

**NUMERICAL ANALYSIS AND
MODELLING IN GEOMECHANICS**

JOHN W. BULL

**Also available as a printed book
see title verso for ISBN details**

Numerical Analysis and Modelling in Geomechanics

Numerical Analysis and Modelling in Geomechanics

John W.Bull



LONDON AND NEW YORK

First published 2003
by Spon Press
11 New Fetter Lane, London EC4P 4EE

Simultaneously published in the USA and Canada
by Spon Press
29 West 35th Street, New York, NY 10001

Spon Press is an imprint of the Taylor & Francis Group

This edition published in the Taylor & Francis e-Library, 2005.

“To purchase your own copy of this or any of Taylor & Francis or Routledge’s collection of thousands of eBooks please go to www.eBookstore.tandf.co.uk.”

© 2003 John W. Bull

All rights reserved. No part of this book may be reprinted or reproduced or utilised in any form or by any electronic, mechanical, or other means, now known or hereafter invented, including photocopying and recording, or in any information storage or retrieval system, without permission in writing from the publishers.

British Library Cataloguing in Publication Data

A catalogue record for this book is available from the British Library

Library of Congress Cataloging in Publication Data

A catalog record for this book has been requested

ISBN 0-203-47128-8 Master e-book ISBN

ISBN 0-203-77952-5 (Adobe eReader Format)

ISBN 0-415-24328-9 (Print Edition)

Contents

<i>List of figures</i>	vi
<i>List of tables</i>	xiii
<i>List of contributors</i>	xv
<i>Preface</i>	xvii
1 The effect of increasing the depth of an underground void on the surface displacements of an airfield runway J.W.BULL AND C.H.WOODFORD	1
2 Numerical and experimental study of compressed air tunnelling A.A.JAVADI	26
3 A general finite element model for wave-seabed-structure interaction D.S.JENG	61
4 The stability of unsaturated soil slopes subjected to rainfall infiltration C.W.W.NG AND Q.SHI	104
5 Computational modelling of ground waves due to pile driving C.L.RAMSHAW AND A.R.SELBY	132
6 Back analysis of geotechnical problems ANNAMARIA CIVIDINI AND GIANCARLO GIODA	168
7 Parameter estimation using extended Bayesian method in tunnelling I.-M.LEE AND D.-H.KIM	201
8 Seismic microzoning using numerical modelling: the Umbria-Marche earthquake of 26 September 1997 F.PERGALANI, V.PETRINI, A.PUGLIESE AND T.SANÒ	223

9	Ground motion modelling using the 2-D Chebyshev spectral element method	258
	ENRICO PRIOLO	
10	Analysis and design of pile groups	283
	F.BASILE	
11	Reservoir compaction, subsidence and well damage	322
	L.BRUN HILBERT, Jr.	
	<i>Index</i>	375

Figures

1.1	Half section of camouflet showing the void and the eight zones	3
1.2	A quarter finite element model of the camouflet for a detonation depth of 8.354 m	12
1.3	A quarter finite element model of the camouflet for a detonation depth of 12.354 m	13
2.1	Variation of the ratio between permeability to air and permeability to water with temperature	29
2.2	Illustration of the principle of pressure balance and over-pressure	32
2.3	Typical tunnel geometry and the boundary conditions	34
2.4	Typical output of the 2D finite element model showing contours of squares of the absolute pore-air pressure heads	36
2.5	Typical output of the 3D model showing the deformed groundwater surface	37
2.6	Method of construction	41
2.7	Geology of the tunnel route	41
2.8	Comparison of the predicted and measured air losses from the tunnel face	43
2.9	Convergence of the genetic algorithm	44
2.10	Air losses from the tunnel perimeter	45
2.11	Total air losses	45
2.12	Change in shear strength with increasing air pressure for specimen 1 (test series 1)	49
2.13	Mohr circles for specimen 1 (test series 1: increasing air pressure)	50
2.14	Change in shear strength due to increase in suction for specimen 2 (test series 2)	51
2.15	Mohr circles for specimen 2 (test series 2: increasing suction)	51
2.16	Variation in shear strength due to increase in effective normal stress for specimen 3 (test series 3: saturated soil)	53
2.17	Mohr circles for specimen 3 (test series 3: saturated soil)	53
2.18	Variation of air permeability of shotcrete with time	54
2.19	Reduction in permeability of cement paste at early age	55
2.20	Failure envelope for the soil tested in the experiments	57
3.1	Principle of repeatability	68
3.2	Configuration of the wave-seabed-pipe interaction	70
3.3	Finite element meshes in the vicinity of a buried pipeline	70

3.4	Distribution of the wave-induced pore pressure amplitude around the pipe in a uniform seabed	71
3.5	Comparison between an anisotropic and isotropic seabed of (a) coarse sand and (b) fine sand	73
3.6	Distribution of the wave-induced pore pressure against θ in an anisotropic seabed for various values of anisotropic constant (n) in (a) coarse sand and (b) fine sand	75
3.7	Distribution of the wave-induced pore pressure against θ in an anisotropic seabed for various values of anisotropic constant (m) in (a) coarse sand and (b) fine sand	76
3.8	Distribution of the wave-induced pore pressure against θ in an anisotropic seabed for various values of anisotropic constant (S) in (a) coarse sand and (b) fine sand	77
3.9	Distribution of the wave-induced pore pressure against θ in an anisotropic seabed for various values of anisotropic constant (b) in (a) coarse sand and (b) fine sand	79
3.10	Distribution of the wave-induced pore pressure against θ in an anisotropic seabed for various values of anisotropic constant (R) in (a) coarse sand and (b) fine sand	80
3.11	Configuration of the cover layer for protection of a buried pipeline	81
3.12	Distribution of the wave-induced pore pressure in the vicinity of a buried pipeline in anisotropic seabeds (a) without a cover layer, (b) with a cover layer of coarse sand, and (c) with a cover layer of gravel	83
3.13	Distribution of the wave-induced pore pressure against θ in an anisotropic seabed for various values of cover layer depth (B) with a cover layer of (a) coarse sand and (b) gravel	84
3.14	Distribution of the wave-induced pore pressure against θ in an anisotropic seabed for various values of cover layer depth (W) with a cover layer of (a) coarse sand and (b) gravel	85
3.15	Configuration of wave-seabed-caisson interaction	88
3.16	Finite element meshes in the vicinity of a caisson	90
3.17	Contour of the wave-induced pore pressure in the vicinity of a composite breakwater in sandy seabeds (solid lines are anisotropic seabed and dashed lines are isotropic seabed)	91
3.18	Vertical distributions of the wave-induced pore pressure versus the soil depth in (a) coarse sand and (b) fine sand	92
3.19	Vertical distributions of the wave-induced pore pressure versus the soil depth for various values of Poisson's ratio μ_{xx} in (a) coarse sand and (b) fine sand	93
3.20	Vertical distributions of the wave-induced pore pressure versus the soil depth for various values of Poisson's ratio μ_{xz} in (a) coarse sand and (b) fine sand	94

3.21	Vertical distributions of the wave-induced pore pressure versus the soil depth for various values of anisotropic constant (n) at different sections in (a) coarse sand and (b) fine sand	95
3.22	Vertical distributions of the wave-induced pore pressure versus the soil depth for various values of anisotropic constant (m) at different sections in (a) coarse sand and (b) fine sand	96
3.23	Vertical distributions of the wave-induced pore pressure versus the soil depth for various values of degree of saturation (S) at different sections in (a) coarse sand and (b) fine sand	98
3.24	Vertical distributions of the wave-induced pore pressure versus the soil depth for various values of caisson width (B) at different sections in (a) coarse sand and (b) fine sand	99
3.25	Vertical distributions of the wave-induced pore pressure versus the soil depth for various values of height of rubble round(H_1) at different sections in (a) coarse sand and (b) fine sand	100
4.1	Variation of degree of saturation with depth during infiltration	106
4.2	Volumetric water content vs pore water pressure	109
4.3	Water permeability vs pore water pressure	110
4.4	Finite element mesh used in the seepage analysis	113
4.5	Pore water pressure distributions at initial steady state	117
4.6	Effect of rainfall intensity on pore pressure distributions at the end of rainfall	118
4.7	Factor of safety vs rainfall intensity	120
4.8	Relations between rainfall intensity and duration	121
4.9	Groundwater rise due to a 2-hour rainstorm following various rainfall durations	122
4.10	Factor of safety vs rainfall duration	123
4.11	Pore water pressure distribution for various water permeabilities	125
4.12	Factor of safety vs water permeability	126
4.13	Effect of permeability anisotropy on initial groundwater table	127
4.14	Ground water response for the anisotropic water permeability	128
4.15	Factor of safety vs anisotropic water permeability	128
5.1	Schematic of ground waves caused by pile driving	133
5.2	Example ground vibrations from an impact hammer	134
5.3	Vibrations caused by vibrodriving	136
5.4	Recommendations for vibration thresholds in structures	138
5.5	8-noded quadrilateral finite element and 5-noded infinite element	140
5.6	P-wave representation	142
5.7	S-wave representation	142
5.8	Rayleigh wave representation	143
5.9	Schematic of response of a FE/IE mesh to geostatic self-weight	144
5.10	Schematic of zoned IEs	144
5.11	Hammer impact model	145
5.12	Schematic view of pile model for axial wave and shear transfer	146

5.13	(a) Displacement-time and (b) force-time functions at the pile head	150
5.14	Radial particle velocities	151
5.15	Verticle particle velocities	152
5.16	Radial particle velocities at (a) 7 m and (b) 16.5 m, impact hammer, Flitwick	154
5.17	Schematics of stage 1 model for vibrodriving, and for shaft/soil	155
5.18	Measured and computed radial particle velocities at 2 m, 7 m and 16.5 m from the vibrodriven pile, Flitwick	157
5.19	Radial velocities at 5.7 m, 14.5 m and 32.9 m, vibrodriving at Second Severn Crossing	157
5.20	Vertical velocities at 5.7 m, 14.5 m and 32.9 m, vibrodriving at Second Severn Crossing	158
5.21	Schematic view of soil plus structure	159
5.22	Frame deformations during passage of a transient wave from impact piling	160
5.23	Wall displacements during passage of a transient wave	161
5.24	Vertical displacements of three surface nodes during vibrodriving, (a) free-ground and (b) with a brickwork wall	163
5.25	Meshes for pipe deformation analyses	164
5.26	Pipe deformation during passage of a P-wave	165
5.27	Pipe deformation at 45°, during passage of an S-wave, and justification	165
5.28	Pipe deformation due to a Rayleigh wave	166
6.1	Construction sequence of the railroad tunnel	177
6.2	Soil profile. The three zones in the grain size distribution denotes, from left to right: gravel, sand and silt	179
6.3	Location of the measurement points	180
6.4	Surface settlements recorded during the tunnel excavation	181
6.5	Finite element mesh for the plane strain back analyses	182
6.6	Elastic moduli of the sand layers obtained by the <i>in situ</i> dilatometer tests and by the elastic back analyses of the displacement measurements	183
6.7	Comparison between the vertical displacements measured in the field and those obtained by the elastic back analysis	184
6.8	Schematic representation of the relationship between average shear stress τ and displacement δ for direct shear tests on a stiff soil sample, and relevant failure envelopes	185
6.9	Variation of the friction angle ϕ with increasing square root of the second invariant of the deviatoric plastic strains J_2	185
6.10	Comparison between the vertical displacements measured at the end of construction and those obtained by the elasto-plastic analysis	186
6.11	Contour lines of the square root of the second invariant of the deviatoric plastic strains	186

6.12	Contour lines of the square root of the second invariant of the deviatoric plastic strains for the modified construction procedure	187
6.13	Comparison between the vertical displacements obtained by the elasto-plastic analyses of the original and modified construction procedures	187
6.14	Rheological model	189
6.15	Horizontal convergence vs time data measured at different tunnel sections	190
6.16	Characteristic lines of a tunnel and of its temporary support	191
6.17	Qualitative plot of the c - ϕ relationship for two tunnel sections with different depth of cover	193
6.18	Qualitative plot of variation of the friction angle along the tunnel axis, assuming a constant value of cohesion	194
6.19	Back calculated friction angle ϕ and cohesion c (I: $\alpha=1.5$, II: $\alpha=1.0$), and number N of rock bolts installed per metre of tunnel, vs the distance d from the tunnel entrance (Italian side)	196
6.20	Experimental convergence vs. time curves (black squares) at different tunnel sections and corresponding numerical results (solid lines) based on the back calculated mechanical parameters ($\alpha=1.5$)	198
7.1	Framework for the feedback system	207
7.2	Measurement of displacement by extensometer from ground surface	209
7.3	Characteristic line of deformation	210
7.4	Geological condition of the hypothetical site	211
7.5	Location of measurement points	212
7.6	Sensitivity of geotechnical parameters on crown settlement	213
7.7	Sensitivity of geotechnical parameters on sidewall settlement	214
7.8	Variation of objective function by the variation of the geotechnical parameters	215
7.9	Idealized ground condition of a subway tunnel in Pusan, Korea	216
7.10	Typical tunnel cross section	217
7.11	Location of measurement points	218
7.12	Characteristic lines (a) Crown (Station I); (b) Side wall (Station I); (c) Crown (Station II); (d) Side wall (Station II)	219
7.13	Plastic zone assessed by Hoek-Brown's criterion	220
7.14	The hyperparameter β vs. AIC value in each model (a) Model I-1; (b) Model I-2; (c) Model II	221
8.1	Italian seismotectonic model identified by 80 seismic source zones	226
8.2	Italian seismotectonic domains (1–9) and volcano-tectonic domain (10)	227
8.3	Elastic pseudo-acceleration response spectra at 10% probability of being exceeded in 50 years for the 60 most damaged municipalities	229
8.4	Seismic hazard distribution of the municipalities	231
8.5	Reference spectra	232
8.6	Non-stationary artificial acceleration time-histories	233
8.7	Scheme 1D of SHAKE	234

8.8	Typical behaviour of shear modulus vs shear strain	234
8.9	Typical behaviour of damping vs shear strain	235
8.10	Scheme 2D of BESOIL	236
8.11	QUAD4 FEM scheme of a valley	240
8.12	Area struck by seismic sequence (earthquakes of Table 4.1, triangles) and location of the investigated villages (circles)	243
8.13	Damping coefficient variation with shear strain	245
8.14	Shear modulus decay with shear strain	246
8.15	(a) Cross-section of Cesi village; (b) Acceleration response spectra computed for Cesi village; (c) Amplification coefficients (F_a) computed for Cesi village	250
8.16	(a) Cross-section of Colfiorito village; (b) Acceleration response spectra computed for Colfiorito village; (c) Amplification coefficients (F_a) computed for Colfiorito village	251
9.1	Example of a quadrangular mesh taken from a study performed near the village of Mels (Udine, Italy)	266
9.2	Base map of the study area, showing the essential information about the geography, the transect position, and the data available	269
9.3	Transect t02: model structure and source position	271
9.4	Snapshots of the acceleration wavefield (amplitude) for the point source	272
9.5	PGA envelopes at the surface of transects t02, t01, t05, and t03, respectively, for the catastrophic earthquake of January 11, 1693	273
9.6	Transect t03	274
9.7	The December 13, 1990, $M \cong 5.8$ Eastern Sicily earthquake	276
9.8	H/V spectral ratios computed for the ENEA-ENEL Catania station	276
9.9	Simplified model of a massive structure	277
9.10	Resonant scattering of the Rayleigh wavefield	278
9.11	The trapezoidal resonant model with $L=50$ m	279
9.12	Amplitude of the horizontal component of ground-roll acceleration at different receivers located at ground level compared with the peak acceleration	280
10.1	Plan view of block failure under lateral load	295
10.2	Comparison of load-settlement response for single pile ($E_p=30$ GPa)	297
10.3	Comparison of load-settlement response for single pile ($E_p=30,000$ GPa)	298
10.4	Comparison of shaft shear stress distribution for single pile at a load level $P/P_u=0.5$	299
10.5	Comparison of different pile group analysis methods for (a) $s/d=2.5$; (b) $s/d=5$	300
10.6	Comparison of axial load distribution to individual piles in 5×5 pile group	301
10.7	Comparison of lateral load distribution to individual piles in 5×5 pile group	302

10.8	Group of 3 piles considered in comparison of methods	303
10.9	Comparison of load-settlement response for single pile	309
10.10	Comparison of load-settlement response for 9-pile group	310
10.11	Comparison of axial load distribution in 9-pile group at a working group load of 2.58 MN	311
10.12	Comparison of axial load distribution in 9-pile group at a group load nearing failure of 5.66 MN	312
10.13	Comparison of load-settlement response for single pile	314
10.14	Comparison of load-settlement response for 5-pile group	314
10.15	Comparison of load-deflection response for single pile	316
10.16	Comparison of load-deflection response for 6-pile group	316
10.17	Comparison of moment profiles of single pile	317
10.18	Comparison of moment profiles of leading row of piles in 6-pile group under the maximum applied lateral load H-10,948 kN	317
11.1	East to west cross section of the South Belridge field	325
11.2	Cross section of a reservoir that has undergone significant reservoir compaction	327
11.3	The yield envelope used in the ABAQUS program	341
11.4	A typical relationship between p_b and ϵ_{vol}^{pl}	342
11.5	The flow potential surface	343
11.6	Showing that the South Belridge field is a north westward tending anticline	350
11.7	The finite element mesh for the model presented in this chapter	352
11.8	Detail of the diatomite reservoir rock	352
11.9a	Pore pressure field contours for 1978	356
11.9b	Pore pressure field contours for 1980	356
11.9c	Pore pressure field contours for 1989	357
11.9d	Pore pressure field contours for 1995	357
11.10	Computed and actual surface subsidence from 1991 to 1995	358
11.11	Relative slip between the Al shale, Dl shale and the Tulare-diatomite unconformity as of 1995 in the simulation	359
11.12	Slip on the Tulare-diatomite unconformity computed in 1987 and the 1995 simulations	360
11.13	Well deformations corresponding to Well 551G	361
11.14	Three-dimensional wellbore model	362
11.15	Deformed casing from a shearing simulation	363
11.16	Comparison of computed and measured casing deformation	364
11.17	Casing displacement plotted against shear displacement	365
11.18	Relative slip plotted against the year of well life	366
11.19	Tool passing through a sheared casing	367
11.20	Passable tool length as a function of casing lateral damage	367
11.21	Bending stress that produces permanent bending in two sizes of tubing	368
11.22	Casing length plotted against lateral displacement	369

Tables

1.1	Young's modulus [MPa] and Poisson's ratio for the 17 material sets	7
1.2	Deflection readings in percent for the undisturbed subgrade	10
1.3	Deflection readings in percent for material set 1; group 1	16
1.4	Deflection readings in percent for material set 2; group 2 part 1	17
1.5	Deflection readings in percent for material set 3; group 2 part 1	17
1.6	Deflection readings in percent for material set 4; group 2 part 1	17
1.7	Deflection readings in percent for material set 5; group 2 part 1	18
1.8	Deflection readings in percent for material set 6; group 2 part 1	18
1.9	Deflection readings in percent for material set 7; group 2 part 1	18
1.10	Deflection readings in percent for material set 8; group 2 part 2	18
1.11	Deflection readings in percent for material set 9; group 2 part 2	19
1.12	Deflection readings in percent for material set 10; group 2 part 2	19
1.13	Deflection readings in percent for material set 11; group 2 part 2	19
1.14	Deflection readings in percent for material set 12; group 3 part 1	19
1.15	Deflection readings in percent for material set 13; group 3 part 1	20
1.16	Deflection readings in percent for material set 14; group 3 part 2	20
1.17	Deflection readings in percent for material set 15; group 3 part 2	20
1.18	Deflection readings in percent for material set 16; group 3 part 2	20
1.19	Deflection readings in percent for material set 17; group 3 part 2	21
2.1	Formulae for determining compressed air pressure	30
2.2	Formulae for determining quantities of air required	31
2.3	The area of tunnel face and method of construction	42
2.4	Perimeter area and thickness of initial layer of shotcrete for each heading	42
2.5	Applied stresses and stress state variables for specimen 1 (test series 1)	49
2.6	Stress state variables for specimen 2 (test series 2: increasing suction)	51
2.7	Stress state variables for specimen 3 (test series 3: saturated soil)	52
3.1	Input data for case study of wave-seabed-pipe interaction	72
3.2	Input data for case study of wave-seabed-caisson interaction	89
4.1	Input parameters based on a 10-year return period (1980–1990)	114
5.1	Human tolerance of vibration, in mm/s	137
5.2	Summary of parameters used in the computation	153
5.3	Examples of bending stresses around pipes due to ovaling	164

6.1	Distance from the tunnel entrance (Italian side) and depth of cover of the various sections	190
6.2	Variation of the coefficient of viscosity with the distance from the tunnel entrance (Italian side)	197
7.1	Ratio of the deformation ahead of the tunnel face to the absolute deformation	210
7.2	Measurement points and displacements	211
7.3	Optimized parameters with changes in the number of measurement points	213
7.4	Results of regression	218
7.5	Results of parameter estimation	219
7.6	Coefficient of variation of geotechnical parameters	222
8.1	Main earthquakes (ML 5) of the Umbria-Marche sequence	241
8.2	Geotechnic parameters for the lithotechnic units	245
8.3	Classifying table for qualitative local effect situations	247
8.4	Reference coefficient Fb of each reference seismic input for normal ductility structures	247
8.5	Results of amplification factors computed in each analysed site	253
8.6	Amplification coefficients for the geologic and geomorphologic situations	255
9.1	Description of the main soil and rock formations used to define the transects	270
9.2	Source parameters adopted for the December 11, 1693 earthquake	270
10.1	Capabilities and limitations of various computer programs for pile group analysis	288
10.2	Features of group behaviour and their effect on corner loads	291
10.3	Parameters for the analyses reported in Figures 10.2–10.4	296
10.4	Parameters for the linear analyses reported in Figures 10.6–10.7	301
10.5	Additional parameters for the non-linear analyses reported in Figures 10.6–10.7	302
10.6	Comparison of different analyses for 3-pile group under general loading conditions	304
10.7	Comparison of alternative numerical analyses for a railway viaduct in North London	308
10.8	Comparison of axial load distribution to individual pile heads in 9-pile group	313
11.1	Material parameters required for a coupled geomechanical surface	344
11.2	Density and elastic moduli for lithologies used in model	353
11.3	Elasto-plastic constitutive parameters for rock units in model	353

Contributors

F.Basile Halcrow Group Ltd, London W6 7BY, UK.

L.Brun Hilbert, Jr. Exponent Failure Analysis Associates Inc, Menlo Park, CA 94025, USA.

John W.Bull Department of Civil Engineering, The University, Newcastle-upon-Tyne NE1 7RU, UK.

Annamaria Cividini Department of Structural Engineering, Politecnico di Milano, Piazza Leonardo da Vinci 32, I-20133 Milano, Italy.

Giancarlo Gioda Department of Structural Engineering, Politecnico di Milano, Piazza Leonardo da Vinci 32, I-20133 Milano, Italy.

A.A.Javadi Department of Engineering, School of Engineering and Computer Science, University of Exeter EX4 4QF, UK.

D.S.Jeng Griffith University Gold Coast Campus, Queensland 9726, Australia.

D.-H.Kim Chief Engineer, Sambo Engineering Co Ltd, Seoul, 138-050, South Korea.

I.-M.Lee Professor of Civil Engineering, Korea University, Seoul, 136-701, South Korea.

C.W.W.Ng Department of Civil Engineering, Hong Kong University of Science and Technology, Clear Water Bay, Kowloon, Hong Kong.

F.Pergalani Department of Structural Engineering, Politecnico di Milano, Piazza Leonardo da Vinci 32, I-20133 Milano, Italy.

V.Petrini Department of Structural Engineering, Politecnico di Milano, Piazza Leonardo da Vinci 32, I-20133 Milano, Italy.

Enrico Priolo Istituto Nazionale di Oceanografia e Geofisica Sperimentale (OGS), Trieste, I-34010, Italy.

A.Pugliese Agenzia Nazionale per la Protezione dell' Ambiente, I-00100 Roma, Italy.

C.L.Ramshaw School of Engineering, University of Durham, DH1 3LE, UK.

T.Sanò Agenzia Nazionale per la Protezione dell'Ambiente, I-00100 Roma, Italy.

A.R.Selby School of Engineering, University of Durham, DH1 3LE, UK.

Q.Shi Ove Arup and Partners (HK) Ltd, Level 5, Festival Walk, 80 Tat Chee Avenue, Kowloon, Hong Kong.

C.H.Woodford Computing Service, The University, Newcastle-upon-Tyne NE1 7RU, UK.

Preface

This book describes numerical analysis, computer simulations and modelling that can be used to answer some of the highly complex questions associated with geomechanics. It then goes on to give an insight into the future direction of these simulation methods.

In geomechanics, existing design methods are very much dependent upon sophisticated on-site techniques to assess ground conditions. Obtaining this practical information is expensive and time consuming. Increasingly, engineers are looking to extending and increasing the accuracy of their design methods by some form of computer simulation. Hence sophisticated numerical analysis and modelling is being pushed to the limits to develop better design methods.

In the area of geomechanics, sophisticated sampling techniques can be used to give impressive amounts of accurate ground and soil information, but only within the initial assumptions and the sampling methods used. If the results of the sampling techniques are accurate such that the material representations used in the mathematical model is adequate, then the engineer is dependent upon the computer simulation model to increase the reliability of the design methods being used.

This book is aimed at the world market of professional engineers who are involved in the designing and building of both onshore and offshore structures, where geomechanical considerations may well be outside the usual codes of practice and where expert advice, specialist advice and research is required.

This book is also a source book for postgraduate researchers and specialist groups in geomechanics who need knowledge of the latest numerical modelling and analysis techniques. This book will soon become a standard textbook for final year degree students who are required to carry out advanced numerical project work in geomechanics.

The topics covered in this book are:

- *The effect of increasing the depth of an underground void on the surface displacements of an airfield runway* describes the effect of an underground detonation on the soil between the void and the surface structure and shows that there are ways of identifying the size, depth and location of the void.

- *Numerical and experimental study of compressed air tunnelling* describes a numerical model that simulates the flow of air through soils and studies the consequences of using compressed air in soils.
- *A general finite element method for wave-seabed-structure interaction* describes the wave-induced oscillatory soil response when seabed structures interact with their soil supports.
- *The stability of unsaturated soil slopes subjected to rainfall infiltration* describes how to predict slope failures and how there is a critical rainfall duration where the factor of safety is the lowest.
- *Computational modelling of ground waves due to pile driving* describes how to model and to predict the effect of induced ground vibrations on buildings and services.
- *Back analysis of geotechnical problems* describes some back analysis techniques applicable in geotechnical engineering and investigates the influence of experimental errors on the results of back calculations.
- *Parameter estimation using extended Bayesian method in tunnelling* describes how field measurements and prior information of underground structures can be combined to best estimate geotechnical parameters.
- *Seismic microzoning using numerical modelling: the Umbria-Marche earthquake of 26 September 1997* describes how earthquake amplification due to local effects was assessed and taken into account in the repair and reconstruction of structures.
- *Ground motion modelling using the 2-D Chebyshev spectral element method* is used to solve engineering seismology problems of ground shaking and ground motion on large structures.
- *Analysis and design of pile groups* describes a practical non-linear approach for the analysis of pile groups under general loading conditions.
- *Reservoir compaction, subsidence and well damage* describes the numerical simulation of compaction of hydrocarbon-bearing rocks as a result of oil, water and gas production.

I would like to express my thanks to my publishers Spon Press for their support and their ability to ensure I produced the work on time! My thanks go also to my wife for her help and her understanding.

John W.Bull

Chapter 1

The effect of increasing the depth of an underground void on the surface displacements of an airfield runway

John W.Bull and C.H.Woodford

Abstract

This research considers the effect of the detonation of a 213 kg mass of explosive in a subgrade at depths of 8.354m, 9.354m, 10.354m, 11.354m, 12.354m, 15.354m and 18.354 m beneath a cement concrete runway. The detonation produces a void in the subgrade and disturbs the subgrade beneath the runway. Seventeen computational models of the void and the disturbed subgrade [camouflet] are considered ranging from where all the detonation-affected subgrade zones are increased in strength to where all the detonation-affected subgrade zones are reduced in strength. Consideration is given to the possibility of using the diameter of the runway deflection bowl as a means of determining the size, depth and position of the void. The results from the computational models are compared with empirical data that states that for the void to have no effect at the air-ground interface, the depth of detonation must exceed a specified value. From this comparison it is found possible to determine the material sets that can be generated feasibly from the detonation. It is also found that for some material sets it is possible to identify the size, depth and location of the void.

Introduction

This research considers the effect of the detonation of a chemical explosive beneath a cement concrete runway on the deflection of the runway when a uniformly distributed downward load is applied to the runway surface. Later research will consider the effect of the detonation on the fatigue life of the subgrade and the runway. When chemical explosives damage a runway, it is a typical requirement that the runway is repaired and operational within three hours and that it will remain operational for thirty days.

When a detonation takes place it may be above ground, at the runway surface or below the air-ground interface in the subgrade. Detonations above the air-ground interface are not considered here, but in previous publications by the authors, research was undertaken into detonations at or below the runway surface [1–14].

Detonations at the runway surface and at shallow depths destroy parts of the runway and eject subgrade such that a crater is formed. These craters are clearly visible and research by the authors has been published into how to repair these craters [1–8]. For detonations below the air—ground interface, where no surface disturbance can be seen, the level of subgrade support remaining to the runway is difficult to assess and methods to detect the detonation are required. In this research it is assumed that the detonation takes place in the subgrade such that a camouflet is formed, as shown in [Figure 1.1](#). A camouflet is a void surrounded by a shell of compacted subgrade, zones 5 and 6 of [Figure 1.1](#). The subgrade between the void and the runway, zones 2, 3, 4 and 5, may or may not be affected by the detonation. There is an inherent weakness in the subgrade due to the void, but if the air—ground interface is undisturbed, then compaction of the subgrade must also have occurred, giving the compacted subgrade additional strength. However as the distance from the detonation point increases beyond the outer diameter of the void, the compaction of the subgrade reduces. This reduction is related to the proximity of the air—ground interface and that interface’s ability to reflect the compression waves from the detonation. It is for this reason that it is difficult to determine the exact strength of the subgrade above the camouflet and why 17 subgrade material sets are considered for numerical analysis later in this chapter.

It is assumed that the subgrade between the void and the runway is disturbed and that the runway does not heave or crack. A damaged or displaced runway would be examined and repaired, not so an apparently undamaged runway. In time the void would collapse with the subgrade falling into the void, thereby reducing subgrade support to the runway and presenting a considerable danger to aircraft using the runway. The shape of the disturbed subgrade above the void is assumed to be that of a cone extending to the underside of the runway, as shown in zones 5, 4, 3 and 2 of [Figure 1.1](#). At the centre of the camouflet is a spherical void. Around the void is a shell of compacted subgrade, zones 5 and 6, with the point of the cone being at the detonation point.

Previous research by the authors has been carried out in a number of parts. In part one, the camouflet, the disturbed subgrade and the undisturbed subgrade surrounding the detonation was modelled. In part two, a uniform pressure was applied to the air—ground interface to assess the resulting subgrade displacement, subgrade stress and inherent camouflet instability. Parts one and two assumed that no runway overlaid the subgrade [9]. Part three was similar to part two but introduced a runway overlaying the subbase and the camouflet [10]. Part four considered a series of possible materials that could be used to fill and stabilise the void to effect a rapid and long-term runway repair [11]. Part five introduced a subsurface barrier layer immediately beneath the runway and suggested a means of determining the presence of a camouflet [12]. Part six considered the fatigue life of the runway, with the void being either filled or unfilled [13]. Part seven considered the effect of tension in the subgrade on the fatigue life of both the subgrade and the runway [14]. The present research is part eight and considers

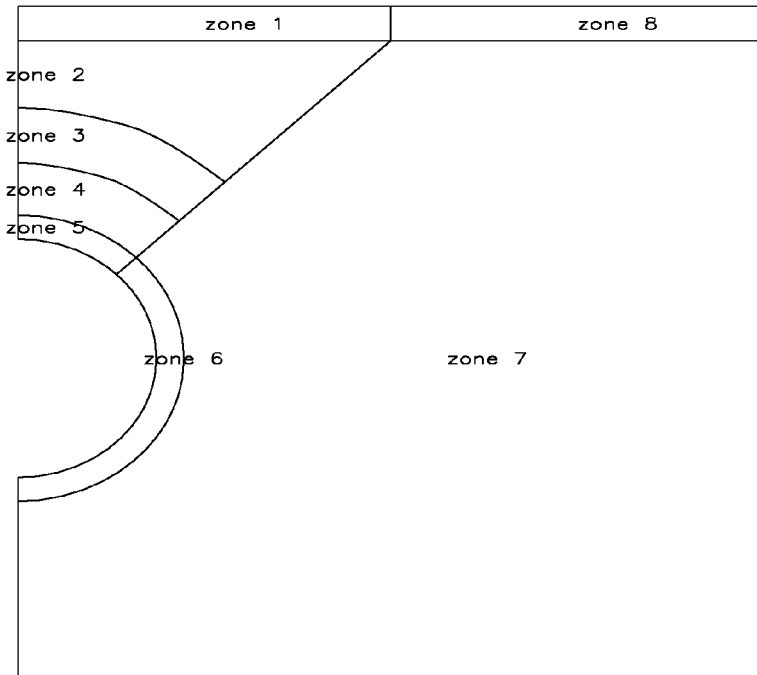


Figure 1.1 Half section of camouflet showing the void and the eight zones.

the effect of the depth of detonation on runway deflection when a downward vertical uniformly distributed load is applied to the runway surface.

Camouflet characteristics

The characteristics of explosively formed craters can be linked directly to dimensional analysis, statistical reasoning and scaling laws [9, 10, 15–22]. The most common relationship being “Hopkinson’s law”, which says that any scaled linear dimension L (m) of the crater may be related to $L/W^{0.33}$ where W (kg), represents the mass of the equivalent yield of TNT of the explosive charge [18, 23]. The factors determining the size and the shape of the crater are the mass of the explosive, the position λ_c of the point of detonation and the medium within which the detonation takes place [16, 17]. The value of λ_c (m) is obtained from the location of the point of detonation (m), which is negative below the runway surface, divided by $W^{0.33}$. If the detonation occurs below the air-ground interface ($\lambda_c < 0$), then the resulting crater is a camouflet if $\lambda_c = -1.388$. The way in which the subgrade reacts to the detonation depends upon the medium within which the detonation takes place. If the medium is rock the detonation forms a void and pushes up a cylindrically shaped column of broken rock which later collapses

into the void. The radius of the column is approximately equal to that of the void [24]. If the medium is a subgrade, the detonation gases dry the void and in time the walls of the void slide down, disturbing the subgrade. The shape of the disturbed subgrade is conical with its base upward [14, 25, 26]. The cone apex angle at the point of detonation is between 82.14° and 93.74° [14, 25].

In sands, following a detonation there is either immediate surface ground heave or small surface settlement followed by continued ground settlement for about an hour. Consolidation of the sand occurs over several hours with water escaping to the surface. The results of standard penetration tests or cone penetration tests taken immediately following detonation will be misleading as the test results will indicate little effect of the detonation, although the clearly visible large surface settlements make clear that considerable density increases have taken place [27].

Clay subgrades have high compressibility, high plasticity and low filtration properties that ensure that voids caused by an underground detonation are almost hermetically sealed. Full-scale experiments have shown that in clay large cavities are distinguished by low stability, but that if these voids are spherical with a diameter of up to 6 to 7.25 metres, they can be relatively stable [28]. To produce a camouflet with $\lambda_c = -1.388$ having a void diameter 7.25 m would require a 333 kg mass of TNT ($1.048W^{0.333}$). The probability of voids being formed near the surface in granular materials is negligible, but the probability does increase as the depth of detonation increases [16, 17].

Test data for camouflets where there is little or no surface disturbance is scarce [25]. When a camouflet is formed, at the air-ground interface there may be no disturbance, a small mound, a depression, a hole or only loose subgrade. The shape of the disturbed subgrade above the camouflet is, as previously described conical, base upward [25]. No specific research has been carried out to determine the apex angle of the cone, although twice the subgrade's angle of repose has been considered as representative [29]. There is no published research on the diameter of the surface disturbance related to the camouflet size and to the depth of detonation.

At the formation of a camouflet, the detonation produces a shock wave. On the shock wave front the subgrade is compressed, while behind it the subgrade expands. When the compressive shock encounters the air—ground interface, a negative stress wave is generated that propagates back into the subgrade. At certain depths, the sum of the two stress waves equals the dynamic tensile strength of the subgrade and pieces of subgrade break away. This produces a new free surface and even more pieces of subgrade break away. At increasing distances between the point of detonation and the air-ground interface, the pressure decreases until it does not exceed the tensile strength of the subgrade. Ultimately, the surface disturbance is only a small elastic movement, with little disruption of the subgrade layers and with surface subsidence occurring perhaps later [30, 31].

The dome of the void formed at the detonation will collapse in single or multiple stages [16, 17, 29, 32]. In rock, the time between detonation and dome collapse may be a few minutes, in water-bearing sands, a few days, while in unsaturated loamy-water subgrades stability may last for years [26, 29]. Dome collapse is complete when one of the three following conditions occurs. First, the height of the collapsed cone develops over the entire detonation to the air-ground interface with a ground settlement funnel being formed on the exposed surface [32]. Second, the void is completely filled with collapsed material, but not extending to the surface. Third, the material in the collapse path is strong enough to form a temporary stable dome. Which of the three conditions that occur depends upon the amount and the volume of the compacted and dilated subgrade. Subgrade compaction occurs close to the point of detonation, with the amount of compaction reducing as the distance from the point of detonation increases. Dilation begins to occur as the shock waves approach the air-ground interface. Hence in the cone of subgrade between the point of detonation and the air-ground interface there is competition between compaction and dilation which makes the strength of the subgrade in the cone uncertain and requires a number of finite element models to be considered. If the camouflet occurs under a runway, the first condition will cause immediate loss of subgrade support, which will be obvious to the repair team. For the second condition, loss of subgrade support will take time to develop, assuming it does actually develop. The second and third conditions present considerable difficulties for the runway repair team. They must determine if, when and at what surface loading the dome will collapse, also the extent of the loss of subgrade support to the runway.

Linked to the difficulties described above and to the possibility of the detonation of undetected unexploded devices, considerable effort was expended in the early 1940s on the detection of both camouflets and unexploded devices, to determine their effect on the subgrade support provided to surface structures [23, 33]. Research showed that the greater the depth of the detonation, the more difficult it became to determine the size of the resulting camouflet [23, 33]. Dimensional analysis suggested that the mass of a charge should increase proportionally to the square root of the depth of detonation to create the same radius of the zone of disturbance [27]. Further experimental research shows that for there to be no surface rupture, the detonation depth has to have a minimum value of between $1.39W^{0.333}$ m and $2.78W^{0.333}$ m, that is between 8.286 m and 16.572 m for the 213 Kg charge considered later in this chapter [23, 33].

To determine the size of the camouflet void, experimental research suggests that the void diameter D be between $1.15W^{0.333}$ m and $1.19W^{0.333}$ m [23]. Experimental research also suggests that the apparent camouflet vertical (D_v) and horizontal (D_h) diameters are equal and between $0.754W^{0.33}$ m and $1.19W^{0.33}$ m [16, 17, 23, 34]. Other experimental research found that the camouflet void was nearly spherical, with a volume V between $2.738W$ m³ and $3.3465W$ m³ and a diameter D between $0.9918W^{0.333}$ m and $1.0711W^{0.333}$ m [33]. Consequently, the diameter of the camouflet is within the range of $0.754W^{0.333}$ m and $1.19W^{0.333}$ m.

This range of diameters is due to the dissipation and absorption of the detonation gases into the voids behind the fracture surface [35]. Surrounding the void is a compacted spherical shell of subgrade with an outer diameter some 20% larger than that of the void [16, 17, 34].

For a camouflet-producing detonation, it is usual for the concrete runway to show signs of distress. This distress may range from a small hole to extensive heaving and cracking [25]. This research considers a detonation that causes no apparent disturbance to the runway. The possibility of determining the position of the camouflet from the location of the projectile's entry point into the subgrade has been considered, but there is no means by which the penetration path of the projectile can be predicted from the projectile's surface penetration point [26].

Camouflet size and material requirements

This research assumes that prior to the detonation, the clay subgrade is homogeneous, isotropic, elastic and has a California Bearing Ratio (CBR) of 9.5%. Notwithstanding the non-linearity of the concrete runway and the subgrade, the ability to carry out linear elastic analysis has proved useful in developing runway design methods [36]. The predominant justification for using elastic theory is that under a single load application, most runways will respond in a resilient manner. Linear elastic analysis can give reasonable solutions for a single load path if sufficient care is taken in determining the material properties. This is also true for the investigation of surface subsidence, provided only compaction takes place [34, 37]. Thus linear elastic analysis is used in this research [36].

This research makes the same reasoned assumptions concerning the dimensions and material properties of the camouflet and the subgrade as in previous research published by the authors [8–14]. That is a 213 kg explosive charge detonates at a depth of approximately $\lambda_c = -1.388$ under a runway and creates a camouflet.

The detonation depth of 8.354 m ($1.401W^{0.333}$ m) is greater than the least value of 8.286 m ($1.39W^{0.333}$ m) for no surface rupture and it is accepted that runway heave could occur for detonation up to 16.555 m ($2.78W^{0.333}$ m). Consideration was given to the range of void diameters of 4.495 m to 7.0948 m ($0.754W^{0.333}$ m to $1.19W^{0.333}$ m) and the value of 6.246 m ($1.048W^{0.333}$ m) was chosen. This is the diameter of the void shown in Figure 1.1. Surrounding the void is a highly compacted subgrade shell extending from the void diameter of 6.246 m to a diameter of 7.495 m [16, 17]. Above the void is a conical-shaped volume of subgrade that was loosened and then resettled to its original level. For the subgrade displacement at the underside of the runway a diameter of 17.622 m was used, giving a cone apex angle of 93.06° .

Earlier it was stated that experimental research had shown that for no surface rupture, the minimum detonation depth for a 213 kg explosive charge was between 8.286 m and 16.572 m [23, 33]. The purpose of this research is to

The numerical model

To satisfy finite element modelling requirements, slight modifications were made to the initial camouflet dimensions used in previous publications by the authors [9–14]. The detonation depth was increased to 8.354 m. The central void of the camouflet has a horizontal diameter of 6.246 m and a vertical diameter of 6.183 m, giving (D_v/D_h) as 99%. The outer radius of the compacted zone, the interface between zones 4 and 5 and 6 and 7 is set at 3.748 m. The radius of the interface between zones 3 and 4 is 5.149 m, with the radius of the interface between zones 2 and 3 being 6.601 m. The origin of the radii is the detonation point. The interfaces of zones 2 and 3, 3 and 4, and 4 and 5 are spherical and contained completely within the frustum of the cone.

Deflection model

For each of the 17 material sets, the depth of the point of detonation $\lambda_c = -1.388$ was considered as depth 0. Then the depth of the detonation point was increased by 1 m, 2 m, 3 m, 4 m, 7 m and 10 m. For each depth, the 17 material sets were computationally modelled. For each depth an additional material set comprising the same finite element model, but with the void filled and representing the subgrade before the detonation took place, was also run. This model was used as a baseline and as a means of checking the accuracy of the displacements obtained from material sets 1 to 17. A total of 136 computer simulations were run.

A uniform downward pressure load of 0.1 MPa was applied to the upper surface of the runway. The origin of the coordinate system for the finite element model was on the top surface of the runway, immediately above the point of detonation. Along the runway surface, measured outwards from the origin, were a series of equally spaced points. The points extended from point 1 at the origin of the coordinates to point 17 at 8.811 m at the zone 1–8 interface. The distance between each point was 0.5507 m. The distances from point 1 to points 4, 8, 12, 16 and 20 were 1.652 m, 3.855 m, 6.058 m, 8.260 m and 10.188 m respectively. For data-recording purposes they were recorded to the third decimal point. Beyond the zone 1–8 interface, there were 12 further points, 18 to 29, at a distance of 0.459 m apart. Points 1 to 16 were located over the area affected by the cone of the camouflet, while points 18 to 29 were located over the subgrade theoretically undisturbed by the camouflet.

To determine the downward vertical deflection of the runway over the undisturbed subgrade, the average of the deflections of points 17 to 29 inclusive were used, provided they did not exceed $\pm 1\%$ of the point 29 value. Points 17 to 29 were used as the baseline deflection because it was initially considered that all the increased deflections due to the camouflet would be confined to points 1 to 16 inclusive, directly over the base of the cone. As the research proceeded it became clear that for some material sets, the effect of the camouflet extended beyond point 17. Consequently, for those material sets, not all the points beyond

point 17 could be used to determine the deflection over the undisturbed subgrade.

For the computer models of the undisturbed camouflet for all seven depths, the downward vertical deflections of points 17 to 29 inclusive were within the 1% limit and this deflection was given the value of 100%. The deflection of points 1 to 16 inclusive was related to the 100% value. For the undisturbed model, when the depth of the camouflet was 8.354 m (column 1 of Table 1.2), the average deflection of points 17 to 29 was 128.6 mm and recorded as 100%. The average deflection for points 1 to 16 inclusive was 131.75 mm (102.5%). This shows that the model of the filled camouflet may give results that for points 1 to 16 inclusive on average overestimate the deflection by 2.5%. To clarify the amount of change from the 100% value that may be expected, the deflections for points 1, 4, 8, 12 and 16 are included in column 2 of Table 2. Table 2 shows that the computer model will overestimate the deflection for all detonation depths up to and including 15.354 m and for all points 1 to 16 inclusive. In this research any detonation deflection results that fall within the deflection overestimation of Table 1.2 are accepted as being undetectable, as also is any deflection between 99% and 101% for detonation depths of 15.354 m and 18.354 m.

For the increasing depth of camouflet a similar analysis was performed for each of the depths of 9.354 m, 10.354 m, 11.354 m, 12.354 m, 15.354 m and 18.354 m. The deflection results are recorded in columns 2, 3, 4, 5, 6 and 7 respectively of Table 1.2. The results show that as the camouflet depth increases the average deflection for points 1 to 16 reduces and tends to 100%. Values are given for points 1, 4, 8, 12 and 16; to illustrate the variation in the individual results included in the average value over zone 1. Clearly for $\lambda_c = -1.388$ the finite element model shows that the accuracy of the undisturbed subgrade model will overestimate the deflection for point 1 by up to 4.4%. But as the depth of the detonation increases this overestimation will reduce to 3.1%, 2.1%, 1.5%, 1%, 0.3% and 0.0%.

In previous publications a series of nine material sets were used to represent the variation in the subgrade caused by the detonation [9–14]. These nine material sets, renumbered, are used in this research with additional material sets to represent other possible variations in the subgrade. The nine previous material sets 1 to 9 inclusive have been renumbered as 5, 7, 6, 13, 14, 16, 12, 3 and 1 respectively of Table 1.1.

Finite element program

PAFEC software [40] was used to model the camouflet and perform the computational analysis. The authors have gained considerable experience in the use of the software and are confident in its application to the research under discussion [41].

For computational modelling purposes the camouflet void was assumed to be spherical and enclosed in a cylinder with a flat surface uppermost. The full

Table 1.2 Deflection readings in percent for the undisturbed subgrade.

Depth of detonation (m)	8.354	9.354	10.354	11.354	12.354	15.354	18.354
Column number	1	2	3	4	5	6	7
Average of points 17 to 29	100	100	100	100	100	100	100
Average of points 1 to 16	102.5	101.7	101.2	100.8	100.6	100.2	100
Deflection at point 16	100.3	100.2	100.2	100.1	100.1	100.1	100
Deflection at point 12	101.2	100.8	100.6	100.4	100.3	100.1	100
Deflection at point 8	102.7	101.8	101.3	100.9	100.6	100.2	100
Deflection at point 4	104.0	102.8	101.9	101.3	100.9	100.3	100
Deflection at point 1	104.4	103.1	102.1	101.5	101.0	100.3	100

model was constructed by rotating a three-dimensional slice about its vertical axis using the interactive facilities of the PAFEC software. It would have been possible to obtain the three-dimensional slice by rotating a two-dimensional cross-section and in so doing form three-dimensional brick and wedge elements from two-dimensional quadrilateral and triangular elements, but this was considered to be an unnecessary simplification. The analysis could not be carried out in two dimensions as the camouflet is a three-dimensional structure with some load combinations, not reported here, also being in three dimensions.

The manual production of the PAFEC data for a single slice would have been a fairly routine matter but in order to allow for varying depths of the camouflet the process was automated. A program was written to produce PAFEC data, which used an input depth parameter to calculate nodal coordinates. In order to keep the total number of elements within reasonable bounds and maintain element aspect ratios consistent with PAFEC guidelines, the relatively thin 300 mm layer of the cement concrete runway and the size of the slice decided effectively the finite element mesh. For the uniform pressure load cases under consideration a single layering of elements was used to model the runway surface layer. The size of the slice was such that five successive 18° rotations produced a quarter section of the cylindrical model, which through considerations of symmetry and by the application of appropriate restraints was sufficient for subsequent analysis. Natural boundary conditions were modelled by fully restraining the lower flat surface of the cylinder. Movement in the curved surface of the cylinder was restricted to the vertical direction.

The subgrade surrounding the camouflet was modelled to a depth below its detonation point equal to the height above. The radius of the modelling cylinder was comparable with its height. By opting for an aspect ratio of approximately 1:3 in the surface elements it was found that the overwhelming majority of remaining elements in the model had aspect ratios within the 1:5 ratio recommended by PAFEC. Breaches of the guidelines, which did occur, were not sufficient to incur error messages and did not occur in significant areas.

A typical cross-section of the finite element mesh is shown in [Figure 1.2](#). There would be up to 4350 elements and 47,750 degrees of freedom. The stress

analysis was completed in less than two hours elapsed time using a workspace of approximately 400 Mb on a SUN workstation connected to the university network. Three-dimensional isoparametric finite elements from the PAFEC 37110 element library were chosen. These elements have curved faces and are provided in a 20-node brick shape and a 15-node wedge shape. Element nodes have three translatory degrees of freedom and the PAFEC analysis provides nodal displacements, nodal stresses, stresses at element centres and at the centres of element faces. The authors were satisfied that this was a realistic model and that any further refinement would not have made a significant impact on the analysis. [Figure 1.3](#) shows a quarter finite element model of the camouflet for a detonation depth of 12.354 m.

Camouflet determination

The requirement to define the extent and the size of a camouflet under a runway is similar to the determination of a void under a highway. Voids under highways have implications for the maintenance, repair and safety of vehicles and people using the highway [42]. Using current technology, some voids in the subgrade under a highway are easily detected, while others are problematic [42]. To improve the detectability of highway voids, the effectiveness of various geophysical and non-destructive testing methods such as ground probing radar, has been proved [42]. Other geophysical techniques such as seismic methods, which use the spectral analysis of surface waves, microgravity surveys and non-destructive test methods such as the falling weight deflectometer have yet to be evaluated.

For highways, the number and types of load applications and vehicular speed are usually unknown, as is the time of the initiation of the void. For runways, construction details and maintenance data, types and frequency of loading are readily and accurately known. Further, the time at which a camouflet occurs is precisely known. What is required is unambiguous evidence to identify that a camouflet is present and to be able to determine its size and its effect on runway support.

Laboratory tests have shown that for a saturated clay subgrade, subjected to static and superimposed cyclic load of low frequency, there is an initial rapid settlement constituting between 60% and 80% of the total permanent settlement and it is completed within the first ten cycles of loading [43]. This is followed by secondary settlement at a slower rate, which continues for up to 15,000 to 20,000 load cycles until equilibrium is reached. Settlement is then practically negligible for all other load cycles. For runways, it is possible to obtain deflection and settlement measurements as heavy aircraft traverse the length of the undamaged runway. These deflection and settlement records allow the determination of whether the runway, prior to the introduction of a camouflet, was in its initial, secondary or equilibrium settlement stages.

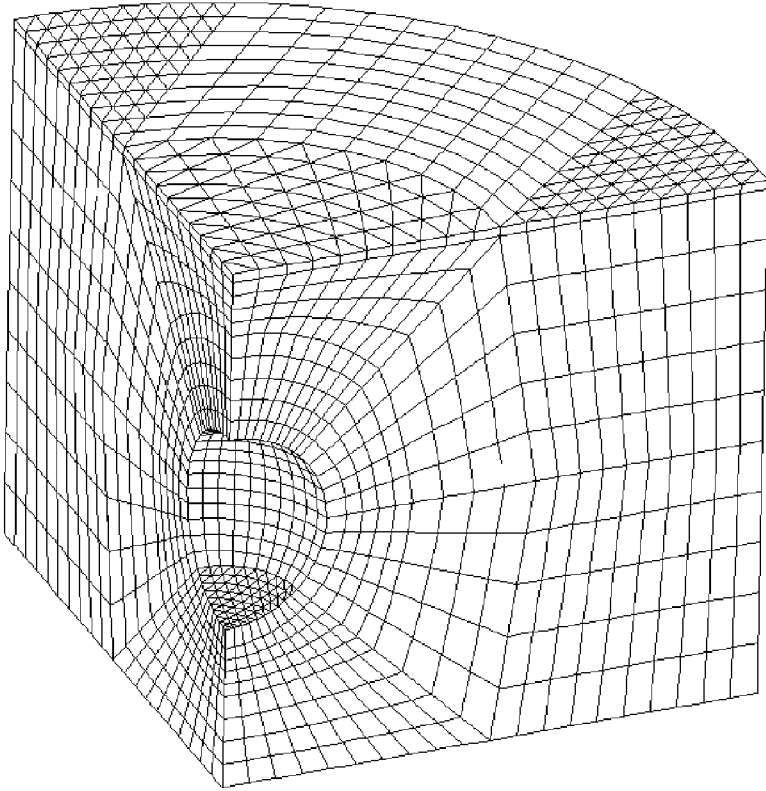


Figure 1.2 A quarter finite element model of the camouflet for a detonation depth of 8.354 m.

The introduction of a camouflet will return the subgrade to a new set of initial rapid settlement conditions and will allow the identification of the location and extent of the camouflet from the deflection bowl the load produces. Further research is required to identify, from the deflection bowl, the precise material set being met.

Depth of the zones above the void

In the original nine material sets the radii of the zonal interfaces 2–3, 3–4, 4–5 and 5-void were not altered and the thickness of the zones 3, 4 and 5 remained constant. The thickness of zone 2 was not constant, as can be seen from [Figure 1.1](#), as although the zone 2–3 interface was spherical, the zone 1–2 interface was horizontal. The thicknesses of zones 2, 3 and 4 on the vertical y -axis, through the centre point of the void were 1.753 m, 1.452 m and 1.375 m respectively. As this research considered the depth of the camouflet being increased, consideration was given to the effect the detonation would have on the

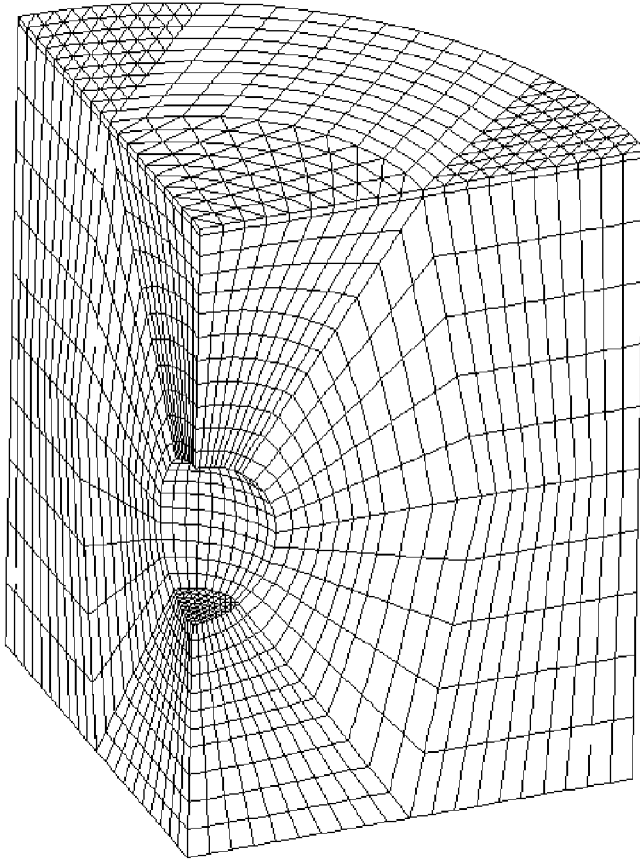


Figure 1.3 A quarter finite element model of the camouflet for a detonation depth of 12., 354m.

thickness of zones 2, 3, 4, 5 and 6. There was no published data on the phenomena. Previous research by the authors had led to a standard thickness being determined for zones 5 and 6 [8, 14, 16, 17, 34]. Further consideration regarding the extent of zones 3 and 4 in relation to the point of detonation and the air-ground interface led the authors to conclude that the thicknesses of these zones should not be altered. Consideration of zone 2 led to the belief that the thickness of that zone would change as it was the zone located nearest to the air-ground interface and the zone most effected by the reflections of the shock waves from that interface. For this reason the thickness of zone 2 was increased in the same steps as the depth of the detonation increased. The thickness of zone 2 was 2.753 m, 3.753 m, 4.753 m, 5.753 m, 8.753 m and 11.753 m as the depth of the detonation changed to 9.354m, 10.354m, 11.354m, 12.354m, 15.354 m and 18.354 m respectively.

Following the detonation, changes take place in the Young's moduli of zones 2, 3, 4, 5 and 6. Previous work shows that the Young's modulus of zones 5 and 6 is likely to increase to 950 MPa [19–22, 25]. However as there is no published data regarding the strength of zones 2, 3 and 4 following a detonation, the authors have made the following reasoned assumptions regarding the Young's modulus values.

The authors divided the changes in the subgrade Young's modulus into three groups related to the Young's modulus of zone 2. Group 1 comprised material set 1, where the Young's modulus was 190 MPa. Group 2 comprised material sets 2, 3, 4, 5, 6, 7, 8, 9, 10 and 11, where the zone 2 Young's modulus was 95 MPa. Group 3 comprised the remaining material sets 12, 13, 14, 15, 16 and 17, where the zone 2 Young's modulus was 7 MPa.

In group 1, as shown in [Table 1.1](#), material set 1, the Young's modulus for zones 2, 3, 4 and 5 is set at 190 MPa on the assumption that the detonation would increase the strength of those zones. The Young's modulus of zone 6 is assumed to have been increased to 950 MPa. Zone 7 remains unaltered by the detonation with its Young's modulus staying at 95 MPa. Zones 1 and 8, the concrete runway, are unaffected by the detonation and remain at 36,000 MPa.

In group 2, as shown in [Table 1.1](#), material sets 2 to 11 inclusive, zone 2 is unaffected by the detonation and remains at 95 MPa. This makes it difficult to detect, by inspection, any void that is beneath the runway. Material sets 2, 4 and 5 assume that zone 5 has been compressed to 950 MPa, that zone 3 remains unchanged at 95 MPa for material sets 4 and 5, and that zone 4 is unchanged at 95 MPa for material set 5. In material sets 2 and 4, zone 4 is increased to 190 MPa, as is zone 3 in material set 2. Material set 3 has zones 3, 4 and 5 increased to 190 MPa. Material set 6 has its zone 5 increased to 190 MPa, but with zones 3 and 4 remaining unaffected at 95 MPa. In material set 7, zones 3, 4 and 5 are unaffected by the detonation and remain at 95 MPa. In material sets 8, 9 and 10, the Young's modulus of zone 3 is reduced to 7 MPa. In zone 4, the Young's modulus of material set 8 remains at 95 MPa, but is reduced to 7 MPa for material sets 9 and 10. The Young's modulus of zone 5 remains at 95 MPa for material sets 8 and 10, but is increased to 950 MPa for material set 9. Material set 11 has zones 3, 4 and 5 reduced to 7 MPa.

In group 3, as shown in [Table 1.1](#), material sets 12 to 17 inclusive, it is assumed that zone 2 has been weakened and that the Young's modulus has been reduced to 7 MPa. In practice this change would be readily observable due to increased load-induced deflections, but difficulties would remain in assessing the strength of zones 3, 4 and 5. For material sets 12, 13, 14 and 16, zones 2 and 5 have a Young's modulus of 7 MPa and 190 MPa respectively. For material set 12, zones 3 and 4 have a Young's modulus of 95 MPa and 190 MPa respectively. For material set 13, zones 3 and 4 have a Young's modulus of 95 MPa as does zone 4 of material set 14. Zone 3 of material sets 14 and 16 has a Young's modulus of 7 MPa as does zone 4 of material set 16. In material sets 15 and 17, zones 3 and 4 have a weakened Young's modulus of 7 MPa as does zone

5 of material set 17. Zone 5 of material set 15 has a strengthened Young's modulus of 950 MPa.

Downward vertical deflections were recorded along the top of the runway from point 1, directly above the detonation point to point 29, 14.32 m from point 1. For the purposes of this research, the deflections for the points numbered 1, 4, 8, 12, 16 and 20 are shown. Points 1, 4, 8, 12 and 16 are on the surface of zone 1, the part of the concrete runway that overlays the subgrade affected by the detonation. Point 20 is in zone 8, the part of the runway overlaying the subgrade not directly affected by the detonation. For some material sets, the effect of the detonation extended to increasing the deflections as far as point 22 in zone 8 if subgrade zones 2, 3, 4 or 5 were weakened.

For no surface rupture for the 213 kg mass of explosive used for this computational modelling, the depth of the detonation must be between 8.286 m and 16.572 m [23, 33]. Consequently, it is expected that the computational results will show that as the depth of detonation exceeds 8.354 m and reaches 16.572 m the surface disturbance will tend to 100% and that when the detonation depth reaches 18.354 m, the 100% deflection will be obtained. That is, no effect of the detonation will be detectable at depths of detonation of 16.572 m and greater.

Discussion of the numerical results

The 17 material sets are considered in three groups. Considering first group 1, material set 1, as shown in Table 1.3, to obtain the 100% value over the undisturbed subgrade, the average of points 21 to 29 inclusive was used. This indicates that the surface deflection detonation effects extended as far as point 20. That is, the deflection due to the detonation extended over the apparently undisturbed subgrade points 18, 19 and 20. When the depth of the detonation was 8.354 m, the deflections at points 1, 16 and 20 were 89.1 %, 96.4% and 99.1 % respectively. Thus increasing the Young's modulus in zones 2, 3, 4 and 5 reduces the deflections as far out as point 20. As the depth of detonation increases, the change in the displacements at points 16 and 20 is small, but there are still reduced surface deflections. Further, for all the remaining deflection points, the surface deflection continues to reduce. For material set 1, the camouflet can be detected for all depths considered, but the size and depth of the camouflet will be overestimated as its deflection bowl exceeds the zone 1–8 interface. The results for material set 1 can be interpreted in two ways. Firstly the experimental work underestimates the depth required for no surface disturbance, or, if the range of depths found experimentally is correct, material set 1 is infeasible.

Group 2 is considered in two parts. In part 1, material sets 2, 3, 4, 5, 6 and 7, Tables 1.4, 1.5, 1.6, 1.7, 1.8, and 1.9 respectively, all the deflections at point 1 for the camouflet depth of 8.354 m are less than 103.7%. Material sets 2 to 7 inclusive have Young's moduli in zones 2, 3, 4 and 5 of 95 MPa or above. For material sets 2, 3 and 4, the deflections for camouflet depth 8.354 m are less than

Table 1.3 Deflection readings in percent for material set 1; group 1.

Depth of detonation (m)	8.354	9.354	10.354	11.354	12.354	15.354	18.354
Average of points 21 to 29	100	100	100	100	100	100	100
Deflection at point 20	99.1	99.1	99.0	99.1	99.1	99.0	99
Deflection at point 16	96.4	96.4	96.4	96.4	96.5	96.5	96.7
Deflection at point 12	92.5	92.7	92.9	93.2	93.4	93.8	94.3
Deflection at point 8	90.2	90.5	90.8	91.2	91.5	92.3	93.0
Deflection at point 4	89.3	89.6	89.8	90.3	90.6	91.5	92.4
Deflection at point 1	89.1	89.4	89.6	90.1	90.5	91.4	92.3

100%. However, as the depth of the camouflet increases, the surface deflection increases and tends to 100%. The deflections of point 16 for material sets 2, 3 and 4 remain between 99% and 100%. The deflection due to the camouflet is contained within points 1 to 17, the zone 1–8 interface. Material sets 2, 3 and 4 become increasingly and almost impossible to detect as the depth of the camouflet increases. At a depth of 18.354 m no surface disturbance is evident. For material set 5, [Table 1.7](#), there is almost no change in the surface deflection over the undisturbed subgrade for all depths of the camouflet. Material set 5 is almost undetectable for all depths and the deflection bowl remains within points 1 to 17, the zone 1 area, as it does for material sets 6 and 7. For material sets 6 and 7, [Tables 1.8](#) and [1.9](#), at a detonation depth of 8.354 m, the point 1 deflections are 102% and 103.7% respectively, but as the depth of detonation increases, the surface deflection reduces to 99.9% and 100% respectively. With a detonation depth of 8.354 m the deflection at point 1 is not identifiable, as it is within the limits given in [Table 1.2](#). As the detonation depth increases it becomes impossible to identify its location. For material sets 2, 3, 4, 5, 6 and 7, the deflection bowl remains within points 1 to 17 and at a detonation depth of 18.354 m the material sets are not detectable. Considering the deflection reading of [Table 1.2](#), material sets 2 and 3 are detectable up to and including depths of 15.354 m. Material sets 4, 5, 6 and 7 are not detectable at any detonation depth. As material sets 2, 3, 4, 5, 6 and 7 are not detectable at a depth of 18.354 m, they are feasible material sets.

For part 2 of group 2, material sets 8, 9, 10 and 11, [Tables 1.10](#), [1.11](#), [1.12](#) and [1.13](#) respectively, the Young's modulus of zone 2 remained at 95 MPa and made it difficult to detect the camouflet by inspection unless the runway was loaded. In material set 8, the Young's modulus of zone 3 was reduced to 7 MPa. In material set 9 the Young's modulus of zones 3 and 4 was reduced to 7 MPa and zone 5 increased to 950 MPa. For material set 10, zones 3 and 4 were reduced to 7 MPa, while in material set 11, zones 3, 4 and 5 were reduced to 7 MPa. To determine the 100% deflection over the apparently undisturbed subgrade under zone 8 for material sets 8, 9, 10 and 11 points 18–29, 19–29, 19–29 and 20–29 respectively were used, showing that the deflection bowl extended beyond the zone 1–8

Table 1.4 Deflection readings in percent for material set 2; group 2 part 1.

Depth of detonation (m)	8.354	9.354	10.354	11.354	12.354	15.354	18.354
Average of points 17 to 29	100	100	100	100	100	100	100
Deflection at point 16	99.2	99.3	99.4	99.6	99.7	99.8	99.9
Deflection at point 12	97.8	98.3	98.7	99.1	99.3	99.7	99.9
Deflection at point 8	95.4	96.7	97.7	98.4	98.8	99.5	99.8
Deflection at point 4	92.3	95.2	96.7	97.8	98.5	99.4	99.8
Deflection at point 1	91.9	94.7	96.4	97.7	98.4	99.4	99.8

Table 1.5 Deflection readings in percent for material set 3; group 2 part 1.

Depth of detonation (m)	8.354	9.354	10.354	11.354	12.354	15.354	18.354
Average of points 17 to 29	100	100	100	100	100	100	100
Deflection at point 16	99.2	99.3	99.4	99.6	99.7	99.8	99.9
Deflection at point 12	97.8	98.3	98.7	99.1	99.3	99.7	99.9
Deflection at point 8	95.4	96.7	97.7	98.4	98.8	99.5	99.8
Deflection at point 4	92.3	95.2	96.7	97.8	98.5	99.4	99.8
Deflection at point 1	91.9	94.7	96.4	97.7	98.4	99.4	99.8

Table 1.6 Deflection readings in percent for material set 4; group 2 part 1.

Depth of detonation (m)	8.354	9.354	10.354	11.354	12.354	15.354	18.354
Average of points 17 to 29	100	100	100	100	100	100	100
Deflection at point 16	99.5	99.6	99.7	99.7	99.8	99.9	100
Deflection at point 12	98.8	99.1	99.3	99.5	99.6	99.8	99.9
Deflection at point 8	97.9	98.5	98.9	99.3	99.4	99.7	99.9
Deflection at point 4	96.6	97.9	98.6	99.1	99.4	99.7	99.9
Deflection at point 1	96.2	97.7	98.6	99.1	99.3	99.7	99.9

interface. Thus the introduction of weak subgrade layers increased the radius of the deflection bowl, giving a false indication of an increased detonation depth and increased size of the camouflet. Material sets 8, 9, 10 and 11 are identifiable for all detonation depths up to and including 15.354 m. The deflections at point 1 at a detonation depth of 8.354 m for material sets 8, 9, 10 and 11 were 136.5%, 144.9%, 145.6% and 148.8% respectively, indicating that as the strength of the subgrade reduced, the surface deflection increased. All four material sets have the same point 1 deflection of 100.4% at the maximum detonation depth of 18.354 m. The authors take the view that the 100.4% falls within the experimental error of the range of detonation depths and thus material sets 8, 9, 10 and 11 would not be detectable at the maximum detonation depth of 18.354 m. Material sets 8, 9, 10 and 11 are feasible material sets.

Turning now to group 3, material sets 12, 13, 14, 15, 16 and 17, Tables 1.14, 1.15, 1.16, 1.17, 1.18 and 1.19, three different values of Young's modulus for zone 5 were used. Material sets 12, 13, 14 and 16 have a Young's modulus of 190 MPa. Material set 15 has a Young's modulus of 950 MPa and material set 17

Table 1.7 Deflection readings in percent for material set 5; group 2 part 1

Depth of detonation (m)	8.354	9.354	10.354	11.354	12.354	15.354	18.354
Average of points 17 to 29	100	100	100	100	100	100	100
Deflection at point 16	99.8	99.7	99.8	99.9	99.9	99.9	100
Deflection at point 12	99.6	99.6	99.7	99.8	99.8	99.9	100
Deflection at point 8	99.8	99.8	99.8	99.9	99.9	99.9	99.9
Deflection at point 4	99.8	99.9	100	100	99.9	99.9	99.9
Deflection at point 1	99.7	99.9	100	100	100	99.9	99.9

Table 1.8 Deflection readings in percent for material set 6; group 2 part 1

Depth of detonation (m)	8.354	9.354	10.354	11.354	12.354	15.354	18.354
Average of points 17 to 29	100	100	100	100	100	100	100
Deflection at point 16	99.8	99.9	99.9	99.9	99.9	99.9	100
Deflection at point 12	100.1	100	100	100	99.9	99.9	99.9
Deflection at point 8	101	100.5	100.3	100.1	100	99.9	99.9
Deflection at point 4	101.8	101.1	100.6	100.4	100.1	99.9	99.9
Deflection at point 1	102	101.3	100.7	100.5	100.1	99.9	99.9

Table 1.9 Deflection readings in percent for material set 7; group 2 part 1.

Depth of detonation (m)	8.354	9.354	10.354	11.354	12.354	15.354	18.354
Average of points 17 to 29	100	100	100	100	100	100	100
Deflection at point 16	99.9	100	100	100	99.9	99.9	100
Deflection at point 12	100.5	100.2	100.1	100.1	100	99.9	100
Deflection at point 8	101.9	101.1	100.5	100.3	100.1	100	100
Deflection at point 4	103.3	101.9	101	100.7	100.3	100	100
Deflection at point 1	103.7	102.2	101.2	100.8	100.4	100	100

Table 1.10 Deflection readings in percent for material set 8; group 2 part 2.

Depth of detonation (m)	8.354	9.354	10.354	11.354	12.354	15.354	18.354
Average of points 18 to 29	100	100	100	100	100	100	100
Deflection at point 16	101.8	101.4	101.0	100.8	100.6	100.2	100.1
Deflection at point 12	107.3	105.1	103.4	102.4	101.7	100.6	100.2
Deflection at point 8	119.3	112.2	107.8	105.2	103.4	101.0	100.3
Deflection at point 4	132.5	119.8	112.2	107.8	105.0	101.3	100.4
Deflection at point 1	136.5	122.1	113.5	108.6	105.4	101.4	100.4

has a Young's modulus of 7 MPa. All the material sets have a zone 2 Young's modulus of 7 MPa. Material sets 14, 15, 16 and 17 have a zone 3 Young's modulus of 7 MPa. The zone 4 Young's modulus of materials sets 15, 16 and 17 is also 7 MPa. With so many of the material sets having a low Young's modulus, the authors expected the deflection bowls to extend beyond point 17. This was the case with all the deflection bowls extending to point 22. The 100% deflection value was determined from points 23–29 for all the group 3 material sets.

Table 1.11 Deflection readings in percent for material set 9; group 2 part 2.

Depth of detonation (m)	8.354	9.354	10.354	11.354	12.354	15.354	18.354
Average of points 19 to 29	100	100	100	100	100	100	100
Deflection at point 16	102.3	101.8	101.3	101.0	100.7	100.3	100.1
Deflection at point 12	109.0	106.2	104.2	102.9	102.0	100.6	100.2
Deflection at point 8	123.6	114.8	109.4	106.1	104.0	101.1	100.3
Deflection at point 4	139.9	123.9	114.6	109.2	105.8	101.5	100.4
Deflection at point 1	144.9	126.6	116.2	110.1	106.3	101.6	100.4

Table 1.12 Deflection readings in percent for material set 10; group 2 part 2.

Depth of detonation (m)	8.354	9.354	10.354	11.354	12.354	15.354	18.354
Average of points 19 to 29	100	100	100	100	100	100	100
Deflection at point 16	102.3	101.6	101.3	101.0	100.7	100.3	100.1
Deflection at point 12	109.2	106.1	104.2	102.9	102.0	100.7	100.2
Deflection at point 8	123.9	114.7	109.4	106.1	104.0	101.1	100.3
Deflection at point 4	140.6	123.9	114.7	109.2	105.8	101.5	100.4
Deflection at point 1	145.6	129.2	116.3	110.0	106.3	101.6	100.4

Table 1.13 Deflection readings in percent for material set 11; group 2 part 2.

Depth of detonation (m)	8.354	9.354	10.354	11.354	12.354	15.354	18.354
Average of points 20 to 29	100	100	100	100	100	100	100
Deflection at point 20	100.5	100.4	100.3	100.2	100.1	100.1	100.0
Deflection at point 16	102.6	101.9	101.4	101.1	100.8	100.3	100.1
Deflection at point 12	109.9	106.6	104.5	103.1	102.1	100.7	100.2
Deflection at point 8	125.6	115.7	109.8	106.4	104.1	101.1	100.3
Deflection at point 4	143.4	125.4	115.3	109.6	106.0	101.5	100.4
Deflection at point 1	148.8	128.3	117.0	110.6	106.5	101.6	100.4

Table 1.14 Deflection readings in percent for material set 12; group 3 part 1.

Depth of detonation (m)	8.354	9.354	10.354	11.354	12.354	15.354	18.354
Average of points 23 to 29	100	100	100	100	100	100	100
Deflection at point 20	105.2	105.3	105.3	105.3	105.3	105.1	104.7
Deflection at point 16	135.8	136.4	136.4	136.1	135.1	132.0	128.7
Deflection at point 12	202.2	206.9	207.6	206.2	203.0	191.9	180.9
Deflection at point 8	255.0	271.3	276.2	275.2	270.5	251.5	232.7
Deflection at point 4	277.1	307.4	318.1	318.6	313.4	289.8	265.8
Deflection at point 1	280.3	315.1	327.6	328.7	323.5	298.8	273.6

The material sets of group 3 are divided into two parts. Part 1 comprises material sets 12 and 13. Part 2 comprises material sets 14, 15, 16 and 17. In part 1, all the depths of detonation are detectable certainly between points 1 and 22. For both material set deflections, the point 1 and point 4 deflections increase for each detonation depth up to 11.354 m and then decrease until the depth of 18.354 m is attained. Points 8 and 12 similarly increase but only up to a depth of 10.354 m,

Table 1.15 Deflection readings in percent for material set 13, group 3 part 1.

Depth of detonation (m)	8.354	9.354	10.354	11.354	12.354	15.354	18.354
Average of points 23 to 29	100	100	100	100	100	100	100
Deflection at point 20	105.3	105.3	105.3	105.4	105.3	105.1	104.7
Deflection at point 16	136.1	136.6	136.4	136.2	135.2	132	128.6
Deflection at point 12	203.5	207.6	207.9	206.5	203.2	191.9	180.9
Deflection at point 8	257.8	272.8	276.9	275.7	270.8	251.5	232.6
Deflection at point 4	281.2	309.7	319.2	319.4	313.9	289.7	265.8
Deflection at point 1	284.8	317.6	328.8	329.5	324.0	298.8	273.6

Table 1.16 Deflection readings in percent for material set 14; group 3 part 2.

Depth of detonation (m)	8.354	9.354	10.354	11.354	12.354	15.354	18.354
Average of points 23 to 29	100	100	100	100	100	100	100
Deflection at point 20	105.7	105.7	105.6	105.6	105.4	105.1	104.7
Deflection at point 16	140.8	139.7	138.5	137.4	136.0	132.4	128.7
Deflection at point 12	224.0	242.2	215.8	211.2	206.0	192.4	181.0
Deflection at point 8	305.7	301.3	293.9	285.6	276.5	252.5	232.8
Deflection at point 4	355.6	352.7	344.2	333.7	322.1	291.1	266.0
Deflection at point 1	366.9	364.7	356.0	345.1	332.9	300.2	273.8

Table 1.17 Deflection readings in percent for material set 15; group 3 part 2.

Depth of detonation (m)	8.354	9.354	10.354	11.354	12.354	15.354	18.354
Average of points 23 to 29	100	100	100	100	100	100	100
Deflection at point 20	106.0	105.9	105.7	105.7	105.7	105.1	104.7
Deflection at point 16	143.2	141.3	139.5	138.0	136.3	132.2	128.9
Deflection at point 12	234.2	226.7	219.5	213.4	207.3	192.6	181.0
Deflection at point 8	328.9	314.9	301.6	290.1	279.1	252.8	232.8
Deflection at point 4	391.1	373.0	355.5	340.1	325.8	291.6	266.0
Deflection at point 1	405.8	386.9	368.4	352.0	336.8	300.8	273.8

Table 1.18 Deflection readings in percent for material set 16; group 3 part 2.

Depth of detonation (m)	8.354	9.354	10.354	11.354	12.354	15.354	18.354
Average of points 23 to 29	100	100	100	100	100	100	100
Deflection at point 20	106.1	105.9	105.7	105.6	105.6	105.1	104.7
Deflection at point 16	143.4	141.4	139.5	138.0	136.3	132.2	128.7
Deflection at point 12	235.0	226.9	219.6	213.4	207.2	192.5	181.0
Deflection at point 8	330.5	315.5	301.9	290.1	279.0	252.8	232.8
Deflection at point 4	393.5	374.0	335.9	340.2	325.6	291.5	266.0
Deflection at point 1	408.5	387.9	368.8	352.1	336.6	300.7	273.8

before the deflections then decrease. Material sets 12 and 13 give very similar deflection results which indicates that there are, for material sets 12 and 13, optimum depths of detonation that cause maximum surface deflections. The only difference in the material sets' Young's moduli is in zone 4, where material set 12 has a value of 190 MPa and material set 13 has a value of 95 MPa. Thus the

Table 1.19 Deflection readings in percent for material set 17; group 3 part 2.

Depth of detonation (m)	8.354	9.354	10.354	11.354	12.354	15.354	18.354
Average of points 23 to 29	100	100	100	100	100	100	100
Deflection at point 20	106.3	106.0	105.8	105.7	105.5	105.1	104.7
Deflection at point 16	144.9	142.2	139.9	138.2	136.5	132.2	128.1
Deflection at point 12	241.1	230.2	221.3	214.2	207.8	192.6	181.0
Deflection at point 8	344.3	322.6	305.5	291.9	280.1	252.8	232.8
Deflection at point 4	414.6	384.6	361.1	342.7	327.1	291.6	265.9
Deflection at point 1	431.7	399.5	374.5	354.9	338.2	300.8	273.8

decrease in Young's modulus in zone 4, from 190 MPa to 95 MPa increases the surface deflection by a small amount.

The large surface deflections in material sets 12 and 13 are due to the weak zone 2 subgrade. The reason for the increase in surface deflection at points 1, 4, 8 and 12 as the depth of detonation increases followed by a reduction in surface deflection as the depth of detonation increases, needs further investigation. This change in deflection could be accounted for by zone 3 arching and interacting with the reducing angle of the cone thus providing additional support to the weak zone 2. As the deflections at point 1 are clearly recognisable at a depth of 18.354 m, material sets 12 and 13 are infeasible.

Turning now to part 2 of group 3, material sets 14, 15, 16 and 17, Tables 1.16, 1.17, 1.18 and 1.19 respectively, the deflections at point 1 for a detonation depth of 8.354 m increases from 366.9% to 405.8% to 408.5% to 431.7% respectively. In each material set the deflections for points 1, 4, 8, 12 and 16 have a maximum value at a detonation depth of 8.354 m and steadily decrease as the detonation depth increases, clearly different to the results for material sets 12 and 13. The deflection results for material sets 15 and 16 are almost identical. The only difference in the Young's modulus is for zone 5, where it has been reduced from 950 MPa to 190 MPa, hence the slightly larger deflections for material set 16. Material set 17 has the largest deflections of part 2 of group 3 and this is explained as zones 2, 3, 4 and 5 have a Young's modulus of 7 MPa. For each of material sets 14, 15, 16 and 17, the deflection at the detonation depth of 18.354 m has the same value of 273.8% and the deflection bowl extends at least as far as point 22. Clearly material sets 14, 15, 16 and 17 of group 3 are infeasible and their deflection bowls overestimate the detonation depth and camouflet size. However if the group 3 material sets could be replicated by the detonation of a chemical explosive, then the effects of a camouflet detonation would be enhanced.

Conclusion

The research considers the effect of the detonation of a 213 kg mass of explosive at depths of 8.354 m, 9.354 m, 10.354 m, 11.354 m, 12.354 m, 15.354 m and 18.

354 m beneath a cement concrete runway on the deflection of the runway surface when a uniformly distributed downward load is applied to the runway. As there is no other published research that details the changes in the subgrade cone above a camouflet detonation, this research computationally modelled 17 material sets as shown in [Table 1.1](#), by changing the Young's modulus of zones 2, 3, 4, 5 and 6 of [Figure 1.1](#). These material sets cover a range of subgrade possibilities, from material set 1 where zones 2, 3, 4 and 5 were all increased in strength to material set 17 where zones 2, 3, 4 and 5 were all reduced in strength. What is known is that for the detonation to have no effect at the air-ground interface, the depth of detonation must exceed a value of between 8.286 m and 16.572 m. For computational reasons, a value of 18.354 m was chosen as the depth at which no air—ground effect could be detected.

Consideration was given to the possibility of using the diameter of the deflection bowl as a means of determining the size, depth and position of the camouflet void. The computational modelling showed that for material sets 1 and 8 to 17 inclusive, the deflection bowl extended beyond the zone 1–8 interface. Thus for these material sets, the deflection bowl will identify a point above the centre of the camouflet void, but the depth and diameter of the void will be overestimated. For the remaining material sets, 2 to 7 inclusive, the size, depth and location of the void can be determined.

It is necessary to consider the validity of the empirical data relating to the depth of the detonation required to produce no surface rupture. Ignoring the empirical data would mean accepting that all 17 material sets are possible outcomes of the detonation. However, the empirical data, although unconfirmed by any other published work, has to be accepted until modified by further data. This means that material sets 1 and 12 to 17 inclusive have to be rejected as possible outcomes of a camouflet-producing detonation. Thus a detonation that produces a camouflet will produce one of material sets 2 to 11 inclusive.

Considering further the material sets that are rejected as being infeasible, material set 1 is the only material set that reduces runway deflections. This is unlikely to occur in practice. Inspecting the remaining infeasible material sets 12 to 17 inclusive, the common theme is that zone 2 has been weakened to 7 MPa. Further research is required to determine the minimum value of the zone 2 Young's modulus of these material sets to make them feasible. An indication is given for material set 13, when it is compared with material set 6. The only difference between the two material sets is that zone 2 of material set 6 has a Young's modulus of 95 MPa while that of material set 13 is 7 MPa. A similar consideration applies to material set 11 when compared with material set 17.

The feasible material sets 2 to 11 inclusive all have a zone 2 Young's modulus of 95 MPa. This suggests that as the depth of the camouflet detonation increases, the arching effect of zone 2 in the base of the cone makes the identification of the camouflet almost impossible. If the zone 2 Young's modulus remains at 95 MPa, then inspection of the subgrade will not reveal the existence of a camouflet. For

material sets 12 and 13, the results indicate that there is an optimum depth of detonation to cause maximum surface deflections.

If the repair team can see no evidence of a camouflet, but believe one is present, they can overrun the runway to determine if the settlement characteristics of the runway have been altered. If this is found to be the case then the fatigue characteristics of the camouflet need to be determined. The authors are pursuing research into the fatigue characteristics of the subgrade and of the cement concrete runway for the 17 material sets.

References

- 1 Bull, J.W. and Woodford, C.H., 1992, Surface repair roughness prediction for concrete hard standing following arbitrary explosive cratering, 4th International Symposium on Numerical Models in Geomechanics (NUMOG IV), Pande, G.N., Pietruszczak, S. (Editors), Balkema Publishers, Rotterdam, pp. 871–878.
- 2 Bull, J.W. and Woodford, C.H., 1993, Damage assessment and repair of explosively formed craters in airfield runways using empirical and numerical modelling, *Journal of Structural Engineering*, Vol 20, No 1, pp. 1–7.
- 3 Bull, J.W. and Woodford, C.H., 1995, The numerical analysis and modelling of repaired runways following chemical explosive crater formation, Chapter 6 in “Numerical analysis and modelling of composite materials,” Bull, J.W. (Editor), Blackie Academic & Professional, Glasgow, Scotland, pp. 128–151.
- 4 Bull, J.W. and Clarke, J.D., 1991, Rapid runway and highway repair using precast concrete raft units, *Proc Int Conf on Rapidly Assembled Structures*, Bulson, P.S. (Editor), Computational Mechanics Publications, Southampton, UK, pp. 139–149.
- 5 Bull, J.W., 1986, An analytical solution to the design of precast concrete pavements, *Int Jour Numerical & Analytical Methods in Geomechanics*, Vol 10, pp. 115–123.
- 6 Bull, J.W., 1991, *Precast concrete raft units*, Blackie and Sons, Glasgow, UK.
- 7 Bull, J.W., 1994, The interaction between precast concrete raft unit pavements and their soil support, Chapter 12 in “Soil-structure interaction, numerical analysis and modelling,” Bull, J.W. (Editor), Chapman and Hall, London, pp. 423–458.
- 8 Bull, J.W. and Woodford, C.H., 1999, The numerical modeling of crater repairs in airfield runways, *Computers and Structures*, Vol 73, pp. 341–353.
- 9 Bull, J.W. and Woodford, C.H., 1999, The effect of camouflets on subgrade surface support, *Computers and Structures*, Vol 73, pp. 315–325.
- 10 Bull, J.W. and Woodford, C.H., 1996, The numerical modelling of camouflets to determine their effect on overlaying runways, 3rd Int Conf in Computational Structures Technology, *Advances in Finite Element Technology*, Budapest, Topping, B.H.V. (Editor) Civil Comp-Press, Edinburgh, pp. 349–356.
- 11 Bull, J.W. and Woodford, C.H., 1998, The prevention of runway collapse following an underground explosion, *Engineering Failure Analysis*, Vol 5, No 4, pp. 279–288.
- 12 Bull, J.W. and Woodford, C.H., 2000, Stress and displacement effects due to subsurface barriers laid under cement concrete runways, *Computers and Structures*, Vol 78, pp. 375–383.

- 13 Bull, J.W. and Woodford, C.H., 1999, The effect of large subgrade voids on the fatigue life of runways, submitted to *Computers and Structures*.
- 14 Bull, J.W. and Woodford, C.H., 1998, Camoufflets and their effect on runway support, *Computers and Structures*, Vol 69, No 6, pp. 695–706.
- 15 Baldwin, R.B., 1949, *The face of the Moon*, University of Chicago Press.
- 16 Waterways Experiment Station, 1961, Cratering from high explosive charges, Analysis of crater data, Technical Report No 2–547, US Army Corps of Engineers, Vicksburg, Mississippi.
- 17 Waterways Experiment Station, 1960, Cratering from high explosive charges, Compendium of crater data, Technical Report No 2–547, Report No 1, US Army Corps of Engineers, Vicksburg, Mississippi.
- 18 Saxe, H.C., 1963, Explosion crater prediction utilising characteristic parameters, *Proceedings 5th Symposium on Rock Mechanics*, University of Minnesota, Fairhurst, C. (Editor), Pergamon Press, pp. 273–306.
- 19 McNeil, G.M., 1973, Cratering of concrete pavements on a clay subgrade, Report No. 73518, MoD, MVEE (Christchurch), UK.
- 20 McNeil, G.M., 1976, The explosion of a 1000 Ib Bomb at Dhekalia, Report No 73 526, MoD, MVEE (Christchurch), UK.
- 21 McNeil, G.M., 1976, Cratering of concrete pavements on a clay subgrade, Part 2, Detonation of 3.6 Kg charges under a 0.075 m pavement, Report No. 75 520, MoD, MVEE (Christchurch), UK.
- 22 McNeil, G.M., 1976, Cratering of concrete pavements on a clay subgrade, Part 3, Analysis of four scaled experiments, Report No. 75 521, MoD, MVEE (Christchurch), UK.
- 23 Chadwick, P., Cox, A.D. and Hopkins, H.G., 1963–1964, Mechanics of deep underground explosions, *Phil. Trans. Royal Soc London, Ser A Maths. Physics. Sci.*, Vol 256, pp. 235–300.
- 24 Boardman, C.R., Rabb, D.D. and McArthur, R.D., 1964, Responses of four rock mediums to contained nuclear explosions, *Journal of Geophysical Research*, Vol 69, No 16, pp. 3457–3469.
- 25 Kvammen, A., Pichumani, R. and Dick, J.L., 1972, Pavement cratering studies, Technical Report No AFWL-TR-72–61, Dec, Civ Eng Research Facility, Univ of New Mexico, New Mexico, USA.
- 26 Bangash, M.Y.H., 1993, *Impact and explosions, analysis and design*, Blackwell Scientific, Oxford, UK.
- 27 Gohl, W.B., Jefferies, M.G., Howie, J.A. and Diggle, D., 2000, Explosive compaction: design, implementation and effectiveness, *Geotechnique*, Vol 50, No 6, pp. 657–665.
- 28 Mikulyak, S.V., 2000, Calculation of the formation processes of underground cavities by blasting methods, *Journal of Mining Science*, Vol 36, No 2, pp. 133–140.
- 29 Knox, J.B. and Terhune, R.W., 1965, Calculation of explosion produced craters high explosive sources, *Journal of Geophysical Research*, Vol. 70, No 10, pp. 2377–2393.
- 30 Chabai, A.J., 1965, On scaling dimensions of craters produced by buried explosives, *Journal of Geophysical Research*, Vol 70, No 20, pp. 5075–5098.

- 31 Nordyke, M.D., 1961, Nuclear craters and preliminary theory of the mechanics of explosive crater formation, *Journal of Geophysical Research*, Vol 66, No 10, pp. 3439–3459.
- 32 Bocharov, M.V., Kudryashov, N.A. and Tsygankova, O.L., 1989, Dome collapse of an underground-blast cavity in a granular medium, *Soviet Mining Science (English translation)*, Vol 24, Pt 2, pp. 118–122.
- 33 Christopherson, D.G., 1946, Report, Structural defence, UK, Ministry of Home Security, Research and Experimental Departments, RC 450.
- 34 Knox, J.B., Rawson, D.E. and Korver, J.A., 1965, Analysis of a groundwater anomaly created by an underground nuclear explosion, *Journal of Geophysical Research*, Vol 70, No 4, pp. 823–835.
- 35 Zverev, A.A. and Fetisov, V.S., 1989, Effect of the leakage of detonation products on the mechanical and elastic characteristics of camouflet explosion, *Combustion, Explosion and Shock Waves (English translation)*, Vol 24, pp. 619–623.
- 36 Brown, S.F., 1996, 36th Rankin Lecture, Soil mechanics in pavement engineering, *Geotechnique*, Vol 46, No 3, pp. 383–26.
- 37 Schrefler, B.A., Lewis, R.W. and Majorana, C.E., 1982, The problem of rebound in subsidence models, in *Finite Element Flow Analysis*, Kawai, T. (Editor), University of Tokyo Press, Tokyo, pp. 689–696.
- 38 Neville, A.M., 1981, *Properties of concrete*, 3rd edition, Pitman, London.
- 39 Neville, A.M., 1995, *Properties of concrete*, 4th edition, Longman Group, London.
- 40 PAFEC-FE Ltd., 1992, Program for automatic finite element calculations, SER Systems Ltd. Nottingham, UK. Web: www.SERuk.com. Email: marketing@SERuk.com.
- 41 Woodford, C.H., Passaris, E.K.S. and Bull, J.W., 1991, *Engineering analysis using PAFEC finite element software*, Blackie & Sons, Glasgow, UK.
- 42 Evans, R., 1997, Detecting voids under highways, *Research Focus*, August, No 30, p. 8.
- 43 Das, B.M. and Shin, E.G., 1997, Cyclic load-induced settlement of foundations on clay, Mouchel Centenary Conference on Innovation in Civil and Structural Engineering, Leeming, M.B. and Topping, B.H.V (Editors), Civil-Comp Press, Edinburgh, pp. 241–246.

Chapter 2

Numerical and experimental study of compressed air tunnelling

A.A.Javadi

Introduction

Compressed air as a means of dewatering the ground and assisting the construction of tunnels has been used for over a hundred years and has been successfully applied to a wide range of geological and construction circumstances. The use of compressed air, particularly with shotcrete lining, has proved to be, in many instances, an economic and effective measure in dewatering the ground, minimising the settlement and stabilising the tunnel face.

Despite having been used for over a century, the adoption of a tunnel pressure and the required volume of air to maintain that pressure, are currently based on judgement and empirical formulae. The risks associated with leakage of air from tunnels are not addressed by these methods. Such risks include surface settlement, uplift of structures, tunnel collapse and blow-out. A principal reason for these shortfalls is that the path and zone of influence of air leakage and the distribution of the air pressure in the ground cannot be predicted. Furthermore, the effects of the compressed air flow on the state of stress, strength and settlement of the ground have not been understood. In view of the paucity of scientific guidance for predicting these, a numerical model has been developed to simulate the flow of air through soils and to study the consequences of using compressed air in soils. In what follows, the details of the numerical model, its validation and a numerical/ experimental procedure which has been established to study the effects of the air flow on the shear strength of the ground will be presented.

Compressed air tunnelling

When driving tunnels under compressed air, an appropriate air pressure is applied in the tunnel to balance the groundwater and stabilise the face. The air displaces the groundwater, desaturates the ground and flows through the ground to the surface. The volume of air flowing through the ground must be compensated by a continuous supply of air from air compressors. An accurate estimation of the compressed air losses is essential at the planning stage to

determine the plant capacity to supply a sufficient volume of air to maintain a safe pressure whilst allowing for leakage from the tunnel. A realistic estimation of air losses can reduce the cost of air supply requirements and preparation for possible changes in air losses with tunnel advance, physical conditions and time.

Numerical modelling

A numerical model has been developed to simulate the flow of air through soils in compressed air tunnelling. The model is based on finite element analysis of the flow of air through the ground in compressed air tunnelling. The numerical model can predict the zone of influence of the air flow, the distribution of the pore-air pressure in the ground, the direction and velocity of the air flow, the deformed shape and position of the groundwater profile and the air losses from the tunnel face and walls. Field data from a tunnel in Germany has been used to verify and calibrate the numerical model.

Furthermore, a relationship has been established to describe the variation of the air permeability of shotcrete tunnel lining with time and the technique of parameter identification has been used to determine the parameters of this relationship. A genetic algorithm has been used in the optimisation procedure. It has been shown that the time-dependency of permeability of shotcrete plays a key role in controlling the air losses in driving tunnels under compressed air with shotcrete as a temporary or permanent lining and this time-dependency should be taken into account in design.

Effect of the air flow on shear strength of the ground

A procedure has been established to predict the changes in the shear strength of the ground due to the flow of air. The procedure is based on integration of the results of the numerical model and some concepts and theories of unsaturated soil mechanics.

A programme of multistage triaxial testing was carried out in a modified triaxial apparatus to study the effects of the flow of air on the shear strength of the partially saturated ground. The results show the way in which the compressed air flow helps to increase the strength and stability of the ground. The results of the tests have been used to define a shear strength envelope, which can be used to predict the change in the shear strength of the ground due to the flow of compressed air and changes in the air pressure.

Factors affecting air losses

The total amount of air lost from a tunnel is the sum of three main sources:

- (1) Air loss from the tunnel face
- (2) Air loss from tunnel perimeter walls

(3) Other losses (including air locks, drainage, and ventilation)

This can be stated as:

$$Q_{\text{total}} = Q_{\text{face}} + Q_{\text{perimeter walls}} + Q_{\text{other}} \quad (2.1)$$

The third item can be estimated from the size of the air lock, the pressure and the frequency of use. However, it is not significant compared with face losses occurring in open ground or losses from the tunnel perimeter walls.

The main factors influencing the air losses from the tunnel face and perimeter walls are the permeability of shotcrete (in cases where it is used as a temporary or permanent lining) and the ground (which is in turn a function of degree of saturation of soil). The permeability of shotcrete varies as it cures, so this time-dependency should be taken into account when analysing the air losses in a tunnel where shotcrete is used as a primary or permanent support.

Permeability of the ground to air

Water permeability of the ground can be determined by *in situ*, laboratory or theoretical methods, of which in-situ tests are more reliable due to the erratic nature of soils.¹ The permeability of a soil to air can be related to its permeability to water using a relationship of the type shown in [Figure 2.1](#).

As compressed air flows through the ground, the groundwater is driven back and a region around the tunnel face becomes unsaturated. The permeability of unsaturated soils to air is a function of many parameters such as type of the soil, relative density, pressure gradient, viscosity of air and water, particle size distribution and degree of saturation. Therefore, the possible relationship would be very complex. At present there is no clear relationship expressing the dependence of the permeability of unsaturated soils to all the above parameters. In this study, the following simple relationship between the permeability of soils to air and to water has been used which considers the dependence of permeability on viscosity and density of the flowing fluid: $k_a/k_w = \eta_w/\eta_a$, where η is dynamic viscosity, which is the ratio of the kinematic viscosity of the fluid to its density.

The viscosity of a flowing fluid varies with changing temperature. Therefore, the ratio of the air permeability to the water permeability of soil is a function of temperature. [Figure 2.1](#) shows the variation of the ratio of air permeability to water permeability with temperature. At 10° C ambient temperature, i.e., the assumed average temperature in the ground, this ratio is approximately equal to 70, i.e.,

$$k_a = 70 \times k_w \quad (2.2)$$

where k_a is the permeability of dry soil to air and k_w is the permeability of saturated soil to water at a temperature of 10° C. The use of this factor of 70 is a

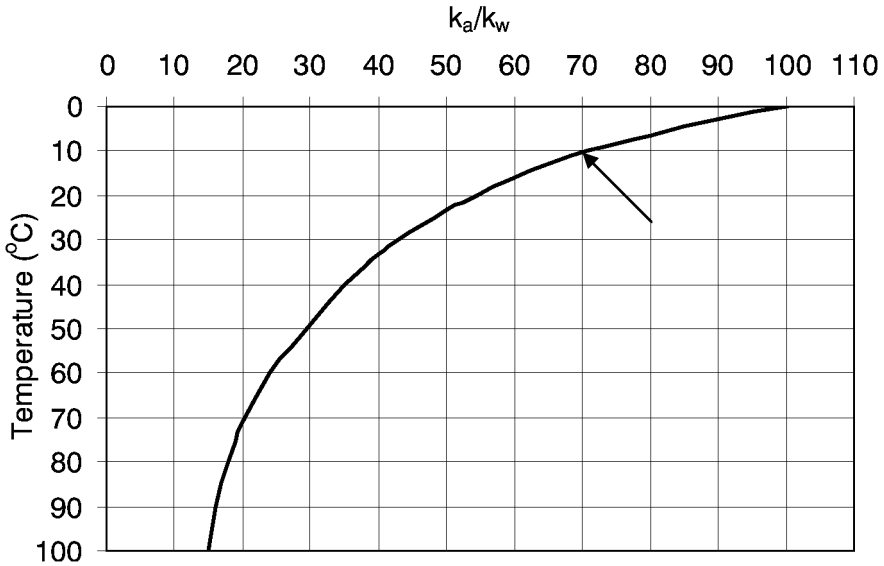


Figure 2.1 Variation of the ratio between permeability to air and permeability to water with temperature (reproduced from Kramer and Semprich³).

common practice in design for compressed air tunnelling. The study of more accurate relationships between permeability of soil to water and air is a subject of ongoing research at the Technical University of Graz².

Current practice in designing for compressed air

Engineers must determine the plant capacity to supply a sufficient volume of air to maintain the pressure whilst allowing for leakage from the tunnel. Typical sources of air loss are leaks in pipe work, airlocks, segment joints, around the shield and through the face of the tunnel, the most significant source being the face. Karlsson⁴ suggested that the air pushes the water away from the tunnel until an equilibrium surface between water and air is formed in the soil in the shape of an elliptical bubble, whereas Krabbe⁵ considered that for the method to work there must be a constant leakage and recharge of air. These different opinions illustrate the range of philosophies for designing for compressed air.

In recognition of the practical considerations, several empirical methods for calculating tunnel pressure P_t (see Table 2.1) and the quantity of air required Q (see Table 2.2) have been proposed. The accuracy of these predictive methods was discussed by Hoad and Gittoes⁶ who concluded that the methods could be appropriate as a rapid first estimate of the air losses. However, they do not account for real influences on air consumption such as multi-layered soils, speed

Table 2.1 Formulae for determining compressed air pressure.

Reference	Formula
Krabbe ⁵ [modified]	$Q = 2k_w 70 \frac{(P_1 - P_2)}{\gamma_w} F \frac{P_1}{P_2} (n_a + n_c)$
Schenck & Wagner ⁸	$Q = \frac{wk_a (P_1 - P_2) (P_1 + P_2)}{\gamma_w L} \frac{A (D - h_k)}{2 P_1 D}$
Hewett & Johannesson ⁹	$Q = 3.7D^2 \text{ to } 7.2D^2 (m^2)$

Where,

P_t is the air pressure in the tunnel

γ_w is the unit weight of water

H_{inv} is the head of water at tunnel invert

a is an on-site adjustment for ground conditions

H is head of water at tunnel crown

σ_s is the surcharge

T_c, T_γ are stability parameters

D is the tunnel diameter

C is the depth of cover

c_u is cohesive strength

F_s is the factor of safety

Table 2.2 Formulae for determining quantities of air required.

Reference	Formula
Anon.	$P_t = \gamma_w (H_{inv} - a)$
Anon.	$P_t = \gamma_w (H + 2/3D)$
Anon. (USA)	$P_t = 0.76H_{inv}$
Atkinson & Mair ⁷	
Cohesive soils	$P_t = \sigma_s - \frac{c_u}{F_s} T_c + 0.5\gamma_w (1 + 2C/D)$
Atkinson & Mair ⁷	
Cohesionless soils	$P_t = \gamma_w DT_\gamma$

Where,

k_w is the coefficient of permeability to water

P_1 is the absolute pressure at the tunnel face to a point of free flow

P_2 is the absolute pressure at the surface

A, F is the face area of the tunnel

n_a relates to the tunnel face and varies from 1 for soft homogeneous ground to 0 for hard ground.

n_b relates to the tail seal of the shield. In soft ground it is 0 with a tail seal and between 1 and 2 without a tail seal.

n_c relates to a typical 500 m length of tunnel behind the face. For a grouted and caulked lining it is 1 and for grouted lining without caulking it is 2.

k_a is the coefficient of permeability for air

L is the length of air flow from the crown

w is a correction factor, typically 2

h_k is the capillary rise

of tunnelling or surface conditions. Furthermore, they do not predict the zone of influence of the air leakage, which is crucial when tunnelling in urban areas.

Deficiencies of the current practice

Although there has been extensive use of this tunnelling method there is no theoretically rigorous method for predicting how the air, water and soil interact. For example, seepage of water into the tunnel can result in groundwater lowering and settlement, over-pressuring can cause ground heave, high air pressures or large quantities of air can fracture or disturb the soil and reduce its strength. Also, the air can travel laterally to adjacent excavations. Records of the Dartford Tunnel¹⁰ refer to high air losses issuing 800 m from the face and a blow-out 100 m from the face. These situations are of immediate concern to those constructing the tunnel, but the threat to deep excavations supported by temporary works, dewatering projects, basements, cuttings, other tunnels and surface structures must also be considered.

An appropriate air pressure must be applied in the tunnel to balance the groundwater pressure and, due to leakage of air from the tunnel, a constant recharge of air must be supplied to maintain that pressure. If air leakage increases, a greater volume of air must be supplied or measures taken to reduce the air losses. However, in its most simplistic form, compressed air as a means of groundwater control is justified on the premise that if the air pressure in the tunnel is equal to the pressure of the water in the ground, a state of equilibrium should be created (see [Figure 2.2](#)).

[Figure 2.2](#) shows the relative pressures for an air pressure set equal to the water pressure at the tunnel invert level. The resulting over-pressure at the tunnel crown, P_r , is the difference between the two pressures. As long as there is no significant flow of water towards the tunnel face, the ground should achieve a satisfactory effective strength for stability at air pressures less than the full head of water.

As well as changing the effective stress conditions, there can be a secondary positive effect of reducing ground settlement. The air pressure provides a support to the tunnel face and walls.

However, it is common for layers of soil with different geological origins and properties to be encountered in driving tunnels. This inhomogeneity is compounded by the flow of air through the ground, which may cause some changes in the structure, state of stress, properties and the strength of the soil. Also a region of the soil is dewatered by the air flow, so the properties of the soil in this region will be different to those in the saturated soil. These conditions result in a very complex geotechnical environment.

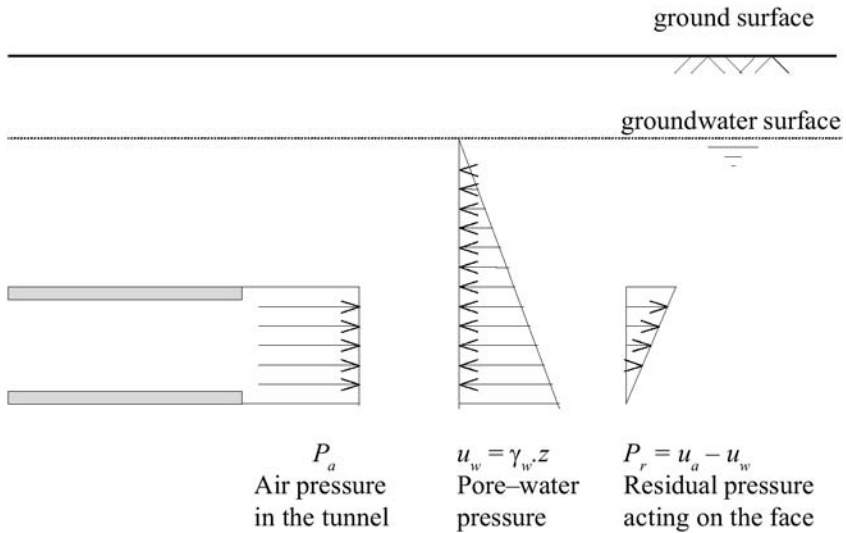


Figure 2.2 Illustration of the principle of pressure balance and over-pressure.

When shotcrete is used as tunnel lining, the permeability of shotcrete to air has a significant effect on controlling the air losses. The permeability of shotcrete to air is strongly governed by shrinkage cracks during the curing process which is a function of its thickness, surface area, temperature and the construction process. Laboratory experiments on small samples do not represent these aspects of the behaviour of in-situ shotcrete. Therefore, at present, back analysis of field measurement is probably the most reliable method to be used for this purpose although complete and reliable field data on compressed air losses are rare.

At present, for estimation of air losses from a tunnel driven under compressed air, a constant value is assumed for the permeability of shotcrete. As will be shown later, the permeability of shotcrete varies significantly with time and this variation has a significant effect on the air losses.

A numerical model for prediction of air losses

A numerical model has been developed to simulate the flow of air from a tunnel face and perimeter walls. The numerical model has two components: one for analysing the air flow from the tunnel face using the finite element method and the other for the estimation of the air flow from the tunnel perimeter walls.

Analysis of air flow through tunnel face

The problem of the flow of air from the tunnel face through partially saturated ground in compressed air tunnelling is a very complex boundary value problem

with complex boundary conditions. In general, the soil is inhomogeneous and anisotropic. The permeability varies with the degree of saturation and both air and soil are compressible. Furthermore, the process of lowering the groundwater is time-dependent. In addition, air and water are miscible fluids. The physical complexity of the problem makes analysis of the flow of air through soils during compressed air tunnelling extremely difficult.¹¹ Due to these complexities and the uncertainty regarding several details of the flow, simplifying assumptions must be made in numerical modelling of the problem.

Assumptions for the numerical model

The air and water permeability of the soil is usually assumed to be constant within a subregion of the ground and so the entire region can be divided into subregions with constant permeabilities. At least two subregions will exist: a saturated subregion below the deformed groundwater surface and an unsaturated region above it. Also different soil layers with different permeabilities can be considered as subregions within these two main subregions. The air permeability of the unsaturated region above the groundwater level will be much higher than that of the saturated subregion below the groundwater level.

Although the whole process of lowering the groundwater level is time-dependent, only the final steady-state condition after establishment of the deformed groundwater profile is considered in the numerical model. Darcy's law is used as the flow law, but it is only valid for laminar flow conditions, which excludes large hydraulic gradients and large soil particles. The analysis is performed for air and water under isothermal conditions.

Air and water are assumed to be immiscible fluids. This implies that the soil mass is subdivided into a fully saturated zone below the deformed water table and an unsaturated zone above it. A free boundary will exist that separates the two zones (see [Figure 2.3](#)). The shape and position of this boundary are a priori unknown and should be determined as part of the solution.

Governing equations

The formulation of the problem is based on the continuity equation, the equation of motion (Darcy's law) and Boyle's law as the equation of state for ideal gases. For the specific case of steady-state flow and in the absence of sources and sinks, the equation of continuity as an expression of the mass conservation can be written as:¹²

$$\nabla \cdot (\rho q) = 0 \quad (2.3)$$

Darcy's law relates the flow rate to the driving potential as:

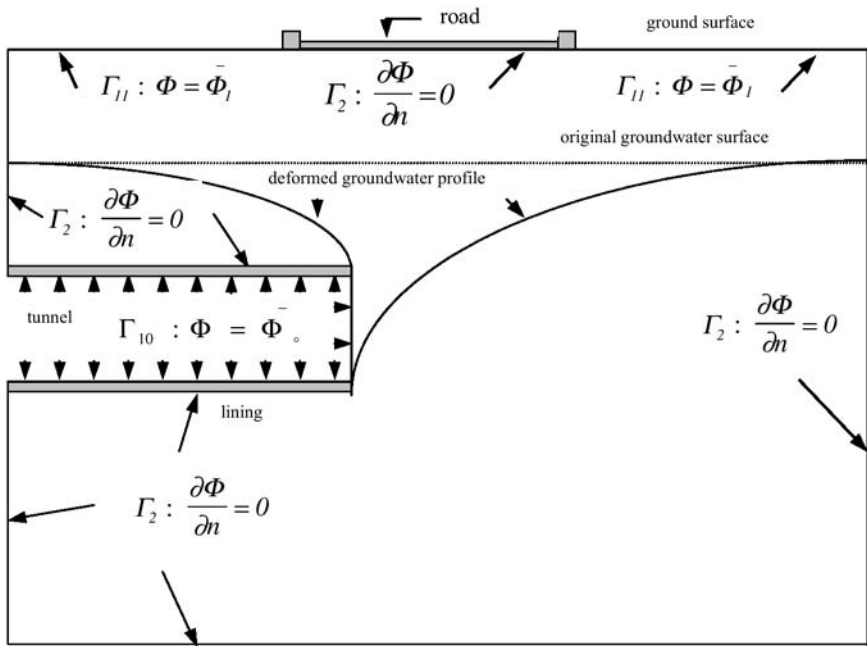


Figure 2.3 Typical tunnel geometry and the boundary conditions.

$$q = K\nabla\Phi \tag{2.4}$$

and Boyle's law expresses the relationship between the pressure, volume and temperature of ideal gases. For an isothermal condition, Boyle's law can be written as:

$$\frac{u_a}{\gamma} = \text{constant} \tag{2.5}$$

In the above equations, ρ is the mass density of air, q is the vector of specific discharge, ∇ is the gradient operator, K is the permeability tensor, γ is the unit weight of the fluid, u_a is the pore air pressure, and Φ is the potential function, defined as:

$$\Phi = \frac{u_a}{\gamma_w} \tag{2.6}$$

Combining equations (2.3), (2.4) and (2.6), the governing equation can be obtained as:

$$\nabla \cdot (K \nabla \Phi^2) = 0 \quad (2.7)$$

Boundary conditions

Typical boundary conditions for this problem can be boundaries of constant air pressure, $\Phi = \text{constant}$, or impermeable boundaries, $\partial\Phi/\partial n = 0$. Figure 2.3 shows the generalised geometry of a tunnel driven under compressed air passing underneath a road, illustrating the typical boundary conditions and the original and the deformed groundwater profiles.

Numerical solution

On the basis of the above assumptions, a numerical model has been developed using the finite element method to simulate the problem on the basis of isothermal, steady-state potential flow and applied to the problem of compressed air tunnelling. The model can predict the distribution of the air pressure in the ground due to the application of, or change in, the tunnel pressure.

The shape and position of the free boundary, separating the saturated and unsaturated zones, are a priori unknown and should be determined as part of the solution. Initially, a position is assumed for the deformed groundwater surface. The problem is then analysed using the assumed boundary and the pore-air pressures are calculated at a number of points (finite element nodes) on or very close to this boundary. The calculated pore-air pressures at various points on the boundary are then compared with the corresponding hydrostatic water pressures. If the pore-air and pore-water pressures are equal (within an acceptable degree of accuracy) on all the nodes on the assumed ground water level, the assumed boundary is accepted as the final position of the deformed groundwater table under the equilibrium conditions. Otherwise, the assumed boundary is updated and the process is repeated until the condition of equal air and water pressures on all nodes on the free boundary is satisfied. In this way, the shape and position of the deformed groundwater surface are determined in an iterative process, as the location of points in the ground at which the air pressure balances the water pressure.

Figure 2.4 shows a typical output of the two-dimensional model showing contours of pore-air pressure heads. Figure 2.5 shows a typical output of the three-dimensional model showing the deformed shape and position of the groundwater table. The model calculates the pore-air pressure distribution in the soil medium, the zone of influence of the air flow, the direction and velocity of the flow of air at every point in this zone, and the final location of the groundwater surface after the application of compressed air. The cumulative air loss from the tunnel can be calculated from this information.^{1, 11}

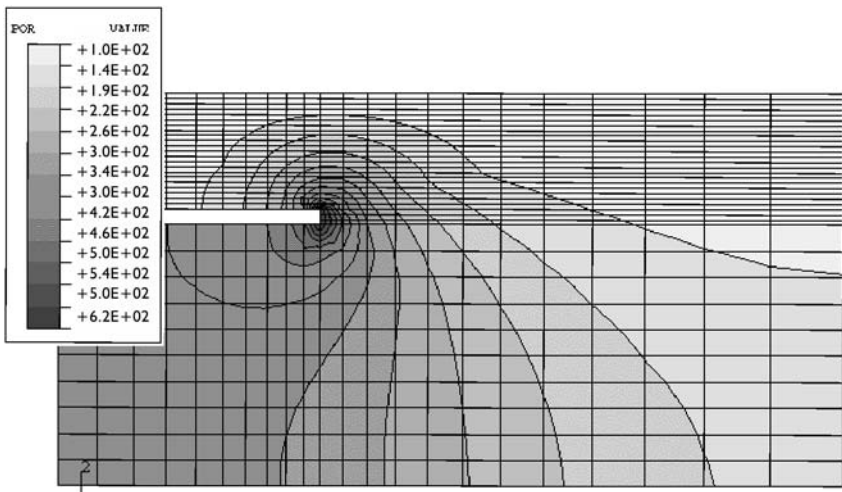


Figure 2.4 Typical output of the 2D finite element model showing contours of squares of the absolute pore-air pressure heads.

Javadi¹¹ compared the results of two- and three-dimensional models in terms of distribution of pore-air pressure, final deformed shape and location of the groundwater surface and computational time. It was shown that the difference between the results of the two- and three-dimensional analyses in terms of pore-air distribution between the tunnel crown and the ground surface was about 6% in average.

The difference between the estimated final shape and the location of the deformed groundwater surface was insignificant, whereas the time for a two-dimensional analysis was only about 2.6% of that of a three-dimensional analysis.¹¹ There is also a considerable difference in the time required for the preparation of the data for two- and three-dimensional analyses.

Although the problem of compressed air tunnelling is a three-dimensional problem, based on the above considerations it has been concluded that the two-dimensional analysis provides results that are accurate enough for most engineering applications. This will also be shown here when comparison is made between the results of the two-dimensional finite element analysis and the measured field data (see Figure 2.8).

Analysis of the air losses from tunnel perimeter walls

The second part of the model simulates the flow of air from the tunnel perimeter walls, based on the equation for the flow of a compressible fluid through porous media. In this part, the permeability of a shotcrete layer is considered in addition to the permeability of the soil layers. Obviously, for the cases where an impermeable lining is installed immediately after excavation, the air losses from

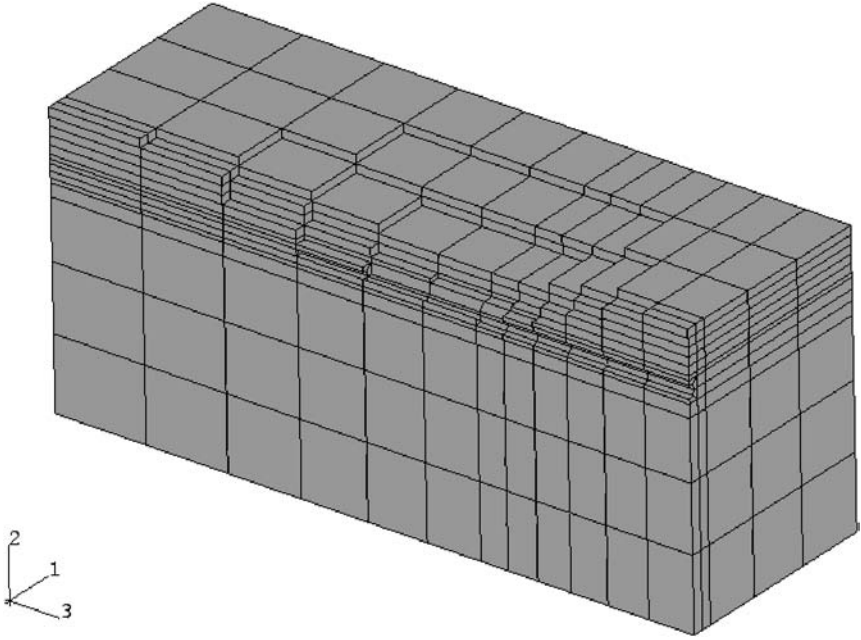


Figure 2.5 Typical output of the 3D model showing the deformed groundwater surface.

the perimeter walls will be negligible. However, for the cases where shotcrete is used as a temporary or permanent lining, the air losses from the tunnel walls will be significant. The computer model can consider the stages of excavation and the corresponding excavation times.

The permeability of shotcrete to air (or water) is not constant and decreases to a certain value during curing. From observation of the field data from a case study, a logarithmic relationship has been used to describe this change as:

$$k_{a,sh} = A - B \log(t) \quad (2.8)$$

where

$k_{a,sh}$ = permeability of shotcrete to air

A, B = constants

t = time in days

Parameter identification, based on back-analysis of the field measurements from the Feldmoching tunnel in Germany, has been used to identify the parameters A and B . Initially the tunnel longitudinal profile is divided into a number of excavation stages and the corresponding time for excavation and installation of the lining for each stage is evaluated from the anticipated rate of tunnel advance. This evaluated time is used to estimate the permeability of the shotcrete at the

corresponding stage, which together with the permeability values of the soil layers can be used to predict the air losses associated with this section (segment). The air loss for each segment is re-evaluated in the next excavation stages to account for the age of the shotcrete. The programme can consider any delay in the construction process such as holidays or other interruptions.

Parameter identification

In order to numerically simulate the flow of compressed air from the tunnel face and walls into the ground, it is necessary to develop appropriate constitutive models of all materials used in the tunnel. The governing equation describing this problem can be obtained by combining the continuity equation and the equation of flow. The flow equation can be expressed by Darcy's (or Pick's) law.^{1, 11} This model contains a number of material parameters which can ideally be determined from experiments on material specimens. The most important material parameters controlling the flow process are the permeability of soil layers and shotcrete tunnel lining.

The first step in the numerical analysis of the problem will be to collect and use the appropriate permeability values for soil layers and shotcrete. For practical purposes, permeability of soil can be assumed to be constant while permeability of shotcrete is not constant and varies with time during the curing process. Thus time-dependency of air permeability of shotcrete lining as it cures, should be taken into consideration and therefore it is very important to establish a relationship which describes the variation of air permeability of shotcrete tunnel lining with time. Obviously, any data collected from laboratory tests on small samples of shotcrete can be unreliable, mainly due to the effect of cracks in the shotcrete lining.

An alternative way of dealing with this problem, which is more reliable and economic, can be the use of a parameter identification technique, provided that some field or experimental data is available. The method is based on finding the material parameters which when introduced to the geotechnical analysis of the problem in hand, provide results as close as possible to the field observations or measurements. The identification problem can then be formulated as an optimisation problem where the function to be minimised is an error function that expresses the difference between the numerical simulation results and the field or experimental data.¹³ This method of parameter identification overcomes the shortcomings of the traditional methods in that it does not necessarily require homogeneous material behaviour.

The basic assumptions of the material parameter identification method are:

- A constitutive model is available which can simulate the behaviour of the material.
- An accurate and efficient computational method incorporating the constitutive model is available to simulate the problem numerically.

Therefore, the material parameter identification technique has three main elements:

- Measurement of some responses of the system,
- Numerical modelling of the same response of the system, and
- A technique to adapt the material parameters in the numerical model by comparing the measured and calculated responses.

In the parameter identification approach used in this study, the error function is defined using the least squares method.

Problem formulation

The material parameters to be identified can be considered as elements of a vector $\mathbf{x} \in R^N$. Then the optimisation problem can be formulated as finding vector \mathbf{x} that minimises the objective function:

$$F(\mathbf{x}) = \sum_{\alpha=1}^M \theta^{\alpha} F^{\alpha}(\mathbf{x}), \quad A_i \leq x_i \leq B_i \quad (i = 1, \dots, N) \quad (2.9)$$

where

M is the total number of individual measured responses which have also been obtained as a result of the numerical simulation, N is the number of parameters to be identified, $F^{\alpha}(\mathbf{x})$ is a dimensionless function defined as:

$$F^{\alpha}(\mathbf{x}) = \left[\sum_{i=1}^{S_{\alpha}} (Rm_i^{\alpha} - Rc_i^{\alpha}(\mathbf{x}))^2 \right] / \left[\sum_{i=1}^{S_{\alpha}} (Rm_i^{\alpha})^2 \right] \quad (2.10)$$

which measures the deviation of the computed α -th individual response, from the measured response, S_{α} is the total number of the discrete set of data points, θ^{α} is the weight coefficient which determines the relative contribution of information yielded by the α -th set of experimental data, A_i, B_i are the lower and upper limits of the values of material parameters stipulated by physical considerations.

Genetic algorithm

Genetic algorithms (GAs) are a group of randomised methods used in function optimisation. They offer a high probability of locating the global optimum in the optimisation variable space for complex optimisation problems. Early developments in the field of GAs are generally credited to Holland¹⁴ and since then they have been successfully applied to various optimisation problems.¹⁵

To implement a GA, the procedure starts by creating a set of binary strings (or chromosomes) of 0s and 1s of a fixed length (the so-called initial population). In

the next step the binary strings are decoded and converted into optimisation variable values (components of vector \mathbf{x}) using a linear scaling. The objective function is evaluated from the established optimisation variable values and a measure of worth or “fitness” is evaluated. For a maximisation problem the objective function is considered as a fitness function but for minimisation, the inverse of the objective function or the negative of the objective function (as used in this chapter) or the difference between a large number and the objective function can be considered as the fitness function. A high fitness value would indicate a better solution than a low fitness value.

The GA creates new populations from old populations. The fitter members in the population are selected to produce new members for the next generation. There are different methods of selection such as ranking, biased roulette wheel, tournament, stochastic remainder sampling and stochastic uniform sampling selection. In this study the tournament selection method was used. In this method several individuals are chosen randomly in groups as parents and then the individual with highest fitness is selected. In the next step, the partial strings of the chosen individuals of the population are exchanged to improve the average fitness of the next generation. The probability of crossover (P_c) shows whether selected members are used in reproduction or not. The most suitable value of P_c from literature is in the range 0.5–1.¹⁵ Different forms of crossover can be implemented (for example, uniform and single-point crossover), crossing two parents at a randomly chosen point. The lowest value of P_c can be used for uniform crossover, and for single-point crossover values of 0.7–1 are recommended. In this study the uniform crossover with $P_c=0.5$ produced good convergence of the optimisation process.

Mutation is another important operator in a GA. If, for example, all the variables in one generation have the same value, then all the new members in the next generation will be the same and premature convergence will be achieved. To avoid this, a mutation operator is used. The operator is based on probability of mutation (p_m) which varies in the range 0.001–0.025. The value of p_m was considered by Goldberg¹⁵ with the suggestion that for small population sizes (35–200), a low mutation probability (p_m 0.0005–0.025) is appropriate. At the end of each generation, convergence is checked and the procedure is repeated until no further improvements can be made to the results.

Case study

The construction of the 635-metre long Feldmoching tunnel, U8 N-8, was started in July 1992 and finished in February 1994. The tunnel was constructed using a top heading and bench method. Compressed air was used to control the groundwater and shotcrete was used as temporary support. The final concrete lining was installed in free air after completion of the tunnel.

The excavation of the first few metres of the tunnel was started with open trench and sheet piling which provided access to the underground work. The first

50 m of the tunnel length was constructed using a twin sidewall drift method (see Figure 2.6a). From 50 m to 320 m, the tunnel was constructed by a single sidewall drift method (see Figure 2.6b) and from 400 m to 635 m, the tunnel was converted to twin tunnels (see Figure 2.6c).

Table 2.3 shows the change in the tunnel face area with tunnel advance for each heading together with the method of construction. Table 2.4 shows the perimeter area (per unit length of the tunnel) and the thickness of the initial and final layer of shotcrete.

Figure 2.7 is a geological section of the tunnel route. The soil layers comprise a coarse gravel layer near to the ground surface overlaid by sand. Beneath the sand is a layer of low permeability silty clay underneath which lies another layer of sand. Also, there is a lens of sand in the silty clay layer between chainages 300 m and 635 m. The groundwater level is approximately 5 metres below the ground surface.

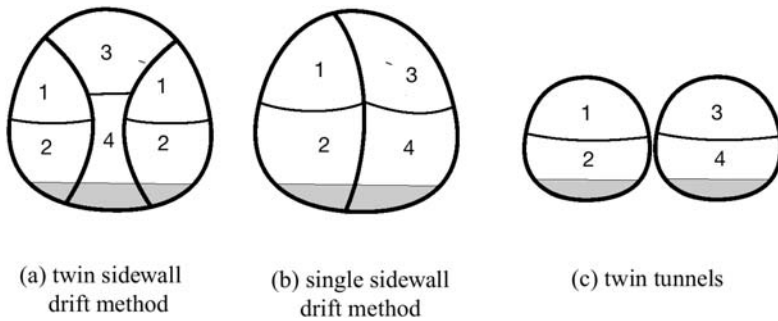


Figure 2.6 Method of construction.

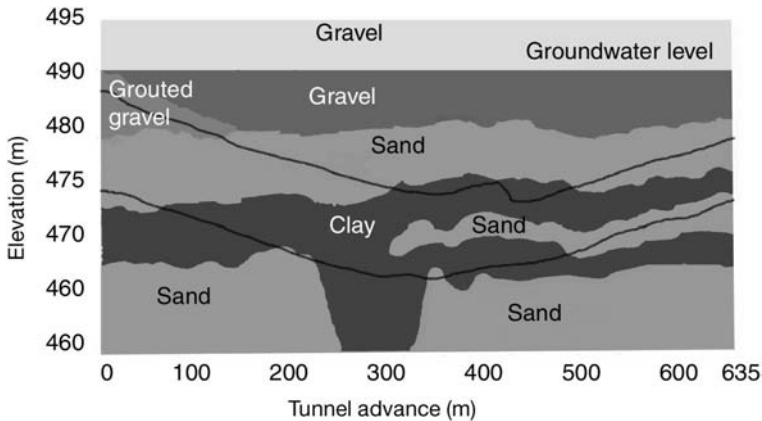


Figure 2.7 Geology of the tunnel route.

Table 2.3 The area of tunnel face and method of construction.

Tunnel length [m]	Area of face [m ²]	Method of excavation
0–50	38.00	Twin sidewall drift method
50–100	41.20	Single sidewall drift method
100–300	37.80	Single sidewall drift method
300–320	43.00	Single sidewall drift method
320–400	35.50	Twin sidewall drift method
400–635	37.60	Twin tunnels

Table 2.4 Perimeter area and thickness of initial layer of shotcrete for each heading.

Tunnel length [m]	Perimeter area [m ² /m]		Thickness of shotcrete [mm]	
	Initial	Final	Initial	Final
0–50	21.96	17.35	270	350
50–320	15.76	15.76	300	300
320–400	21.96	17.06	270	350
400–635	21.06	21.06	200	200

At the beginning of excavation work, the tunnel face was entirely in sand and gravel layers, and so high air losses were expected. Therefore, grouting was carried out to reduce the permeability. The tunnel face advanced gradually into the lower permeability clay layer such that at a chainage of about 300 m the whole face was in the clay layer and the air losses were reduced significantly. From about 470 m, the tunnel face gradually moved out of the clay layer and consequently the air losses increased.

The range of the water permeability of the layers was as follows:

gravel	$k_w=1 \times 10^{-3} - 5 \times 10^{-3}$ m/sec
grouted gravel	$k_w=1 \times 10^{-5} - 5 \times 10^{-5}$ m/sec
sand	$k_w=2 \times 10^{-5}$ m/sec
silty clay	$k_w=1.9 \times 10^{-9}$ m/sec

Two methods were used to reduce air losses from the shotcrete:

- 1) A layer of mortar was applied to the inner surface of the shotcrete lining.
- 2) A second layer of shotcrete was applied at the tunnel roof.

Numerical analysis and comparison

The air losses from the tunnel face and perimeter walls were analysed separately using the numerical model. The air losses from the face were determined for a

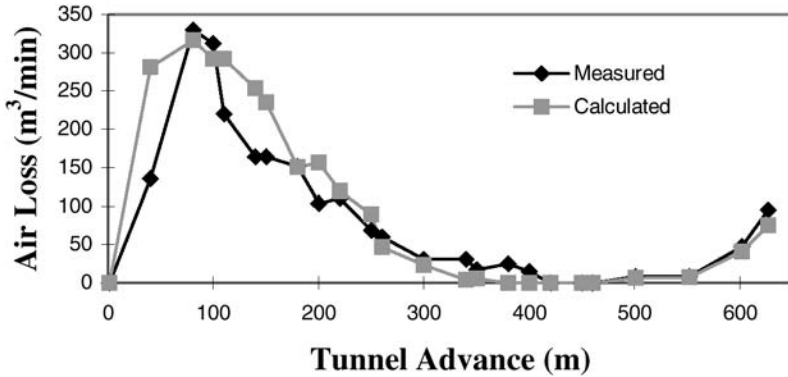


Figure 2.8 Comparison of the predicted and measured air losses from the tunnel face.

number of sections along the tunnel length. In Figure 2.8, the calculated values of the air losses at these locations have been plotted against the measured values.

The figure shows that the results of the numerical model are in close agreement with the measured values. The slight differences between the calculated and the measured values are likely to be due to the heterogeneity of the ground.

The air losses from the perimeter walls were calculated using the second part of the numerical model where the excavation sequence and the age of the installed shotcrete lining at each stage were considered. The tunnel length was divided into a number of segments and the permeability of the shotcrete was calculated for each segment from equation (2.8) considering the time of installation and age of shotcrete. The air losses for each segment were then calculated using the corresponding permeability and thickness of shotcrete and soil layers. For every location of the tunnel face, the total air loss from the perimeter walls was considered as the sum of the air losses from the segments behind the face. Delays in construction, such as those due to local collapse of the tunnel or holidays, were taken into consideration.

Coefficients A and B in equation (2.8) were determined by minimising the discrepancies between the measured and calculated values of air losses as described earlier. The final values were:

$$A = 1.43 \times 10^{-8} \text{ m/sec}$$

$$B = 3.09 \times 10^{-9} \text{ m/sec}$$

Figure 2.9 shows the results of the GA analysis in the identification process in terms of variation of the objective function value against the number of generations. The figure shows the rapid convergence of the algorithm and high efficiency of the method. The following parameter values were used in the GA:

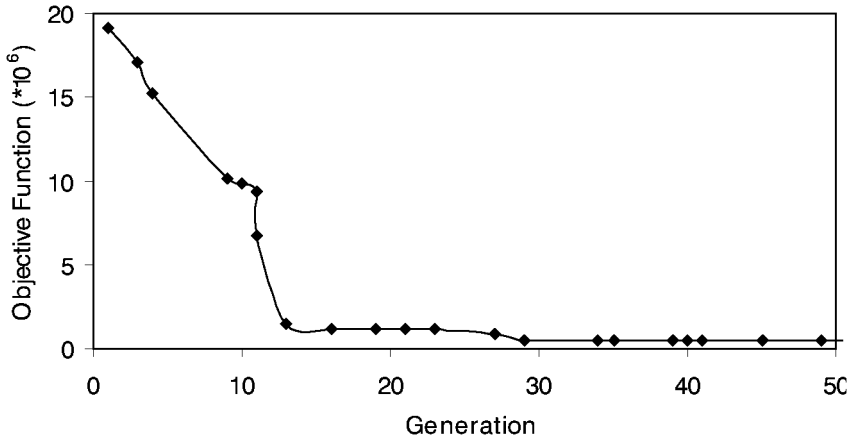


Figure 2.9 Convergence of the genetic algorithm.

Length of population = 20
 Length of binary strings = 20
 Probability of crossover = 0.05 (uniform crossover)
 Probability of mutation = 20

Practically, convergence was achieved after 29 generations and the CPU time used for 49 generations was 175 seconds on a Sun SPARC station using Solaris 2, giving 3.5 seconds for each generation.

Figures 2.10 and 2.11 show the calculated and measured values of the air losses from the tunnel perimeter walls and the total losses respectively. The occasional divergence of the two curves in Figures 2.10 and 2.11, can be related to construction activities. The cross-sections at which the major events occurred during the construction of the tunnel, are indicated in Figure 2.11. These events governed the trend of changes in the air losses and also the occasional divergence of the calculated and measured air losses. At the location of the tunnel face indicated by number 1 in Figure 2.11, a layer of mortar was added to the inner surface of the shotcrete lining. The addition of this relatively impermeable layer caused a considerable decrease in the actual air loss from the tunnel perimeter walls and the total loss (Figures 2.10 and 2.11) which was not considered in the numerical simulation. At location 2, another layer of shotcrete was added to the inner surface of the lining at the tunnel crown, which decreased the actual air losses which again was not considered in the numerical simulation. At location 3, the tunnel face started moving into the low-permeability clay layer, so the air losses from the face and the perimeter walls decreased dramatically. Between 300 m and 470 m, the tunnel was completely embedded in the clay layer and also the air pressure was reduced from 1.5 to 1.38 bar, so only a small

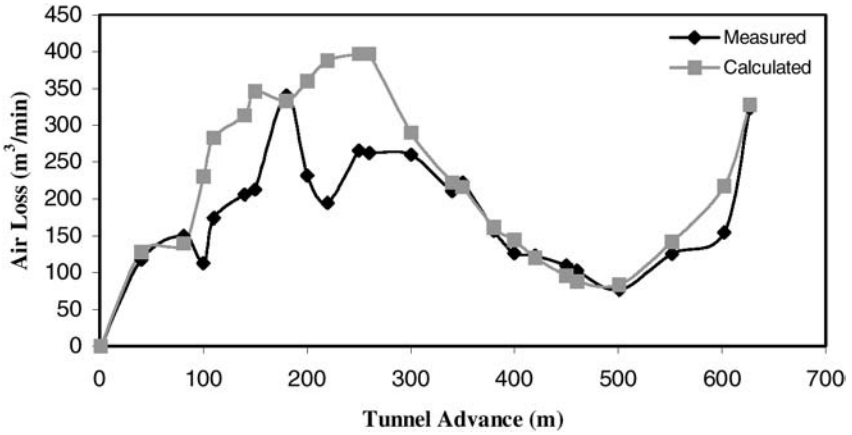


Figure 2.10 Air losses from the tunnel perimeter.

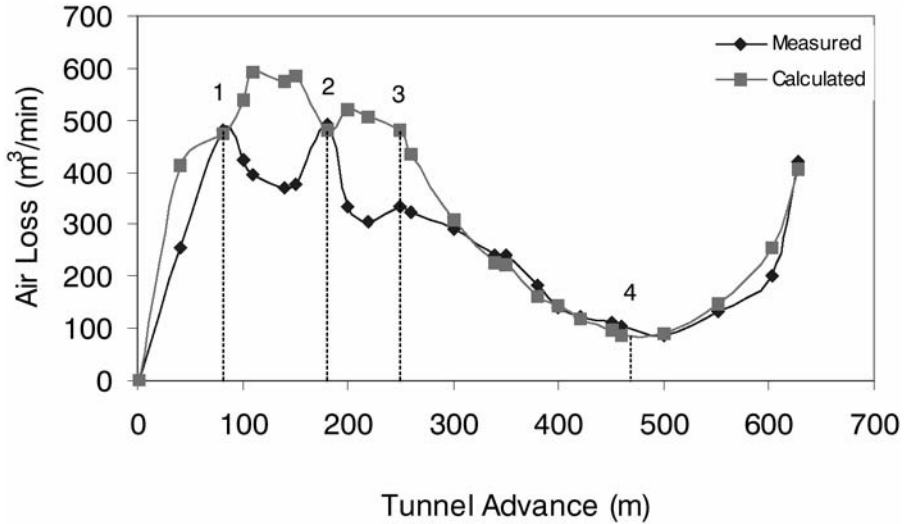


Figure 2.11 Total air losses.

amount of air was lost. At location 4 in Figure 2.11, the tunnel face started moving out of the clay layer and so the air losses increased.

Effects of air flow on shear strength of the soil

Theory of shear strength for unsaturated soils

Fredlund *et al.*¹⁶ proposed a shear strength equation for unsaturated soils, as an extension to that of saturated soils:

$$\tau = c' + (\sigma - u_a) \tan \phi' + (u_a - u_w) \tan \phi^b \quad (2.11)$$

where τ is shear strength of the soil, c' is effective cohesion, σ is total stress, u_a and u_w are pore-air pressure and pore-water pressure respectively, ϕ' and ϕ^b are effective friction angles with respect to changes in net normal stress and matric suction respectively, $(\sigma - u_a)$ is net normal stress and $(u_a - u_w)$ is matric suction.

This equation incorporates two independent stress state variables. The effective cohesion, c' , and the internal friction angles, ϕ' , and ϕ^b , are the strength parameters and relate the shear strength of an unsaturated soil to the stress state variables. The shear strength parameters represent many factors simulated in the test such as density, void ratio, degree of saturation, mineral composition, stress history, and strain rate. In other words, these factors are combined and expressed mathematically as the strength parameters.¹⁷ Equation (2.11) describes a planar surface called the “extended Mohr-Coulomb failure envelope”. This surface is tangent to the Mohr circles at failure.

The state of stress at failure can also be represented by the stress point failure envelope. A Mohr-Coulomb failure envelope and a stress point envelope can both be used to represent the stress state of a soil at failure; the former is obtained by drawing a surface tangent to the Mohr circles while the latter is a surface connecting the stress points of the failure Mohr circles. The stress point envelope is usually assumed to be planar and can be defined by the following equation¹⁷ although evidence of nonlinearity of the failure surface has been reported in the literature:¹⁶

$$q_f = d' + p_f \tan \Psi' + r_f \tan \Psi^b \quad (2.12)$$

where

q_f is half of the deviator stress at failure (i.e., $(\sigma_1 - \sigma_3)_f / 2$),

σ_{1f} and σ_{3f} are major and minor principal stresses at failure respectively,

d' is the intercept of the stress point envelope on the q -axis,

$P_f = ((\sigma_1 + \sigma_3)_f / 2 - u_a)$ is the mean net normal stress at failure,

$r_f = (u_a - u_w)_f$ is the matric suction at failure, and

Ψ' and Ψ^b are slopes of the stress point envelope with respect to the mean net stress and matric suction respectively.

In this study, the stress point failure envelope has been used to predict the shear strength behaviour of the soil due to the air flow in compressed air tunnelling.

Laboratory tests

Donald¹⁸ carried out a series of shear tests on unsaturated fine sands and coarse silts in a direct shear test box. The tests were run with atmospheric pore-air pressure (zero gauge pressure) and negative pore-water pressure. The results of the tests indicated that by increasing the matric suction, the soil strength increased to a peak value and then decreased to a nearly constant value. Ho and Fredlund¹⁹ studied the effect of matric suction, $(u_a - u_w)$, on the shear strength of soil. The results can be applied to engineering problems in which only one stress state variable (i.e. matric suction) is changed such as in slope stability and the swelling of expansive soils. However, in compressed air tunnelling, a change in the internal air pressure, u_a , will cause a change in matric suction and also a change in net normal stress. Therefore, the stress path followed in this special problem is different from the other problems studied so far in the literature.

The laboratory test associated with an engineering problem should closely simulate the loading conditions that are likely to occur in the field. Therefore, a suitable testing programme to study the effect of air flow in compressed air tunnelling, should account for the variation of both independent stress state variables.

Testing programme

Triaxial shear strength tests were carried out on a decomposed granitic soil sample to study the effect of air flow on the shear strength of the ground in compressed air tunnelling. The testing programme comprised three test series as follows:

- i. Simultaneous variation of both net normal stress and matric suction by changing the air pressure,
- ii Variation of only matric suction, keeping the net normal stress constant, and
- iii Variation of net normal stress at constant (zero) matric suction (saturated sample).

In order to eliminate the effect of variability of the soil sample, a multistage triaxial testing programme was used, as proposed by Ho and Fredlund.¹⁹ In this way, considerable information could be obtained from a limited number of samples. The tests were carried out in a modified triaxial apparatus.¹¹

Apparatus

Due to the presence of both air and water in the soil, the testing procedure for unsaturated soils is more complicated than that for saturated soils. Special design considerations are required for development of equipment for testing unsaturated soils under different loading conditions. A suitable design should be able to

accommodate several aspects of the behaviour and loading of unsaturated soils. The basic requirement is that it must allow independent control and/or measurement of all individual components of stress, i.e., total stress, σ , pore-water pressure, u_w , and pore-air pressure, u_a .

A triaxial cell was modified and used for the shear strength tests.¹¹ The flow of air was controlled from the top and the flow of water was controlled and measured from the bottom of the specimen. Three geotechnical digital systems (GDS) controllers were used to control and measure the cell pressure, the deviator stress, and the pore-water pressure and pore-water volume change. The controllers were connected to a computer and a complete set of data was recorded by the computer.

PORE-WATER PRESSURE CONTROL

For controlling the pore-water pressure, a 5 bar, 0.635 cm thick, high entry ceramic disk was sealed onto the pedestal of the triaxial cell. The disk has small pores and allows the passage of water but resists the flow of air and in this way serves to separate the pore-air and pore-water pressures. So long as the difference between the pore-air and pore-water does not exceed the “air entry value” of the disk, there is a continuous column of water from the specimen to the pore-water pressure transducer below the porous disk and the pore-water pressure can then be independently controlled and measured.

PORE-AIR PRESSURE CONTROL

A special hydrophobic membrane was used to control the pore-air pressure. The hydrophobic membrane was fitted between the two parts of a specially designed top cap. The hydrophobic membrane allows the passage of air but resists water flow. As long as the difference between the pore-water and pore-air pressures is less than the capacity of the membrane, there will be no water flow from the top cap to the air pressure line.

Testing procedure

The testing procedure consisted of three main tests. The difference between the tests was the saturation procedure and application of the stresses.

TEST SERIES 1: INCREASING AIR PRESSURE

The first test series was a multistage triaxial drained test. After the specimen was prepared and saturated, the stresses associated with the first stage of the test were applied through an isotropic consolidation procedure and the specimen was allowed to consolidate under the applied stresses. [Table 2.5](#) shows the stresses

Table 2.5 Applied stresses and stress state variables for specimen 1 (test series 1).

Stage	σ_3 (kPa)	u_o (kPa)	u_w (kPa)	$(\sigma_3 - u_a)$ (kPa)	P_f (kPa)	r_f (kPa)	q_f (kPa)
1	400	100	100	300	762.7	0	462.7
2	400	150	100	250	815.1	50	565.1
3	400	200	100	200	771.9	100	571.9
4	400	250	100	150	703.7	150	557.3
5	400	300	100	100	595.4	200	495.4

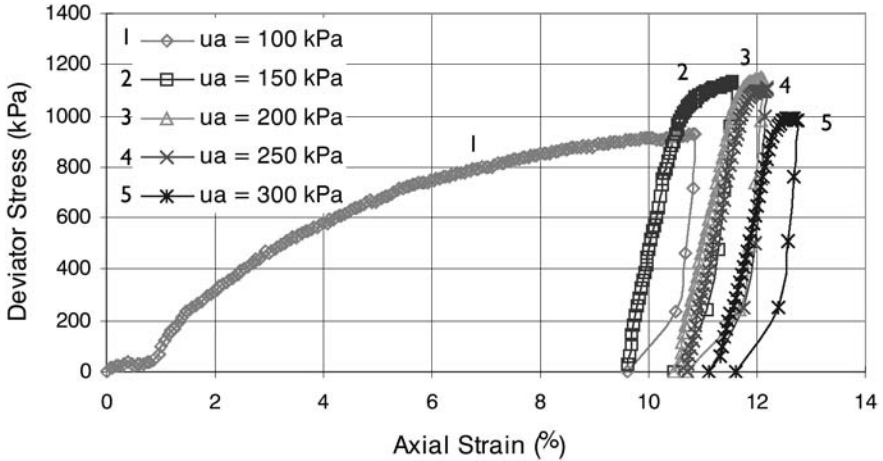


Figure 2.12 Change in shear strength with increasing air pressure for specimen 1 (test series 1).

and stress state variables associated with the five stages of loading for which the air pressure was increased in steps. After consolidation, when there was no further volume change detected by the back pressure controller, the specimen was loaded under a constant strain rate of 0.042 mm/h. Readings were taken of strain and deviator stress until the deviator stress passed the peak point. The peak point was recognised as the point after which the deviator stress versus axial strain curve became nearly horizontal (Figure 2.12). After that, the deviator stress was reduced to zero in a few steps while recording the changes in axial strain at the end of each step. Then the stresses associated with the next stage of loading were applied and the consolidation and shear tests were repeated with the new set of stresses. The procedure was repeated for each successive stage of loading according to Table 2.5. At the end of each stage of loading, a part of the axial strain was recovered while an irrecoverable part remained in the sample.

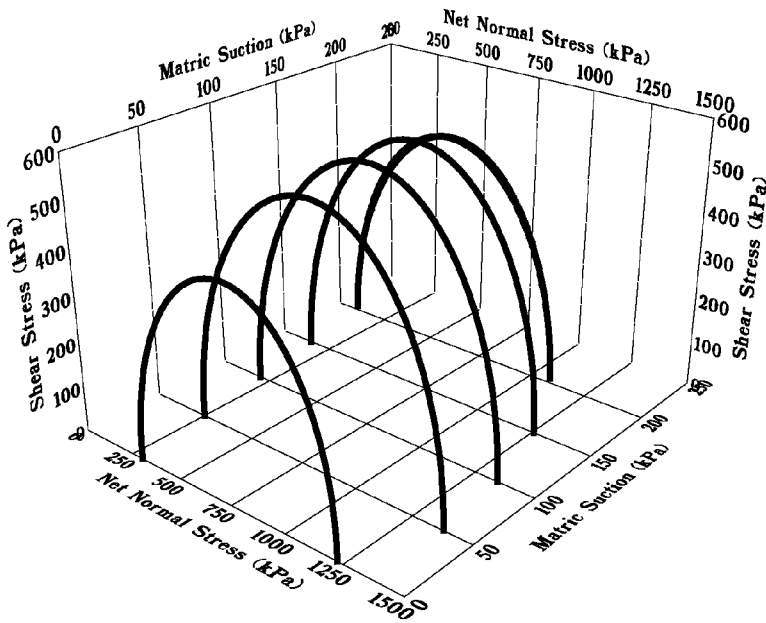


Figure 2.13 Mohr circles for specimen 1 (test series 1: increasing air pressure).

Figure 2.12 shows the change in the shear strength with increasing the air pressure and the corresponding Mohr circles are shown in Figure 2.13. The results show that as the air pressure increased, the water content of the soil decreased (the soil became dryer) and the shear strength of the soil increased. Figures 2.12 and 2.13 also shown that as the air pressure increased the shear strength increased to a peak value and then decreased. In fact, the strength decreased when the air pressure was increased beyond a limiting value. The results show that for the soil tested, for variation of the air pressure up to about 150 kPa (1.5 bar), the failure envelope was more or less planar, however, at high values of air pressure, the failure envelope became non-linear.

TEST SERIES 2: INCREASING SUCTION

The second test series was a multistage triaxial drained test in which the effect of variation of only matric suction on the shear strength of the soil was studied. This test series comprised three stages at which water pressure, u_w , was kept constant and σ_3 and u_a were changed so that the net normal stress, $(\sigma_3 - u_a)$, remained constant (Table 2.6). The associated stress state variables are also shown in Table 2.6. The testing procedure was the same as for test series 1. Figure 2.14 shows the variation of the shear strength as a consequence of increasing matric suction and the Mohr circles are shown in Figure 2.15. It is

Table 2.6 Stress state variables for specimen 2 (test series 2: increasing suction).

Stage	σ_3 (kPa)	u_o (kPa)	u_w (kPa)	$(\sigma - u_a)$ (kPa)	p_f (kPa)	r_f (kPa)	q_f (kPa)
1	250	100	50	150.0	541.8	50.0	391.8
2	350	200	50	150.0	608.3	150.0	458.3
3	500	350	50	150.0	642.3	300.0	492.3

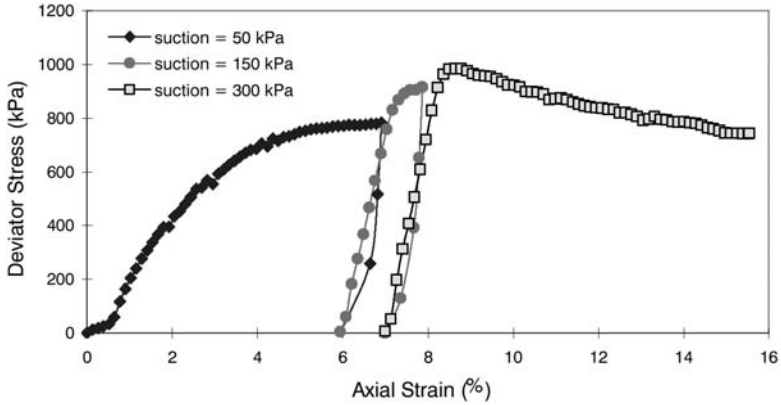


Figure 2.14 Change in shear strength due to increase in suction for specimen 2 (test series 2).

shown that the shear strength increased with increasing matric suction. The results show that the failure envelope for variation of suction up to 300 kPa is nearly linear.

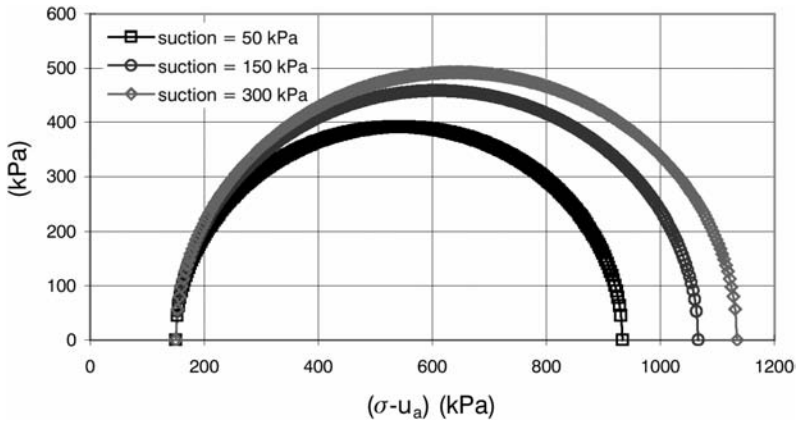


Figure 2.15 Mohr circles for specimen 2 (test series 2: increasing suction).

Table 2.7 Stress state variables for specimen 3 (test series 3: saturated soil).

Stage	σ_3 (kPa)	u_w (kPa)	$(\sigma - u_w)$ (kPa)	P_f (kPa)	r_r (kPa)	q_f (kPa)
1	250	100	150.0	393.0	0.0	243.0
2	400	100	300.0	733.0	0.0	433.0
3	550	100	450.0	1014.3	0.0	564.3

TEST SERIES 3: SATURATED SOIL

The third test series comprised a multistage triaxial drained test on saturated specimens. The specimen was initially saturated by a saturation ramp test and then the stresses for the first stage of testing were applied in an isotropic consolidation test. Table 2.7 shows the stresses and stress state variables associated with the three stages of loading for the saturated specimen. After consolidation, when there was no further volume change detected by the back pressure controller, the specimen was loaded at a constant strain rate. Figure 2.16 shows the change in the shear strength of the saturated soil with change in confining pressure and the Mohr circles are shown in Figure 2.17. The failure envelope is linear for the saturated soil.

Discussion of the results

Comparison of the results of the numerical analysis with the measured values of air losses shows that the numerical model is capable of predicting the air flow from the tunnel face and walls with a high accuracy. The divergence of the calculated air losses from the measured values on two occasions (locations 1 and 2 in Figure 2.11) was due to the application of a second layer of mortar or shotcrete to the inner surface of the initial shotcrete layer. There was no detailed information on the properties of the mortar, the duration of the construction process and the time for the application of the second layer of shotcrete along the tunnel length. Obviously, the second layer of shotcrete was younger and had higher permeability than the first layer, which was older and less permeable at the time of installation of the second layer. Furthermore, at location 2 in Figure 2.11, at a chainage of about 180 metres, the second layer of shotcrete was applied only at the tunnel crown. Inevitably, this led to a discrepancy between the measured and calculated air losses from the tunnel perimeter walls and the total losses. Although this difference was expected, it was understood that this divergence was due to construction activities which were not taken into account in the numerical model.

On the other hand, this effect was expected to be temporary because, as shown in Figure 2.18, the rapid reduction in the permeability of shotcrete occurs in the first few weeks after installation, and after that the rate of reduction in

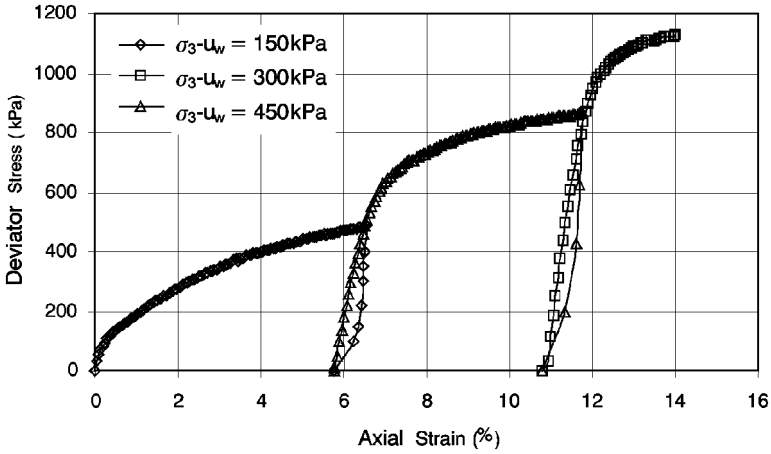


Figure 2.16 Variation in shear strength due to increase in effective normal stress for specimen 3 (test series 3: saturated soil).

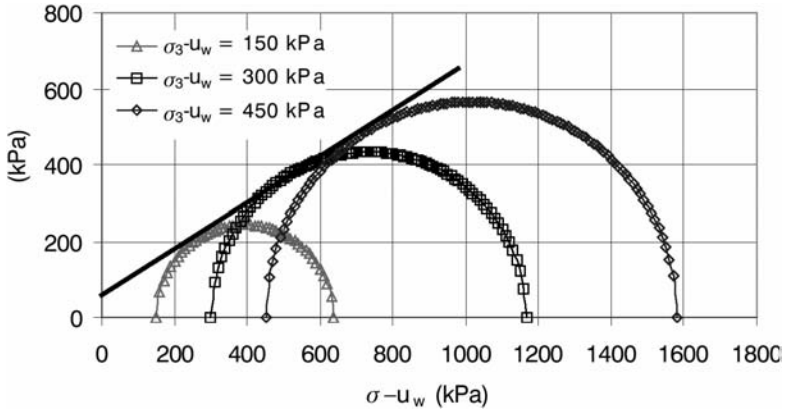


Figure 2.17 Mohr circles for specimen 3 (test series 3: saturated soil).

permeability decreases dramatically. Therefore, as the two shotcrete layers became older, the difference between the permeability of the young and old layers became much smaller, which caused the divergence between the measured and calculated results to dissipate with time, as shown in Figures 2.10 and 2.11.

Figure 2.18 shows the variation of the permeability of shotcrete with time for a period of 2 years, predicted using equation (2.8) and the parameters, A and B , obtained in this study. It is shown that the permeability of shotcrete decreases with time and the rate of reduction at the early age is greater by several orders of magnitude compared with later times.

Figure 2.19 shows the variation of permeability of cement paste with time, reported by Illston.²⁰ Comparison of Figures 2.18 and 2.19 shows that the predicted behaviour of permeability of shotcrete is quite similar to the behaviour

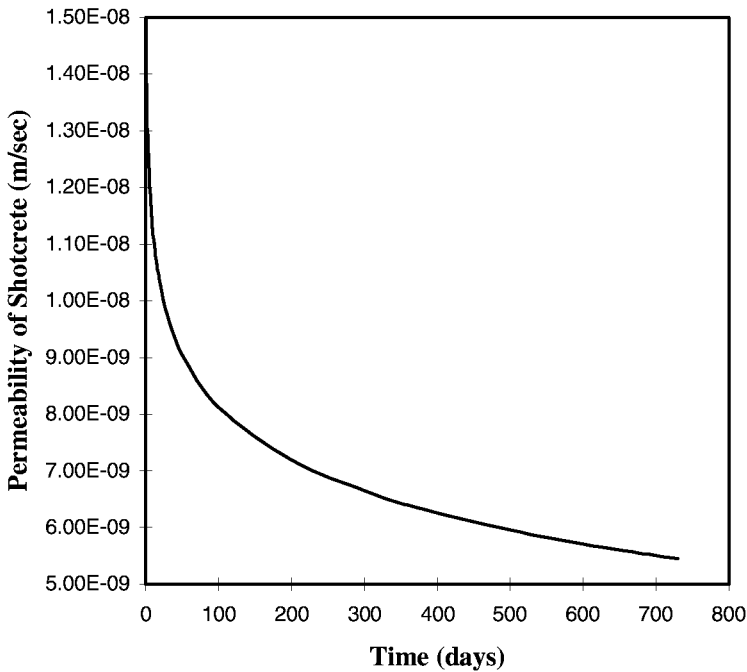


Figure 2.18 Variation of air permeability of shotcrete with time.

of cement paste and concrete, as one would expect. Illston²⁰ argues that in the curing process of cement, the hydration products infill the skeleton structure, blocking the flow channels and so reduce the permeability. During the early age, the hydration proceeds rapidly and so the reduction in permeability is higher. The rate of reduction in permeability reduces by several orders of magnitude in the first few weeks for cement paste (see Figure 2.19).

Mehta and Monterio²¹ state that with increasing age of cement as hydration proceeds, the pore diameter is reduced and the rate of reduction in pore diameter is much higher at the early age. Illston²⁰ explains that similar factors, as with cement paste, control the permeability and strength of concrete and therefore, similar changes in permeability can be expected for concrete and shotcrete. Nyame²² states that the permeability of concrete is reduced with time.

This shows that the predicted behaviour of permeability of shotcrete is reasonable and comparable to similar materials, like cement paste and concrete, which follow similar procedures during the curing process.

This can be further justified by the evidence from the Feldmoching tunnel project. When the tunnel moved into the clay layer, although the exposed area of shotcrete lining increased continuously with increasing tunnel length, a significant reduction occurred in the measured total air loss and air loss from the tunnel walls. This can only be explained by the continuous and rapid reduction in the air permeability of shotcrete with time.

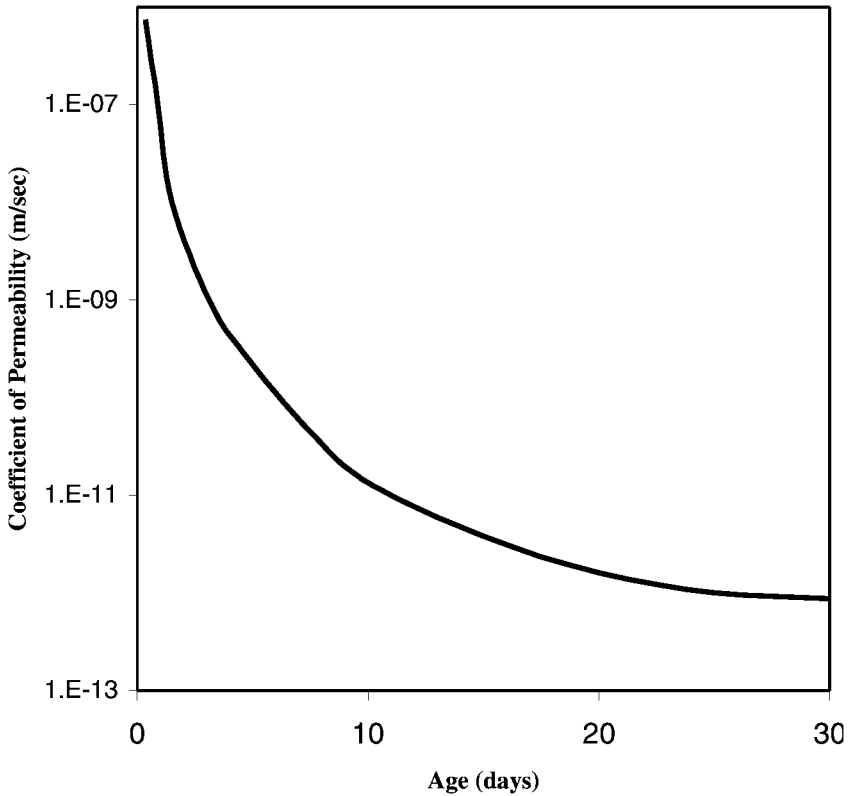


Figure 2.19 Reduction in permeability of cement paste at early age (reconstructed from Illston²⁰).

Inspection of Figures 2.7 and 2.11 shows that after a tunnel length of about 300 m, when the tunnel face moved in the clay layer with a very low permeability, although the tunnel length increased, the air loss from the tunnel walls and the total losses decreased with time. This happened while the perimeter area of the tunnel in the permeable ground remained constant, so the usual engineering assumption of constant permeability of the shotcrete lining would lead to constant air losses. As this was not the case, the explanation of the decrease in the actual air losses is that the time-dependency of the permeability of shotcrete as it cures plays a key role in controlling the amount of air losses.

The results of the experimental study show that the application of air pressure increases the shear strength of the soil. As the air pressure in the tunnel increases, the water content of the soil decreases (the soil becomes dryer) and the shear strength of the soil increases. By increasing the air pressure, the strength of the soil increases to a peak value beyond which further increase in the air

pressure can result in a decrease in the soil strength and reduce the stability of the tunnel.

The results of the tests can be used to predict the change in shear strength of the ground due to the flow of air in compressed air tunnelling. From the results of the experiments, it can be seen that for the practical range of changes in the air pressure, the variation of the shear strength with the stress state variables can be considered to be linear. The internal air pressure applied in driving tunnels under compressed air is usually about one atmosphere and because of safety considerations it is rarely increased beyond two (or at most three) atmospheres. So the assumption of a planar failure envelope for the Mohr circles is reasonable. If the equations for the assumed planar stress point envelope for the soil at failure and the change in the stress state variables are known, then the change in the shear strength of the soil with change in the air pressure can be predicted.

A planar surface was assumed for the stress point failure envelope and a surface fitting technique was used to determine the closest fit planar surface to the results obtained from the laboratory tests. In the equation of the failure surface (equation (2.12)), p_f and r_f were known parameters from the test results (Tables 2.5, 2.6 and 2.7), and the three unknown parameters d' , Ψ' and Ψ^b were to be identified. For the soil specimens tested, the results of the surface fitting analysis indicated that the following values for the unknown parameters gave the best fit between the test results and the assumed planar surface:

$$d' = 56.2$$

$$\Psi' = 28.7^\circ$$

$$\Psi^b = 25^\circ$$

Therefore, for the soil tested, the equation for the failure envelope will be:

$$q_f = 56.2 + p_f \tan(28.7^\circ) + r_f \tan(25^\circ)$$

Figure 2.20 shows the planar failure envelope for the soil tested which is the graphical presentation of equation (2.12).

Conclusion

Selection of an air pressure and supply requirements for tunnelling is currently based on judgement and empirical formulae. The judgements are overly simplistic and the formulae do not account for the true behaviour of the materials.

A numerical model has been developed that can predict air losses from a tunnel driven under compressed air. The model predicts the air losses from the tunnel face as well as from the perimeter walls.

A relationship has been presented for the time-dependency of the air permeability of shotcrete and the parameters of this relationship have been

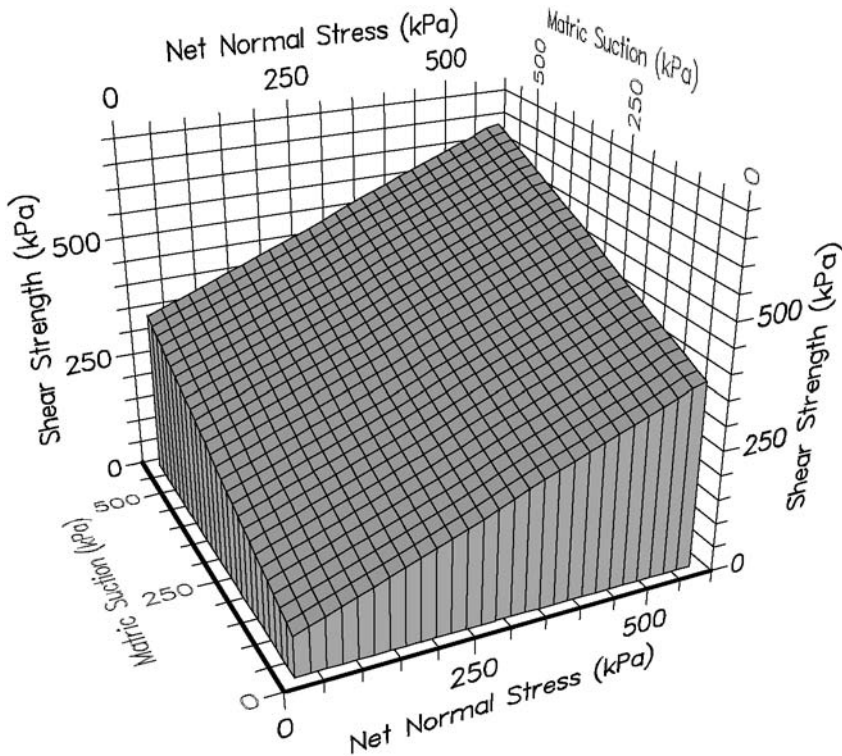


Figure 2.20 Failure envelope for the soil tested in the experiments.

identified using a parameter identification technique from back analysis of some measured data from a tunnel. It was shown that the predicted variation of the permeability of shotcrete as it cures is comparable to that of concrete and cement paste reported in the literature.

A genetic algorithm and weighted least squares approach was used in the optimisation procedure in the identification process. A genetic algorithm has the advantage of simplicity and high efficiency in locating the global optimum solution in the optimisation process.

The calculated and measured air losses from a tunnel were compared. The comparison shows that the established relationship for variation of permeability of shotcrete and the numerical model produce realistic results. The proposed relationship was verified against a case study. However, although the tunnel passed through various soil conditions in this case study, the results of the numerical prediction show the same trend as the measured data in the field. It is recommended that this relationship and the procedure are tested against other case studies but case studies on field measurements in compressed air tunnelling are rare.

Parameters A and B in the proposed equation (2.8) are related to a specific make of shotcrete used in the Feldmoching tunnel in Germany. However, the proposed procedure is generic and can be used for any tunnel driven under compressed air with shotcrete as a temporary or permanent lining.

In this study, an existing theoretical relationship between the permeability of soil to air and water has been used in the numerical model. This relationship does not address all the parameters affecting the air permeability of partially saturated soils. This needs further investigation. A study on the air permeability of partially saturated soils is the subject of current research. However, again, the presented procedure is generic and should an improved relationship emerge, it can easily be incorporated in the numerical procedure.

The change in the shear strength of the soil in compressed air tunnelling has been studied qualitatively and quantitatively. A method has been presented to quantify the change in shear strength of the soil due to the flow of the compressed air through the ground. The method is based on the integration of the results of the testing procedure and the numerical analysis described above. The numerical model can predict the change in the pore-air pressure in the ground due to the air flow through the ground, from which the change in the state of stress in the soil (represented by the stress state variables) can be calculated. A series of tests can be carried out on the soil samples representative of the *in situ* soil to study the shear strength behaviour of the ground qualitatively. The equation for the failure envelope of the soil, which describes the change in the shear strength of the soil with the change in the stress state of the soil, can be obtained from results of the tests. By integration of the results of the numerical model with the laboratory test results within the established procedure, the effects of the change in the internal air pressure in the tunnel on the shear strength of the soil can be estimated. This is particularly useful if a laboratory testing programme is required for the investigation of a site for tunnelling under compressed air.

The results of the tests indicate that the application of internal air pressure during the excavation of a tunnel, besides being an internal support to the excavation, leads to an increase in the strength of the soil. However, increasing the air pressure beyond a certain limit could lead to a decrease in soil strength and cause a stability problem for the excavation. This is consistent with tunnelling practice and is commonly referred to as a blow-out.

The method proposed in this study can be used to provide a more realistic estimation of air losses during compressed air tunnelling. This is critical information for planning and design of underground construction when compressed air is considered as a method of controlling groundwater. The proposed method can also be used to assess the risk of tunnel collapse and blow-out. It improves current understanding of the interaction between this tunnelling method and the ground.

Acknowledgements

This work forms part of a wider study of numerical modelling of compressed air tunnelling. The author would like to acknowledge his gratitude to Professor H.J. Bösch from the Technical University of Munich for his valuable co-operation regarding the field data and to the Ministry of Higher Education of Iran and CVCP for financial support for this research.

References

- 1 Javadi, A.A. and Snee, C.P.M. New method in predicting air losses in compressed air tunnelling. *Proc. Tunnelling '97 Conf. Institution of Mining and Metallurgy*, London, 2–4 September, 1997, pp. 57–69.
- 2 Fuchsberger, M. and Semprich, S. Air flow through partially saturated soil, *Proc. First Int. Conference on Unsaturated Soils*, Paris, France, vol. 1, Sept. 1995, pp. 491–497.
- 3 Kramer, J. and Semprich, S. Erfahrungen über Druckluftverbrauch bei der Spritzbeton bauweise. Taschenbuch für den Tunnelbau, 1989, pp. 91–153.
- 4 Karlsson, N.G. A complicated tunnel driving method, *Tunnels and Tunnelling*, 1973; **5**(8):452–457.
- 5 Krabbe, W. Die wasserhaltung beim schildvortrieb durch grundwasserabsertung und druckluft, In: Hamburg Editor. *Baugrundtagung*. Deutsche Gesellschaft fuer Erd-und Grundbau ev Essen, 1968.
- 6 Hoad, R.S. and Gittoes, G.P. Estimation of compressed air losses. *Proc. Conf. Engineering and Health in Compressed Air Work*, CIRIA, 1992, pp. 157–175.
- 7 Atkinson, J.H. and Mair, R.J. Soil mechanics aspects of soft ground tunnelling. *Ground Engineering*, 1981; **14**(5):20–26.
- 8 Schenck, W. and Wagner, H. Luftverbrauch v. Überdeckung beim tunnelvortrieb mit druckluft. *Bautechnik* 2, 1963.
- 9 Hewett, B.H.M. and Johannesson, S. *Shield and Compressed Air Tunnelling*. New York: McGraw-Hill, 1922.
- 10 Glossop, R. The invention and early use of compressed air to exclude water from shafts and tunnels during construction. *Geotechnique*, 1976; **26**(2):253–280.
- 11 Javadi, A.A. Compressed air tunnelling; Geotechnical aspects and numerical modelling, PhD Thesis, University of Bradford, UK, 1998.
- 12 Snee, C.P.M. and Javadi, A.A. Prediction of compressed air leakage from tunnels. *Tunnelling and Underground Space Technology*, 1996; **11**(2):189–195.
- 13 Javadi, A.A., Farmani, R., Toropov, V.V. and Snee, C.P.M. Identification of parameters for air permeability of shotcrete tunnel lining using a genetic algorithm. *Journal of Computers and Geotechnics*, 1999; **25**(1):1–24.
- 14 Holland, J.H. *Application of Naturl and Artificial Systems*. Ann Arbor: University of Michigan Press, 1975.
- 15 Goldberg, D.E. *Genetic algorithms in search, optimisation and machine learning*, Boston, MA: Addison-Wesley, 1989.
- 16 Fredlund, D.G., Rahardjo, H. and Gan, J.K.M. Non-linearity of strength envelope for unsaturated soils. *Proc. 6th Int. Conf. Expansive Soils*, New Delhi, India, 1–3 December 1987, vol. 1, pp. 49–54.

- 17 Fredlund, D.G. and Rahardjo, H. *Soil Mechanics for Unsaturated Soils*. New York: John Wiley, 1993.
- 18 Donald, I.B. Shear strength measurements in unsaturated non-cohesive soils with negative pore pressures. *Soil Mechanics and Foundation Engineering, Proc. 2nd Australia-New Zealand Conf.*, Christchurch, New Zealand, 1956, pp. 200–205.
- 19 Ho, D.Y.F. and Fredlund, D.G. A multi-stage triaxial test for unsaturated soils. *ASTM Geotech. Testing J.*, 1982; **5**(1/2):18–25.
- 20 Illston, J.M. *Construction Materials, Their Nature and Behaviour*, London: Chapman and Hall, 1994.
- 21 Mehta, P.K. and Monterio, P.J.M. *Concrete: Structure, Properties and Materials*, London, Prentice-Hall International, 1993.
- 22 Nyame, B.K. Permeability and pore structure of hardened cement paste and mortar, PhD Thesis, University of London, King's College, 1979.

Chapter 3

A general finite element model for wave-seabed-structure interaction

D.S.Jeng

Introduction

The mechanism of wave-seabed-structure interaction is an important concern for designing offshore facilities, such as pipelines, anchors, marine platforms and breakwaters. In the field, concrete armour blocks at the toes of many marine structures have been found to subside into the seabed; wave-induced liquefaction has been identified as the reason for this problem (Silvester and Hsu, 1989). Moreover, it has been reported that some such structures have possibly failed due to seabed instability (Lundgren *et al.*, 1989; Silvester and Hsu, 1989).

Waves propagating in shallow water create a significant dynamic pressure on the sea floor. This pressure field induces a stress field and associated pore water pressure fluctuations within the seabed. With excess pore-pressure and diminishing vertical effective stresses, part of the seabed may become unstable or even liquefied. This causes a *quicksand* effect in which external loads cannot be supported. Furthermore, when liquefaction occurs, the soil particles are likely to be carried away as a fluid by any prevailing bottom current or by mass transport due to the wave action.

Two mechanisms of wave-induced soil response have been observed in laboratory experiments and field measurements (Zen and Yamazaki, 1990; Nago *et al.*, 1993). The first is caused by the *progressive* development of excess pore pressure that occurs after a certain number of wave cycles. This type of soil response is similar to that induced by an earthquake. The second is generated by the *oscillatory* nature of the excess pore pressure, which appears periodically many times during a storm sequence. In most cases, the wave-induced soil response is oscillatory in nature except for some special cases of non-cohesive sediments with loose to medium density (Seed and Rahman, 1978). In this study, we will focus on the wave-induced oscillatory soil response.

Many variables influence the wave-induced soil response in a porous seabed; anisotropy in soil behaviour is an important issue that must be considered in the wave-seabed interaction problem. In the field, most marine sediments display a certain degree of anisotropy, with different elastic properties in different directions, owing to the manner of their deposition, particle shape and stress

history. However, many materials show more limited forms of anisotropy. A cross-anisotropic material is an example. This material has the same properties in all horizontal directions, but different properties in the vertical direction. When soils are deposited vertically and subjected to equal horizontal stresses, they will exhibit a vertical axis of symmetry and be transversely isotropic (Pickering, 1970; Graham and Houlsby, 1983).

The mechanism of the wave-seabed-structure interaction has been studied from the aspect of either coastal or geotechnical engineering. The wave forces (pressure) acting on the marine structure have been the main concerns of coastal engineering. Although some researches have considered the sediment transport around the structures, only the movement of sediment along the seabed surface was considered. On the other hand, geotechnical engineers have focused on the distribution of stress under the structure loading, rather than wave loading. However, the interaction between wave, structure and seabed has rarely been linked from both the coastal and the geotechnical point of view. This study attempts to link wave loading, seabed response, and marine structure in a single model.

This chapter is divided into two parts. In the first part, a general finite element model for the wave-seabed-structure interaction is proposed. The full finite element formulations are presented. Also, a detailed numerical procedure used for the simulation of wave-seabed-structure interaction is included. In the second part, two practical examples (pipelines and caissons) are used to demonstrate the application of the proposed model.

Theoretical formulations

Boundary value problem

In this study, the consolidation equation (Biot, 1941), which has been generally accepted as the governing equation for the flow of a compressible pore fluid in a compressible porous medium, is adopted to treat the wave-seabed-structure interaction with variable permeability as

$$K\nabla^2 p - \gamma_w n' \beta \frac{\partial \varepsilon}{\partial t} = \gamma_w \frac{\partial \varepsilon}{\partial t}, \quad (3.1)$$

where p is the wave-induced pore pressure, K is permeability in all directions, n' is soil porosity, and γ_w is the unit weight of the pore fluid.

In equation (3.1), the volumetric strain (ε) and compressibility of pore fluid (β) are defined as

$$\varepsilon = \frac{1}{K_{w0}} + \frac{1-S}{P_{w0}} \quad \text{and} \quad \varepsilon = \frac{\partial u}{\partial x} + \frac{\partial w}{\partial z}, \quad (3.2)$$

where S is the degree of saturation; K_{w0} is the true bulk modulus of pore water, which is normally taken as 2×10^9 N/m²; P_{w0} is the absolute static water pressure ($= \gamma_w d$, d is the water depth).

It is well known that the elastic properties of an isotropic material can be described by two parameters: Young's modulus (E) and Poisson's ratio (μ). However, the elastic properties of an anisotropic material can be described by five parameters (Pickering, 1970):

- Young's modulus (E_x and E_z);
- Poisson's ratios, μ_{xx} and μ_{xz} ;
- The modulus of shear deformation in the vertical plane (G_z)

Another two dependent parameters, Poisson's ratio (μ_{zx}) and the shear modulus in the horizontal plane (G_x) can be interrelated by

$$\frac{\mu_{zx}}{\mu_{xz}} = \frac{E_x}{E_z} = n \quad \text{and} \quad G_x = \frac{E_x}{2(1+\mu_{xx})}. \quad (3.3)$$

It is noted that the non-dimensional parameter n is equal to one for an isotropic soil.

The shear modulus in the vertical plane, G_z , can be expressed in terms of Young's modulus E_z as

$$G_z = mE_z, \quad (3.4)$$

where m is an anisotropic constant (Gazetas, 1982) that is equal to $E/2(1+\mu)$ for an isotropic soil. Now, the five anisotropic parameters listed above can be changed to E_z , μ_{xx} , μ_{xz} , n and m . The possible ranges of the above parameters for different materials have been discussed in (Jeng, 1997a, 1997b).

Based on the generalised Hooke's law (Pickering, 1970) and under the condition of plane strain, the incremental effective stresses and strains in a cross-anisotropic seabed can be expressed as

$$\sigma'_x = E_z \left(C_{11} \frac{\partial u}{\partial x} + C_{13} \frac{\partial w}{\partial z} \right), \quad (3.5a)$$

$$\sigma'_z = E_z \left(C_{13} \frac{\partial u}{\partial x} + C_{23} \frac{\partial w}{\partial z} \right), \quad (3.5b)$$

$$\tau_{xz} = nE_z \left(\frac{\partial u}{\partial z} + \frac{\partial w}{\partial x} \right) = \tau_{zx}, \quad (3.5c)$$

In (3.5), and are the effective normal stresses in the x - and z -directions, respectively, and τ_{xz} is the shear stress in the x - z plane. It is noted that compressive stresses are taken as positive here. Therefore, the effective stress is defined by

$$\begin{Bmatrix} \sigma_x \\ \sigma_z \end{Bmatrix} = \begin{Bmatrix} \sigma'_x \\ \sigma'_z \end{Bmatrix} + p, \quad (3.6)$$

in which σ_x and σ_z are the total stresses in the x - and z -directions, respectively.

In (3.5), the C_{ij} coefficients are given by

$$C_{11} = n(1 - \mu_{xz}\mu_{zx}) / \Delta, \quad (3.7a)$$

$$C_{13} = n(1 + \mu_{xx}) / \Delta, \quad (3.7b)$$

$$C_{33} = m(1 - \mu_{xx}^2) / \Delta, \quad (3.7c)$$

$$\Delta = (1 + \mu_{xx})(1 - \mu_{xx} - 2\mu_{xz}\mu_{zx}). \quad (3.7d)$$

Based on the concept of effective stresses, the equations of overall equilibrium for a poro-elastic medium with the absence of body forces can be expressed as

$$\frac{\partial \sigma'_x}{\partial x} + \frac{\partial \tau_{xz}}{\partial z} = -\frac{\partial p}{\partial x} \quad \text{and} \quad \frac{\partial \tau_{xz}}{\partial x} + \frac{\partial \sigma'_z}{\partial z} = -\frac{\partial p}{\partial z}, \quad (3.8)$$

It is noted that the governing equations (1) and (8) do not include inertial effects. In general, such effects can be ignored for most cases with small amplitude waves (Jeng *et al.*, 1999). It is also noted that the body force (the soil self-weight) is ignored in this study.

Substituting (3.5) into (3.8), the equations for the force equilibrium in a porous media can be re-written as

$$E_z \left[C_{11} \frac{\partial^2 u}{\partial x^2} + m \frac{\partial^2 u}{\partial z^2} + (C_{13} + m) \frac{\partial^2 w}{\partial x \partial z} \right] = -\frac{\partial p}{\partial x}, \quad (3.9a)$$

$$E_z \left[m \frac{\partial^2 w}{\partial x^2} + C_{33} \frac{\partial^2 w}{\partial z^2} + (C_{13} + m) \frac{\partial^2 u}{\partial x \partial z} \right] = -\frac{\partial p}{\partial x}, \tag{3.9b}$$

in the x - and z -directions, respectively.

Appropriate boundary conditions are required to solve the governing equations (3.1) and (3.9). For a porous flow in a seabed, the boundary conditions at the impermeable rigid bottom require that the dynamic fluctuations of all the physical quantities vanish, i.e.,

$$u = w = \frac{\partial p}{\partial z} = 0 \text{ at } z = -h. \tag{3.10}$$

For the lateral boundaries of the computation domain, since the existence of the structure only affects the wave-induced soil response near the structure, the disturbed components due to the existence of a structure will vanish far away from the structure. Thus, the soil response at these points should be that induced by waves without any structures (see Yamamoto *et al.*, 1978; Jeng, 1997b). These lateral boundary conditions should be determined before including the structure into the whole model. The details of the numerical procedure will be described in the section headed ‘Numerical procedure’.

Besides the bottom boundary conditions, the seabed surface conditions are also required for the wave-seabed-structure interaction. Since these boundary conditions will vary with the type of structure, they will be described in each example.

General finite element model for wave-seabed-structure interaction (GFEM-WSSI)

Since the wave-induced oscillatory soil response fluctuates periodically in the temporal domains under harmonic wave loading, the wave-induced soil response can be assumed to take the form

$$\begin{Bmatrix} p(x, z; t) \\ u(x, z; t) \\ w(x, z; t) \end{Bmatrix} = \begin{Bmatrix} p_r(x, z) \\ u_r(x, z) \\ w_r(x, z) \end{Bmatrix} + i \begin{Bmatrix} p_c(x, z) \\ u_c(x, z) \\ w_c(x, z) \end{Bmatrix} e^{i\omega t}, \tag{3.11}$$

where subscripts “r” and “c” represent the real and imaginary parts of the soil response, respectively.

Substituting (3.11) into (3.1) and (3.9), then directly applying the Galerkin method (Zienkiewicz and Taylor, 1989) to these equations, the finite element analytical formulations can be expressed in matrix form as

$$\int_S N_i [Q_e] dS = \int_V B_1^T D_1 B_1 dV [P] + \int_V B_2^T D_2 B_2 dV [P] + \int_V B_3^T D_3 B_3 dV [U] \quad (3.12)$$

$$\int_S N_i [F_e] dS = \int_V B_4^T D_4 B_4 dV [U] + \int_V B_5^T D_5 B_5 dV [P] \quad (3.13)$$

in which

$$[Q_e] = \begin{bmatrix} (q_{nr})_1 & 0 & \Lambda & (q_{nr})_{n_e} & 0 \\ 0 & (q_{nc})_1 & \Lambda & 0 & (q_{nc})_{n_e} \end{bmatrix} \quad (3.14)$$

$$[F_e] = \begin{bmatrix} (f_{xr})_1 & 0 & (f_{xr})_1 & 0 & \Lambda & (f_{xr})_{n_e} & 0 & (f_{xr})_{n_e} & 0 \\ 0 & (f_{xc})_1 & 0 & (f_{zc})_1 & \Lambda & 0 & (f_{xc})_{n_e} & 0 & (f_{zc})_{n_e} \end{bmatrix} \quad (3.15)$$

$$\left(\begin{matrix} q_{nr} \\ q_{nc} \end{matrix} \right)_i = \left(\frac{K}{\gamma_w} \left\{ \frac{\partial P_r}{\partial x} \right\} n_x + \frac{K}{\gamma_w} \left\{ \frac{\partial P_r}{\partial z} \right\} n_z \right)_i \quad (3.16)$$

$$\left(\begin{matrix} f_{xr} \\ f_{xr} \\ f_{xc} \\ f_{zc} \end{matrix} \right) = \left(\begin{matrix} S_{xr} \\ S_{xr} \\ T_r \\ T_c \end{matrix} \right) n_x + \left(\begin{matrix} T_r \\ T_c \\ S_{xr} \\ S_{zc} \end{matrix} \right) n_z \quad (3.17)$$

$$[P] = \begin{bmatrix} (P_r)_1 & 0 & \Lambda & (P_r)_{n_e} & 0 \\ 0 & (P_c)_1 & \Lambda & 0 & (P_c)_{n_e} \end{bmatrix} \quad (3.18)$$

$$[U] = \begin{bmatrix} (U_r)_1 & 0 & (W_r)_1 & 0 & \Lambda & (U_r)_{n_e} & 0 & (W_r)_{n_e} & 0 \\ 0 & (U_c)_1 & 0 & (W_c)_1 & \Lambda & 0 & (U_c)_{n_e} & 0 & (W_c)_{n_e} \end{bmatrix} \quad (3.19)$$

where n_e is the number of nodes per element, N_i is the shape function of the i -th node, and coefficient matrices B_i and D_i can be derived from the governing equations.

Numerical procedure

The present model is able to simulate the wave-seabed interaction problem as well as the wave-seabed-structure interaction by the general finite element model described in the previous section with different meshes.

The first step to solve the wave-seabed-structure interaction problem is to obtain the lateral boundary conditions. To do so, the wave-seabed interaction can be solved by employing the principle of repeatability (Zienkiewicz and Scott, 1972). As shown in Figure 3.1, the wave-induced pore pressure and soil displacements at sections AA and BB should be identical, because the seabed is under a periodical loading. That is,

$$\begin{aligned} p(x = AA, z; t) = p(x = BB, z; t), u(x = AA, z; t) = u(x = BB, z; t) \\ \text{and } w(x = AA, z; t) = w(x = BB, z; t). \end{aligned} \quad (3.20)$$

This concept is particularly convenient for periodical loading such as the present problem (Jeng *et al.*, 1998).

Once the lateral boundary conditions are obtained, the whole wave-seabed-structure problem can be solved with the boundary conditions for different types of structures. Because a concentration of stresses is to be expressed, the local refinement of the finite element mesh always has to be taken into account in the region near a structure.

To ensure the accuracy of numerical calculations without increasing the finite element mesh, an eight-node element is used in the presented model. An isoparametric element is used near the structures, and a rectangular element is used in the seabed.

Applications

To demonstrate the application of the proposed general finite element model, two classic marine structures are used as examples in this study a buried pipeline and a caisson-type breakwater. Based on the model, but with different finite element meshes, the wave-seabed-structure interaction problem can be solved.

Wave-seabed-pipe interaction

Offshore pipelines are extensively used to transport hydrocarbons to shore. There is also widespread application for ocean disposal of municipal waste. Design of marine pipelines with respect to their stability is a complicated problem, and improved design represents one of the main areas currently targeted by oil majors for reducing the costs of offshore oil and gas developments. Wave-induced failure of offshore pipelines has been well documented (Herbich, 1977). Failure may occur as a result of wave-induced scour, liquefaction, or slope instability. To protect the pipeline from possible damage caused by waves or

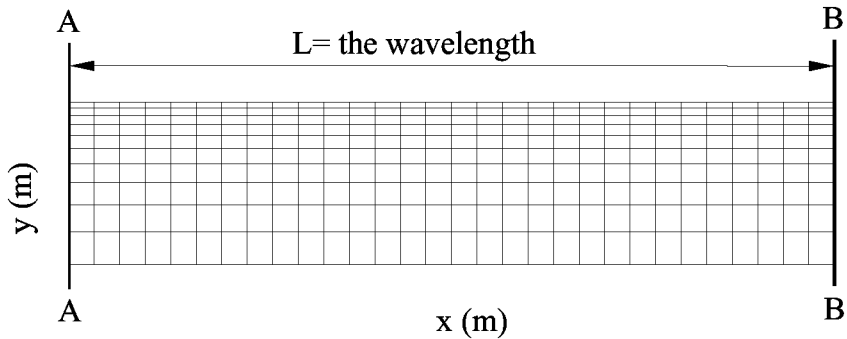


Figure 3.1 Principle of repeatability.

currents, it is common to use an appropriate covering layer with rock-fill or other coarse material. This expenditure often accounts for a large proportion of the total budget of a pipeline project.

Various numerical investigations for the wave-seabed-pipe interaction have been carried out in the past. Cheng and Liu (1986) proposed a boundary element model to examine the wave-induced pore pressure and effective stresses around a buried pipeline. They discovered the great influence of the soil parameters on the pore pressure concentration around the buried pipeline. Later, Magda (1996, 1997, 2000) carried out a series of studies on the wave-induced pore pressure and lift forces on buried pipelines. These studies were carried out using finite element modelling. Magda considered a similar case to Cheng and Liu (1986) with a wider range in the degree of saturation. In both Cheng's model and Magda's model, they considered the pipeline to be buried in a region surrounded by impermeable walls. In fact, realistically, the buried pipeline is surrounded by a cover layer, which consists of a coarser material. Thus, the lateral boundary conditions for the wave-seabed-pipe interaction problem should be permeable, rather than using impermeable walls.

Recently, Jeng and Cheng (2000) proposed a finite difference method in a curvilinear coordinate system to investigate the wave-induced seabed instability around a buried pipeline. They found that the soil particles always move away from the pipe when the wave crest passes the centre of the pipeline. However, their model did not work for finer materials (for example, permeability smaller than 5×10^{-4} m/sec) under a certain combination of wave and soil conditions. Based on the numerical model proposed by Jeng *et al.* (1998), the mechanism of the wave-seabed-pipe interaction has been investigated (Jeng and Lin, 1999, 2000; Postma, 2000; Jeng, 2001; Jeng *et al.*, 2001b). Some important results will be presented in this section.

Application of GFEM-WSSI

This section, will demonstrate the application of the proposed general finite element model on the wave-seabed-pipe interaction problem. The configuration of the problem is depicted in [Figure 3.2](#). In the problem, the boundary condition at the seabed surface can be written as

$$\sigma'_z = \tau_{xz} = 0 \quad \text{and} \quad p = \frac{\gamma_w H}{2 \cosh kd} \cos(kx - \omega t) = p_0 \text{Re} \left[(\cos kx + i \sin kx) e^{i\omega t} \right] \quad (3.21)$$

where p_0 denotes the amplitude of the wave pressure at the surface of the seabed, d is water depth, H is the wave height, k is the wave number and ω is the wave frequency. In (3.21), “Re” represents the real part of the function in the brackets.

Since there is no flow through the pipeline wall, thus the pressure gradient on the surface of the pipeline $r=R$, i.e.,

$$\frac{\partial p}{\partial n} = 0 \quad \text{at} \quad r = \sqrt{(x - x_0)^2 + (z - z_0)^2} = R \quad (3.22)$$

where x_0 and z_0 denote the co-ordinates of the centre of the pipe and n is the normal direction to the surface of the pipeline. As mentioned previously, because a concentration of stresses is expected, the local refinement of the finite element mesh always has to be taken into account in the region near the structure, as shown in [Figure 3.3](#).

To verify the proposed finite element model for the wave-seabed-pipe interaction, the experimental data from Turcotte *et al.* (1984) is used here ([Figure 3.4](#)). The experimental study was conducted in the J.H. Depress Hydraulic Laboratory at Cornell University. The input data of the experiment are listed in [Figure 3.4](#). As Turcotte *et al.* (1984) reported, the sediment was considered to be uniform and isotropic. Although the case that Cheng and Liu (1986) considered is slightly different from the present study, their results are also included in the example. In [Figure 3.4](#), the solid line represents the present model, • denote the experimental data, and are the results of Cheng and Liu (1986). As seen in the figure, the present model reasonably agrees with the experimental data.

To enhance the current understanding of the mechanism of the wave-seabed interaction in the vicinity of an offshore pipeline, several important parameters will be investigated in this section. The input data for the numerical examples are given in [Table 3.1](#).

Effects of soil characteristics

[Figure 3.5\(a\)](#) demonstrates the difference in pore pressure (p/p_0) between isotropic and cross-anisotropic seabeds of coarse sand. There is a slight difference between the two different soils. An examination around the pipeline

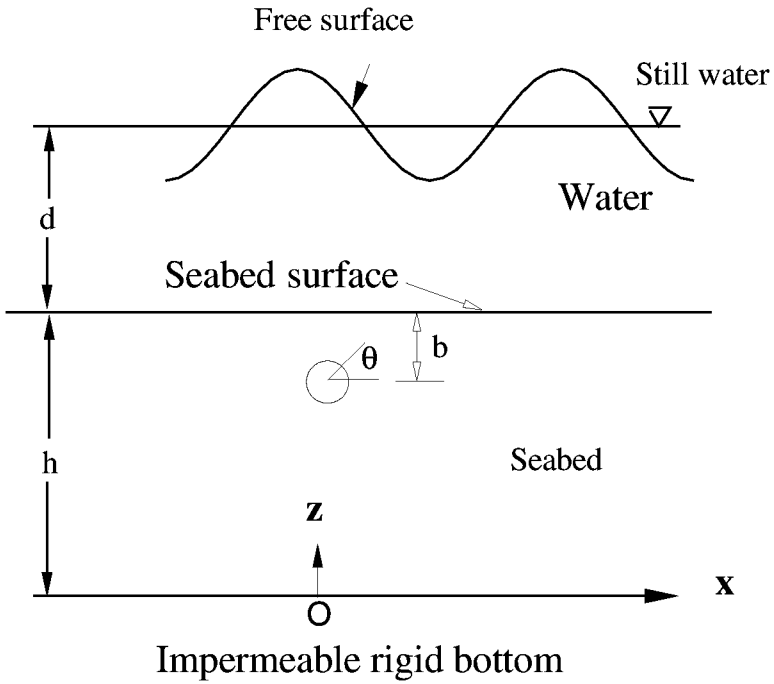


Figure 3.2 Configuration of the wave-seabed-pipe interaction.

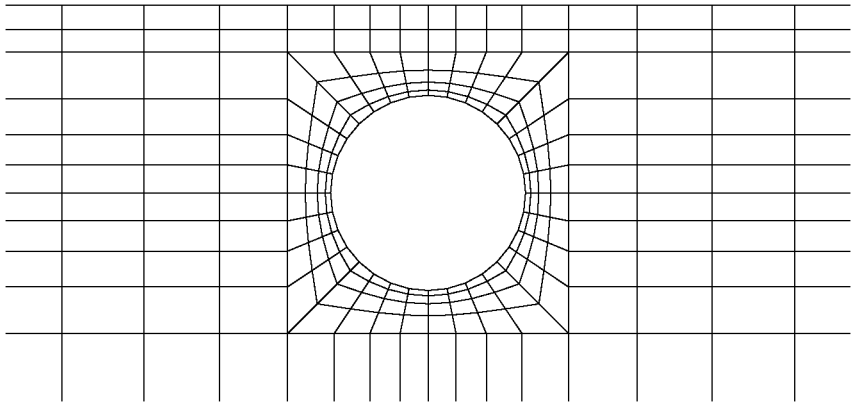


Figure 3.3 Finite element meshes in the vicinity of a buried pipeline.

reveals that the pore pressure around the pipeline is marginally lower around the whole pipe for a cross-anisotropic seabed. The major difference between the two can be seen directly under the lower half of the pipeline where the pore pressure is lowest. It is lowest on the underside of the pipeline because the pore pressure decreases with an increase in the soil depth. An isotropic seabed obviously has

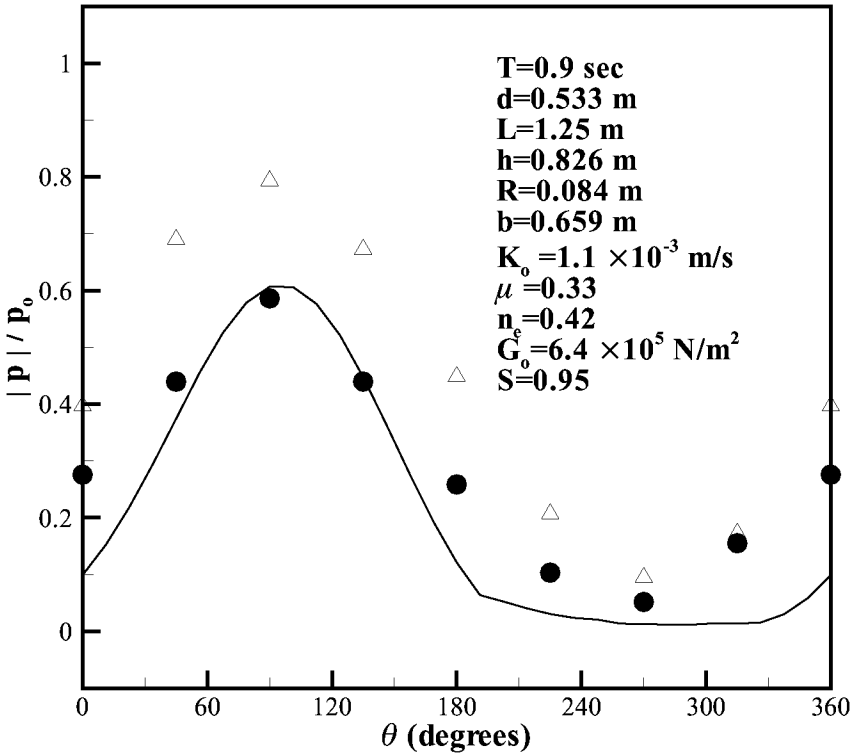


Figure 3.4 Distribution of the wave-induced pore pressure amplitude around the pipe in a uniform seabed. The solid line is the present model, “•” denotes the laboratory data and “△” are the results of Cheng and Liu (1986).

the same properties in all directions, which means that the water will penetrate the pores within the seabed at a constant rate in all directions. However, there is a trade-off between the horizontal and vertical directions of penetration in an anisotropic seabed. Furthermore, it is suspected that the rate of penetration in the horizontal direction is much greater than in the vertical direction, which would obviously result in a lower pore pressure with a subsequent increase in the burial depth of the pipeline.

Figure 3.5(b) shows the pore pressure, p/p_0 , around the buried pipeline in fine sand. The pore pressure follows a very similar path to that of coarse sand with both isotropic and anisotropic soil behaviour. However, the pore pressure is considerably lower as would be expected in fine sand. It is expected that the pore pressure would be less because the fine sand has smaller pores between the individual particles. There is also a significant difference between anisotropic and isotropic seabeds, with a lower pore pressure in an anisotropic seabed. This would also be expected as the properties in the vertical direction are different to those in the horizontal direction. Also, there is a bigger difference between the

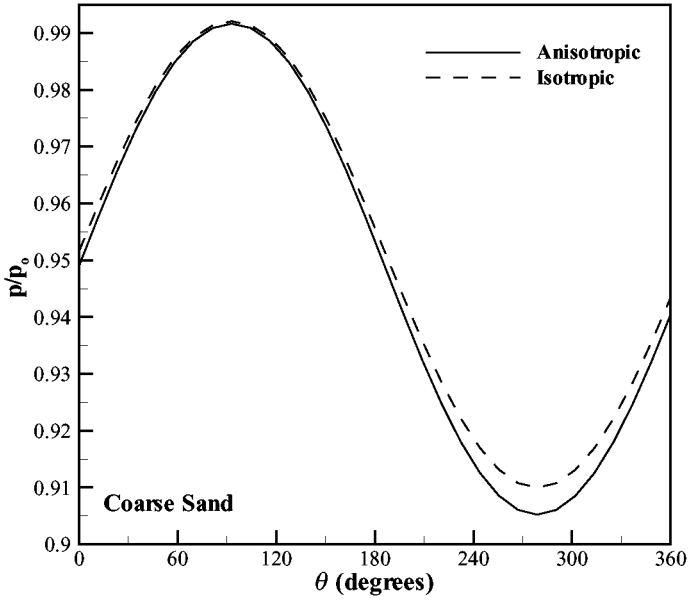
Table 3.1 Input data for case study of wave-seabed-pipe interaction

Wave characteristics	
Wave period T	10.0 sec
Water depth d	20 m
Wavelength L	121.171 m
Wave height H	2 m
Soil characteristics	
Thickness of seabed h	40 m
Poisson's ratio $\mu_{xx}, \mu_{xz}, \mu_{zx}$	0.4 or various
Porosity n'	0.4
Permeability K	10^{-1} m/sec (gravel)
	10^{-2} m/sec (coarse sand)
	10^{-4} m/sec (fine sand)
Young's modulus E_z	2×10^8 N/m ² (gravel)
	7×10^7 N/m ² (coarse sand)
	2×10^7 N/m ² (fine sand)
Degree of saturation S	0.95 – 1.0
Anisotropic constant n	0.4 or various
	m
Geometry of the pipe	
Pipe radius R	0.5 m or various
Burial depth b	0.5 m or various
Centre of the pipe (x_o, z_o)	$(L/2, h-b)$

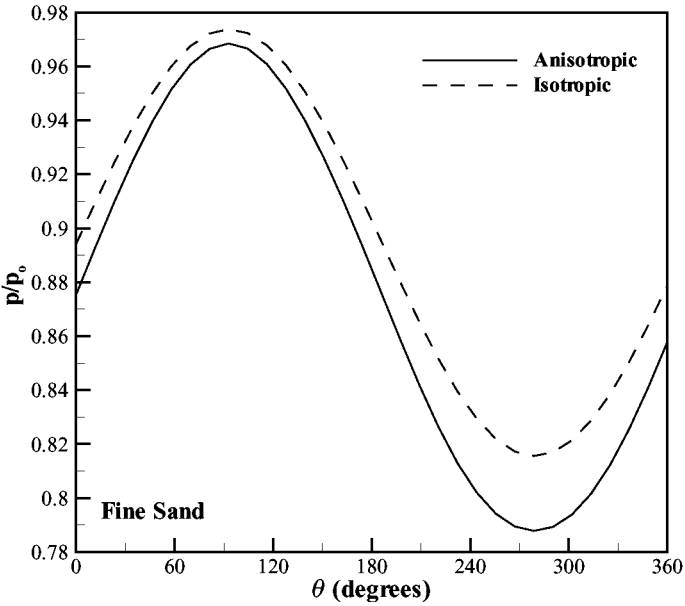
anisotropic and isotropic soil behaviour in fine sand, which strongly highlights the difference between the two cases.

To investigate further the influences of anisotropic soil behaviour on the pore pressure distribution along the pipeline surface, a parametric study has been performed. The preliminary results indicate that two anisotropic constants (n and m) have more significant influence on the wave-induced pore pressure than other anisotropic soil parameters in the wave-seabed-pipe interaction. Thus, we only discuss the influence of n and m on the wave-induced pore pressure in this section.

The anisotropic constant n establishes the relationship between μ_{xz} and μ_{zx} , as well as E_x and E_z . The elastic constant n can be increased when either the Young's modulus in the horizontal direction (E_x) is increased or the Young's modulus in the vertical direction (E_z) is decreased. As a result of E_x increasing, the soil will be able to retain its structure better in the horizontal direction. For isotropic soils, n equals one, n varies between 0.2 and 1.0 for most anisotropic soils. Figure 3.6 shows the effect of changing the cross-anisotropic constant (n) in both coarse and fine sand. With an increase in n , there is an increase in the pore pressure, p/p_o , producing greater rigidity in the vertical direction. As a result, it is easier for the water to penetrate the seabed in the horizontal direction, which



(a) coarse sand



(b) fine sand

Figure 3.5 Comparison between an anisotropic and isotropic seabed of (a) coarse sand and (b) fine sand.

leads to higher pore pressure. In the same manner, with a decrease in E_z the soil will be weaker in the vertical direction than in the horizontal direction. This encourages greater seepage in the vertical direction, which again leads to higher pore pressure.

Figure 3.7 illustrates the effect of changing the cross-anisotropic constant, m , in both coarse and fine sand. With an increase in m there is a subsequent increase in the pore pressure, p/p_o . With an increase in the shear modulus, G_z , or a decrease in the Young's modulus, E_z , there is an increase in the cross-anisotropic constant, m . As a result of m increasing, there is an increase in the pore pressure. The pore pressure increases as the water will be able to penetrate the seabed easier in the vertical direction than in the horizontal direction. The pore pressure in coarse sand is greater, however there is less variation with the increase in m (Figure 3.7(a)). As shown in Figure 3.7(b), the increase in m has a great influence on the pore pressure. Thus, the value of m can be said to be more critical in fine sand.

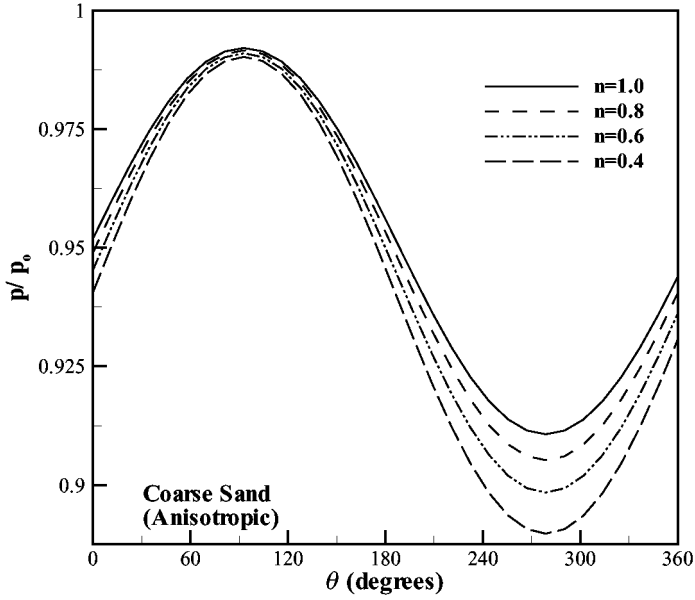
It is common to find gas within marine sediments. For example, samples taken from Mississippi Delta sediments, equilibrating when they are exposed to atmospheric pressure, have a degree of saturation between 75% and 95% (Esrig and Kirby, 1977). It is believed that most marine sediments have degrees of saturation very close to unity, implying nearly full saturation (Pietruszczak and Pande, 1996). However, it is rare that full saturation can be attained in field or laboratory conditions, except for an ideal condition.

Figure 3.8 highlights the influence of a varying degree of saturation on the pore pressure (p/p_o) around the buried pipeline. Obviously, with a higher degree of saturation the pore pressure should be larger. The pore pressure around the pipe is much higher in coarse sand (Figure 3.8(a)), compared with that in fine sand (Figure 3.8(b)).

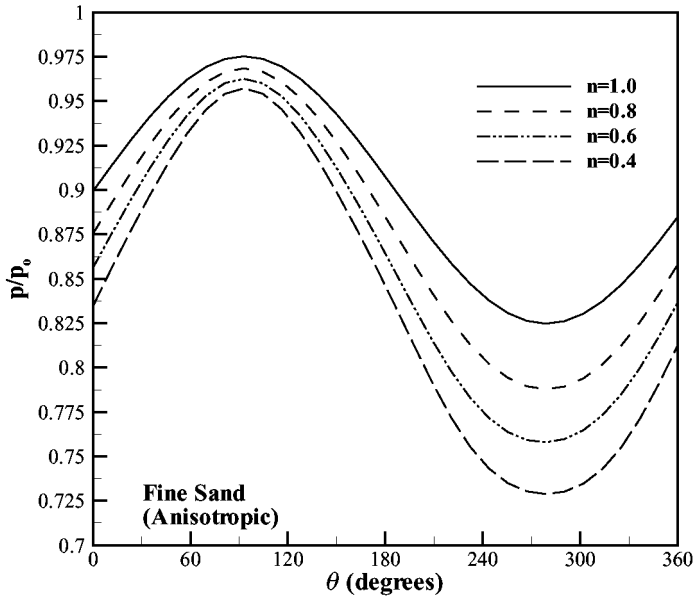
Effects of geometry of the pipe

Besides the influences of soil characteristics, the geometry of the buried pipe is another important factor that must be considered in the analysis of the wave-seabed-pipe interaction problem. The geometry of the pipe (including the burial depth and pipe radius) is particularly important for the design of the pipeline with respect to economic concerns.

Burial depth is an important factor that must be taken into consideration for the design of the pipeline. The burial depth of the pipeline (b) is defined as the distance from the seabed surface to the top of the pipeline. The influence of the burial depth (b) on the wave-induced pore pressure against the polar angles around the pipe surface is illustrated in Figure 3.9. In the figure, the pore pressure (p/p_o) in coarse sand is slightly higher than in fine sand. This would be expected as coarse sand is more porous than fine sand, as larger voids are present. However, it should be noted that the pore pressure is only marginally

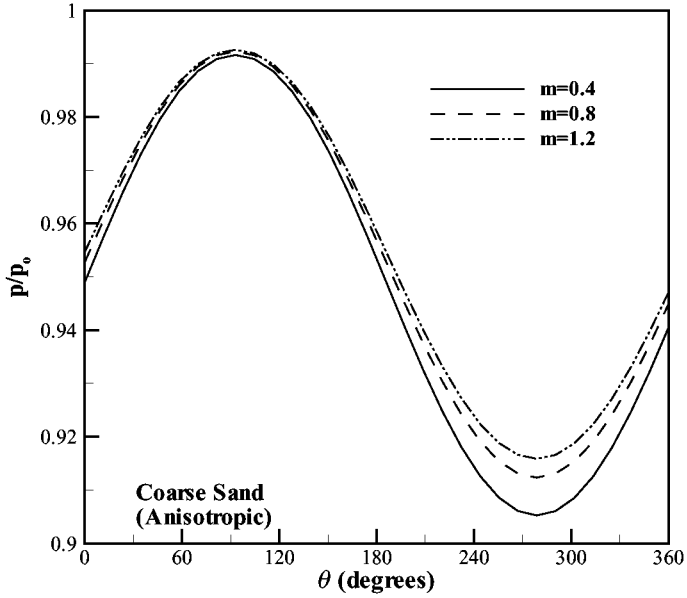


(a) coarse sand

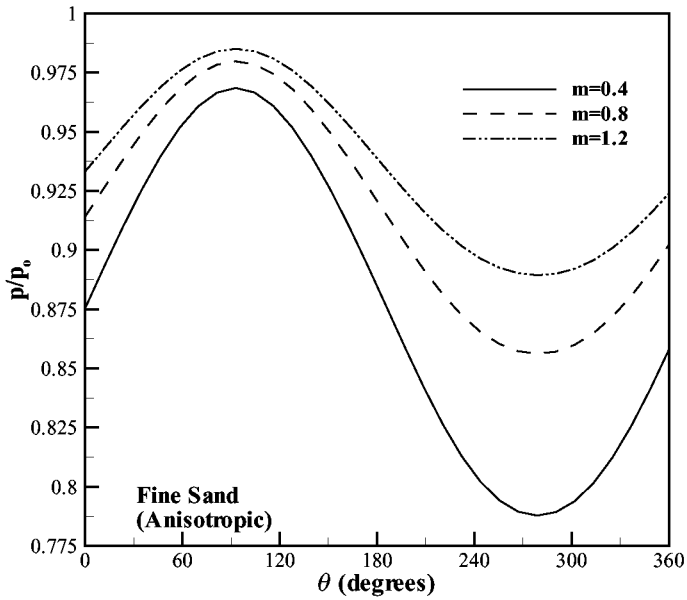


(b) fine sand

Figure 3.6 Distribution of the wave-induced pore pressure against θ in an anisotropic seabed for various values of anisotropic constant (n) in (a) coarse sand and (b) fine sand.

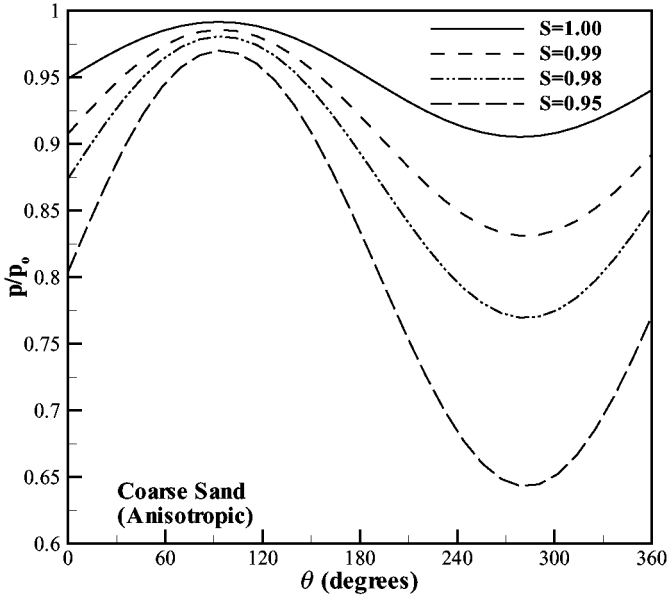


(a) coarse sand

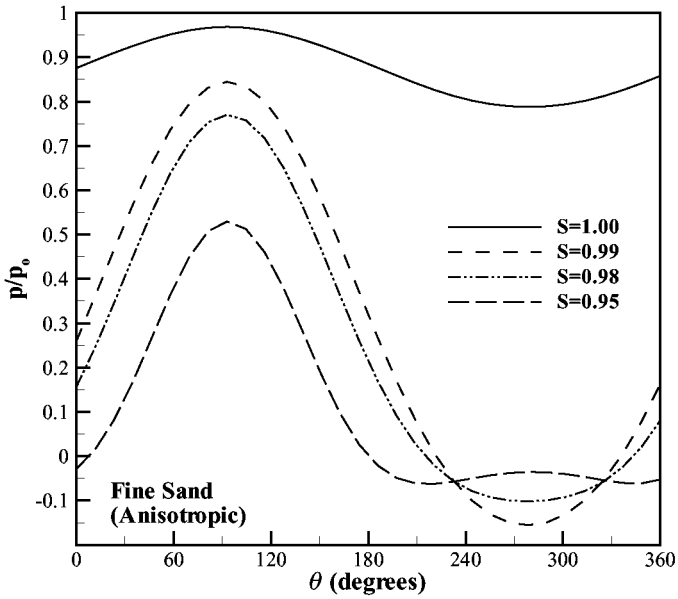


(b) fine sand

Figure 3.7 Distribution of the wave-induced pore pressure against θ in an anisotropic seabed for various values of anisotropic constant (m) in (a) coarse sand and (b) fine sand.



(a) coarse sand



(b) fine sand

Figure 3.8 Distribution of the wave-induced pore pressure against θ in an anisotropic seabed for various values of anisotropic constant (S) in (a) coarse sand and (b) fine sand.

higher and will ultimately rely on the water depth, d . With an increase in the burial depth there is a substantial reduction in the pore pressure.

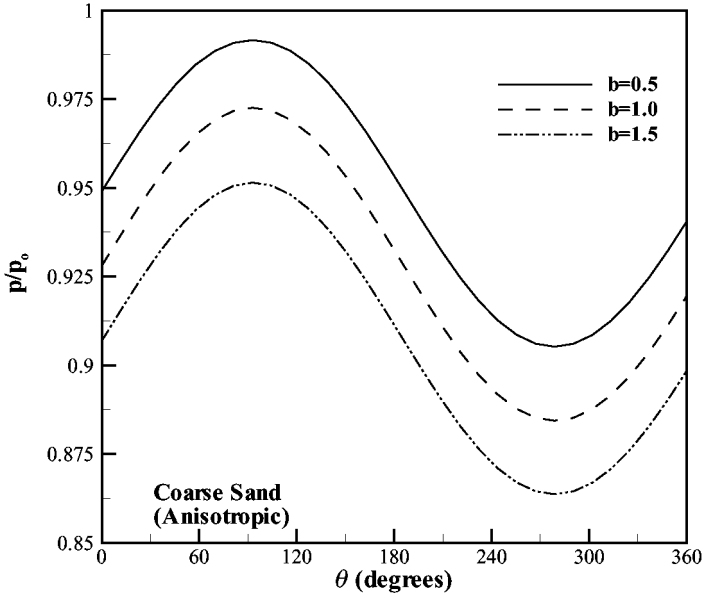
Compared with coarse sand, it can be seen that there is a larger range of pore pressure (p/p_o) in fine sand (Figure 3.9(b)). The pore pressure around the pipeline is less than in coarse sand, especially around the lower extent of the pipe. There is a definite trend, as seen in each of the cases in Figure 3.9. The greater the burial depth (b) of the pipeline, the smaller the pore pressure present around the pipeline. However, it would be a very costly exercise if the pipe was to be positioned deep within the seabed. The standard installation of underwater pipelines is very costly to begin with, and to increase further the burial depth will only add to the cost. There will thus need to be a compromise between the burial depth and the allowable pore pressure. It should also be noted that the greater the burial depth, the greater the subsequent overburden pressure. Thus careful consideration must be given before commitment to the final design.

Pipe radius (R) is another important factor that directly affects the distribution of the wave-induced seabed response. The distribution of the wave-induced pore pressure around the pipe for various pipe radii is illustrated in Figure 3.10. The figure indicates that the pipe radius only slightly affects the top portion of the pipeline. However, with rotation around the pipeline to the lower extent there is a significant reduction in the pore pressure (p/p_o) with an increase in the pipe radius. As a result the pore pressure is very similar on the top portion of the pipeline at $\theta=90^\circ$. The increasing reduction in pore pressure results because at each successive point around the pipeline with an increasing radius, it is situated deeper within the seabed. The reduction in pore pressure is most noticeable in the fine sand, as shown in Figure 3.10(b).

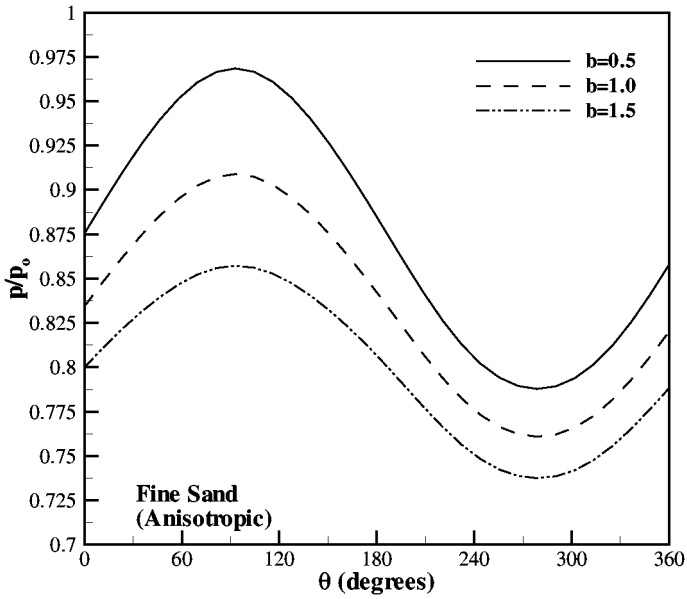
Effects of cover layer

It is well known that buried pipelines are damaged by wave-induced seabed instability (such as liquefaction and scour). The wave pressure at the surface of the seabed will push soil particles upward under wave troughs, while it pushes soil particles downward under wave crests. This is the reason why liquefaction occurs near wave troughs, and densification occurs near wave crests. Along with the vertical soil movement, there can also be horizontal movement, which is a result of the soil failing in shear. This occurs with the forward thrust of the waves. By installing a coarser and more permeable material around the pipe, it is expected to protect the seabed from scouring which will ultimately lead to the failure of the pipeline.

In this example, a simple cover layer is considered. The configuration of the cover layer is illustrated in Figure 3.11. Both the width (W) and depth (B) of the cover layer will be altered and a detailed analysis will again be made on pore pressure around the pipeline, as well as the resulting internal stresses within the pipe. Both coarse sand and gravel will be used in the cover layer, whilst the surrounding seabed will consist of fine sand. It is envisaged that the coarser the

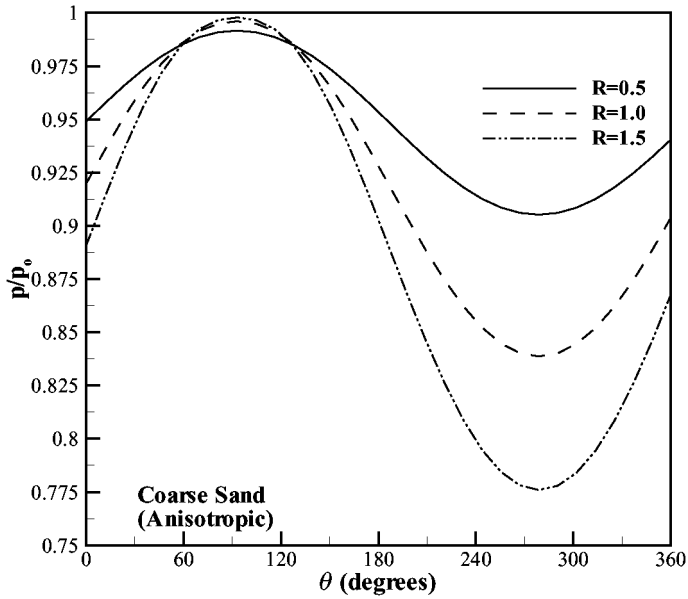


(a) coarse sand

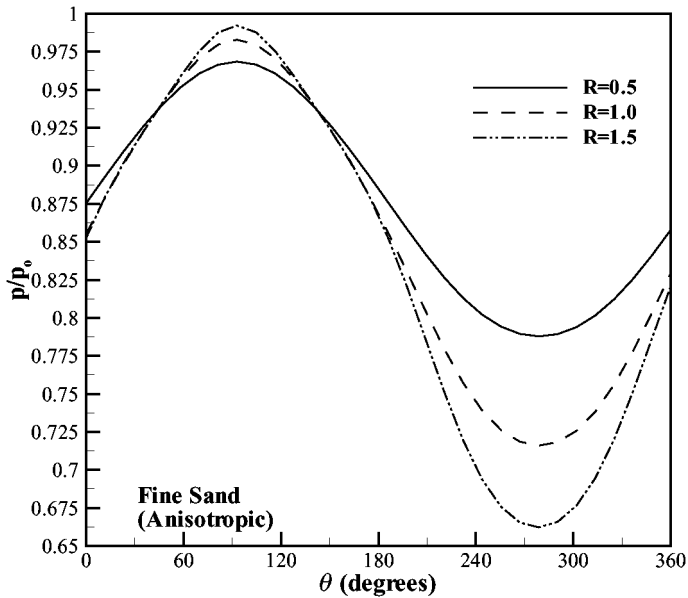


(b) fine sand

Figure 3.9 Distribution of the wave-induced pore pressure against θ in an anisotropic seabed for various values of anisotropic constant (b) in (a) coarse sand and (b) fine sand.



(a) coarse sand



(b) fine sand

Figure 3.10 Distribution of the wave-induced pore pressure against θ in an anisotropic seabed for various values of anisotropic constant (R) in (a) coarse sand and (b) fine sand.

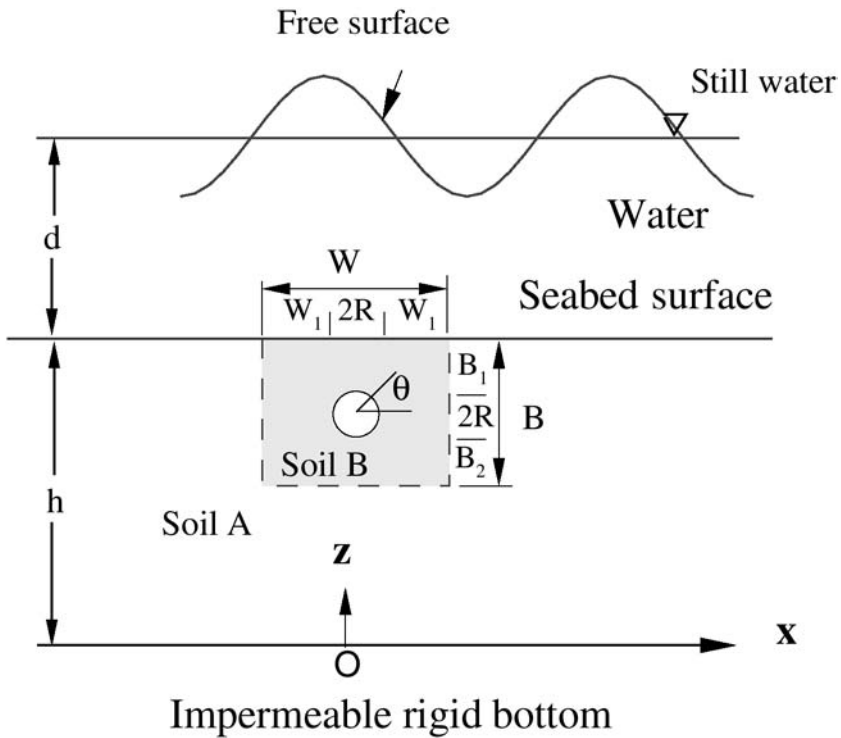


Figure 3.11 Configuration of the cover layer for protection of a buried pipeline.

material used within the cover layer, the greater the stability will be. With higher stability it is also hoped that there will also be a reduction in the internal stresses within the pipeline. The common values used in this model are again given in Table 3.1.

Before evaluating the effects of the geometry of the cover layer (including the width and thickness), the influence of the material present in the cover layer will be examined. It is envisaged that the coarser the material present within the cover layer, the higher the resulting pore pressure will be in the vicinity of the pipeline. The influence of placing coarse sand and gravel in the cover layer will be examined.

Figure 3.12 demonstrates the influence on the pore pressure in the vicinity of a buried pipeline by varying the material present in the cover layer. Initially, there is no cover layer in place and the seabed consists solely of fine sand, as shown in Figure 3.12(a). The distribution of pore pressure is quite large and quickly diminishes with a successive increase in depth into the seabed. With a cover layer of coarse sand, the pore pressure increases significantly, especially in the region above the pipeline (Figure 3.12(b)). Furthermore, with a cover layer of

more coarse material such as gravel (Figure 3.12(c)), there is a further increase in pore pressure. Thus, it can be concluded that the coarser the material present is within the cover layer, the greater the pore pressure will be. The pore pressure increases proportionally when a coarser material is introduced in the cover layer as there is an increase in permeability. An evaluation of both the width and depth of the cover layer (W and B) will now proceed and a comparison will be drawn between coarse sand and gravel.

Figure 3.13 illustrates the distribution of the wave-induced pore pressure (p/p_o) around a buried pipeline for various values of the depth of the cover layer (B). In this example, the width, W has been fixed at 2.0 m. It can be seen that with an increase in the depth (B), there is a reduction in the pore pressure around the pipeline. Relatively speaking, it would be expected that there would be an increase in the pore pressure. However, this is not only the case with an increase in the depth (B) but also with an increase in the burial depth. This increase in the burial depth comes about because the pipe is always situated in the centre of the cover layer. A higher pore pressure is expected to be present around the pipeline when gravel is the medium used in the cover layer (see Figure 13(b)). The figure clearly demonstrates that the pore pressure around the pipeline is much greater in gravel and there is much less variation around the pipeline, which is logical.

An evaluation of the effects of pore pressure (p/p_o) by varying the width of the cover layer (W) can also be made. Figure 3.14 shows the difference in pore pressure with increasing width (W), where both coarse sand and gravel were again both evaluated. The depth of the cover layer has been fixed at 2.0 m in the example and the width (W) increases from 2.0 m to 4.0 m. Unlike when varying the depth of the cover layer B , where there was no direct increase in pore pressure due to a relative increase in burial depth, b , an increase in pore pressure was experienced with an increase in the width of the cover layer (W).

Figure 3.14 also indicates that an increase in pore pressure was achieved, as more water was able to penetrate horizontally in towards the pipeline. Again, a much higher pore pressure was experienced around the pipeline when gravel was introduced into the cover layer because of the higher permeability. The range of pore pressure around the pipeline decreased with an increase in the width of the cover layer, however the pore pressure was much higher. There was also a much greater difference in pore pressure (p/p_o) on the underside of the pipeline compared with the top of the pipeline. Greater water penetration was thus being achieved in the upper extent of the cover layer around the pipeline.

When gravel was present in the cover layer the resulting pore pressures on the lower half of the pipe were a little ambiguous. It could be seen that when coarse sand was present in the cover layer and there was a successive increase in the width (W), there was also an increase in the pore pressure (p/p_o). However, in the gravel there was actually a minor decrease in the pore pressure with successive increases in the width (W) and around the lower extent of the pipe the pore pressure varied quite strangely. However, it should be noted that the pore pressure was actually much higher, which was to be expected. Also, the

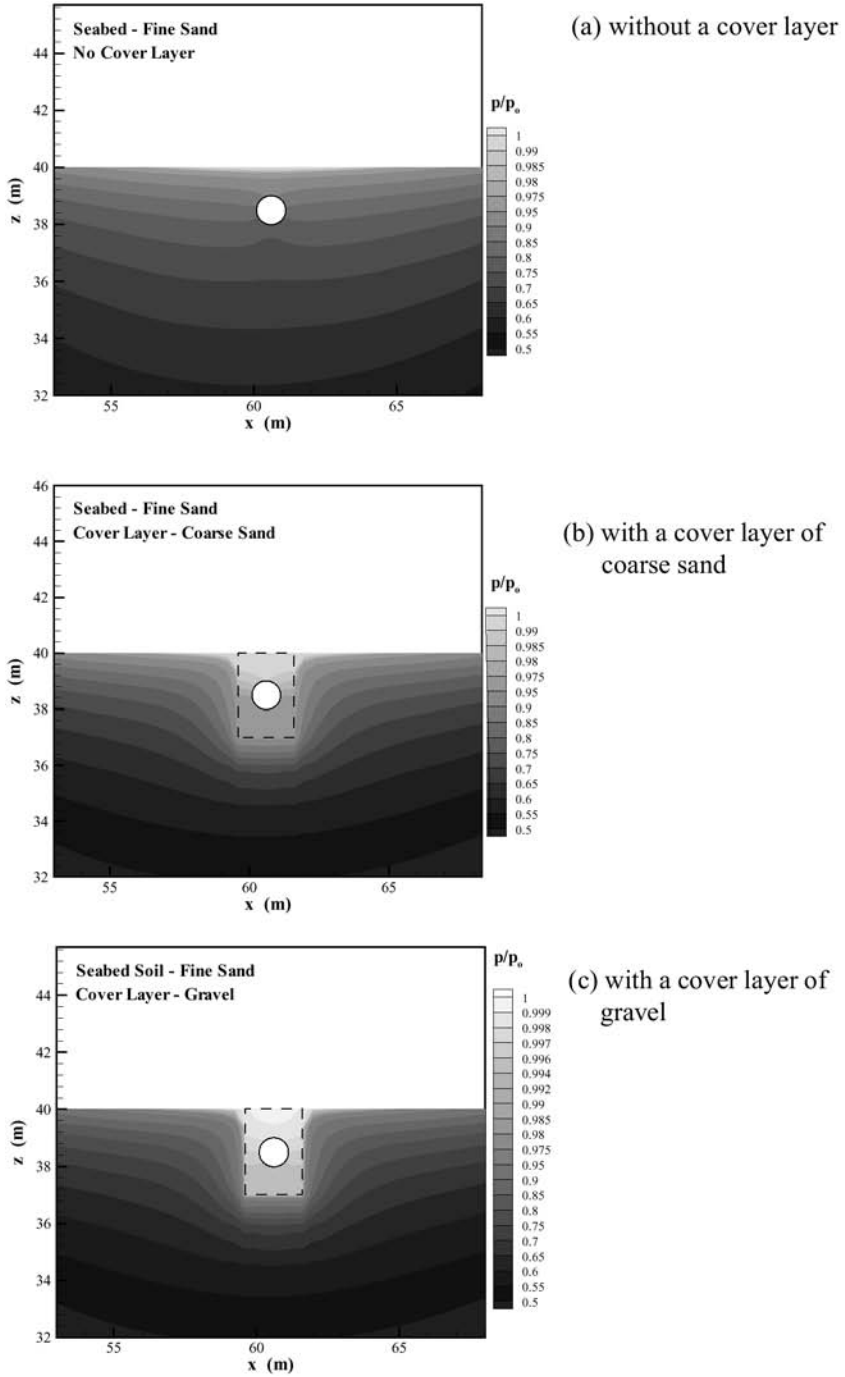
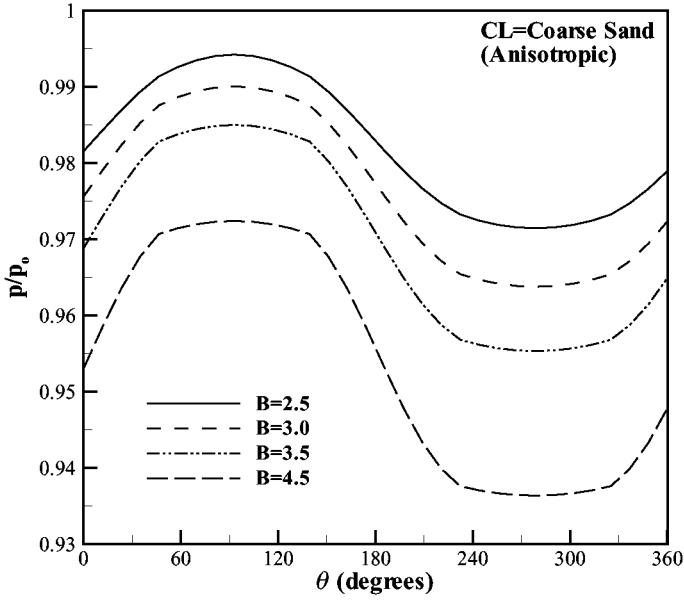


Figure 3.12 Distribution of the wave-induced pore pressure in the vicinity of a buried pipeline in anisotropic seabeds (a) without a cover layer, (b) with a cover layer of coarse sand, and (c) with a cover layer of gravel.



(a) with a cover layer of coarse sand

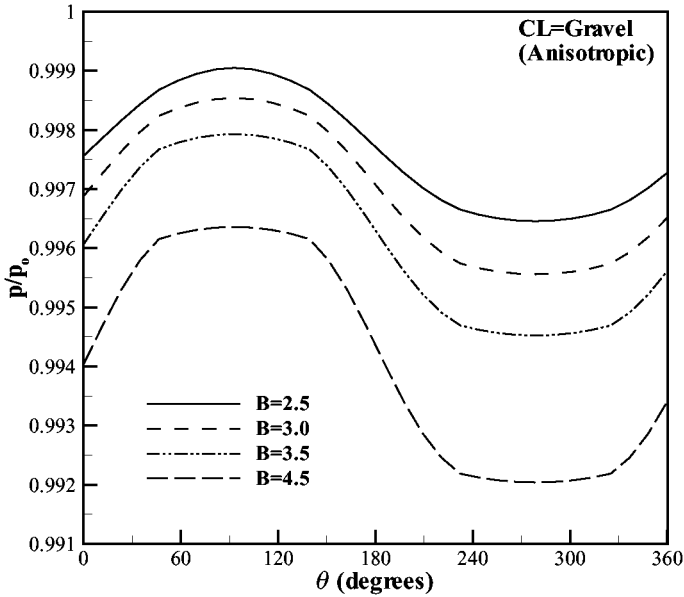
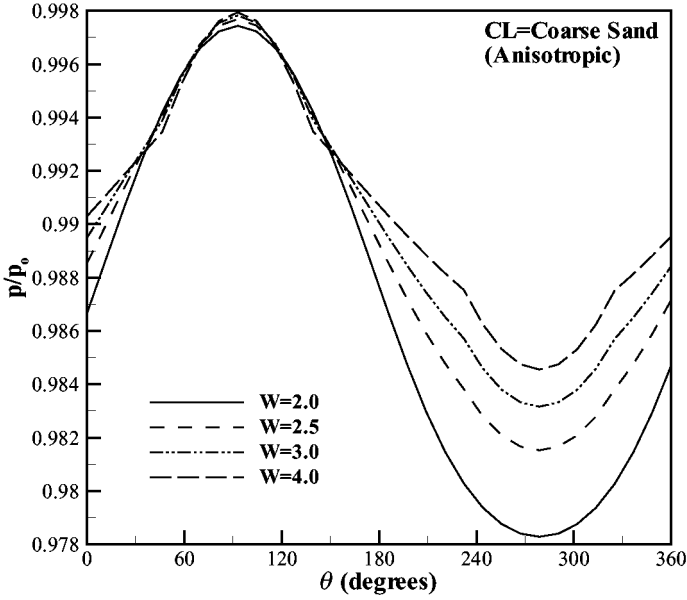
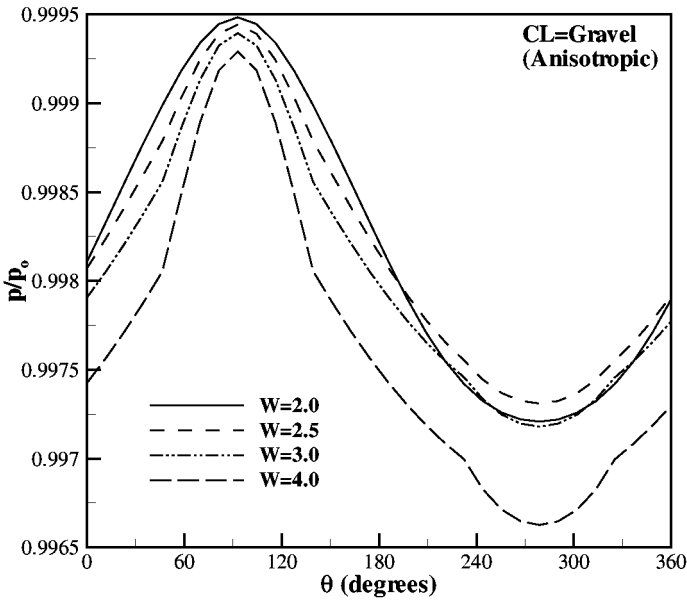


Figure 3.13 Distribution of the wave-induced pore pressure against θ in an anisotropic seabed for various values of cover layer depth (B) with a cover layer of (a) coarse sand and (b) gravel.

magnification in the gravel is quite large which may actually take account of this



(a) with a cover layer of coarse sand



(b) with a cover layer of gravel

Figure 3.14 Distribution of the wave-induced pore pressure against θ in an anisotropic seabed for various values of cover layer depth (W) with a cover layer of (a) coarse sand and (b) gravel.

strange variance.

Wave-seabed-caisson interaction

Considerable efforts are devoted to the protection of marine structures (such as caissons, seawalls, etc.). The major reason is that marine structures such as caissons and seawalls are commonly adopted for coastal defence. Recently, caissons have also been used more widely as foundation elements for offshore structures. Although the protection of caisson-type breakwaters has been extensively studied in recent years, the understanding of their interaction with waves and the seabed is far from complete.

Some investigations into wave-induced pore pressure in the vicinity of a caisson have been carried out through analytical and numerical approaches (Mynett and Mei, 1982; Tsai *et al.*, 1990; Mase *et al.*, 1994; Mizutani and Mostafa, 1998; Jeng *et al.*, 2000, 2001a). Among these, Mynett and Mei (1982) proposed a boundary-layer approximation for a rectangular caisson located on an isotropic seabed without a rubble mound base. Later, Tsai *et al.* (1990) extended the model to a seabed of finite thickness, and also including three different mechanisms of interaction between waves, caisson and seabed. However, it has been demonstrated that boundary-layer approximation is only suitable for finer sandy beds, not for coarser materials (Hsu and Jeng, 1994).

Numerical modelling has been widely used for the wave-seabed-caisson interaction problem, due to the complicated configuration of such a problem, which is difficult to handle by analytical approximation. Mase *et al.* (1994) proposed a finite element model to investigate the wave-induced seabed response around a composite breakwater, including a rectangular caisson and rubble mound base. In their model, the lateral boundary conditions were directly given by the analytical solution proposed by Yamamoto (1977), and they treated the derivative terms with respect to time by finite difference methods. The initial values of the pore pressure and soil displacements were assumed to be zero in their model. This may not provide a solution that accurately performs the oscillatory fluctuation in the initial stage of the time series. Furthermore, they considered the rubble mound base as gravels, but they took the values of permeability (K) as 10^{-1} m/sec and 10^{-2} m/sec. In fact, the common value of the permeability of gravel is 10^{-1} m/sec, while 10^{-2} m/sec is the common value of coarse sand. Mase *et al.* (1994) did not discuss in detail the effects of wave and soil characteristics on the wave-induced soil response near to the composite breakwater. Furthermore, the lateral boundary conditions they used were only a simple isotropic solution, not a general solution for more complicated soil behaviour.

Later, Mizutani and Mostafa (1998) developed a combined boundary element model and finite element model to investigate the wave-seabed-caisson interaction in an isotropic homogeneous seabed. In their model, the wave field and porous seabed are coupled in a combined numerical model. However, their

approximation only considered the isotropic soil behaviour and a homogeneous seabed. Recently, the general finite element model proposed by Jeng *et al.* (1998) was extended to the wave-seabed-caisson interaction problem by including the cross-anisotropic soil behaviour, and demonstrates the significant effects of cross-anisotropic soil behaviour on the wave-induced pore pressure (Cha, 2000).

Application of GFEM-WSSI

In this section, we will demonstrate the application of the proposed general finite element model on the wave-seabed-caisson interaction problem. The configuration of the problem is depicted in [Figure 3.15](#). The boundary condition at the seabed surface, rubble mound foundation and caisson can be written as

$$n_x \sigma'_x + n_z \tau_{xz} = -n_x p \quad \text{and} \quad n_x \tau_{xz} + n_z \sigma'_z = -n_z p \quad (3.23)$$

and

$$p = \frac{\gamma_w H \cosh kz}{\cosh kd} \cos(kx) \cos(\omega t) \quad (3.24)$$

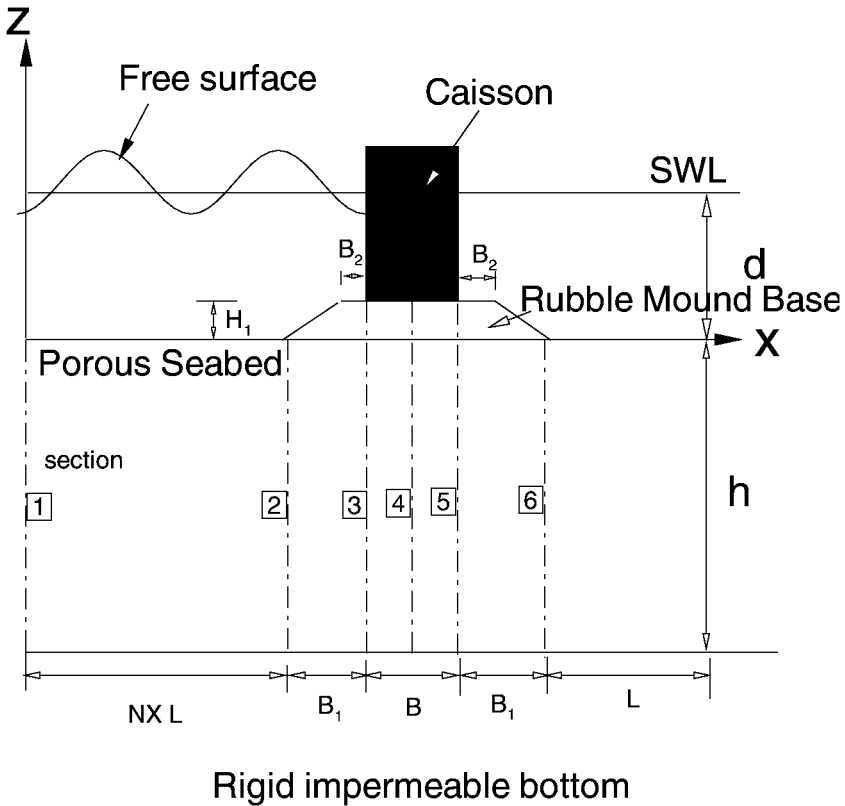
for the part subjected to wave motion, and $p=0$ for the part subjected to no wave action. It is noted that only dynamic wave pressure is considered in the study. The static wave pressure is not included here, since it remains a constant in the whole computing domain.

To give a basic understanding of the mechanism of the wave-seabed interaction around a caisson, we examine several characteristics in this section. In the following examples, we consider the rubble mound as gravel, and the seabed to be coarse and fine sand. The wave crests are assumed to arrive fronting the caisson. The detail of soil properties, wave conditions, caisson and rubble mound are given in [Table 3.2](#).

An example of a finite element mesh for the wave-seabed-caisson interaction is given in [Figure 3.16](#). As shown in the figure, a finer mesh is used near the rubble mound and caisson to enhance the accuracy near the interface of different materials.

Contours of pore pressure distribution

[Figure 3.17](#) illustrates the contour of the wave-induced pore pressure in the vicinity of a caisson. In the figure, the result of the wave-induced pore pressure in both isotropic seabed (dashed line) and cross-anisotropic seabed (solid line) are included.



Rigid impermeable bottom

Figure 3.15 Configuration of wave-seabed-caisson interaction.

As seen in the figure, the effect of anisotropic soil behaviour on the wave-induced pore pressure around the caisson is quite significant, at least in this numerical example.

To give a better understanding of the vertical distribution of the wave-induced pore pressure, the results of six different sections are presented in Figure 3.18. The locations of the five sections are indicated in Figure 3.15. Section 1 represents the results far away from the structure, i.e., there is no disturbed pressure generated by the existence of the structure. Section 2 is the toe of the rubble mound, while section 3 is the interface point of the caisson and rubble mound. Section 4 is the cross-section beneath the centre of the caisson, while sections 5 and 6 represent the cross-sections behind the structure.

Figure 3.18 presents the pore pressure distribution at different sections for both coarse sand and fine sand. As seen in the figure, the distribution of pore pressure in coarse sand is slightly different from that in fine sand. In coarse sand, the pore pressure changes smoothly, while it changes dramatically near the interface of the rubble mound and the sandy seabed in fine sand (Figure 3.18

Table 3.2 Input data for case study of wave-seabed-caisson interaction.

Wave characteristics	
Wave period T	12.5 sec
Water depth d	20 m
Wavelength L	159.91 m
Wave height H	2 m
Soil characteristics	
Thickness of seabed h	40 m
Poisson's ratio μ_{xx}, μ_{xz}, μ	0.4 or various (sandy bed) 0.34 (rubble mound)
Porosity n'	0.4 (sandy bed) 0.45 (rubble mound)
Permeability K	10^{-1} m/sec (rubble mound) 10^{-2} m/sec (coarse sand) 10^{-4} m/sec (fine sand)
Young's modulus E_z	2×10^8 N/m ² (rubble mound) 7×10^7 N/m ² (coarse sand) 2×10^7 N/m ² (fine sand)
Degree of saturation S	0.98 or various
Anisotropic constant n	0.4 or various
m	0.8 or various
Geometry of caisson and rubble mound base	
Width of caisson B	2 m or various
Width of rubble mound B_1	8 m or various
Width of rubble mound B_2	3 m or various
Height of rubble mound H_1	3 m or various

(b)). It is also noted that the maximum pore pressure occurs at section 3, which is the intersecting point of caisson and rubble mound. Since sections 2, 3 and 4 are the three most dangerous regions for most marine structures, only results at these three sections will be discussed below.

Effects of cross-anisotropic soil behaviour

Poisson's ratio (μ_{xx}) describes the strain in one horizontal direction caused by the strain in another horizontal direction normal to the first direction. On the other hand, Poisson's ratio (μ_{xz}) also describes the strain in the horizontal direction caused by the strain in the vertical direction. Their effects on the wave-induced pore pressure are discussed in this section.

Figure 3.19 shows the vertical distribution of the wave-induced normalised pore pressure (p/p_o) at different sections for various values of Poisson's ratio (μ_{xx}) in coarse sand and fine sand, respectively. Generally speaking, the wave-induced pore pressure increases as μ_{xx} increases. The figure indicates that the effects of μ_{xx} are more significant at section 4 in fine sand. Compared with

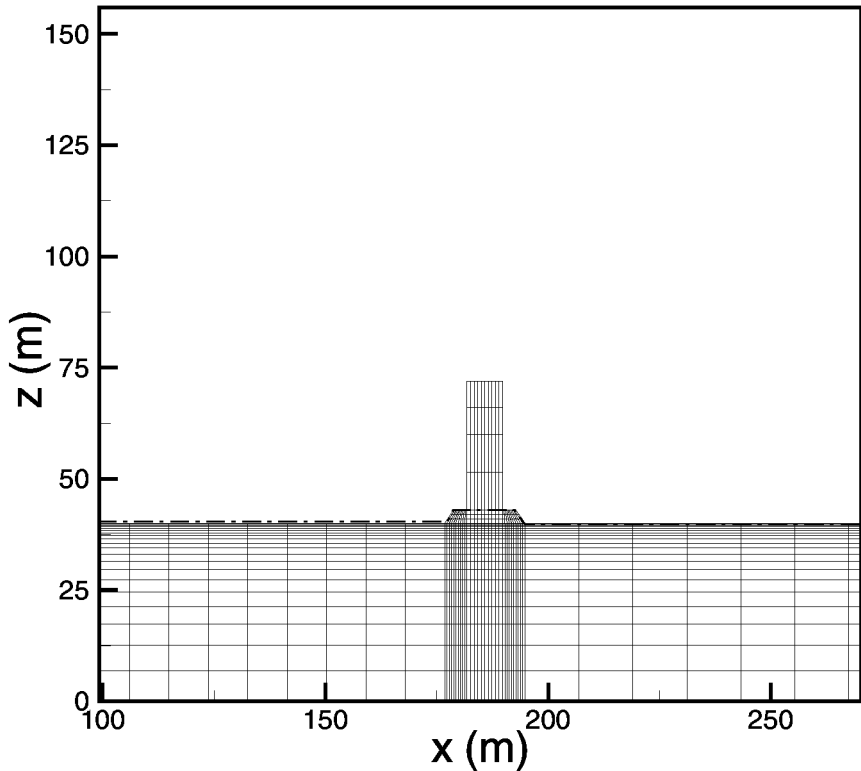


Figure 3.16 Finite element meshes in the vicinity of a caisson.

μ_{xx} in coarse sand, the effects of Poisson's ratio (μ_{xz}) on the wave-induced pore pressure is much more significant, as seen in Figure 3.20.

Besides the two Poisson's ratios (μ_{xx} and μ_{xz}), there are three other cross-anisotropic parameters (E_x , E_z and G_z). As defined by equations (3.3) and (3.4), these three anisotropic parameters are related to two non-dimensional parameters, n and m . The influences of n and m on the wave-induced pore pressure are examined here. Figure 3.21 illustrates the effects of anisotropic constant n on the wave-induced pore pressure. Basically, pore-pressure (p/p_o) increases as n decreases. It is observed that the anisotropic constant n has greater influence on the pore pressure beneath the caisson (i.e. at section 4) than at sections 2 and 3 (graphs not shown here), especially in fine sand.

Figure 3.22 illustrates the vertical distribution of the wave-induced pore pressures (p/p_o) for various values of anisotropic constant (m) in coarse sand and fine sand, respectively. In general, the pore pressure decreases as m increases. It is noted that the wave-induced pore pressure is unaffected by m in coarse sand, while the influence of m is observed in fine sand. However, compared with n , the

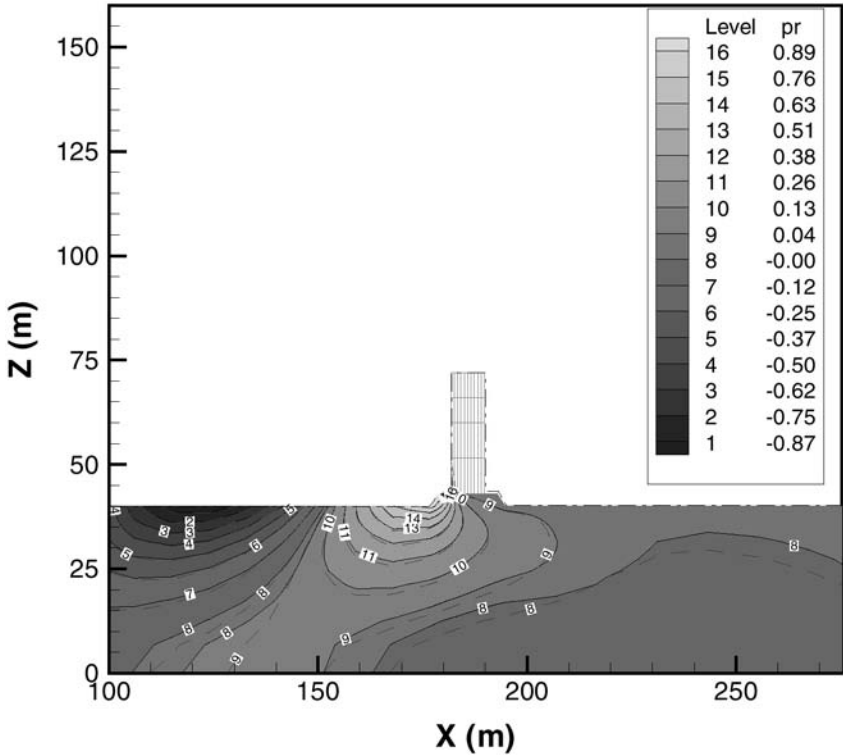


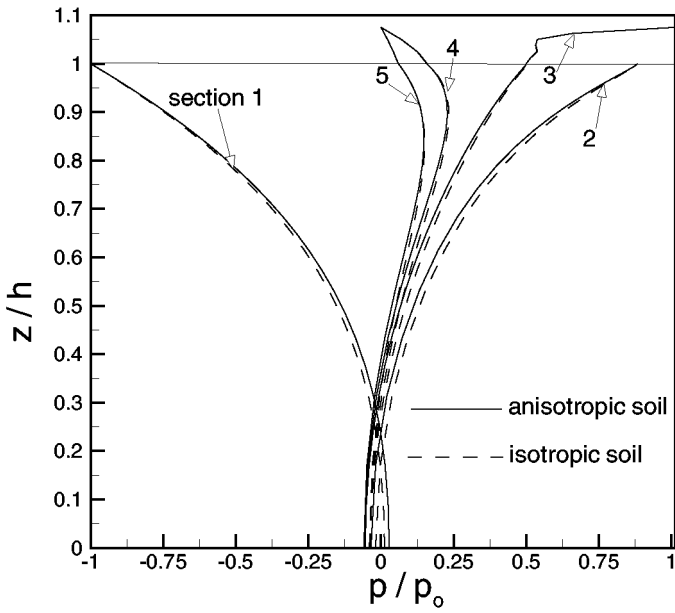
Figure 3.17 Contour of the wave-induced pore pressure in the vicinity of a composite breakwater in sandy seabeds (solid lines are anisotropic seabed and dashed lines are isotropic seabed).

effect of anisotropic constant m on the wave-induced pore pressure is insignificant.

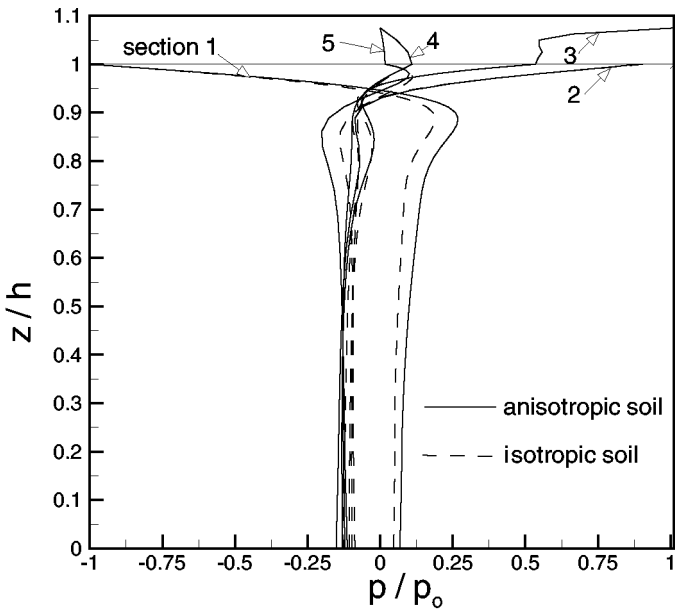
In summary, among the anisotropic parameters (μ_{xx} , μ_{xz} , n and m), it can be concluded that Poisson's ratio (μ_{xz}) and the anisotropic constant (n) have more significant influences than other parameters in the evaluation of the wave-induced pore pressure at the section beneath the caisson (i.e. section 4), in comparison with sections 2 and 3.

Effects of basic soil characteristics

Many variables affect the wave-induced seabed response, for example, shear modulus, permeability, degree of saturation, seabed thickness etc. A detailed discussion of the influence of these parameters was given in Jeng (1997b). Here, we only discuss two important parameters (degree of saturation and soil type (in terms of permeability and shear modulus)) on the wave-seabed-structure interaction. It is common to observe gas in marine sediments (Okusa, 1985). It

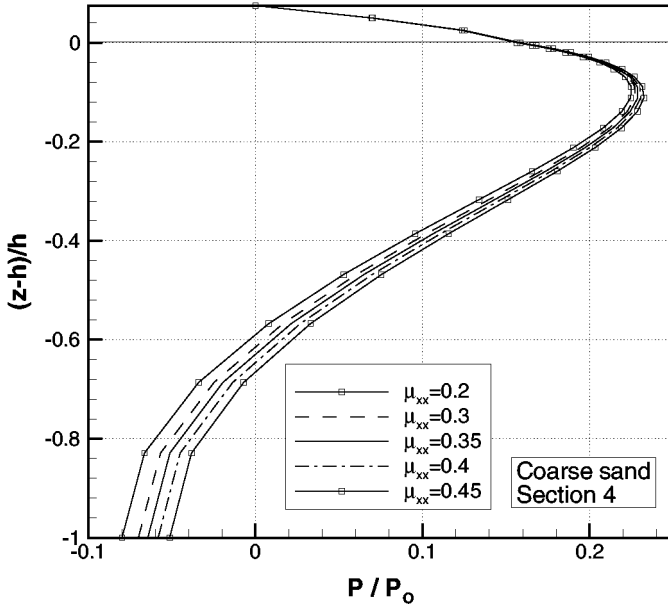


(a) coarse sand

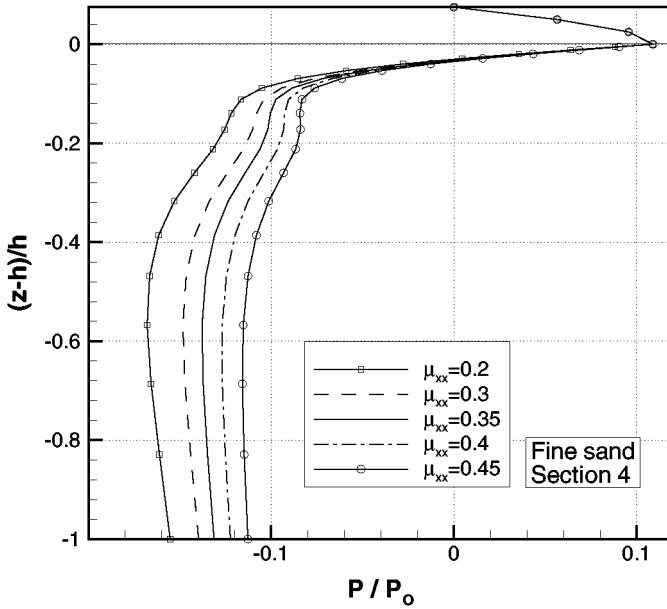


(b) fine sand

Figure 3.18 Vertical distributions of the wave-induced pore pressure versus the soil depth in (a) coarse sand and (b) fine sand.

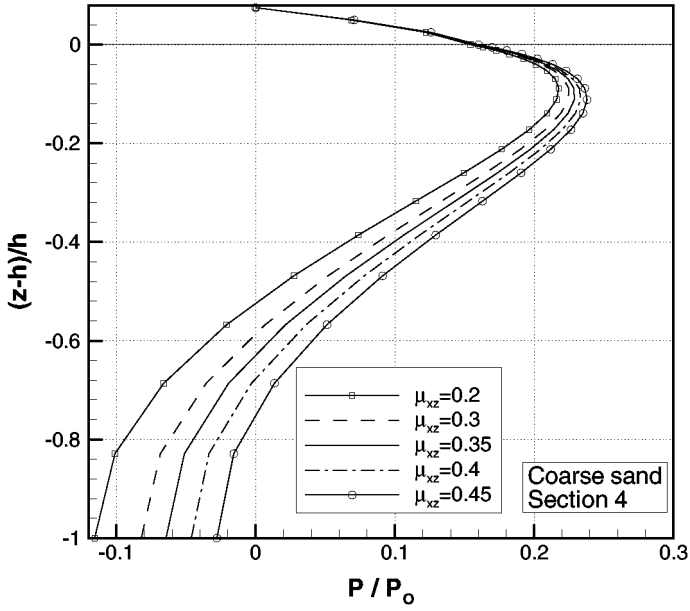


(a) coarse sand

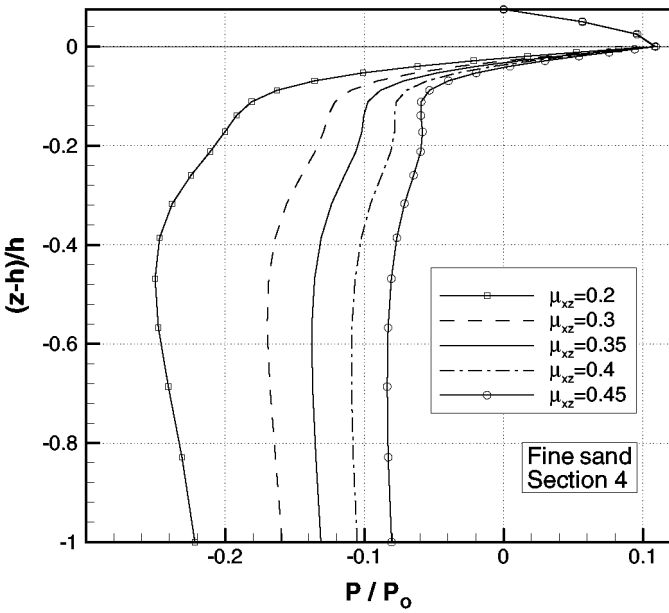


(b) fine sand

Figure 3.19 Vertical distributions of the wave-induced pore pressure versus the soil depth for various values of Poisson's ratio μ_{xx} in (a) coarse sand and (b) fine sand.

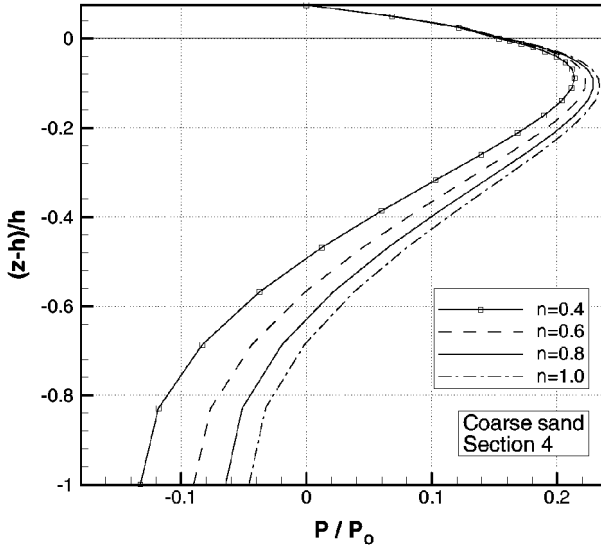


(a) coarse sand

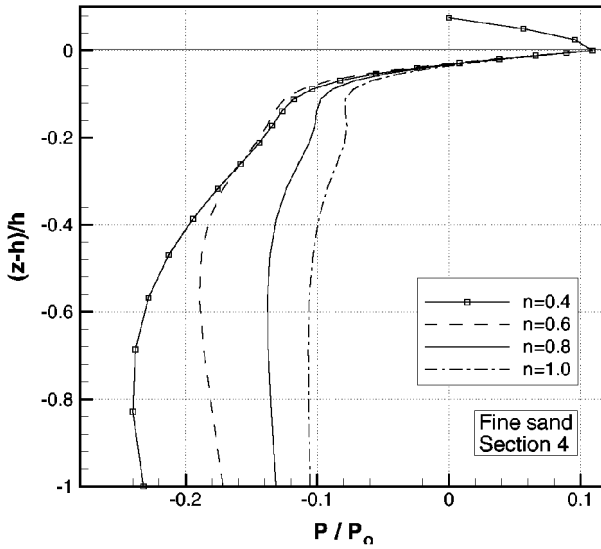


(b) fine sand

Figure 3.20 Vertical distributions of the wave-induced pore pressure versus the soil depth for various values of Poisson's ratio μ_{xz} in (a) coarse sand and (b) fine sand.



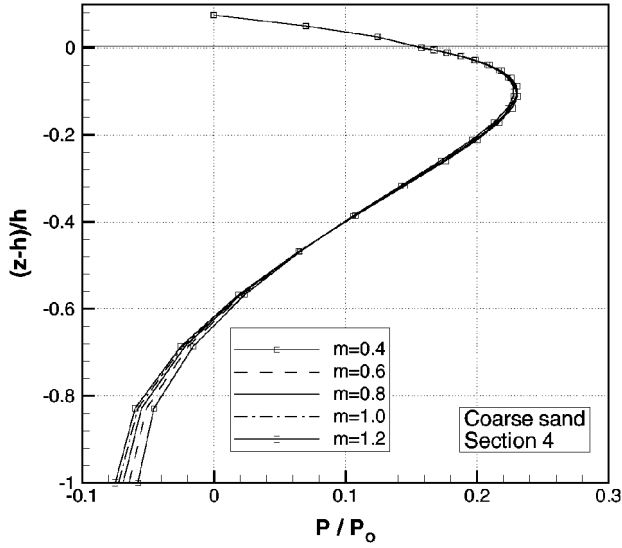
(a) coarse sand



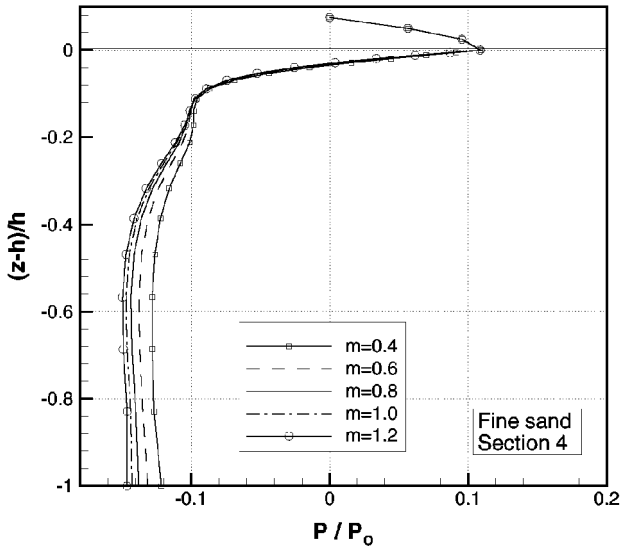
(b) fine sand

Figure 3.21 Vertical distributions of the wave-induced pore pressure versus the soil depth for various values of anisotropic constant (n) at different sections in (a) coarse sand and (b) fine sand.

has been reported that the degree of saturation plays an important role in the evaluation of the wave-induced seabed response without structures (Okusa,



(a) coarse sand



(b) fine sand

Figure 3.22 Vertical distributions of the wave-induced pore pressure versus the soil depth for various values of anisotropic constant (m) at different sections in (a) coarse sand and (b) fine sand.

1985; Hsu and Jeng, 1994). As shown in Figure 3.23, the degree of saturation significantly affects the wave-induced pore pressure, especially near a structured

seabed. This phenomenon is particularly obvious at the sections between seabed and structure beneath the caisson (i.e. section 4). Its influence will increase as the degree of saturation increases. Similar trends can be found in fine sand (Figure 3.23).

Figure 3.23 also indicates the different trend of pore pressure distribution at $S=0.95$, compared with other values of degree of saturation ($S=0.975$ and 1). It is noted that the results presented in the figure are the real component of the solution, i.e., the phase change component of pore pressure (i.e., imaginary component). The trend at $S=0.95$ is a significant phase change occurring at the unsaturated seabed, as reported by Okusa (1985) and Hsu and Jeng (1994). The occurrence of phase lag comes from the flow transfer between different media (solid and fluid).

Soil type is a dominant factor in the evaluation of the wave-induced pore pressure (Jeng, 1997a). Two different sandy beds (coarse sand and fine sand) are considered in this study. The major differences between them are the permeability and shear modulus.

Comparing Figures 3.19–3.23, a common trend is observed between coarse sand and fine sand. That is, the effect of other soil parameters on the wave-induced pore pressure in fine sand is more significant than that in coarse sand.

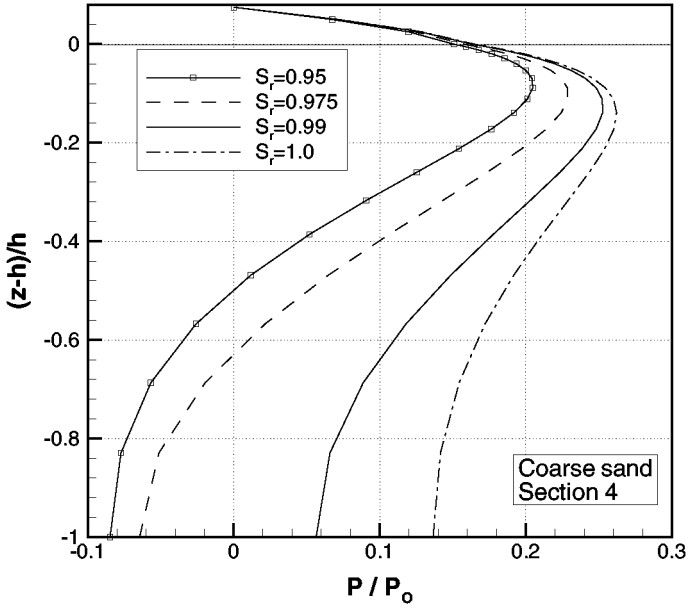
Effects of geometry of caisson and rubble mound

The geometry of the caisson is an important factor, which must be taken into account in the design of structures. The width of the caisson may vary from 2 m to 20 m in engineering practice. In this case, the width of the caisson is considered to vary between 2 m and 8 m. We intend to examine the effects of the width of the caisson on the pore pressure distribution.

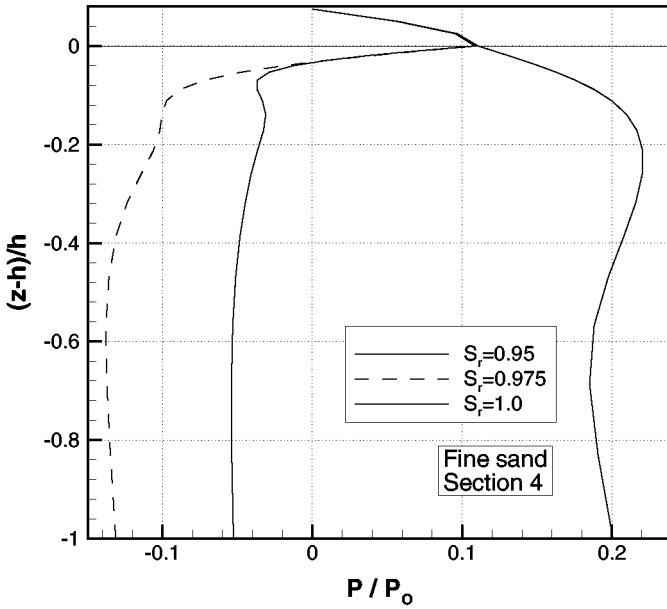
Figure 3.24 presents the vertical distribution of pore pressure for various widths of the caisson at section 4 in both coarse and fine sand, respectively. The figure indicates that the width of the caisson only significantly affects the pore pressure beneath the caisson (i.e. section 4). It is noted that the width of the caisson also affects the pore pressure distribution in the rubble mound, unlike other characteristics.

The geometry of the rubble mound base, including its width (B_1 and B_2) and height (H_1) (as depicted in Figure 3.15) is expected to affect the distribution of the wave-induced pore pressure. After some preliminary parametric tests, the influences of B_1 and B_2 can be ignored. Thus, we will present the results of varying H_1 in this section.

Figure 3.25 illustrates the vertical distribution of the wave-induced pore pressure (p/p_0) with various heights of the rubble mound base (H_1). In general, the pore pressure increases as H_1 increases. The effects of the height of the rubble mound (H_1) on the wave-induced pore pressure are significant at sections 3 and 4, especially inside the rubble mound base and in the region near the seabed surface, as shown in Figure 3.25. The figure also demonstrates a greater

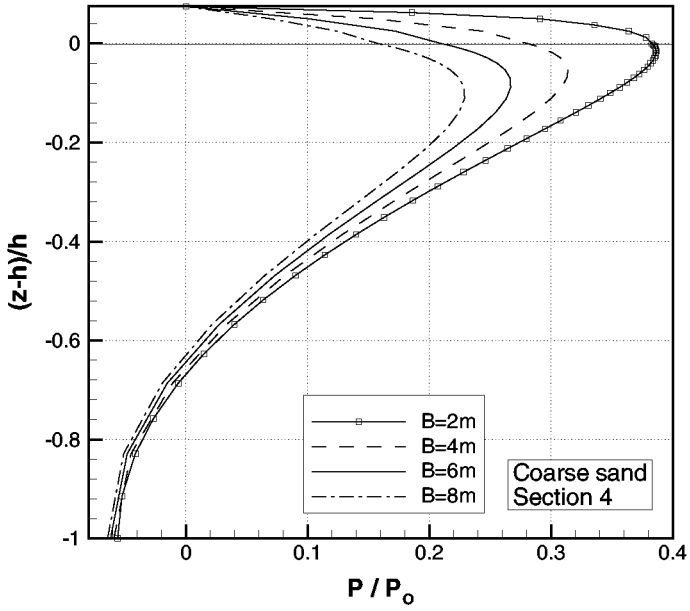


(a) coarse sand

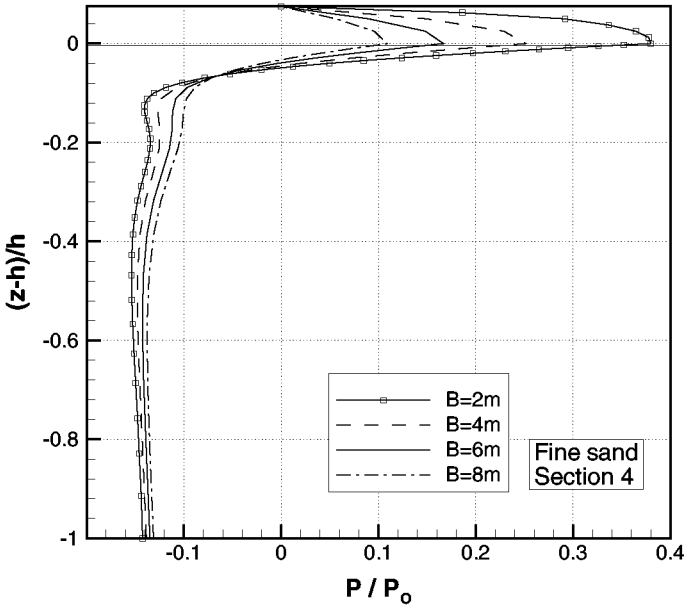


(b) fine sand

Figure 3.23 Vertical distributions of the wave-induced pore pressure versus the soil depth for various values of degree of saturation (S) at different sections in (a) coarse sand and (b) fine sand.

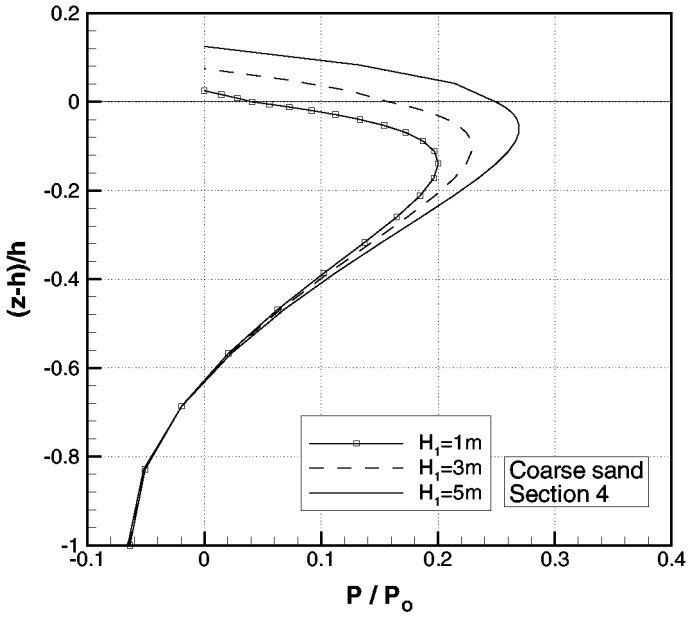


(a) coarse sand

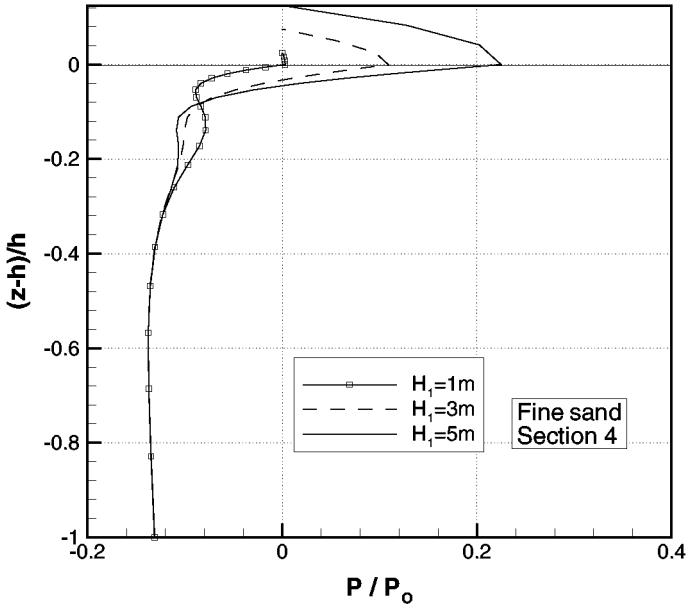


(b) fine sand

Figure 3.24 Vertical distributions of the wave-induced pore pressure versus the soil depth for various values of caisson width (B) at different sections in (a) coarse sand and (b) fine sand.



(a) coarse sand



(b) fine sand

Figure 3.25 Vertical distributions of the wave-induced pore pressure versus the soil depth for various values of height of rubble mound (H_1) at different sections in (a) coarse sand and (b) fine sand.

influence on the pore pressure beneath the caisson (i.e. section 4), especially in fine sand.

Conclusions

In this chapter, a general finite element model for the wave-seabed-structure interaction (GFEM-WSSI) is presented. The proposed model overcomes the major difficulty, i.e. encountered in the WSSI problem the determination of the lateral boundary conditions. To demonstrate the application of the GFEM-WSSI model, two practical examples with a pipeline and a caisson-type breakwater have been used. The GFEM-WSSI model can also be extended further to other structures such as offshore piles, piers and so on, as well as three-dimensional cases in the future.

Acknowledgements

The author thanks Mr Cha and Mr Postma for their help with the generation of graphs and routine computing work. The initial idea for the GFEM-WSSI model was formed while the author worked at the Special Research Centre for Offshore Foundation Systems (at the University of Western Australia), which was supported by the Australian Research Council (ARC) Special Research Centre Program. Financial support from the Australia-Taiwan exchange program (1999), two ARC Small Grants (Griffith University) during 2000–2001 and the ARC Large Grant (2001–2003) under Project no. A00104092 is also appreciated.

References

- Biot, M.A. (1941) 'General theory of three-dimensional consolidation' *Journal of Applied Physics*, 12, 2:155–164.
- Cha, D.H. (2000) *Wave-induced pore pressure in an anisotropic seabed in the vicinity of a caisson*. Undergraduate Student Thesis, School of Engineering, Griffith University Gold Coast Campus, 61pp.
- Cheng, A.H.D. and Liu, P.L.F. (1986) 'Seepage force on a pipeline buried in a poroelastic seabed under wave loadings' *Applied Ocean Research*, 8, 1:22–32.
- Esrig, M.I. and Kirby, R.C. (1977) 'Implication of gas content for predicting the stability of submarine slopes' *Marine Geotechnology*, 2, 2:81–100.
- Gazetas, G. (1982) 'Stresses and displacement in cross-anisotropic soils' *Journal of Geotechnical Engineering Division, ASCE*, 108, 4:532–553.
- Graham, J. and Houlsby, G.T. (1983) 'Anisotropic elasticity of a natural clay' *Geotechnique*, 33, 2:165–180.
- Herbich, J.B. (1977) 'Wave-induced scour around offshore pipelines' *Proceedings Offshore Technical Conference*, Houston, TX, 79–90.
- Hsu, J.R.C. and Jeng, D.S. (1994) 'Wave-induced soil response in an unsaturated anisotropic seabed of finite thickness' *International Journal for Numerical and Analytical Methods in Geomechanics*, 18, 11:785–807.

- Jeng, D.S. (1997a) 'Soil response in cross-anisotropic seabed due to standing waves' *Journal of Geotechnical and Geoenvironmental Engineering, ASCE*, 123, 1:9–19.
- Jeng, D.S. (1997b) *Wave-induced seabed response in front of a breakwater*, PhD Dissertation, The University of Western Australia, 297pp.
- Jeng, D.S. (2001) 'Numerical modelling for wave-seabed-pipe interaction in a non-homogeneous porous seabed' *Soil Dynamics and Earthquake Engineering*, 21, 8: 699–712.
- Jeng, D.S. and Cheng, A.H.D. (2000) 'Wave-induced seabed instability around a buried pipe in a poroelastic seabed' *Ocean Engineering*, 27, 2:127–146.
- Jeng, D.S. and Lin, Y.S. (1999) 'Pore pressure on a submarine pipeline in a cross-anisotropic non-homogeneous seabed under wave loading' *Canadian Geotechnical Journal*, 36, 3:563–572.
- Jeng, D.S. and Lin, Y.S. (2000) 'Response of in-homogeneous seabed around buried pipeline under ocean waves' *Journal of Engineering Mechanics, ASCE*, 126, 4: 321–332.
- Jeng, D.S., Cheng, L. and Lin, Y.S. (1998) 'Numerical study of wave-seabed interaction in Gibson soils' *8th Biennial Computational Techniques and Application Conference*, Adelaide, Australia, 321–328.
- Jeng, D.S., Rahman, M.S. and Lee, T.L. (1999) 'Effects of inertia forces on wave-induced seabed response' *International Journal of Offshore and Polar Engineering*, 9, 4: 307–313.
- Jeng, D.S., Cha, D.H., Lin, Y.S. and Hu, P.S. (2000) 'Analysis on pore pressure in an anisotropic seabed in the vicinity of a caisson' *Applied Ocean Research*, 22: 317–329.
- Jeng, D.S., Cha, D.H., Lin, Y.S. and Hu, P.S. (2001a) 'Wave-induced pore pressure around a composite breakwater' *Ocean Engineering*, 28, 10:1413–1435.
- Jeng, D.S., Postma, P.F. and Lin, Y.S. (2001b) 'Stresses and deformation of a buried pipe under ocean wave loading' *Journal of Transportation Engineering, ASCE*, 127(5), 127, 5:398–407.
- Lundgren, H., Lindhardt, J.R.C. and Romhild, C.J. (1989) 'Stability of breakwaters on poor foundation' *Proceedings 12th International Conference on Soil Mechanics and Foundation Engineering*, 451–454.
- Magda, W. (1996) 'Wave-induced uplift force acting on a submarine buried pipeline: Finite element formulation and verification of computations' *Computers and Geotechnics*, 19, 1:47–73.
- Magda, W. (1997) 'Wave-induced uplift force on a submarine pipeline buried in a compressible seabed' *Ocean Engineering*, 24, 6:551–576.
- Magda, W. (2000) 'Wave-induced cyclic pore pressure perturbation effects in hydrodynamic uplift force acting on submarine pipeline buried in seabed sediments' *Coastal Engineering*, 39:243–272.
- Mase, H., Sakai, T. and Sakamoto, M. (1994) 'Wave-induced porewater pressure and effective stresses around breakwater' *Ocean Engineering*, 21, 4:361–379.
- Mizutani, N. and Mostafa, A.M. (1998) 'Non-linear wave-induced seabed instability around coastal structure' *Coastal Engineering Journal*, 40:131–160.
- Mynett, A.E. and Mei, C.C. (1982) 'Wave-induced stresses in a saturated poro-elastic seabed beneath a rectangular caisson' *Geotechnique*, 33, 3:293–305.
- Nago, H., Maeno, T., Matsumoto, T. and Hachiman, Y. (1993) 'Liquefaction and densification of loosely deposited sand bed under wave pressure variation':

Proceeding of 3 (1993) International Offshore and Polar Engineering Conference, 578–584.

- Okusa, S. (1985) 'Wave-induced stresses in unsaturated submarine sediments' *Geotechnique*, 35, 4:517–532.
- Pickering, D.J. (1970) 'Anisotropic elastic parameters for soil' *Geotechnique*, 20, 3: 271–276.
- Pietruszczak, S. and Pande, G.N. (1996) 'Constitutive relations for partially saturated soils containing gas inclusions' *Journal of Geotechnical Engineering, ASCE*, 122, 1: 50–59.
- Postma, P.F. (2000) *Mechanism of Wave-seabed-pipe interaction*, Undergraduate Student Thesis, School of Engineering, Griffith University Gold Coast Campus, 88 pp.
- Seed, H.B. and Rahman, M.S. (1978) 'Wave-induced pore pressure in relation to ocean floor stability of cohesionless soils' *Marine Geotechnology*, 3, 2:123–150.
- Silvester, R. and Hsu, J.R.C. (1989) 'Sines revisited' *Journal of Waterways, Port, Coastal and Ocean Engineering, ASCE*, 115, 3:327–344.
- Tsai, Y.T., McDough, W.G. and Sollitt, C.K. (1990) 'An analytical model for ocean wave-soil-caisson interaction' *Proceedings of 20th International Conference on Coastal Engineering, ASCE*, 3:2314–2328.
- Turcotte, B.R., Liu, P.L.F. and Kulhawy, F.H. (1984) 'Laboratory evaluation of wave tank parameters for wave-sediment interaction' *Joseph F. Defree Hydraulic Laboratory Report 84-1*, School of Civil and Environmental Engineering, Cornell University.
- Yamamoto, T. (1977) 'Wave induced instability seabeds' *Proceedings ASCE Special Conference on Coastal Sediment*, Charleston, SC, 898–913.
- Yamamoto, T., Konning, H.L., Sellmeijer, H. and van Hijum, E.V. (1978) 'On the response of poro-elastic bed to water waves' *Journal of Fluid Mechanics*, 87, 2: 193–206.
- Zen, K. and Yamazaki, H. (1990) 'Mechanism of wave-induced liquefaction and densification in seabed' *Soils and Foundations*, 30, 4:90–104.
- Zienkiewicz, O.C. and Scott, F.C. (1972) 'On principle of repeatability and its application in analysis of turbine and pump impellers' *International Journal for Numerical Methods in Engineering*, 9:445–452.
- Zienkiewicz, O.C. and Taylor, R.L. (1989) *The Finite Element Method*, McGraw-Hill, New York.

Chapter 4

The stability of unsaturated soil slopes subjected to rainfall infiltration

C.W.W.Ng and Q.Shi

Abstract

Slope instability in unsaturated residual soils and loose fills has attracted increasing attention in recent years around the world in such countries as Brazil, South Africa, Japan and in the Far East. Rain-induced failures are the most common failures. Rainfall leads to the development of a perched water table, increasing the main groundwater level and soil erosion (due to concentrated water flow), resulting in an increase in pore water pressure or a reduction in soil matrix suction. This, in turn, results in a decrease in shear strength on the potential failure surface to a point where equilibrium can no longer be sustained in the slope and then failures occur. However, the present understanding of the influence of transient seepage in unsaturated soils, due to water infiltration under various boundary and ground conditions, and hydrogeological regimes on slope stability, is still relatively poor compared with other elements of geomechanics.

To investigate the influence of various rainfall events and initial ground conditions on transient seepage and hence slope stability, a parametric study has been conducted using the finite element method. A typical steep unsaturated cut slope in Hong Kong has been adopted for the parametric study. Variables considered in the parametric study include soil isotropic and anisotropic permeability, and rainfall intensity and duration. Pore water pressures or suctions predicted during the transient seepage analyses are then used as input groundwater conditions for subsequent limit equilibrium analyses of the stability of the slope. A factor of safety is calculated using Bishop's simplified method, with a modified Mohr—Coulomb failure criterion to allow for shear strength variation due to the presence of matrix suction. Infiltration due to rain-water causes a reduction of matrix suction, but an increase in moisture content and water permeability in unsaturated soils. A perched water table is developed above the main water table. The factor of safety is not only governed by the intensity of rainfall, the initial groundwater table and the anisotropic permeability ratio, but it also depends on antecedent rainfall duration. A critical rainfall duration can be identified, at which the factor of safety is the lowest.

Introduction

Slope instability in unsaturated residual soils and loose fills is attracting increasing attention in many countries around the world such as Brazil, Italy, South Africa, Japan and in the Far East. The causes of landslides in these slopes are attributed to a number of factors. Rain- induced failures are the most common ones around the world (Brand [1], Fukuoka [2], Premchitt *et al.* [3], Wolle and Hachich [4], Fourie [5], Lim *et al.* [6]). For instance, the annual number of landslides caused by rainfall in Japan is in excess of 10,000 and could be as high as 100,000 (Fukuoka [2]). Pore water pressure (u_w) in the shallow depth of these residual soil and loose fill slopes is generally negative with respect to the atmospheric pressure (u_a). The presence and the magnitude of matrix suction ($u_a - u_w$) have been found to be absolutely crucial to the stability of unsaturated soil slopes (Fredlund and Rahardjo [7]).

Infiltration of rain-water or ingress of a wetting front (Lumb [8]) leads to the development of a perched water table, rising in the main groundwater level and washing out (soil erosion due to concentrated water flow), resulting in an increase in pore water pressure or a reduction in soil matrix suction. This, in turn, results in a decrease in shear strength on the potential failure surface to a point where equilibrium can no longer be sustained in the slope and then failures occur. Slope failure mechanisms found in these landslides generally consist of both shallow and deep-seated slips, depending mainly on the thickness of these residual soils and loose fills. Deep-seated static soil liquefaction occurred in some loose fill slopes under intense rainfall (Brand [1]).

The physical processes of infiltration of rainwater into the ground and its seepage through the soil stratum have been studied by hydrogeologists, soil scientists and geotechnical engineers. Equations and numerical models have been derived and developed for use (Lumb [9], Leach and Herbert [10], Anderson and Pope [11], Lam *et al.* [12], Pradel and Raad [13]). However, several important limitations on the use of these equations and models are discussed in the following paragraphs.

Lumb [9] derived an expression for the advance of the “wetting front”, with the assumption that diffusion is negligible at the end of an intensive rainfall:

$$h_w = \frac{k_s t}{n(S_f - S_o)} \quad (4.1)$$

where n is porosity, k_s is saturated water permeability, t is time, and S_o and S_f are the initial and final degree of saturation respectively. The soil will only be fully saturated near the surface, but will be wet (degree of saturation, $S=0.8$ to 0.9) down to a depth h (see Figure 4.1). The method was frequently used in the 1970s and 1980s to design the water table for slopes by superimposition of the depth of wetting front onto the main groundwater table at the end of a wet season. However, this equation does not take account of sloping ground conditions,

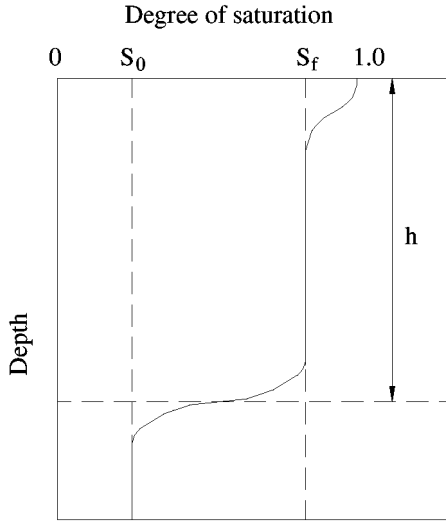


Figure 4.1 Variation of degree of saturation with depth during infiltration [9].

downslope flows, rainfall intensity, or most importantly, the dependence of water permeability on moisture content. The determination of S_0 and S_f is somewhat speculative (Brand [1]).

For achieving saturation of the soil to some critical depth (z_w) in a slope, Pradel and Raad [13] postulated that the rainfall must be intense enough to exceed the infiltration rate of the soil and must last long enough to saturate the slope to that depth. They showed that the time (T_w) necessary to saturate the soil to depth z_w is:

$$T_w = \frac{(\theta_s - \theta_0)}{k_w} \left[z_w - C_s \ln \left(\frac{C_s + z_w}{C_s} \right) \right] \tag{4.2}$$

where θ_s and θ_0 are the saturated and field volumetric water content respectively, k_w is the coefficient of hydraulic conductivity of the soil in the wetted zone, and C_s is the wetting-front capillary suction. The infiltration rate v_i at which water enters the soil surface is:

$$v_i = k_w \left(\frac{C_s + z_w}{z_w} \right) \tag{4.3}$$

To ensure that the wetting front penetrates to a depth z_w , the critical rainfall duration and intensity must not be smaller than T_w and v_i respectively. It seems that any variations of water permeability in the unsaturated soil zone are not considered in this approach.

Leach and Herbert [10] developed a finite difference semi-empirically based multi-layer model to predict and identify possible changes in piezometric pressure resulting from extreme rainfall events with a duration of less than 1 hour. The governing two-dimensional time-variant groundwater flow equation used to describe the changes in pressure head (h) with time in a continuous aquifer having variable values of the specific storage (S_s) and the saturated water permeability (k), is:

$$\nabla^2 h = \left(\frac{S_s}{k} \right) \left(\frac{\partial h}{\partial t} \right) \quad (4.4)$$

In a fixed slope geometry, the response to rainfall is a direct function of the ratio k/S_s . The higher the value of the ratio, the faster the heads will rise and decay, and the shorter will be the response time of the system to storm events. Parameters used in the model were obtained and adjusted from back-analysed rainfall records. As a constant saturated permeability value is assumed, this approach may give rise to misleading predictions in unsaturated soil regimes which are commonly present in Hong Kong. In addition, transient water flow due to various rainfall intensities are not considered.

Anderson and Pope [11] incorporated unsaturated flow into a hydrological model to investigate the stability of a typical slope in Hong Kong. In the unsaturated flow zone, water movement was assumed to be vertical (one-dimensional), whilst in the saturated zone, water could flow in both horizontal and vertical directions. Water permeability was no longer a constant value in the unsaturated zone and it depended on the degree of saturation. Thus a soil-moisture permeability relation for the specific soils was defined in their analysis. Pore pressure and suction predicted by the model were adopted as input parameters for limit equilibrium stability calculations. They showed that the minimum factor of safety occurred when the storm duration just exceeded one day, thereafter it remained approximately constant for the 4-day duration considered. In their analyses, the flow and stability calculations were treated in a completely uncoupled manner, similar to the approach adopted by Thomas and Rees [14]. However, advances have been made recently to fully couple flow and deformation analyses in unsaturated soils (Thomas and He [15]).

In practice, the ground conditions in the unsaturated region which may affect the groundwater level at any point are generally very complex and it is difficult to predict reliably the pore pressure distributions for stability calculations. The current knowledge of the influence of transient seepage under various boundary and ground conditions and hydrogeological regimes on slope stability calculations is relatively poor compared with other elements of geomechanics. In this paper, a finite element parametric study of transient flow has been carried out to investigate the influence of various rainfall events, initial ground conditions and water permeability on transient seepage in unsaturated soils and hence the soil slope stability. A typical steep, unsaturated slope in Hong Kong has been used for

this parametric study. The rainfall events considered correspond to 1 in 10-year return period storms. In addition to water permeability, rainfall intensity and duration are treated as variables for the parametric studies. For the slope stability analysis, results from the parametric study are used as input groundwater conditions for limit equilibrium calculations. The factor of safety is obtained using Bishop's simplified method, with modified Mohr-Coulomb failure criterion to allow for shear strength variation due to the presence of matrix suction. The transient seepage analyses (assuming a non-deforming soil) and slope stability calculations (assuming rigid perfectly plastic soil behaviour) were treated in a completely uncoupled manner.

The objectives of this study are, firstly, to illustrate and clarify the nature of the pore pressure distribution in a typical unsaturated slope; secondly, to demonstrate the sensitivity of transient flow systems to various initial hydraulic boundary conditions, rainfall intensities and duration, and *in situ* soil permeabilities; and finally to show and report the sensitivity of the factor of safety to these variables.

Theory of water flow in unsaturated soils

Water flow through unsaturated soils is governed by the same physical law—Darcy's law—as fluid flow through saturated soils. The major difference between water flow in saturated and unsaturated soils is that the coefficient of permeability (hydraulic conductivity), which is conventionally assumed to be a constant in saturated soils, is a function of degree of saturation or matrix suction in the unsaturated soils. The pore water pressure generally has a negative gauge value in the unsaturated region, whereas the pore water pressure is positive in the saturated zone. Despite the differences, the formulation of the partial differential flow equation is similar in the two cases.

The governing differential equation (Lam *et al.* [12]) for water flow through a two-dimensional unsaturated soil element is as follows:

$$\frac{\partial}{\partial x} \left(k_x \frac{\partial h}{\partial x} \right) + \frac{\partial}{\partial y} \left(k_y \frac{\partial h}{\partial y} \right) + Q = \left(\frac{\partial \theta_w}{\partial t} \right) \quad (4.5)$$

where h is total hydraulic head, k_x and k_y are the hydraulic conductivity in the x -direction and y -direction respectively, Q is the applied boundary flux, θ_w is the volumetric water content. The equation illustrates that the sum of the rates of change of flows in the x -direction and y -direction plus an external applied flux is equal to the rate of change of the volumetric water content with respect to time.

The amount of water stored within the soil depends on the matrix suction and the moisture retention characteristics of the soil structure (see Figure 4.2). The slope of the curve represents the retention characteristics of a soil, i.e., it represents the rate of water taken or released by the soil as a result of a change in

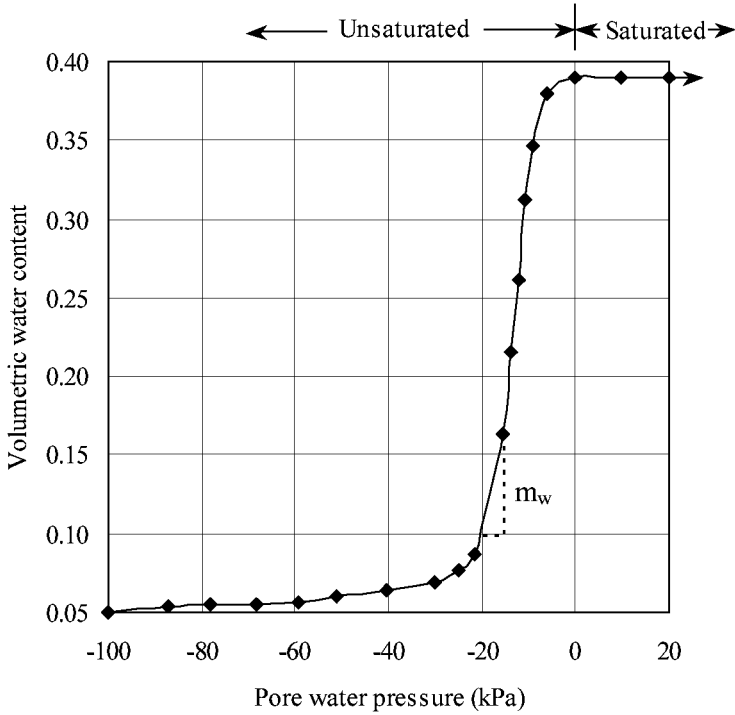


Figure 4.2 Volumetric water content vs pore water pressure.

the pore water pressure. At 100% saturation, the volumetric water content is equivalent to the soil porosity.

In unsaturated flow, the hydraulic conductivity is highly dependent on the water content of a soil. This is because of the heterogeneous volume distribution of the pore water (or water content or matrix suction) within the soil mass. It is generally assumed that water flows along a web of interconnected but continuous conduits, and that as the water content increases, the size and number of conduits increase, thereby enhancing the capability to conduct water through the soil. Since a unique relationship is assumed between the water content and pore water pressure, the hydraulic conductivity is thus also a function of pore water pressure as shown in Figure 4.3.

For an isotropic unsaturated soil element, the constitutive equation for the water phase (Lam *et al.* [12]) is:

$$\partial\theta_w = m_a \partial(\sigma - u_a) + m_w \partial(u_a - u_w) \quad (4.6)$$

where m_a and m_w can be regarded as constants for a particular time step during a transient process. Under saturated conditions, m_a is equivalent to the conventional

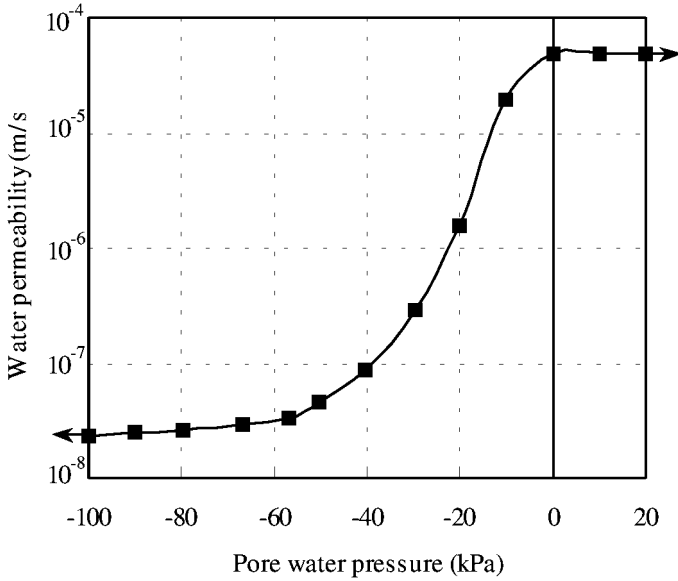


Figure 4.3 Water permeability vs pore water pressure.

coefficient of volume change, m_v . For transient seepage analysis, it can be assumed that the total stress in the soil mass and the pore air pressure remain constant. This means that $(\sigma - u_a)$ does not have any effect on the change in volumetric water content. In addition, no hysteresis is assumed between drying and wetting paths in the water retention curve (as shown in Figure 4.2). Then, a change in volumetric water content can be related to a change in pore water pressure by:

$$\partial\theta_w = m_w \partial u_w \quad (4.7)$$

Substituting equation (4.7) into (4.5), leads to the following governing differential equation for water flow in unsaturated soils:

$$\frac{\partial}{\partial x} \left(k_x \frac{\partial h}{\partial x} \right) + \frac{\partial}{\partial y} \left(k_y \frac{\partial h}{\partial y} \right) + Q = m_w \left(\frac{\partial u_w}{\partial t} \right) \quad (4.8)$$

where m_w is equal to the slope of the water retention curve (see Figure 4.2), which can readily be determined by experiments (Fredlund and Rahardjo [7]). If the water permeability is homogenous and isotropic, *i.e.* $k_x = k_y = k$, and $Q = 0$, equation (4.8) can be reduced to the following equation:

$$\nabla^2 h = \left(\frac{\gamma_w m_w}{k} \right) \left(\frac{\partial h}{\partial t} \right) \quad (4.9)$$

By comparing equations (4.4) and (4.9), it can be deduced that $S_s = \gamma_w m_w$. For water flow in saturated soils, $u_a = u_w$, then equation (4.6) becomes:

$$\partial \theta_w = m_a \partial (\sigma - u_w) \quad (4.10)$$

where m_a is equivalent to the coefficient of volumetric change m_v which is common to saturated soil mechanics.

Theory of shear strength for unsaturated soils

The mechanical behaviour of soils is governed by stress state variables which control the equilibrium of the soil structure. Physically meaningful stress state variables must be expressed in terms of measurable quantities such as the total stress σ , the pore water pressure u_w , and the pore air pressure, u_a . Matyas and Radhakrishna [16] introduced the two stress state parameters, $(\sigma - u_a)$ and $(u_a - u_w)$, to describe the volumetric behaviour of unsaturated soil. These two stress state parameters were subsequently adopted by Fredlund and Morgenstern [17] to conduct stress analysis of unsaturated soils on the basis of multi-phase continuum mechanics.

For soil located above the main water-table, the pore water pressure is negative with respect to the atmospheric pressure. This negative pore water pressure is commonly referred to as the matrix suction of soil. To account for the influence of this negative pore water pressure on soil shear strength and hence the factor of safety, Fredlund *et al.* [18] developed a modified form of the Mohr-Coulomb failure criterion for unsaturated soils, as follows:

$$\tau = c' + (\sigma_n - u_a) \tan \phi' + (u_a - u_w) \tan \phi^b \quad (4.11)$$

where σ_n is normal stress and ϕ^b is an angle defining the increase in shear strength for an increase in matrix suction. Based on some recent triaxial test results on completely decomposed granite (CDG) with suction measurements (Gan and Fredlund [19]), effective cohesion $c' = 10 \text{ kPa}$, angle of friction $\phi' = 38^\circ$ and $\phi^b = 15^\circ$ were adopted in the limit equilibrium analyses. It should be noted that shear strength varies with matrix suction in a non-linear fashion (Gan *et al.* [20]). The value of ϕ^b decreases with increasing suction. However, for simplicity and the small suction range considered in the stability analyses, a constant ϕ^b value was assumed.

The mid-levels on Hong Kong island

Hong Kong is located at the mouth of the Pearl River on the south east coast of China. The Mid-levels considered in this study is located on the northern slopes of Hong Kong Island. The geology of Hong Kong has been reported by many researchers (Davis [21]). The predominant rock types in Hong Kong are granitic, volcanic and sedimentary rocks. Chemical and physical weathering processes have resulted in the formation of mantles of saprolitic and residual soils, which are up to 50 m thick over the granite, with a saturated water permeability varying between 1.5×10^{-6} m/sec and 8.0×10^{-6} m/sec (Premchitt *et al.* [3]). The average saturated permeability of the underlying bedrock is 2×10^{-7} m/sec.

One important issue relating to the slope stability problems in Hong Kong is the presence of colluvium (clayey, sandy silt) which covers many of the footslopes. Colluvium is a mixture of soil and decomposed rock debris produced from landslips migrating progressively downslope. Many slope failures are associated with the collapse of colluvium during rainstorms. Colluvium on the upper slopes of the Mid-levels is an interlocked boulder scree with little or no matrix. However, this progressively changes downslope to a sequence of cobbles and boulders in a matrix of clayey, sandy silt (Leach and Herbert [10]). The thickness of the colluvium varies from place to place, ranging from 1 m to 36 m thick in the Seymour area, with saturated permeability varying between 5×10^{-6} m/sec and 3.5×10^{-4} m/sec (GCO [22]). Since the thickness of each soil layer varies from place to place, it was decided to idealise the complex hillside geology as a single soil layer together with a relatively impermeable rock stratum for parametric studies presented in this chapter (see Figure 4.4). The practical range of the saturated water permeability considered is given in Table 4.1.

Rainfalls in Hong Kong originate from two different processes, either slow-moving low pressure troughs or tropical cyclonic storms (Lumb [8]). Very often the troughs bring continuous rain over several days, i.e., trough to succeed another trough after a few days of dry weather. The storms are always associated with strong winds, which may reach typhoon strength, and can produce very intensive rainfall over several hours. However, these rainstorms rarely cause more than two or three days of continuous rainfall.

The average annual rainfall in Hong Kong is 2225 mm, with 80% of this occurring between May and September each year (Premchitt *et al.* [3]). During the rainstorms, hourly rainfall intensities can exceed 100 mm/hr and those in excess of 50 mm/hr are not uncommon. Based on the actual rainfall record, a 10-year return period spanning from 1980 to 1990 (Lam and Leung [23]) has been selected for parametric study in this chapter (refer to Table 4.1). In fact, the amount of rainfall can vary substantially with time and location. However, for the scope of the parametric study, the exact magnitude of rainfall is not particularly important and so any slight discrepancies will not affect any conclusions arising from this study.

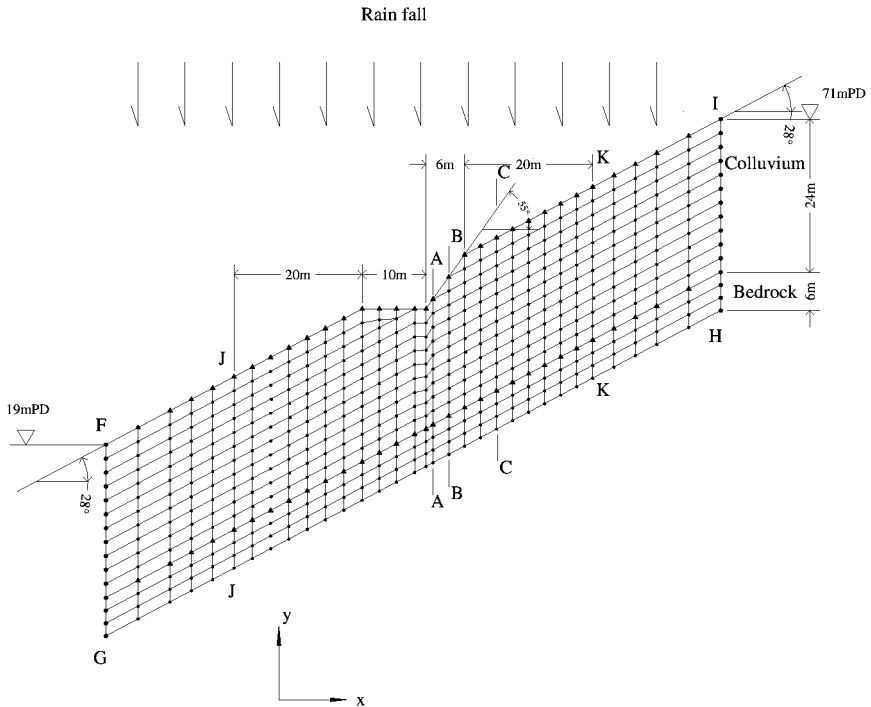


Figure 4.4 Finite element mesh used in the seepage analysis.

Between the end of 1970s and the early 1980s, the Geotechnical Control Office conducted some extensive pore pressure measurements at the Mid-levels using tensiometers and piezometers (GCO [22]). Very scattered suction values, varying from 0 to 80 kPa (practical upper limit of the tensiometers) were measured in colluvium, CDG and completely decomposed volcanic (CDV). These measured values depend on locations, depths and season.

Numerical experiments using the finite element method

Figure 4.4 shows the finite element mesh of a typical unsaturated hillside with a steep cut slope in Hong Kong for the parametric study. The ground conditions at the site comprise a 28° natural slope which consists of a 24m thick soil layer which may be colluvium or CDG underlain by a 6 m thick bedrock. In the middle of the hillside, a 55° cut slope has been formed for providing a 10 m wide carriage-way. For the purposes of parametric studies, a constant hydraulic head is specified along the boundaries FG (at 6 mPD) and HI (at 62 mPD unless stated otherwise), whereas the bedrock is assumed to be an impermeable layer. The appropriateness of the specified hydraulic heads at the two boundaries can be verified by comparing the predicted and measured suction values in the slope (see below). On the exposed sloping surface (FI), infiltration due to rainfall is modelled by applying flux (Q) across the side of an element with varying

Table 4.1 Input parameters based on a 10-year return period (1980–1990).

Parameter	Rainfall intensity (mm/day)	Duration	Saturated permeability, k_s	Saturated θ_w	k_x / k_y	Remarks
basic run	267	24 hours	4.8×10^{-5} m/s	0.39	1	
i1	181	24 hours	4.8×10^{-5} m/s	0.39	1	
i2	267	24 hours	4.8×10^{-5} m/s	0.39	1	
i3	394	24 hours	4.8×10^{-5} m/s	0.39	1	
du1	0	0	4.8×10^{-5} m/s	0.39	1	an intense 2-hr
du2	394	24 hours	4.8×10^{-5} m/s	0.39	1	rainstorm
du3	82	7 days	4.8×10^{-5} m/s	0.39	1	(148 mm) is
du4	46	15 days	4.8×10^{-5} m/s	0.39	1	added at the end
du5	29.4	31 days	4.8×10^{-5} m/s	0.39	1	of each run
k1	267	24 hours	4.8×10^{-4} m/s	0.37	1	
k2	267	24 hours	4.8×10^{-5} m/s	0.39	1	
k3	267	24 hours	4.8×10^{-6} m/s	0.34	1	
an1	267	24 hours	4.8×10^{-5} m/s	0.39	1	
an2	267	24 hours	4.8×10^{-5} m/s	0.39	2	
an3	267	24 hours	4.8×10^{-5} m/s	0.39	4	

Notes

i1, i2, i3=intensities; du1, du2, du3, du4, du5=durations; an1, an1, an3=anisotropic permeability ratios; k1, k2, k3=water permeabilities.

intensity (mm/day) at the boundary. Since the thickness of colluvium and CDG vary from place to place, a single uniform soil layer is assumed initially for the purposes of parametric seepage and stability analysis.

The two-dimensional finite element program SEEP/W (Geo-slope [24]) has been adopted for the parametric study. This program can be used to model both saturated and unsaturated flows under steady-state and transient conditions. Based on laboratory measurements of fine sand and silt (Ho [25]), the volumetric water content function and water permeability-pore pressure characteristic function for colluvium and CDG are derived as shown in Figures 4.2 and 4.3 respectively. Recently, experimental evidence (Ng and Pang [26]) suggests that the volumetric water content function of CDV can be strongly affected by stress state. The influence of stress-state dependency of volumetric water content on the stability of unsaturated soil slopes has been investigated recently (Ng and Pang [27]) and a lower factor of safety has been found if the influence of stress state has been included in the analysis for some ground conditions. For simplicity, the influence is not included in this study.

For studying the sensitivity of water permeability, the saturated water permeability is modified according to data available in Hong Kong (see Table 4.1). However, the shape of the curve has been kept the same. The derived permeability functions or curves are believed to be sufficiently accurate for the purposes of the parametric analyses.

In presenting various pore water pressure distributions after rainfall and associated factors of safety for slope stability in this chapter, the presented results all relate to a time immediately after completion of rainfall. It should be noted that the factor of safety may not be always a minimum value immediate after the rainfall. This is because water will continue to seep downwards through the soil after the rainfall ceases, so that, if the critical slip surface is at depth, the minimum factor of safety may not be reached until some time after the rain stops. However, as most of slope failures in Hong Kong are shallow in depth, the time delay for reaching the minimum factor of safety for deep-seated failures is not relevant for the parametric study of the stability of the steep cut slope presented in this chapter.

Influence of rainfall Intensity

Traditionally, interpretations of what rainfall conditions are needed to initiate slope failure have frequently been based on a statistical approach. Vargas [28] and Brand [1] correlated a number of landslides with rainfall intensity and concluded that if the rainfall intensity of a rainstorm exceeded a threshold value (70 mm/hr in Hong Kong), the probability of landslide was very high. Their statistical studies do not seem to have considered the influence of initial geological and hydrological conditions on the slope failures and the variations of pore water pressure in the ground before and after the landslides.

For investigating the influence of transient rainfall intensity on pore pressure distributions in the slope and hence slope stability, three 1 in 10-year return daily rainfall intensities were considered (see Table 4.1). Except for the rainfall intensity, relevant mean values (e.g. $k_s=4.8 \times 10^{-5}$ m/sec) from Table 4.1 were adopted for the transient parametric seepage analyses using SEEP/W. Before any transient seepage analysis is carried out, the initial groundwater condition is set up by conducting a steady state seepage analysis (i.e. $Q=0$) under the specified boundary hydraulic head conditions. This is based on the assumption that evapotranspiration from the ground surface is negligible. For comparing the ground response with various rainfall intensities with an upslope specified water table at 62 mPD (9 m below ground level), critical sections regarding the stability of the cut slope are considered (see Figure 4.4), which include Section A-A near the toe, Section B-B at the mid-height, and Section C-C above the cut slope. The computed initial pore pressure distribution varying with depth at these three critical sections is shown in Figure 4.5. As expected, the pore water pressures are negative above the main water table. The pore pressure distributions vary linearly with depth, with suction values up to 50 kPa predicted within the top 10m from the exposed slope surface. The predicted initial main water tables at these three critical sections, A-A, B-B and C-C, are at 39.8 mPD, 41.3 mPD and 45.5 mPD respectively (i.e., 2.3 m, 4.4 m and 6.5 m below the corresponding ground levels). The numerical predictions are in reasonable agreements with field measurements described previously. This implies that the realistic equipotential values were applied at the upslope and downslope boundaries.

Since the pore water pressure responses to various rainfall intensities are similar in nature, only a set of typical pore water distributions (along three critical sections) with depth is shown in Figure 4.6. During the one-day rainfall of 267 mm/day, it can be seen that the pore pressure response varies from section to section. At Section C-C, the ground surface is at 52 mPD and the main groundwater table (45.5 mPD) is at 6.5 m below the ground surface, the deepest among the three sections considered. By comparing with the initial conditions shown in Figure 4.5, it is clearly that the main water table is hardly affected by the 1-day rainfall. Based on some typical values of CDG, equation (4.1) would predict that the advancement of 100% saturation wetting front is in the order of 15–20 m. This significant discrepancy is likely caused by the low unsaturated water permeability that existed in the ground, which was not taken into account by equation (4.1).

However, the pore water pressure regime above the main groundwater table at Section C-C is substantially affected by the rainfall. The magnitude of negative pore water pressure is reduced by a considerable amount, which depends on the intensity of the rainfall simulated. For the rainfall intensity of 267 mm/day, a perched water table appears at 51.8 mPD. This offers a theoretical illustration to support the explanations of some of the observed slope failures in Lantau Island in Hong Kong (Wong and Ho [29]).

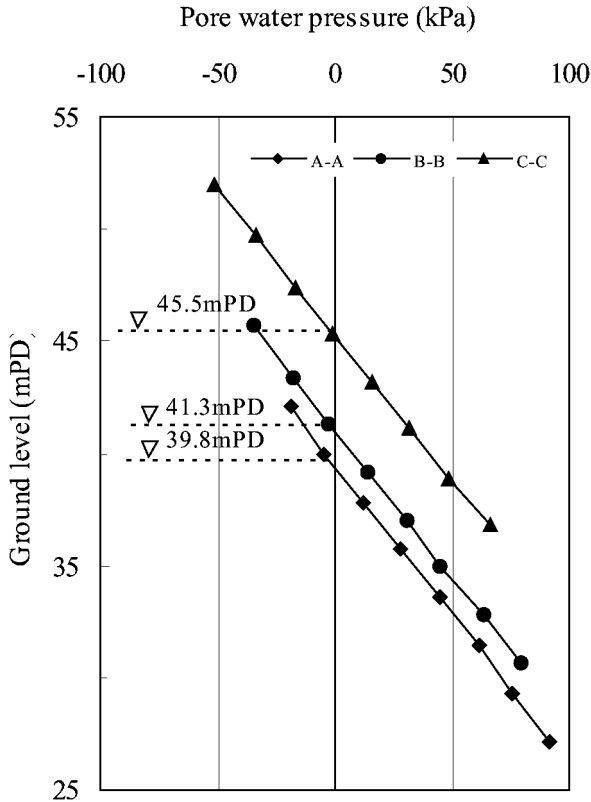


Figure 4.5 Pore water pressure distributions at initial steady state.

By considering equation (4.8), it can be deduced that for an isotropic and homogeneous soil, the rise of the main water table is not only governed by the ratio k/S_s , but it is controlled also by the ratio Q/k , even for a given set of slope geometry and boundary conditions. At Section B-B, the initial main groundwater table rises from 41.3 mPD (4.7 m below the ground surface) to 41.6 mPD. The amount that the water table rises is found to be approximately proportional to the rainfall intensity. This is consistent with the study reported by Pradal and Raad [13]. The magnitude of negative pore water pressure at the ground surface reduces to about half the initial value. However, the amount of reduction seems to be relatively unaffected by the intensity of rainfall (compare Figures 4.6a and 4.6b).

Due to the proximity of the main water table to the ground surface at Section A-A, as expected, rainfall of various intensities not only causes a rise of the main water table but it also results in a reduction in the magnitude of negative of pore water pressure at the ground surface. The rise of the main water table is greater at this section than other sections (B-B and C-C). This is because of the

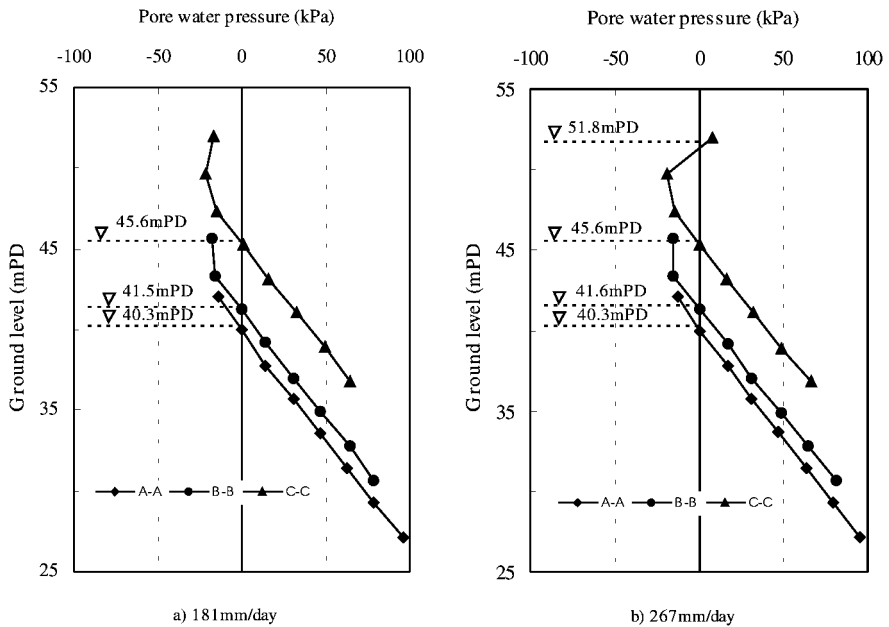


Figure 4.6 Effect of rainfall intensity on pore pressure distributions at the end of rainfall.

downward and horizontal seepage from the upslope in both saturated and unsaturated soil zones.

The effects of various rainfall intensities on the stability of the cut slope are shown in Figure 4.7 for the three different initial hydraulic boundary conditions. Both positive and negative pore water pressures predicted by SEEP/W were used as input groundwater conditions for limit equilibrium analyses of the stability of the slope. The factor of safety was calculated using Bishop's simplified method, with a modified Mohr-Coulomb failure criterion to allow for shear strength variation due to the presence of matrix suction (see equation (4.11)). It can be seen that for a given set of water permeability, slope geometry and initial ground-water conditions, the factor of safety of the slope decreases as rainfall intensity increases. The decrease of the factor of safety was attributed to the reduction in matrix suctions and a consequent fall in shear strengths caused by the rise in pore water pressures.

The influence of initial groundwater conditions on the factor of safety is also investigated by specifying different hydraulic heads at the upslope of the hill (i.e., at HI in Figure 4.4). It can be seen in Figure 4.7 that the initial groundwater condition has a significant influence on the stability calculations. This series of parametric analyses clearly illustrates that the factor of safety of a slope not only depends on the rainfall intensity but is also affected by the initial pore pressure distribution prior to the rainfall. This implies that the use of a single threshold

rainfall intensity (e.g., 70 mm/hr adopted in Hong Kong) as a landslide warning signal could be potentially very misleading. In other words, a slope can be perfectly stable if the initial main water table is low, even if subjected to extremely high rainfall intensity.

Influence of rainfall duration

The relevance of long periods of rainfall to slope stability has attracted considerable attention and debate over the years. Based on empirical correlation found between rainfall and landslide data, researchers such as Peck [30] and Lumb [8] have suggested the significance of 10-day and 15-day antecedent rainfall on slope stability respectively. By making use of automatic rain gauges to obtain better and more data of rainfall distribution and intensity, Brand [1] and Premchitt *et al.* [3] concluded that the majority of landslides are induced by localised short duration rainfall events of high intensity. Antecedent rainfall is not of major significance. However, all these traditional correlations between rainfall data and slope failure events ignore local geological and hydrological conditions.

To investigate the effects of rainfall duration on slope stability, 1 in 10-year rainfall records collected by the Hong Kong Royal Observatory between 1980 and 1990 (Lam and Leung [23]) were adopted for parametric studies. The rainfall events considered are shown in Figure 4.8. In the parametric analyses, it is assumed that the rate of infiltration is equal to the rainfall intensity. The hydraulic heads at HI and FG (see Figure 4.4) were specified at 62 mPD and 6 mPD respectively, and other relevant mean values from Table 4.1 were adopted for the parametric analyses. At the end of each prolonged rainfall, a 2-hour rainstorm of high intensity (74 mm/hr) is also included in each analysis to investigate the influence of antecedent rainfall on the subsequent performance of the slope subjected to the intensive 2-hour rainstorm.

Figure 4.9 shows the locations of the main water table between sections JJ and KK of the natural slope under various rainfall conditions. It can be seen from Figure 4.9a that the intensive 2-hr rainstorm cause a significant rise of the main water table at the toe of the cut slope (near to Section A-A). This can probably explain why many slopes with a marginal factor of safety fail after an intensive rainstorm. For slopes with a higher factor of safety, a substantial amount of rain-water may be needed to cause landslides.

Figures 4.9b and 4.9c show a typical groundwater profile after 7-day and 15-day prolonged rainfall events with an average intensity of 82 mm/day and 46 mm/day respectively. Because of limited space, only some computed results are included. The main groundwater table rises globally. By comparing with Figure 4.9a, the influence of the 2-hr intensive rainstorm on the level of the main water table is more significant after the 7-day and 15-day prolonged rainfall events in terms of the amount and extent of the rise of the main water table. This is probably due to the increase of water permeability (hydraulic conductivity) as a

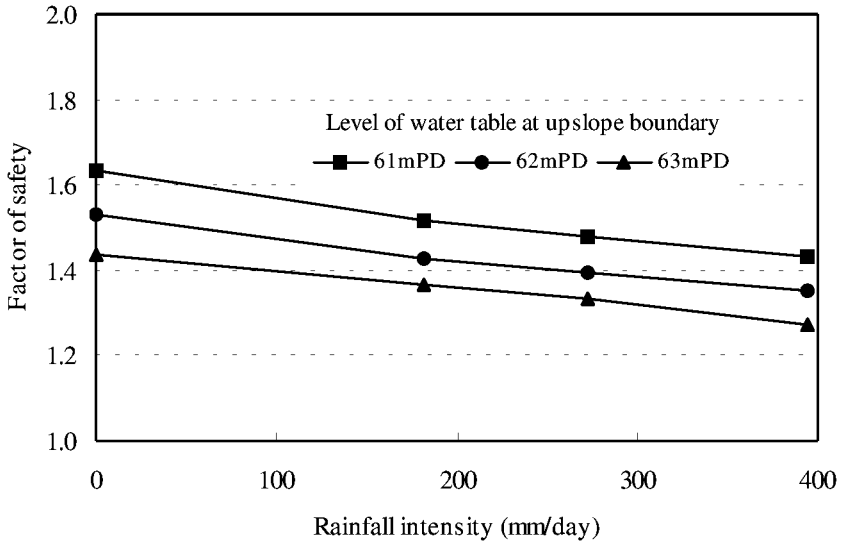


Figure 4.7 Factor of safety vs rainfall intensity.

result of the reduction of matrix suction in the unsaturated zone (refer to Figure 4.3).

Figure 4.10 shows the variation of the factor of safety with duration of rainfall. The factor of safety decreases with an increase in duration of rainfall, until a “critical duration” is reached. The initial fall in the factor of safety (f_1) is attributed to the rise of the main groundwater table as the duration increases. However, if the rainfall lasts longer than the critical duration, the rise of the main water table actually decreases as the duration increases. This is because the average rate of rainfall drops significantly with duration (see Figure 4.8).

Based on the analysed results, a critical rainfall duration exists, which leads to the lowest factor of safety. For the present investigation, the critical rainfall duration is found to lie between 3 and 7 days. The concept of the existence of a critical duration is in fact consistent with field measurements of groundwater response at the Mid-levels to rainfalls (GCO [22]). It was found that a critical duration of storm could be identified in both CDG and colluvium to characterise the pore water pressure response to a rainstorm for a given location. Typically the critical duration was found to lie between 2 and 7 days. Before reaching the critical duration, infiltration of rain-water is continuing to improve the initially low permeability of unsaturated soils and it results in a gradual rise of the main water table, until the main water table reaches its maximum at the critical duration. As the average rainfall intensity decreases rapidly with time (see Figure 4.8), the main water table will not rise further for rainfalls with duration which is longer than the critical value. Infiltrated groundwater will be drained away by soils with sufficient high permeability after “soaking”. The concept and existence of a critical duration can be further justified by considering landslides

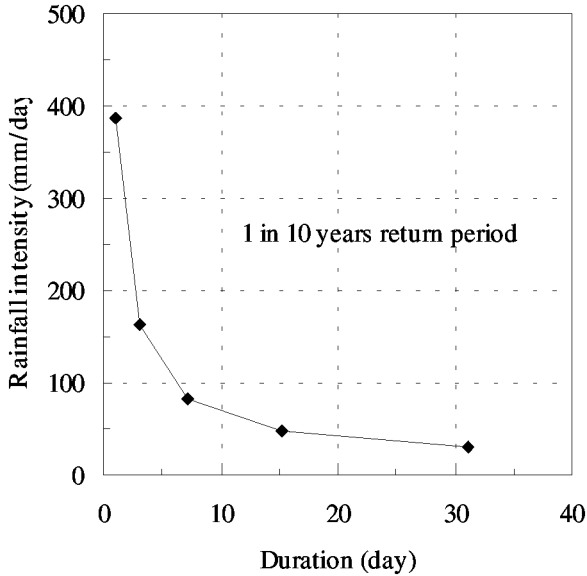


Figure 4.8 Relations between rainfall intensity and duration.

reported in the literature. Based on extensive field observations on failures, Vaughan [31] reported that slope failures occurred on the third day of prolonged heavy rainfall. Costa Nunes *et al.* [32] discussed how in slope failures in Rio de Janeiro, landslides only developed after 18 days of continuous rainfall.

Based on the field data and the current numerical investigation, it is anticipated that a critical duration is likely to be governed by the ratios Q/k and m_w/k for given geometry and boundary conditions and rainfall patterns (or characteristics), as shown in Figure 4.8.

The relative importance of rainfall duration and short-duration rainstorms with high intensity on factor of safety is clearly illustrated in Figure 4.10. For rainfalls with duration shorter than the critical duration, an antecedent rainfall results in a larger fall in the factor of safety (f_2) during the subsequent 2-hr rainstorm. This finding is contradictory to the conclusions drawn by Brand [1] and Premchitt *et al.* [3]. It is clear from Figures 4.7, 4.9 and 4.10 that high intensity rainfall may be a triggering factor for landslides in those slopes with a marginal factor of safety. However, there are other factors such as duration which are also important and contribute to the occurrence of landslides. Senanayaka *et al.* [33] investigated slope failures in Sri Lanka and provided convincing evidence that the chance of a slope failure is not only affected by intensity but it is also determined by duration. The rule of thumb that they developed is “if more than 200 mm rainfall had occurred on the hill slopes in a period of 3 days and if wet weather was continuing, then the possibility of landslides looms ahead.”

A prolonged period of rainfall will certainly lead to an increase of water permeability in unsaturated soils. From equation (4.8), it can be deduced that the

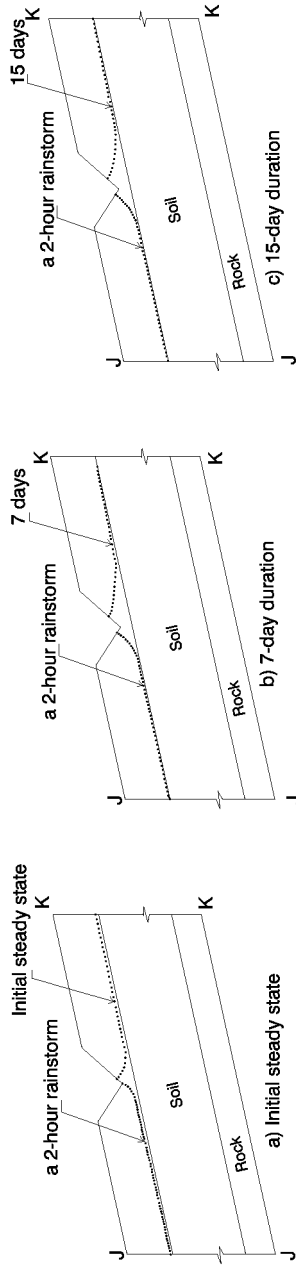


Figure 4.9 Groundwater rise due to a 2-hour rainstorm following various rainfall durations.

ground response to infiltration is a function of the ratio (k/m_w) , the higher the value of (k/m_w) , the faster the water table will rise and decay. The rapid rise of

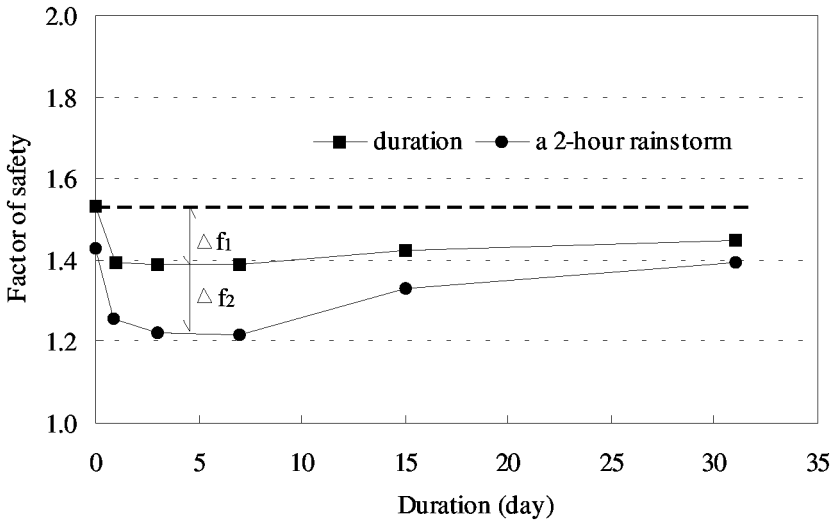


Figure 4.10 Factor of safety vs rainfall duration.

the main water table following a 2-hour rainstorm is shown in Figure 4.9 for various antecedent rainfall duration, and the influence of the 2-hour rainstorm on the factor of safety of the slope is illustrated in Figure 4.10. As expected, the 2-hour rainstorm affects the factor of safety with and without an antecedent rainfall. However, the degree of influence of the 2-hour rainstorm on the factor of safety depends on the duration of antecedent rainfalls. For an antecedent rainfall duration shorter than the critical duration (7 days), the drop in the factor of safety (f_2) caused by the 2-hour rainstorm increases with the duration. On the other hand, however, (f_2) becomes smaller when the duration of an antecedent rainfall event is longer than the critical value. This suggests that the risk of a landslide is highest during a short-duration rainstorm when the slope has been subjected to an antecedent rainfall event of the critical duration. This is because an antecedent rainfall event of critical duration not only causes an increase in water permeability due to the advancement of the wetting front, but it also causes a rise in the main water table. A subsequent 2-hour rainstorm of high intensity leads to a sharp fall in the factor of safety and causes a major landslide, especially for those slopes with a marginal factor of safety.

Influence of saturated water permeability

Making use of equations (4.2) and (4.3), Pradel and Raad [13] studied the effect of permeability on surficial stability of homogenous slopes in Southern California and concluded that soils with a low permeability such as clayey and silty soils are more prone to slope failure than granular materials. For given

boundary conditions, rainfall infiltration and duration, they also found that soils with a permeability greater than a certain limiting value will not become saturated.

In fact, two extreme cases can be considered, i.e. k tending to infinity and k tending to zero. In the former extreme, there will be no infiltration of water into a slope during rainfall, hence no increase in pore water pressure and no drop in the factor of safety. At the latter case, water will infiltrate the slope but will immediately drain away through the boundaries, so that again there is no increase in pore water pressures and no drop in the factor of safety. However, at intermediate permeability values, water will infiltrate the slope to a certain degree and will not entirely drain away, hence giving rise to an increase of pore water pressures and a reduction in the factor of safety. This implies that a critical saturated water permeability exists which corresponds to the minimum factor of safety.

To investigate the sensitivity of the factor of safety to saturated water permeability in Hong Kong soils, a typical range of saturated soil permeabilities have been adopted (see Table 4.1). The range of saturated soil permeabilities is taken with reference to the measured limits in colluvium and CDG, ranging from 1.0×10^{-3} to 1.0×10^{-7} m/sec (GCO [22]). Since only a limited but practical range of saturated soil permeabilities have been selected, there is no guarantee that the critical saturated water permeability will fall within the selected range.

Initially homogeneous isotropic flow is considered, i.e., the saturated water permeability in the x -direction (k_x) and in the y -direction (k_y) are assumed to be equal. Examining the governing groundwater flow equation (4.8), it can be deduced that in a model of fixed geometry and rainfall intensity, the response to infiltration is a function of the ratios k/m_w and Q/k .

Figures 4.11a and b show the pore water pressure distributions with depth, corresponding to saturated soil permeabilities of 4.8×10^{-4} m/sec and 4.8×10^{-6} m/sec respectively. The pore water pressure distribution with depth for a saturated water permeability of 4.8×10^{-5} m/sec is shown in Figure 4.6b. For a given slope and rainfall intensity (Q) of 267 mm/day (3.1×10^{-6} m/sec), there is no significant difference between the ground pore water response for $k=4.8 \times 10^{-4}$ m/sec and 4.8×10^{-5} m/sec (see Figures 4.11a and 4.6b), except that the degree of saturation (indicated by the formation of a perched water table) above the main water table at Section C-C is higher for soils with lower permeability. This is consistent with the findings reported by Pradel and Raad [13]. The groundwater response is dominated by the ratio (k/m_w) when the rainfall intensity is small relative to the saturated water permeability, i.e., negligible Q/k . The higher the ratio of k/m_w , the faster the water table rises and decays.

For soils with very low permeability of 4.8×10^{-6} m/sec, the main groundwater rises significantly at Sections B-B and C-C (see Figure 4.11b) and the degree of saturation increases further at Section A-A, comparing Figure 4.6b and Figure 4.11b. As the magnitude of saturated water permeability (4.8×10^{-6} m/sec) is comparable with the rainfall intensity (3.1×10^{-6} m/sec), the ratio Q/k is one

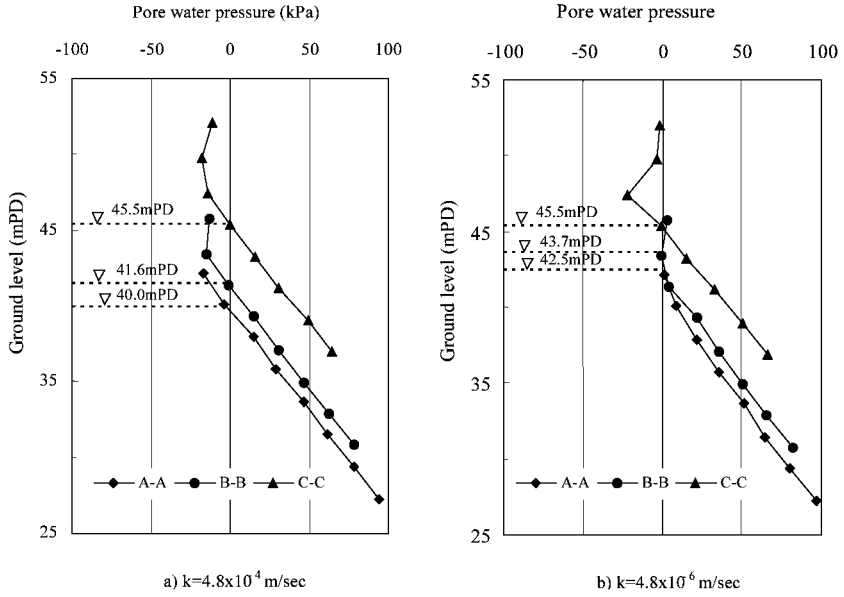


Figure 4.11 Pore water pressure distribution for various water permeabilities.

and two orders of magnitude larger than the previous two cases, shown in Figure 4.6 and Figure 4.11a respectively. Thus, the ratio Q/k governs the response of pore water pressure for the low permeability soil and this leads to high pore water pressure being developed in the ground, as shown in Figure 4.6b.

Figure 4.12 shows the variation of the factor of safety with saturated water permeability for a given slope and rainfall intensity. As expected, the factor of safety reduces with decreasing saturated water permeability but the rate of reduction of the factor of safety is relatively small for high water permeability with respect to the rainfall intensity. On the other hand, the factor of safety drops more significantly when the saturated water permeability is of a comparative magnitude to the rainfall intensity.

Back-analysis of subsurface water flows in slopes at the Mid-levels conducted by Leach and Herbert [10] have concluded that it is necessary to consider heterogeneous anisotropic flows in order for their model to predict correctly the observed groundwater changes. The governing differential equation for their model (see equation (4.4)) is essentially the same as equation (4.8), except that flux was not considered.

In this chapter, heterogeneous anisotropic flow means that the permeability in the x -direction (horizontal), k_x , and in the y -direction (vertical), k_y , are not equal, but that the ratio (k_x/k_y) is a constant at any point within the soil mass. The magnitude of k_x and k_y can also vary with a change of the moisture content or of

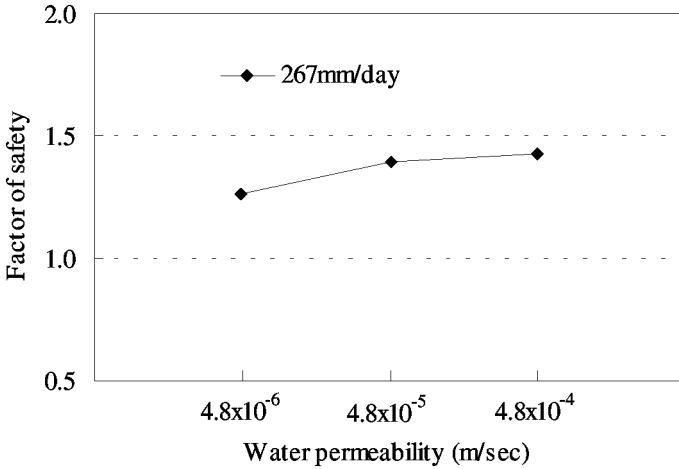


Figure 4.12 Factor of safety vs water permeability.

the matrix suction. For parametric studies, two anisotropic cases are considered: $(k_x/k_y)=2$ and 4, keeping $k_x=4.8 \times 10^{-5}$ m/sec unchanged but reducing k_y . The effects of anisotropic permeability on the initial (i.e. $Q=0$ in equation (4.8)) groundwater table are shown in Figure 4.13. It can be seen that permeability anisotropy has a significant influence on the position of the initial groundwater table. Reduction of permeability in the vertical direction (k_y) limits the amount of water flowing in the y -direction for a given slope and time. Since the hydraulic boundaries of the hillside slope are fixed, to maintain the continuity of flow, the main groundwater table has to rise and the rising of the main groundwater table is higher in the lower part than the one in the upper part of the natural hillside slope. This results in the “divergence” of the main groundwater tables for the two anisotropic cases, $k_x/k_y=1$ and 2, from the upper to the lower slope. For the case of permeability anisotropy $k_x/k_y=4$, the main groundwater table rises substantially on the upper part of the hillside slope. The sloping surface of the cut slope behaves as a low permeability membrane to cause a substantial rise of the main groundwater table.

Figures 4.14a and b show the pore water pressure distribution with depth during a rainfall intensity of 267 mm/day for the two anisotropic soil permeabilities, $k_x/k_y=2$ and $k_x/k_y=4$ respectively. Comparing with the pore water pressure distribution for the case of isotropic water permeability shown in Figure 4.6, a substantial rise of the main groundwater table (more than 1 m) is observed for the three cross-sections considered in the soil with $k_x/k_y=2$. This is mainly attributed to the increase in the ratio Q/k_y , as due to the reduction of k_y (refer to equation (4.8)). However, a negative pore water pressure (unsaturated) zone still exists in the slope.

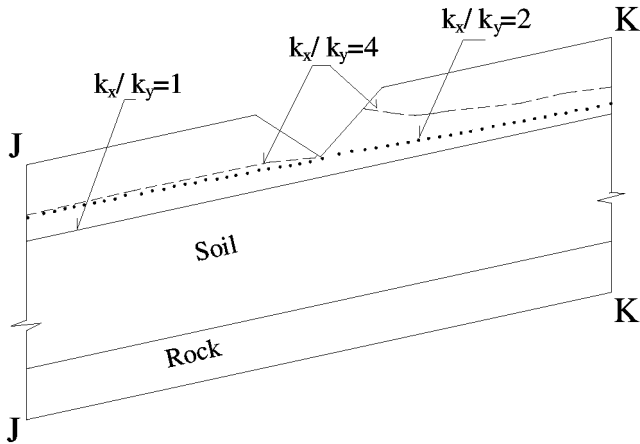


Figure 4.13 Effect of permeability anisotropy on initial groundwater table.

For the case of higher anisotropic ratio, $k_x/k_y=4$, the main groundwater table rises substantially at all three sections considered. The substantial increase in pore water pressures at Sections A-A and B-B is somewhat unexpected. This could be due to some small numerical errors occurred at the air-water interface on the sloping surface.

Figure 4.15 shows the influence of various anisotropic permeability ratios (k_x/k_y) on the stability of the cut slope. As expected, the large increase in pore water pressure in the vicinity of the cut slope has significant implications on its stability. At the initial steady state, the factor of safety of the cut slope decreases as the anisotropic permeability ratio (k_x/k_y) increases. The factor of safety decreases further when the slope is subjected to a daily rainfall of 267 mm/day and the cut slope fails if $k_x/k_y=4$. For the range of heterogeneous anisotropic flows analysed, the factor of safety of the slope is very sensitive to the anisotropic permeability ratio. The higher the degree of hydraulic anisotropy, the lower the factor of safety becomes.

Conclusions

A series of finite element parametric analyses has been conducted to investigate the influence of various rainfall events and initial ground and boundary conditions on transient seepage and hence slope stability in unsaturated soils. A typical steep unsaturated cut slope on a hillside in Hong Kong has been used to illustrate key results from the parametric studies.

Infiltration due to rain-water causes a reduction of matrix suction and an increase in moisture content and water permeability in the unsaturated zones. A perched water table is developed above the main water table. This offers a theoretical explanation and illustration of some slope failures in Hong Kong. For an initially low main water table in the ground, infiltration will not result in a

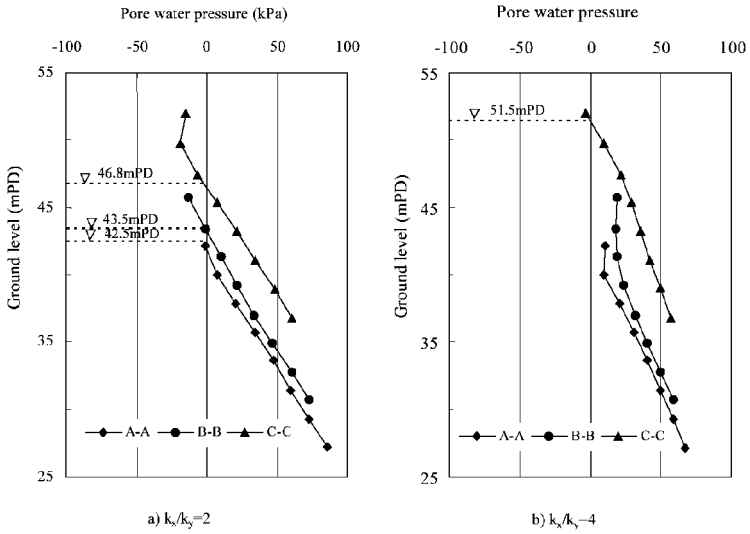


Figure 4.14 Ground water response for the anisotropic water permeability.

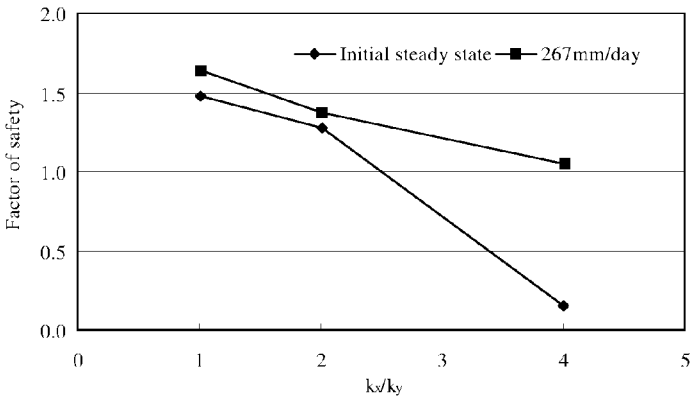


Figure 4.15 Factor of safety vs anisotropic water permeability.

significant rise of the main water table, but it can substantially change the negative pore water pressure regime above the main groundwater table. The reduction of the magnitude of negative pore water pressure, which seems to depend on the intensity of the rainfall, leads to a fall in the factor of safety for a given slope.

The location of the initial groundwater table has a significant effect on the stability of a slope. The current parametric analyses clearly illustrate that the factor of safety of the slope not only depends on the rainfall intensity but it also relies on the initial groundwater conditions prior to the rainfall. This implies that

the traditional approach of using a single rainfall intensity (threshold value) as a landslide warning signal could be potentially misleading. In other words, a slope can be perfectly stable if the initial main water table is low, even if it is subjected to extremely intense rainfall.

Antecedent rainfalls have significant influence on the stability of the slope. The degree of influence depends on their duration. The factor of safety decreases as the duration of rainfall increases, until a critical duration is reached. For the given geological and hydrological conditions of the cut slope, the critical duration has been found to lie between 3 and 7 days. At this critical duration, the factor of safety is the lowest. More importantly, antecedent rainfalls with duration less than or equal to the critical duration adversely affect the stability of the cut slope during a subsequent heavy rainstorm. On the other hand, antecedent rainfalls with duration longer than the critical duration do not seem to affect the stability of the slope during a subsequent heavy rainstorm.

For rainfalls lasting longer than the critical duration, the factor of safety gently increases due to the reduction of average rainfall intensity over the entire rainfall duration considered. The concept of the existence of a critical duration is consistent with field measurements of groundwater response to rainfall at the Mid-levels. High-intensity rainfall can be a triggering factor for landslides but there are other factors such as antecedent rainfall duration, which are also important and contributed to the occurrence of landslides.

The factor of safety of the slope decreases with water permeability, but the rate of reduction in the factor of safety is relatively small for soils with high permeability, with respect to the rainfall intensity. However, the factor of safety drops sharply when the water permeability has a comparative magnitude to the rainfall intensity and this factor is extremely sensitive to the anisotropic permeability ratio (k_x/k_y). The higher the ratio, the lower the factor of safety becomes.

Acknowledgements

Reprinted from *Computer and Geotechnics*, Vol. 22, C.W.W.Ng and Q.Shi, A numerical investigation of the stability of unsaturated soil slopes subjected to transient seepage, pages 1–28, 1998, with permission from Elsevier Science.

This research was conducted under a grant awarded to the first author by the RGC Direction Allocation Grant at the Hong Kong University of Science and Technology. The authors would like to thank Mr K.K.S.Ho, Dr Alex Li and Dr H.W.Sun of the Geotechnical Engineering Office for their useful discussions.

References

- 1 Brand, E.W. (1984) Landslides in south Asia: a state-of-art report, Proceedings of 4th International Symposium on Landslides, Toronto, 1, 17–59.

- 2 Fukuoka, M. (1980) Landslides associated with rainfall. *Geotechnical Engineering Journal, Southeast Asia Society of Soil Engineering*, 11, 1–29.
- 3 Premchitt, J., Brand, E.W. and Phillipson, H.B. (1986). Landslides caused by rapid groundwater changes. *Groundwater in Engineering Geology, Proceedings of 21st Annual Conference Engineering Group of Geological Society, London*, 87–94.
- 4 Wolle, C.M. and Hachich, W. (1989). Rain-induced landslides in south-eastern Brazil. *Proceedings of 12th International Conference on Soil Mechanics & Foundation Engineering, Rio de Janeiro, Vol. 3*, 1639–1644.
- 5 Fourie, A.B. (1996). Predicting rainfall-induced slope instability. *Geotechnical Engineering, Proceedings of the Institution of Civil Engineers*, 119, 211–218.
- 6 Lim, T.T., Rahardjo, H., Chang, M.F. and Fredlund, D.G. (1996). Effect of rainfall on matrix suctions in residual soil slope. *Canadian Geotechnical Journal*, 33, 618–628.
- 7 Fredlund, D.G. and Rahardjo, H. (1993). *Soil mechanics for unsaturated soils*. John Wiley & Sons.
- 8 Lumb, P.B. (1975). Slope failures in Hong Kong. *Quarterly Journal of Engineering Geology, London*, 8, 31–65.
- 9 Lumb, P.B. (1962). Effects of rainstorms on slope stability. *Symposium on Hong Kong Soils, Hong Kong*, 73–87.
- 10 Leach, B. and Herbert, R. (1982). The genesis of a numerical model for the study of the hydrology of a steep hillside in Hong Kong. *Quarterly Journal of Engineering Geology, London*, 15, 243–259.
- 11 Anderson, M.G. and Pope, R.G. (1984). The incorporation of soil water physics models into geotechnical studies of landslide behaviour. *Proceedings of the 4th International Symposium on Landslides*, vol. 4, 349–353.
- 12 Lam, L., Fredlund, D.G. and Barbour, S.L. (1987). Transient seepage model for saturated-unsaturated soil systems: a geotechnical engineering approach. *Canadian Geotechnical Journal*, 24, 565–580.
- 13 Pradel, D. and Raad, G. (1993). Effect of permeability on surficial stability of homogenous slopes. *Journal of Geotechnical Engineering Division, American Society of Civil Engineers*, 119, No. 2, 315–332.
- 14 Thomas, H.R. and Rees, S.W. (1994). Seasonal ground movement in unsaturated clay: an examination of field behaviour. *Géotechnique*, Vol. 44, No. 2, 353–358.
- 15 Thomas, H.R. and He, Y. (1995). Analysis of coupled heat moisture and air transfer in a deformable unsaturated soil. *Géotechnique*, Vol. 45, No. 4, 677–689.
- 16 Matyas, E.L. and Radhakrishna, H.S. (1968). Volume change characteristics of partially saturated soils. *Géotechnique*, Vol. 18, No. 4, 432–448.
- 17 Fredlund, D.G. and Morgenstern, N.R. (1977). Stress state variables for unsaturated soils. *Journal of Geotechnical Engineering Division, American Society of Civil Engineers*, 103, No. 5, 447–466.
- 18 Fredlund, D.G., Morgenstern, N.R. and Widger, A. (1978). Shear strength of unsaturated soils. *Canadian Geotechnical Journal*, 15, 313–321.
- 19 Gan, J.K.M. and Fredlund, D.G. (1996). Direct shear and triaxial testing of a Hong Kong soil under saturated and unsaturated conditions. GEO Report No. 46. Geotechnical Engineering Office, Hong Kong Government.
- 20 Gan, J.K.M., Fredlund, D.G. and Rahardjo, H. (1988). Determination of the shear strength parameters of an unsaturated soil using the direct shear test. *Canadian Geotechnical Journal*, 25, 500–510.

- 21 Davis, S.G. (1952). *The geology of Hong Kong*. The Government Printer, Hong Kong.
- 22 GCO (1982). Mid-levels study: report on geology, hydrology and soil properties. Geotechnical Control Office, Public Works Department of Hong Kong.
- 23 Lam, C.C. and Leung, Y.K. (1995). Extreme rainfall statistics and design rainstorm profiles at selected locations in Hong Kong. Technical Note No. 86. Royal Observatory, Hong Kong.
- 24 Geo-slope (1995). *User's guide for SEEP/W*, version 3. Geo-slope International Ltd, Calgary, Alberta, Canada.
- 25 Ho, P.G. (1979). The prediction of hydraulic conductivity from soil moisture suction relationship. BSc Thesis, University of Saskatchewan, Canada.
- 26 Ng, C.W.W. and Pang, Y.W. (2000). Experimental investigation of soil-water characteristics of a volcanic soil. *Canadian Geotechnical Journal*, Vol. 37, No. 6, 1252–1264.
- 27 Ng, C.W.W. and Pang, Y.W. (2000). Influence of stress state on soil-water characteristics and slope stability. *Journal of Geotechnical and Geo-environmental Engineering, ASCE*, Vol. 126, No. 2, 157–166.
- 28 Vargas, M. (1971). Effect of rainfall and groundwater levels. Proceedings of 4th Pan American Conference on Soil Mechanics & Foundation Engineering, San Juan, Puerto Rico, 138–141.
- 29 Wong, H.N. and Ho, K.K.S. (1995). General report on landslips on 5 November 1993 at man-made features in Lantau. GEO Report No. 44, Civil Engineering Department, Hong Kong Government.
- 30 Peck, R.B. (1967). Stability of natural slopes. *Journal of Geotechnical Engineering Division, American Society of Civil Engineers*, 93, No. 4, 403–418.
- 31 Vaughan, P.R. (1985). Pore pressures due to infiltration into partly saturated slopes. Proceedings of the 1st International Conference on Tropical, Lateritic and Saprolitic Soils, Brasilia, 2, 61–71.
- 32 Costa Nunes, A.J., Couto Fonseca, A.M., De M.Fernandes, C.E. and Craizer, W. (1989). Intense rainstorms and ground slides. Proceedings of 12th International Conference on Soil Mechanics & Foundation Engineering, Rio de Janeiro, Vol. 3, 1627–1630.
- 33 Senanayaka, K.S., Sithampton, P.M. and Herath, N.W. (1994). Salient aspects of landslides in Sri Lanka. Proceedings of 13th International Conference on Soil Mechanics & Foundation Engineering, New Delhi, Vol. 3, 1103–1106.

Chapter 5

Computational modelling of ground waves due to pile driving

C.L.Ramshaw and A.R.Selby

Introduction

A number of construction processes require high energy input to achieve their objectives. They include blasting for tunnelling and quarrying, rock ripping and breaking-out, ground improvement by vibro-compaction, dynamic compaction or vibratory rolling, pile-driving, the movement of heavy site plant, and demolition. All of these processes also cause severe ground vibrations close to the source activity. While many of these are used only in locations remote from buildings and services, piles must frequently be installed in urban development sites and residential areas. Here ground vibrations cause disturbance to residents and occupants of buildings, and may create a risk of cosmetic or structural damage (e.g. Wiss, 1967; Selby, 1991; Head and Jardine 1992; Malam, 1992; Dowding 1996). In such situations it is important to be able to predict ground vibrations and to monitor and control peak levels; it is important also to estimate the effects of the vibrations on buildings and buried services, see [Figure 5.1](#).

A variety of pre-formed piles exists which must be installed by high energy drivers. Steel sheet piles are used for quay walls, temporary cofferdams, retaining walls and integral bridge abutments. Steel bearing piles may be of tube, box or 'H' section, and may be driven vertically or to a rake and may be 40 m or more in length. Driven concrete piles may be precast reinforced or prestressed segmental units or driven and cast-in-place. In Canada and Scandinavia timber piles are sometimes used.

A wide range of hammers has been developed over the years, which can be classified as impact, vibratory and special. The character of ground vibrations is primarily a function of hammer type and energy.

Impact hammers

The simplest, and oldest, hammer is the drop weight, which is raised and released into 'free' fall by the main lift wire of a crane. It is cheap but of low efficiency, and may cause equipment wear. Air hammers (originally steam) are powered by compressed air; they have a high strike rate with low energy per

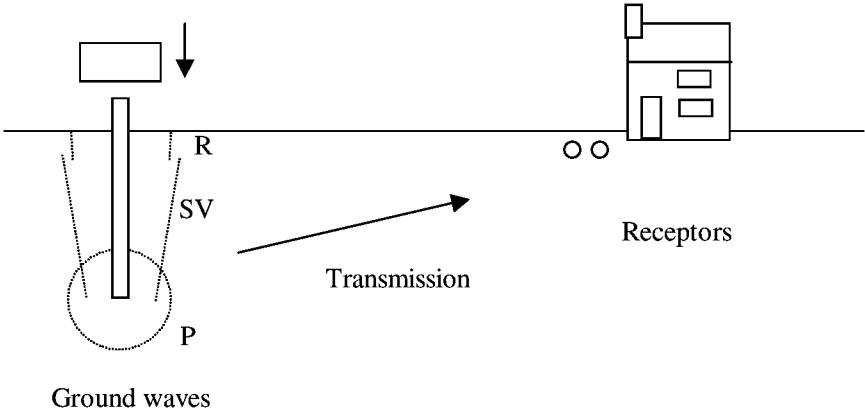


Figure 5.1 Schematic of ground waves caused by pile driving.

blow. They are noisy, which limits their use in residential areas. Diesel hammers are economical and effective but they are not controllable and they cause air pollution, so they are now rarely used. The hydraulic hammer, single or double acting, is efficient, controllable and environment-friendly, and is now the standard choice of impact hammer, whether for small pile elements on land or for very large tubes offshore.

All the above hammers are effective in installing piles into most soil types, provided that the correct hammer is selected for the work and that the pile drive is guided effectively, e.g. panel driving should be used for sheet pile walls, pile guide frames for long piles. The presence of a dolly, i.e. packing material between hammer and pile head to cushion the impact, changes the shape of the force-time impulse, reducing the peak and extending the time duration.

Many records of ground vibrations have been made in the last 30 years (e.g. Attewell and Farmer, 1973; Uromeihy, 1990; Hiller, 2000), so that the general pattern of vibrations is well known. At any surface measurement station within some 2 m to 50 m from the pile, there are three components of disturbance in the radial, transverse and vertical directions. The shape of the vibration as a function of time is typically a half-wave with pre- and post-cursor minor fluctuations, see Figure 5.2.

The magnitude of vibration of a soil particle can be defined in terms of maximum acceleration, velocity or displacement. The most commonly used parameter is maximum velocity, v_{\max} , partly because it is easily measured, and also because ground strain is defined approximately by

$$\varepsilon_g = \frac{v_{\max}}{c} \quad (5.1)$$

where c is the wave transmission velocity.

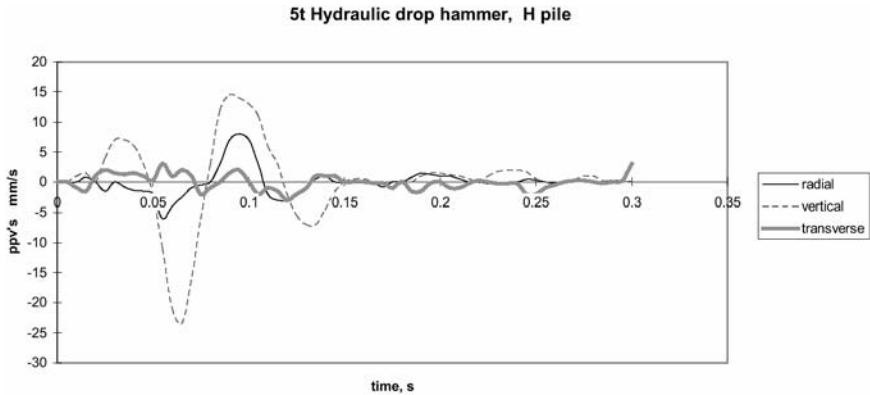


Figure 5.2 Example ground vibrations from an impact hammer.

The three components of velocity can be combined into a single vector trace by taking the values of radial, transverse and vertical velocities *at each instant in time*, and combining them to give the true peak particle velocity, ppv. The vector direction is ignored.

$$\text{ppv} = \sqrt{v_r^2 + v_t^2 + v_v^2} \quad (5.2)$$

The practice of taking the peaks of each signal regardless of time, and applying equation (5.2) gives a spurious value which is typically 20% in excess of the true value (Hiller and Hope, 1998). Conversely, the practice of using vertical peak velocity alone underestimates the true value by 20% or more. Indeed there is no obvious pattern to show which component is the largest of the three; vertical vibration may be largest close to a pile with large toe depth, while radial vibration may be largest at greater distance from the pile.

The peak particle velocity attenuates with distance away from the source, as energy density around the expanding wave front is reduced, i.e. geometric damping. However, the rate of attenuation is not well defined because the observed signal contains components of primary P-wave, vertical shear, SV, and surface or Rayleigh, R, waves, which attenuate differentially. The soils contribute a small degree of material damping. The non-uniformity of attenuation has been observed and discussed by Attewell *et al.* (1991) and Hiller (2000).

For practical purposes, a simplified estimate for ppv has been developed from Attewell and Farmer (1973), through BS5228 part 4 (1992), and culminating in Eurocode 3 Ch 5 (1996), as

$$\text{ppv} = \frac{C \cdot \sqrt{W}}{r} \quad (5.3)$$

where ppv has units of mm/s, C is an empirical constant ($= 0.5$ in soft ground, 0.75 in stiff soils, and 1.0 in hard ground), W is hammer energy per blow in joules, and r (m) is horizontal distance from the source. This is not an exact estimate, and considerable scatter of measured data is to be expected. A statistical approach was evaluated by Attewell *et al.* (1992), in which curves of 0.5 and 1.0 standard deviations in excess of best fit curves on log-log scales were produced.

There is a clear need for computational analysis of this complex system of ground vibrations, in order to clarify some of the issues observed in site data measurements.

Vibratory hammers

Vibratory hammers or ‘vibrodrivers’ are now widely used to install steel piles into granular soils. The strong vertical vibration of the whole pile causes liquefaction of the soils close to the pile shaft and toe, which causes the pile to sink into the ground under its self-weight plus the weight of the vibrodriver unit. Vibrodrivers are much less effective in advancing a pile through cohesive soil strata, which do not liquefy, but slow progress is possible as a result of the hammering action. They are very effective in pile extraction when the support crane applies an upward static force.

Vibrodrivers consist of eccentric contra-rotating masses which impose a vertical cyclic force onto the pile head, but horizontal effects are self-cancelling. The vibrator unit must be firmly clamped to the pile head, which is done by hydraulic gripper, with adapter where necessary for steel tube or box piles. Standard vibrodrivers cause the whole pile to oscillate vertically at some 25 Hz, but higher frequency equipment (c. 40 Hz) is often preferred in an urban location, to reduce the disturbance to buildings and occupants. A ‘resonant free’ system has been developed recently to avoid the problem of pile-soil resonance at about 5 – 10 Hz during run-up to operating frequency and run-down to rest. The system uses rotating discs which are in balance during run-up, and when operating speed is reached, then eccentric masses are deployed.

Many site records of ground surface vibrations have been taken (e.g. Uromeihy, 1990; Oliver and Selby, 1991; Hiller, 2000), all of which show a characteristic pattern of strongly sinusoidal radial transverse and vertical vibrations as a function of time, see [Figure 5.3](#). As before, the three components can be combined at instants in time to produce a vector trace using equation 5.2, and a true peak particle velocity.

The signal generally attenuates with distance from the source, but with some anomalies observed during site measurements. Ramshaw (2001) proposed that the signal may include a standing wave component. Attewell *et al.* (1992) produced curves based on log-log plots of amplitude/distance. Equation 5.3 gives practical estimates of ppv , as quoted in BS5228 and Eurocode 3, but for all soils, BS5228 recommends $C=1.0$, while Eurocode 3 proposes $C=0.7$.

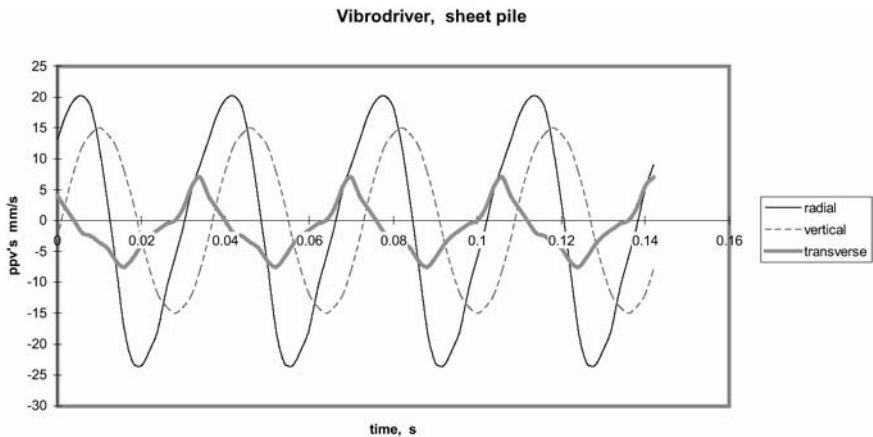


Figure 5.3 Vibrations caused by vibrodriving.

More controversially, Hiller and Crabbe (2000) found little change in ppv with hammer energy, which is usually quoted as energy per cycle, calculated as power divided by cyclic frequency in units of joules/cycle.

Within this context of varied observations and non-uniformity of attenuation, it is desirable to develop a computational procedure to analyse ground vibrations.

Special hammers

In locations which are highly sensitive to vibrations, e.g. close to hospitals or micro-electronics laboratories, special measures are required. Hydraulic jacking systems are available for sheet piling, which push one pile into the ground using the uplift resistance of adjacent piles and the weight of the plant for vertical reaction. For bearing piles, pre-augering may be sufficient, otherwise alternative systems may be required such as continuous flight auger or bored piles.

Sensitivity of humans and of buildings

The human body is highly sensitive to vibrations, and typically can detect vibrations as low as 0.1 mm/s in the frequency range of 1–80 Hz, see BS6472 (1992). Sensitivity varies depending upon the body position, i.e. seated, lying horizontally, or standing. Fingertip touch is more highly sensitive. Vibrations of some 5–10 mm/s may cause alarm or discomfort. Continuous vibration is less tolerable than intermittent, and long duration further reduces tolerance. BS6472 gives recommendations in terms of vibration dose value, VDV, but more easy to apply is the table from Eurocode 3, which is reproduced in summary in [Table 5.1](#).

Table 5.1 Human tolerance of vibration, in mm/s.

Duration D in days	$1 \leq D < 6$ days	$6 \leq D < 26$ days	$26 \leq D \leq 78$ days
Level I	1.5	1.3	1.0
Level II	3.0	2.3	1.5
Level III	4.5	3.8	2.0

Notes

1. Level I Under this level the vibration should be accepted
 Level II Acceptable with advanced warning. Complaints possible
 Level III Above these values—unacceptable.

2. The above values relate to 4 hrs of vibrations in the working day. For different durations of vibrations,

$$v_{tc} = \frac{V_4}{2} \sqrt{\frac{T_1}{T_c}}$$

where v_{tc} =transverse wave transmission velocity, V_4 =4 hours of vibrations, T_1 =16 hours and T_c is the exposure time in hours per day.

3. The limiting values apply for all environments other than hospitals, precision laboratories and libraries, in which vibrations of up to 0.15 mm/s should be acceptable.

There is little evidence to suggest that vibrations from piling *alone* cause even minor cracking damage to buildings in good repair, BRE Digest 353 (1990). BS5228 part 4 (1992) and BS7385 part 2 (1993) give recommendations for limits of transient vibrations. However, their threshold values are significantly different, with the values from BS5228 being lower in most conditions. Values for *continuous* vibrations are taken at 50% of transient values. Values for domestic and industrial buildings are plotted in Figure 5.4.

Further guidance for old buildings, buried services and retaining walls is available,

Objectives of the current study

The study takes place against a background of conflicting opinions on vibrations caused by impact and vibratory pile driving, and their consequences upon buildings and occupants. The overall objective has been to develop computational models to estimate outgoing ground vibrations, and to calibrate and refine the models by reference to a number of high quality site measurement data sets.

At a more detailed level, the following should be studied:

- Patterns of surface and below-surface ground waves.
- The non-uniform attenuation of transient vibrations from impact driving, and in particular the ‘quiescent zone’ identified by Hiller (2000).
- Proportionality of vertical and horizontal components of vibration.

Vibration thresholds for domestic and heavy industrial structures

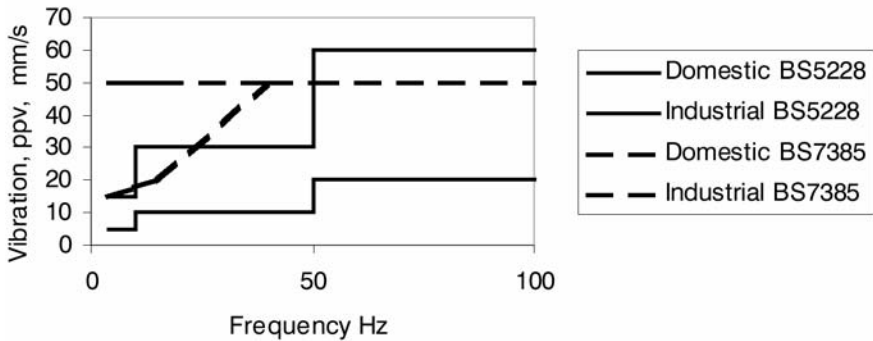


Figure 5.4 Recommendations for vibration thresholds in structures.

- Ground waves caused by vibrodriving, as a function of energy per cycle, and attenuation.
- Ultimately, the interactive response of buildings and services to outgoing waves.

The procedure followed was to build two- or three-stage computational models using axisymmetric finite and infinite elements for the soil half-space. The detailed behaviour of the pile-soil system was modelled separately for impact and vibratory hammers. For impact driving, a three-stage computation was found to be most effective, following the method of Deeks and Randolph (1993); firstly, the hammer-pile impact was modelled using a spring-mass-damper system; secondly the waves travelling down the pile shaft were computed with soil represented by springs and dampers; and finally the soil forces were imposed onto an axisymmetric mesh of FEs (finite elements) and IEs (infinite elements), to compute the outgoing waves. Infinite elements were used to avoid spurious reflections at the boundaries of a finite mesh. At all stages a time-stepping transient analysis was required which implied restrictions on element size and time step.

Vibrodriver simulation required a two-stage model; the vibrodriver, a rigid pile and springs and dampers for the soil was oscillated vertically. Then the deduced cyclic soil force-time functions were applied to an FE/IE axisymmetric soil mesh. A transient analysis was chosen in preference to a forced vibration (i) because waves radiated from the source localised to the pile shaft and toe, and (ii) because the far boundary of infinite elements was effective in reducing spurious reflections to a very small level, but was not a perfect representation as would be desired for a harmonic excitation analysis.

Finite element and infinite element models

This section contains a preliminary verification of the capability of the chosen elements to give a faithful representation of primary, P, shear, S, and Rayleigh, R, waves. Infinite elements are then assessed for their performance in limiting or eliminating reflected waves, and the simultaneous limit of P, S and R-wave reflection at the model boundaries. The multi-stage models for impact and for vibratory driving are then explained in detail. All computational analyses were undertaken using the Abaqus (1999) suite.

Element verification

The normal choice for axisymmetric analysis is the 8-noded quadrilateral, which is most effective when its aspect ratio is close to unity. For transient analysis, a suitable mesh will have some 10 nodes per wavelength, and the time-step interval should meet the stability criterion of $\Delta x = c \Delta t$, where Δx is the mesh spacing, c is the wave transmission velocity and Δt is the time step. Around the boundaries of the FE mesh it is necessary to include infinite elements, which contain 5 nodes to be compatible with the 8-noded quadrilateral, [Figure 5.5](#). The normal mesh used for the soil half-space comprised a 50×50 mesh of $1 \text{ m} \times 1 \text{ m}$ square axisymmetric FEs, with a surround of IEs on the outer vertical and base-horizontal boundaries.

These elements were tested for purity of transmission of P, S and R waves and for limitation of wave reflection (Ramshaw *et al.* 1998a). Consider the P-wave test. A small mesh of FEs was set up in plane-strain, with constrained vertical movement at top and bottom boundaries, and a compressive sine wave was imposed at each end of the mesh with appropriate time delay, based on the transmission velocity c_p of

$$c_p = \sqrt{\frac{\lambda + 2G}{\rho}} \quad (5.4)$$

where G is shear modulus, λ is a Lamé constant and ρ is density.

A pure sine wave was observed. The right-hand boundary was then meshed into infinite elements, and again a pure sine wave was observed, see [Figure 5.6](#).

The geometric attenuation of the P-wave was studied by imposing a compressive sine wave on a plane strain model, an axisymmetric mesh, and a spherical expansion. The plane strain showed negligible attenuation, the axisymmetric mesh gave attenuation of peak displacement proportional to $1/r$, while amplitudes in spherical expansion were proportional to $1/r^2$, in accordance with standard wave theory (Ramshaw *et al.* 1998b), where r is distance from the source.

Tests on S-wave generation and transmission were similar to those for the P-wave, but with modified top and bottom boundary restraints, and with imposed sinusoidal shear-waves, based on transmission velocity c_s of

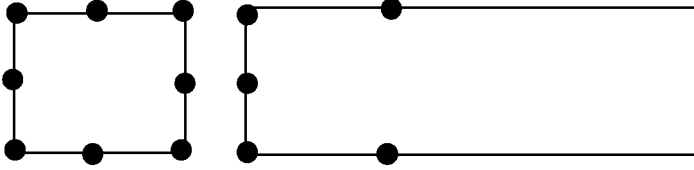


Figure 5.5 8-noded quadrilateral finite element and 5-noded infinite element.

$$c_s = \sqrt{\frac{G}{\rho}} \quad (5.5)$$

where the symbols are as above.

A pure wave was generated with either a double shear-wave, or with a shear-wave and infinite elements, Figure 5.7. Attenuation could be tested only with plane-strain and axisymmetric computations, the latter showing amplitude decaying as $1/r$.

Verification of the Rayleigh wave was undertaken with a free top surface, and with both vertical and horizontal components of excitation:

$$u = D \left[e^{0.8475ky} - 0.5573e^{0.3933ky} \right] \sin(kx - \omega t) \quad (5.6)$$

$$v = D \left[-0.8475e^{-0.8475ky} + 1.4679e^{0.3933ky} \right] \cos(kx - \omega t) \quad (5.7)$$

where k is the wave number, x is frequency and the constants correspond to a chosen value for Poisson's ratio of 0.25. The transmission velocity v_r is

$$v_r = 0.9194 \sqrt{\frac{G}{\rho}} \quad (5.8)$$

The pattern of surface disturbance and the near-purity of wave form are shown in Figure 5.8.

While a mesh with imposed wave pattern at input left-hand end and at output right-hand end gave pure wave forms, the infinite element method was not absolutely successful. This indicates the limitations of the basic infinite element method in absorbing more than one single wave component of fixed transmission velocity. Indeed, when an impure wave input such as that from a driven pile is the excitation of the FE/IE system, with outgoing P, S and R-waves, then the basic infinite element method is not adequate, and other methodologies are needed.

Infinite elements

The use of infinite elements to model continua has been developed particularly by Bettess (1992). The standard infinite element method available within Abaqus, see [Figure 5.5](#), is very effective in preventing spurious reflection when a single wave type and transmission velocity strikes the boundary. However, it is less effective when the wave pattern contains components of different velocities and/or directions.

A further difficulty may arise if static forces such as self-weight are to be applied prior to the dynamic analysis. The formulation of the dynamic damper is in terms of resistance to velocity, not displacement, with the result that the configuration of a pile in an elastic half-space has no resistance to rigid body movement of the FE mesh. Geostatic stresses are necessary when considering Coulomb slip at the interface between pile and soil, but would cause unrestrained extreme displacements, [Figure 5.9](#).

A number of strategies were used to achieve satisfactory analyses:

- 1 The viscous boundary developed by Lysmer and Kuhlemeyer (1969) was programmed into Abaqus as a 'user-defined' element. With respect to pure P or S-waves, this performed as well as the Abaqus element (Ramshaw, 1999) but caused significant extensions in run time, because of the toggling between formulations. However, it also had limitations with respect to Rayleigh waves (Lysmer and Kuhlemeyer, 1969).
- 2 Lysmer and Kuhlemeyer also proposed a Rayleigh wave damper where dashpots are tuned to the frequency of the incoming waves. This was also programmed in as user-defined, and produced a substantial improvement over the Abaqus element, albeit at the expense of extended run times (Ramshaw, 2001).
- 3 A combination of IEs was used, where geostatic stress was not required, as in [Figure 5.10](#), which was found to give satisfactory performance.
- 4 When considering interface slip at the pile-soil interface, it was necessary to generate normal stress between the pile and soil, which increases with depth. Application of soil self-weight caused the above problem of gross rigid-body movement. A device to generate the normal stresses was developed, in which a 'pseudo-pile' was expanded non-uniformly against the soil to generate the necessary stresses. Application of a Coulomb friction factor, μ , was then feasible.
- 5 Experience of actual wave patterns due to impact driving led to the conclusion that the most time-efficient computational model was a large FE mesh with rigid boundaries, eliminating the need for IEs. Careful scrutiny of the wave patterns showed that the significant waves were the first outgoing P-wave, followed by an S-wave which degenerated into an R-wave at the surface. Following wave bands were of much smaller amplitude. Consequently, the significant disturbance within say 20 m of the pile could

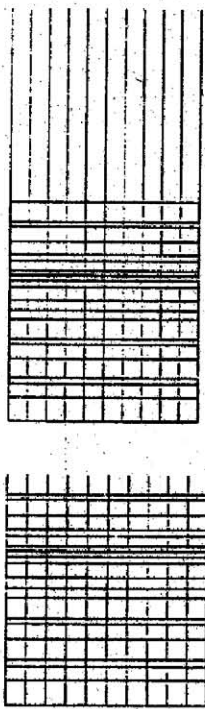
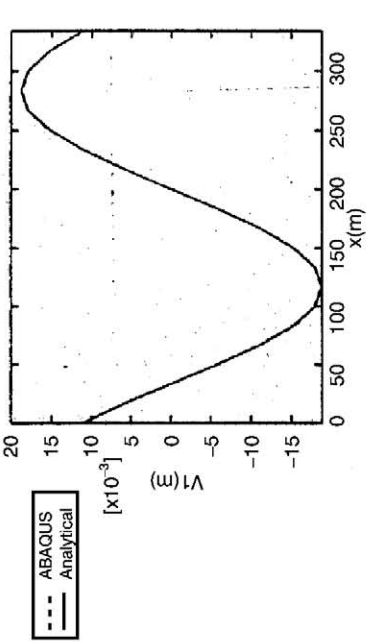


Figure 5.6 P-wave representation.

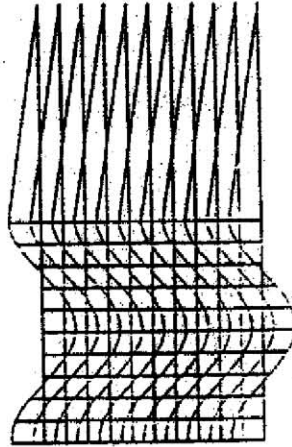
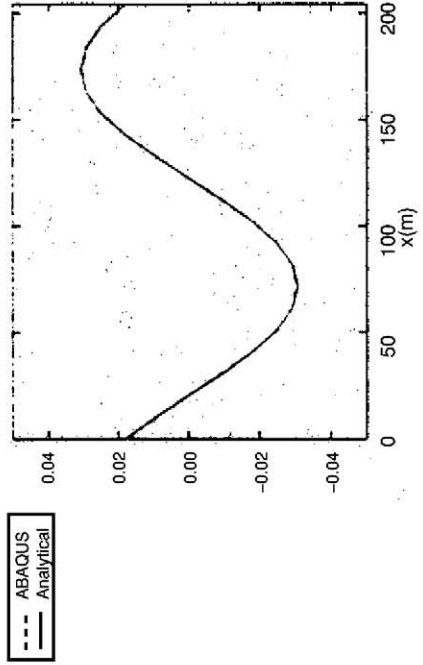


Figure 5.7 S-wave representation.

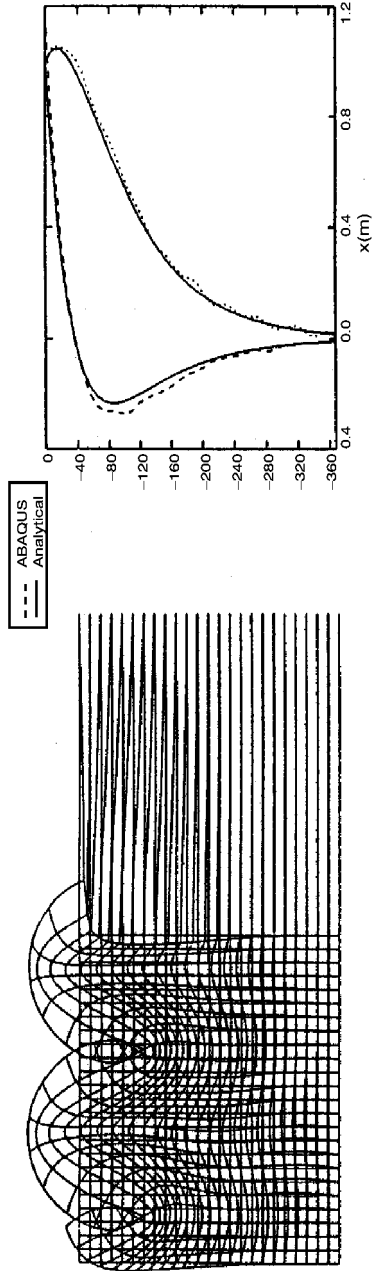


Figure 5.8 Rayleigh wave representation.

be identified within the transients, before any reflected wave from the rigid boundary had returned close enough to cause interference.

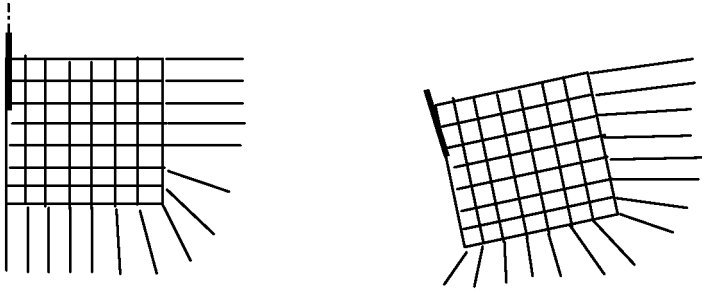


Figure 5.9 Schematic of response of a FE/IE mesh to geostatic self-weight. (Actual FE mesh was 50×50 or more.)

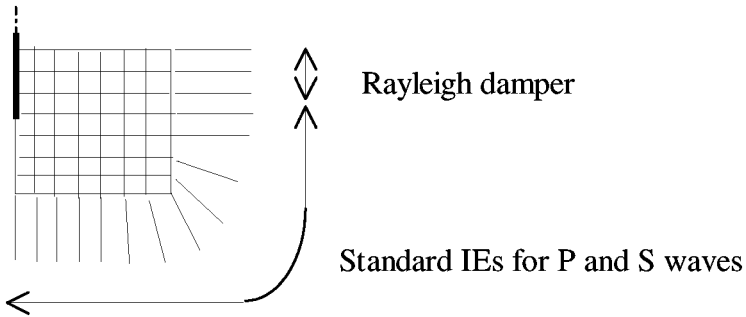


Figure 5.10 Schematic of zoned IEs. (Actual mesh was 50×50.)

6 Vibrodriving. An important choice of form of analysis was the selection of time-stepping transient, in preference to forced vibration with harmonic excitation. The choice was made partly because of the difficulty of boundary definition, and also to allow closer comparison with the site data. It was initially considered essential to generate accurate IE boundaries for this analysis, and good results were obtained when using scheme 3 above. However, it was again found to be the case that a larger FE mesh without IEs was sufficient to allow the set-up of the second or third cycle of an outgoing wave set, which was a good representation of the steady state vibrations, before reflected waves returned to interfere.

Impact hammers

The input excitation to an FE or FE/IE axisymmetric mesh due to the impact of a drop or hydraulic hammer is complex, and for efficiency of computation is better treated in three separate stages:

- i) Hammer impact model to identify the force-time characteristic imposed onto the pile head.

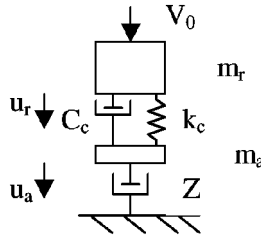


Figure 5.11 Hammer impact model.

- ii) Transmission of a compression wave down the pile,
- iii) Outward propagation of ground waves into the soil.

The advantages are that each parameter can be studied individually, and also greater mesh efficiency can be obtained by separating the transient wave analyses down the pile shaft and outward into the soil.

Stage 1

Firstly, the impact of the hammer onto a dolly on top of the pile can be analysed by a model (Deeks and Randolph, 1993) consisting of discrete masses of hammer and anvil/pile head, a spring and dashpot for the cushion, and a dashpot to represent the pile at this stage, see Figure 5.11.

Within Abaqus, the several units are represented by uni-axial springs and dampers, and by discrete masses, and the excitation of the transient time-stepping analysis is the velocity V_0 of the hammer at the moment of strike. The output from the analysis is a force-time function (derived as head velocity-time multiplied by pile impedance).

The pile is represented by its impedance, Z , as

$$Z = \frac{E_p \cdot A_p}{c_p} \tag{5.9}$$

where the pile is of elastic modulus E_p , area A_p and has axial wave velocity c_p .

Deeks and Randolph (1993) derived dimensionless parameters for the cushion stiffness, k_c^* , the anvil mass, m_a^* , and the cushion damping, C_c^* , as follows:

$$k_c^* = \frac{k_c \cdot m_r}{Z^2} \tag{5.10}$$

$$m_a^* = \frac{m_a}{m_r} \tag{5.11}$$

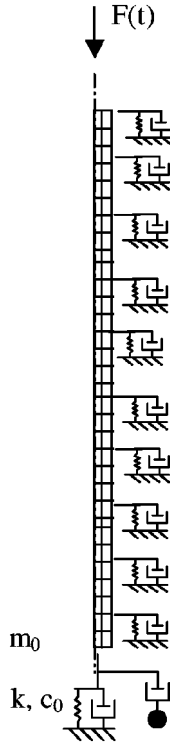


Figure 5.12 Schematic view of pile model for axial wave and shear transfer.

$$c_c^* = \frac{c_c}{Z} \tag{5.12}$$

where k_c is the stiffness of the cushion spring, m_r is the mass of the hammer ram, m_a is the anvil mass and c_c is the damping in the cushion.

Stage 2

In the second stage, the transmission of the compression wave down the pile shaft is simulated, following the method proposed by Deeks and Randolph (1995), see Figure 5.12. For the solution, the pile shaft is modelled by an axisymmetric mesh of 8-noded finite elements. A mass-spring-dashpot represents the toe resistance, (Wolf, 1988; Deeks, 1992). A series of springs and dampers is sufficient to model the shaft/soil interface, for this stage, which can transmit shear-waves independent of frequency. Excitation is imposed as a force-time function, and the required ‘solution’ is the force-time functions at each of the shaft spring-dampers, and at the toe, with respective time delays.

The parameters can be conveniently expressed in dimensionless terms. The frequency of the applied load, ω , is non-dimensionalised with respect to the radius of the pile base, R , and the shear-wave velocity of the soil, c_s .

$$a_s = \frac{\omega \cdot R}{c_s} \quad (5.13)$$

The static spring stiffness, k , is taken as

$$k = \frac{4 \cdot GR}{1 - \nu} \quad (5.14)$$

For convenience, non-dimensionalised mass and damping parameters α_0 , α_1 , β_0 and β_1 , are defined as:

$$\alpha_0 = \frac{m_0}{k} \left(\frac{c_s}{R} \right)^2 = 0 \quad \text{and} \quad \alpha_1 = \frac{m_1}{k} \left(\frac{c_s}{R} \right)^2 \quad (5.15)$$

$$\beta_0 = \frac{c_0}{k} \left(\frac{c_s}{R} \right) = 0 \quad \text{and} \quad \beta_1 = \frac{c_1}{k} \left(\frac{c_s}{R} \right) \quad (5.16)$$

Further, Deeks (1992) proposed the following expressions to accommodate variations in Poisson's ratio, ν , as:

$$\alpha_1 = 0.63 - 3.6\nu + 6\nu^2 \quad (5.17a)$$

$$\beta_1 = 1.58 - 10.3\nu + 19\nu^2 \quad (5.17b)$$

The pile shaft/soil interface described above is the frequency independent transmitting boundary for axisymmetric shear waves derived by Deeks (1992). This boundary is equivalent to viscous dashpots with a distributed damping constant of $\rho \cdot c_s$ (identical to a viscous boundary) and a distributed spring constant of $G/2r_b$, where ρ is the density of the soil, c_s is the shear-wave velocity in the soil, G is the shear stiffness of the soil and r_b is the pile radius.

Stage 3

The third and final stage of the procedure is to impose the displacement-time functions onto a large FE or FE/IE axisymmetric mesh of the surrounding soils. The pile response is transferred to the ground model by way of an unrestrained 'false' pile made up of axisymmetric finite elements.

The pile-soil interface is modelled using a surface-based contact simulation, with slip controlled by a Coulomb friction model with $\mu=0.1$ (Mabsout and Tassoulas, 1994). In order to simulate the horizontal stresses on the pile from the soil, the false pile is expanded laterally into the soil by a predetermined distance. (This avoids the problem of rigid body motion.) Once the horizontal stresses have equilibrated, the vertical displacements computed from the pile model are applied to the pile shaft nodes of the false pile and the soil nodes immediately under the pile toe in a dynamic analysis with time steps of 0.001 s.

Outward transmission of ground waves is then computed using elastic soil properties. Massarsch (1992) demonstrated that most of the energy is transmitted in elastic waves beyond about a pile radius from the pile. Parametric studies of site records of arrival times of waves at various distances from the pile indicate that the dynamic soil stiffness exceeds the static stiffness. This has been observed by several workers, e.g. Matthews *et al.* (1996). An appropriate FE mesh would typically be a 50×50 mesh of 8-noded quadrilateral elements, each of $1 \text{ m} \times 1 \text{ m}$. One of the more effective boundary strategies is also required, either of grouped IEs, or expansion of the FE mesh to allow study of outgoing waves without interference from spurious reflections.

Calibration of the impact driving model

Two sets of site data are next considered. The three-stage procedure described above was used, and the parameters were adjusted in turn, so as to obtain the best match between computed and site ground surface vibrations in both the vertical and radial directions. However, it was anticipated that a perfect match would never be achieved because of the assumptions of a pure axial impact, shaft guide location, energy transfer and uniform elastic soils.

Impact driving at the M66

One of the rare occasions when site data included both pile head force-time, and also adjacent ground surface vibrations was observed during dynamic testing of driven cast *in situ* piles for bridge foundations on the M66 motorway near Manchester.

Ten piles, 750 mm diameter and 21 m long, were tested by the SIMBAT system (Stain, 1992). A concrete pile cap was cast and strain gauges, accelerometers and an electronic theodolite target were attached. Signals were recorded during blows from a 2.2 tonne hammer falling through 1.2 m. Ground vibrations were measured by geophones placed on the ground surface at distances of 5.5 m, 10 m and 16.5 m. Ground conditions comprised firm to stiff clay soils from the surface to 10.5 m depth, underlain by dense sands. Static elastic moduli were $13 \times 10^6 \text{ Pa}$ and $24 \times 10^6 \text{ Pa}$ respectively, but a *dynamic* soil stiffness of $150 \times 10^6 \text{ Pa}$ was found to be appropriate for dynamic small strains.

The impact of the hammer onto the pile head was modelled with the conceptual model, and various values for the parameters α , β and γ were considered. The closest match with site pile head records was achieved with $\alpha = 0.01$ and $\beta = 0.01$. Typical ranges of values for the parameters are $\alpha = 0.001$ to 0.1 and $\beta = 0.001$ to 0.1 . The values for stiffness of the dolly and mass of the anvil are slightly outside these bands because of the special pile cap required for the SIMBAT tests.

The correlation between field measured and computed pile head displacement-time and force-time functions was quite close in magnitudes, but the force duration was overestimated, [Figure 5.13](#).

In stage 2 the force-time function was imposed onto the head of the model of pile shaft plus springs and dampers. The displacement-time functions were computed at each of the spring and damper sets on the shaft and toe.

In stage 3, the displacement-time functions were imposed onto the shaft and toe interface nodes of the FE/IE mesh. The computed surface vibrations at 5.5 m, 10m and 16.5 m from the pile are compared with measured values in [Figures 5.14](#) and [5.15](#).

Some discrepancies are apparent in the radial values, with measured S-waves generally larger than those computed. Also, there appears to be an observed early P-wave component, probably due to an eccentric strike, and a later hammer bounce trace. However, close agreement is shown in the vertical waves. Overall, however, the agreement is encouraging, considering the ground variability and the imperfect impacts.

Impact driving at Flitwick, Bedfordshire

A second calibration exercise is now presented, for the driving of a 12m long steel H-pile (305×305×89 kg/m), using a 3200 kg drop hammer falling through 1.0 m. The soil conditions comprised topsoil and soft clays to 2.4 m, loose sand and gravel at 2.4–4.8 m, then very dense uniform sands to considerable depth. The water table (WT) was at 2.4 m. Although the static elastic moduli for the three layers were estimated to be 5 MPa, 20 MPa and 50 MPa respectively, the *dynamic* stiffnesses used for the stage 3 computation were identified as 20 MPa above the WT and 200 MPa below. The three-stage computation was conducted for the condition of 7 m penetration depth.

A summary of some of the parameters used in the analyses of the hammer impact, the pile shaft and the pile toe is given in [Table 5.2](#).

Although no pile head signals were available during driving, the ground surface vibrations were recorded, and comparisons with the computed values are shown in [Figure 5.16](#), for radial particle velocities at 7 m and 16.5 m distances from the pile. The observed signals appear to include an extra peak from an early P-wave arrival, which is accentuated at 16.5 m, and was probably caused by an eccentric strike. Otherwise close correlation is achieved.

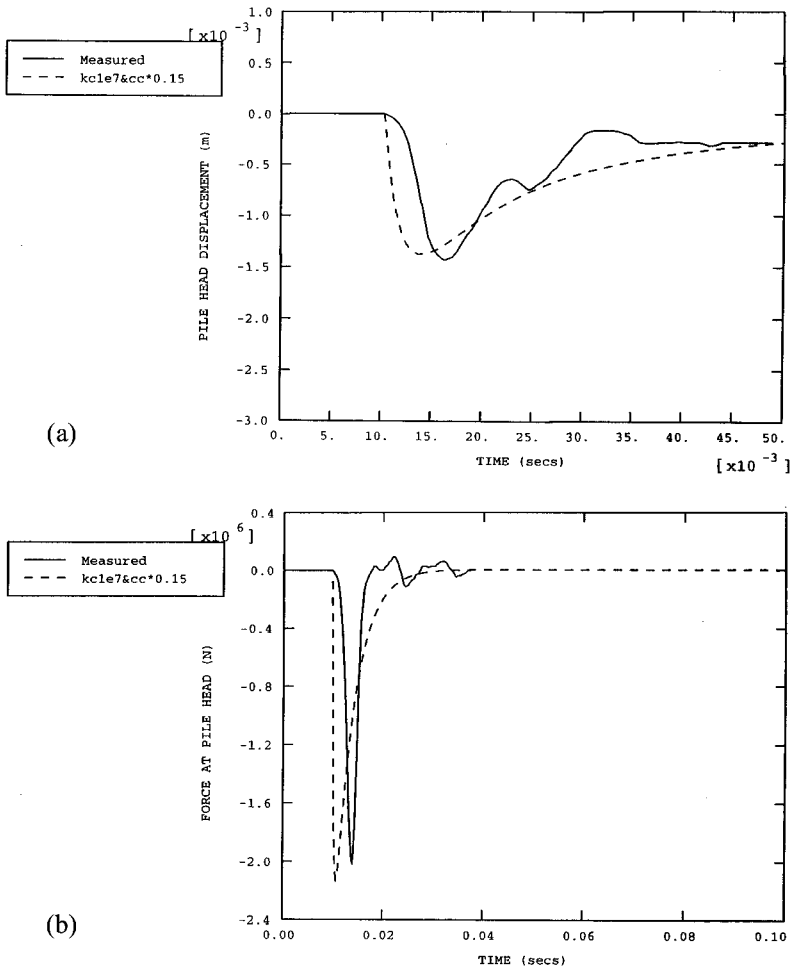


Figure 5.13 (a) Displacement-time and (b) force-time functions at the pile head (computed=solid line, measured=dashed line).

Vibrodrivers

Pile installation by vibrodriver is fundamentally different to impact driving, the installation being achieved by liquefaction of soils immediately adjacent to the pile. The method is most effective in saturated fine sands. The vertical cyclic force $F(t)$ is sinusoidal in form, and the pile is excited into rigid body oscillation, at the driving frequency, and with amplitude which is dependent on the total pile mass and the soil resistance on the shaft and toe.

$$F(t) = m.e.\omega^2 . \sin \omega t \tag{5.18}$$

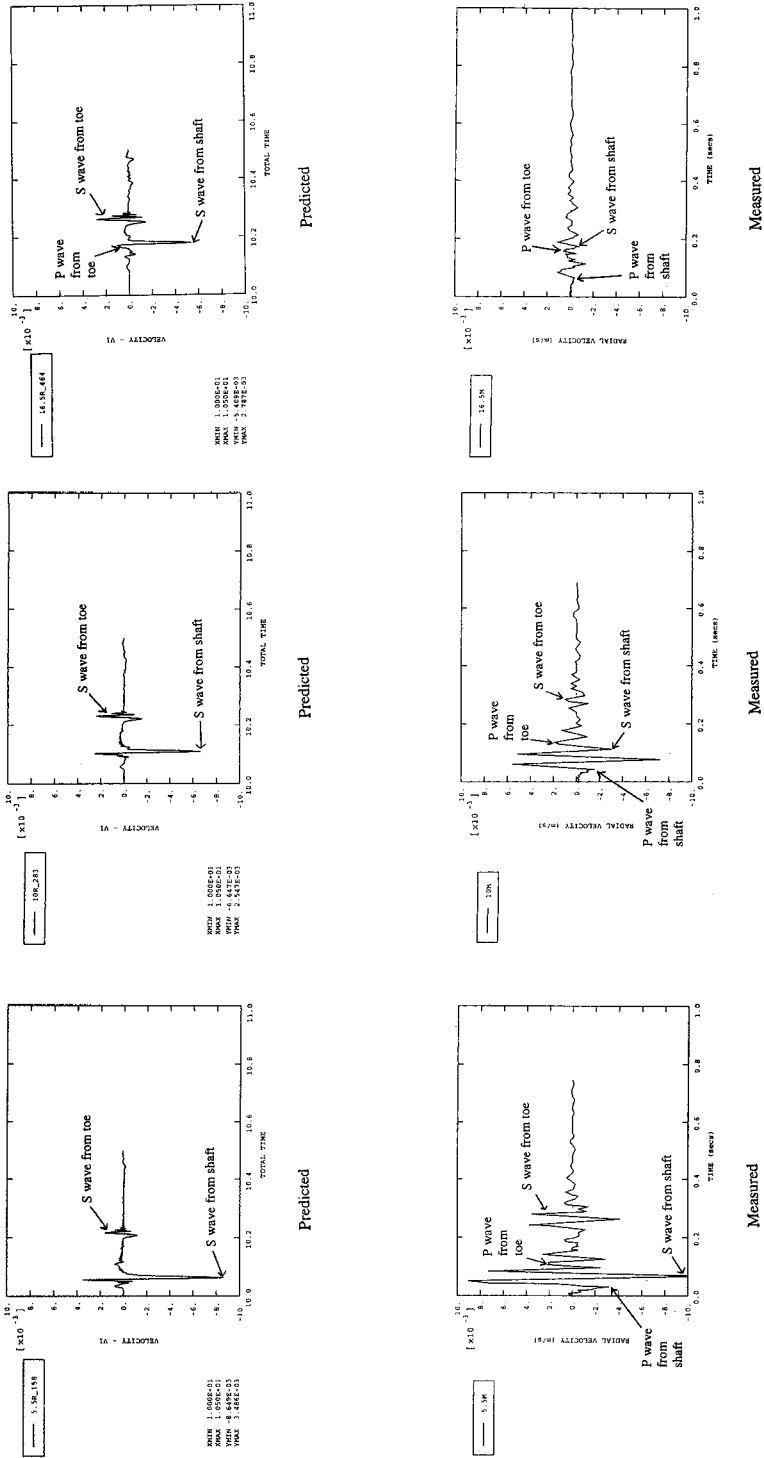


Figure 5.14 Radial particle velocities (computed and measured)

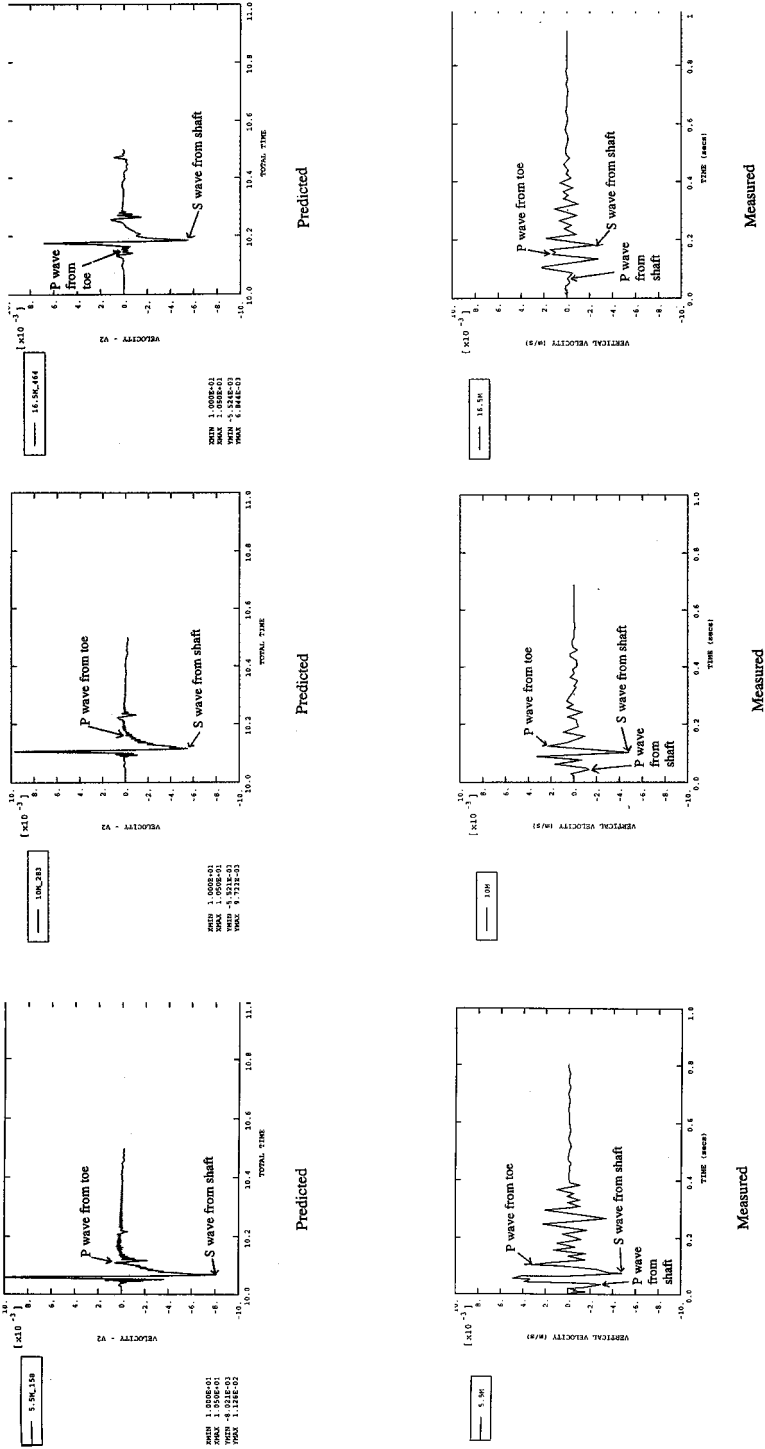


Figure 5.15 Verticle particle velocities (computed and measured)

Table 5.2 Summary of parameters used in the computation.

<i>Pile head</i>	<i>Pile shaft</i>	<i>Pile toe</i>
$m_r = 3200 \text{ kg}$	$k_s = 24.65 \times 10^6 \text{ N/m}$ (sands and gravels)	$m_0 = 0$
$k_c = 63.8 \times 10^6 \text{ N/m}^2$	$k_s = 65.6 \times 10^6 \text{ N/m}$ (dense sand)	$k = 16.3 \times 10^6 \text{ N/m}$
$c_c = 226 \times 10^3 \text{ N/ms}$	$c_s = 114.7 \times 10^3 \text{ N/ms}$ (sands and gravels)	$c_0 = 19.85 \times 10^3 \text{ N/ms}$
$m_a = 320 \text{ kg}$	$c_s = 200.0 \times 10^3 \text{ N/m}$ (dense sand)	$m_1 = 3.97 \text{ kg}$
$Z = 452 \times 10^3 \text{ Ns/m}$	Coulomb friction $\mu = 0.4$	$c_1 = 4.78 \times 10^3 \text{ N/ms}$

where m is the total mass rotating at eccentricity e , at ω rad/s.

Computational procedure

The computational procedure for modelling pile response to cyclic excitation and outgoing ground waves is undertaken in two stages.

In the first stage, the objective is to establish the rigid body vertical oscillation of the pile in response to the cyclic vibrodriever force applied to the pile head. The developed model comprises rigid axisymmetric elements for the pile shaft, a limited axisymmetric FE/IE mesh for the soil around the shaft, and a spring/damper model for soil at the toe (Lysmer and Richart, 1966), see [Figure 5.17](#). Values for the spring and damper constants were used, where

$$k = \frac{4GR}{1-\nu} \quad \text{and} \quad c = 0.85 \cdot \frac{kR}{c_s} \quad (5.19)$$

The shaft-soil interface consists of a two-surface contact controlled by Coulomb friction, μ . A static computation is run first to calculate soil self-weight stresses at the interface nodes. A forced harmonic computational analysis is then conducted to give the steady state response of the rigid pile.

The second stage of the computation is based on a 50×50 mesh of FEs surrounded by IEs as discussed previously. The sinusoidal displacements of the shaft nodes and at the base, from stage 1, are imposed as Fourier series, and a transient analysis is conducted for the outgoing ground waves. Infinite elements can be set up to be effective in eliminating artificial boundary reflections, or alternatively the FE mesh can be expanded so that the steady state is achieved within say 20 m of the pile, before reflections return. Material damping of the waves during transmission through the ground can be included using a typical value for the damping ratio of some 5% (Massarsch, 1992), although its effect is small.

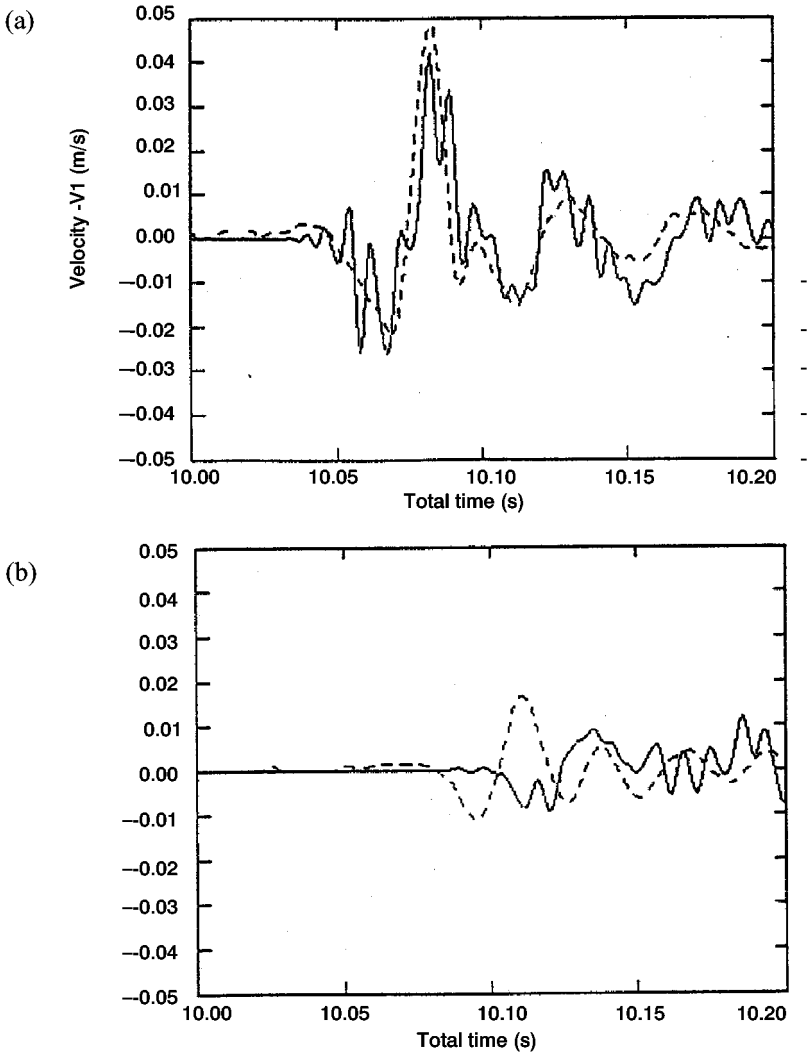


Figure 5.16 Radial particle velocities at (a) 7 m and (b) 16.5 m, impact hammer, Flitwick (computed=solid line, measured=dashed line).

Calibration of the vibrodriver model

The modelling procedure was calibrated against several site records, two of which are now reported, which have very different soil conditions. The first data set was recorded at Flitwick during an extensive pile driving trial. The second set was taken during driving of casings at the Second Severn Crossing, where soil conditions were not best suited to vibratory installation.

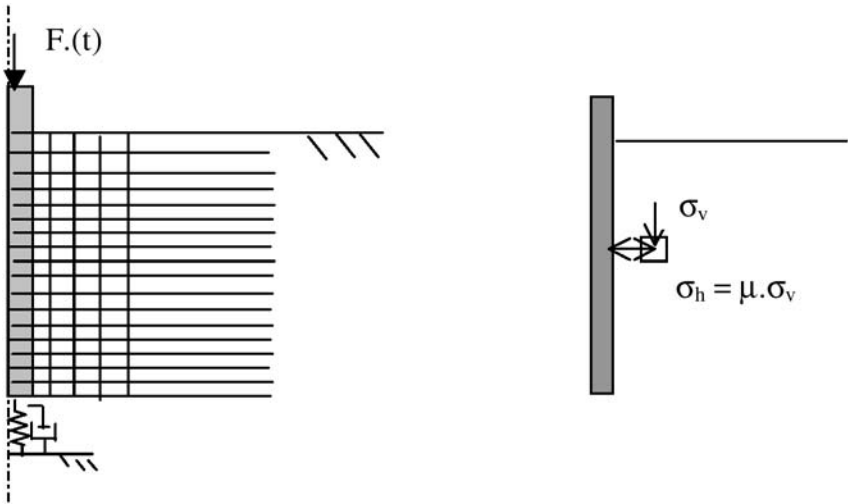


Figure 5.17 Schematics of stage I model for vibrodriving, and for shaft/soil.

Vibrodriving at Flitwick

The case considered was that of a 12m long steel H-pile being installed using a PTC 13HF1 vibrodriver, with an eccentric moment of 13 m.kg, operating at 19.1 Hz. The pile toe depth at the time of the record was 7 m. The soil conditions comprised topsoil and soft clays to 2.4 m, loose sand and gravel at 2.4–4.8 m, then very dense uniform sands to considerable depth. The water table was at 2.4 m. Although the static elastic moduli for the three layers were estimated to be 5 MPa, 20 MPa and 50 MPa respectively, the *dynamic* stiffness used for the second stage of the computation was a uniform value of 155 MPa. The pile shaft-soil interface slip was controlled by a Coulomb friction factor $\mu=0.5$. A damping ratio of 5% was applied for small strain dynamic behaviour. Ground surface vibrations were recorded at 2 m, 7 m and 16.5 m from the pile, and the radial values are compared in [Figure 5.18](#) with the computed values.

The form of the traces is strongly sinusoidal, although the closest measured trace has a slight kick, suggesting either poor contact with the ground of one geophone or a contact somewhere within the driver or guide mechanisms. It is interesting to note that both the measured and computed ppv's show little attenuation between 2 m and 7 m, but with a stronger reduction at 16.5 m. The reasons for this observation are unclear, and may be due either to interaction of shaft and toe effects or to locations chosen with respect to a standing wave component of the signal.

Overall, adequate agreement is obtained between measured and computed vibrations by careful selection of appropriate values for a number of pile and soil parameters.

Vibrodriving at the Second Severn Crossing

A detailed study was made of the installation of steel 1050 mm diameter casings for one of the foundations for the approach viaduct to the main cable-stayed spans of the Second Severn Crossing. The ground conditions consisted of soft to firm clays to a depth of 13.8 m, overlying firm to stiff marl. These conditions are far from ideal for Vibrodriving, since liquefaction is unlikely. However, penetration to 15.5 m was achieved using a PTC 50H3 vibrodriver with an eccentric moment of 50 m.kg, and running at 15.8 Hz. Ground surface vibrations were measured using geophone triaxial sets at distances of 5.7 m, 14.5 m and 32.9 m. Comparisons are made between measured and computed ground vibrations in [Figure 5.19](#) for the radial components, and in [Figure 5.20](#) for the vertical components.

Overall, close agreement is obtained in terms of form, amplitude and attenuation, for both radial and vertical particle velocities.

Ground wave modelling and applications

In the previous two sections, methods have been presented for computing outgoing ground waves, taking as the starting point the driving force from either an impact hammer or a vibrodriver. For effectiveness of computation, and for identification of the effects of parametric variation, the impact model has been separated into three stages, while the vibrodriving has been split into two stages.

The three-stage model for impact hammers requires a number of parameters to be evaluated. Of particular significance are the spring and damper values ascribed to the dolly or packing; low stiffness and damping imply a force-time relation with a lower peak and longer duration. Soil parameters for both shaft and toe are also significant with respect to displacements of interface nodes as input to the third stage of the model.

The two-stage model of the vibrodriver has a well-defined input excitation, since the cyclic vertical force is known as a function of the eccentric masses and their frequency of rotation, and in particular because the vibrodriver is firmly clamped to the pile head. However, the shaft and toe interaction with the soils is less predictable, with liquefaction as a key mechanism.

With both procedures, the above uncertainties are present, together with ground non-uniformities, and imperfections in the driving process in terms of non-axial forces and guide-frame weakness. In consequence, the modelling procedures are shown to be highly effective when used in a back-analysis mode, but their ability to *predict* ground waves is less secure. On-going work to back-analyse a number of site cases with measured ground surface vibrations will improve the predictive capability.

A major advance arising from the modelling capability is the potential for computing the dynamic response of structures or buried services adjacent to the pile driving, with full soil-structure interaction. When undertaking computer

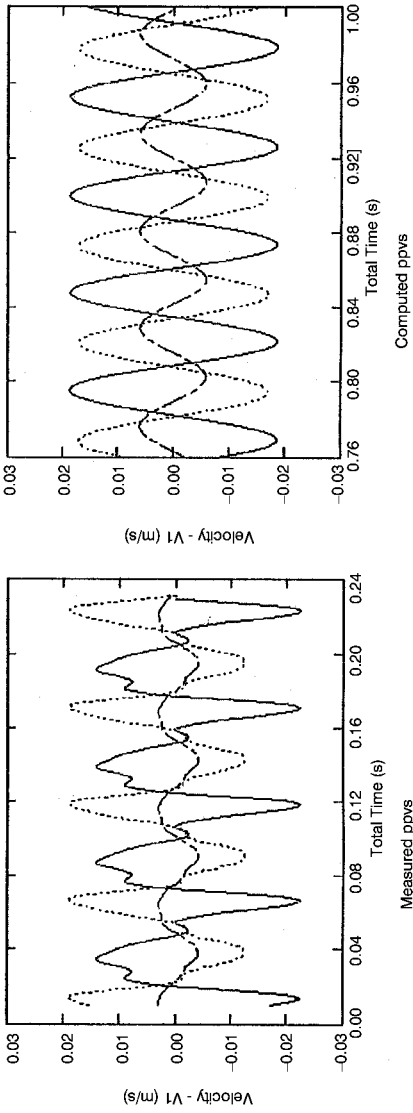


Figure 5.18 Measured and computed radial particle velocities at 2 m, 7 m and 16.5 m from the vibrodriven pile, Flitwick.

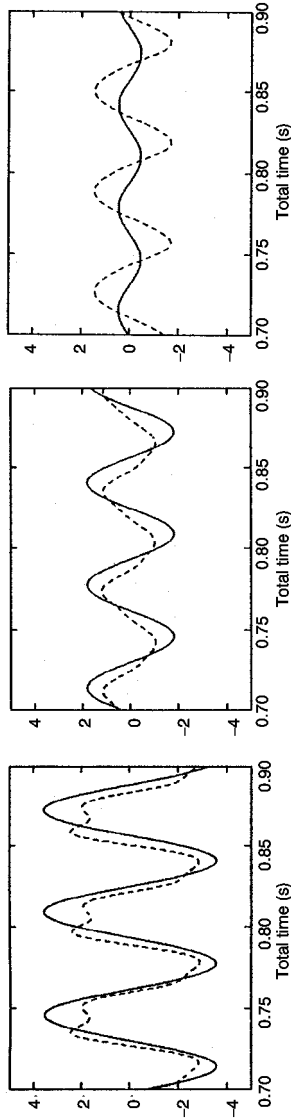


Figure 5.19 Radial velocities at 5.7 m, 14.5 m and 32.9 m, vibrodriving at Second Severn Crossing (computed= solid line, measured=dashed line).

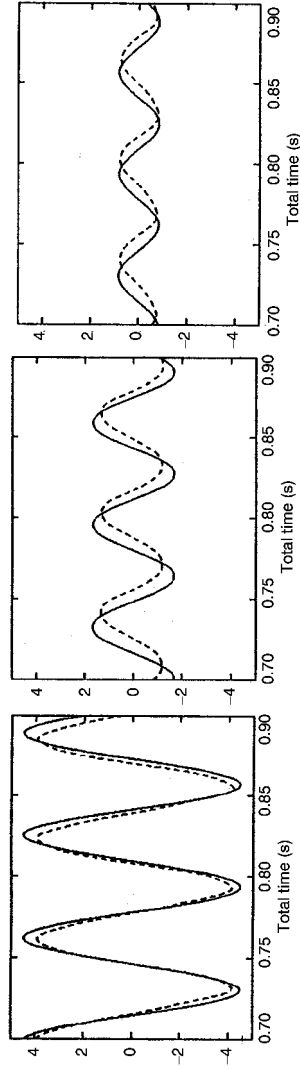


Figure 5.20 Vertical velocities at 5.7 m, 14.5 m and 32.9 m, vibrodriving at Second Severn Crossing (computed=solid line, measured =dashed line).

estimates of the transient or cyclic response of structures, it may be essential to recognise that the presence of a stiff structure will modify the ground waves; the structure will *not* deform to follow the transient free-ground movements. Transient response of three conceptual structures is now demonstrated briefly, with respect to a simple rectangular steel portal, a brickwork wall, and a buried gas main. Appropriate mesh forms are described.

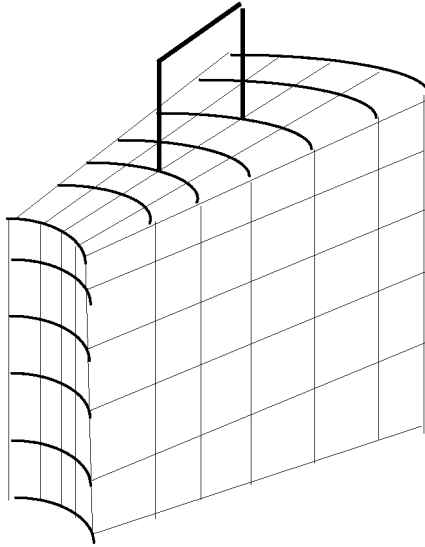


Figure 5.21 Schematic view of soil plus structure.

Rectangular steel portal frame

A large number of light industrial and commercial buildings consist of steel portal frames founded on pad footings, with a variety of cladding options. The natural choice of computational model is plane stress. This is incompatible with an axisymmetric model of pile and soil. A fully three-dimensional solution is unsuitable because the solution time would be totally excessive, and mesh size would suffer for any realistic solution.

An effective compromise solution has been found, comprising a ‘wedge’ of the axisymmetric model, represented with 3D fanned elements. This allows correct connectivity with the 2D portal frame, whilst ensuring geometric damping of the outgoing waves, and allowing realistic computing time. A simplified view of the soil-structure system is shown in [Figure 5.21](#).

The mesh used in practice was considerably refined from that in [Figure 5.21](#). For impact driving the mesh represents stage 3 of the model, and the FE mesh was extended sufficiently that the behaviour of the soil and the frame were identified before reflections had returned. In the case of vibrodriving, IEs were added around the outer boundaries. Excitation of the system in terms of transient or sinusoidal displacements was imposed onto the inner curved face of the mesh, as derived by stages 1 and 2 for impact and stage 1 for vibrodriving. Preliminary calibrations of the wedge mesh compared with axisymmetric analyses showed very close agreement, with effective geometric attenuation.

The method was applied to a uniform soil with dynamic modulus of 200 MPa, and a single steel portal on pad foundations. The portal had a span of 12.5 m,

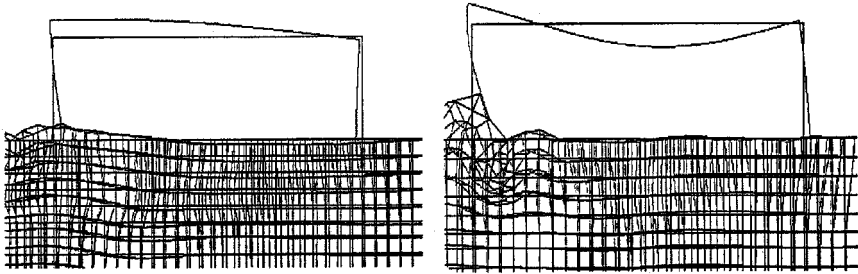


Figure 5.22 Frame deformations during passage of a transient wave from impact piling.

was 3 m high, and comprised 203×203×60 kg/m Universal Columns and a 610×229×125 kg/m Universal Beam. The dynamic modulus of steel was 2.1×10^{11} Pa, no different to the static modulus. Typical frame deformations are shown in Figure 5.22 as the waves passed outwards through the soil around the portal. The response is a function of ground wavelength and form, with peak distress to the columns caused by horizontal movements of the frame feet in anti-phase. Beam bending was more complex, due to components of feet movement both vertical, radial, and with enforced rotation, and also with inertial effect. Comparison with free-ground transient displacements showed negligible difference, from which it is inferred that a single portal is sufficiently flexible that it does not modify ground movements, and soil-structure interaction is not important. In such cases, it is computationally more efficient simply to calculate free-ground displacements, and then to impose these onto the frame. However, a multi-bay or multi-storey frame might impose more restraint on the ground, and require a fully interactive computation.

Plane brickwork wall

In this computation, a brickwork wall, 10m long, 6 m high and 0.2 m thick was superimposed onto the wedge of soil, so that it was subjected to in-plane transient disturbance. The wall dimensions approximate to a domestic house wall, but neglecting cut-outs for doors or windows, and cross-wall stiffening. A value of 30×10^9 Pa was chosen for the dynamic modulus of the brickwork. The response of the wall to transient waves was typical of a very stiff structure, in that the wall showed rigid body motions of lift and pitch, but only very minor deformations of shape, see Figure 5.23. Inspection of in-plane stresses showed that the dominant effect was due to restraint of *horizontal ground strain*, rather than restraint of curvature in bending. This structural element should not be analysed by imposition of ground strain; a fully interactive soil-structure computation is required.

The same soil and brickwork wall were then subjected to cyclic excitation from vibrodriving. The free-ground vertical displacements are compared with

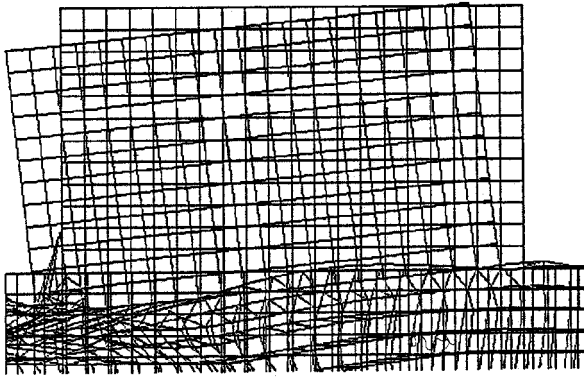


Figure 5.23 Wall displacements during passage of a transient wave.

displacements at three interface nodes with the wall in place, and the restraining effect of the wall is plain to see in Figure 5.24. Clearly, the mass of the wall reduces the overall vertical displacements of the ground surface, but also the curvature of the wall is very small, being about 0.01 mm in 10 m, compared with 0.3 mm in 10 m for the free ground.

The degree of soil restraint is substantial in this situation. However, it is strongly a function of the relationship between wavelength and building dimension. If the wavelength is long, and the building is short the building will 'ride' the wave, in rigid-body pitch and heave, reducing soil movements because of extra mass only. If the building is longer than the half-wavelength then the ground waves will be much reduced by the building stiffness in addition to its mass, i.e. there is significant soil-structure interaction.

Buried gas main

The Transco distribution network consists of some 6000 km of national pipeline and 12,000 km of local pipelines, of X60 or X80 steel. The national pipelines range from 30 inch to 42 inch diameter, pressurised at up to 85 bar. Local pipelines range from 12 in to 18 in diameter, pressurised to a maximum of 38 bar. Standard depth of cover to the crown is 1.1 m, but pipes may run at 3 m, or exceptionally at 10 m in locations beneath embankments or buildings.

The situation was analysed where piling took place to one side of a pipeline, and outgoing ground waves impinged upon the buried pipe, causing deformation of the thin wall of the pipe cross-section. Realistic bending and compression of a very thin pipe wall could be modelled effectively only by 3-node curved beam elements. Such elements are not compatible with axisymmetric elements. The combination chosen (Besford, 2000) was to use the curved beams with plane-strain 8-noded elements, which have interconnection of x - and y -displacements

with the beams but not rotation. This model could not compute geometric attenuation of the ground waves, so the strategy used was to input reasonable impact or vibratory excitation around a pile space, and to compute pipe strains when the ppv's at the ground surface directly above the pipe were 10 mm/s. This relates to Transco's field practice. Figure 5.25 shows an FE mesh for a 10 m deep pipe and an impact hammer, and an FE/IE mesh for a 2 m deep pipe with vibrodriver.

A number of cases were analysed, and some peak bending stresses induced in the pipe cross-section are summarised in Table 5.3.

The stresses induced into the pipe by bending deformation of the cross-section are very small, and are negligible in comparison with the yield stress of the pipe steel of 413 MPa or 552 MPa respectively. There is strong evidence that the stresses induced by deformation of the cross-section are negligible. However, other forms of distress to pipelines may be caused by wave-generated mechanisms, such as joint pull-out or pipe-branch joint damage.

The deformed shapes of the pipe cross-section in response to P, S and R-waves were particularly interesting and not entirely expected. The passage of a P-wave was fairly predictable in causing ovaling of the cross-section with the major axis normal to the direction of travel of the wave front, Figure 5.26. This deformation caused the lowest stress during passage of ground waves.

The response of the cross-section of the pipe as an S-wave passed through showed a maximum deformation with a major axis at 45° to the direction of the wave travel. This can be verified by consideration of the effect of an S-wave upon a square element, as shown in Figure 5.27.

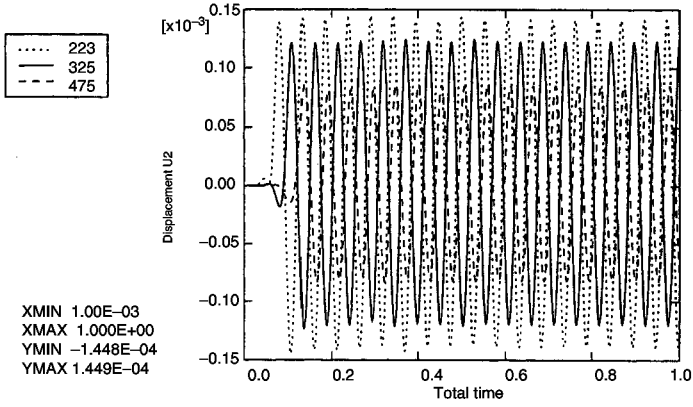
Finally, deformation of the pipe section near to ground surface caused by a Rayleigh wave is even more complex, as can be anticipated, because of the combination of vertical and horizontal movements of a soil particle in a retrograde elliptic path, see Figure 5.28.

Conclusions

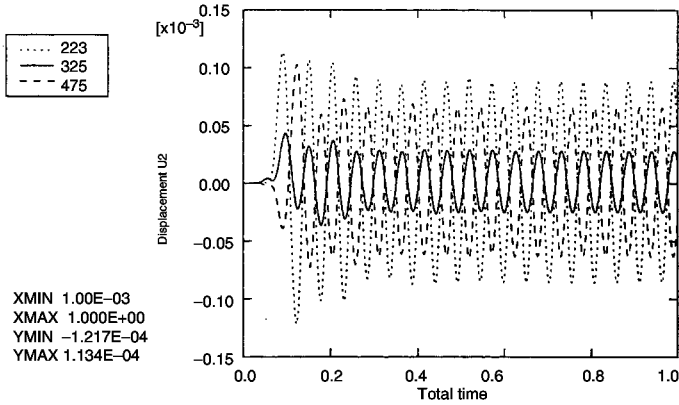
Impact driving of a pre-formed pile causes significant transient ground vibrations, which attenuate non-uniformly with distance from the pile. Vibration, expressed as ppv's, is a function of hammer energy, hammer-pilehead impact, and, to a lesser extent, of soil type.

A three-stage computational model has been shown to be capable of good quality back-analysis of the impact and of the definition of outgoing ground vibrations. The method is less reliable in pre-estimating vibrations because of the variability of driving parameters, of soil properties and of site construction features. The selection of an appropriate *dynamic* soil modulus has been discussed.

Pile installation and extraction by vibrodriving is highly effective in saturated fine sands and silty soils. A two-stage computational procedure has been developed which shows close agreement with site records of ground surface



(a) No structure



(b) With brick wall

Figure 5.24 Vertical displacements of three surface nodes during vibrodriving, (a) free-ground and (b) with a brickwork wall.

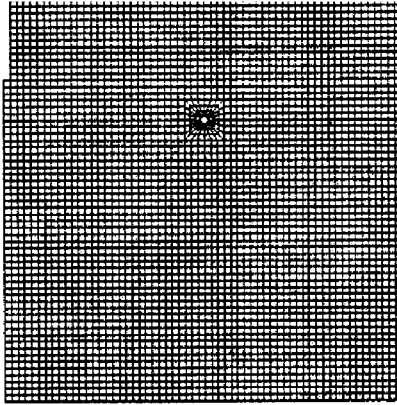
vibrations. The vibrations are strongly sinusoidal, matching the driving frequency. Attenuation is non-uniform, possibly due to the presence of a standing wave.

The choice of axisymmetric mesh of finite elements is governed by the wavelength and transmission speed. In addition, spurious boundary reflections must be eliminated from the computation within the zone of interest. This may be achieved by the use of infinite elements of various kinds, or by expanding the finite element mesh sufficiently. Specific problems and advantages of infinite elements have been discussed.

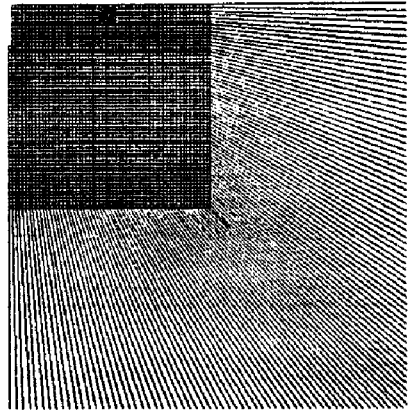
Detailed wave analysis generally requires considerable computer power and time, above that which is available for normal piling activities. The empirical

Table 5.3 Examples of bending stresses around pipes due to ovalling.

Pipe diam (mm)	Depth (m)	Max. bending stress, P-wave, (MPa)	Max. bending stress, S-wave or R-wave (MPa)
600	3	0.1	0.93
100	3	0.1	0.87
600	1.5	—	1.4
100	1.5	—	1.7



10 m deep pipe



2m deep pipe

Figure 5.25 Meshes for pipe deformation analyses.

expressions and guidance given in British Standards and in Eurocode 3 offer useful methods of site working.

A major benefit of generating realistic, or fully calibrated, waves is the facility of imposing them onto a range of structural forms, with full soil-structure interaction. However, reconstruction of the mesh representing the ground may be necessary to accommodate structures or buried service pipes. Examples of such reconstructions have been given.

Acknowledgements

Funding from EPSRC grant GR/L 18679/01 is gratefully acknowledged.

Advice on infinite elements has been generously given by Professor Bettess. Computations on buried pipes were conducted by Mr I.Besford. Data on the M66 and Second Severn Crossing were supplied by Dr D.Hiller.

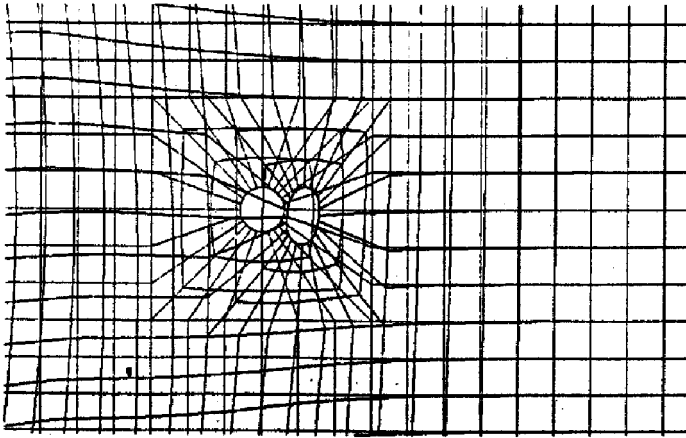


Figure 5.26 Pipe deformation during passage of a P-wave.

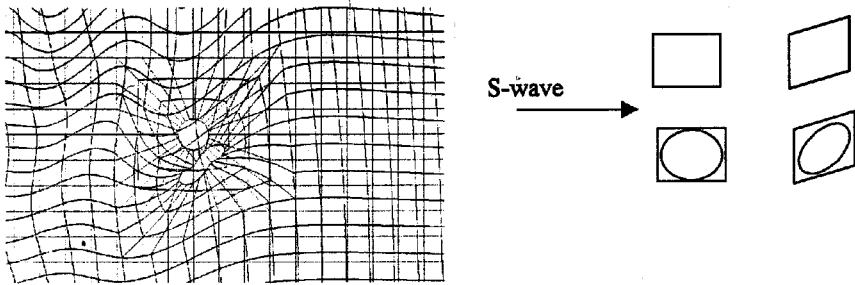


Figure 5.27 Pipe deformation at 45° , during passage of an S-wave, and justification.

References

- Abaqus (1999) HK&S (UK), Warrington.
- Attewell P.B. and Farmer, I.W. (1973) Attenuation of ground vibrations from pile driving. *Ground Engineering* Vol 6 No 4 pp 26–29.
- Attewell P.B., Selby A.R. and Uromeihy A. (1991) Non-monotonical decay of ground surface vibrations caused by pile-driving. In *Earthquake, blast and impact*. Elsevier, London, pp 463–481.
- Attewell P.B., Selby A.R. and O'Donnell L. (1992) Estimation of ground vibration from driven piling based on statistical analyses of recorded data. *Geotech & Geol. Eng.* Vol 10 pp 41–59.
- Besford I. (2000) Stresses induced in pipelines from nearby pile driving. Internal Rep. Durham Univ.
- Bettess P. (1992) *Infinite elements*. Penshaw Press, Sunderland.
- BRE Digest 353* (1990) Damage to structures from ground-borne vibration. Building Research Establishment, Garston.
- British Standard BS5228 part 4 (1992) *Noise control on construction and open sites*. BSI London.

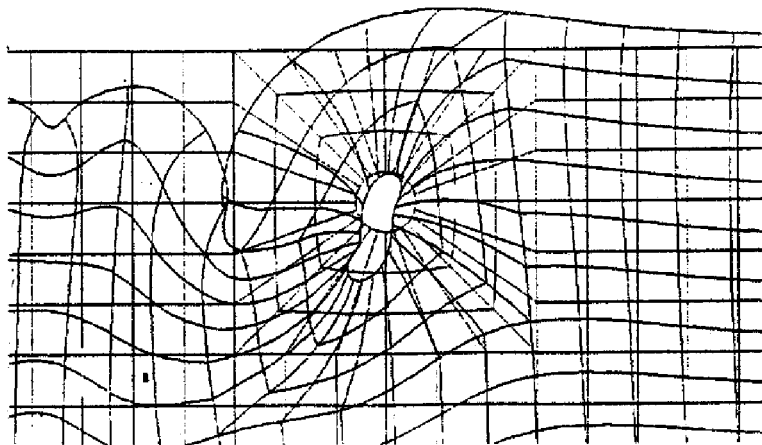


Figure 5.28 Pipe deformation due to a Rayleigh wave.

British Standard BS6472 (1992) *Evaluation of human exposure to vibration in buildings* (1 Hz to 80 Hz). BSI London.

British Standard BS7385 part 2 (1993) *Evaluation and measurement for vibration in buildings*. BSI London.

Deeks A.J. (1992) Numerical analysis of pile driving dynamics. PhD thesis, Univ of W Australia.

Deeks A.J. and Randolph M.F. (1993) Analytical modelling of hammer impact for pile driving. *Int J for Num. and Analytical Methods in Geomechanics* 17 pp 279–302.

Deeks A.J. and Randolph M.F. (1995) A simple model for inelastic footing response to transient loading. *Int J for Num and Analytical Methods in Geomechanics* 19 pp 307–329.

Dowding C.H. (1996) *Construction vibrations*. Prentice-Hall, Upper Saddle River, New Jersey.

Eurocode 3 (1996) Design of steel structures. Pt 5. Piling CEN/TC 250/SC3/PT5.

Head J.M. and Jardine P.M. (1992) *Ground-borne vibrations arising from piling*. TN142 CIRIA, Storey's Gate, Westminster.

Hiller, D.M. (2000) Prediction of ground borne vibrations caused by mechanised construction works. PhD thesis Univ of Surrey.

Hiller, D.M. and Crabbe G.I. (2000) Groundborne vibration caused by mechanised construction works. TRL Report 429. Crowthorne.

Hiller D.M. and Hope, V.S. (1998) Groundborne vibration generated by mechanised construction activities. *Proc Instn Civ Engrs. Geotech Eng* 131 pp 223–232.

Lysmer J. and Kuhlemeyer R.L. (1969) Finite dynamic model for infinite media. *J Eng Mech Div ASCE* pp 859–877.

Lysmer J. and Richart F.E. (1966) Dynamic response of footings to vertical loading. *J of SM and F Div Proc ASCE* Vol 92 SM1 pp 65–91.

Mabsout M.E. and Tassoulas, J.L. (1994) A finite element model for the simulation of pile driving. *Int J for Num Methods in Eng* 37 pp 257–278.

Malam, D. (1992) *Groundborne vibration and structural damage*. SECED, ICE London.

- Massarsch K.R. (1992) Static and dynamic soil displacements caused by pile driving. *Application of stress-wave theory to piles*, ed Barends F.B.J. Balkema, Rotterdam, pp 15–24.
- Matthews M.C., Hope V.S. and Clayton C.R.I. (1996) The use of surface waves in the determination of ground stiffness profiles. *Pr Instn Civ Engrs. Geotech Eng* 119 pp 84–95.
- Oliver A. and Selby A.R. (1991) Estimation of piling-induced ground vibrations. In *Earthquake, blast and impact*. SECED, Elsevier, London, pp 395–110.
- Ramshaw C.L. (1999) The use of Abaqus to model vibrations generated by pile driving. Abaqus Users Conf. Chester.
- Ramshaw C.L. (2001) Computer simulation of ground waves due to pile installation. PhD thesis, Durham University .
- Ramshaw C.L., Selby A.R. and Bettess P. (1998a) Computation of the transmission of waves from pile driving. In *Ground dynamics and man made processes*, ed Skipp B.O. T.Telford, London, pp 115–128.
- Ramshaw C.L., Selby A.R. and Bettess P. (1998b) Computed ground waves due to pile driving. In *Geotechnical earthquake engineering and soil dynamics III*, ed Dakoulas P., Yegian M. and Holtz R.D. Geot Sp Pub No 75 ASCE pp 1484–1495.
- Selby, A.R. (1991) Ground vibrations caused by pile installation. 4th Int DFI Conf, Balkema, Rotterdam, pp 497–502.
- Stain R.T. (1992) *SIMBAT- a dynamic load test for bored piles. Piling: European practice and worldwide trends*. T.Telford, London, pp 198–205.
- Uromeihy, A. (1990) Ground vibration measurements with special reference to pile driving. PhD thesis Durham Univ.
- Wiss J.F. (1967) Damage effects of pile driving vibrations. *Highways Res B* 155 pp 14– 20.
- Wolf J.P. (1988) *Soil-structure-interaction analysis in time domain*. Prentice-Hall, New Jersey.

Chapter 6

Back analysis of geotechnical problems

Annamaria Cividini and Giancarlo Gioda

Abstract

Some back analysis techniques applicable in geotechnical engineering are summarised, considering both their deterministic and probabilistic aspects. The discussion is limited to static conditions. First, two alternative back analysis approaches are described in a deterministic context, referred to as “direct” and “inverse” techniques. Subsequently, a probabilistic Bayesian technique is discussed which aims at investigating the influence of the experimental errors on the results of back calculations. Finally, two applications to actual tunnelling problems are summarised.

Introduction

Back analysis techniques are nowadays often used in geotechnical engineering practice for determining the mechanical characteristics of soil/rock masses on the basis of field measurements performed during excavation or construction works [1–4].

In this context, a back analysis consists in finding the values of the parameters of the geotechnical medium that, when introduced in the stress analysis of the problem under examination, lead to results (e.g. displacements, stresses, etc.) as close as possible to the corresponding *in situ* measurements.

In general terms, two “tools” are necessary to perform a back analysis. The first is a stress analysis procedure for determining the stress, strain and displacement distributions for the problem at hand. The second is a suitable optimisation algorithm which minimises, with respect to the “unknown” mechanical parameters of the soil/rock mass, a non-linear function representing the discrepancy between the quantities measured in the field and the corresponding data obtained by the stress analysis.

Here some aspects of the back analysis procedures in the field of geotechnical engineering are illustrated, adopting the finite element method as a suitable solution technique and limiting the discussion to static conditions.

First, two alternative approaches for the back analysis, referred to as “direct” and “inverse” (with respect to the stress analysis) procedures are illustrated in a deterministic context. Subsequently, the influence of the experimental error on the back-calculated parameters is discussed on the basis of a probabilistic Bayesian approach. Finally, two applications to actual tunnelling problems are presented.

Notation: Upper and lower case underlined letters denote, respectively, matrices and column vectors. The superscripts T and -1 mean transpose and inverse.

An inverse method for elastic back analysis

The back analysis of mechanical parameters is a non-linear problem even in the simple case of linear elastic material behaviour. In order to show this characteristic, let us briefly recall the basic aspects of a technique for the back analysis of elastic constants which is based on a finite element approach originally proposed in [5]. This method can be defined as “inverse”, with respect to the corresponding stress analysis, since it requires the “inversion” of the equations governing the linear elastic stress analysis problem.

To apply this procedure it is necessary to establish a linear relationship between the stiffness matrix of each finite element \underline{K}^e and the unknown mechanical parameters. In the case of isotropic material behaviour, such a relationship can be obtained easily by describing the elastic behaviour in terms of bulk B and shear G moduli,

$$\underline{K}^e = B \cdot \underline{K}_B^e + G \cdot \underline{K}_G^e \quad (6.1)$$

The two matrices on the right-hand side of eq. (6.1) are, respectively, the volumetric and the deviatoric stiffness matrices of the e -th element. Consequently, the stiffness matrix \underline{K} of the assembled finite element model can be written in the following form,

$$\underline{K} = \sum_{i=1}^{2n} p_i \cdot \underline{K}_i \quad (6.2)$$

where n is the number of different materials ($2n$ being the number of unknown elastic parameters) and \underline{K}_i is the assembled stiffness matrix obtained by setting all the parameters to zero, but with the i -th parameter set equal to 1.

Assuming that m displacement components are measured in the field, and that the measurement points coincide with nodes of the finite element grid, the system of linear equations describing the behaviour of the finite element discretization can be partitioned as follows,

$$\begin{bmatrix} \underline{K}_{11} & \underline{K}_{12} \\ \underline{K}_{21} & \underline{K}_{22} \end{bmatrix} \begin{Bmatrix} \underline{u}_1^* \\ \underline{u}_2 \end{Bmatrix} = \begin{Bmatrix} \underline{f}_1 \\ \underline{f}_2 \end{Bmatrix} \quad (6.3)$$

where vector collects all the measured displacements, and \underline{f}_1 and \underline{f}_2 are known nodal force vectors.

A static condensation of eq.(6.3) leads to,

$$(\underline{K}_{11} - \underline{Q} \cdot \underline{K}_{21}) \cdot \underline{u}_1^* = \underline{f}_1 - \underline{Q} \cdot \underline{f}_2 \quad (6.4)$$

where

$$\underline{Q} = \underline{K}_2 \cdot \underline{K}_{22}^{-1} \quad (6.5)$$

Eq. (6.4), by taking into account eq. (6.2), can be written in the following form,

$$\sum_{i=1}^{2n} p_i \cdot \underline{r}_i = \underline{f} - \underline{Q} \cdot \underline{f}_2 \quad (6.6)$$

where

$$\underline{r}_i = (\underline{K}_{11,i} - \underline{Q} \cdot \underline{K}_{21,i}) \cdot \underline{u}_i^* \quad (6.7)$$

The stiffness matrices in eq. (6.7) are obtained by partitioning matrix \underline{K}_i with the same criteria used in eq. (6.3) for matrix \underline{K} .

Grouping the unknown parameters in the $2n$ vector \underline{p} , and grouping vectors \underline{r}_i in the $m \times 2n$ matrix \underline{R} ,

$$\underline{R} = [\underline{r}_1 | \underline{r}_2 | \dots | \underline{r}_{2n}] \quad (6.8)$$

eq. (6.6) yields the following relationship that governs the back analysis problem,

$$\underline{R} \cdot \underline{p} = \underline{f}_1 - \underline{Q} \cdot \underline{f}_2 \quad (6.9)$$

Assuming that the number of measured displacements exceeds the number of unknown elastic constants, a standard least square minimisation can be applied to eq. (6.9), which leads to the following non-linear equation system,

$$\underline{R}^T \cdot \underline{R} \cdot \underline{p} = \underline{R}^T \cdot (\underline{f}_1 - \underline{Q} \cdot \underline{f}_2) \quad (6.10)$$

The non-linear nature of eq. (6.10) derives from the fact that the matrix of coefficients \underline{R} depends, through matrix \underline{Q} , on the unknown vector \underline{p} .

The solution of this equation system is reached through an iterative procedure. Each iteration requires the inversion of the sub-matrix \underline{K}_{22} of the assembled stiffness matrix (cf. eq. (6.5)). The assembled matrix is evaluated on the basis of the parameter vector \underline{p} determined at the end of the preceding iteration.

Other approaches for the back analysis of elastic parameters have been proposed in the literature, still leading to a set of non-linear equations. The one proposed in [4] could be mentioned; which offers the advantage of being applicable also in the case of non-linear or time dependent material behaviour.

Direct solution technique

An alternative back analysis procedure can be based on the minimisation of the discrepancy between the field measurements and the corresponding numerically evaluated quantities. This approach presents the advantage of avoiding the “inversion” of the stress analysis equations, which was required by the technique discussed in the previous section.

The following error function E_r can be adopted to define the discrepancy between the measured displacements (denoted by a star) and those deriving from a numerical stress analysis in which a given set of material parameters \underline{p} is used,

$$E_r(\underline{p}) = \sum_{i=1}^m \left[u_i^* - u_i(\underline{p}) \right]^2 \quad (6.11)$$

Note that the error function depends, through the numerical results, on the parameters being back calculated, which in this context has a rather general meaning and may correspond to elasticity or shear strength properties, viscosity coefficients, etc. Consequently, the back analysis reduces to determining the set of parameters that minimises the error function, i.e. that leads to the best approximation of the field observation through the chosen numerical model.

The error defined by eq. (6.11) is in general a complicated non-linear function of the unknown quantities, and in most cases the analytical expression of its gradient cannot be determined. This is particularly evident for non-linear or elasto-plastic problems. Therefore, the adopted minimisation algorithm must handle general non-linear functions and should not require the analytical evaluation of the function gradient.

Methods of this kind, known in mathematical programming as direct search methods, are iterative procedures that perform the minimisation process only by successive evaluations of the error function [7, 8]. In the present contest, each evaluation requires a stress analysis of the geotechnical problem on the basis of the trial vector \underline{p} chosen for that iteration.

In most practical cases some limiting values exist for the unknown parameters. For instance, the modulus of elasticity or the cohesion cannot have negative values. These limits, expressed by inequality constraints, can be easily

introduced into a direct search algorithm by means of a penalisation procedure. When a point in the space of the free variables is reached outside the feasible domain, the error function is assigned a large value so that the minimisation algorithm automatically drives back the optimisation path into the feasible region.

This penalty approach is general and simple to implement. In fact, no assumptions are required on the characteristics of the constraints and the computer program for constrained minimisation can be easily obtained with few modifications of the code for unconstrained minimisation.

From the computational viewpoint the back analysis approach requiring the minimisation of the error function expressed by eq. (6.11) presents non-negligible differences with respect to that based on the least square method (eq. (6.10)). In fact, the inverse technique, specifically developed for the calibration of elasticity parameters, requires a number of iterations in general smaller than that of the direct method.

On the other hand, each iteration of the direct method involves the inversion of a partitioned stiffness matrix, which is in general computationally more cumbersome than the solution of the equation system required by the direct procedure.

It is not straightforward to work out a general criterion for choosing the most convenient algorithm for back analysis. However, it should be observed that inverse techniques are particularly convenient when dealing with a relatively large number of unknown parameters and when the finite element mesh has a small number of nodal variables. On the contrary, the direct procedures are preferable when a few parameters are back analysed using large finite element meshes.

Another point to be taken into account concerns the programming effort for implementing these techniques. In this respect the back analysis methods based on direct search algorithms present a non-negligible advantage compared with the inverse procedures. In fact, while the inverse procedures require the implementation of an *ad hoc* computer program, the direct approach can be implemented on the basis of standard computer codes for non-linear function minimisation in which the finite element program for stress analysis is introduced as a subroutine. This requires some simple changes to the original finite element code, and a limited programming effort. In addition, the same stress analysis and minimisation programs can be used for various back analysis problems, merely by considering the calculated quantities as functions of the current unknown parameters, regardless of their physical nature.

Probabilistic back analysis

The field measurements that represent the data of the back analysis are in general affected by errors that depend on the nature of the measured quantities, on the characteristics of the adopted devices, on the field conditions, etc. Various techniques have been proposed in the literature to evaluate the influence of these

errors on the computed mechanical parameters. Among them, two will be mentioned here.

A first approach, is based on the so-called Monte Carlo, or simulation, technique. Following this method, the influence of the measurement error, and of the number of input data, is evaluated through a series of numerical tests [9]. Each of them consists of a set of back analyses based on suitable generated input measurements (e.g. displacements).

The input data are obtained by adding to the “exact” measurements a disturbance that represents the experimental “errors”. Independent generators of random numbers, with chosen probability distributions and zero mean value, are used to work out these errors. The number of generators coincides with that of the input measurements. Their probability distributions depend on the characteristics of the measuring devices and of the measured quantities.

The “exact” displacements either can be evaluated on the basis of actual field measurements or could be simulated through a preliminary stress analysis of the problem at hand, in which reference values of the material parameters are introduced [9].

This procedure permits establishing a probabilistic correlation between the resolution of the measuring device, the number of measurements and the accuracy of the computed parameters characterising the soil/rock mass.

The simulation technique offers the advantage of an extremely simple implementation, but requires a computational effort rapidly increasing with the number of free variables of the numerical model and with the number of unknown parameters.

This drawback could be limited by making recourse to probabilistic approaches [10–13]. Among them, the so-called Bayesian approach will be discussed here, which was adopted in [14] and [15] for a rock mechanics problem and for the back analysis of the field measurements performed during the construction of a railroad embankment.

A typical feature of the Bayes approach is that “a priori” information on the unknown parameters can be introduced in the back analysis, together with the data deriving from *in situ* measurements. In most cases, the a priori information consists of an estimation of the unknown parameters based on the engineer’s judgement or on available general information. This leads to a numerical calibration procedure that combines the knowledge deriving from previous, similar problems with the results of the *in situ* investigation. For the sake of brevity, only the bases of the approach are outlined here.

Consider the experimental measurements, collected in vector \underline{u}^* , and the corresponding errors, seen as random variables, grouped in vector \underline{u} . Let us assume that the expected average value of the error vector, expressed by the “expectation” operator E_x , vanishes,

$$E_x |\Delta \underline{u}| = \underline{0} \quad (6.12)$$

and that the error covariance matrix \underline{C}_u , which depends on the accuracy of the measuring device, is known,

$$\underline{C}_u = E_x \left| \Delta \underline{u}_i \cdot \Delta \underline{u}_i^T \right| \quad (6.13)$$

If all measurements are statistically independent, \underline{C}_u is a diagonal matrix the entries of which (variances) are related to the resolution of the instruments.

Also the unknown parameters \underline{p} are regarded as random quantities and it is assumed that the following expectations are known,

$$\underline{p}_0 = E_x \left| \underline{p} \right| \quad (6.14)$$

$$\underline{C}_{p,0} = E_x \left| \left[\underline{p} - \underline{p}_0 \right] \cdot \left[\underline{p} - \underline{p}_0 \right]^T \right| \quad (6.15)$$

In the above equations, \underline{p}_0 and $\underline{C}_{p,0}$ depend on the a priori information on the unknown parameters. If the entries of vector \underline{p}_0 are uncorrelated, $\underline{C}_{p,0}$ is a diagonal matrix. Note that the values of the entries of this matrix increase with decreasing accuracy of the initial information on the unknown parameters.

The Bayesian back analysis consists in combining a priori and experimental information in order to achieve the best estimate of the unknown parameters. Also in this case, as for the deterministic back analysis, a numerical model is set up which allows us to calculate the quantities \underline{u} , corresponding to the measured ones \underline{u}^* , on the basis of the current parameter vector \underline{p} .

Consider first the simple case in which \underline{u} is linearly dependent on \underline{p} through a constant matrix \underline{L} and constant vectors \underline{u} and \underline{p} ,

$$\underline{u}(\underline{p}) = \underline{u}' + \underline{L} \cdot \left[\underline{p} - \underline{p}' \right] \quad (6.16)$$

The best estimate of \underline{p} can be obtained by minimising, with respect to \underline{p} , the following error function E_r ,

$$E_r = \left[\underline{u}^* - \underline{u}(\underline{p}) \right]^T \cdot \underline{C}_u^{-1} \cdot \left[\underline{u}^* - \underline{u}(\underline{p}) \right] + \left[\underline{p}_0 - \underline{p} \right]^T \cdot \underline{C}_{p,0}^{-1} \cdot \left[\underline{p}_0 - \underline{p} \right] \quad (6.17)$$

which consists of two parts: the first represents the discrepancy between measured and calculated data, while the second is the discrepancy between assumed and current parameters.

These discrepancies are weighted by means of the inverted covariance matrices, which tend to vanish with decreasing accuracy of the a priori information and of the experimental data.

By introducing eq. (6.16) into eq. (6.17), and by imposing that the derivatives of E_r with respect to \underline{p} vanish, the following system of linear equations is arrived at, the solution of which leads to the optimal vector ,

$$\left[\underline{L}^T \cdot \underline{C}_u^{-1} \cdot \underline{L} + \underline{C}_{p,0}^{-1} \right] \cdot \underline{p} = \underline{L}^T \cdot \underline{C}_u^{-1} \cdot \left[\underline{u}^* - \underline{u}' + \underline{L} \cdot \underline{p}' \right] + \underline{C}_{p,0}^{-1} \cdot \underline{p}_0 \quad (6.18)$$

To obtain the covariance matrix associated with vector \underline{p} is necessary to recall that if a vector \underline{a} is linearly dependent on a vector \underline{b} of random variables through matrix \underline{A} ,

$$\underline{a} = \underline{A} \cdot \underline{b} \quad (6.19)$$

the following relationship exists between the covariance matrices, \underline{C}_a and \underline{C}_b , associated with the two vectors

$$\underline{C}_a = \underline{A} \cdot \underline{C}_b \cdot \underline{A}^T \quad (6.20)$$

On the basis of eq. (6.18), a linear relation can be established between vectors \underline{p}_0 and \underline{u}^* ,

$$\underline{\bar{p}} = [\underline{I} - \underline{M}_0 \cdot \underline{L}] \cdot \underline{p}_0 + \underline{M}_0 \cdot \underline{u}^* - \underline{M}_0 \cdot [\underline{u}' - \underline{L} \cdot \underline{p}'] \quad (6.21)$$

where \underline{I} is the identity matrix, and matrix \underline{M}_0 has the following expression,

$$\underline{M}_0 = [\underline{L}^T \cdot \underline{C}_u^{-1} \cdot \underline{L} + \underline{C}_{p,0}^{-1}]^{-1} \cdot \underline{L}^T \cdot \underline{C}_u^{-1} \quad (6.22)$$

Since \underline{p}_0 and \underline{u}^* are statistically independent, eq. (6.20) allows expressing the covariance matrix associated to vector \underline{p} in the following form,

$$\underline{C}_p = [\underline{I} - \underline{M}_0 \cdot \underline{L}] \cdot \underline{C}_{p,0} \cdot [\underline{I} - \underline{M}_0 \cdot \underline{L}]^T + \underline{M}_0 \cdot \underline{C}_u \cdot \underline{M}_0^T \quad (6.23)$$

Eqs.(6.18) and (6.23) cannot be directly applied to the majority of calibration problems in the field of geomechanics, due to the fact that \underline{u} is in general a non-linear function of \underline{p} (even in the simple case of linear elastic behaviour of the soil/ rock mass). In this case an iterative procedure can be adopted, by linearising the relationship between \underline{u} and \underline{p} , in the neighbourhood of the current parameter vector \underline{p} , through a Taylor's series expansion truncated at the linear terms (cf. eq. (6.16)),

$$\underline{u}(\underline{p}) = \underline{u}(\underline{p}') + \underline{L}(\underline{p}') \cdot [\underline{p} - \underline{p}'] \quad (6.24)$$

The main steps of the iterative solution procedure can be summarised as follows:

- 1) At the beginning of iterations the current parameter vector \underline{p} is set equal to the initial estimate.

- 2) The quantities u_i , corresponding to the *in situ* measurements, are determined by means of a finite element stress analysis based on the current parameter values.
- 3) The current “sensitivity” matrix $\underline{L}(\underline{p})$ is evaluated numerically as a finite difference approximation. This requires the solution of n stress analysis problems (n being the number of unknown parameters p_i). The vector of parameters used in each analysis coincides with vector \underline{p} but the i -th component is perturbed by a small quantity Δp_i . Denoting by Δu_i the difference between the quantities obtained at step (2) and those derived from the i -th stress analysis, the sensitivity matrix can be expressed as,

$$\underline{L}(\underline{p}') = [\Delta \underline{u}_1 / \Delta p_1, \dots, \Delta \underline{u}_n / \Delta p_n] \tag{6.25}$$

- 4) Vector \underline{u} is evaluated by solving the equation system (6.18), where the current values of \underline{L} , \underline{u} and \underline{p} are introduced.
- 5) The iterative procedure ends when the difference between \underline{p} and \underline{p}' is smaller than a pre-assigned tolerance, otherwise \underline{p} is set equal to \underline{p}' and the process is continued from step (2). The main diagonal of the covariance matrix calculated at the end of the iterative process through eq.(6.23) represents the variances of the estimated values of the parameters.

It is worthwhile observing that the Bayesian approach is applicable also when the number of unknown parameters exceeds the number of *in situ* measurements, if a reliable initial guess on the parameters can be formulated.

Consider in fact the limit case in which no experimental information is available. This case is equivalent to the situation in which the accuracy of the experimental data is so poor that the entries of the corresponding inverted covariance matrix \underline{C}_u vanish. Consequently, eq.(6.18) reduces to a trivial form expressing the equivalence between the optimal values of the parameters and their initial estimate \underline{p}_0 .

Another limit case is when no a priori information is available, or when its reliability is so low that the corresponding inverted covariance matrix vanishes. In this case eq. (6.18) becomes,

$$[\underline{L}^T \cdot \underline{C}_u^{-1} \cdot \underline{L}] \cdot \underline{p} = \underline{L}^T \cdot \underline{C}_u^{-1} \cdot [\underline{u}^* - \underline{u}' + \underline{L} \cdot \underline{p}'] \tag{6.26}$$

Furthermore, if all the (uncorrelated) *in situ* measurements have the same accuracy, matrix \underline{C}_u can be eliminated from eq. (6.26), thus obtaining the following least square expression for the best estimate of the unknown parameters,

$$\underline{L}^T \cdot \underline{L} \cdot \underline{p} = \underline{L}^T \cdot [\underline{u}^* - \underline{u}' + \underline{L} \cdot \underline{p}'] \tag{6.27}$$

Note, however, that the covariance matrix of the measurements still affects the covariance matrix associated with the best estimate of the parameters. In fact eq. (6.23) becomes,

$$\underline{C}_p = \underline{M}_0 \cdot \underline{C}_u \cdot \underline{M}_0^T \tag{6.28}$$

where

$$\underline{M}_0 = [\underline{L}^T \cdot \underline{C}_u^{-1} \cdot \underline{L}]^{-1} \cdot \underline{L}^T \cdot \underline{C}_u^{-1} \tag{6.29}$$

The influence of the measurement errors on the results of back analysis has been discussed in [9] and [14] with reference to a simple rock mechanics problem. The first study is based on the mentioned Monte Carlo or simulation approach, while the second adopts the Bayesian procedure. To compare the results of the two approaches, eqs. (6.27) and (6.29) were adopted in the Bayesian solution procedure, instead of eqs. (6.18) and (6.23), since no a priori information can be introduced in the “simulation” back analysis.

The results of the two studies showed that both approaches lead practically to the same results, in terms of the relationships between the resolution of the measuring devices and the uncertainty of the estimated parameters. However, the computer time required by the simulation process is appreciably larger than that required by the Bayesian back analysis.

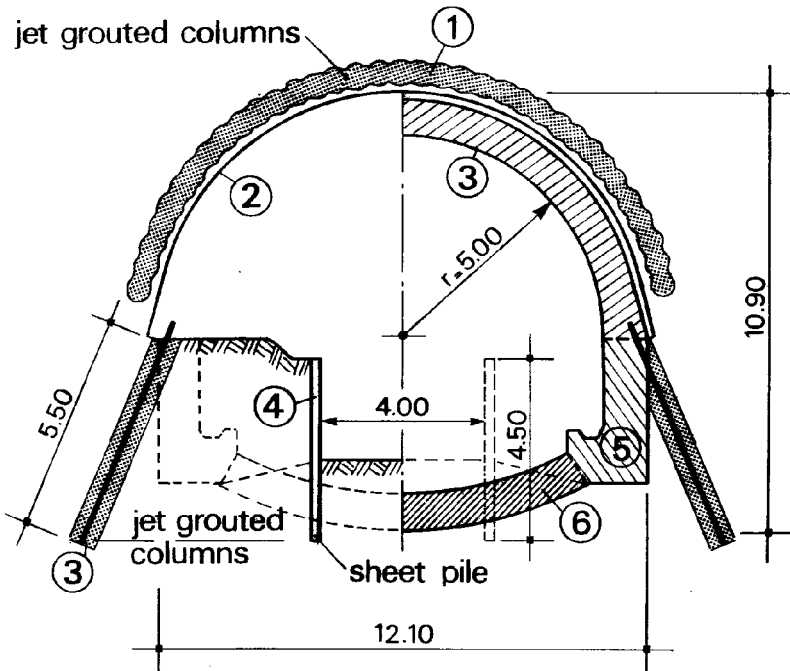


Figure 6.1 Construction sequence of the railroad tunnel.

Back analysis of a tunnel in a granular deposit

Tunnel characteristics

The back analysis problem discussed here concerns the construction of a new tunnel of the Gotthard railroad connecting Italy to Switzerland. This two-track tunnel has an internal radius of 5 m, a length of 7.2 km and a portion of it (750 m in length) crosses an alluvial deposit, consisting mainly of fine sand, at a depth of about 35m. The water table is located below the invert arch level.

To limit the difficulties of driving a tunnel in a cohesionless soil, jet grouted columns were adopted for consolidating the sand ahead of the excavation and to stabilise the tunnel face. The construction steps, illustrated in detail in [16], are summarised in Figure 6.1. First, the top part of the tunnel was excavated for a considerable length. Subsequently the bottom excavation was carried out and the permanent lining was set in place.

During excavation, the surface settlements and the vertical displacements within the sand deposit were measured at two sections of the tunnel through topographic survey and sliding micrometers [17]. Figures 6.2 and 6.3 show, respectively, the soil profile for one of these sections and the location of the measurement points. The surface settlements measured during the advancing of the excavation are shown in Figure 6.4. The maximum settlement measured at the end of the top excavation was about 3 cm. It increased to about 6 cm after the completion of the opening.

After construction, a back analysis of the *in situ* measurements performed at Section 2 (cf. Figure 6.4) was attempted [18]. This had two main purposes: (a) to identify the “mechanism” that governs the development of the displacements around the opening, and (b) to evaluate the effectiveness of possible improvements of the construction procedure in reducing the surface settlements.

Among various back analysis techniques applicable to tunnelling problems [3, 19, 20], the previously described direct approach was used, in a deterministic context, for this application.

Elastic back analysis

A first back analysis was carried out, assuming a linear elastic material behaviour, in order to determine the equivalent elastic parameters of the sand deposit. To this purpose the deposit was subdivided into six layers, the secant elastic moduli of which represent the free variables of the problem. The mesh adopted in the plane strain calculations is shown in Figure 6.5. The meaning of the dark zone in this figure will be discussed subsequently.

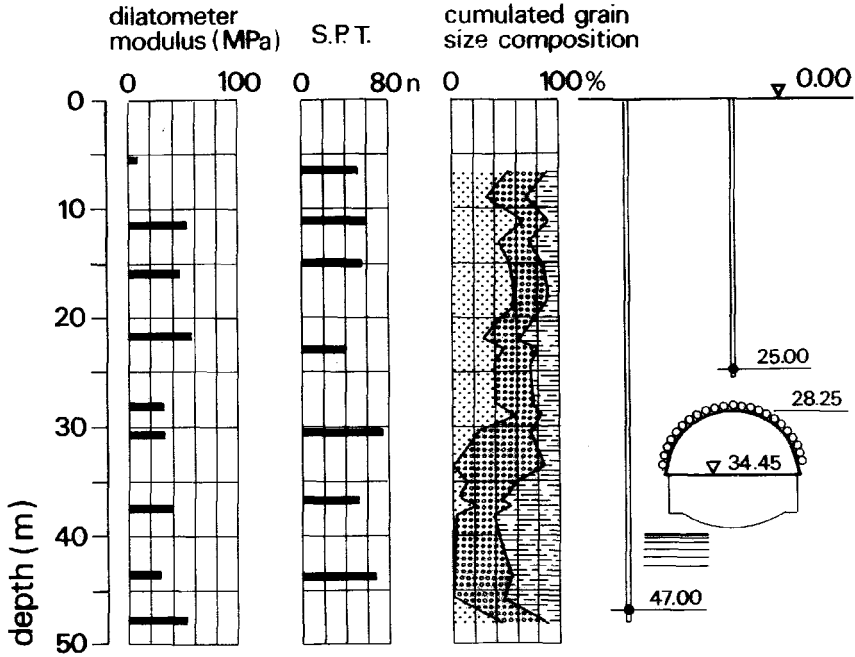


Figure 6.2 Soil profile. The three zones in the grain size distribution denotes, from left to right: gravel, sand and silt.

To obtain an acceptable approximation of the excavation process, which has a three-dimensional nature, by means of a two-dimensional finite element model, two stress analyses were carried out for each step of the error minimisation process. The first concerns the first excavation stage, i.e. the top part of the tunnel. This is done by applying to the tunnel walls a set of forces equivalent to 30% of initial stress distribution, by introducing the elements discretising the crown support and by applying the remaining part of the equivalent forces. The second stage of analysis considers the excavation of the bottom part of the tunnel, the installation of the sub-vertical jet grouting columns (representing the foundation of the crown arch) and the completion of the permanent lining.

This first back analysis did not lead to satisfactory results; in fact an appreciable difference was observed between the displacements measured in the vicinity of the tunnel and those computed on the basis of the back calculated “optimal” elastic constants.

The results presented in [21] and [22] provide a possible explanation of this difference. They show, in fact, that in the vicinity of shallow tunnels, driven in soil deposits characterised by low values of the coefficient of earth pressure at rest, the shear strains tend to concentrate within narrow zones forming almost vertical bands.

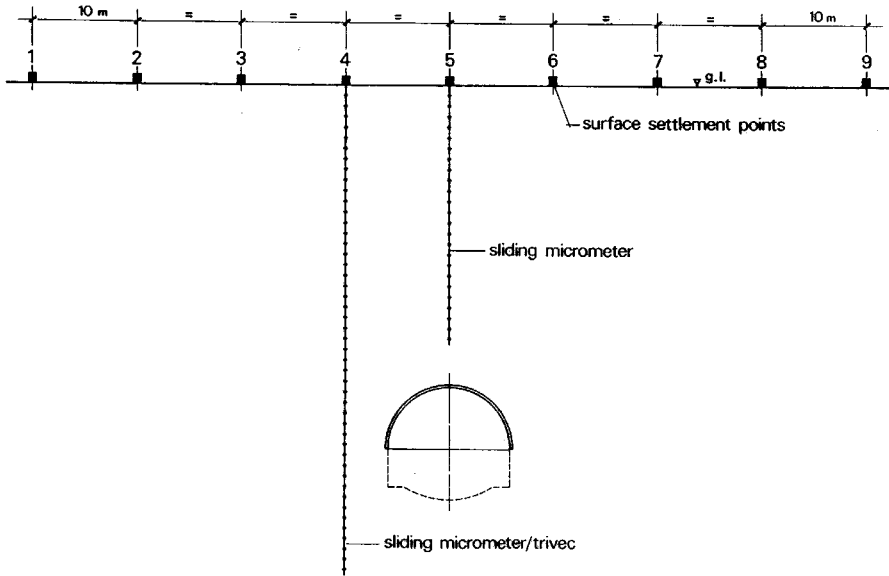


Figure 6.3 Location of the measurement points.

This effect was introduced in the elastic back analysis through the band indicated by a dark zone in Figure 6.5. To take into account the overall loss of stiffness of the sand in this zone, the moduli of elasticity were assumed equal to those of the mentioned six layers multiplied by a reduction factor α , constant for all layers. The elastic moduli of each layer and the reduction factor α represent the free variables of a second back analysis problem.

Two calculations were performed considering as input data the displacements measured, respectively, at the end of the first and second stages of excavation. Figure 6.6 compares the elastic moduli obtained by the back analyses for the two excavation stages with the loading and unloading moduli obtained by the dilatometer tests carried out *in situ* before the beginning of excavation. This back analysis led to a reduction factor within the “weak” zone equal to 0.23 and to 0.26 for the top and bottom excavations, respectively. The computed and measured vertical displacements at the end of excavation are shown in Figure 6.7.

It can be observed that, apart from the reduction factor, the elastic moduli obtained by the back analysis of the first excavation stage are quite close to those calculated at the end of the bottom excavation, but for the soil layers located at the tunnel depth. This depends on the fact that the bottom excavation produces appreciable incremental strains in the soil close to the tunnel with respect to those obtained at the end of the top excavation. This is interpreted by the elastic back analysis as a reduction of the equivalent secant modulus of the sand in that zone.

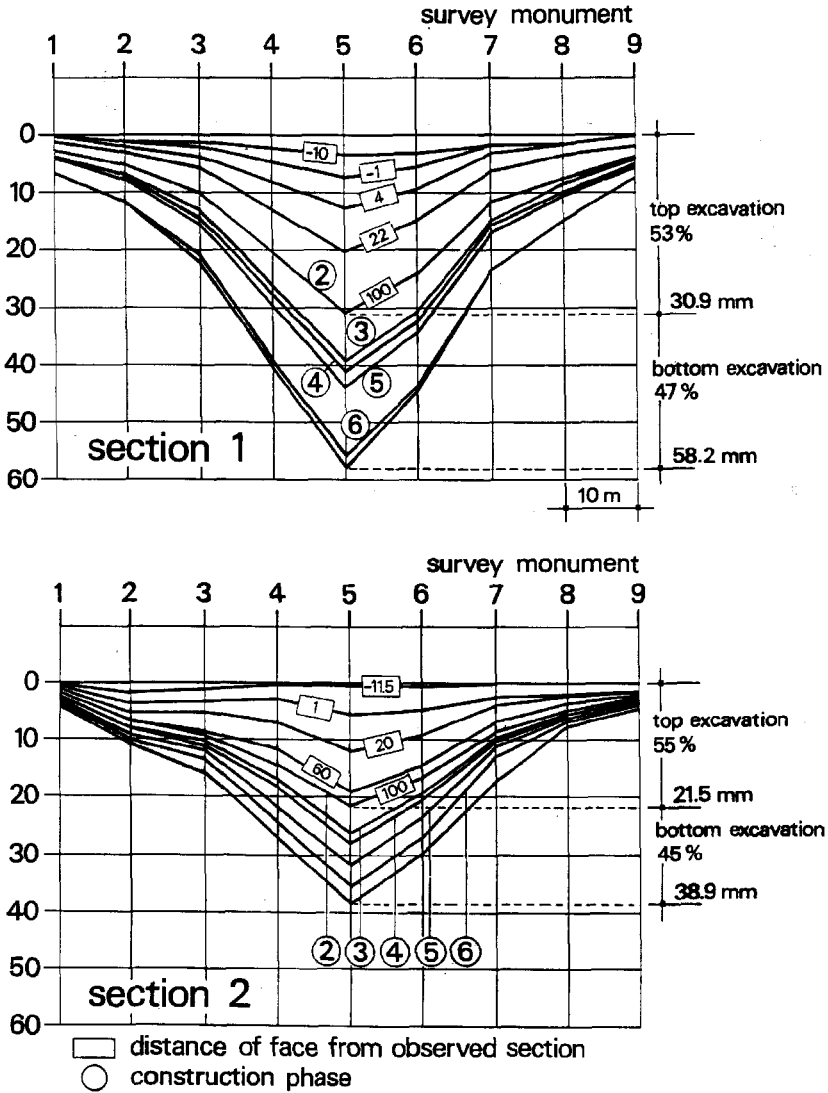


Figure 6.4 Surface settlements recorded during the tunnel excavation.

These results suggested some possible changes to the construction technique, to limit the settlements during the second stage of excavation. They should increase the bearing capacity of the foundations of the crown arch, for instance, by introducing additional sub-vertical jet grouted columns at the liner shoulders.

Since this modified technique involves relevant technical problems, and an increase of the cost of excavation, it was decided to carry out a preliminary evaluation of its effectiveness by means of a finite element simulation. It was

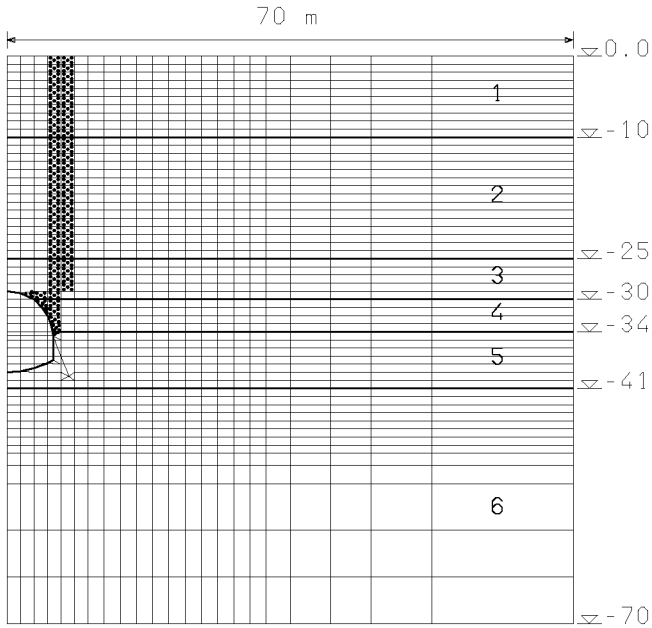


Figure 6.5 Finite element mesh for the plane strain back analyses.

observed, however, that the numerical model “tuned” by the elastic back analyses could not be adopted for the analysis of a different construction procedure. In fact, the shape and size of the “weak” zone were a priori chosen in the calculations, and it is quite likely that a change of the method of excavation would involve, in turn, a change of this zone.

Elasto-plastic calculations

In order to circumvent the above-mentioned drawback it was decided to develop an elasto-plastic model able to analyse the spreading of the “plastic” zone around the railroad tunnel. To this purpose, a simple elasto-plastic material model was considered, which is based on experimental observations from compression and shear tests on “stiff” soil samples [23].

Among the various features of the mechanical behaviour of these geological materials only the so-called strain softening was considered, even though other aspects, anisotropy in particular, could play a non-negligible role in defining the overall stress-strain response.

Figure 6.8 shows a qualitative representation of the results of a direct shear test on a stiff soil sample under a constant, average vertical stress σ , in terms of the diagram between the average shear stress τ and the horizontal displacement δ .

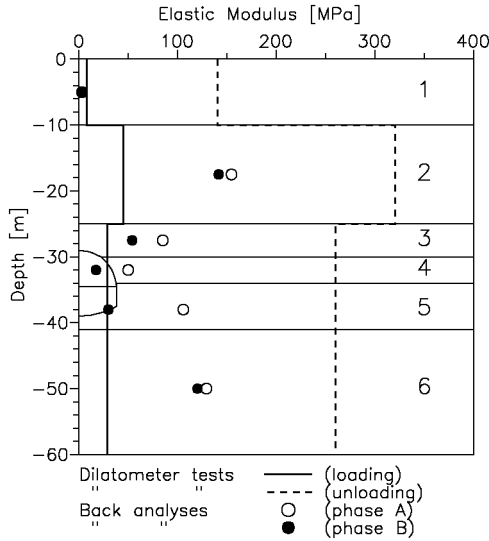


Figure 6.6 Elastic moduli of the sand layers obtained by the *in situ* dilatometer tests and by the elastic back analyses of the displacement measurements.

The τ - δ relationship can be schematically subdivided into three main parts. In the first, the average shear stress increases until its peak value is reached. This corresponds, in the average normal stress-shear stress (σ - τ) plane, to the so-called peak failure envelope characterised by peak cohesion and friction angle. Relatively small additional increments of displacements produce a reduction of the shear resistance, caused by an almost complete loss of the peak cohesion. This leads to a second (fully softened) failure condition. Finally, further large increments of the horizontal displacement bring the friction angle to its residual value, which represents the only non-vanishing parameter of the residual failure envelope. During this process also a reduction of the instantaneous elastic modulus could take place.

In order to account for this material behaviour in a finite element stress analysis it is necessary to define a law governing the reduction of cohesion, friction angle and elastic moduli from peak to residual values. This was based on the relationship graphically depicted in Figure 6.9.

It is assumed that shear strength and stiffness parameters are functions of a measure of the (irreversible) plastic deformation, represented by the square root of the second invariant J_2 of the deviatoric plastic strains.

The friction angle keeps its peak value until J_2 reaches a “peak” limit J_{2p} . Then a reduction occurs until a second limit J_{2r} is attained, which corresponds to the residual friction angle. Analogous relationships, with different limits on J_2 , are adopted also for the remaining mechanical parameters.

In order to account for the effects of dilatancy, the plastic flow rule is related to the variation of the friction angle. In particular, an associated flow rule is

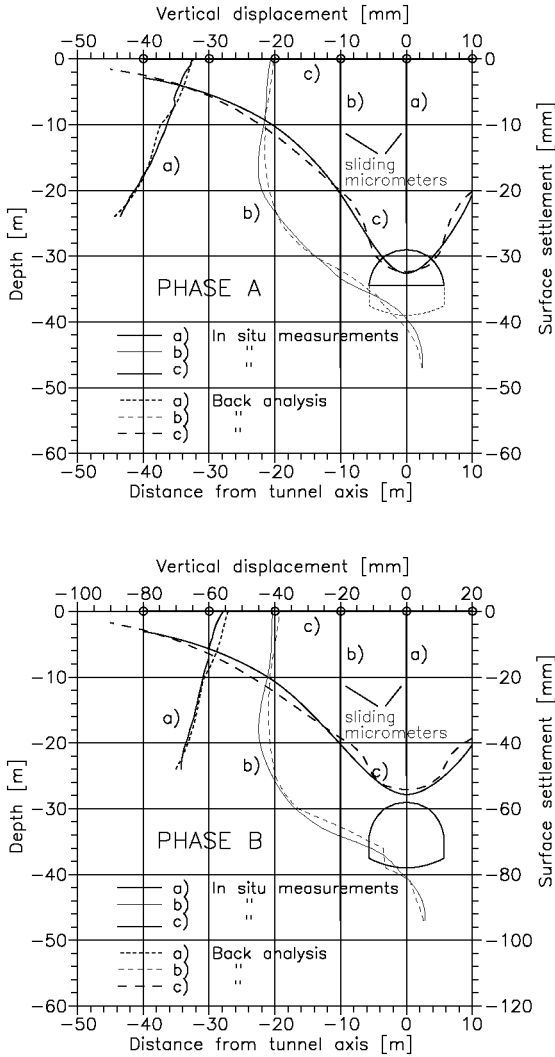


Figure 6.7 Comparison between the vertical displacements measured in the field and those obtained by the elastic back analysis.

assumed for the peak failure envelope. Then the angle of dilatancy decreases with increasing plastic deformation and it vanishes when the residual failure condition is reached.

Details of the finite element implementation of this simple strain softening constitutive model have been presented in [23].

This constitutive model was first applied to the analysis of the original construction procedure of the railroad tunnel, using the same mesh and steps already described for the elastic back analysis. The elastic moduli were those

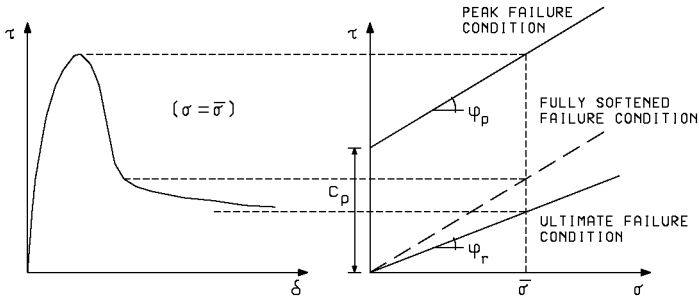


Figure 6.8 Schematic representation of the relationship between average shear stress τ and displacement δ for direct shear tests on a stiff soil sample, and relevant failure envelopes.

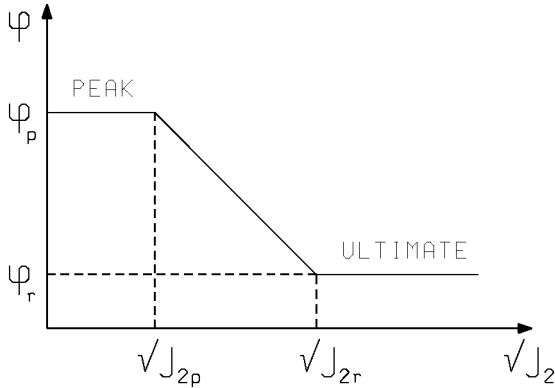


Figure 6.9 Variation of the friction angle ϕ with increasing square root of the second invariant of the deviatoric plastic strains J_2 .

obtained by the back analysis of the top excavation, but the zone characterised by the reduction factor a was eliminated. The described softening material law, with no cohesion, was introduced to account for the loss of stiffness and strength in this zone. The analysis is initiated assuming for all elements a “peak” friction angle. When the state of stress reaches the failure condition the friction angle is suddenly reduced to its residual value. Also the modulus of elasticity is reduced, multiplying it by the reduction factor obtained from the previous elastic back analysis.

This elasto-plastic calculation led to the final displacements and to the contour lines of the second invariant of the deviatoric plastic strains shown, respectively, in Figures 6.10 and 6.11. These results indicate that the “softening” calculation is able to provide an acceptable approximation of the measured surface settlements, without requiring specific assumptions on the shape and size of the zone where the plastic strains concentrate.

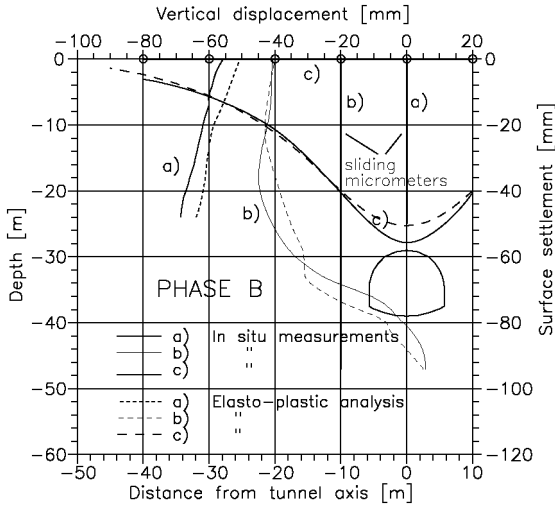


Figure 6.10 Comparison between the vertical displacements measured at the end of construction and those obtained by the elasto-plastic analysis.

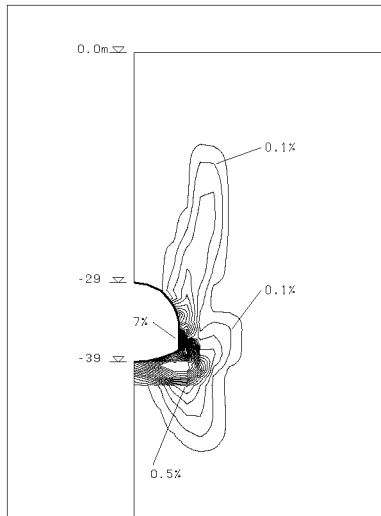


Figure 6.11 Contour lines of the square root of the second invariant of the deviatoric plastic strains.

On these bases, the finite element model was applied to the analysis of the modified construction procedure for the railroad tunnel for evaluating the consequent reduction of the surface settlements.

The change in the construction procedure is easily introduced into the finite element analysis simply by refining the mesh at the tunnel shoulders and assigning the property of the grouted soil to a larger number of elements with

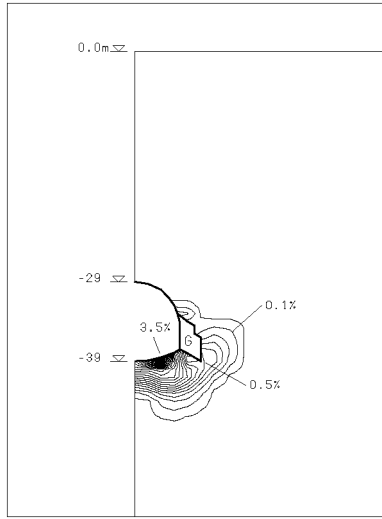


Figure 6.12 Contour lines of the square root of the second invariant of the deviatoric plastic strains for the modified construction procedure (G denotes the grouted zone representing the foundation of the tunnel crown).

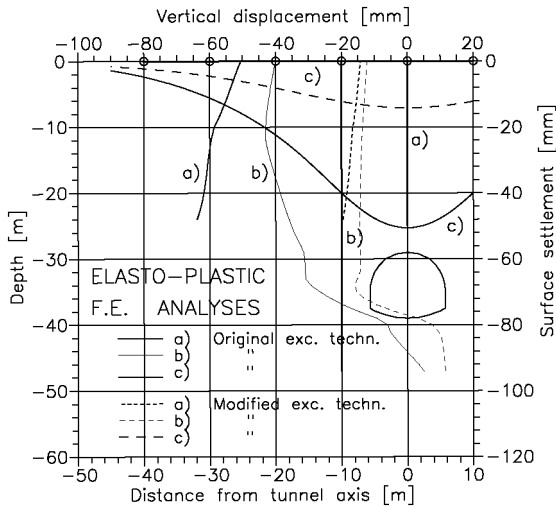


Figure 6.13 Comparison between the vertical displacements obtained by the elasto-plastic analyses of the original and modified construction procedures.

respect to those used in the previous calculations. The other characteristics of the analysis (e.g. sequence of excavation/loading steps, material model, values of the material parameters, etc.) are unchanged.

Figure 6.12 shows the plastic zone at the end of excavation, by means of the contour lines of the square root of the second invariant of deviatoric plastic strains. In the same figure, zone *G* denotes the grouted zone that represents the modified foundation of the upper arch.

It can be observed that the modified construction procedure involves a marked reduction of the extension of the plastic zone with respect to that characterising the original procedure. This, in turn, leads to a decrease of the surface settlements, as shown in Figure 6.13 by comparison of the vertical displacements calculated for the two excavation procedures.

As previously observed, the accuracy of the elasto-plastic model could be improved, since its parameters were not calibrated on the basis of a back analysis. In spite of this, some useful information is obtained by the numerical analysis, concerning in particular the surface settlements which are reduced by a factor of about 2 to 2.5 with respect to those calculated for the original excavation procedure.

This information can be used, together with that related to the increment of the cost of excavation, to predict the effects of the reduced (but still non-negligible) settlements on buildings in the construction area, etc. as one of the parameters for evaluating the effectiveness of the modified technique.

Back analysis of a tunnel in a ‘viscous’ rock mass

Tunnel characteristics

A second application concerns the back analysis of the displacements measured *in situ* during the excavation of the Frejus motorway tunnel. This tunnel, excavated between 1975 and 1979, crosses the Alps and joins the towns of Modane (France) and Bardonecchia (Italy). Its total length is approximately 13 km.

The main portion of the tunnel on the Italian side is excavated in a schistose rock, with a depth of cover ranging from 700 m to about 1700 m. The rock mass is characterised by three major joint sets that intersecting the schistosity could lead to the formation of unstable wedges at the excavation crown.

The tunnel has a horseshoe-shaped section, with a height of 9 m and a vertical radius of 6 m. The construction was based on conventional methods, using mainly rock bolts and shotcrete as a primary support. The rock bolts have a diameter of 24 mm, their length varies from 3 to 5 m and their “density” is about 1 bolt every 1.4 m². The shotcrete is approximately 10 cm thick.

Steel ribs were also used in the zones where the rock quality was particularly poor. The permanent concrete lining, 80 cm thick, was installed 300 to 400 m behind the excavation face.

Comprehensive geomechanical studies were carried out during construction [24, 25]. They included plate load and flat jack tests, for the evaluation of the

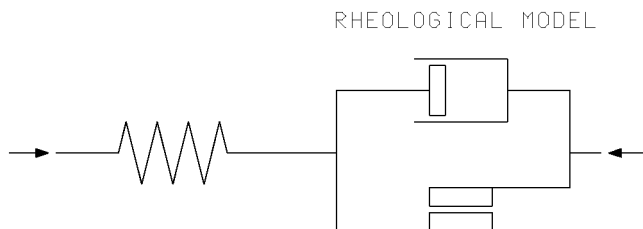


Figure 6.14 Rheological model.

elastic modulus of the rock mass, and laboratory shear tests, for determining the peak and residual values of the friction angle along the schistosity.

The elastic modulus for the rock mass ranged between 6000 and 14,700 MN/m². The shear tests provided average values of peak and residual friction angles of about 60° and 34°, respectively. The relatively large value of the peak friction angle depends on the appreciable influence of its “geometrical” portion.

In addition to the above investigation, the following measurements were also carried out during excavation to monitor the overall stability of the opening:

- 1) Size of the relaxed zone around the tunnel using multiple point extensometers to a depth of 6 to 10m.
- 2) Convergence of the opening contour.
- 3) Axial force in the rock bolts.
- 4) Seismic wave velocity by geophysical survey.

Model for the analysis

The mentioned *in situ* measurements showed an appreciable time-dependent deformation of the opening. This suggested to base the back analyses on the rheological material model depicted in Figure 6.14. It consists of a linear spring (governing the instantaneous response of the rock mass), a friction block (with limit resistance governed by the Mohr-Coulomb criterion) and a linear dashpot (that accounts for the observed time-dependent behaviour).

The rock mass surrounding the tunnel did not exhibit an appreciable volume increase (or swelling) during time. This allows the disregarding of the volumetric part of the viscous behaviour, i.e. the one related to the spherical component of the state of stress, and to consider only one deviatoric viscosity coefficient η for the rheological model.

The shear strength c , φ and viscosity η parameters of the rock mass represent the free variables of the back analysis. The values of the elastic constants were chosen on the basis of *in situ* investigations. As suggested in [24], the average value of the elastic modulus from the plate load tests ($E=10,000$ MN/m²) was adopted, and Poisson’s ratio was estimated equal to 0.3.

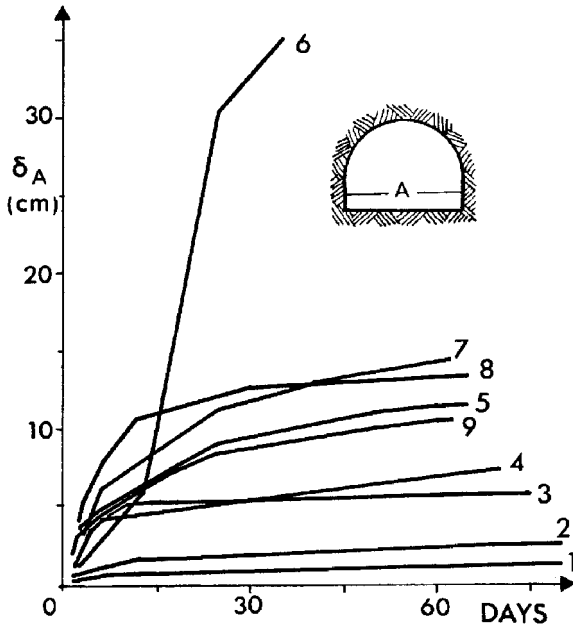


Figure 6.15 Horizontal convergence vs time data measured at different tunnel sections (after [25]).

Table 6.1 Distance from the tunnel entrance (Italian side) and depth of cover of the various sections.

Section	Distance (m)	Depth (m)
1	845	490
2	861	500
3	2772	580
4	3954	590
5	4507	740
6	5172	1200
7	5533	1400
8	5950	1530
9	6066	1640

Among the performed *in situ* measurements, the inward displacements of the tunnel walls (convergence) were adopted as input data for the back analyses. These measurements were carried out at various sections along the tunnel axis and, as usual, along different directions.

The input data of a back analysis should depend on the overall behaviour of the rock mass and should not be influenced by local effects such as, for instance, the movements of rock wedges that could develop in the vicinity of the tunnel

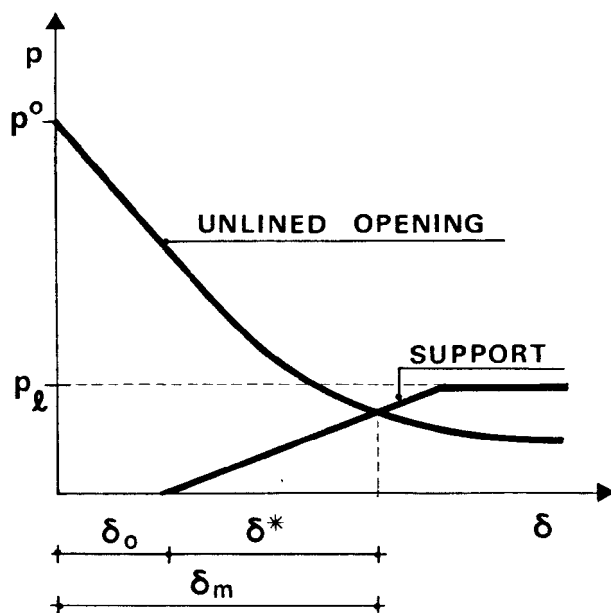


Figure 6.16 Characteristic lines of a tunnel and of its temporary support.

crown. Consequently, only the convergence along the horizontal diameter of the tunnel was considered in the calculations.

Figure 6.15 shows the recorded variation with time of the horizontal part of the vertical diameters of nine different sections of the tunnel [25]. The distances of these sections from the Italian entrance of the tunnel, and their depths of cover, are reported in Table 6.1.

Since the poor quality of the rock mass at section 6 did not permit a reliable monitoring of the convergence, the data of that section were not considered in the back analyses.

The calibration problem was solved in two subsequent phases. First, the values of cohesion and friction angle (c and ϕ) were determined, considering only the maximum (long-term) values of the measured displacements. Subsequently, the viscosity coefficient η was back calculated, taking into account the increase of displacements with time.

The back analysis of the average mechanical parameters of the rock mass was based on the assumptions of axial symmetry with respect to the tunnel axis, and of plane strain regime. Hence, the tunnel is equivalent to a circular opening in a homogeneous and isotropic, weightless medium, subjected to a hydrostatic *in situ* stress state p_0 , and the excavation process is simulated by decreasing the pressure p on the opening contour, from its initial value p_0 .

The “equivalent” radius of the circular opening is 7 m and the hydrostatic *in situ* stress is equal to the unit weight of the rock multiplied by the depth of cover of the various sections.

The first calibration problem was dealt with by adopting the analytical solution for a circular hole in an elasto-plastic medium obeying the Mohr-Coulomb yield criterion, see e.g. [26]. This solution leads to the so-called “characteristic curve” of the tunnel or, in other words, to the relationship between the convergence δ and the uniform rock pressure p (cf. Figure 6.16).

The possible increment of the rock pressure on the tunnel support due to possible “loosening” effects was introduced in an approximated manner. In fact, the pressure obtained with the elasto-plastic solution was increased by the ratio between a chosen percentage (50%) of the weight of the rock where plastic strain occurs and the circumference of the tunnel.

Under the assumption of elastic ideally plastic behaviour for the primary support, three additional parameters are needed to evaluate the stress and strain regimes developing after its installation, namely:

- its radial stiffness K ,
- the limit radial pressure p_l bearable by the support,
- the convergence δ_0 that takes place before its installation.

An overall radial stiffness K of 30 MN/m³ was estimated for the primary support. This represents the slope of the p – δ curve of the support in Figure 6.16. The limit pressure p_l was determined by assuming, according to the available experimental information, a compression strength of 12 MN/m² for the shotcrete and an equivalent tensile strength of 0.22 MN/m² for the rock bolts.

The maximum displacement δ_m of the tunnel wall (representing the input data of the back analysis) depends on the initial displacement δ_0 and on the measured displacement δ^* (cf. Figure 6.16),

$$\delta_m = \delta_0 + \delta^* = \alpha \cdot \delta^* \quad (6.30)$$

Since no experimental information was available about the initial displacement δ_0 , different values of α were introduced in the calculations, namely 1.0 and 1.5, to evaluate its influence on the results of back analyses.

The mentioned elasto-plastic solution permits estimating the long-term radial displacement of the primary support, and the corresponding average rock pressure, through the intersection of the characteristic curves of the opening and of the support.

The second back analysis concerns the determination of the deviatoric viscosity coefficient η . The numerical model adopted in this case is based on the finite element approach developed for the analysis of the “squeezing” effects around tunnels [27].

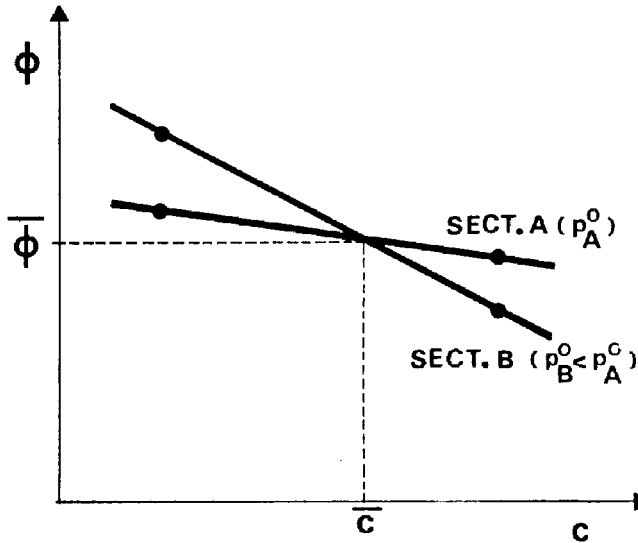


Figure 6.17 Qualitative plot of the c - ϕ relationship for two tunnel sections with different depth of cover.

A plane strain, axisymmetric finite element scheme was set up, which enables simulating the excavation process (by decreasing the internal pressure p) and the installation of the primary support (by applying an equivalent non-linear “spring” at the tunnel wall).

The optimal value of the viscosity coefficient was evaluated through the direct back analysis approach, by minimising the difference between the convergence measured during time and the corresponding numerical results.

Evaluation of the shear strength parameters

A first back analysis was attempted to evaluate the average values of cohesion and friction angle for the entire rock mass. These calculations were carried out assuming a linear elastic behaviour for the primary support and $\alpha=1.5$ (cf. eq.6.30).

To this purpose, each tunnel section was considered separately, excluding section 6. Since two unknowns, c and ϕ , are sought for each section on the basis of only one displacement δ_m , the optimal values of the shear strength parameters describe a line in the c - ϕ plane for each section. This curve turns out to be almost linear, with slope depending on the *in situ* stress p_0 (cf. Figure 6.17). Its evaluation for each section is straightforward. It is sufficient, in fact, to choose two values of c and to evaluate (by means of a one-dimensional minimisation) the corresponding values of ϕ leading to the displacement δ_m for that section.

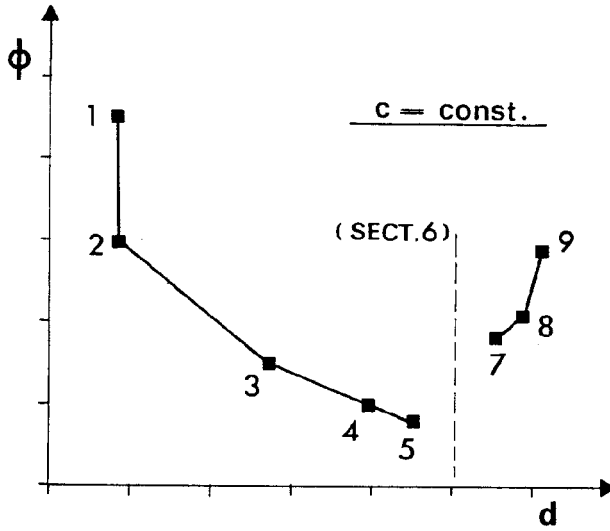


Figure 6.18 Qualitative plot of variation of the friction angle along the tunnel axis, assuming a constant value of cohesion.

If the lines of all sections intersect each other “almost” at the same point, that point defines the average values of shear strength parameters for the entire rock mass.

Unfortunately, the results of the calculations did not lead to a unique intersection point. On the contrary, a marked variation of the shear strength parameters was obtained with the distance d from the tunnel entrance. A qualitative representation of these results is given in Figure 6.18, where the variation of the back calculated friction angle is shown vs. the distance d , for a constant value of cohesion. This preliminary analysis suggests the following observations:

- An exceedingly large friction angle, with respect to the values obtained in the other sections, is evaluated at section 1. This could depend on some local effects influencing the experimental readings in section 1, and suggests disregarding this section in subsequent analyses.
- The average friction angle for the various sections is close to the residual value obtained by the direct shear tests. This is likely to depend on the assumption of linear elastic behaviour of the primary support, which leads to overestimating the load carried by the support itself, thus causing a reduction of the back calculated strength of the rock mass. Therefore, the more realistic assumption of elastoplastic behaviour for the support should be adopted in subsequent analyses.

- The diagram in Figure 6.18 indicates a reduction of the friction angle approaching section 6, where large inward displacements are observed. This reduction is probably associated to a similar decrease of cohesion; both effects should be accounted for in subsequent analyses.

On the basis of these observations a new calibration problem was formulated, concerning the determination of the variation of both c and φ along the tunnel axis that, under the assumption of elasto-plastic behaviour of the support, corresponds to the best approximation of the displacements δ_m for all sections.

The law governing the variation of cohesion and friction angle for this second analysis should not involve more than seven parameters. In fact, in a deterministic back analysis the number of free variables cannot exceed the number of input data that, in the present case, is equal to 7 (excluding, as previously observed, the displacements measured at sections 1 and 6).

The following bi-linear law was adopted which fulfils the above requirement, and takes into account two different variations of the shear strength parameters (suggested by the diagram of Figure 6.18) for sections 2 to 5 and for sections 7, 8 and 9:

- The values of c and φ are expressed as the product of reference quantities, C_0 and φ_0 , by a non-dimensional function f of the distance d ,

$$c = c_0 \cdot f(d) \quad (6.31a)$$

$$\varphi = \varphi_0 \cdot f(d) \quad (6.31b)$$

- Two expressions for f are introduced holding, respectively, for sections 2, 3, 4, 5 and 7, 8, 9,

$$f = f_1 = a_1 + a_2 \cdot d \quad , \quad \text{for sections 2, 3, 4, 5, and}$$

$$f = f_2 = a_3 + a_4 \cdot d \quad , \quad \text{for sections 7, 8, 9.}$$

The back analysis is based on the direct approach, hence its solution requires the minimisation of the discrepancy (or error) between the input data δ_m (cf. eq.(6.30)) for all sections and the corresponding numerically evaluated displacements δ . The error is a non-linear function of six variables, since the numerical results depend on c and φ , which in turn are functions of six unknown parameters c_0 , φ_0 , a_1, \dots, a_4 .

The results of the back analysis are presented in Figure 6.19 by means of the diagrams of cohesion and friction angle vs. the distance d , obtained by assuming $\alpha=1.5$ (curve I) and $\alpha=1.0$ (curve II). The φ vs. d diagram reports also the peak, φ_p ,

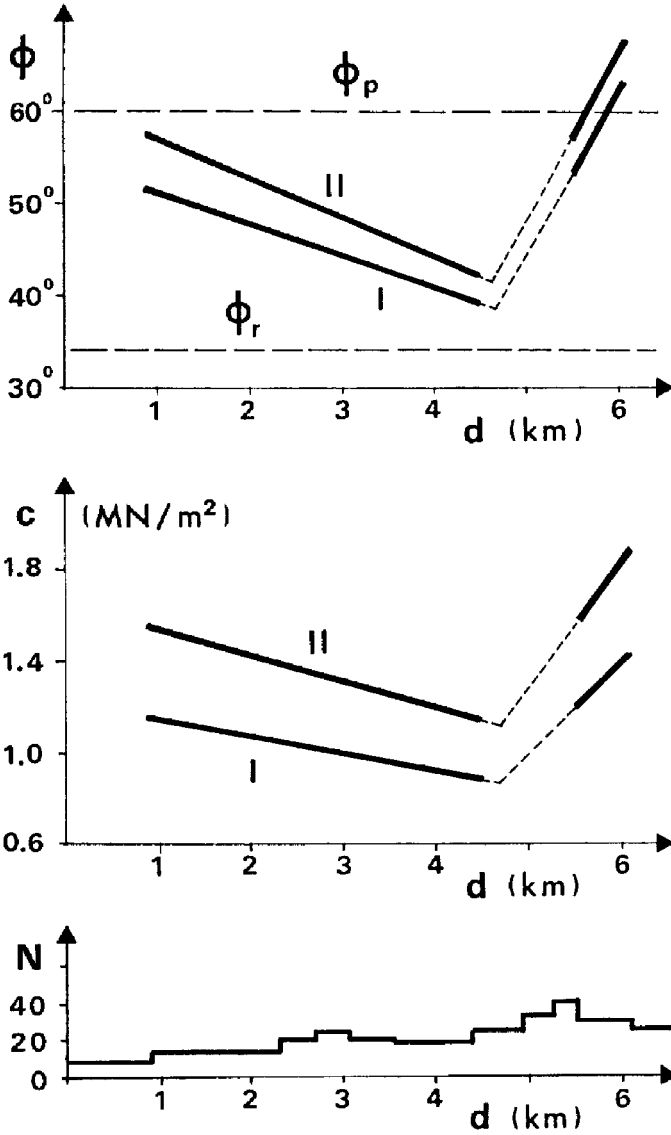


Figure 6.19 Back calculated friction angle ϕ and cohesion c (I: $\alpha=1.5$, II: $\alpha=1.0$), and number N of rock bolts installed per metre of tunnel, vs the distance d from the tunnel entrance (Italian side).

and residual, ϕ_r , values of the friction angle. The dashed parts of the diagrams refer to the zone close to section 6, where no reliable measurements are available.

Table 6.2 Variation of the coefficient of viscosity with the distance from the tunnel entrance (Italian side).

Section	Distance (m)	η (MPa \times day)
3	2772	1000
4	3954	1600
5	4507	1400
7	5533	2200
8	5950	1000
9	6066	2500

These data show a decrease of the shear strength parameters approaching section 6. This may be the cause of the large displacements observed at that section and of the consequent need to reinforce the primary support. In fact, it has been reported in [25] that the average number of 10–20 rock bolts installed per metre of tunnel increased to above 30 (cf. Figure 6.19) when reaching section 6 ($d \cong 5000\text{m}$).

Note that the decrease of the coefficient α from 1.5 to 1.0 leads to an increase in the back calculated shear strength parameters. This can be easily explained by considering that the reduction of α reduces, in turn, the displacements δ_m introduced in the calibration analysis, but does not affect the pressure applied by the rock on the support, which depends on δ^* . Consequently, since the same pressure has to be reached with a lower convergence, the back calculated shear strength parameters tend to increase.

Evaluation of the viscosity coefficient

The second phase of the back analysis was aimed at defining the values of the viscosity coefficient η for the various sections of the tunnel.

The analysis was carried out through the direct approach, by minimising for each section the difference between the displacement vs. time data recorded in the field and the corresponding curve obtained by the visco-plastic finite element model (which, in turn, depends on η).

Here only the results obtained assuming $\alpha=1.5$ are presented. Table 6.2 reports the values of viscosity at the same sections considered also in the first phase of the calibration problem, except for section 2. In fact, this section exhibits a nearly linear elastic behaviour, the value of the time dependent displacement being barely appreciable.

The back calculated viscosity does not show the variation affecting the shear strength parameters; in fact an independent calibration problem was solved for each section, without assuming any a priori relationship between η and d .

It could be observed, however, that the average viscosity for sections 3, 4 and 5 is smaller than that of sections 7, 8 and 9, similar to what happens for the cohesion and friction angle. This seems to indicate that the average rock quality

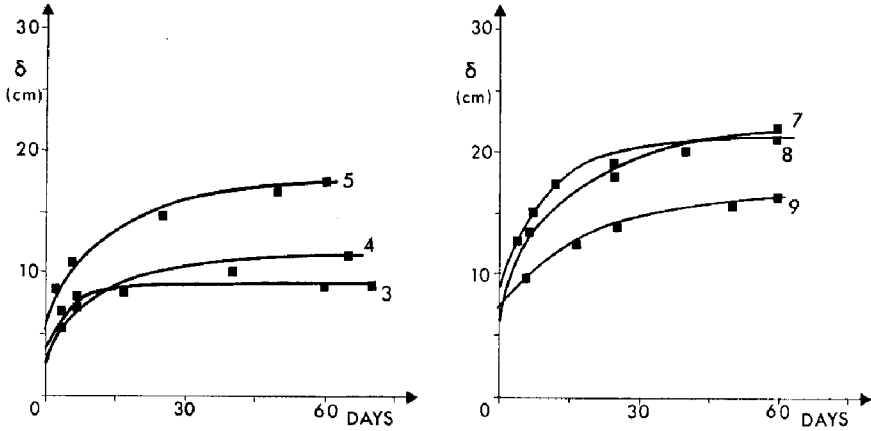


Figure 6.20 Experimental convergence vs time curves (black squares) at different tunnel sections and corresponding numerical results (solid lines) based on the back calculated mechanical parameters ($\alpha=1.5$).

in the first part of the tunnel, before section 6, is slightly poorer than that encountered after section 6.

Finally, the comparison between calculated and measured displacement vs. time data is shown for all sections in Figure 6.20. Here the curves corresponding to the numerical results were obtained by adopting the optimal values of the mechanical parameters of the rock previously evaluated for each section.

Conclusions

Some procedures have been illustrated for the solution of back analysis problems in geotechnical engineering, considering both their deterministic and probabilistic aspects.

These procedures represent a practical tool for reducing the uncertainties that often affect the parameters to be used in the design of complex geotechnical works, in particular when the calculations are based on suitable numerical models.

Once the numerical model able to describe the behaviour of the rock mass has been calibrated, the model itself can be used to foresee the “response” of the soil/rock mass to changes in the construction/excavation procedure, leading to a possible refinement of the design. An example of this “observational” design procedure has been discussed with reference to the excavation of a shallow railroad tunnel.

Nowadays a marked increase is observed in the use of back analysis procedures in geotechnical engineering practice and in the research for new, more efficient, back analysis techniques. This effort concerns, in particular, the use

of complex constitutive models, the extension to dynamic problems and studies oriented to probabilistic approaches.

An attempt in this last direction has been discussed here, with reference to a Bayesian calibration technique, but also other approaches, such as the Kalman filtering technique, appear to be quite promising. In fact, they exploit both the *a priori* knowledge of the problem at hand and the sequential evolution of the experimental information during the excavation/construction works.

Acknowledgements

The examples presented in this paper are part of studies supported by the Ministry of the University and Research of the Italian Government. They are based on the pioneering researches of G.Maier and S.Sakurai on structural and geotechnical back analysis. Their scientific guidance is gratefully acknowledged.

References

- [1] Asaoka A., Matsuo M., An inverse problem approach to the prediction of multi-dimensional consolidation behaviour. *Soils and Foundations*, Vol. 24, No. 1, pp. 49–62, 1984.
- [2] Sakurai S., Shimizu N., Matsumuro K., Evaluation of plastic zone around underground openings by means of displacement measurements. *Proc. 5th Int. Conf. on Numerical Methods in Geomechanics*, Nagoya, 1985.
- [3] Gioda G., Sakurai S., Back analysis procedures for the interpretation of field measurements in geomechanics. *Int. J. Numer. Anal. Methods in Geomechanics*, Vol. 11, pp. 555–583, 1987.
- [4] Ichikawa Y., Ohkami T., A parameter identification procedure as a dual boundary control problem for linear elastic materials. *Soils and Foundations*, Vol. 32, No. 2, pp. 35–44, 1992.
- [5] Gioda G., Indirect identification of the average elastic characteristics of rock masses. *Proc. Int. Conf. on Structural Foundations on Rock*, Sydney, 1980.
- [6] Kavanagh K.T., Clough R.W., Finite element application in the characterisation of elastic solids. *Int. J. Solids and Structures*, Vol. 7, pp. 11–23, 1971.
- [7] Rosenbrock H.H., An automatic method for finding the greatest or least value of a function. *The Computer Journal*, Vol. 3, 1960.
- [8] Powell M.J.D., An efficient method of finding the minimum of a function of several variables without calculating derivatives. *The Computer Journal*, Vol. 7, 1964.
- [9] Cividini A., Jurina G., Gioda G., Some aspects of characterization problems in geomechanics. *Int. J. Rock Mechanics and Mining Sciences*, Vol. 18, pp. 487–503, 1981.
- [10] Asaoka A., Matsuo M., Bayesian approach to inverse problem in consolidation and its application to settlement prediction. *Proc. 3rd Int. Conf. on Numerical Methods in Geomechanics*, Aachen, 1979.
- [11] Isenberg J., Collins J.D., Kavanagh J., Statistical estimation of geotechnical material model parameters from *in situ* test data. *Proc. ASCE Spec. Conf. on Probabilistic Mechanics and Structural Reliability*, Tucson, 1979.

- [12] Murakami A., Hasegawa T., Application of Kalman filtering to inverse problems. *Theoretical and Applied Mechanics*, Vol. 43, pp. 3–14, 1993.
- [13] Gens A., Ledesma A., Alonso E.E., Back analysis using prior information—Application to the staged excavation in rock. *Proc. 6th Int. Conf. on Numerical Methods in Geomechanics*, Innsbruck, pp. 2009–2016, 1988.
- [14] Cividini A., Maier G., Nappi A., Parameter estimation of a static geotechnical model using a Bayes' approach. *Int. J. Rock Mechanics and Mining Sciences*, Vol. 20, pp. 215–226, 1983.
- [15] Cancelli A., Cividini A., An embankment on soft clays with sand drains: numerical characterization of the parameters from *in situ* measurements. *Proc. Int. Conf. on Case Histories in Geotechnical Engineering*, St.Louis, 1984.
- [16] Ceppi G., Maggioni F., De Paoli B., et al., Horizontal jet grouting as a temporary support for the “Monteolimpino 2” tunnel. *Proc. Int. Congress on Progress and Innovation in Tunnelling*, Toronto, 1989.
- [17] Kovari K., Amstad C., Fundamental of deformation measurements. *Proc. Int. Symp. on Field Measurements in Geomechanics*, Zurich, 1983.
- [18] Gioda G., Locatelli L., Back analysis of the measurements performed during the excavation of a shallow tunnel in sand. *Int. J. Numer. Anal. Methods in Geomechanics*, Vol. 23, No. 13, pp. 1407–1426, 1999.
- [19] Sakurai S., Displacement measurements associated with the design of underground openings. *Proc. Int. Symp. on Field Measurements in Geomechanics*, Zurich, pp. 1163–1178, 1983.
- [20] Sakurai S., Shinji M., A monitoring system for the excavation of underground openings based on microcomputers. *Proc. ISRM Symp. on Design and Performance of Underground Excavations*, Cambridge, pp. 471–476, 1984.
- [21] Cording E.J., Hansmire, W.H., Displacements around soft ground tunnels. *Proc. 5th Panamerican Congress SMFE*, Buenos Aires, 1985.
- [22] Wong R.C.K., Kaiser P.K., Performance assessment of tunnels in cohesionless soils. *J. of Geotechnical Engineering, ASCE*, Vol. 117, No. 12, pp. 1880–1901, 1991.
- [23] Cividini A., Gioda G., Finite element analysis of direct shear tests on stiff clays. *Int. J. Numer. Anal. Methods in Geomechanics*, Vol. 16, 1992.
- [24] Barla G., Cravero M., Parametric analysis of the lining of the Frejus motorway tunnel (in Italian). Technical Report, Department of Mining Engineering, Politecnico di Torino, Turin, 1979.
- [25] Lunardi P., Application de la mécanique des roches aux tunnels autoroutiers, exemple des tunnels du Fréjus (côte Italic) et du Gran Sasso. *Revue Française de Géotechnique*, Vol. 12, pp. 5–43, 1980.
- [26] Cividini A., Gioda G., Sterpi D. Application of elasto-plastic analysis to tunnelling. *In Advanced Numerical Applications and Plasticity in Geomechanics* (D.V.Griffiths, G.Gioda eds), CISM Courses and Lectures, Springer-Verlag, Wien, 2001.
- [27] Cividini A., Gioda G., Numerical methods for the analysis of tunnel performance in squeezing rock. *Rock Mechanics and Rock Engineering*, Vol. 29, No. 4, pp. 171–193. 1996.

Chapter 7

Parameter estimation using extended Bayesian method in tunnelling

I.-M.Lee and D.-H.Kim

Abstract

This chapter addresses a parameter estimation technique to be applied in tunnelling. The extended Bayesian method (EBM) is adopted, which can systematically combine field measurements and prior information of underground structures in order to obtain the best estimate of geotechnical parameters. For the EBM, the relative importance of prior information over field measurements is defined by the parameter, β , which is determined from the sensitivity of geotechnical parameters and the uncertainty existing in the prior information and the measurements. In the present study various geotechnical parameters were determined, including the elastic modulus (E), the initial horizontal stress coefficient (K_0), the cohesion (c) and the internal frictional angle (ϕ). The validity of the feedback system proposed herein was demonstrated through an elasto-plastic example problem. The proposed method was applied to an actual tunnel site in Pusan, Korea and has shown to be highly effective in actual field problems.

Introduction

In spite of dramatic developments in underground technology, there are still many uncertainties that exist in the design and construction of underground structures. This is mainly due to the discrepancy between laboratory and *in situ* tests and limitations of site investigation techniques during the design stage. In order to reduce these uncertainties, field instrumentation results obtained during construction are compared with initially estimated ground properties. A feedback system can be used to estimate optimum ground properties by minimizing the difference between predicted and measured ground motions.

The ordinary least squares (OLS) method is widely used, because of its easy application to non-linear geotechnical problems without complex mathematical concepts. However, this method cannot consider prior information in the process of parameter estimation. The Bayesian approach incorporates both prior information and measurement data (Cividini, Maier and Nappi 1983:215). In the

conventional Bayesian approach, the objective function is composed of two components:

$$J(\theta) = J_o(\theta) + J_p(\theta) \quad (7.1)$$

where $J_o(\theta)$ and $J_p(\theta)$ are the observed and predicted objective functions, respectively. A significant drawback of the Bayesian method is the incommensurate matching between the two components, since the objective function is equally divided between them. To overcome this, Neuman and Yakowitz (1979) introduced the adjusting positive scalar β term, which adjusts the weights of $J_o(\theta)$ and $J_p(\theta)$:

$$J(\theta) = J_o(\theta) + \beta J_p(\theta) \quad (7.2)$$

where $J_o(\theta)$ and $J_p(\theta)$ are objective functions of the observed and predicted parameters, respectively. This concept is called the extended Bayesian method or EBM (Honjo, Wen-Tsung and Sakajo 1994:5; Honjo, Wen-Tsung and Guha 1994: 709).

Model identification is the procedure to select the best model describing the problem. Complex models may reduce possible model errors, but may increase uncertainties of parameters, and vice versa. Therefore, the choice of the most appropriate model should be based not only on the accuracy of a model but also on the quantity of available information. A methodology of model identification utilizing the EBM is also proposed herein to identify the geometrical and geotechnical parameters that are the most influential in assessing the ground motions caused by underground excavation. To select the best model in the Bayesian method, the Akaike Information Criterion is proposed (Akaike 1973: 267).

Background of the extended Bayesian method

Model identification

The techniques proposed so far for parameter estimation focus only on the estimation of model parameters for a given model, and they do not provide any information regarding the selection of the most appropriate model among alternative models. To make possible the selection of the best model for the Bayesian approach, the Akaike Information Criterion (AIC) will be introduced (Akaike 1973:267). The AIC for the k th alternative model is expressed as:

$$AIC(x) = (-2) \ln \left\{ f_k \left(x \mid \theta_k(x) \right) \right\} + 2 \dim(\theta_k) \quad (7.3)$$

where x =arbitrary input vector, $f_k(x|\theta_k)$ =probability distribution function of the k th alternative model, and $\dim(\theta_k)$ =number of model parameters for the k th model. The best model among the various alternatives can be identified when the $AIC(x)$ value in Equation (7.3) is minimized.

The posterior distribution of model θ can be expressed as Equation (7.4) in the Bayesian approach:

$$g(\theta|x) = \frac{f(x|\theta)\Pi(\theta)}{\left\{ \int f(x|\theta)\Pi(\theta)d\theta \right\}} \tag{7.4}$$

where θ is a model parameter vector, x is the input data vector, and $\Pi(\theta)$ is a prior distribution of θ . The denominator is independent of θ ; this is simply a normalizing constant required to make $g(\theta|x)$ a proper density function. Therefore, a Bayesian estimator of θ can be obtained by θ value that maximizes Equation (7.5):

$$\max_{\theta} g(\theta|x) = \max_{\theta} f(x|\theta)\Pi(\theta) \tag{7.5}$$

The major problem in employing the Bayesian approach is the selection of an appropriate prior distribution $\Pi(\theta)$. Since this selection is subjective, Akaike (1973) proposed a likelihood function, Equation (7.6):

$$p(x) = \int \Pi_k(\theta)f(x|\theta)d\theta \tag{7.6}$$

where $\Pi_k(\theta)$ is an alternative prior distribution. Sometimes, a family of prior distributions $\Pi_k(\theta|\beta)$ is employed instead of $\Pi_k(\theta)$ to indicate the possible prior distribution, where β is called the ‘hyperparameter’, being generally less than the model parameter θ . To select the best hyperparameter β , the AIC concept is again used as follows:

$$AIC(\beta) = (-2)\ln\{p(x|\beta)\} + 2\dim\beta \tag{7.7a}$$

where

$$p(x|\beta) = \int \Pi(\theta|\beta)f(x|\theta)d\theta \tag{7.7b}$$

The first term in Equation (7.7a) indicates the degree of model fitness to the observed data, and $\dim\beta$ of the second term means the number of model parameters. Equation (7.7a) is called the Bayesian version of the AIC, and it is used to select the most appropriate prior information and model among the various alternative models. Application of Equation (7.7a) to geotechnical parameter estimation will be shown in the later section ‘Parameter estimation’.

Formulation of extended Bayesian method

The observation data vector can be expressed as:

$$u^{*u} = u^k(x|\theta) + \varepsilon^k \tag{7.8}$$

where u^{*u} =field observation data vector at step k , u^k =calculated results vector at k by an employed physical model with a chosen parameter vector, ε^k =error vector assumed to follow $\varepsilon^k \sim N(0, V_u)$, where V_u is an $N \times N$ covariance matrix, x =known input data vector, θ =model parameter vector to be estimated, and N =total number of observation points. Then the observation expressed as a multivariate normal distribution is given by

$$g(u^* | \theta) = (2\pi)^{-NK/2} |V_u|^{-K/2} \times \exp\left\{-\frac{1}{2} \sum_{k=1}^K \{u^{*k} - u^k(x|\theta)\}^T V_u^{-1} \{u^{*k} - u^k(x|\theta)\}\right\} \tag{7.9}$$

where K =total number of measured steps. The prior information vector is assumed as follows:

$$\theta = p + \delta \tag{7.10}$$

where p =prior (initially estimated) mean vector of the model parameter vector θ , δ =uncertainty of the prior information assumed to follow $\delta \sim N(0, V_p / \beta)$ where V_p is an $M \times M$ covariance matrix, β =a scalar adjustment of the magnitude of the uncertainty, and M =number of model parameters. Then the prior distribution, also assumed normal, can be expressed as:

$$f'(\theta | \beta) = (2\pi)^{-M/2} \beta^M |V_p|^{-1/2} \exp\left\{-\frac{1}{2} \beta(\theta - p)^T V_p^{-1} (\theta - p)\right\} \tag{7.11}$$

By the Bayesian theorem, the posterior distribution can be expressed as:

$$\begin{aligned} f''(\theta | u^*, \beta) &\propto f'(\theta | \beta) g(u^* | \theta) \\ &= (2\pi)^{-(NK+M)/2} \beta^M |V_u|^{-K/2} |V_p|^{-1/2} \\ &\times \exp\left\{-\frac{1}{2} \sum_{k=1}^K \{u^{*k} - u^k(x|\theta)\}^T V_u^{-1} \{u^{*k} - u^k(x|\theta)\} - \frac{1}{2} \beta(\theta - p)^T V_p^{-1} (\theta - p)\right\} \end{aligned} \tag{7.12}$$

This equation is conceptually the same as Equation (7.7b). The Bayesian estimator θ is the one that maximizes Equation (7.12) or minimizes the following function with respect to θ :

$$J(\theta | \beta) = \sum_{k=1}^K \{u^{*k} - u^k(x|\theta)\}^T V_u^{-1} \{u^{*k} - u^k(x|\theta)\} + \beta(\theta - p)^T V_p^{-1} (\theta - p) \tag{7.13}$$

where β =a positive scalar adjustment of the relative importance of the observed data to the prior information, p =prior mean of the model parameter θ , and V_p = prior covariance matrix of θ .

The main difference between the EBM and conventional Bayesian analysis is the introduction of the scalar, β . The β parameter can be estimated again by the Bayesian theorem maximizing the following function:

$$L(\beta | u^*, p) = \int f'(\theta | \beta)g(u^* | \theta)d\theta \tag{7.14}$$

u^* can be linearized as

$$u^{*k} \cong \phi^k + S^k\theta + \varepsilon \tag{7.15a}$$

where

$$\phi^k = u^k(\hat{\theta}) - S^k\hat{\theta} \tag{7.15b}$$

$$S^k = \left(\frac{\partial u^k}{\partial \theta^k} \right)_{\theta=\hat{\theta}} \tag{7.15c}$$

By employing Equation (7.14), the log-likelihood function can be obtained as

$$l(\beta | u^*, p) = \ln\{L(\beta | u^*, p)\} \cong -\frac{1}{2}NK \ln\{J_0(\hat{\theta}) + \beta J_p(\hat{\theta})\} + \frac{1}{2} \ln \left\{ \frac{\beta^M |V_p^{-1}|}{\left[\sum_{k=1}^K S^{(k)T} V_u^{-1} S^{(k)} + \beta V_p^{-1} \right]} \right\} + const \tag{7.16}$$

β should be chosen to maximize Equation (7.16). The AIC value can be expressed, for the present study, as

$$AIC = 2 \ln\{L(\beta | u^*, p)\} + 2 \dim \beta \tag{7.17}$$

where $\dim \beta$ is one for the proposed model.

Once we obtain β from Equation (7.16), parameter θ is to be estimated. Either the Gauss-Newton method or a modified Box-Kanemasu iteration method can be used to estimate θ by minimizing Equation (7.13) (Beck and Arnold 1977).

Uncertainty evaluation of model parameters

It is possible to reduce uncertainties by comparing the uncertainty of initially estimated parameters (the prior estimation) with the uncertainty of the estimated

values utilizing the EBM (the posterior estimation). Unfortunately, the posterior distribution is not a simple normal distribution with respect to θ due to the fact that u^k is a non-linear function of θ , which causes the covariance matrix to be non-linear. In order to resolve this problem, with u^k the estimated value, θ is linearized. With the linearized u^k , it is possible to obtain the posterior covariance matrix with the conventional Bayesian theory (Honjo, Wen-Tsung and Guha 1994: 709):

$$\Sigma_p = \left\{ \sum_{k=1}^K (S^k)^T V_u^{-1} S^k + \beta V_p^{-1} \right\}^{-1} \quad (7.18)$$

As shown in Equation (7.18), the covariance matrix of the posterior estimation (Σ_p) is composed of the prior estimation (V_p) and the covariance matrix of measurements (V_u). It is interesting to observe that when the first term in Equation (7.18) is added to the second term, it reduces the variance of the posterior estimation since the covariance matrix of measurements is added to the prior estimation in inverse matrix form.

Numerical method for back analysis

For problems involving geometries, external loadings, and engineering properties, it is generally not possible to obtain an analytical solution. Hence, we need to rely on numerical methods, such as the finite element method, to predict the ground motion caused by underground excavation. For the finite element program, we can either use conventional software or write our own program. The existing elastoplastic finite element program, developed by Owen and Hinton (1980), was modified by the authors to simulate a tunnel excavation and support system. The Mohr-Coulomb failure criterion was used to represent the plastic behavior.

Framework of the feedback system

General

This section introduces the implementation of the extended Bayesian method, combined with the finite element method, for parameter estimation in underground structures. The procedure for the proposed feedback analysis technique is summarized as a flowchart in [Figure 7.1](#).

The initially estimated values of ground parameters (the prior information) as well as measured data are utilized for the feedback analysis. Geotechnical parameters to be estimated in the current analysis are chosen and formulated statistically. *In situ* measured values also have observation errors and may contain bias terms due to initial ground movement that occurred before the

installation of the measurement system. The method to estimate the unbiased values from observed data will be discussed in the section ‘Treatment of measured displacements’.

Selection of model parameters

Ground motion in underground structures depends on geotechnical parameters such as elastic modulus (E), initial horizontal stress coefficient (K_0), mass density (γ), Poisson’s ratio (ν), cohesion (c), and internal friction angle (ϕ). This is the case where the Mohr-Coulomb criterion is used as a failure criterion. If the Hoek-Brown criterion is used, strength parameters c and ϕ should be replaced by m and s (Hoek and Brown 1980).

Assuming the mass density and Poisson’s ratio constant and adopting the Mohr-Coulomb model, the model parameter vector $\hat{\theta}$ and mean vector p are expressed as follows:

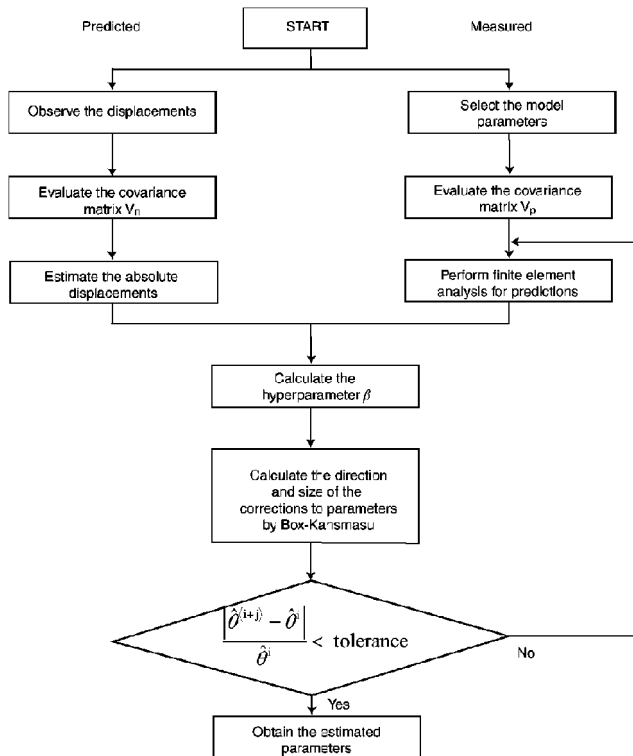


Figure 7.1 Framework for the feedback system.

$$\hat{\theta} = \begin{Bmatrix} \hat{E} \\ \hat{K}_o \\ \tan \hat{\phi} \\ \hat{c} \end{Bmatrix} \tag{7.19}$$

$$p = \begin{Bmatrix} \bar{E} \\ \bar{K}_o \\ \tan \phi \\ \bar{c} \end{Bmatrix} \tag{7.20}$$

where a bar over a symbol indicates the mean of the model parameters. Assuming there are no correlations among the parameters, the covariance matrix is expressed as:

$$V_p = \begin{bmatrix} \text{Var}(E) & 0 & 0 & 0 \\ 0 & \text{Var}(k_o) & 0 & 0 \\ 0 & 0 & \text{Var}(\tan \phi) & 0 \\ 0 & 0 & 0 & \text{Var}(c) \end{bmatrix} \tag{7.21}$$

where $\text{Var}(\cdot)$ is the variance of (\cdot) .

If the ground motion due to underground excavation is more or less elastic, the number of parameters is reduced to two as follows:

$$\hat{\theta} = \begin{Bmatrix} \hat{E} \\ \hat{K}_o \end{Bmatrix} \tag{7.22}$$

$$p = \begin{Bmatrix} \bar{E} \\ \bar{K}_o \end{Bmatrix} \tag{7.23}$$

and

$$V_p = \begin{bmatrix} \text{Var}(E) & 0 \\ 0 & \text{Var}(K_o) \end{bmatrix} \tag{7.24}$$

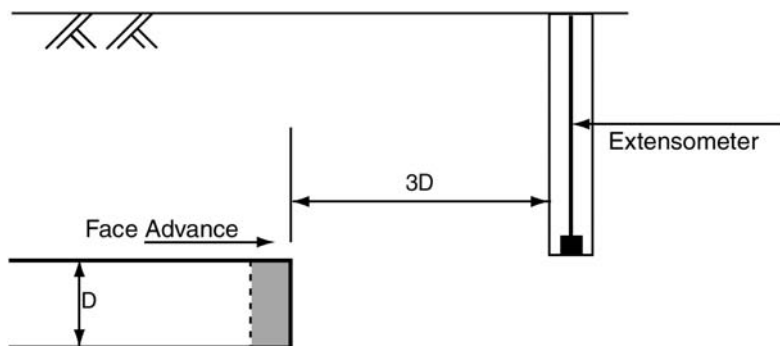


Figure 7.2 Measurement of displacement by extensometer from ground surface.

Treatment of measured displacements

As displacements measured from borehole extensometers and convergence are more reliable than stresses (Sakurai 1983:1163), observed displacements are mainly used in this study. If the overburden height of the underground opening is less than 60 m, extensometers can be installed from the ground surface using groutable anchors and mechanical transducers as shown in Figure 7.2 (Dunncliff 1988). The displacements measured by these schemes appear to be reliable. However, convergence is generally measured inside the tunnel because of its simplicity; the measured convergence inside the tunnel is only a part of the total deformation. To estimate the absolute displacement, mathematical analyses should be performed using an appropriate characteristic line of deformation.

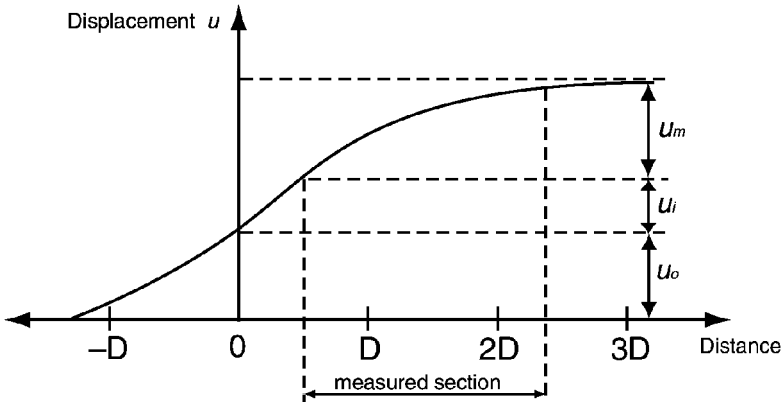
It is known that ground movement begins to take place about one to three tunnel diameters ahead of a tunnel face, and is completed when the tunnel face advances to a distance of about three diameters of the tunnel (Lo, Lukajic and Ogawa 1984:128). The characteristic line of deformation due to face advance is presented in Figure 7.3.

As shown in Figure 7.3, the absolute displacement is the sum of three components: deformation ahead of the face (u_0), missed deformation behind the face (u_i), and measured deformation (u_m). Therefore, to obtain an unbiased (absolute) deformation, u_i and u_0 must be estimated. To estimate u_i , a characteristic line is assumed based on the measured convergence shape, and by the extrapolation technique (Gerald and Wheatley 1994). The deformation occurring ahead of the tunnel face (u_0) can be obtained empirically or numerically. It is known that u_0 constitutes about 30 percent of the absolute displacement (Hanafy and Emery 1980:119; Panet and Guenot 1982:197). However, this value might be mostly applicable to hard rock conditions. Three-dimensional finite difference analysis was performed and compared with the two-dimensional analysis to obtain the ratios in three typical ground conditions (Lee, Kim, Choi and Choi 1996:87): weathered rock, soft rock, and hard rock. The

ratios of the tunnel deformation ahead of the face to the absolute deformation are shown in Table 7.1. In summary, the unbiased (absolute) displacement is estimated by using Table 7.1 for u_o and by using an extrapolation technique for u_i .

Table 7.1 Ratio of the deformation ahead of the tunnel face to the absolute deformation

Ground condition	Ratio (%)
Weathered rock	45
Soft rock	30
Hard rock	20



- D : Tunnel diameter
- u_o : Deformation occurring ahead of the face
- u_i : Missed deformation behind the face
- u_m : Measured deformation

Figure 7.3 Characteristic line of deformation.

Evaluation of the proposed scheme

Data preparation

A comprehensive evaluation of the proposed feedback system was carried out for the elasto-plastic case in a hypothetical site. The geological condition of the site is presented in Figure 7.4, and the tunnel is assumed to be located in the residual soil layer. The typical cross-section of the tunnel is a horseshoe shape having a diameter of 10 m, and the primary support system consisting of 10 cm thick soft shotcrete. Typical values of the geotechnical parameters are considered as the initial estimated geotechnical parameters (prior information) for this case.

Since the site is hypothetical, the observed data are calculated using the finite difference method code, FLAC-2D. The measurement points and displacements are summarized in Figure 7.5 and Table 7.2.

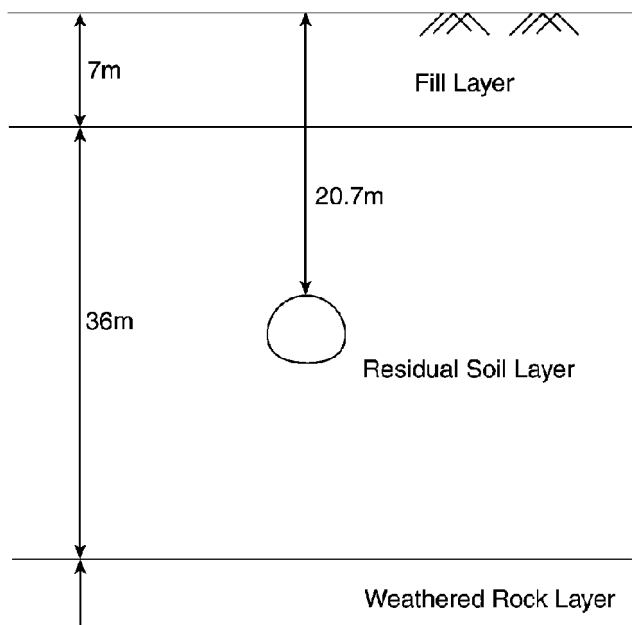


Figure 7.4 Geological condition of the hypothetical site.

Sensitivity analysis

Sensitivity analysis is carried out to check the change in the ground response due to perturbation in the parameters. Figures 7.6–7.8 show the results of the sensitivity analysis. During the sensitivity analysis for a chosen parameter, the other parameters are fixed with initially estimated values. These figures show that the ground motion depends on the elastic modulus and the initial horizontal stress coefficient during elastic behavior. If plastic deformation occurs, the elastic modulus and the internal

Table 7.2 Measurement points and displacements

No.	Distance from tunnel centre (m)	Measured (assumed) displacements (mm)
1	4.5	74.5
2	5.5	66.3
3	6.5	59.6
4	7.5	54.5
5	8.5	50.4
6	4.55	30.8
7	5.7	13.5
8	6.7	4.6
9	7.7	2.0
10	8.7	0.9

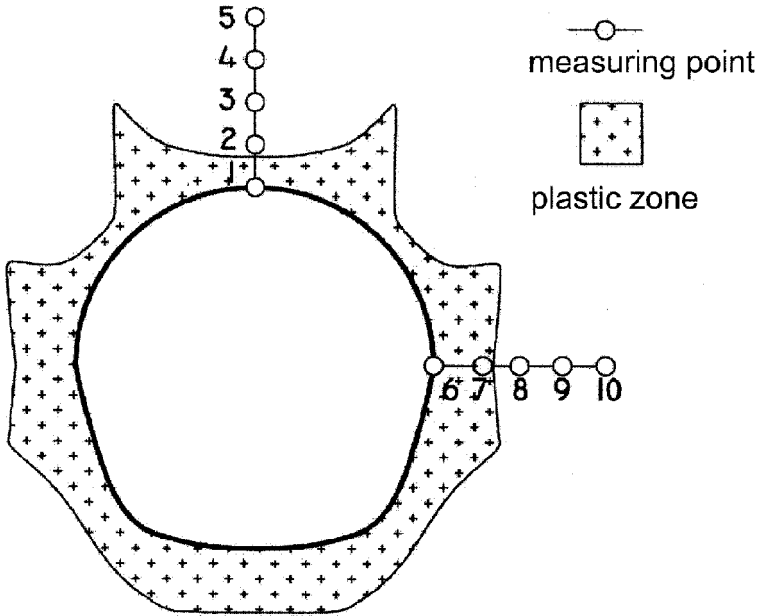


Figure 7.5 Location of measurement points.

friction angle will be major influencing factors on ground motion. It has also been concluded that the ground motion is insignificantly affected by cohesion.

Parameter estimation

As shown in [Figure 7.5](#), plastic deformation occurs around the tunnel. Therefore, four parameters must be estimated: the cohesion, the internal friction angle, the elastic modulus, and the initial horizontal stress coefficient. Since the tunnel crown is located within the residual soil layer, only the parameters for the residual soil layer are assessed. The coefficient of variation of model parameters is assumed to be 0.3 considering that large uncertainties are encountered.

In order to check the effect of the number of measurement points in the feedback system, they are varied during the analysis. The results of the analysis are listed in [Table 7.3](#) and the prior estimates are also tabulated for comparison. [Table 7.3](#) shows that at least six measurement points must be installed to obtain a reliable estimation.

Case study

The application of the proposed method is extended to a subway tunnel in Pusan, Korea, to illustrate the applicability of the EBM beyond parameter estimation. Applications in this chapter concentrate on the following. First, in order to

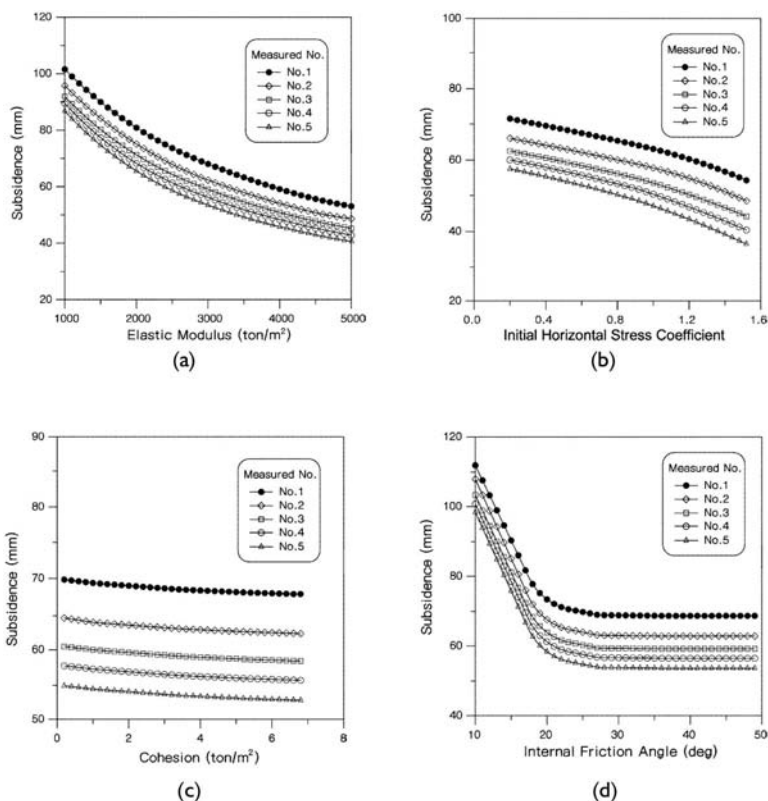


Figure 7.6 Sensitivity of geotechnical parameters on crown settlement (a) Elastic modulus; (b) Initial horizontal stress coefficient; (c) Cohesion; (d) Internal friction angle.

Table 7.3 Optimized parameters with changes in the number of measurement points

Number of measurement points	E (t/m^2)	K_0	c (t/m^2)	ϕ (deg)
Assumed values	3,000	0.50	3.00	30.0
2	3,182.1	0.51	3.00	31.5
4	3,008.8	0.52	3.01	26.2
6	3,013.9	0.47	3.02	27.6
8	3,013.7	0.46	3.01	27.6
10	3,013.6	0.46	3.02	28.0

determine the most influential geotechnical parameters, the model identification process is performed by the Akaike Information Criterion. Then the parameter estimation process is performed for all the models. Lastly, the reduction of uncertainties by utilizing the EBM is assessed so that the proposed methodology is proved to be a means of systematic consideration of uncertainties.

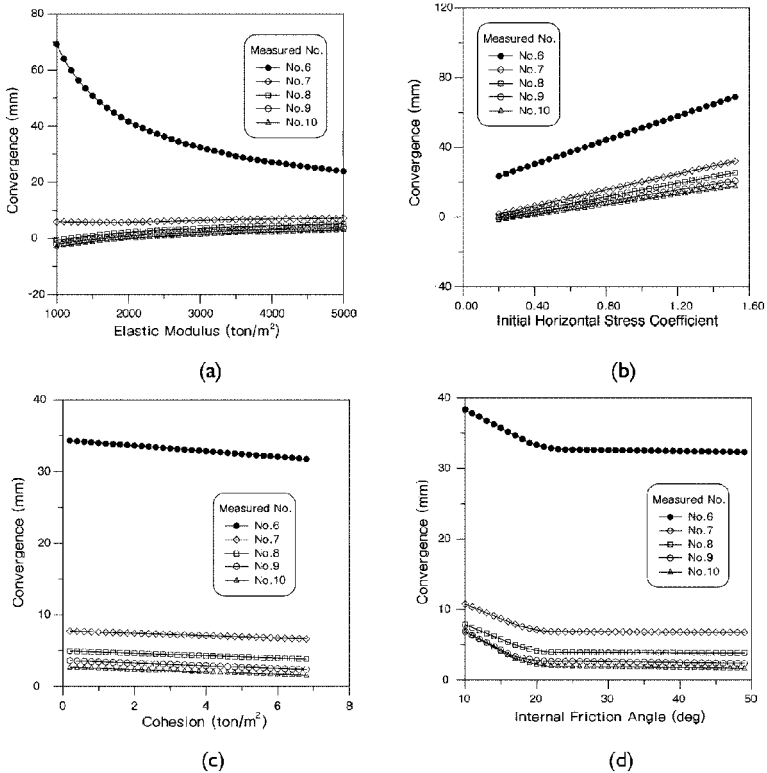


Figure 7.7 Sensitivity of geotechnical parameters on sidewall settlement (a) Elastic modulus; (b) Initial horizontal stress coefficient; (c) Cohesion; (d) Internal friction angle.

Ground condition

The ground at the site consists of a fill layer (cohesionless soil), residual soil and highly weathered rock from the ground surface, as shown in Figure 7.9. Below the overburden, it is composed of Bulkuksa granite. The tunnel was constructed through the highly weathered rock, which is classified as ‘poor rock’ with a rock mass rating (RMR) description. A typical cross-section of the tunnel is shown in Figure 7.10.

Measurement

The crown subsidence and sidewall convergence measured by tape extensometers are used as the observed data. The location of measurement points is shown in Figure 7.11. The characteristic lines are obtained from the extrapolation of the measured data. Figure 7.12 and Table 7.4 show obtained characteristic lines and absolute displacements. In this case, the ratio of deformation which occurred ahead of the tunnel face was 45 percent of the

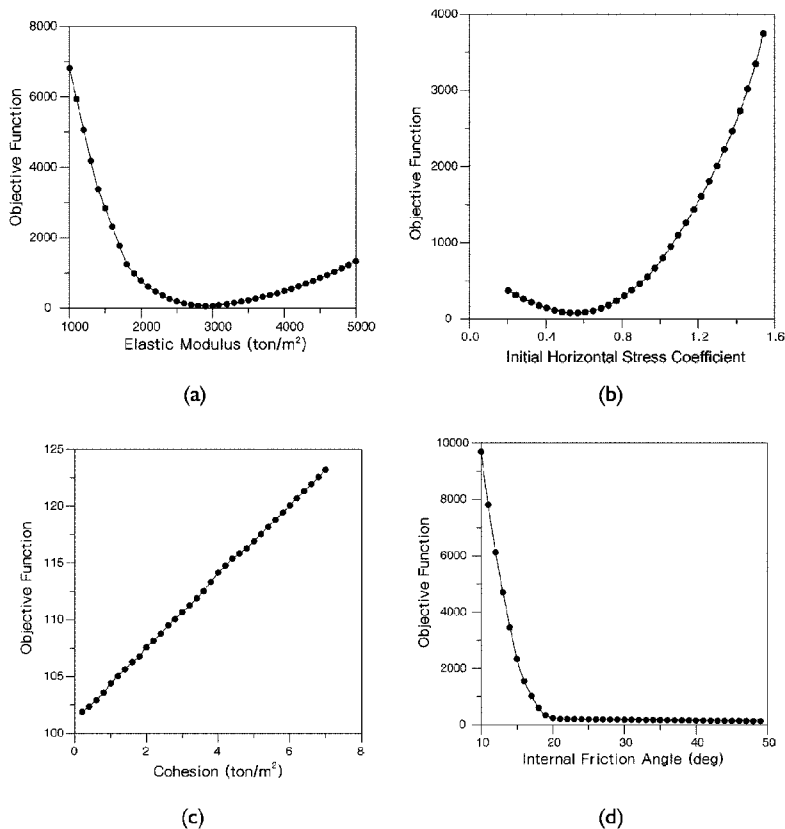


Figure 7.8 Variation of objective function by the variation of the geotechnical parameters (a) Elastic modulus; (b) Initial horizontal stress coefficient; (c) Cohesion; (d) Internal friction angle.

absolute displacements, as shown in Table 7.1. Two stations located within close proximity are chosen for the tunnel convergence measurements; however, for the application of the EBM, the two stations are combined by endowing each section with time steps 1 and 2.

Selection of model parameters

The zone in which the ground shows plastic deformation due to tunnel excavation is assessed by comparing the stress obtained from the elastic finite element calculation and the strength obtained from the Hoek-Brown model. As shown in Figure 7.13, the ground motion is almost elastic except at the invert corner zones. Therefore, elastic analysis appears appropriate for this site.

Since the residual soil of granite origin is mostly cohesionless, it is almost impossible to obtain undisturbed samples with typical sampling techniques. The

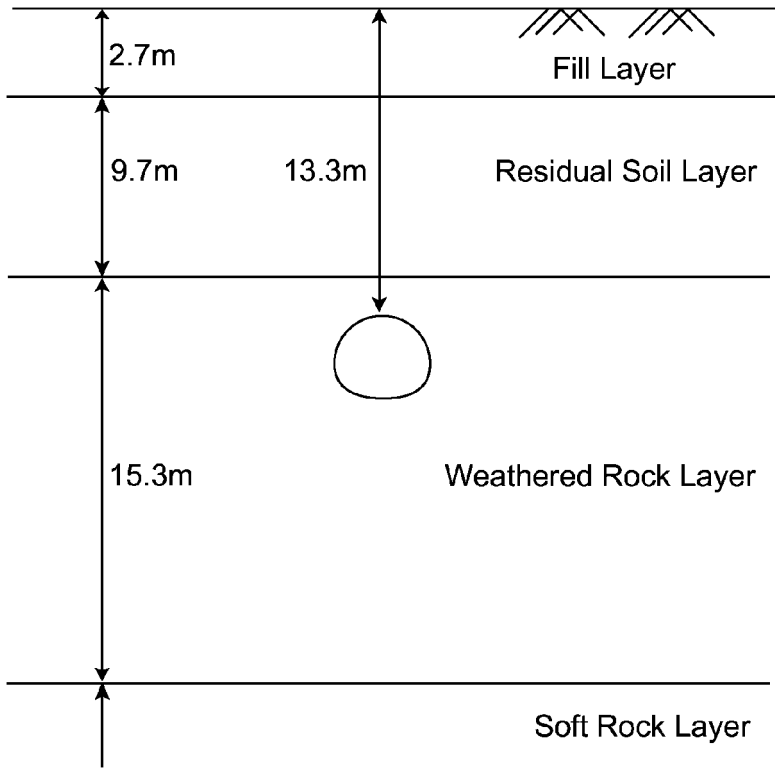


Figure 7.9 Idealized ground condition of a subway tunnel in Pusan, Korea.

elastic modulus and strength parameters can be empirically estimated from correlations with standard penetration test (SPT) N -values. Estimation of the K_0 value is even more difficult. Therefore, some typical values using Figure 7.9 are used as the prior information in this case study. The coefficient of variation of the SPT N -value is about 0.26 (Harr 1987). The coefficient of variation of E and K_0 is selected as 0.3, including uncertainty of the SPT N -value.

Model identification

In order to assess the best model, three models are introduced. Model I-1 is adopted directly from site investigation (see Figure 7.9). Since the elastic modulus of the residual soil selected in model I-1 seems too small, model I-2 adopts a larger elastic modulus for the residual soil layer. The estimated elastic modulus of the granite soil for model I-2 was about $10,000 \text{ ton/m}^2$, which was obtained from triaxial tests conducted by Kim (1994). In model II, residual soils and weathered rocks are considered as a single 'weathered zone'.

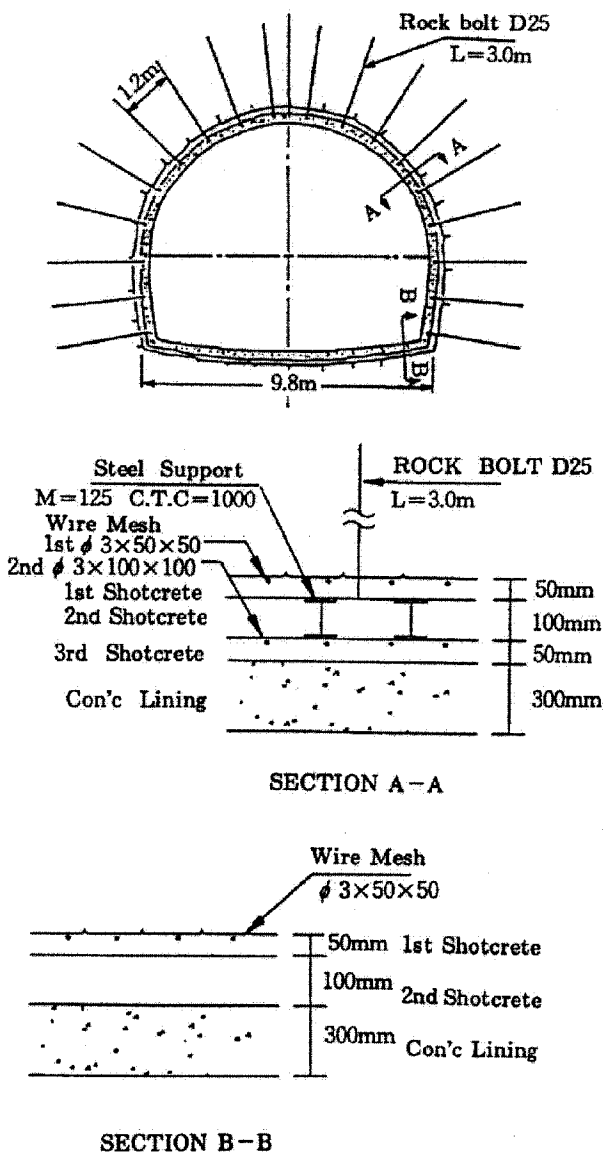


Figure 7.10 Typical tunnel cross section.

The measurement error, V_u might then be significant by field conditions; however, since the relative magnitude of V_u to V_p can be adjusted by applying β , V_u

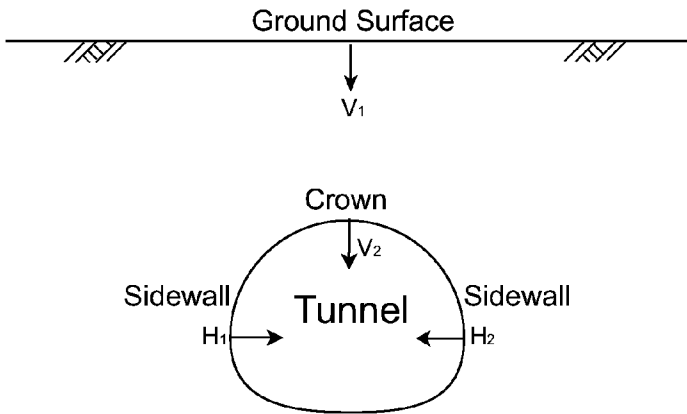


Figure 7.11 Location of measurement points.

Table 7.4 Results of regression

Location	Functions	Displacements from regression analysis (mm)	Absolute displacements ^a (mm)	
Station I	Sidewall	$u(x)=2.593(1-e^{-0.096x})$	3.56	6.47
	Crown	$u(x)=7.316(1-e^{-0.126x})$	7.38	13.42
	Surface	—	3.41	6.20
Station II	Sidewall	$u(x)=2.833(1-e^{-0.165x})$	3.48	6.32
	Crown	$u(x)=2.593(1-e^{-0.122x})$	7.77	14.12
	Surface	—	3.41	6.20

Note

^a Absolute displacement is the sum of the displacement occurring ahead of the tunnel face and the displacement from regression analysis.

is assumed to be a unit matrix for the comparison of model I-1, model I-2 and model II by the AIC (shown in Figure 7.14). It is found from Figure 7.14 that model I-1 gives the maximum AIC among the three models, and model II also looks small, even though slightly larger than model I-2.

Parameter estimation

Using the β values obtained in the previous stage, the optimized parameters are obtained. As shown in Table 7.5, the objective functions of model I-2 and model II are quite small compared with the function of model I-1.

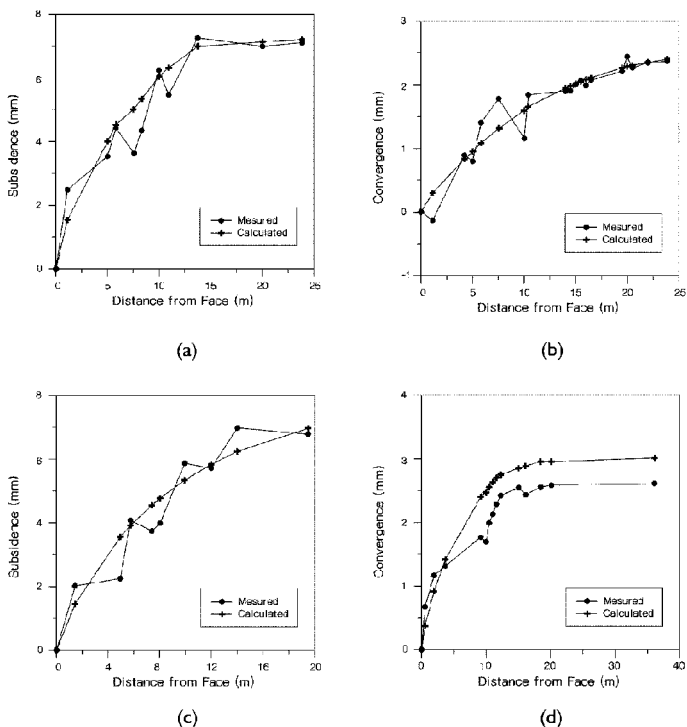


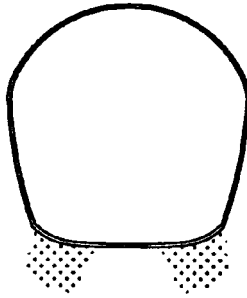
Figure 7.12 Characteristic lines (a) Crown (Station I); (b) Side wall (Station I); (c) Crown (Station II); (d) Side wall (Station II).

Table 7.5 Results of parameter estimation

	Ground condition	Elastic modulus (t/m ²)		Initial horizontal stress coefficient		Objective function
		Prior information	Optimized value	Prior information	Optimized value	
Model I-1	R.S.	3,000	4,610	0.50	0.49	28.69
	W.R.	20,000	22,630	0.50	0.50	
Model I-2	R.S.	10,000	11,990	0.50	0.50	0.26
	W.R.	20,000	19,620	0.50	0.505	
Model II	W.Z. ^a	20,000	18,990	0.50	0.49	0.76

Uncertainty evaluation

The error ratio of mechanical instrumentation is generally within ± 4 percent (Hanna 1985). However, gross errors may include reading errors, computational errors, incorrect installation, missed installation time, etc. Therefore, it is likely



■ Plastic Zone

Figure 7.13 Plastic zone assessed by Hoek-Brown's criterion.

Note

^a W.Z. weathered zone.

to be a larger value in the field. Measurement errors of 4, 20 and 30 percent are considered in this study to evaluate the influence of measurement accuracy on the magnitude of uncertainty. Table 7.6 shows the reduction of uncertainties from prior to posterior with the variation of measurement errors in model I-2. The elastic modulus of the weathered rock layer is more sensitive to the changing of measurement accuracy.

Concluding remarks

Introduced in this chapter is a new feedback system in which field measurements and prior information are systematically combined together. The extended Bayesian method (EBM) was adopted for the feedback analysis. The main advantage of the extended Bayesian method is the introduction of the hyperparameter β which is influenced by the sensitivity of the parameters and uncertainties existing in both the prior information and the measurement. A small value of β implies that the measurement possesses more weight than the initially estimated information, and vice versa. Therefore, by observing the value of β , the relative importance of feedback analysis can be easily seen.

References

- Akaike, H., 'Information Theory and an Extension of the Maximum Likelihood Principle', *Second International Symposium on Information Theory*, 1973, pp. 267-281.
- Beck, J.V. and Arnold, K.J., *Parameter Estimation in Engineering and Science*, New York, John Wiley & Sons, 1977.
- Cividini, A., Maier, G., and Nappi, A., 'Parameter Estimation of a Static Geotechnical Model Using a Bayes's Approach', *Int. J. Rock Mech. Min. Sci. & Geomech. Abstr.*, 1983, vol. 20, pp. 215-226.

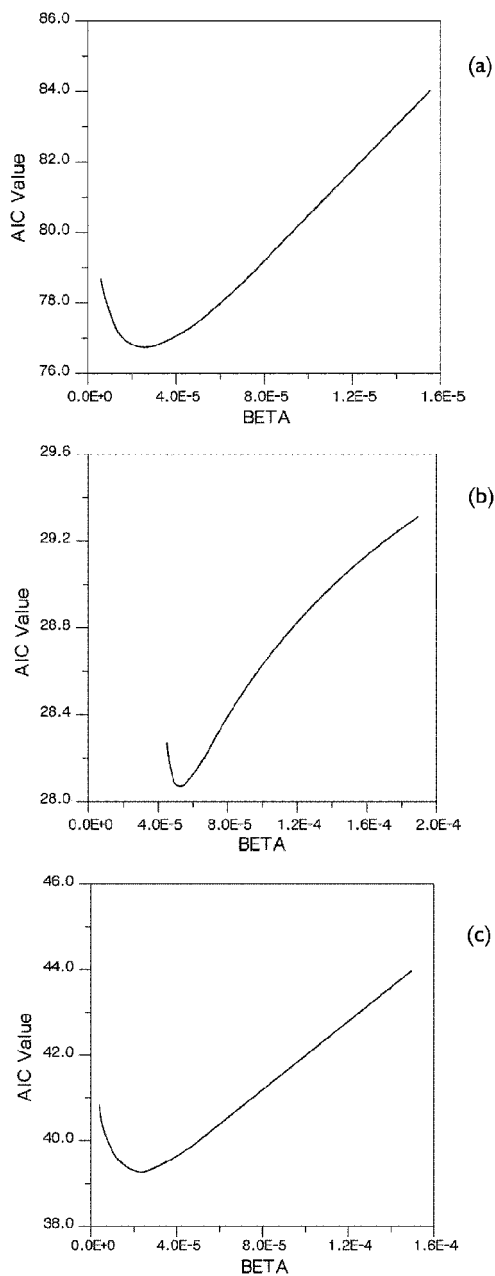


Figure 7.14 The hyperparameter β vs AIC value in each model (a) Model I-1; (b) Model I-2; (c) Model II.

Table 7.6 Coefficient of variation of geotechnical parameters

		Ω (E)		Ω (K_p)	
		R.S.	W.R.	R.S.	W.R.
<i>Prior error</i>		0.3	0.3	0.3	0.3
Posterior error	Measurement error $\Omega = 0.3^a$	0.26	0.24	0.30	0.29
	Measurement error $\Omega = 0.2$	0.22	0.19	0.25	0.25
	Measurement error $\Omega = 0.04$	0.05	0.05	0.06	0.06

Note

^a $\Omega(\cdot)$: coefficient of variation.

Dunnicliff, J., *Geotechnical Instrumentation for Monitoring Field Performance*, New York, John Wiley & Sons, 1988.

Gerald, F.C. and Wheatley, *Applied Numerical Analysis*, Addison-Wesley, 1994.

Hanafy, F.A. and Emery, J.J., 'Advancing Face Simulation of Tunnel Excavations and Lining Placement', *13th Canadian Rock Mechanics Symposium*, CIMM, Montreal, 1980, pp. 119–125.

Hanna, T.H., *Field Instrumentation in Geotechnical Engineering*, Trance Tech Publication, 1985.

Harr, M.E., *Reliability-Based Design in Civil Engineering*, New York, McGraw-Hill, 1987.

Hoek, E. and Brown, E.T., *Underground Excavation in Rock*, London, Institution of Mining & Metallurgy, 1980.

Honjo, Y., Wen-Tsung, L. and Guha, S., 'Inverse Analysis of an Embankment on Soft Clay by Extended Bayesian method', *Int. J. Numer. Anal. Methods Geomech.*, 1994, vol. 18, pp. 709–734.

Honjo, Y., Wen-Tsung, L. and Sakajo, S., 'Application of Akaike Information Criterion Statistics to Geotechnical Inverse Analysis: the Extended Bayesian Method', *Structural Safety*, 1994, vol. 14, pp. 5–29.

Kim, Y.J., *Constitutive Characteristics of Decomposed Korean Granites*, Thesis, Department of Civil Engineering, Korea University, 1994.

Lee, I.M., Kim, D.H., Choi, H.S. and Choi S.I., 'The 3-Dimensional Tunnel Analysis Considering Stress Concentration; Load-Distribution Ratio', *Journal of Korean Geotech. Soc.*, 1996, vol. 12, no. 1, pp. 87–108.

Lo, K.Y., Lukajic, B., and Ogawa, T., 'Interpretation of Stress-Displacement Measurements', *Proceedings of Two Sessions at Geotech '84*, ASCE, 1984, pp. 128–155.

Neuman, S.P. and Yakowitz, S., 'A Statistical Approach to the Inverse Problem of Aquifer Hydrology-1. Theory', *Water Resources Research*, 1979, vol. 15, no. 4, pp. 845–860.

Owen, D.R.J. and Hinton, E., *Finite Elements in Plasticity: Theory and Practice*, Swansea, Pineridge Press, 1980.

Panet, M. and Guenot, A., 'Analysis of Convergence Behind the Face of a Tunnel', *Tunnelling 82*, IMM, Brighton, 1982, pp. 197–204.

Sakurai, S., 'Displacement Measurements Associated with the Design of Underground Openings', *Proc. International Symposium on Field Measurements in Geomechanics*, Zurich, 1983, pp. 1163–1178.

Chapter 8

Seismic microzoning using numerical modelling

The Umbria-Marche earthquake of 26 September 1997

F.Pergalani, V.Petrini, A.Pugliese and T.Sanò

Introduction

After the Umbria-Marche (Central Italy) Ms 5.9 earthquake of 26 September 1997 the Italian Government decided that the amplification due to local effects had to be taken into account in repair and reconstruction. The area to be analysed was quite large, including about 1000 villages, and the analysis had to be completed in about six months to avoid excessive delay in the starting of reconstruction; the available budget was also limited to about 1,550,000 euros.

A working group, formed by researchers of the Servizio Sismico Nazionale (SSN) and the Istituto di Ricerca sul Rischio Sismico-Consiglio Nazionale delle Ricerche (IRRS-CNR), was charged to define a procedure able to give reliable results under the above-mentioned constraints. The working group was also charged with guiding the activity.

Therefore the working group decided to proceed in two phases. In the first phase the researchers of the working group performed the following steps:

- 1 Selection of 60 sample villages: the criterion was to select those showing the highest degree of damage and representative of the main geologic and geomorphologic features of the area struck by the earthquake, in view of the extrapolation of the results to the entire area;
- 2 Collection of the basic geologic, geomorphologic and geotechnic data;
- 3 Field surveys, which implied a geologic and geomorphologic survey at a detailed scale (1:5000);
- 4 Definition of the seismic input for the numerical analysis;
- 5 Computation of site amplifications through one-dimensional and two-dimensional soil modelling, by finite and boundary element methods.

As a result a set of standard local effect situations and a table giving the values of the amplification factors for each situation were defined.

In the second phase, a group of geologists expert in the area extended the field surveys, again applying the geologic and geomorphologic survey at 1:5000

scale, to all the villages and gave to each local situation a value of the amplification factor on the basis of the table defined at the end of the first phase.

It is worth noting that the feeling of mutual support in an emergency was the main reason for the positive results of the process.

Considerable work was done on site effect analysis: some researchers used experimental approaches, others developed numerical codes for the evaluation of the amplification. In the field of experimental approaches both strong events, and microtremors and small events were used and numerical methods are available for 1D, 2D and 3D analysis. In this particular case, experimental approaches were discarded for reasons of both time and cost, as explained above. The choice of 1D and 2D techniques derives from the quantity and quality of input data available and the need for fast computation in order to fulfil the time requirement previously mentioned.

The Umbria Region is now applying a similar procedure in the areas that have not been affected by the earthquake, as a support for urban planning in the frame of prevention policies.

The seismic input

The area affected by the earthquake sequence of September 1997 is located in a region with several dissected seismic structures, still not very well known and identified as defined seismic sources. Therefore, it being impossible to separate the seismic hazard contribution coming from all the possible sources to each village, the cumulative contribution, on a probabilistic basis, was derived from all relevant neighbouring seismogenetic areas. The probabilistic approach also fits with the aim of the project, that is, the evaluation of a set of parameters to be entered in code for building restoration and new building design.

Calculations were made treating seismic source zones as areas of uniformly distributed seismicity following a Poisson process. According to Cornell's (1968) methodology the expected ground motion values, for a 10% probability of exceedence within a reference time period of 50 years, were computed.

The hazard analysis results are summarized through uniform hazard response spectra and an equivalent set of time-histories suitable for microzoning study.

Hazard analysis

The seismic hazard calculation is an application of the total-probability theorem (Harr, 1987) and it is usually presented in the following form:

$$P(A > a, t) \cong \sum_i v_i t \int \int_{M R} p[A > a | m, r] f_{R_i|M_i}(r | m) f_{M_i}(m) dr dm \quad (8.1)$$

where P is the probability that a ground-motion amplitude A is greater than a in time t ; f_M denotes the probability density function of the magnitude distribution;

f_R denotes the probability density function of the source to site distance; and the summation of the activity rates ν_i extends over all the seismic sources.

In particular, for a Poisson process, the exceedence probability that a ground motion amplitude A is greater than a in time t is given by:

$$P[A > a, t] = 1 - e^{-\lambda t} \quad (8.2)$$

where λ is the yearly frequency of exceedence of the ground motion amplitude A .

The hazard analyses were carried out with the following assumptions:

- The activity rate at each magnitude corresponds to the 50th percentile of the frequency-magnitude relationship;
- Strong ground motion uncertainties resulting from the attenuation relationships of Sabetta and Pugliese (1996) were taken into account;
- A threshold magnitude of 4.7 was adopted, to avoid a misleading contribution to the seismic hazard coming from the integration in equation (8.1) of small magnitudes of little engineering interest (McCann and Reed, 1989);
- In each seismic source zone the maximum magnitude coincides with the maximum historical magnitude.

Seismic sources

The current Italian seismotectonic model is constituted of 80 seismic source zones (Figure 8.1) based on a kinematic model of the most recent tectonic units (Scandone *et al.*, 1990; Patacca *et al.*, 1993; Scandone *et al.*, 1996).

The zones belong to nine main seismotectonic domains and one volcano-tectonic domain (Figure 8.2). The mountainous Alpine arc (domain 1) is characterized by a prevalently compressive regime, with thrust or reverse faults, and secondary strike-slip faults. In north-eastern Italy this domain represents the compressive margin between the Adriatic micro-plate and the Eurasian plate (Albarello *et al.*, 1995). The northern Apennines are divided into domains elongated parallel to the chain (Lavecchia *et al.*, 1994). On the western side (domain 5—zones 27, 31, 41, 42, 49) prevails a rifting regime with a moderate seismicity along normal faults. The eastern side of the chain (domain 3—zones 30, 35, 38, 39, 48, 53) is representative of a compressive regime due to the residual inflection of the Adriatic micro-plate going under the Apennine chain (roll-back mechanism; Scandone, 1996). The resulting fault mechanisms are both compressive along the front of the Apennine chain over-thrusting the Adriatic micro-plate and normal to transcurrent along the flexural inflection of the plate itself. Along the chain axis (domain 4— zones 28, 29, 32, 33, 34, 36, 37, 44, 45, 46, 47, 50, 51, 52; domain 6—zones 58, 62, 63, 64 and domain 7—zones 66, 67, 69, 70, 71, 72) the uplift prevails, reaching maximum rates in the southern Apennines (Cinque *et al.*, 1993; Moretti *et al.*, 1994). Focal mechanisms are

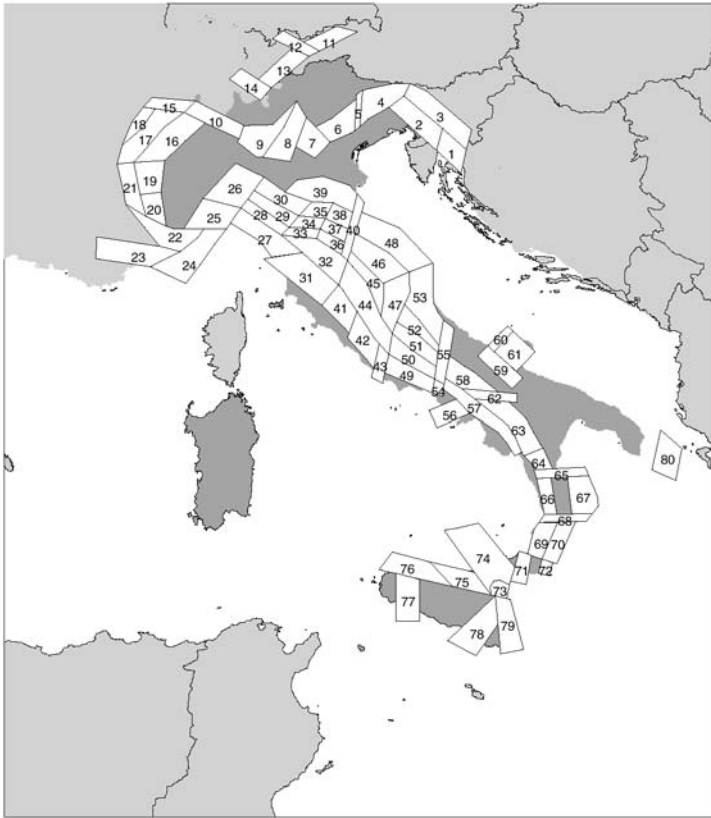


Figure 8.1 Italian seismotectonic model identified by 80 seismic source zones (Scandone *et al.*, 1996).

governed by normal faults. Along all the Apennines some “transfer” zones (domain 2—zones 25, 26, 40, 43, 54), transverse to the chain elongation, interrupt the continuity of the chain structure, with a regime of prevalently transcurrent faults. One of the most important is the “Ortona Roccamonfina” lineament (zone 55), that represents the southern boundary of domain 3 (Patacca *et al.*, 1992). In the northern Sicily (domain 8—zones 74, 75, 76; Albarello *et al.*, 1993) strike-slip fault mechanisms prevail. The foreland domain (9—zones 59, 60, 61, 77, 78, 79, 80) is easily recognizable from the Adriatic sea to the Ionian sea and in Sicily it is characterized by dip-slip and strike-slip mechanisms. The Vesuvius and Etna volcanic areas (domain 10—zones 56, 73) are characterized by high activity rates and low to moderate magnitudes.

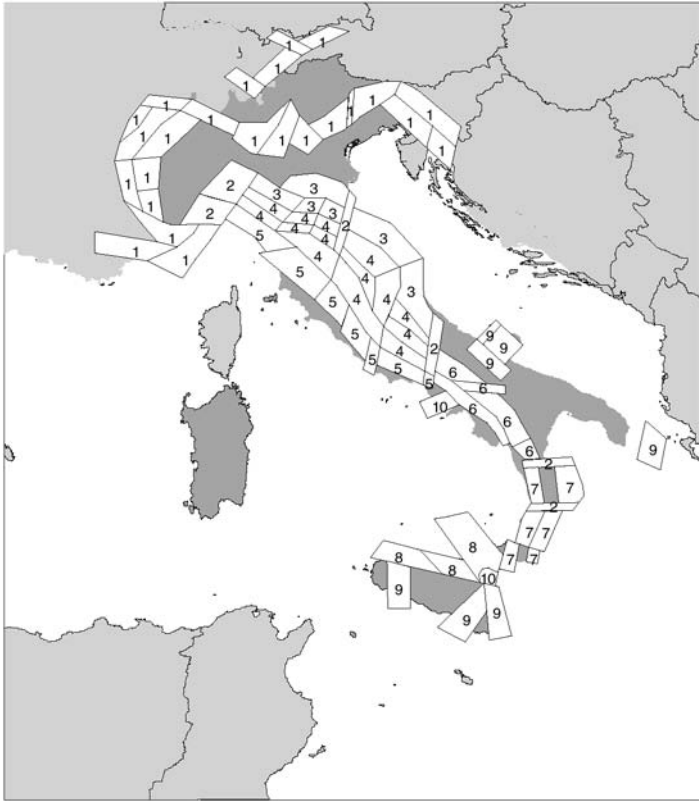


Figure 8.2 Italian seismotectonic domains (1–9) and volcano-tectonic domain (10) (Scandone *et al.*, 1996).

Earthquake catalogue

Italian seismicity is well described by historical chronicles, reportage, manuscripts, and so on, due to the rich cultural tradition and history of the country. Among the most complete catalogues available in Italy for this study we selected the Camassi and Stucchi (1996) catalogue, because it was specifically assembled for hazard studies. In fact this catalogue contains only mainshocks and the events are associated to the seismic source zones in Figure 8.1. The seismicity is described by the epicentral intensity and the surface wave magnitude.

The catalogue lists earthquakes that occurred in Italy from AD 1000 to 1980; we updated the catalogue up to 1996, adding earthquakes above magnitude 4.6 contained in the instrumental catalogue of the National Institute of Geophysics.

The resulting catalogue consists of 2028 earthquakes relevant for Italy distributed over the 81 seismic source zones and 150 earthquakes belonging to a

wider background area. Most of the destructive earthquakes ($M_s > 6$) are distributed along the Apennine chain and the eastern Alpine belt, which represent the youngest folded areas of the peninsula. The largest earthquakes ($M_s > 7$) are concentrated in central and southern Italy and particularly in the Calabrian arc (zones 65 to 71 in [Figure 8.1](#)).

Activity rates

A key question in the use of historical seismicity for seismic hazard assessments is given by the completeness of the earthquake catalogue, usually based on statistical analyses. Following the procedure proposed by Tinti and Mulargia (1985), the cumulative number of earthquakes against time was plotted and the possible completeness intervals were selected by looking at the increase in slope or detection rate.

The activity rate of each seismic source zone was then estimated through a least square regression analysis, assuming a Gutenberg-Richter (1954) frequency-magnitude relation.

Source zone 47 (Umbria-Marche area) has the highest activity rate, followed by source zone 4 (Friuli region), with at least one event above M_s 4.7 every 10 years.

Attenuation relationships

Despite the availability of much historical information, the Italian strong motion data do not allow the development of attenuation laws for different seismotectonic domains. Currently two attenuation models have been developed for the whole country (Tento *et al.*, 1992; Sabetta and Pugliese, 1996). The attenuation equations proposed by Sabetta and Pugliese (1996) have been developed for a wider range of seismic parameters and for both the horizontal and the vertical components of the ground motion.

The adopted form of the ground-motion attenuation equation is the following:

$$\log_{10}(Y) = a + bM + c \log_{10} \sqrt{R^2 + h^2} + e_1 S_1 + e_2 S_2 \pm \sigma \quad (8.3)$$

where Y is the ground motion parameter to be predicted; M is the magnitude; R is the distance (fault or epicentral); h is a fictitious depth determined through a non-linear regression analysis; S_1 , and S_2 are flags characterizing the local site conditions, referring to shallow and deep alluvium sites, respectively; and σ is the standard deviation of the logarithm of the estimated ground motion Y .

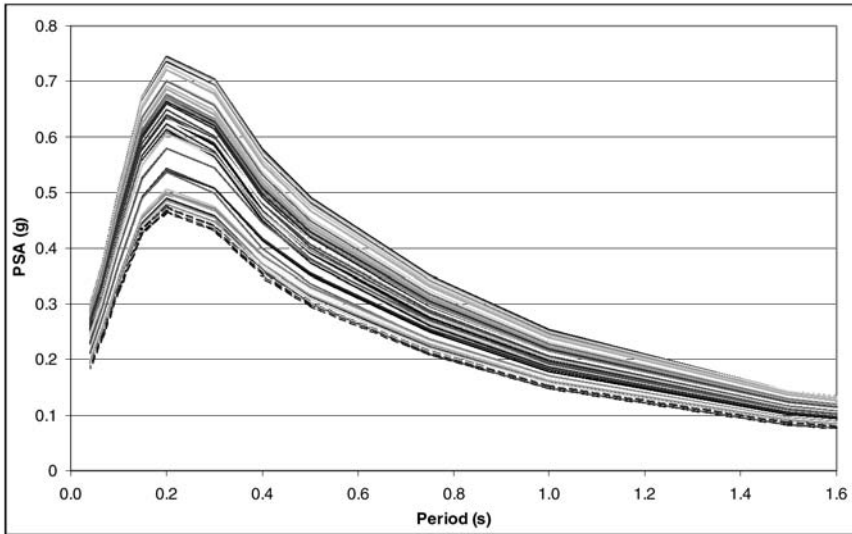


Figure 8.3 Elastic pseudo-acceleration response spectra at 10% probability of being exceeded in 50 years for the 60 most damaged municipalities (Pergalani *et al.*, 1999).

Identification of the response spectra and accelerograms for the analysis

In Figure 8.3 shows the elastic pseudo-acceleration response spectra with 10% probability of being exceeded in 50 years for the 60 most damaged municipalities; they refer to rock or stiff soil conditions in free field. The maximum values of the spectral ordinates are in the range 0.45–0.75g at a period of 0.2 s. In the analyses only the spectra labelled Gualdo Tadino, Spello and Preci were used, applying the Gualdo Tadino spectrum for all municipalities with maximum spectral ordinates lower than 0.55g, the Spello spectrum for all municipalities with maximum spectral ordinates between 0.55 and 0.65g and the Preci spectrum for the municipalities with maximum spectral ordinates higher than 0.65g.

Figure 8.4 shows the spatial distribution of the municipalities belonging to the three groups; the seismic hazard increases from north to south, due to the influence of the Val Nerina seismic zone, located on the southernmost side of the area and struck in 1979 by a Ms 5.9 earthquake.

The reference spectra (Figure 8.5) correspond approximately to three reference earthquakes of magnitude 6 scaled in distance (about 5, 10 and 15 km); Figure 8.5 also shows, for comparison, the elastic spectrum derived from the design spectrum for the area of the Italian code: the design spectrum has been scaled by a factor of 9, accounting for the safety factor and the behaviour factor.

Since most of the site amplification analyses required accelerograms as reference input, artificial time-histories were simulated following the method proposed by Sabetta and Pugliese (1996).

The method has features that make it particularly interesting:

- It reproduces the non-stationarity, in amplitude and frequency, of the real ground motions;
- It allows the simulation of a family of time-histories, requiring only the magnitude of the reference earthquake, the distance from source to site, and the local site geology as input parameters;
- The simulated time-histories fit the recorded Italian accelerograms in terms of several ground motion amplitude measures such as peak acceleration, peak velocity, Fourier spectra, and response spectra.

To match the reference spectra and the peak ground accelerations of the three reference villages, the non-stationary time-histories were further modified by scaling the amplitude of each Fourier spectrum without modifying the phase; the resulting accelerograms are shown in [Figure 8.6](#).

Analysis methods

The present chapter, given the space limitations, cannot pretend to provide an exhaustive survey of the whole literature but does provide a brief outline of the computer programs used to estimate the “ground shaking” site effects in the Umbria-Marche region, and to emphasise the main issues as yet unsatisfactorily answered by the methods used and the limits of their application.

Three kinds of computer programs have been used. The first, SHAKE or PSHAKE, is based on a simple model that was developed in the 1970s, and is now almost routinely used in engineering practice (1D linear or linear equivalent approach). The second, QUAD4 or QUAD4M, based on the Finite Element Method, FEM, was used in our work to solve the site effect problems essentially in the case of very soft valleys in 2D geometry. The third, BESOIL (Sanò, 1996), is based on the Indirect Boundary Element Method, IBEM, and allows accounting for very complex 2D geometry and wave propagation.

1D model

The computer program SHAKE was written in 1970–71 by Schnabel and Lysmer and was published in December 1972 by Schnabel *et al.* This has been by far the most widely used program for computing the seismic response of horizontally layered soil deposits. A new improved version, SHAKE91, has recently been published (Idriss and Sun, 1992).



Figure 8.4 Seismic hazard distribution of the municipalities (Pergalani *et al.*, 1999).

The soil profile is idealized as a system of homogeneous, visco-elastic sublayers of infinite horizontal extent; the idealized physical model is shown in Figure 8.7. The response of this system is calculated considering vertically propagating shear waves. The algorithm (Schnabel *et al.*, 1972) is based on the continuous solution to the wave equation, which was adapted for transient motions using the fast Fourier transform techniques of Cooley and Tukey (1965). The wave equation in this case of only horizontal displacements is:

$$\sigma \frac{\delta^2 u}{\delta t^2} = G \frac{\delta^2 u}{\delta x^2} + \xi \frac{\delta^3 u}{\delta x^2 \delta t} \quad (8.4)$$

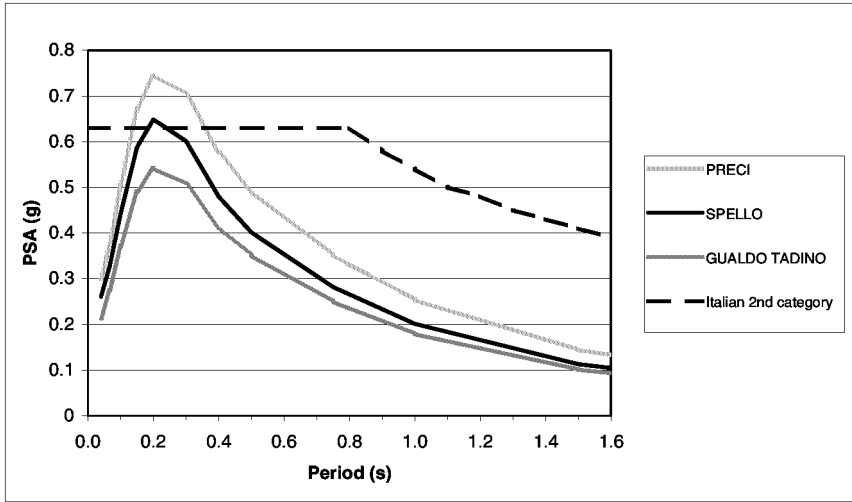


Figure 8.5 Reference spectra (Pergalani *et al.*, 1999).

where u is the horizontal displacement, G is the shear modulus, ρ is the density and ξ is the damping ratio of the soil, and t is the time.

The equation (8.4) is analytically solved in each homogeneous stratum for each incident and reflected wave of frequency ω . Their amplitudes, i.e. two unknowns for each layer, can be solved by imposing the continuity conditions of displacements and shear stresses on each interface among layers and null shear stress on the free surface. Based on the solution of the consequent algebraic equations, the transfer function can be found between any two layers in the system. Hence, if the motion is known in any one layer, the motion can be computed in any other layer.

In case of half-space, that is when the soil system is removed, if the surface motion is known, the amplitudes of the incident and reflected wave components, I_N and R_N in Figure 8.7, are easily computed. In fact the shear stresses are zero at any free surfaces; thus $I_N=R_N$ and the incident wave is completely reflected with a resulting amplitude $2I_N$. Thus the incident wave component, I_N , is equal to half the known surface motion in every system shown in Figure 8.7.

In this way the SHAKE program can compute the responses for a design motion given anywhere in the system, combining the effect of each wave, of frequency ω , in which an accelerogram can be composed by the Fourier transform. Thus accelerograms obtained from instruments on outcrop rock, or even on soil deposits, can be used to generate new rock motion which, in turn, can be used as reference motion for other soil deposits.

Since the mechanical properties of soil, shear modulus and damping, are dependent upon shear deformations (Seed and Idriss, 1970; Seed *et al.*, 1986; Sun *et al.*, 1988), the non-linearity plays an important role in the response.

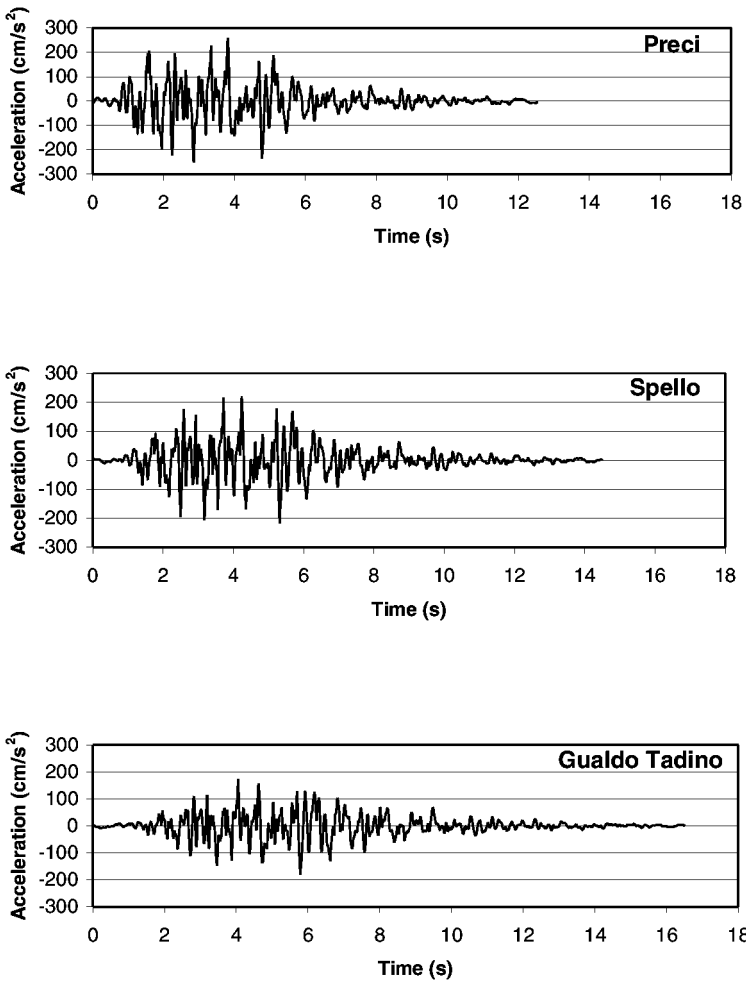


Figure 8.6 Non-stationary artificial acceleration time-histories (Pergalani *et al.*, 1999).

Figures 8.8 and 8.9 show that the non-linearity can be very important for strong ground motion for which a significant soil shear deformation exists.

Such non-linearity is accounted for by the use of equivalent linear analysis (Seed *et al.*, 1986) using an iterative procedure to obtain, in each iteration, the characteristics of the soil compatible with the effective strain in each layer.

In performing the microzoning of the Umbria-Marche region, extensive use was made of another computer program, called PSHAKE (Sanò and Pugliese, 1991). This program allows the direct use of a response spectrum instead of a time history as input. A power spectrum of a family of ground motions on the outcropping rock is obtained through an iteration on the given acceleration response spectrum, taking into account its exceedence probability.

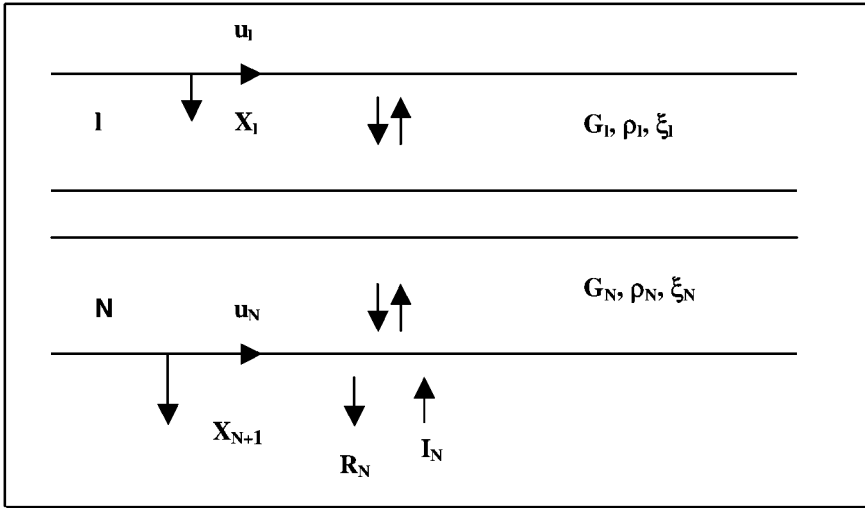


Figure 8.7 Scheme 1D of SHAKE.

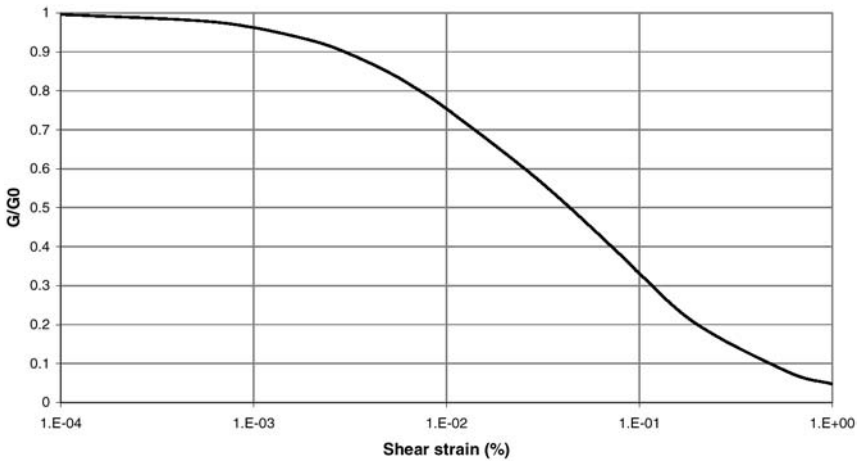


Figure 8.8 Typical behaviour of shear modulus vs shear strain.

Once the amplification function is computed using the SHAKE method, the power spectrum of any top of layer and the corresponding response spectrum at any level of exceedence probability is obtained.

The limitations of the 1D model are:

- The hypothesis that layers are perfectly horizontal and unbounded. Such an ideal situation rarely exists in reality;
- The hypotheses that waves are vertically propagating and composed by pure shear components;

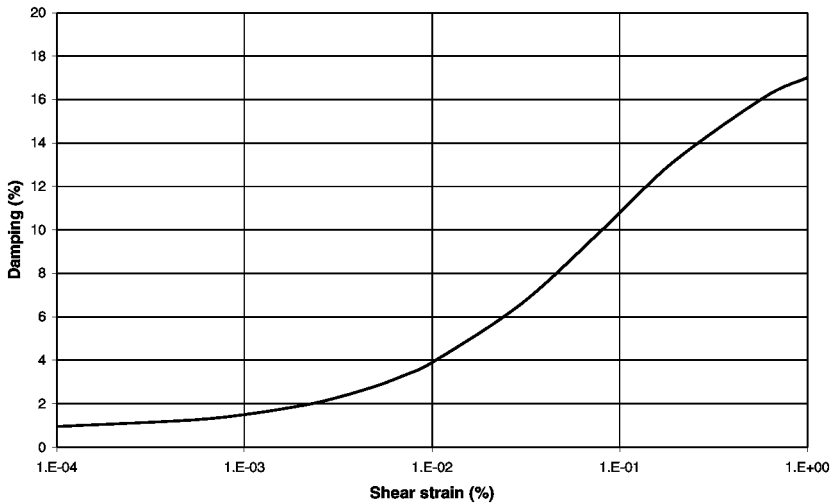


Figure 8.9 Typical behaviour of damping vs shear strain.

- The equivalent non-linear procedure can give imprecise results especially in the field of high frequencies.

In spite of those approximations, the long experience of the use of the SHAKE program shows that it can give good results also in the case of inclined impinging waves and even in the case of a relevant surface wave contribution to the ground motion.

2D models

The BESOIL program

The computer program BESOIL (Sanò, 1996) is based on the Boundary Element Method, BEM (Brebbia, 1984), applied to wave propagation in soils. This method has gained increasing popularity, having advantages over domain approaches, i.e. the Finite Element Method (FEM), due to the reduction by one of the problem dimensions, the relatively easy fulfilment of radiation conditions at infinity and the high accuracy of results. The method is based on the mathematical work on integral equations (more specifically on Somigliana's integral representation formulae established in 1886) as formulations of linear boundary value problems alternative to those in terms of partial differential equations. Excellent surveys of the available literature on the BEM in elastodynamics are those of Kobayashi (1987) and Manolis and Beskos (1988). The BEM approaches are divided into direct and indirect ones. In the first

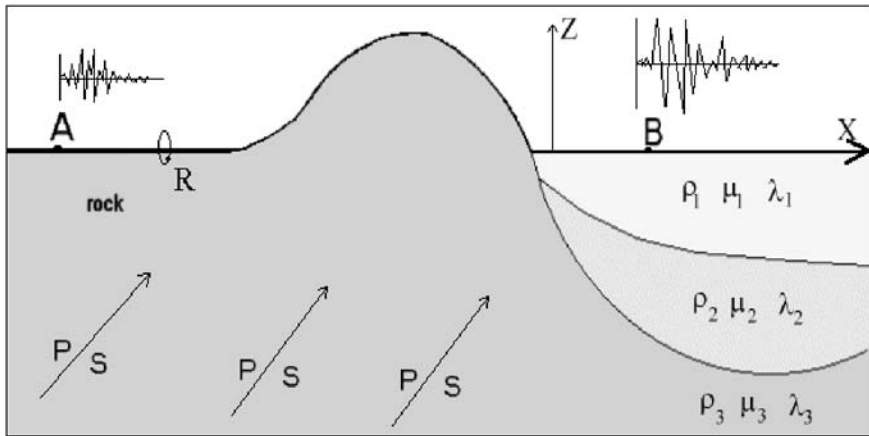


Figure 8.10 Scheme 2D of BESOIL (Sanò, 1996),

formulation, the most popular, the unknowns are the values of displacements and tractions. In the second, the problem is formulated in terms of force or moment boundary densities; it is less popular in spite of the fact that such a distribution of forces can give a better insight on the physical phenomenon of wave propagation. BESOIL uses the indirect method and strictly follows the works of Sanchez-Sesma *et al.* (1993); Sanchez-Sesma (1978, 1987, 1990); Dravinski and Mossessian (1987) and Kawase (1988).

The basic hypotheses are the following:

- Plane motion, i.e. the soil particle velocities and displacements, lies on a plane (x and z in Figure 8.10). This implies that all the soil mechanical properties are independent of y ;
- The seismic source is so far from the site that also waves are plane;
- The elastic medium is divided into plane regions with homogeneous mechanical properties, i.e. density ρ , shear modulus G , Lamé modulus λ and damping ξ .

Consider the elastic material in a homogeneous region V with boundary S ; the displacement field at a generic internal point r can be described, in the absence of body forces, by a boundary integral:

$$u_i(r) = \int_{S'} \phi_j(r') * G_{ij}(r, r') dS' \quad (8.5)$$

where $u_i(r)$ is the i -th component of displacement at r , $G_{ij}(r, r')$ is Green's tensor, i.e. the displacement in the direction i at point r due to the unit force applied in

direction j at point r and $\phi_j(r)$ is the force density on the boundary in direction j . The closed-form solution of the Green function has been derived for two-dimensional elastodynamic problems of the whole space (Kummer *et al.*, 1987). Equation (8.5) shows that the displacement at any internal point can be determined as a sum of the effects of forces applied at the boundaries. Such an equation stems from the Somigliana identity, which is the base of the direct approach of the BEM. Kupradze (1963) showed that the displacement field is continuous across the boundary, S , if ϕ_{ij} is continuous along S .

Stresses and tractions can be calculated by direct application of Hooke's law except at the boundary singularities, i.e. when $r \rightarrow r'$ on the boundary. In this situation the Green function, G_{ij} , has a logarithm-type integrable singularity, but its derivative can be computed only if the singularity is extracted (Kupradze, 1963). The integral can be calculated by a limiting process based on equilibrium considerations around the singularity, in the following form:

$$t_i = C\phi_i(r) + \int_{S'} \phi_j(r') * T_{ij}(r, r') * dS' \quad (8.6)$$

where t_i is the i -th component of traction at the boundary and C is equal to zero outside the boundary and equal to ± 0.5 for a smooth boundary. The signs $+$ and $-$ are valid respectively for the interior and exterior domain. $T_{ij}(r, r')$ is the traction Green function and represents the traction in direction i at point r on the boundary due to the application of a unit force in the direction j applied at r' .

The equations (8.5) and (8.6) are the basic formulations for solving the problem of wave propagation. Consider the space in [Figure 8.10](#), in the homogeneous infinite domain external to the valleys on the right, under incidence of elastic waves. It is usual to distinguish the resultant motion as composed of the free field motion, i.e. the incident waves, and the "scattered" waves, i.e. those reflected, diffracted and refracted from the boundary. In fact the ground motion in this irregular configuration physically comes from the interference of incoming waves with those generated by the boundaries. On the contrary, in the limited areas of the valleys, on the right-hand side of [Figure 8.10](#) and also called inclusions, the motion is due only to diffracted waves. The resultant motion is expressed by:

$$\underline{u} = \underline{u}^o + \underline{u}^s \quad (8.7)$$

where u^o is the incoming and u^s the scattered motion. It is assumed that both the waves also exist for $z > 0$, that is in the air, fulfilling the same analytical expression valid for $z < 0$.

Similarly for stresses and tractions the resultant value is:

$$\underline{t} = \underline{t}^o + \underline{t}^s \quad (8.8)$$

Substituting equations (8.5) and (8.6) into (8.7) and (8.8), we obtain:

$$\int_S \phi_j \cdot T_{ij} \cdot dS - m v_i = 0 \quad (8.9)$$

$$\frac{1}{2} \phi_i + \int_S \phi_j \cdot T_{ij} \cdot dS - m f_i = 0 \quad (8.10)$$

which are valid in each homogenous region with the convention that m is equal to 1 in the infinite domain and equal to zero in the inclusions. F_i and v_i are respectively the stresses and displacements due to the incoming waves and ϕ_i physically represent the point sources distributed on the boundary, which modify the displacement field generated by the incoming waves. The sources ϕ_i are unknown while G_{ij} , T_{ij} , f_i and v_i are known. Equations (8.9) and (8.10) can be discretized assuming ϕ_i constant over each of N boundary segments into which the entire boundary has been divided. Then imposing the continuity conditions over the boundary between adjacent homogeneous regions and the conditions of null stress on the interface with the air, the previous integral equations can be transformed into a system of algebraic equations and solved in the unknown ϕ_i .

The two major limitations to the method are the high frequency and the non-linearity. In order to get a good approximation the dimension of each boundary element should be a fraction (between and) of the wavelength. In the case of a long valley with soft soil conditions this limitation requires a great number of elements to treat the high frequency field. A valley 1000 m long, with V_s shear wave velocity of 240 m/s, has a wavelength of 8 m at a frequency of 30 Hz and requires about 600 elements. Moreover it is also necessary to model the rocky region, that is the infinite homogeneous region, at a distance in the x direction at least 2 times the dimension of the valley on each side. The numbers of degrees of freedom can reach very large values especially in the case of multiple layers of soft soil. This is a great limitation, also taking into account that the solution matrix is imaginary and sparse.

The problem of non-linearity can be overcome using a simpler program to assess approximately the deformation of the soil under the seismic excitation, i.e. the SHAKE program. Such deformation can be used to compute the modified characteristic of the soil to apply to BESOIL for the final analysis.

The QUAD4M program

The QUAD-4 program is based on the Finite Element Method, FEM. It has been implemented by Idriss *et al.* (1973), and updated as QUAD4M by Hudson *et al.* (1993). In this method the actual continuum is represented by an assemblage of elements interconnected at a finite number of nodal points. Details of the formulation of the general method are available in several publications (e.g. Desai and Abel, 1972; Zienkiewicz, 1977; Bathe, 1982).

In earthquake response evaluations, the following set of equations are solved:

$$[M]\{\dot{u}\} + [C]\{u\} + [K]\{u\} = \{R(t)\} \quad (8.11)$$

in which:

- $[M]$ = mass matrix for the assemblage of elements shown in [Figure 8.11](#). The dimension of the matrix is $2N \times 2N$ where N is the number of nodes external to the lower boundary, i.e. the interface with the rigid soil.
- $[C]$ = damping matrix for the assemblage of elements,
- $[K]$ = stiffness matrix for the assemblage of elements,
- $\{u\}$ = nodal displacements vector (dots denote differentiation with respect to time), and
- $\{R(t)\}$ = earthquake load vector.

The equations of motion (8.11) are most readily solved by a direct numerical method such as the step-by-step method (Wilson and Clough, 1962).

The solution proceeds by assigning modulus and damping values to each element. Because these values are strain-dependent, they would not be known at the start of the analysis and an iteration procedure is required as in case of the SHAKE program. Thus, at the outset, values of shear modulus and damping are estimated and the analysis is performed. Using the computed values of average strain developed in each element, new values of modulus and damping are determined from appropriate data relating these values to strain (Seed and Idriss, 1970; Hardin and Drnevich, 1972). Proceeding in this way, a solution is obtained incorporating modulus and damping values for each element, which are compatible with the average strain developed.

The main features of the QUAD4 program are the following.

The first feature regards the high frequency range. In order to get a good response the dimension of elements should be a fraction, to , of the wavelength of incident waves; this affects the dimensions of the matrices in equation (8.11), that is the number of equations to solve, and the computing time. Moreover the equivalent non-linear procedure can give imprecise results, especially in the field of high frequencies.

The second, and more important, feature regards the lower boundary of the FEM model, that is the interface with rigid soil. The FEM method assumes that the boundary nodes move simultaneously, which means that the soil at the bottom is infinitely rigid. This can be approximately right in many cases when a well-defined contrast exists between underlain rock and soft soil. A consequence of the previous condition is that such rigid boundaries can reflect and trap waves going away from the soft soil. This can produce an overestimate of soil amplification.



Figure 8.11 QUAD4 FEM scheme of a valley.

Application

Some characteristics of The Umbria-Marche seismic sequence

The seismic sequence started in the Umbria-Marche Apennine region on 4 September 1997 with an ML 4.4 earthquake located near the village of Colfiorito, close to the boundary between the Marche and Umbria regions. Several aftershocks with magnitude lower than 4 followed in the subsequent weeks. On 26 September at 00.33 GMT, an Ms 5.5 earthquake occurred with epicentre located between the villages of Cesi and Colfiorito. It was followed by a stronger earthquake at 09.40 GMT (Ms 5.9; Mw 6.0; [Table 8.1](#)), which represents the largest earthquake of the entire seismic sequence and caused damage as large as IX on the MCS macroseismic intensity scale. The epicentre was located north of the previous one, between the villages of Colfiorito and Annifo. A few minutes later a third shock occurred (ML 4.7) located more northward. Strong ground motion accelerographs of the National Electric Company, recorded peak ground accelerations as high as 0.5g at the

Table 8.1 Main earthquakes (ML 5) of the Umbria-Marche sequence (Pergalani *et al.*, 1999)

Date	GMT	ML	Ms	Mw	Long. E	Lat. N	Depth (km)	Io (MCS)
97.09.26	00.33	5.5	5.5	5.7	12.89	43.02	7.0	VIII
97.09.26	09.40	5.8	5.9	6.0	12.84	43.01	8.0	VIII-IX
97.10.03	08.55	5.1			12.84	43.05		VII
97.10.06	23.24	5.3			12.84	43.02		VII-VIII
97.10.12	11.08	5.1	5.2		12.97	42.87		VI-VII
97.10.14	15.23	5.5	5.5	5.6	12.94	42.91	5.0	VIII
98.03.26	16.26	5.5		5.3	12.85	43.20	50.0	VII
98.04.03	07.26	5.0		5.1	12.79	43.20	6.0	VII

village of Nocera Umbra in both the main earthquakes. In the following weeks the seismic activity was very high with more than 2000 shocks between 26 September and 11 October with about 20 earthquakes exceeding magnitude 4 up to 14 October. [Table 8.1](#) gives a list of earthquakes with magnitude greater than or equal to 5.

It is interesting to note the migration of the seismic activity during the entire sequence. Up to 12 October, the seismic activity, which was initially concentrated in the northern part of the area ([Figure 8.12](#)), migrated to the southern part, between the villages of Sellano and Preci, where on 14 October, at 15.23 GMT an earthquake of Ms 5.5 occurred. Finally, in March and April 1998, two earthquakes with magnitude greater than 5 occurred more than 20 km north of the first sequence ([Table 8.1](#)). This activity seems to highlight the activation

of several interconnected faults rather than a single segment of a main seismogenic structure.

The epicentral distribution of the first two sequences shows a NW-SE trend for a total length of about 30 km. Fault plane solutions, computed by the Centroid Moment Tensor (CMT) method, indicate a dip-slip mechanism along a primary NW-SE plane, with a T-axis oriented NE-SW. The depth of the foci shows a concentration between 4 and 8 km, increasing westward.

These directions are in good agreement with the structural framework of the area, represented by a conjugate system of normal faults oriented along the axis of the Apennines. The repeated earthquakes gave cumulative effects: the final estimated maximum intensity was as high as IX-X on the MCS scale. This peculiar seismic sequence caused the collapse of several buildings and severe damage to many of them, also because of the high vulnerability of old masonry buildings. Despite the amount of damage, fortunately only 11 people died, 126 were injured, but the homeless numbered more than 25,000. The estimated monetary losses were more than 2 billion dollars.

Geologic and geomorphologic overview and sample area selection

The investigated area is located in the central Apennines, across the Umbria-Marche regional boundary. The Umbria-Marche sedimentary sequence, composed of limestones, marly limestones, marls and flysch sequences, represents the stratigraphy of the study area.

The central Apennines are made up of several tectonic units formed since the Oligocene as a result of convergence and collision between the continental margins of the Corsica-Sardinia block and the Adriatic block (Cello *et al.*, 1995). The main compressive phase started in the Tortonian and the lack of Pliocene-Pleistocene marine deposits proves that after the Miocene the area was definitively uplifted. The compressive structures were dissected by normal faults during the Quaternary, and, according to the most recent studies (Calamita *et al.*, 1994; Lavecchia *et al.*, 1994), these are related to the crustal thinning processes occurring in the Tyrrhenian Tuscan area. The Quaternary normal faults led to the formation of intra-mountain basins, of which the Colfiorito plain is a clear example, and the seismicity of the area is mainly related to the activity of these faults.

The geomorphologic setting is characterized by a general conformity between structural-lithologic elements and morphologies. High relief zones are found in correspondence with the calcareous ridges, and hilly and smooth areas correspond to the flysch deposits in the zone of Nocera Umbra and Camerino. Even the drainage network is influenced by the structural pattern and the main drainage lines are located along the trace of the main faults and fractures. Climatic factors, especially the last glacial and interglacial period, influenced the landscape evolution and the deposition type. Stratified periglacial slope waste



Figure 8.12 Area struck by seismic sequence (earthquakes of Table 8.1, triangles) and location of the investigated villages (circles) (Pergalani *et al.*, 1999).

deposits, mainly formed by Scaglia Rossa and Maiolica cobbles, occur extensively on calcareous slopes (Coltorti *et al.*, 1979; Dramis, 1983; Coltorti and Dramis, 1988). The alluvial terraces also refer to the glacial periods; they are placed at different levels over the valley bottom and are often inter-bedded with slope deposits; three main levels are found in the area but the number can vary according to local conditions.

Lacustrine deposits are found in correspondence of intra-mountain basins; they can reach thickness of 100 m and are formed by more or less regular alternances of conglomerates, clays and sands; they are dated lower-middle Pleistocene. Finally, travertine deposits are widespread all over the area; they are mainly

formed by spring water whose chemical content is connected to the activity of deep faults and fractures; the age of these deposits is from middle Pleistocene up to the present.

According to the geomorphologic framework of the area, three main geomorphologic features were taken into account for the site selection:

- Hill tops (mainly on limestones and marly limestones);
- Valley-like morphologies (formed by alluvial deposits, lacustrine deposits or slope waste deposits and travertine);
- Slopes (slope deposits, travertine or colluvial deposits).

Geologic and geotechnic data

The collection of geologic, geomorphologic and geotechnic data is fundamental for the site geology reconstruction. The survey aimed to identify the relationships between lithologic units, to map the main structural features and to estimate the thickness of surface deposits and their degree of cementation, in order to assign the proper geotechnic value. Therefore soil columns and data from geophysics or geotechnic site tests and geotechnic laboratory tests were always reported on forms, where available. Two-dimensional cross-sections were drawn to better understand the stratigraphic and tectonic features of each site. The geomorphologic map was only intended to represent the forms and the processes acting on the examined landscape.

The lithotechnic map was derived from the geologic map by grouping geologic units considered homogeneous from the physical and mechanical point of view; the available data, from laboratory and geophysics tests, allowed to assign to each lithotechnic unit the geotechnic parameters needed for the dynamic analyses: the shear wave velocity, the Poisson coefficient, the soil unit weight, the initial shear modulus and the initial damping coefficient (Table 8.2).

The relationships between shear modulus decay and damping coefficient variation as a function of the shear strain were also assessed (Figures 8.13 and 8.14).

Analysis

The amplification effects were evaluated in two main steps. First, hazardous situations were identified for each of the 60 villages and classified according to

Table 8.2 Geotechnic parameters for the lithotechnic units (V_s shear wave velocity; ν Poisson coefficient; γ soil unit weight; G_0 shear modulus at low strain; ξ initial damping coefficient) (Pergalani *et al.*, 1999)

Surface deposits (ordered by increasing values of V_s)	V_s (m/s)	ν	γ (kN/m ³)	G_0 (MPa)	ξ
Colluvial deposits	300	0.35	17.7	162	0.03
Debris	400	0.35	19.6	320	0.01
Clayey fluvial-lacustrine deposits and silty-clayey alluvial deposits	400	0.4	19.6	320	0.04
Sandy-gravel fluvial-lacustrine deposits and sandy-gravel alluvial deposits (type 1-2)	400-700	0.35	19.6	320-980	0.01
Travertine (type 1-2)	550-1000	0.3	19.6	605-2000	0.02
Bedrock formations (in stratigraphic order)	V_s (m/s)	ν	γ (kN/m ³)	G_0 (MPa)	ξ
Flysch deposits	1000	0.3	20.6	2100	0.005
Schlier	1000	0.3	21.6	2200	0.005
Bisciario	1200	0.25	22.6	3312	0.005
Scaglia Cinerea (average values)	1000	0.3	21.6	2200	0.005
Scaglia Variegata	1200	0.25	22.6	3312	0.005
Scaglia Rossa	1500	0.25	23.5	5400	0.005
Marne a Fucoidi	1200	0.25	22.6	3312	0.005
Maiolica	1500	0.25	23.5	5400	0.005
Calcare Massiccio	2000	0.25	24.5	10,000	0.005

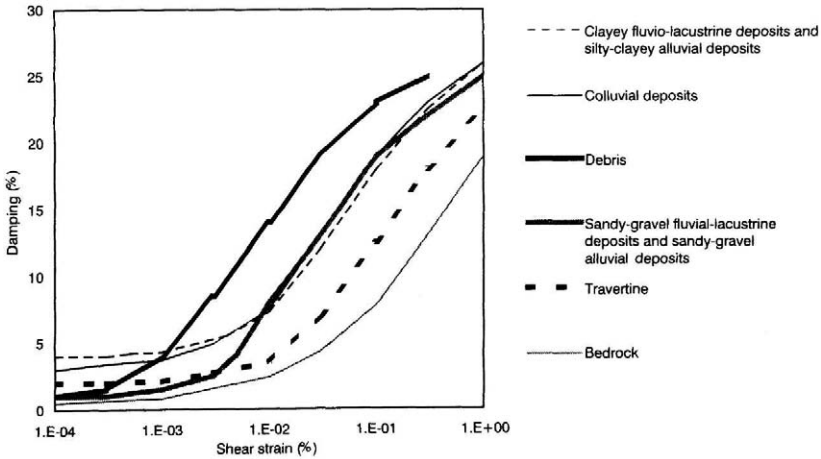


Figure 8.13 Damping coefficient variation with shear strain (Pergalani *et al.*, 1999).

Table 8.3. As a second step, a numerical analysis was performed on point sites or two-dimensional sections, crossing the inhabited areas.

The programs available for the analysis evaluate the entity of local site amplifications with different methods; the most suitable program was selected for every site condition.

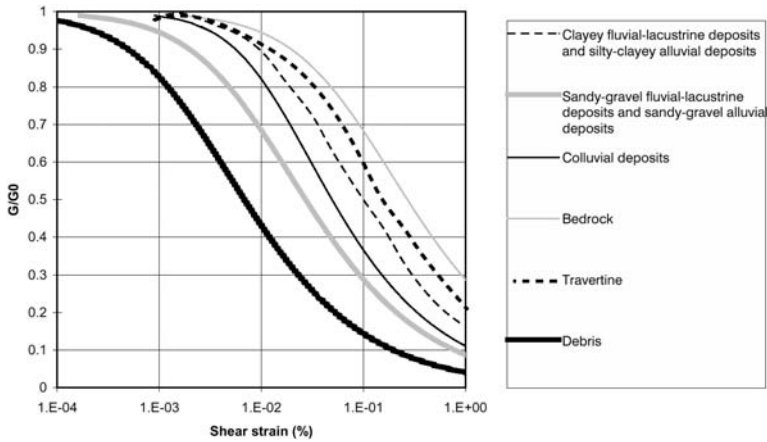


Figure 8.14 Shear modulus decay with shear strain (Pergalani *et al.*, 1999).

Response parameters

The soil response was synthetically expressed in terms of elastic spectra, calculated either for soil columns in the one-dimensional analyses, or for each nodal point on the ground surface in the two-dimensional analyses.

The spectral intensity SI (Housner, 1952) computed in the period range 0.1–0.5 s, which is the range of fundamental periods of most of the structures in the area, was selected to represent the seismic amplification:

$$SI(PSV) = \int_{0.1}^{0.5} PSV(T, \xi) dT \quad (8.12)$$

where PSV are the pseudo-velocity spectral ordinates, T is the period and ξ is the damping, set to 5% of the critical damping.

The spectral intensities were computed for the following seismic motions:

- 1 SI (input), spectral intensity of each reference spectrum;
- 2 SI (output), spectral intensity of each computed amplification spectrum;
- 3 SI (code), spectral intensity of the Italian code spectrum for the second seismic category zones.

Then, three coefficients were defined on the basis of the following ratios:

$$Fa = \frac{SI(\text{output})}{SI(\text{input})} \quad (8.13)$$

is the amplification coefficient pertaining to local site conditions;

Table 8.3 Classifying table for qualitative local effect situations (Pergalani et al., 1999)

Code	Type
1	Active landslide
2	Dormant landslide
3	Potentially unstable area
4	Soft soil (low density fills, saturated soils with abundant fine fraction)
5	Cliff with height ≥ 10 m
6	Ridge area
7	Valley filled by alluvial deposits
8	Slope toe, slope debris and alluvial fan
9	Stratigraphic-tectonic contact between two lithologic units with different geotechnic characteristics

Table 8.4 Reference coefficient F_b of each reference seismic input for normal ductility structures (Pergalani et al., 1999)

Reference seismic input	$F_b (q = 4.5)$
Preci	1.00
Spello	0.85
Gualdo Tadino	0.70

$$F_b = \frac{SI(\text{input})}{SI(\text{code})} \quad (8.14)$$

is the amplification coefficient which states the relation between seismic hazard for reference site conditions (rock or stiff soil) and the seismic protection level imposed by the Italian seismic code, for the second category zone, in absence of site amplifications;

$$A = \frac{SI(\text{output})}{SI(\text{code})} = F_a \cdot F_b \quad (8.15)$$

is the amplification coefficient, accounting for both site effects and seismic hazard variability.

To derive $SI(\text{code})$ a set of assumptions is needed, as the Italian seismic code only gives the design spectrum. In particular two factors should be considered: the ratio between the allowable stresses and the yield stresses, α , and the behaviour factor, q . For the former an average value of 2 can be assumed according to the Italian code, while for the latter the value may vary in the range 3–6 for typical buildings.

If the value 2 is assumed for the first factor and the value 4.5 for the behaviour factor, the resulting F_b values are given in Table 8.4.

For any value other than 4.5, other values of Fb^* can be calculated, keeping the a constant, as:

$$Fb^*(q) = Fb(4.5/q) \quad (8.16)$$

where q is the assumed behaviour factor. Therefore the coefficient $Fb^*(q)$ is only a scaling parameter depending on the level of structural ductility which is adopted. According to the Italian seismic code (Decree of 16 January 1996 of the Ministry of Public Works) for static analysis, seismic actions are represented by a set of horizontal forces proportional to the weight, through a seismic coefficient K :

$$K = C \cdot R \cdot \varepsilon \cdot \beta \cdot \gamma \cdot I \quad (8.17)$$

where C is a coefficient of seismic intensity, which depends on the seismic category zone (0.07 for second category zones), that is the seismic protection level assumed by the law in absence of site amplifications; R is a response coefficient which assumes the value of 1 in the period range 0–0.8s; ε is the “foundation coefficient”, which assumes the value of 1 for rock or stiff soil and 1.3 for loose alluvial deposits shallower than 20 metres; β , γ , I are coefficients depending on the structure typology, geometry and class of importance.

It was proposed to modify the seismic coefficient as follows:

$$K^* = C \cdot Fb^*(q) \cdot R \cdot Fa \cdot \beta \cdot \gamma \cdot I \quad (8.18)$$

introducing the coefficient $Fb^*(q)$ to take into account the seismic hazard given on a probabilistic basis, for reference site conditions, and substituting the foundation coefficient ε with the amplification coefficient Fa , to account for geotechnic and topographic effects.

Example of application

Field surveys and numerical computations of the local seismic response of the two villages of Cesi and Colfiorito, located in the near field area of the seismic sequence, are shown below, as an example of the adopted methodology. They show geologic and geomorphologic settings typical of the Umbria-Marche Apennine framework.

CESI VILLAGE

The village of Cesi, located in the epicentral area of the 26 September 00.33 GMT, Ms 5.5 earthquake, suffered damage up to degree IX on the MCS scale. The damage distribution was inhomogeneous, having been stronger in the lower part of the village, where some buildings collapsed and many were seriously

damaged. The upper part of the village, Cesi Villa, suffered less damage, reaching not more than degree VII on the MCS scale.

The lower part of the village lies partly on a toe slope formed by debris and colluvium and partly in a valley filled by colluvial and fluvial-lacustrine fine deposits; the upper part directly lies on bedrock made by marls and marly limestones belonging to the Scaglia formations. An evident strong influence of local geologic conditions governed the damage distribution and such situations were monitored and analysed in detail (Pergalani *et al.*, 1999).

Some aftershocks up to magnitude 5, recorded just a few days after the mainshock on 26 September, were used to calibrate the geotechnic model suggested by the field geologic survey. In particular, above a 35 metres depth of fluviallacustrine silty-clayey deposits with an average shear wave velocity of 400 m/s, a thin cover of loose colluvial deposits has been hypothesized from the analyses of the accelerometric recordings. The good agreement between the recorded seismic signals and the results of the analysis confirmed the validity of the geotechnic characteristics attributed to the soils.

In Figure 8.15a a schematic cross-section through Cesi Villa and Cesi valley is shown (Sanò *et al.*, 1998); the nodes, where the local seismic response has been computed by the BESOIL program, are labelled with capital letters. The corresponding response spectra are drawn in Figure 8.15b, and in Figure 8.15c the site effects are summarised in terms of F_a amplification factors. It is worth noting the increment in the spectral accelerations and the decrease in the fundamental period of vibration proceeding from the centre of the valley toward the slope toe. The response is maximum at station F, about 100 metres far from the slope toe, for a period of about 0.3 s.

COLFIORITO VILLAGE

The village of Colfiorito is located very close to the main epicentral areas of 26 September, 00.33 and 09.40 GMT. The macroseismic intensity, updated to 20 October, is VII–VIII MCS and 38% of buildings were made unusable.

The geologic setting is that of a typical inter-mountain tectonic depression of the central Apennines. The Umbria-Marche thrust sequence is here dissected by normal faults whose major trend is NW-SE. The depression acted as a shallow lake during the Quaternary and it has been filled up by a sequence of lacustrine and fluvial deposits mainly composed of gravels, clays and silts. The local thickness in the Colfiorito area has been estimated to be about 30–60 m from two available bore-hole logs located in the plain (Pergalani *et al.*, 1999).

A simplified two-dimensional section, drawn across the Colfiorito valley (Figure 8.16a), has been analysed with the aid of the QUAD4M program. The results in terms of acceleration spectra (Figure 8.16b) show how spectral ordinates increase in the central part of the valley (points 8 and 17), reaching about 3g in the period range 0.2–0.3s. Lower values of the spectral ordinates of about 2g in the period range 0.05–0.15s are obtained in proximity of the valley

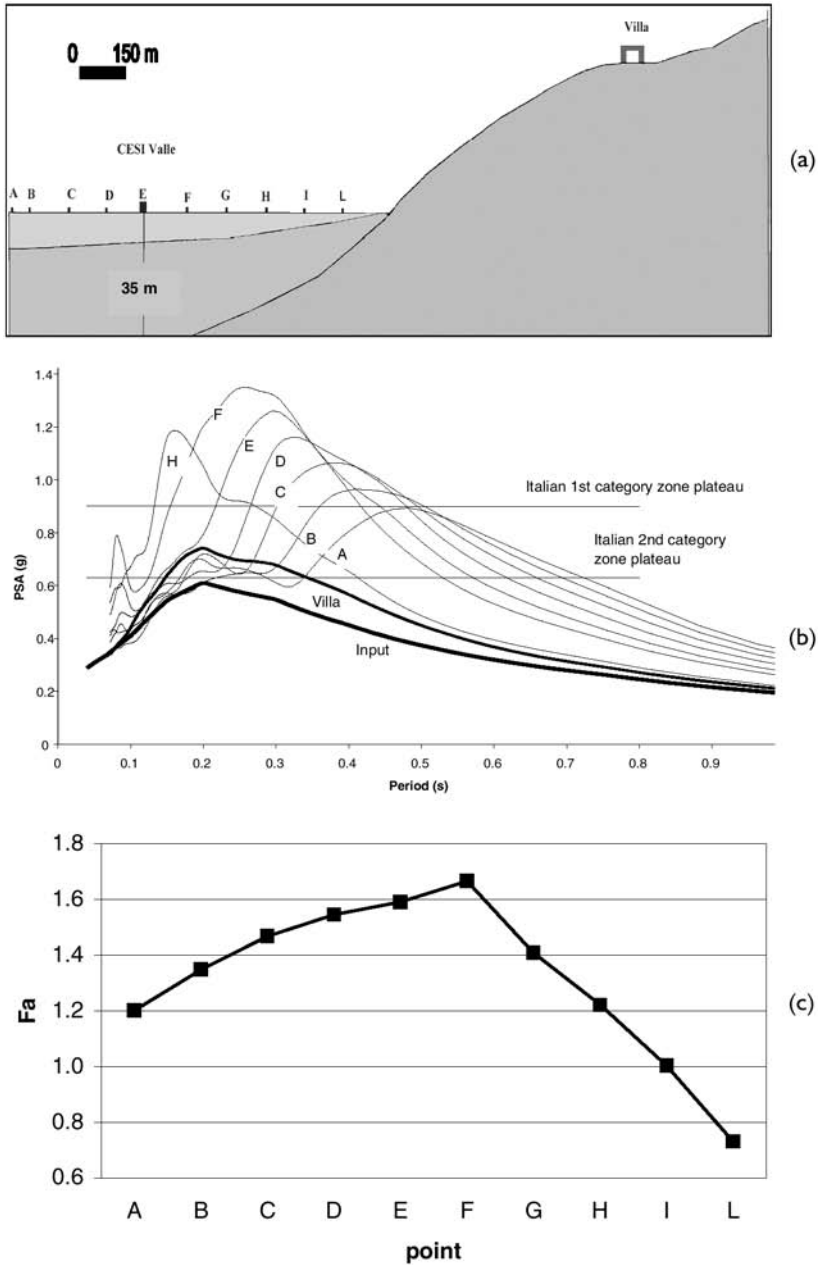
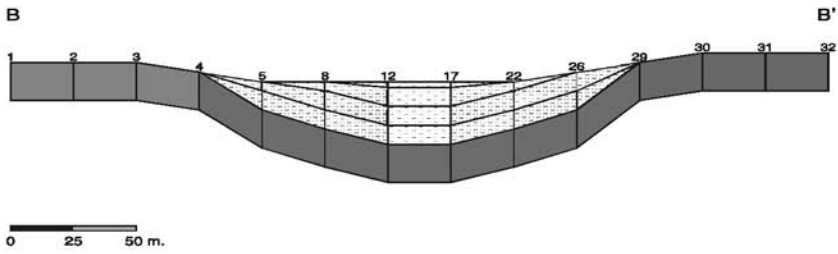
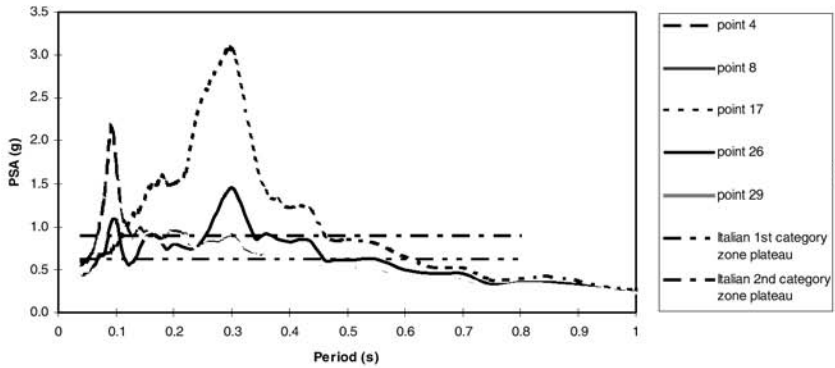


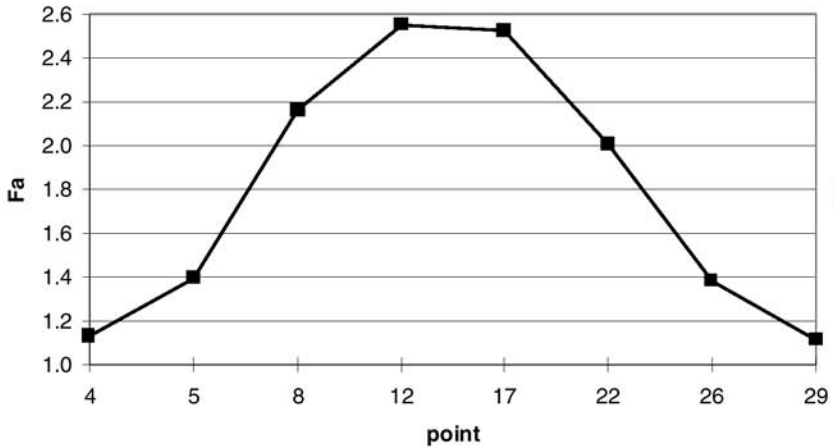
Figure 8.15 (a) Cross-section of Cesi village; (b) Acceleration response spectra computed for Cesi village; (c) Amplification coefficients (Fa) computed for Cesi village (Pergalani *et al.*, 1999).



(a)



(b)



(c)

Figure 8.16 (a) Cross-section of Colfiorito village; (b) Acceleration response spectra computed for Colfiorito village; (c) Amplification coefficients (F_a) computed for Colfiorito village (Pergalani *et al.*, 1999).

sides. [Figure 8.16c](#) summarizes the site effects in terms of the Fa amplification factor. As well as the acceleration, the highest amplification factor of about 2.5 is found in correspondence of the central part of the valley, where the sediment thickness is higher, while the amplification factor Fa decreases close to the valley sides. The village is located on the eastern side of the valley, which is the zone of relatively small amplification, that is about 1.5 if expressed as Fa , as reported in [Figure 8.16c](#) (points 26 and 29).

Practical application

Observations made on the analysed sample villages allowed clustering of some particular stratigraphic and topographic features. [Table 8.5](#) gives the average and the standard deviation of the coefficients Fa and A as well as their maximum values computed in each analysed section, grouped by four morphostratigraphic features. Fa and A mean values are averaged along all the nodes of the analysed section, crossing the villages' area, in order to smooth some particularity due to very local site conditions, which could strongly affect the attribution of the amplification coefficient to the entire area as the columns labelled Fa -max and A -max show.

In particular, in the few cases of slope toe sites analysed, an increment of the amplifications can be observed from the centre of the valley toward the slope toe, due to the refraction of the seismic waves at the contact (ramp) between bedrock and the valley fillings (see Cesi village). Similarly the focusing of the seismic waves near cliff edges produced a systematic increment in the amplification coefficients for a length of about 3 times the cliff height.

After analysing the 60 sample villages, a generalization of the stratigraphic and morphologic situations was produced, to characterize the geologic framework of the area struck by the seismic sequence. This generalization is synthesized in [Table 8.6](#), where the zones of possible amplifications are grouped by morphology types (valleys, ridges or slopes), lithologic units and thickness, and a value of Fa is assigned to each group.

As [Table 8.6](#) points out, the largest amplifications are produced by slope toe, slope debris and alluvial fan morphostratigraphic features, generally characterized by loose deposits and by lithologic sequences with high seismic impedance contrast between bedrock and overlying soils, such as fluvial-lacustrine clays, silts and colluvium.

Superposition has been assumed between stratigraphic and morphologic effects, such as a ridge in uncemented formations; in this case the resulting amplification coefficient is the product of the coefficients of the two effects.

Table 8.5 Results of amplification factors computed in each analysed site (Pergalani et al., 1999)

Cliff						
Locality	<i>Fa</i> -mean	<i>Fa</i> -max	<i>Fa</i> -std.dev.	<i>A</i> -mean	<i>A</i> -max	<i>A</i> -std.dev.
Bagni B-B' type 1	1.1	1.2	0.07	0.9	1.0	0.06
Bagni B-B' type 2	1.0	1.0	0.02	0.9	0.9	0.01
Sorifa C-C' type 1	2.0	3.9	0.73	1.7	3.2	0.62
Sorifa C-C' type 2	1.4	2.0	0.29	1.2	1.7	0.25
Le Cese A-A' type 1	1.2	1.2	0.09	1.0	1.0	0.07
Le Cese A-A' type 2	1.1	1.1	0.06	0.9	0.9	0.05
Fonni	1.3	1.3	0.01	1.3	1.3	0.01
Pale	1.3	1.3	0.01	1.3	1.3	0.01
Ridge						
Locality	<i>Fa</i> -mean	<i>Fa</i> -max	<i>Fa</i> -std.dev.	<i>A</i> -mean	<i>A</i> -max	<i>A</i> -std.dev.
Bastia	1.3	1.3	0.00	0.9	0.9	0.00
Belvedere	1.2	1.4	0.26	0.9	0.9	0.18
Ceresole	1.0	1.1	0.07	0.9	1.0	0.06
Colle	1.1	1.2	0.01	1.0	1.0	0.01
Cupigliolo	1.2	1.2	0.00	1.2	1.2	0.00
Dignano	1.2	1.2	0.00	1.2	1.2	0.00
Montesanto	1.3	1.3	0.00	1.3	1.3	0.00
Riofreddo	1.3	1.6	0.29	1.2	1.6	0.28
Nocera Umbra A-A'	1.2	1.3	0.19	1.0	1.1	0.16
Nocera Umbra B-B'	1.2	1.3	0.17	1.0	1.1	0.15
Sellano C-C'	1.2	1.3	0.09	1.1	1.3	0.09
Sellano D-D'	1.3	1.5	0.25	1.3	1.4	0.24
Valley						
Locality	<i>Fa</i> -mean	<i>Fa</i> -max	<i>Fa</i> -std.dev.	<i>A</i> -mean	<i>A</i> -max	<i>A</i> -std.dev.
Casenove C-C' type 1	1.5	2.0	0.34	1.4	2.0	0.33
Casenove C-C' type 2	1.2	1.3	0.13	1.6	1.3	0.13
Colfiorito B-B'	1.8	2.5	0.60	1.7	2.5	0.60
Piaggia A-A' type 1	1.6	2.3	0.43	1.6	2.2	0.43
Piaggia A-A' type 2	1.2	1.5	0.17	1.2	1.5	0.16
Piaggia B-B' type 1	1.4	1.9	0.33	1.4	1.8	0.32
Piaggia B-B' type 2	1.2	1.6	0.11	1.1	1.3	0.11
Selvapiana A-A'	1.3	1.5	0.14	1.3	1.5	0.14
Selvapiana B-B'	1.4	1.5	0.18	1.4	1.5	0.18
Selvapiana C-C'	1.4	1.8	0.27	1.4	1.8	0.27
Serravalle B-B' type 1	1.5	2.1	0.42	1.5	2.1	0.42
Serravalle B-B' type 2	1.4	2.3	0.39	1.4	2.3	0.38
Serravalle C-C' type 1	1.4	2.0	0.36	1.4	1.9	0.35
Serravalle C-C' type 2	1.3	1.8	0.29	1.3	1.7	0.28
Capodacqua C-C'	1.8	2.8	0.75	1.8	2.7	0.73
Capodacqua D-D'	1.5	2.2	0.45	1.5	2.3	0.44
Nocera Scalo	1.0			0.9		
Bagnara A-B type 1	1.4	1.9	0.39	1.2	1.6	0.33
Bagnara A-B type 2	1.1	1.2	0.08	0.9	1.0	0.07

Table 8.5

Slope toe, slope debris and alluvial fan						
Locality	Fa-mean	Fa-max	Fa-std.dev.	A-mean	A-max	A-std.dev.
Costa (Serravalle) C-D	1.5	1.9	0.27	1.5	1.9	0.26
Acquapagana E-F	1.6	2.1	0.33	1.6	2.1	0.32
Costa (Nocera Umbra)	1.4			1.2		
Cupo	1.4			1.0		
Isola A	1.0			0.9		
Isola B	1.2			1.0		
Isola C	1.4			1.2		
Cesi	1.3	1.7	0.29	1.3	1.6	0.28

References

- Albarello, D., Mantovani, E. and Viti, M. (1993). Numerical modeling of the present deformation pattern in Sicily and surrounding regions. *Atti XII Conv. GNGTS* (Rome, 24–26 Nov. 1993), 2, 651–661.
- Albarello, D., Mantovani, E., Babbucci, D. and Tamburelli, C. (1995). Africa-Eurasia kinematics: main constraints and uncertainties. *Tectonophysics*, 243, 25–36.
- Bathe, K.J. (1982). *Finite element procedures in engineering analysis*. Prentice-Hall, Englewood Cliffs, New Jersey.
- Brebbia, C.A. (1984). *The boundary element method for engineers*. Pentech Press, London.
- Calamita, F., Cello, G., Deiana, G. and Paltrinieri, W. (1994). Structural styles, chronology rates of deformation, and time space relationships in the Umbria-Marche thrust system (central Apennines, Italy). *Tectonics*, 13, pp. 873–881.
- Camassi, R. and Stucchi, M. (1996). NT4.1 un catalogo parametrico di terremoti di area italiana al di sopra della soglia del danno. CNR-GNDT, Milano, November 1996, 1–86, <http://emidius.itim.mi.cnr.it/NT.html>.
- Cello, G., Turco, E. and Zuppetta, A. (1995). Cinematica del settore centrale del Mediterraneo ed implicazioni sulla struttura dell'arco calabro. *Cinquant'anni di attività didattica del Professor Felice Ippolito*, G. Bonardi, B. De Vivo, P. Gasparini, and A. Vallario (eds), Liguori Editore, Napoli, pp. 293–301.
- Cinque, A., Patacca, E., Scandone, P. and Tozzi, M. (1993). Quaternary kinematic evolution of the Southern Apennines. Relationships between surface geological features and deep lithospheric structures. *Annali di Geofisica*, 36, pp. 249–260.
- Coltorti, M. and Dramis, F. (1988). The significance of slope-waste deposits in the Quaternary of Umbria-Marche Apennines, Central Italy. *Geomorph.*, N.F., Supp. Bd 71, pp. 59–70.
- Coltorti, M., Dramis, F., Gentili, B. and Pambianchi, G. (1979). Stratified slope-waste deposits in the Umbria-Marche Apennines. *Proc. 15th meeting "Geomorphology survey and mapping"*, Modena, pp. 205–212.
- Cooley, J.W. and Tukey, J.W. (1965). An algorithm for the machine calculations of complex fourier series. *Mathematics of Computation*, Vol. 19, No. 90.
- Cornell, C.A. (1968). Engineering seismic risk analysis. *Bull. Seism. Soc. Am.*, 67, 4.
- Desai, C.S. and Abel, J.F. (1972). *An introduction to the finite element method*. Van Nostrand Reinhold, New York.
- Dramis, F. (1983). Morfogenesi di versante nel Pleistocene superiore in Italia: i depositi detritici stratificati. *Geogr. Fis. Din. Quat.*, 6(2), pp. 180–182.

Table 8.6 Amplification coefficients for the geologic and geomorphologic situations (Pergalani *et al.*, 1999)

<i>Local effect situations</i>	<i>Lithologic units</i>	<i>Thickness</i>	<i>F_a</i>
Cliff with height ≥ 10 m	Debris	< 10 m	1.2
		10–20 m	1.4
		20–30 m	1.6
	Travertine	< 10 m	1.1
		10–20 m	1.3
		20–30 m	1.4
Valley filled by alluvial deposits	Clayey fluvial-lacustrine deposits and silty-clayey alluvial deposits; colluvium	< 10 m	1.2
		10–20 m	1.5
		20–30 m	1.7
Slope toe, slope debris and alluvial fan	Sandy-gravel fluvial-lacustrine deposits and sandy-gravel alluvial deposits	< 10 m	1.1
		10–20 m	1.2
		20–30 m	1.4
Ridge area	Ratio height/width	< 10 m	1.2
		10–20 m	1.5
		20–30 m	1.7
		<i>F_a</i>	
Unstable area and potentially unstable area	Investigations to evaluate the instability and to define the feasibility of interventions of stabilization	< 0.1	1.0
		0.1–0.2	1.2
		0.2–0.3	1.4
Soft soil (low density fills, saturated soils with abundant fine fraction)	Investigations to evaluate the feasibility of interventions of consolidation		
Stratigraphic-tectonic contact between two lithologic units with different geotechnic characteristics	Investigations to evaluate the differential sinking under seismic conditions and the consequent interventions on foundations		

- Dravinski, M. and Mossessian, T.K. (1987). Scattering of plane harmonic P, SV and Rayleigh wave by dipping layers of arbitrary shape, *Bull. Seism. Soc. of Am.*, Vol 77, No. 1, pp. 212–235.
- Gutenberg, B.E. and Richter, C.F. (1954) *Seismicity of the Earth and Associated Phenomena*, Princeton University Press, NJ, 2nd ed., 310 pp.
- Hardin, B.O. and Drnevich, V.P. (1972). Shear modulus and damping in soils: design equations and curves. *Journal of the Soil Mechanics and Foundations Division, ASCE*, Vol. 98, No. SM7, July.
- Harr, M.E. (1987). *Reliability-based design in civil engineering*. McGraw-Hill, New York, 290 pp.
- Housner, G.W. (1952). Spectrum intensities of strong motion earthquakes. *Proceedings of the Symposium on Earthquakes and Blast Effects on Structures*, Earth. Eng. Res. Inst.

- Hudson, M.B., Idriss, I.M. and Beikae, M. (1993). *QUAD4M, A computer program for evaluating the seismic response of soil structure by variable damping finite element procedures*. Report of Dip. of Civil and Environmental Eng., University of California, Davis.
- Idriss, I.M. and Sun, J.I. (1992). *User's manual for SHAKE91, a computer program for conducting equivalent linear seismic response analyses of horizontally layered soil deposits*. Report of Dip. of Civil and Environmental Eng., University of California, Davis.
- Idriss, I.M., Lysmer, J., Hwang, R. and Seed, H.B. (1973). *QUAD4 a computer program for evaluating the seismic response of soil structures by variable damping finite element procedures*. Report No. UCB/EERC-73/16, Earthquake Engineering Research Center, University of California, Berkeley.
- Kawase, H. (1988). Time-domain response of a semicircular canyon for incident SV, P, and Rayleigh waves calculated by the discrete wave number boundary element method. *Bull. Seism. Soc. Am.*, 78, pp. 1415–1437.
- Kobayashi, S. (1987). Elastodynamics, *Boundary Element Methods in Mechanics*. North-Holland, Amsterdam.
- Kummer, B., Behle, A. and Dorau, F. (1987). Hybrid modelling of elastic wave propagation in two-dimensional laterally inhomogeneous media. *Geophysics*, 52, pp. 765–771.
- Kupradze, V.D. (1963). Dynamical problems in elasticity. *Progress in Solid Mechanics*, Vol. III, I.N. Sneddon and R.Hill (eds), North Holland, Amsterdam
- Lavecchia, G., Brozzetti, F., Barchi, M., Menichetti, M. and Keller, J.V.A. (1994). Seismotectonic zoning in east-central Italy deduced from an analysis from the Neogene to present deformations and related stress fields. *Geol. Soc. Am. Bull.*, 106, pp. 1107–1120.
- Manolis, G.D. and Beskos, D.E. (1988). *Boundary Element Methods in Elastodynamics*. Unwin Hyman, London.
- McCann, M.W. and Reed, J. (1989). *Lower-bound magnitude for probabilistic seismic hazard assessment*. EPRI Report, EPRI NP-6496, Mountain View, CA.
- Moretti, A., Currà, M.F. and Guerra, I. (1994). Shallow seismic activity in the southeastern Tyrrhenian Sea and along the Calabria-Lucania border, Southern Italy. *Boll. Geof. Teor. Appl.*, 36, pp. 399–409.
- Patacca, E., Scandone, P., Bellatalla, M., Perilli, N. and Santini, U. (1992). La zona di giunzione tra l'arco appenninico settentrionale e l'arco appenninico meridionale nell'Abruzzo e nel Molise. *Studi Geologici Camerti*, Vol. Spec. (1991–92), pp. 417–441.
- Patacca, E., Sartori, R. and Scandone, P. (1993). Tyrrhenian basin and Apennines. Kinematic evolution and related dynamic constraints. *Recent Evolution and Seismicity of the Mediterranean Region*, E.Boschi, E.Mantovani, A.Morelli (eds), Kluwer Academic Publ., pp. 161–171.
- Pergalani, F., Romeo, R., Luzi, L., Petrini, V., Pugliese, A. and Sanò, T. (1999). Seismic microzoning of the area struck by Umbria-Marche (central Italy) Ms 5.9 earthquake of the 26 September 1997. *Soil Dynamic and Earthquake Engineering*, Elsevier Science, 18, pp. 279–296.
- Sabetta, F. and Pugliese A. (1996). Estimation of response spectra and simulation of nonstationary earthquake ground motion. *Bulletin of the Seismological Society of America*, Vol. 86, No. 2, pp. 337–352.

- Sanchez-Sesma, F.J. (1978). Ground motion amplification due to canyon of arbitrary shape. *Proc. 2nd Conf. "Microzonation"*, 2, pp. 729–742.
- Sanchez-Sesma, F.J. (1987). Site effects on strong ground motion. *Soil Dynamic and Earthquake Engineering*, 6, pp. 124–132.
- Sanchez-Sesma, F.J. (1990). Elementary solutions for the response of a wedge-shaped medium to incident SH and SV waves. *Bull. Seism. Soc. Am.*, pp. 737–742.
- Sanchez-Sesma, F.J., Ramos-Martinez, J. and Campillo, M. (1993). An indirect boundary element method applied to simulate the seismic response of alluvial valleys for incident P, S and Rayleigh Waves. *Earthq. Engrg. Struct. Dyn.*, 22, pp. 279–295.
- Sanò, T. (1996). *BESOIL—Un programma per il calcolo della propagazione delle onde sismiche*. Italian National Seismic Service, Rapporto Tecnico SSN/RT/96/9.
- Sanò, T. and Pugliese, A. (1991). *PSHAKE—Analisi probabilistica della propagazione delle onde sismiche*. Rapporto Tecnico ENEA/RT/DISP/91.
- Sanò, T., Pugliese, A., Romeo, R.W. and Marsan, P. (1998). Effetti locali a Cesi (Pg) durante la sequenza sismica del settembre ottobre 1997. *Ingegneria Sismica* No. 3.
- Scandone, P. (1996). Linea di Ricerca 2 "Sismotettonica". *L'attività del GNDT nel triennio 1993–1995*, A.Corsanego, E.Faccioli, C.Gavarini, P.Scandone, D.Slejko, M.Stucchi (eds), CNR-GNDT, Rome, pp. 67–96.
- Scandone, P., Patacca, E., Meletti, C., Bellatalla, M., Perilli, N. and Santini, U. (1990). Struttura geologica, evoluzione cinematica e schema sismotettonico della penisola italiana. *Atti del Convegno GNDT*, Pisa, Vol. 1, pp. 119–135.
- Scandone, P., Patacca, E. and Meletti, C. (1996). Main recent deformation and seismotectonics in the Central Mediterranean region. Int. School Earth and Planetary Science (Siena, 1–4 April 1996), Workshop on *Geodynamics of the Mediterranean area and implications on volcanic and seismic hazards*.
- Schnabel, P.B., Lysmer, J. and Seed, H.B. (1972). *SHAKE: A computer program for earthquake response analysis of horizontally layered sites*. Report No. UCB/EERC-72/12, Earthquake Engineering Research Center, University of California, Berkeley, December, 102 pp.
- Seed, H.B. and Idriss, I.M. (1970). *Soil moduli and damping factors for dynamic response analysis*. Report No. UCB/EERC-70/10, Earthquake Engineering Research Center, University of California, Berkeley, December, 48 pp.
- Seed, H.B., Wong, R.T., Idriss, I.M. and Tokimatsu, K. (1986). Moduli and damping factors for dynamic analyses of cohesionless soils. *Journal of the Geotechnical Engineering Division, ASCE*, Vol. 112, No. GT11, November, pp. 1016–1032.
- Sun, J.I., Golesorkhi, R. and Seed, H.B. (1988). *Dynamic moduli and damping ratios for cohesive soils*. Report No. UCB/EERC-88/15, Earthquake Engineering Research Center, University of California, Berkeley, 42 pp.
- Tento, A., Franceschina, L. and Marcellini, A. (1992). Expected ground motion evaluation for Italian sites. *Proc. 10th World Conf. on Eqk. Engng.*, Madrid (Spain), A.A. Balkema, Vol. 1, pp. 489–494.
- Tinti, S. and Mulargia, F. (1985). Completeness analysis of a seismic catalog. *Ann. Geophys.*, 3, pp. 407–414.
- Wilson, E.L. and Clough, R.W. (1962). Dynamic response by step-by-step matrix analysis. *Proceedings of Symposium "On the Use of Computers in Civil Engineering"*, Lisbon, Portugal, October.
- Zienkiewicz, O.C. (1977). *The Finite Element Method*. McGraw-Hill.

Chapter 9

Ground motion modelling using the 2-D Chebyshev spectral element method

Enrico Priolo

Abstract

The 2-D Chebyshev spectral element method (SPEM) and its application to engineering seismology problems is reviewed in this paper. The SPEM is a high-order finite element technique, which is particularly suitable to compute numerically accurate solutions of the full wave equations in complex media. The chapter first gives an overview of the theoretical bases of the method and discusses some methodological topics of interest for practical applications. Then, the effectiveness of the method is illustrated through two case histories, i.e. the ground shaking prediction in Catania (Sicily, Italy) for a catastrophic earthquake, and the analysis of the ground motion in the presence of a massive structure.

Introduction

The spatial variability of the ground motion following an earthquake has been observed in a large number of cases and is, nowadays, a widely accepted phenomenon. Several studies have shown how it manifests itself (e.g., incoherent arrival phases, local amplifications in narrow frequency bands etc., especially for the acceleration field and frequencies higher than 2 Hz), and have explained its possible causes. The great majority of the spatial ground motion variability is tied to the rupture process at the source and the propagation of the radiated wavefield through three-dimensionally complex, geologic structures. It is also known that the ground structure and soils close to the surface (a 30 m thickness is a widely accepted reference for “surface soils”) have the largest influence on a local scale. The damage distribution to buildings and infrastructures can be very inhomogeneous, with dramatic variations within a few tens of metres (Hartzell *et al.*, 1997). Only techniques that allow accurate modelling of the seismic wavefield through complex geologic structures can faithfully reproduce those phenomena, and this is one of the main reasons that has led to the development of the spectral element method in its various forms.

The global Chebyshev spectral element method (SPEM), which is overviewed here, is a high-order finite element technique, which solves the variational

formulation of the seismic wave propagation equations. The computational domain is discretised into an unstructured grid composed of irregular quadrilateral elements. This property makes the SPEM particularly suitable to compute numerically accurate solutions of the full wave equations in complex media, which can be taken into account to the finest detail. The earthquake is simulated following an approach that can be considered “global”, that is, all the factors influencing the wave propagation—source, crustal heterogeneity, fine details of the near-surface structure, and topography—are taken into account and solved simultaneously.

In this chapter, the author reorganises and synthesises material from his last ten years’ work. The chapter is organised into four main sections. First, the author summarises the basic theory, the spectral element numerical solution, and focuses on some implementation issues. The method’s effectiveness in dealing with real applications is illustrated through the description of two case studies: the strong ground motion estimation in Catania (Sicily, Italy) for a catastrophic earthquake, and the study of the influence of a massive structure on the nearby ground motion.

Mathematical formulation of the SPEM

The Chebyshev spectral element method (SPEM) is a high-order finite element technique, which solves the variational formulation of the equation. The computational domain is decomposed into non-overlapping quadrilateral subdomains. In each subdomain, the solution of the variational problem is expressed as a truncated expansion of Chebyshev orthogonal polynomials, as in the spectral methods. This section describes the mathematical formulation and the modelling algorithm.

Equations of motion

The equations of the linear elastodynamics, which govern the wave propagation, split in 2-D into two uncoupled equations (Eringen and Suhubi, 1975), which describe the in-plane (P-SV vector equation) and antiplane (SH scalar equation) particle motion, respectively. In the differential formulation they are written in the well-known form as (Marfurt, 1984):

$$\frac{\partial}{\partial t} \left(\rho \frac{\partial u_y}{\partial t} \right) - \nabla \cdot (\mu \nabla u_y) = f_y, \quad (9.1)$$

for the SH case, and

$$\frac{\partial}{\partial t} \left(\rho \frac{\partial \mathbf{u}}{\partial t} \right) - \nabla [(\lambda + \mu) \nabla \cdot \mathbf{u}] - \nabla \times (\mu \nabla \mathbf{u}) = \mathbf{f}, \quad (9.2)$$

for the P-SV (plain strain) case. Here, $u_y(x, z, t)$ and $\mathbf{u}(x, z, t) = (u_x, u_z)$, $f_y(x, z, t)$ and $\mathbf{f}(x, z, t) = (f_x, f_z)$, define the (horizontal) out-of-plane, and in-plane components of the displacement and exciting force, respectively; $\rho(x, z)$ is the density, and $\lambda(x, z)$ and $\mu(x, z)$ are Lamé's constants of the medium. Equations (9.1) and (9.2) are defined for $(x, z) \in \Omega$ and $t \in [0, T]$, where Ω is a two-dimensional, bounded, inhomogeneous medium, and $[0, T]$ is a bounded time interval.

The 2-D wave propagation problem is completed by the acoustic equation, which describes the propagation of a 2-D pressure field. This is a scalar equation which is formally similar to equation (9.1), and is written as:

$$\frac{\partial}{\partial t} \left(\frac{1}{\rho c^2} \frac{\partial p}{\partial t} \right) - \nabla \cdot \left(\frac{1}{\rho} \nabla p \right) = f, \quad (9.3)$$

where $p(x, z, t)$ is the pressure field, $\rho(x, z)$ is the density, $c(x, z)$ is the wave velocity, and $f(x, z, t)$ is the source forcing term, which equals the divergence of the body force divided by the density.

Equations (9.1–9.3) are completed with suitable boundary and initial conditions for the unknown fields.

The SPEM starts writing equations (9.1–9.3) in an equivalent variational formulation (Marfurt, 1984; Priolo *et al.*, 1994). In all cases, the equivalent problem is to find Ξ such that:

$$\frac{d^2}{dt^2} (\mathbf{w}, \rho \Xi)_{\Omega} + a(\mathbf{w}, \Xi)_{\Omega} = (\mathbf{w}, \mathbf{f})_{\Omega} \quad \forall \mathbf{w} \in H_0^1(\Omega) \quad (9.4)$$

where is the space of all functions that vanish on the boundaries, and which, together with their first derivatives, are square integrable over Ω . The functions $w(x, z)$ are called weight (or test) functions. The symbols $a(\bullet, \bullet)_{\Omega}$ and $(\bullet, \bullet)_{\Omega}$ denote symmetric, bilinear forms, and are specified for each case.

In the P-SV case (equation (9.2)), $\Xi = \mathbf{u}$, and

$$a(\mathbf{w}, \mathbf{u})_{\Omega} = \int_{\Omega} \mathbf{w}^{\top} \mathbf{D}^{\top} \mathbf{C} \mathbf{D} \mathbf{u} \, d\Omega, \quad (9.5)$$

$$(\mathbf{w}, \rho \mathbf{u})_{\Omega} = \int_{\Omega} \rho \mathbf{w}^{\top} \bullet \mathbf{u} \, d\Omega, \quad (9.6)$$

$$(\mathbf{w}, \mathbf{f})_{\Omega} = \int_{\Omega} \mathbf{w}^{\top} \bullet \mathbf{f} \, d\Omega. \quad (9.7)$$

\mathbf{D} is the differential operator, given by

$$\mathbf{D} = \begin{bmatrix} \partial_1 & 0 \\ 0 & \partial_2 \\ \partial_2 & \partial_1 \end{bmatrix},$$

and \mathbf{C} is the elastic stiffness matrix, given by

$$\mathbf{C} = \begin{bmatrix} \lambda + 2\mu & \lambda & 0 \\ \lambda & \lambda + 2\mu & 0 \\ 0 & 0 & \mu \end{bmatrix}$$

Using this notation, the generalized Hooke's law is written as $\boldsymbol{\sigma} = \mathbf{C}\boldsymbol{\varepsilon}$, and the components of the strain vector $\boldsymbol{\varepsilon}$ are related to the displacement field by $\boldsymbol{\varepsilon} = \mathbf{D}\mathbf{u}$.

In the SH case (equation (9.1)), $\Xi = u_y$, and

$$a(\mathbf{w}, u_y)_\Omega = \int_\Omega \nabla \mathbf{w} \bullet (\mu \nabla u_y) \, d\Omega, \quad (9.8)$$

$$(\mathbf{w}, u_y)_\Omega = \int_\Omega \mathbf{w} \rho u_y \, d\Omega, \quad (9.9)$$

$$(\mathbf{w}, f_y)_\Omega = \int_\Omega \mathbf{w} f_y \, d\Omega. \quad (9.10)$$

Finally, in the case of the pressure waves equation (9.3), the bilinear forms are similar to those of the SH case (9.8–9.10), with the following changes: $p \rightarrow u_y$, $1 / (\rho c^2) \rightarrow \rho$ and $1/\rho \rightarrow \mu$.

Equation (9.5) can easily account for a more general constitutive equation, just by changing matrix \mathbf{C} coefficients. See, for instance, Seriani and Priolo (1995) for the extension to the case of a transversely isotropic medium.

In the following two sections, the author first introduces the discretisation of the physical domain, and then that of the wave equation. For the sake of brevity, the latter is done only for the P-SV case (equations 9.4–9.7), which is the most general. A detailed treatment of other cases can be found in: Priolo and Seriani (1991) for the 1-D acoustic equation; Seriani *et al.* (1991, 1994) for the 2-D acoustic equation with straight and curved elements, respectively; Seriani *et al.* (1992) for the 2-D elastic equation with curved elements.

Discretisation of the physical domain

The first step of the discretisation process is to build up the approximating functional spaces. To do this, the spatial domain is decomposed into

subdomains. Then, an approximating function is defined on each subdomain as a truncated expansion of Chebyshev polynomials. For the simpler 1-D case, the procedure is described in Priolo and Seriani (1991). In the case of two-dimensional problems, the original spatial domain Ω is decomposed into non-overlapping quadrilateral elements Ω_e , where $e=1, \dots, n_e$, and n_e is the total number of elements. As approximating functions on each element Ω_e , functions belonging to the space \mathcal{P}_e are chosen, i.e., polynomials of degree N_1 in x_1 and of degree N_2 in x_2 . Then a global approximating function is built up as a sum of the elemental approximating functions. The resulting function is a continuous piecewise polynomial defined on the decomposition $\tilde{\Omega}$ of the original domain Ω . In this case, the polynomial space is constructed by using the Chebyshev orthogonal polynomials and for simplicity it is assumed that $N_1=N_2=N$, i.e., the order of the polynomials is the same in both directions x_1 and x_2 .

It can be shown (Canuto et al., 1988) that a function $f(\xi)=f(\xi_1, \xi_2)$, defined on the square interval $[-1, 1] \times [-1, 1]$, can be approximated by a truncated expansion using a tensor product of Chebyshev polynomials as follows:

$$\tilde{f}(\xi) = \sum_{i=0}^N \sum_{j=0}^N \tilde{f}_{ij} \varphi_i(\xi_1) \varphi_j(\xi_2) \equiv \sum_{i=0}^N \sum_{j=0}^N \tilde{f}_{ij} \Phi_{ij}(\xi) \tag{9.11}$$

where \tilde{f}_{ij} are the grid values of the function f , and φ_i are Lagrangian interpolants satisfying the relation within the interval $[-1, 1]$, and identically zero outside. Here, δ_{ik} denotes the Kronecker-delta symbol, and ζ stands for ξ_1 or ξ_2 . The Lagrangian interpolants are given by

$$\varphi_i(\zeta) = \frac{2}{N} \sum_{p=0}^N \frac{1}{\bar{c}_i \bar{c}_p} T_p(\zeta_i) T_p(\zeta), \quad \text{with } \bar{c}_i = \begin{cases} 1 & \text{for } i \neq 0, N \\ 2 & \text{for } i = 0, N \end{cases} \tag{9.12}$$

where T_p are the Chebyshev polynomials and ζ_i are the Chebyshev Gauss-Lobatto quadrature points $\zeta_i = \cos(\pi i/N)$ for $i=0, \dots, N$. The coordinates $\xi_{ij} = \{\xi_{1i}, \xi_{2j}\}$ of the internal nodes for the discretisation of the rectangular domain $[-1, 1] \times [-1, 1]$ are obtained as Cartesian products of the ζ_i points. In order to apply these interpolants and construct the approximating function space, there needs to be defined the mapping $\Lambda^{(e)}(\mathbf{x}): \mathbf{x} \in \Omega_e \rightarrow \xi^{(e)} \in [-1, 1]^2$ between the points \mathbf{x} of each element $\Omega_e = [a_e, a_{e+1}] \times [b_e, b_{e+1}]$ of the decomposition Ω in the physical space and the local element coordinate system $\{\xi_1, \xi_2\}$ by

$$\Lambda^{(e)}(\mathbf{x}) \equiv \left\{ \xi_1^{(e)}, \xi_2^{(e)} \right\} = \left\{ \frac{2}{\Delta_1^e} (x_1 - a_e) - 1, \frac{2}{\Delta_2^e} (x_2 - b_e) - 1 \right\} \tag{9.13}$$

with the dimensions of the element Ω_e . Then the global approximating function is formed by the sum of the elemental approximating functions (9.11) defined on each element.

Discretisation of the wave equation

In order to obtain the spectral-element approximation of equations (9.4–9.7), Ω is decomposed into rectangular non-overlapping elements Ω_e , and on the decomposition the trial functions $\mathbf{u}(\mathbf{x}, t)$ and the weight functions $\mathbf{w}(\mathbf{x})$ are defined such that

$$\tilde{\mathbf{u}}(\mathbf{x}, t) = \bigcup_{e=1}^{n_e} \mathbf{u}_e(\mathbf{x}, t), \quad \tilde{\mathbf{w}}(\mathbf{x}) = \bigcup_{e=1}^{n_e} \tilde{\mathbf{w}}_e(\mathbf{x}), \quad (9.14)$$

where \mathbf{u}_e and $\tilde{\mathbf{w}}_e$ denote the restrictions to Ω_e of $\tilde{\mathbf{u}}$ and $\tilde{\mathbf{w}}$, respectively. According to the Galerkin approach, the functions \mathbf{u}_e and $\tilde{\mathbf{w}}_e$ take the following form in the local coordinate system:

$$\tilde{\mathbf{u}}_e(\xi, t) = \sum_{i=0}^N \sum_{j=0}^N \tilde{\mathbf{u}}_e(\xi_{ij}^{(e)}, t) \phi_{ij}(\xi), \quad \tilde{\mathbf{w}}_e(\xi) = \sum_{i=0}^N \sum_{j=0}^N \tilde{\mathbf{w}}_e(\xi_{ij}^{(e)}) \phi_{ij}(\xi) \quad (9.15)$$

where $\xi_{ij}^{(e)}$ and $\tilde{\mathbf{w}}_e(\xi_{ij}^{(e)})$ are the grid values of the unknown solution and of the weight functions, respectively. Using the approximating function spaces (9.14) to solve equation (9.2), it follows that the two-dimensional wave propagation problem is equivalent to finding \mathbf{u}_e such that for all the following equations are satisfied in each element Ω_e :

$$\frac{d^2}{dt^2} (\tilde{\mathbf{w}}_e, \rho \tilde{\mathbf{u}}_e)_N + a(\tilde{\mathbf{w}}_e, \tilde{\mathbf{u}}_e)_N = (\tilde{\mathbf{w}}_e, \tilde{\mathbf{f}}_e)_N \quad (9.16)$$

enforcing the continuity condition for the solution on the element boundaries, and where $a(\bullet, \bullet)_N$ and $(\bullet, \bullet)_N$ are symmetric, bilinear forms computed according to definitions (9.5–9.7) at the element level.

Using the definition of $\phi_i(\zeta)$ given in equation (9.13), we can compute the derivative matrix $D_{ij} = d\phi_i(\zeta_j)/d\zeta$, and then the semidiscrete differential operator

$$\mathcal{D}_{ij}^{(e)} = \sum_{k=0}^N \begin{vmatrix} D_{ik} \phi_{kj} & 0 \\ 0 & D_{jk} \phi_{ik} \\ D_{jk} \phi_{ik} & D_{ik} \phi_{kj} \end{vmatrix}. \quad (9.17)$$

The expansions (9.15) are now applied to the terms of equation (9.16) and the resulting elemental integrals are evaluated using the mapping $\Lambda^{(e)}(\mathbf{x})$ and the semidiscrete operator \mathcal{D} . Requiring that the variational equation be satisfied for all $\tilde{\mathbf{w}}_e$, the spectral element approximation of the original equation finally yields a set of linear differential equations

$$\mathbf{M}\ddot{\mathbf{U}} + \mathbf{K}\mathbf{U} = \mathbf{F} \quad (9.18)$$

with $\mathbf{U}(0)=\mathbf{U}_0$, $(\dot{\mathbf{U}})_0=0$ as initial conditions, where the unknown vector \mathbf{U} contains the values of the discrete solution \mathbf{u} at all Chebyshev points, for $i, j=0, \dots, N$ and for all $e=0, \dots, n_e$. A dot above a variable denotes differentiation with respect to time. In equation (9.18), \mathbf{M} is the mass matrix, \mathbf{K} is the stiffness matrix, and \mathbf{F} is the force vector obtained after a global nodal renumbering and assembly of all the elemental matrices and force vector contributions. They can be computed by using the following expressions:

$$\mathbf{M} = \sum_{e=1}^{n_e} \mathbf{M}^{(e)}, \quad \mathbf{K} = \sum_{e=1}^{n_e} \mathbf{K}^{(e)}, \quad \text{and} \quad \mathbf{F} = \sum_{e=1}^{n_e} \mathbf{F}^{(e)} \quad (9.19)$$

where Σ denotes the matrix element summation over all the elements, and $\mathbf{M}^{(e)}$, $\mathbf{K}^{(e)}$ and $\mathbf{F}^{(e)}$ are the elemental matrices and force vector, respectively. The contributions from nodes that are common to an element pair are summed—this approach is called *stiff* summation (Hughes, 1987)—to enforce the continuity requirement of the solution on the element boundaries. The elemental matrices and force vector are given by

$$\mathbf{M}^{(e)} = [\mathbf{M}_{ijlm}^{(e)}], \quad \mathbf{M}_{ijlm}^{(e)} = \delta_{\alpha\beta} \int_{\Omega_e} \phi_{ij} \rho \phi_{lm} d\Omega, \quad \text{with } \alpha, \beta = 1, 2, \quad (9.20)$$

$$\mathbf{K}^{(e)} = [\mathbf{K}_{ijlm}^{(e)}], \quad \mathbf{K}_{ijlm}^{(e)} = \int_{\Omega_e} \mathcal{D}_{ij}^{(e)\top} \mathcal{C} \mathcal{D}_{lm}^{(e)} d\Omega, \quad (9.21)$$

$$\mathbf{F}^{(e)} = \{\mathbf{F}_{ij}^{(e)}\}, \quad \mathbf{F}_{ij}^{(e)} = \int_{\Omega_e} \phi_{ij} \mathbf{f} d\Omega, \quad (9.22)$$

where and are the nodal submatrices and vector respectively.

The global matrices \mathbf{M} , \mathbf{K} and \mathbf{F} are sparse, symmetric and positive-definite. Equation (9.18) is a linear, second-order ordinary differential equation with constant coefficients, which must be integrated over the time interval $[0, T]$. Time integration is performed using the “three-point-recurrence weighted residual” scheme (Zienkiewicz and Wood, 1987), which is a two-step finite difference scheme belonging to the Newmark family. This scheme is implicit, unconditionally stable and accurate to the second order. The solution \mathbf{u} is computed solving a symmetric positive-definite sparse linear system at each time step.

Issues specific to the implementation

The order of the polynomials can be set arbitrarily. Usually, orders equal to six or eight are chosen, which, for this kind of formulation, have been shown to be the best compromise between accuracy, computational efficiency, and memory requirement (Padovani *et al.*, 1994). The method needs a low number of grid points per wavelength (G), and the accuracy does not degrade even for very long propagation times. For example, values of $G=4.5$ and $G=5.2$ are typically used with polynomial orders $N=8$ and $N=6$, respectively. Material inhomogeneity is modelled simply by defining different material parameters for adjacent elements. Material characteristics do not vary inside each element. The free-surface boundary condition is obtained simply by imposing no constraints at boundary nodes (Hughes, 1987). The inner reflection of the outgoing wavefield at external boundaries is eliminated through absorbing strips where the wavefield is smoothly attenuated (Cerjan *et al.*, 1985). Attenuation Q is introduced in a simplified form (Graves, 1996) with a single value for both P and S waves. In this approximation, Q is set for a reference frequency, and it depends linearly on the frequency. It can be shown that this form approximates the constant Q fairly well for frequencies near the reference frequency. The value of Q is set on the shear wave velocities, which are the dominant waves in the wavefield generated by an earthquake.

The method presented here is 2-D. This means that both model structure and source extend infinitely in the direction perpendicular to the vertical model plane. The earthquake source is a point shear dislocation with no torsion, and it is equivalent to a point double-couple. It is introduced through a field of external forces. The 2-D hypothesis implies that the point source is actually a 3-D line source orthogonal to the model plane. The time history used to simulate earthquakes, i.e. the slip velocity function, is a unit Ohnaka impulse (Herrmann, 1996) of the form:

$$\dot{s}(t) = \alpha^2 t \exp(-\alpha t).$$

This function is defined by only one parameter α , which relates to the corner frequency f_c by $\alpha=2\pi f_c$. The Fourier amplitude spectrum has a typical ω^2 decay. The source is scaled by setting the slip magnitude and duration through some empirical relations (Wells and Coppersmith, 1994; Somerville *et al.*, 1999).

The use of irregular grids and isoparametric high-order elements makes it possible to adjust the element size to the minimum wave velocity locally, and follow all structure interfaces exactly (Figure 9.1). Technically, the mesh of the computational model is generated by two steps. First, the model is decomposed into several sub-regions, which are meshed one at a time. Then the complete mesh is obtained by sticking together all the meshed sub-regions. Irregular regions are first meshed (Priolo, 2001) into triangles using an element size that is double the final one; then the triangles are joined two by two; uncoupled

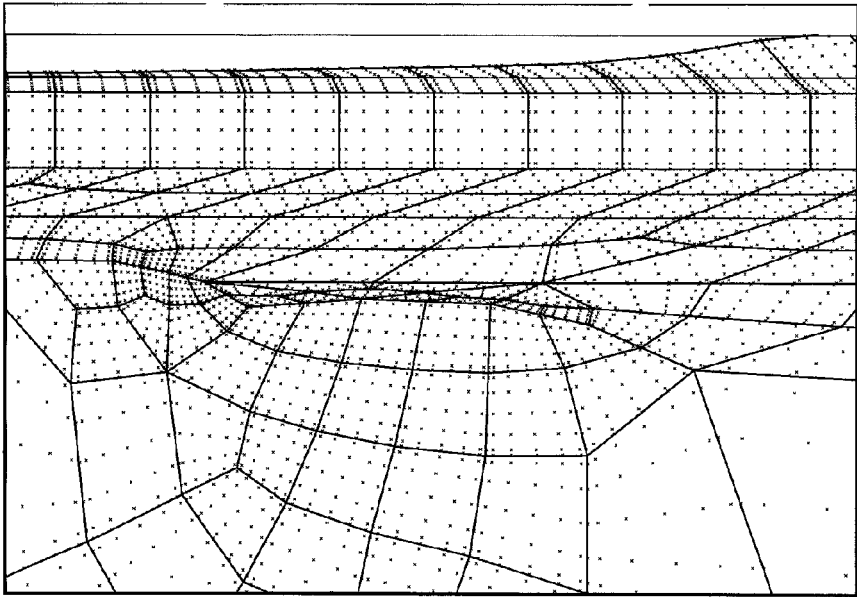


Figure 9.1 Example of a quadrangular mesh taken from a study performed near the village of Mels (Udine, Italy). The picture clearly displays how the grid adapts both in shape, to fit the near surface structure and surface topography, and size, to fit the shear wave velocity locally (from Siro (2001)). The small cross marks within each element show the internal nodes (a total number of 25, corresponding to a polynomial order $N=6$).

triangles are eliminated by splitting triangles into (three) quadrangles, and quadrangles into (four) quadrangles; finally, the mesh is regularised.

The main advantages of using the SPEM are (i) the flexibility of the unstructured grids in describing realistic geometries; and (ii) the high computational accuracy, which derives from the use of high-order Chebyshev polynomials. In inhomogeneous media, SPEM has proved to be more accurate than other grid methods (Seriani and Priolo, 1994), especially in the case of inclined and curved interfaces, since grid lines can be exactly aligned to material interfaces (e.g. [Figure 9.1](#)). Moreover, the total number of grid nodes is strongly reduced, compared with methods based on structured grids. These properties of SPEM make it particularly suitable to compute numerically accurate solutions of the full wave equations in complex media.

More details about the numerical solution, implementation, and computational efficiency and accuracy can be found in Padovani *et al.* (1994). A discussion about the use of the method in real applications, and in particular for engineering seismology purposes (e.g. quadrangular mesh generation, source definition and scaling, numerical accuracy and computational efficiency, and limitations and advantages of using a 2-D approach), can be found in Priolo (2001).

Recent developments

The kernel of the 2-D SPEM, as described in this paper, goes back to the early 1990s. Afterwards, however, the approach underwent some noteworthy improvements. Following a similar approach, that is a high-order finite element formulation, Komatitsch and Vilotte (1998) developed a method in both 2-D and 3-D, using Legendre polynomials as interpolants.

Faccioli *et al.* (1996) followed a somewhat different approach, and developed a code that is more suitable for engineering applications. Here, the spectral elements are very large and are connected by a domain decomposition technique based on a variational principle. In each element, the wave equation is solved by a global pseudo-spectral Fourier or Fourier-Legendre method. The method solves both 2-D and 3-D cases, can also handle non-linear soil behaviour, and allows for the simultaneous use of spectral and classical low-order finite elements.

The Chebyshev SPEM itself is still being developed. Seriani (1997, 1998) implemented the *element-by-element* technique into the Chebyshev SPEM for the acoustic equation. Here, the matrix coefficients are computed on the fly at each time step while solving the linear system, thus avoiding global matrix assembly. Seriani and Priolo (2000) introduced new heterogeneous elements, which account for medium variations inside the element itself. The advantages are that a finely heterogeneous medium can be described in a finer way than the problem solution, and the medium heterogeneity can be represented numerically by the most appropriate shape function and polynomial order. Laurenzano and Priolo (2001) are working on a simplified construction of the computational mesh for a complex structure, based on few control points and geometrical constraints, and an optimal adaptation of the mesh size to the medium properties. As a consequence, the applicability of the 2-D Chebyshev spectral element method to geo-problems is improved.

All the above methods are also implemented for parallel computers.

Method demonstration: two case histories

This section illustrates two real applications that have been tackled by the 2-D SPEM. The first concerns the construction of a detailed scenario of ground motion in Catania (Sicily, Italy) for a catastrophic earthquake. The second aims at estimating, through a parametric approach, how and how much the presence of a massive structure built at ground surface (e.g. an embankment or an earth dam) may influence the ground motion.

Ground shaking scenario in Catania (Sicily, Italy)

This study was developed within *The Catania Project*, a three-year national research programme funded by the *National Research Council-National Group*

for the *Defence Against Earthquakes (CNR-GNDT)* and devoted to evaluating the seismic risk of a highly urbanised area, such as that of Catania, located in a seismically active region. All details about the study are reported in Priolo (1998, 1999, 2000).

The ground motion was calculated along four vertical transects (t01, t02, t03, and t05 in [Figure 9.2](#)), which span the Catania municipal area along four different directions and provide a good spatial sampling of the northern part. The model along these transects represent the upper 20 km of the Earth's structure in terms of seismic velocities, density, and attenuation. Particular emphasis was given to the definition of the surface structure, with the finest local detail. Data consist of three geological profiles, several pre-interpreted seismic lines, data relative to deep wells, a complete geotechnical survey of the area, and several studies regarding Eastern Sicily and the area surrounding Catania, in particular. On a regional scale, the main units of the crustal structure are: (i) the carbonatic basement of the Hyblean Foreland, (ii) the sedimentary formations of the Northern Chain, (iii) the volcanic body of Mt. Etna, (iv) the Ibleo-Maltese escarpment running offshore in the NNW-SSE direction, and, on a smaller scale, (v) the Gela-Catania Foredeep, with the sedimentary basin of the Catania Plain. [Table 9.1](#) summarises the parameter values adopted for the main formations in the models.

The reference earthquake simulates the $M7$ event of January 11, 1693. This destructive event is commonly associated to rupture with normal mechanism along the Ibleo-Maltese system of faults. This is a system of sub-vertical normal faults, NNW-SSE oriented, which runs for about 70–100 km offshore along the Ionian coast of Sicily. The reference earthquake of this study is associated to the northern part of the system, which is simplified in a segment about 25 km long (s. IBM in [Figure 9.2](#)). [Table 9.2](#) summarises the values of the main source parameters. The source mechanism is of pure normal faulting. The wavefield amplitude is scaled by the value assumed for the fault-slip D .

Two groups of sources are considered. The first group uses a point source model with the aim of studying the effect induced by a variation in the fault orientation and source position. With the second group, the purpose is to simulate an extended source. To do this, the fault is discretised into three elementary point sources, aligned along the fault dip direction ([Figure 9.3](#)). In this way, three different directions of rupture propagation are reproduced.

The main results of this study are synthetic seismograms, peak ground acceleration (PGA) envelopes, and response spectra. Seismograms are computed up to a maximum frequency of 7.5 Hz and for a total propagation time of 25 s. The time step is 15 ms. On average, the size of the computational models is 45 km×25 km and the meshes contain 170,000–200,000 nodes ([Figure 9.3](#)).

[Figure 9.4](#) shows snapshots of wave propagation through transect t02. The main pressure and shear wavefronts— P_+ – P_- and S_1 – S_2 , respectively—can be clearly distinguished, as well as the reflected wavefronts (S'_1) [Figure 9.5](#) summarises the spatial distribution of PGA. On average, values range between 0.

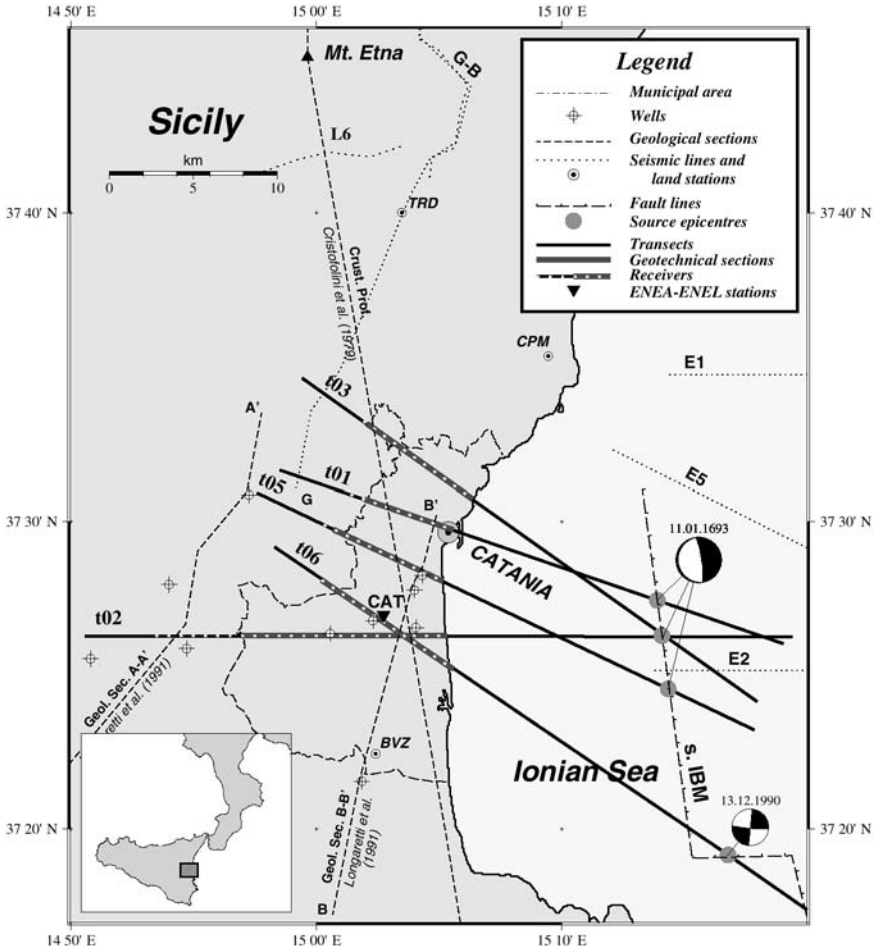


Figure 9.2 Base map of the study area, showing the essential information about the geography, the transect position, and the data available. The grey circles show the assumed positions of the two reference earthquakes, of January 11, 1693, and December 13, 1990, respectively (from Priolo (2001)).

1 and 0.5g, and, with the exception of a few local peaks, the largest PGA does not exceed 0.7g. The predicted values do not vary appreciably in the four transects. However, the inability to model ruptures that propagate laterally, makes the 2-D methodology applied in this study unsuitable for these last kinds of conclusions. An unexpected and remarkable feature, which contradicts the classical laws of attenuation, is the appreciable increase of the PGA for large epicentral distances (i.e. starting from 9 km inland in transect t02). As the simulations performed with the point source show, it is caused by the reflection of a shear wavefront

Table 9.1 Description of the main soil and rock formations used to define the transects. The following parameters are reported: density (ρ) compressional and shear wave velocities (V_p , V_s), and attenuation (Q). The attenuation is computed for a reference frequency of 2 Hz.

<i>Material description</i>	<i>Id</i>	ρ (km/m ³)	V_p (m/s)	V_s (m/s)	Q (s ⁻¹)
Clay and silt interbedded with sand	Asg	1950	490	250	12–20
Clay interbedded with sand	Aa _#	1950–2000	486–950	250–500	15–30
Fine alluvium deposits	Alf	1900	370	190	15
Recent alluvium deposits	Alg	1850	408	210	12
Beach deposits (sands)	M	1830	430	220	12
Filling material, soils, and detrita	R _#	1800–1900	400–480	210–250	12–15
Sand, coarse gravel, and conglomerate	SG _#	2000	858–875	450	20
Pliocenic sediments and alloctonous	Spa _#	2000–2150	1400–2800	775–1570	40–100
Scoriaceous and blocky lava	X	1800	408	230	15
Lava	E	2300	1730	1000	50–100
Vulcanits	V _#	2580–2630	3900–4100	2250–2335	100–120
Limestone (carbonatic basement)	Cc _#	2580–2835	4700–7000	2680–3970	120–300

Table 9.2 Source parameters adopted for the December 1 1, 1693 earthquake. The following parameters are reported: dimensions of the Ibleo-Maltese northern segment ($L \times W$), source mechanism (strike ϕ , dip δ , and rake λ), magnitude (M), seismic moment (M_0), stress-drop (σ), average value of the fault slip (D), and corner frequency (f_c).

$L \times W$	ϕ	δ	λ	M	M_0	$\Delta\sigma$	D	f_c
(km)	(degrees)	(degrees)	(degrees)		(Nm)	(bar)	(m)	(Hz)
15×25	352	90–65	–90	7	$2-3 \times 10^{19}$	150	1.2–1.3	0.7

from deep interfaces (S'_i in Figure 9.4) and occurs only for particular positions of the source with respect to the deep reflectors.

Local soil conditions strongly affect the response on a smaller spatial scale, and can change the amplitude dramatically. The ground motion amplitude is amplified by soft or moderately stiff sediments (e.g. at 4–6.5 km, 0–2.5 km, 1.5–3 km, and 2.5–4 km in transects t02, t05, t01, and t03, respectively (Figure 9.5)), and the highest peaks are found especially at the transition between lava and sediments. Thus, seismograms over lava or soft sediments may differ by a factor of two even at a very short distance.

To demonstrate the method's effectiveness, the results obtained along one transect only, namely transect t03, are discussed in more detail. The surface structure (Figure 9.6a) is characterised by two stiff and thick lava banks. The horizontal PGA (Figure 9.5) features a peak ($>0.5g$) at 2.5–4 km from the coastline, where the soft and low velocity soil outcrops. The ground motion can be better understood by looking at the acceleration response spectra along the surface (Figure 9.6b). Below 1.5 Hz, the amplitude decays rather smoothly with increasing epicentral distance, and has no local anomalies. At higher frequencies,

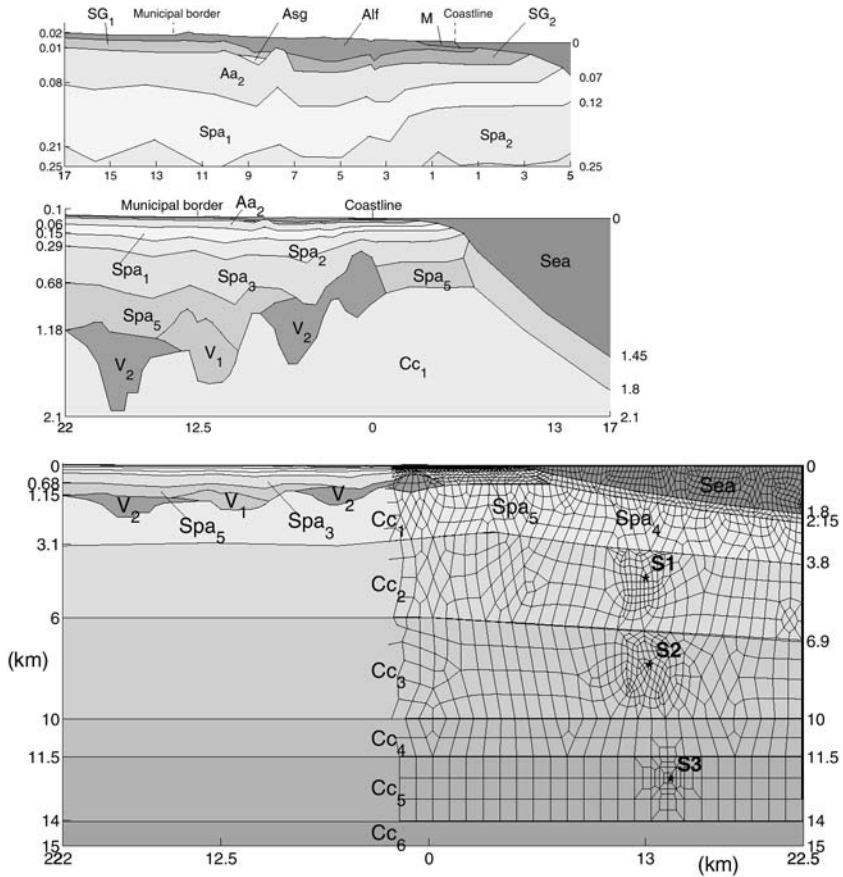


Figure 9.3 Transect t02: model structure and source position. The bottom panel shows the whole model with part of the spectral element mesh superimposed on it. The upper two panels zoom progressively into the near surface part of the velocity model. Units are in m. East and West correspond to positive and negative abscissas, respectively. The vertical scale is exaggerated, and different horizontal/vertical ratios are used for each panel. Material parameters are described in Table 9.1 (from Priolo (1999)).

the zone of the largest amplification corresponds to that of the largest PGA (2.8–3.7 km). In this zone, three almost evenly spaced peaks are distinguished. The largest peak falls on the transition between stiff/scoriaceous lava to soft soil. Here, the amplification is increased by the irregular geometry of the western edge of the lava bank, which traps energy. The Arias intensity displayed in Figure 9.6c shows that the maximum seismic destructiveness falls exactly where the ground motion is strongly amplified. The peak values are of about $I_A=500$ cm/s. Figure 9.6e and f directly compare the ground motion predicted at two near receivers located on lava and on soft soil, respectively. Seismograms feature a nearly impulsive response on lava, while a ringing effect and longer coda can be

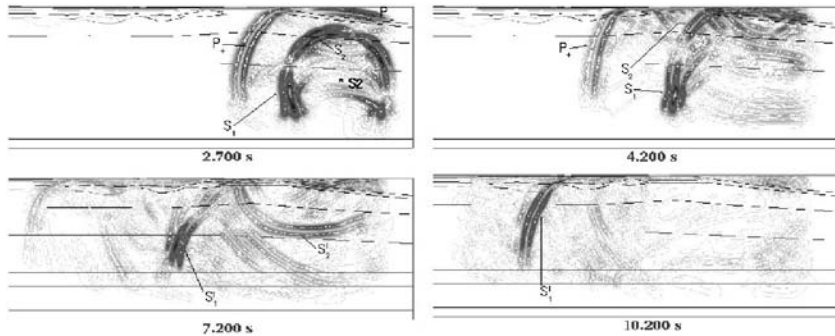


Figure 9.4 Snapshots of the acceleration wavefield (amplitude) for the point source (indicated by a * S2 in the first panel) with dip equal to 65° . Propagation times are indicated at the bottom of each panel. Letters mark the main wavefronts: P_+ and P_- the dilatational and compressional wavefronts of the pressure wave, respectively; S_1 and S_2 the shear wavefronts of the lobes orthogonal to and in-line with the fault plane, respectively. The quote indicates reflected wavefronts. At model boundaries the wavefield is attenuated by the presence of absorbing strips (from Priolo (2001)).

seen at the receiver on soft soil, as a result of the energy that is trapped within the uppermost layers. The response spectra confirm this analysis, although the vertical component features a smaller amplification, which is localised in a higher frequency band (3–5 Hz).

A rather important consideration is that the most dangerous frequencies for civil buildings, that is 1.5–4 Hz, are amplified mostly in the horizontal components. They correspond to the eigenfrequencies of a stack of sediment layers about 30–100 m thick, where the average shear-wave velocity is about 500–600 m/s. On the other hand, the very thin and soft superficial layers (e.g. R_2 in *Figure 9.6a*), are too thin to interfere constructively with the exciting wavefield. They just increase the overall amplitude. It follows that, for a reliable prediction of the strong ground motion, a detailed knowledge of the seismic properties of the uppermost layers, down to a depth of about 100–150 m, is of crucial interest.

Finally, *Figure 9.6d* shows the maximum displacement difference predicted along the transect surface. This quantity may be important for predicting damage to lifelines and bridges. As expected, the largest values (about 2.5 cm for a distance of 50 m) occur at the transition between lava and soft soil.

No records are currently available for earthquakes occurring along the fault segment considered in this study. Therefore, the approach was validated by simulating a nearby event which occurred recently (Priolo, 2000). This earthquake is the *M*5.7 earthquake, which struck Eastern Sicily on December 13, 1990. It is associated to the rupture of the transcurrent segment of the Ibleo-Maltese fault, and was recorded by the Catania station of the ENEA-ENEL accelerometric network (CAT in *Figure 9.2*).

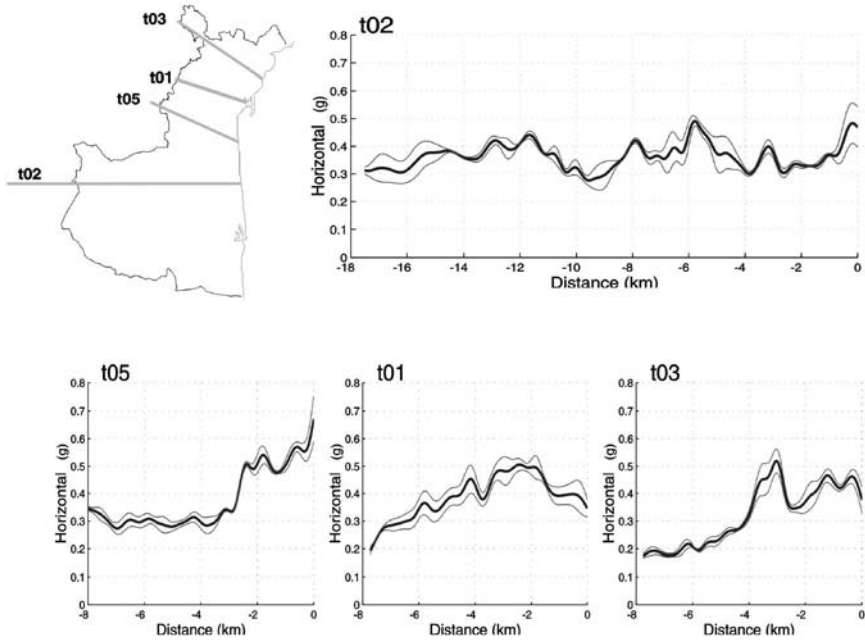


Figure 9.5 PGA envelopes at the surface of transects t02, t01, t05, and t03, respectively, for the catastrophic earthquake of January 11, 1693. The envelopes are computed for the extended source with three different kinds of rupture propagation. The thick and thin lines represent the mean and the mean plus/ minus the first standard deviation, respectively. Values represent the average of the two horizontal components. The abscissa represents the distance from the coastline. Decreasing abscissas correspond to westward direction and increasing epicentral distances. The coastline-epicenter distance (reference epicenters are indicated by gray circles in Figure 9.2) is 14.5 km for transects t05 and t03, and 13 km for transects t01 and t02, respectively (from Priolo (2001)).

The computational model is defined along transect t06. The structure is consistent with that of the other transects of this study. The source is a point, and the fault mechanism is defined by $(\phi, \delta, \lambda) = (96^\circ, 85^\circ, 180^\circ)$. Corner frequency, source depth, and fault-slip amplitude are set at $f_c = 1.3$ Hz, $z_s = 20$ km, and $D = 0.7$ m, respectively. Seismograms are computed up to a maximum frequency of 6 Hz and for a total propagation time of 40 s.

Figure 9.7 displays seismograms predicted at and recorded by the ENEA-ENEL Catania station. They compare well in terms of the overall shape, polarity of the main arrivals, S-wave amplitude, and seismogram duration. A slightly larger amplification of all P-waves is observed in the synthetics (e.g., in the early 4 s). This can be ascribed to the rather low V_p values imposed on the surface soils, and needed to overcome the inability of the method to deal with surface soils characterised by large V_p/V_s ratios. Also, it is noted here that, even if a simple point source is adopted, the calculated seismograms are extremely

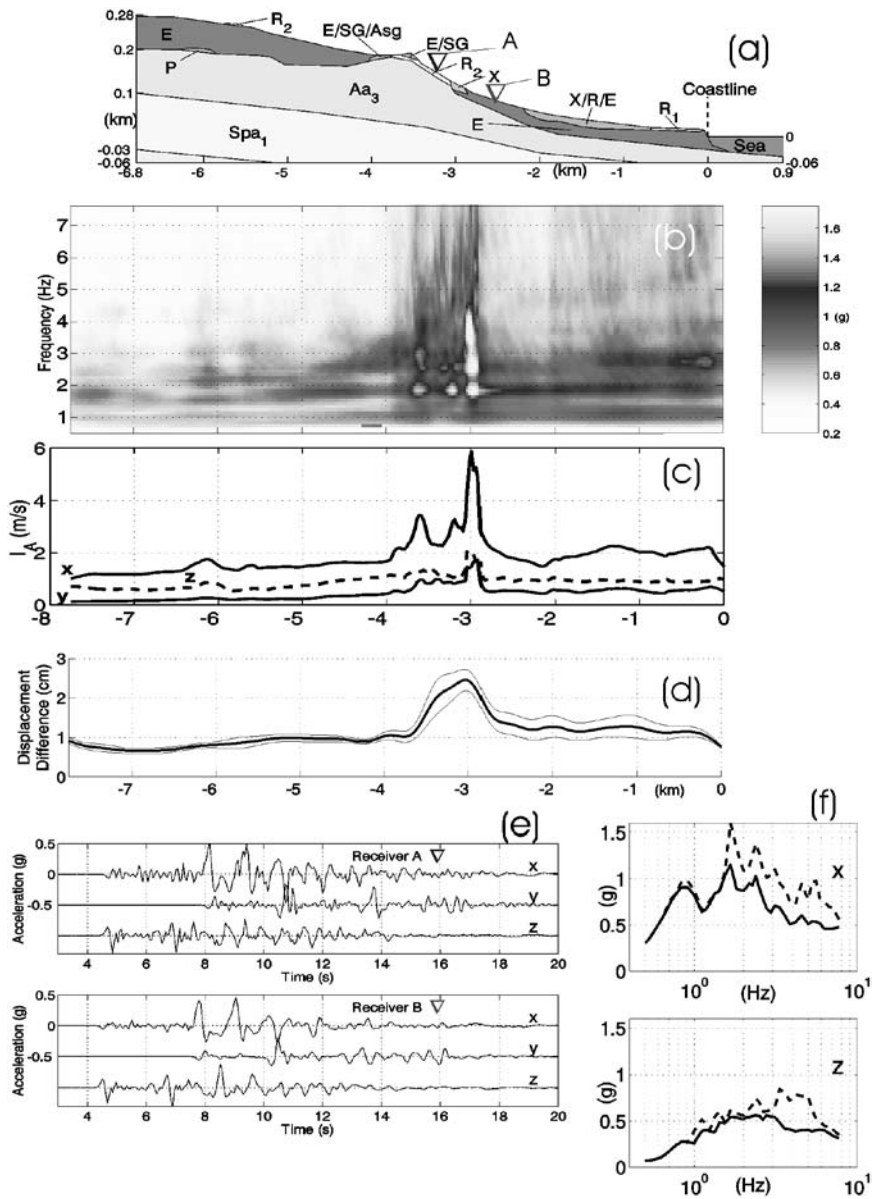


Figure 9.6 Transect t03. (a) Detail of the uppermost part of the model. See Table 9.1 for the model parameters. Surface distribution of (b) response spectra (5% damping) and (c) displacement difference (horizontal component) computed for a receiver distance $x=50$ m. (d) Seismograms (three components) and (e) response spectra (radial and vertical components) predicted at two near receivers (see panel (a)) located on sediments (A) and lava (B), respectively (from Priolo (2000)).

realistic. This supports the need for methods that accurately model realistic geologic structures.

In addition to the earthquake data, environment microtremors were recorded at the same site of the Catania station (Priolo *et al.*, 2001). The aim of this data acquisition was to improve our prediction of the seismic ground motion locally. To this end, Nakamura's approach was followed which, as proven, provides the main features of the dynamic ground response through the calculation of the spectral ratio between the horizontal and vertical components (i.e., H/V ratio) of background microtremors (Nakamura, 1989). In [Figure 9.8](#), the H/V spectral ratios obtained from (i) the environment seismic noise, (ii) the seismograms recorded by the accelerometric station during the December 13, 1990 $M=5.8$ Eastern Sicily earthquake, and (iii) the seismograms computed by the 2-D spectral element method for the same earthquake, are compared. The ratios obtained from the seismic noise measurements well detect the fundamental mode of vibration at about 1.5 Hz, but they miss the peak at the higher frequency of 4–5 Hz. This fact may either confirm that Nakamura's method is only reliable for identifying the fundamental mode of vibration, or that the peak at 4–5 Hz in the earthquake records is a feature of the earthquake source. The H/V ratios determined from the synthetic seismograms are generally noisier, but they well reproduce the behaviour of the spectral ratios determined from the full ENEA-ENEL recordings for frequencies larger than 1 Hz. The origin of the two additional peaks at 0.4–0.8 Hz is currently under investigation.

Influence of a massive structure on the free surface ground motion

In this study, the 2-D SPEM was used to investigate how seismic ground motion is affected by the presence of a massive structure. The analysis of soil-structure interaction in seismic hazard studies is usually concerned with its influence on the response of and damage to the structure itself. One should expect, however, that large massive loads perturb the free-field ground motion in their surroundings. Recent numerical investigations indicate, in fact, that long-range soil-structure interaction for large buildings may have had a role in determining the abnormal amount of damage on the Mexico City clay basin during the 1985 Michoacan earthquake (Wirgin and Bard, 1996). The aim of this work was to investigate how much, and over what distance range, surface loads alter the free-field ground motion.

Two-dimensional models were considered where a linear elastic structure with a quadrangular cross-section, resting on an elastic homogeneous half-space, is impinged upon by the surface waves generated by a vertical and impulsive point source located on the ground surface at some distance ([Figure 9.9](#)). The scattering of Rayleigh waves and the response of the structure are extensively analysed in a parametric way: by varying the size, mechanical parameters, and

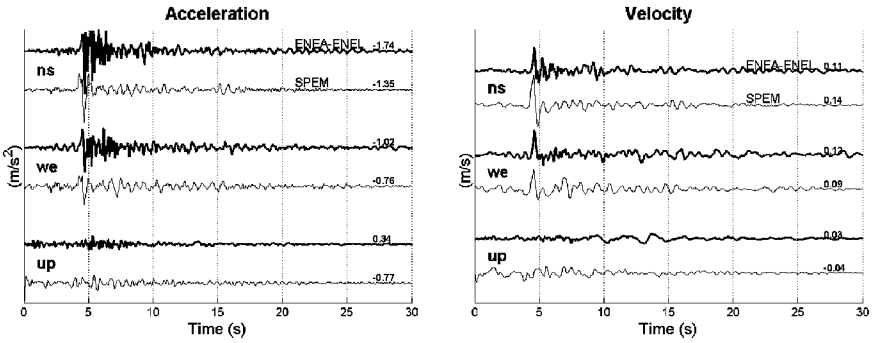


Figure 9.7 The December 13, 1990, M5.8 eastern Sicily earthquake. Three-component acceleration (left panel) and velocity (right) seismograms recorded by ENEA-ENEL Catania station (thick lines), and those predicted using 2-D spectral element modeling (thin lines). The ENEA-ENEL seismograms are band-pass filtered at 0.25-6 Hz. The ENEA-ENEL velocity is obtained by time integration of the acceleration records. The origin time of predicted seismograms has been aligned to that of the recorded seismograms (from Priolo (2001)).

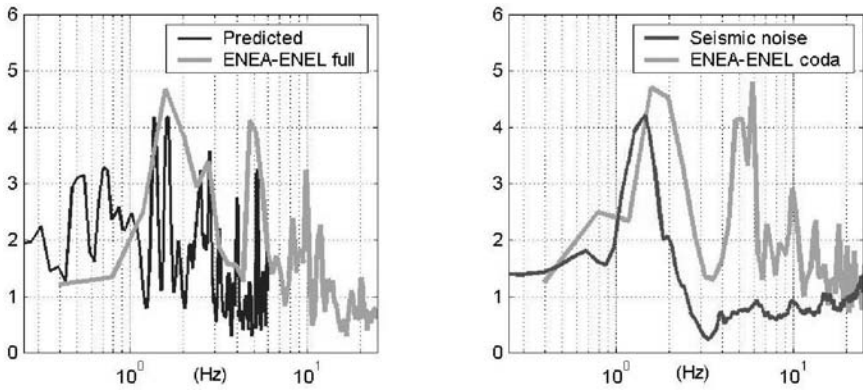


Figure 9.8 H/V spectral ratios computed for the ENEA-ENEL Catania station. Both panels, gray curves: ratios determined from the recordings of the December 13, 1990 Eastern Sicily earthquake (full record and coda from 20 to 45 s, left and right panels, respectively). Left panel, black curve: ratio simulated for the same event and using the SPEM 2-D spectral element code. Right panel, black curve: ratio obtained from the seismic noise measurements (from Priolo 2000)).

shape of the load. Some of the models considered are representative of embankments and earth dams.

In the experiments, the source is applied at a distance of 3600 m from the massive load. The time history is a Ricker wavelet with central frequency $f_c=6$ Hz. The computational domain is decomposed into 35×10 elements of order $N=6$. The embankment is made up of one additional element (Figure 9.10). The mesh is regular everywhere, except for a column of elements underlying the structure.

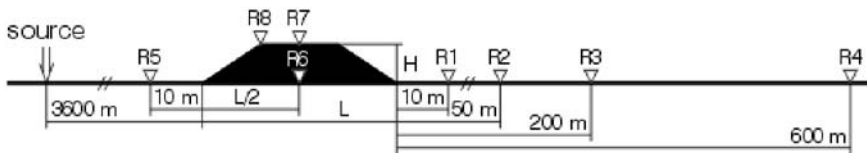


Figure 9.9 Simplified model of a massive structure. The picture shows the model geometry and the locations of source and receivers (triangles). The structure height H is held fixed at 10 m in all experiments (from Chiaruttini *et al.* (1996)).

The size of the rectangular elements in the half-space is equal to $180 \text{ m} \times 180 \text{ m}$, and corresponds to $G=5.2$ nodes per minimum wavelength.

The simulations show that some models indeed resonate, storing part of the incoming energy. With realistic parameters, the lowest resonance frequency is due to pure shear deformation and is controlled by the shear velocity V_s and height H of the load ($f=V_s/4H$), rather than by the inertial properties. Flexural modes are excited only at higher frequencies. The acceleration predicted at the top of the structure may be 5 to 7 times higher than at the base, depending on the mass of the structure (Figures 9.11 and 9.12). The gradual release of trapped energy produces a ground-roll which lasts several seconds after the wave front has passed. The ground-roll amplitude depends on the structure's mass and can be as large as 30% of the peak acceleration. Outside the resonance conditions, the ground motion is almost unaffected by the presence of the artifact, and the horizontal motion on top of it is nearly twice the motion at ground level. The shape of the embankment has only a marginal influence. The perturbation obviously reaches its highest values close to the structure, but it may still be relevant at several hundred metres distance (Figure 9.12), especially for the largest structures. For instance, for an embankment with $L=200 \text{ m}$ and $H=10 \text{ m}$, the level of ringing remains as high as 25%, up to distances of at least 600 m. Similar results should be expected when the incident field is an upcoming shear wave. Finally, the presence of an elastic attenuation in the embankment does not significantly alter the preceding conclusions, unless it has very high values (e.g. $Q<15$).

The modelling results indicate that the soil-structure interaction may substantially alter the free-field ground motion. From a practical point of view, the main conclusions of this study are: (1) careful analysis is necessary when interpreting seismic records collected in the vicinity of large artifacts; (2) seismic hazards at a site may depend on the presence of man-made structures such as embankments, dams, tall and massive buildings. Finally, this study can easily be extended to simulate the presence of multiple structures.

Conclusions

In this paper, the 2-D Chebyshev spectral element method (SPEM) to help solving engineering seismology problems has been reviewed. Its effectiveness in

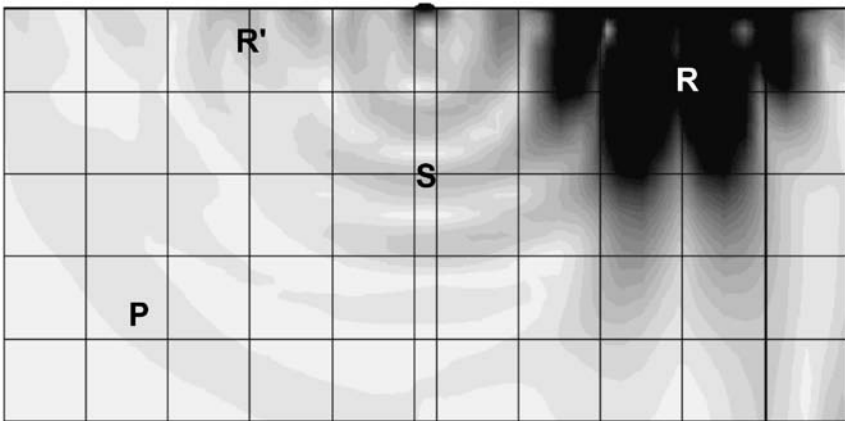


Figure 9.10 Resonant scattering of the Rayleigh wavefield. The letters indicate the incoming Rayleigh wave (R), and the scattered pressure (P), shear (S), and Rayleigh waves (R'), respectively. The picture also shows part of the computational mesh near the massive structure (from Chiaruttini *et al.* (1996)).

tackling real cases has been demonstrated by two case histories, i.e. the estimation of ground shaking in the area of Catania (Sicily, Italy), and the study of the influence of a massive structure on the nearby ground motion. In the present implementation, the approach has some drawbacks (Priolo, 2001), such as the difficulty of generating the quadrangular mesh, the sporadic occurrence of numerical instabilities resulting in large problems, as well as the heavy computational needs related to the use of global matrices. However, recent work carried out by several authors clearly shows the still large possibilities of improvement.

Acknowledgements

This work has been partially funded by the *National Group for the Defence Against Earthquakes (GNDT)*. Figure 9.2 was made by GMT software (Wessel and Smith, 1995). I wish to thank Giovanna Laurenzano for her recent contribution to the improvement of the method.

Figure 9.3 is reprinted *Journal of Seismology*, Vol 3, 2001, pp. 289–309, Priolo, E., ‘2-D spectral element simulations of destructive ground shaking in Catania (Italy)’, Figure 2, with kind permission of Kluwer Academic Publishers.

Figures 9.9, 9.10, 9.11 and 9.12 are reprinted from *Soil Dynamics and Earthquake Engineering*, Vol 15, Chiaruttini, C., Grimaz, S., and Priolo E., ‘Modelling of ground motion in the vicinity of massive structures’, Figures 3, 5, 9 and 14, pp. 75–82, 1996, with permission of Elsevier Science.

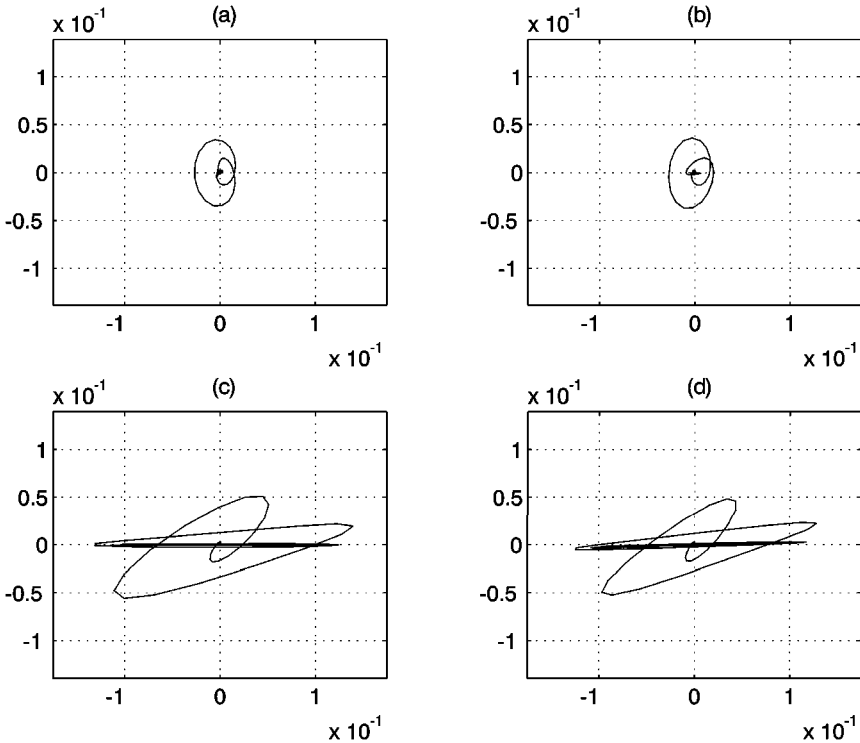


Figure 9.11 The trapezoidal resonant model with $L=50$ m. Displacement hodograms in the vertical plane at ground level (receivers (a) R5 and (b) R6) and on top of the structure level (receivers (c) R7 and (d) R8), respectively (from Chiaruttini *et al.* (1996)). A shear resonance features the ground motion at the top of the structure.

References

- Canute, C., Hussaini, M.Y., Quarteroni, A., and Zang, T.A. (1988) *Spectral Methods in Fluid Dynamics*, New York: Springer-Verlag.
- Cerjan, C., Kosloff, D., Kosloff, R., and Reshef, M. (1985) 'A nonreflecting boundary condition for discrete acoustic and elastic wave equations', *Geophysics* 50:705–708.
- Chiaruttini, C., Grimaz, S., and Priolo, E. (1996) 'Modelling of ground motion in the vicinity of massive structures', *Soil Dynam. Earthq. Eng.* 15:75–82.
- Eringen, A.C., and Suhubi, E.S. (1975) *Elastodynamics, Vol. II: Linear Theory*, Academic Press.
- Faccioli, E., Maggio, F., Quarteroni, A., and Tagliani, A. (1996) 'Spectral-domain decomposition methods for the solution of acoustic and elastic wave equations', *Geophysics* 61:1160–1174.
- Graves, R.W. (1996) 'Simulating seismic wave propagation in 3D elastic media using staggered-grid finite-differences', *Bull. Seism. Soc. Am.* 86:1091–1106.

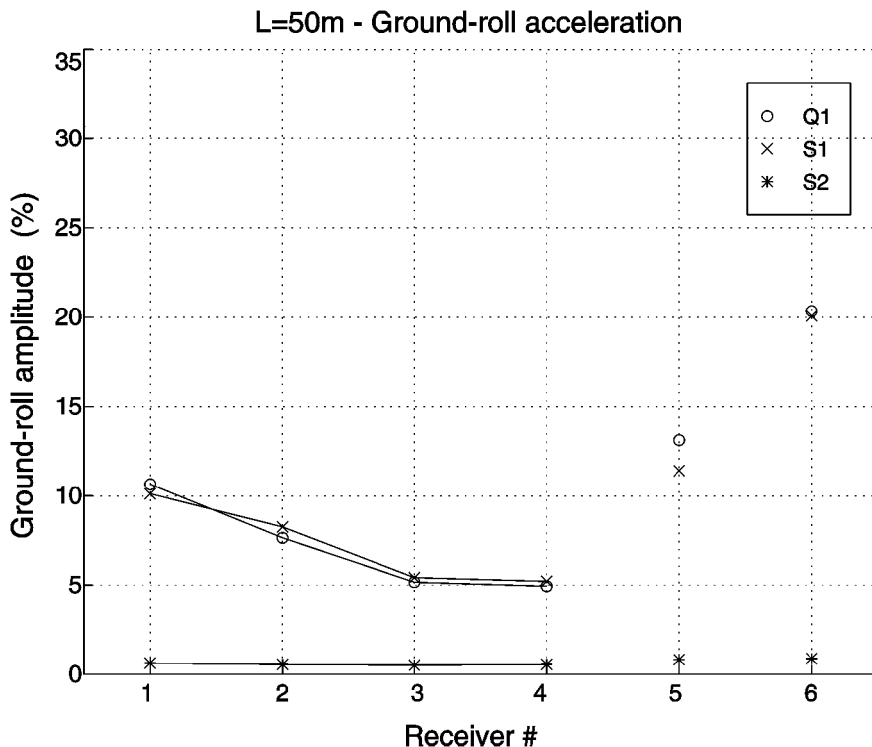


Figure 9.12 Amplitude of the horizontal component of ground-roll acceleration at different receivers located at ground level compared with the peak acceleration. Models with $L=50$ m: Q1: rectangular shape, $V_s=290$ m/s; S1: trapezoidal shape, $V_s=290$ m/s; S2: trapezoidal shape, $V_s=580$ m/s (from Chiaruttini *et al.* (1996)).

Hartzell, S., Cranswick, E., Frankel, A., Carver, D., and Meremonte, M. (1997) 'Variability of site response in the Los Angeles urban area', *Bull. Seis. Soc. Am.* 87: 1377–1400.

Hughes, T.J.R. (1987) *The finite element method*, New Jersey: Prentice-Hall.

Komatitsch, D., and Vilotte, J.-P. (1998) 'The spectral element method: an efficient tool to simulate the seismic response of 2D and 3D geological structures', *Bull. Seis. Soc. Am.* 88:368–392.

Laurenzano, G., and Priolo, E. (2001) 'Modeling of seismic wave propagation with optimally varying mesh size', *Proc. 10th Int. Conf. on Soil Dynamics and Earthquake Engineering (SDEE '2001)*, Philadelphia, USA, October 7–10, 2001.

Murfurt, K.J. (1984) 'Accuracy of finite-difference and finite-element modelling of scalar and elastic wave-equations', *Geophysics*, 49, 5:533–549.

Nakamura, Y. (1989) 'A method for dynamic characteristics estimation of subsurface using microtremor on the ground surface', *QR Railway Tech. Res. Inst.* 30, 1:25–33.

Padovani, E., Priolo, E., and Seriani, G. (1994) 'Low- and high-order finite element method: Experience in seismic modeling', *J. Comp. Acoust.* 2:371–422.

- Priolo, E. (1998) '2-D crustal models for ground shaking estimations in the municipal area of Catania (Sicily, Italy)', in P.Bisch, P.Labbé, and A.Pecker (eds) *Proc. 11th Europ. Conf. Earth. Eng.*, Paris, 6-11 Sept., 1998, Abstract Volume and CD-ROM.
- Priolo, E. (1999) '2-D spectral element simulations of destructive ground shaking in Catania (Italy)', *J. of Seismology* 3:289-309.
- Priolo, E. (2000) 'Spectral element simulation of the ground motion for a catastrophic earthquake', in Faccioli, E., and Pessina, V. (eds) *The Catania Project: Earthquake damage scenarios for a high risk area in the Mediterranean*, Rome: CNR-GNDT, 225 pp. 67-73.
- Priolo, E. (2001) 'Earthquake ground motion simulation through the 2-D spectral element method', *J. Comp. Acoust.* 9, 4:1561-1582.
- Priolo, E., and Seriani, G. (1991) 'A numerical investigation of Chebyshev spectral element method for acoustic wave propagation', in R.Vichnevetsky (ed.) *Proc. 13th IMACS Conf. on Comp. Appl. Math.*, Dublin, 551-556
- Priolo, E., Carcione, J.M., and Seriani, G. (1994) 'Numerical simulation of interface waves by high-order spectral modeling techniques', *J. Acoust. Soc. Am.* 95:681-693.
- Priolo, E., Michelini, A., Laurenzano, G., Addia, R., and Puglia, A. (2001) 'Seismic response from microtremors in Catania (Sicily, Italy). *Boll. Geof. Teor. Appl.*; Special Issue on: Site Response Estimation from Observed Ground Motion Data. E.Priolo, A. Michelini, and L.Huitchings (eds) 42, (3-1):337-362.
- Seriani, G. (1997) 'A parallel spectral element method for acoustic wave modeling', *J. Comp. Acous.* 5:53-69.
- Seriani, G. (1998) '3-D large-scale wave propagation modeling by spectral element method on Cray T3E multiprocessor', *Comp. Meth. in Appl. Mech. Eng.* 164: 235-247.
- Seriani, G., and Priolo, E. (1991) 'High-order spectral element method for acoustic wave modeling', in *Expanded abstracts of Seg. 61st Ann. Int. Mtg.*, Houston, Texas, Vol 2, Soc. Expl. Geophys., 1561-1564.
- Seriani, G., and Priolo, E. (1994) 'Spectral element method for acoustic wave simulation in heterogeneous media', *Finite Elements in Analysis and Design* 16:337-348.
- Seriani, G., and Priolo, E. (2000) 'Heterogeneous Chebyshev spectral elements for acoustic wave modelling', in E.Ornate, G.Bugeda, and B.Suarez (eds), *ECCOMAS 2000: Finite element schemes for waves problems*. CIMNE Publ., Barcelona, Spain. 13 pp., CD-ROM.
- Seriani, G., Priolo, E., and Pregarz, A. (1995) 'Modelling waves in anisotropic media by a spectral element method', in Cohen, G. (ed.) *Mathematical and numerical aspects of wave propagation*, SIAM-INRIA, 289-298.
- Seriani, G., Priolo, E., Carcione, J.M., and Padovani, E. (1992) 'High-order spectral element method for elastic wave modeling, in *Expanded Abstracts of Sef. 62nd Ann. Int. Mtg.*, New-Orleans, Louisiana, Soc. Expl. Geophys., 1285-1288.
- Siro, L. (Scient. Resp.) (1992) *Valutazione quantitativa del pericolo di liquefazione del terreno in siti ubicati nella regione del Friuli. Rapporto della fase 4 del contratto; Modellazione. Conclusioni finali*. Osservatorio Geofisico Sperimentale (OGS), Trieste, Italy. In Italian.
- Wessel, P., and Smith, W.H.F. (1995) 'New version of the Generic Mapping Tools', *EOS Trans. American Geophysical Union* 76:329 pp.
- Wirgin, A., and Bard, P.Y. (1996) 'Effects of building on the duration and amplitude of ground motion in Mexico City', *Bull. Seism. Soc. Am.* 86:914-920.

Zienkiewicz, O.C., and Wood, W.L. (1987) 'Transient response analysis', in H. Kardestuncer and D.H.Norrie (eds) *Finite Element Handbook*, McGraw-Hill, 2.275–2.314.

Chapter 10

Analysis and design of pile groups

F.Basile

Introduction

In his 2000 Rankine Lecture, Professor Atkinson has emphasised the importance of considering soil non-linearity in routine design. For pile group problems, this issue has not yet been satisfactorily addressed, and current design practice is still generally based on linear approaches. The main drawback to the application of linear models to pile group problems is that they ignore the non-linear load-deformation characteristics of soil and hence misrepresent the forces in piles, specifically by giving higher stresses in group corners. The cost of this in practice is high and there is an urgent need in industry for efficient non-linear analysis methods.

An attempt at removing these limitations is represented by the load-transfer approach which is the most widely adopted technique for the non-linear analysis of single piles. However, this approach suffers from some significant restrictions when extended to pile group problems.

A more practical non-linear approach for the analysis of pile groups under general loading conditions (i.e. vertical loads, horizontal loads and moments) has recently been proposed by Basile (1999) and some further developments and applications of the method are described in this chapter. A review of available computer programs for pile group analysis is presented, including some applications in both the linear and non-linear range. The critical question of estimation of geotechnical parameters is addressed, and attention is focused on correlations between these parameters and commonly available *in situ* test data. Finally, attention is turned to the application of available numerical methods to practical problems involving real soils. A number of published case histories are considered, and the predictions from selected methods of analysis are compared with the field measurements.

Numerical methods for pile group analysis

Estimation of the deformations and load distributions in a group of piles subjected to general loading conditions normally requires the use of computer-

based methods of analysis. Numerical techniques for pile group analysis may be broadly classified into the following two categories:

- (a) continuum-based approaches;
- (b) load-transfer (or subgrade reaction) approaches.

The latter category, based on Winkler spring idealisation of the soil, employs load-transfer functions to represent the relationship between the load at any point along the pile and the associated soil deformation at that point. Such a semi-empirical method is widely adopted for the analysis and design of single piles, especially where non-linear soil behaviour has to be considered and/or soil stratification is complicated (e.g. the “*t-z*” or “*p-y*” curve methods of analysis). The computer programs PILGP1 (O’Neill *et al.*, 1977), FLPIER (Hoit *et al.*, 1996) and GROUP (Reese *et al.*, 2000) are included in this category. The main limitations associated with this approach are as follows:

- 1 The modulus of subgrade reaction is not an intrinsic soil property but instead gives the overall effect of the soil continuum as seen by the pile at a specific depth, and hence its value will depend not only on the soil properties but also on the pile properties and loading conditions. Thus, no direct tests can be conducted to establish force-displacement relationships for that particular pile and soil type, and hence these curves have to be derived from the data obtained by conducting a field test on an instrumented pile. However, due to the high costs, such a test is rarely justifiable for onshore applications and hence standard load-transfer curves are usually adopted in practice. This implies that a significant amount of engineering judgement is needed when formulating these curves for site conditions which differ markedly from the recorded field tests. Murchison and O’Neill (1984) have compared four commonly adopted procedures for selecting *p-y* curves with data from field tests, and their results show that errors in pile-head deflection predictions could be as large as 75%. Huang *et al.* (2001) employed several sets of *p-y* curves derived from DMT data for the analysis of laterally loaded piles, and none of the *p-y* curves yielded reasonable predictions of the measured pile deflections.
- 2 The load-deformation relationship along the pile is modelled using discrete independent springs and no information is available from the analysis regarding the deformation pattern around the pile. Disregarding continuity through the soil makes it impossible to find a rational way to quantify the interaction effects between piles in a group. Thus, in evaluating group effects, recourse is made to an entirely empirical procedure in which the single pile load-transfer curves are modified on the basis of small-scale and full-scale experiments performed on pile groups in different types of soil. Although Reese and Van Impe (2001) reported some successful analyses of this kind for pile groups under lateral loading, the uncertainties on the

general use of the approach in routine design remain (Rollins *et al.*, 1998; Rollins *et al.*, 2000; Huang *et al.*, 2001).

- 3 It is uncertain how the p - y curves are influenced by pile-head fixity. To date, this issue has hardly been addressed, although Reese *et al.* (1975) showed that the p - y relationships are affected by pile-head fixity. The relevance of this aspect is obvious if the p - y curves from single pile tests are to be used for pile group predictions where the pile-heads are restrained by a cap.

In conclusion, the load-transfer approach may be regarded as a link between the interpretation of full-scale pile tests and the design of similar piles rather than a general design tool for pile group predictions.

Several hybrid approaches which combine a load-transfer analysis for single pile response and a continuum model to estimate pile-soil-pile interaction have been proposed (Chow, 1986a, 1987; Mandolini and Viggiani, 1997). However, such analyses do not overcome the main limitation of the load-transfer approach that is the questionable assessment of the empirical constants which define the non-linear relationship on the basis of intrinsic soil properties.

The above shortcomings may be removed by means of soil continuum based solutions which are generally based on the finite element method (FEM) (Ottaviani, 1975) or the boundary element method (BEM) (Butterfield and Banerjee, 1971). These solutions provide an efficient means of retaining the essential aspects of pile interaction through the soil continuum and hence a more realistic representation of the problem. Further, the mechanical characteristics to be introduced into the model now have a clear physical meaning and they can be measured directly. Finite element analyses are valuable for clarifying the mechanism of load transfer from the pile to the surrounding soil but, especially for pile groups, are not readily applicable to practical problems. The considerable effort of data preparation and the high computational cost (particularly if non-linear soil behaviour is to be considered) preclude the routine use of such techniques in design. Some idea of the computational resources required may be obtained from the non-linear FEM analysis of a laterally loaded 9-pile group by Kimura and Adachi (1996) who reported a CPU time of 85 hours on a SPARC II work-station.

By contrast, BEM provides a complete problem solution in terms of boundary values only, specifically at the pile-soil interface. This leads to a drastic reduction in unknowns to be solved for, thereby resulting in substantial savings in computing time and data preparation effort. This feature is particularly important for three-dimensional problems such as pile groups.

The following computer programs may be included in this category. DEFPIG (Poulos, 1990), based on a simplified BEM analysis and the use of interaction factors, models soil non-linearity in an approximate manner by means of an elastic-plastic interface model. Two main shortcomings are associated with this model: (1) the non-linear features of stress-strain behaviour are not captured

until the load corresponding to the yield of the first interface element is reached; (2) deformations are often seriously underestimated at high load levels. An alternative approach is offered by the widely used computer program MPILE, originally developed by Randolph (1980) under the name of PIGLET. The analysis is based on a semi-empirical method which makes use of approximate analytical solutions for single pile response and for interaction between two piles, in which linear elastic soil behaviour is assumed.

It is important to note that the interaction factor approach (such as is employed in DEFPIG and MPILE) solves the group problem by calculating the influence coefficients for each pair of piles and by merely superimposing the effects. This approximate procedure produces a number of limitations: (a) it ignores the stiffening effect of intervening piles in a group, thereby leading to an overestimation of interaction between piles; (b) its use becomes questionable for cases in which not all the piles are identical; (c) it only gives the loads and bending moments at the pile heads, but not their distributions along the piles; these may only be approximated utilising the single pile solutions with the corresponding pile head loads and bending moments.

The above limitations on the use of interaction factors may be removed by simultaneous consideration of all the piles within the group, i.e. performing a "complete" analysis of the group. The computer program PGROUP, originally developed by Banerjee and Driscoll (1976), is included in this category but is restricted to linear elastic analyses and problems of small dimensions because of the very large computational resources required. The latter aspect makes the program inapplicable in normal design. An even more rigorous linear analysis is performed by the numerical code GEPAN (Xu and Poulos, 2000) in which the boundary elements are meshed in partly cylindrical or annular surfaces. The program provides a benchmark for assessing the accuracy of simplified procedures in the linear range and can also analyse loadings induced by ground movements. However, the relatively high computational cost makes questionable its potential use for routine design problems.

The main feature of the proposed PGROUPN program (Basile, 1999) lies in its capability to provide a complete non-linear BEM solution of the soil continuum while retaining a computationally efficient code. One of the main advantages of a non-linear analysis system over a linear one is that it has the desirable effect of demonstrating a relative reduction of the corner loads in pile groups in both the vertical and horizontal senses. This observation is of basic importance in practice, and offers the prospect of significant improvements in design techniques and potential saving of materials. The choice of soil parameters for PGROUPN is simple and direct: for a linear analysis, it is only necessary to define two soil parameters whose physical interpretation is clear, i.e. the soil modulus (E_s) and the Poisson's ratio (ν_s). If the effects of soil non-linearity are considered, the strength properties of the soil also need to be specified, i.e. the undrained shear strength (C_u) for cohesive soils and the angle of friction (ϕ') for cohesionless soils. These parameters are routinely measured in

soils investigation. This aspect represents a significant advantage over the t - z and p - y curve approaches which are based on empirical parameters which may only be derived from the results of pile load tests. However, in many practical situations it is not possible to carry out such testing, at least in the preliminary stages of design.

A summary of the main capabilities and limitations of some of the computer programs discussed above is presented in [Table 10.1](#).

Load distribution in pile groups

The distribution of load between piles in a group is of basic importance in design. When a group of piles connected by a rigid “free-standing” cap (a common assumption for this kind of problem) is subjected to a system of vertical loads, horizontal loads and moments, the following features of behaviour play a major role in the prediction of the load distribution between the piles:

1 Pile-to-pile interaction

Due to pile-to-pile interaction, groups of piles tend to deform more than a proportionally loaded single pile. This is because neighbouring piles are within each others’ displacement fields and hence the load per pile to generate a given displacement is reduced for the central piles and increased for the outer ones. Therefore, in a group of piles, the distribution of load is not uniform, i.e. the corner piles carry the greatest proportion of load, while those near the centre carry least. This feature of behaviour is commonly modelled using the interaction factor approach (e.g. in MPILE and DEFPIG). However, as discussed previously, this approximate method suffers from some significant limitations.

2 Group stiffening effect

The simultaneous presence of all the piles within the soil mass has the effect of “stiffening” the soil continuum. Therefore, the central pile of a group (the most affected by the presence of the other piles) is subjected to a reduction of the head deformation due to the greater stiffness of the surrounding soil, “reinforced” by the presence of the other piles. This increased stiffness of the central pile results in a higher proportion of the applied load taken by the pile and hence the non-uniformity of load distribution resulting from pile-to-pile interaction (Feature No. 1) is reduced. It has been shown that these group stiffening effects are more marked in a laterally loaded pile group than in an axially loaded one (Burghignoli and Desideri, 1995; Basile, 1999), and they become more significant for increasing the number of piles in a group.

It is therefore important to recognise that each pile interacts with the surrounding soil with a twofold effect: on the one hand, the displacement of the other piles tends to increase as a result of the stresses transferred to the

Table 10.1 Capabilities and limitations of various computer programs for pile group analysis

<i>Program name</i>	<i>PGROUPN</i>	<i>MPILE</i>
<i>Latest version</i>	1.18	1.50
<i>Year</i>	2002	2000
<i>DOS User Interface</i>	Text Interface	Text Interface
<i>Windows User Interface</i>	Graphical Interface ⁽¹⁾	NA
<i>Max no. of piles</i>	200	100
<i>Max no. of pile elements</i>	50	No pile discretization
<i>Loading</i>	Vertical, horizontal and moment (note: horizontal loads and moments acting in two directions)	Vertical, horizontal, moment and torsional (note: horizontal loads and moments acting in two directions)
<i>General output</i>	Cap displacements and rotations; profiles of pile shear/normal stresses, axial/lateral loads and moments	Cap displacements and rotations; axial/lateral loads and moments at pile heads only; approximate profiles of moments
<i>Analysis method</i>	Complete BEM solution	Semi-empirical analysis using interaction factors
<i>Soil model</i>	Linear or non-linear (using hyperbolic continuum-based interface model)	Linear
<i>Soil profile</i>	Multi-layered	Homogeneous or Gibson
<i>Soil layer</i>	Finite or semi-infinite	Semi-infinite
<i>Soil modulus</i>	Independent profiles for axial and lateral loading	Independent profiles for axial and lateral loading
<i>Cap stiffness</i>	Fully rigid	Fully rigid or fully flexible (for vertical loading only)
<i>Cap-soil contact</i>	Non-effective	Non-effective
<i>Pile modulus</i>	Can vary	Same for all
<i>Pile lengths</i>	Can vary	Same for all
<i>Pile shaft diameters</i>	Can vary	Can vary
<i>Pile base diameters</i>	Can vary	Can vary
<i>Pile rake</i>	In two directions	In two directions
<i>Pile-head fixity at cap</i>	Rigidly fixed	Rigidly fixed or pinned

surrounding soil (Feature No. 1); this increase may be expressed in terms of “interaction factors”. On the other hand, by reinforcing the continuum in which the piles are located, the effects of interaction with the other piles are

Table 10.1

<i>PGROUP</i>	<i>DEFPIG</i>	<i>GROUP</i>
3.0	1.6	5.0
1981	1990	2000
NA	NA	NA
NA	NA	Graphical Interface
200	36	100
11	26 (under vertical loading), 50 (under horizontal loading)	100 ⁽²⁾
Vertical, horizontal and moment in one direction	Vertical, horizontal and moment in one direction	Vertical, horizontal, moment and torsional (note: horizontal loads and moments acting in two directions)
Cap displacements and rotation; normal stresses at cap-soil interface; profiles of pile shear/normal stresses, axial/lateral loads and moments	Cap displacements and rotation; approximate profiles of pile displacements, shear/normal stresses, axial/lateral loads and moments	Cap displacements and rotations; profiles of pile displacements, shear/normal stresses, axial/lateral loads and moments
Complete BEM solution	Simplified BEM analysis using interaction factors	Load-transfer approach (Winkler spring model)
Linear	Linear or non-linear (approximated using elastic-plastic interface model)	Non-linear (using $t-z$, $q-w$ and $p-y$ curves)
Homogeneous, Gibson or two-layered	Multi-layered	Multi-layered
Semi-infinite	Finite or semi-infinite	NA
Same profile for axial and for lateral loading	Independent profiles for axial and lateral loading	NA
Fully rigid	Fully rigid or fully flexible	Fully rigid
Effective or Non-effective	Effective or non-effective	Non-effective
Same for all	Same for all	Can vary
Can vary	Same for all	Can vary
Can vary	Same for all	Can vary
Can vary	Same for all	Equal to shaft diameters
In one direction	In one direction	In two directions
Rigidly fixed	Rigidly fixed or pinned	Rigidly fixed, pinned or restrained

Notes

NA=Not applicable; (1) available through Commercial Software Repute (Geocentrix, 2002); (2)=finite difference discretization.

decreased (Feature No. 2). The latter aspect cannot be reproduced in the interaction factor method and it can only be accounted for by a “complete” approach.

3 *Load-deformation coupling*

Pile-soil interaction is a three-dimensional problem, and each of the load components has deformation-coupling effects, i.e. there is an interaction between the axial and lateral response of the piles. Modelling of this aspect becomes important when a pile group is subjected to a combination of vertical and horizontal loads. In this case, only a proper consideration of the interaction between the axial and lateral response will lead to a realistic estimate of the loads acting on the piles, which will be increased for the piles in the leading rows and decreased for those in the trailing rows of the group. However, in current design practice, such interaction effects are not properly accounted for, and the axial and lateral responses of the piles are treated separately.

4 *Soil non-linearity*

A fundamental limitation of the linear elastic methods is that they result in a considerable overestimation of the load concentration at the outer piles of the group, and this may lead to an overconservative design. Indeed, it has long been recognised that consideration of soil non-linearity results in a reduction of the stiffness of the piles, the reduction being greater for piles at a greater load level, i.e. for the corner piles. Consequently, as the total applied load increases, the share of the load carried by the corner piles progressively decreases. This results in a redistribution of the loads in the individual piles, leading to a more uniform distribution than that predicted by linear models. Ideally, for an axially loaded pile group, all piles will carry the same load as the total applied load approaches the ultimate load capacity of the group.

Table 10.2 summarises the above-mentioned features and their effect on the prediction of load at group corners. The table also shows the ability of the computer programs discussed above to model such aspects of group behaviour. It is worth noting that all the features mentioned above may be modelled using the PGROUPN analysis, whereas the other programs can only model some of these aspects, thereby neglecting important features of group behaviour. There is thus a number of compelling arguments for adopting a design methodology which deals with group effects on a more fundamental basis.

PGROUPN method of analysis

The PGROUPN analysis is based on a complete non-linear BEM formulation, extending an idea first proposed by Butterfield and Banerjee (1971) and incorporated into a number of computer programs, including PGROUP (Banerjee and Driscoll, 1976), GAPFIX (Poulos and Hewitt, 1986) and that developed by

Table 10.2 Features of group behaviour and their effect on corner loads

Features of group behaviour	Effect on corner load	PGROUPN	MPILE	PGROUP	DEFFIG	GROUP
(1) Pile-to-pile interaction	↑	x	x	x	x	x
(2) Group stiffening effect	↓	x		x		
(3) Loading-deformation coupling	↑	x		x		
(4) Soil non-linearity	↓	x			x ⁽¹⁾	x

Note

× indicates capability: (1)=using elastic-plastic soil model

Burghignoli and Desideri (1995). The analysis involves discretisation of only the pile-soil interface into a number of cylindrical elements, while the base is represented by a circular (disc) element. The method employs a substructuring technique in which the piles and the surrounding soil are considered separately and then compatibility and equilibrium conditions are imposed at the interface. A description of the basic theoretical formulation of the PGROUPN analysis has been presented elsewhere (Basile, 1999) and hence only a brief description will be given here. However, the additional features that have recently been introduced will be described in some detail.

Soil domain

The boundary element method involves the integration of an appropriate elementary singular solution for the soil medium over the surface of the problem domain, i.e. the pile-soil interface. With reference to the present problem, the well-established solution of Mindlin (1936) for a point load within a homogeneous, isotropic elastic half-space has been adopted, yielding:

$$\{u_s\} = [G_s] \{t_s\} \quad (10.1)$$

where $\{u_s\}$ are the soil displacements, $\{t_s\}$ are the soil tractions and $[G_s]$ is the flexibility matrix obtained from Mindlin's solution. The singular part of the $[G_s]$ matrix is calculated via analytical integration of the Mindlin functions. This is a significant advance over previous work (e.g. PGROUP) where these have been integrated numerically, since these singular integrals require considerable computational resources.

Treatment of multi-layered soil profiles

Mindlin's solution is strictly applicable to homogeneous soil conditions. However, in practice, this limitation is not strictly adhered to, and the influence of soil non-homogeneity is often approximated using some averaging of the soil moduli. PGROUPN handles multi-layered soils according to the averaging procedure first examined by Poulos (1979) and widely accepted in practice (Chow, 1986a, 1987; Poulos, 1989, 1990; Xu and Poulos, 2000): in the evaluation of the influence of one loaded element on another, the value of the soil modulus is taken as the mean of the values at the two elements. This procedure is adequate in most practical cases but becomes less accurate if large differences in soil modulus exist between adjacent elements or if a soil layer is overlain by a much stiffer layer (Poulos, 1989).

Finite soil layer

Mindlin's solution has been used to obtain approximate solutions for a layer of finite thickness by employing the Steinbrenner approximation (Steinbrenner, 1934) to allow for the effect of the underlying rigid base in reducing the soil displacements (Poulos and Davis, 1980; Poulos, 1989).

Pile domain

If the piles are assumed to act as simple beam-columns which are fixed at their heads to the pile cap, the displacements and tractions over each element can be related to each other via the elementary beam theory, yielding:

$$\{u_p\} = [G_p]\{t_p\} + \{B\} \quad (10.2)$$

where $\{u_p\}$ are the pile displacements, $\{t_p\}$ are the pile tractions, $\{B\}$ are the pile displacements due to unit boundary displacements and rotations of the pile cap, and $[G_p]$ is a matrix of coefficients obtained from the elementary (Bernoulli-Euler) beam theory.

Solution of the system

The soil and pile equations (10.1) and (10.2) may be coupled via compatibility and equilibrium constraints at the pile-soil interface. Thus, by specifying unit boundary conditions, i.e. unit values of vertical displacement, horizontal displacement and rotation of the pile cap, these equations are solved, thereby leading to the distribution of stresses, loads and moments in the piles for any loading condition.

Limiting pile-soil stresses

It is essential to ensure that the stress state at the pile-soil interface does not violate the yield criteria. This can be achieved by specifying the limiting stresses for the soil.

Cohesive soil

For cohesive soils, a total stress approach is adopted. The limiting shear stress in the slip zone (i.e. the pile shaft for the axial response) is taken as:

$$t_{ss} = \alpha C_u \quad (10.3)$$

where C_u is the undrained shear strength of the soil and α is the adhesion factor. The limiting bearing stress on the pile base is calculated as:

$$t_{sc} = 9C_u \quad (10.4)$$

The limiting bearing stress on the pile shaft for the lateral response is calculated as:

$$t_{sc} = N_c C_u \quad (10.5)$$

where N_c is a bearing capacity factor increasing linearly from 2 at the surface to a constant value of 9 at a depth of three pile diameters and below, much as was originally suggested by Broms (1964) and widely accepted in practice (Fleming *et al.*, 1992).

Cohesionless soil

For cohesionless soils, an effective stress approach is adopted. The limiting shear stress in the slip zone (i.e. the pile shaft for the axial response) is taken as:

$$t_{ss} = K_s \sigma'_v \tan \delta \quad (10.6)$$

where K_s is the coefficient of horizontal soil stress, σ'_v is the effective vertical stress and δ is the angle of friction between pile and soil. The limiting bearing stress on the pile base is calculated as:

$$t_{sc} = N_q \sigma'_v \quad (10.7)$$

where N_q is calculated as a function of the soil angle of friction (Φ) and the length-to-diameter ratio (L/d) of the pile, much as was originally established by Berezantzev *et al.* (1961). The limiting bearing stress on the pile shaft for the lateral response is calculated as (Fleming *et al.*, 1992):

$$t_{sc} = K_p^2 \sigma'_v \quad (10.8)$$

where K_p is the passive earth pressure coefficient, equal to $(1+\sin\phi)/(1-\sin\phi)$.

Group “shadowing” effect

Under lateral loads, closely spaced pile groups are subjected to a reduction of lateral capacity. This effect, commonly referred to as “shadowing”, is related to the influence of the leading row of piles on the yield zones developed in the soil ahead of the trailing row of piles. Because of this overlapping of failure zones, the front row will be pushing into virgin soil while the trailing row will be pushing into soil which is in the shadow of the front row piles. A consequence of this loss of soil resistance for piles in a trailing row is that the leading piles in a group will carry a higher proportion of the overall applied load than the trailing piles. This effect also results in gap formation behind the closely spaced piles and an increase in group deflection. It has been shown both theoretically and experimentally that the shadowing effect becomes less significant as the spacing between piles increases and is relatively unimportant for centre-to-centre spacing greater than about six pile diameters (Cox *et al.*, 1984; Brown and Shie, 1990; Ng *et al.*, 2001).

The shadowing effect has been modelled into the PGROUPN analysis using the approach outlined by Fleming *et al.* (1992). Following this approach, it has been assumed that a form of block failure will govern when the shearing resistance of the soil between the piles is less than the limiting resistance of an isolated pile. Referring to Figure 10.1, the limiting lateral resistance for the pile which is in the shadow of the front pile may be calculated from the lesser of the limiting bearing stress for a single pile (as calculated from Equations (10.5) and (10.8)) and $s t_s$, where s is the centre-to-centre pile spacing, d is the pile diameter and t_s is the friction on the sides of the block of soil between the two piles. The value of t_s may be taken as C_u for cohesive soil and $\tan \phi$ for cohesionless soil.

The outlined approach provides a simple yet rational means of estimating the shadowing effect in closely spaced groups, as compared with the purely empirical “ p -multiplier” concept which is employed in load-transfer analyses (e.g. in GROUP and FLPIER).

Extension to non-linear soil behaviour

Non-linear soil behaviour is incorporated, in an approximate manner, by assuming that the soil Young’s modulus varies with the stress level at the pile-soil interface. A simple and popular assumption is to adopt a hyperbolic stress-strain relationship, in which case the tangent Young’s modulus of the soil E_{tan} may be written as (Duncan and Chang, 1970; Poulos, 1989; Randolph, 1994):

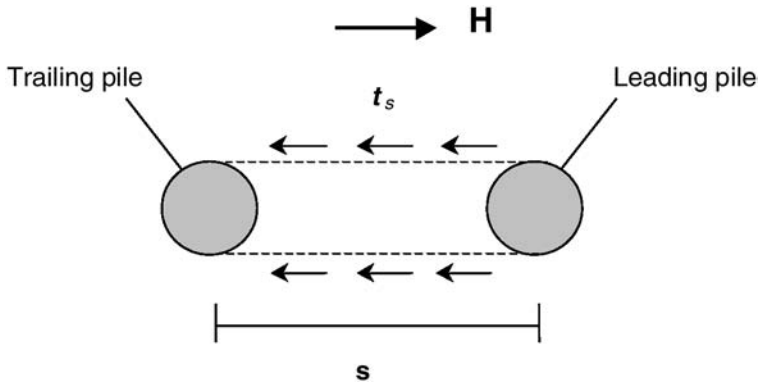


Figure 10.1 Plan view of block failure under lateral load (after Fleming et al., 1992).

$$E_{\tan} = E_i \left(1 - \frac{R_f t}{t_{\text{lim}}} \right)^2 \quad (10.9)$$

where E_i is the initial tangent soil modulus, R_f is the hyperbolic curve-fitting constant, t is the pile-soil stress and t_{lim} is the limiting value of pile-soil stress obtained from Equations (10.3)–(10.8). Thus, the boundary element equations described above for the linear response are solved incrementally using the modified values of soil Young's modulus of Equation (10.9) and enforcing the conditions of yield, equilibrium and compatibility at the pile-soil interface.

The hyperbolic curve fitting constant R_f defines the degree of non-linearity of the stress-strain response and can range between 0 (an elastic-perfectly plastic response) and 1.0 (an asymptotic hyperbolic response in which the limiting pile-soil stress is never reached). Different values of R_f should be used for the axial response of the shaft and the base, and for the lateral response of the shaft. For the axial response of the shaft, there is a relatively small amount of non-linearity, and values of R_f in the range 0–0.5 are appropriate (Poulos, 1989, 1994; Hirayama, 1991), the higher values being associated with relatively rigid piles. The (axial) response of the base is highly non-linear, and a value of R_f in the range 0.9–0.99 is recommended (Poulos, 1989, 1994). For the lateral response of the shaft, values of R_f in the range 0.5–0.99 generally give a reasonable fit with the observed behaviour, the higher values being recommended to avoid underestimation of deflections at high load levels.

Numerical results

The results obtained from alternative numerical methods for single piles and pile groups subjected to vertical and horizontal loads are compared and discussed.

Benchmark solutions in the linear and non-linear range are presented, and the significant influence of soil non-linearity on load distribution between individual piles in a group is highlighted.

Single pile response

In comparing non-linear solutions for single pile response to axial loading, the problem examined is that reported by Poulos (1989) in his Rankine Lecture. This example offers the opportunity to assess the validity of the non-linear hyperbolic model adopted by PGROUPN by comparison with well-established numerical solutions. The input parameters are reported in Table 10.3 and, in order to cover a wide range of pile-soil relative stiffnesses ($K=E_p/E_s$), two values of pile Young's modulus have been considered, 30GPa and 30,000GPa (the latter would be unrealistically stiff in practice). Figures 10.2 and 10.3 report the pile head load-settlement response obtained from a FEM analysis by Jardine *et al.* (1986) which can be used as a benchmark. Such analysis involves the use of a non-linear soil model in which the Young's modulus decreases markedly from an initial value of 1056 MPa as the axial strain level increases. Figures 10.2 and 10.3 also show the load-settlement curves obtained from the following two BEM analyses by Poulos (1989): (a) an elastic-perfectly plastic continuum-based interface model, using a constant soil Young's modulus of 1056 MPa; (b) a hyperbolic non-linear continuum-

Table 10.3 Parameters for the analyses reported in Figures 10.2–10.4

Parameter	Value
Pile length, L (m)	30
Pile diameter, d (m)	0.75
Depth of soil layer (m)	50
Pile Young's modulus, E_p (GPa)	30, 30000
Soil Young's modulus, E_s (MPa)	1056
Soil Poisson's ratio, ν_s	0.49
Limiting shear stress, t_{sc} (kPa)	220

based interface model (similar to PGROUPN), using an initial tangent soil Young's modulus of 1056 MPa and a hyperbolic curve fitting constant (R_f) of 0.9 for both the shaft and the base. The PGROUPN solutions have been obtained for three sets of hyperbolic curve fitting constants: (1) $R_f=0.5$ for the shaft and $R_f=0.9$ for the base (this set attempts to reproduce the FEM results); (2) $R_f=0$ for both the shaft and the base (to be compared with curve (a) by Poulos); (3) $R_f=0.9$ for both the shaft and the base (to be compared with curve (b) by Poulos).

It is worth noting that, for the more compressible and realistic pile (Figure 10.2), all BEM analyses (perhaps excluding the analyses including $R_f=0.9$ for both the shaft and the base) are capable of predicting a very similar load-settlement response to that obtained from the FEM solution which utilises a non-

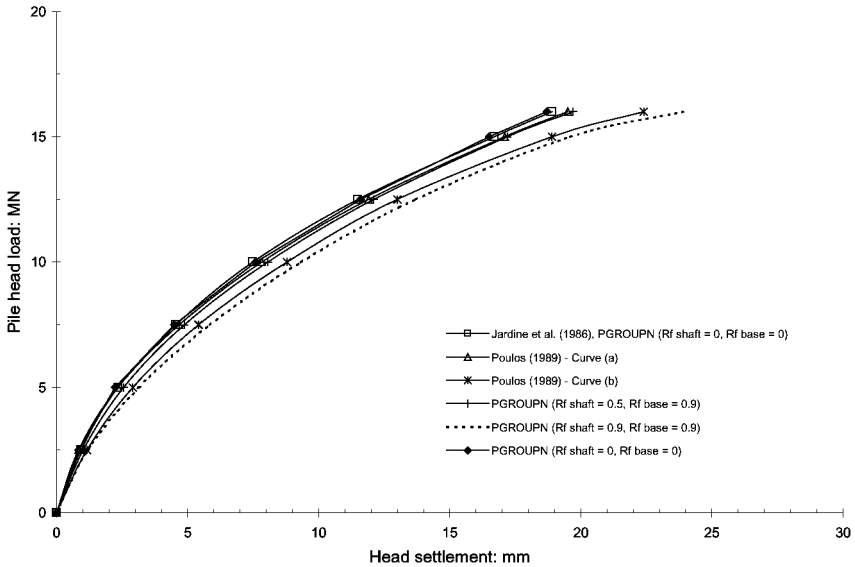


Figure 10.2 Comparison of load-settlement response for single pile ($E_p=30$ GPa).

linear constitutive model of soil behaviour. For the stiffer pile (Figure 10.3), the agreement between the curves is not as close, and only the PGROUPN analysis using $R_f=0.5$ for the shaft and $R_f=0.9$ for the base is in good agreement with the FEM solution. It is clear that, for very stiff piles, the details of the pile-soil interface model have a greater influence on the load-settlement response than for more compressible piles. For this type of problem, two features of behaviour are worthy of note: (1) the elastic-perfectly plastic model, such as is employed in curve (a) (and also in DEFPIG), is not capable of capturing the non-linear features of stress-strain behaviour; (2) the use of $R_f=0.9$ for the shaft within a hyperbolic non-linear model leads to a significant overprediction of pile settlements, especially at high load levels.

Finally, Figure 10.4 reports the mobilisation of shaft resistance t_s / C_u for a factor of safety (FoS) of 2 (i.e. at a load level $P/P_u=0.5$, where P is the applied axial load and P_u is the ultimate axial capacity of the pile). The results show that the distribution of shear stress (t_s) predicted by PGROUPN (using $R_f=0.5$ for the shaft and $R_f=0.9$ for the base) is very consistent with that obtained from the FEM analysis of Jardine and colleagues.

Pile group settlement

In order to investigate pile group settlement predictions in the linear range, Figure 10.5 compares PGROUPN results with those obtained by some of the computer programs mentioned above. Results are expressed in terms of the normalised group stiffness $k_p / (nsG)$ of square groups of piles at different

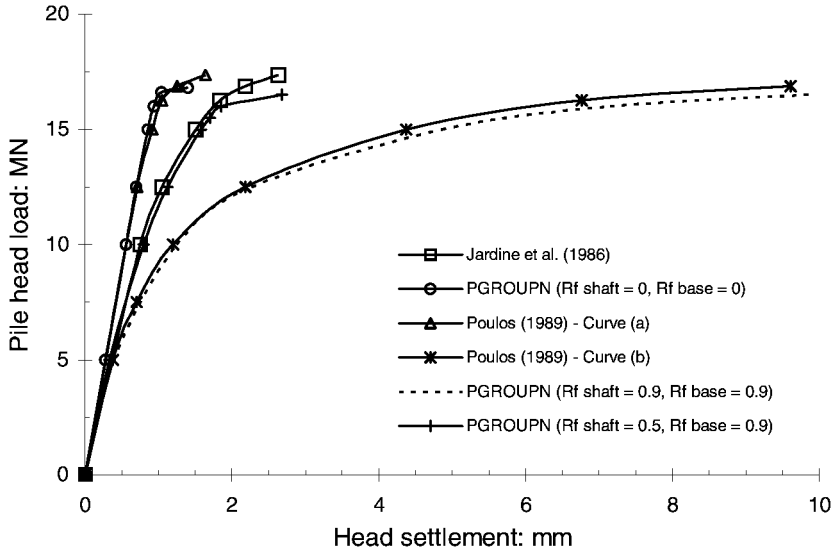


Figure 10.3 Comparison of load-settlement response for single pile ($E_p=30,000$ GPa).

spacings (where k_p is the ratio of the total vertical load acting on the group to the average settlement of the group, n is the number of piles in the group, s is the pile spacing and G is the soil shear modulus). In the analyses of PIGLET and GRUPPALO, it is assumed that axial interaction effects between piles become insignificant for a pile spacing greater than a limiting value s_{max} equal to (Randolph and Wroth, 1979):

$$s_{max} = 2.5L(1 - \nu_s) + r_g \tag{10.10}$$

where ν_s is the soil Poisson's ratio and r_g , for rectangular pile group configurations, may be taken as the radius of the circle of equivalent area to that covered by the pile group. In the analyses of DEFPIG, PGROUP and PGROUPN, no limiting value for axial interaction effects has been adopted.

It may be observed that DEFPIG and PIGLET approaches give divergent results, while a reasonable agreement is obtained between PGROUPN and the computer program GRUPPALO (Mandolini and Viggiani, 1997). It is worth noting that results from PGROUPN are in excellent agreement with the rigorous BEM solution of PGROUP, but the latter is limited to groups of 8×8 piles, due to the magnitude of computer resources required to analyse larger groups. In contrast, PGROUPN took about 30 CPUs on an ordinary desktop computer for the 20×20 pile group, considering the symmetry of the pile arrangement. This observation is of great significance because it demonstrates the applicability of the complete BEM approach to large pile groups, whereas previous work (i.e. PGROUP) was restricted to small pile groups.

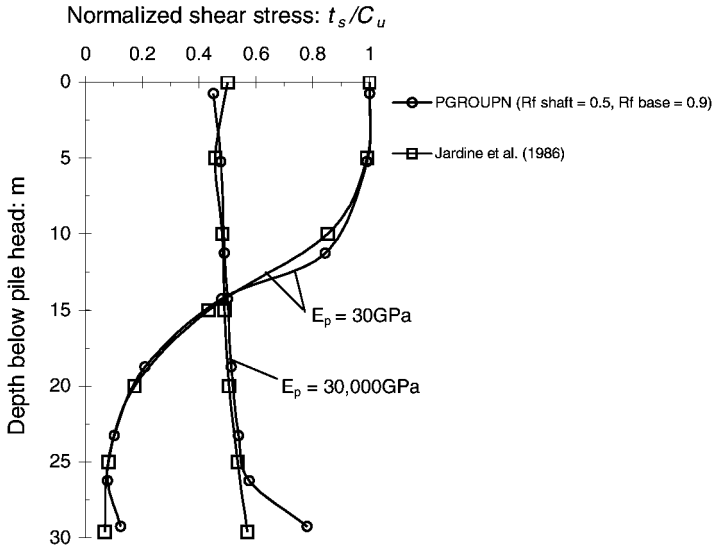


Figure 10.4 Comparison of shaft shear stress distribution for single pile at a load level $P/P=0.5$.

Finally, it may be noted that, for very large pile groups, where the ratio of pile group width to pile length becomes much greater than unity, the group stiffness should approach that of a shallow foundation. This would correspond to a limiting stiffness of about 4.5 (Fraser and Wardle, 1976), as indicated in Figure 10.5.

Axial load distribution

Figure 10.6 shows a comparison of the distribution of axial load in a 5×5 pile group in homogeneous soil which has been obtained from selected numerical codes.

The results from a simplified BEM analysis using interaction factors by Poulos and Davis (1980) are also included. The load distribution is expressed in terms of the ratio of load on pile to the average pile load in the group (P/P_{av}), and is plotted against the normalised pile spacing (s/d). The input parameters of the analyses are given in Tables 10.4 and 10.5 for the linear and non-linear range, respectively. In the linear range, the load distribution predicted by PGROUPN compares favourably with that predicted by MPILE, whereas the results of DEFPIG and Poulos and Davis (1980) give slightly higher corner loads.

In the non-linear range, the PGROUPN results have been obtained by applying a total load on the group of 29.0 MN (corresponding to a group FoS of 2.0) and 38.6 MN (corresponding to a group FoS of 1.5). It is evident that consideration of the non-linear soil response yields a significant reduction in the load concentration at the corner piles and a more uniform load distribution. Clearly,

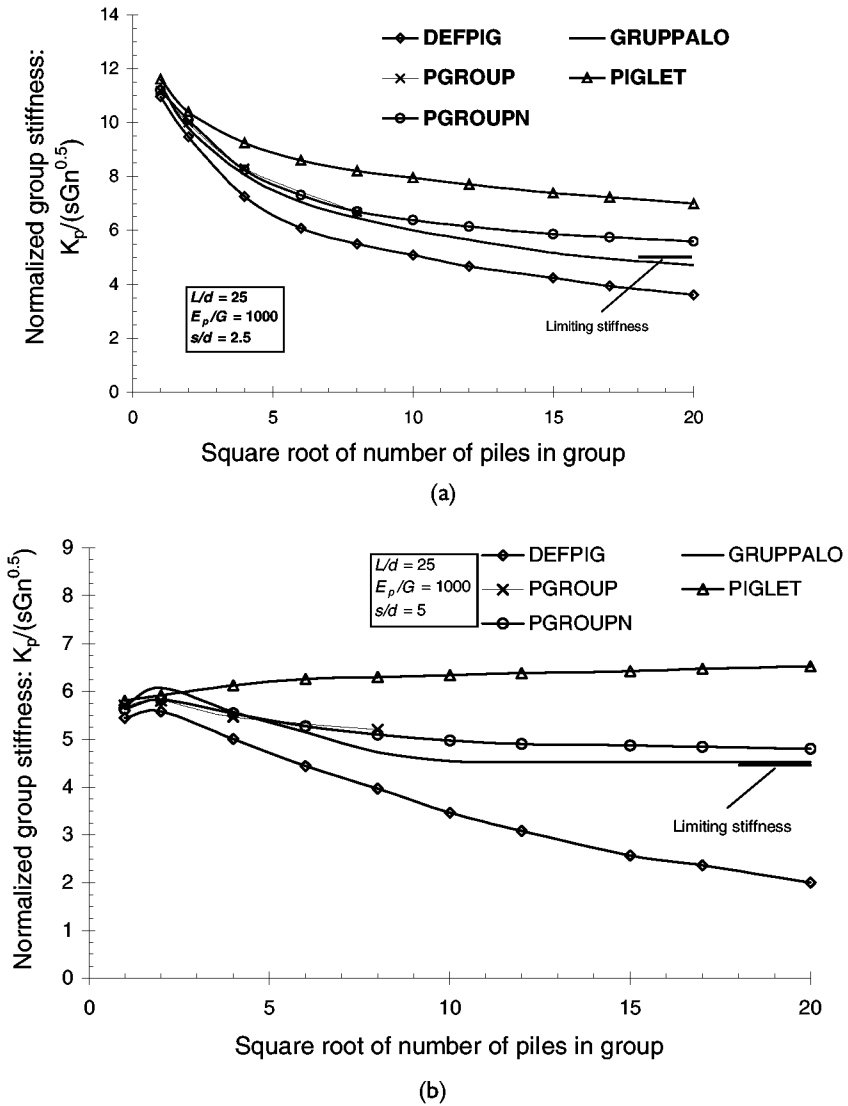


Figure 10.5 Comparison of different pile group analysis methods for (a) $s/d=2.5$; (b) $s/d=5$.

the lower the factor of safety, the higher the reduction in the load concentration at the corner piles obtained by the non-linear analysis.

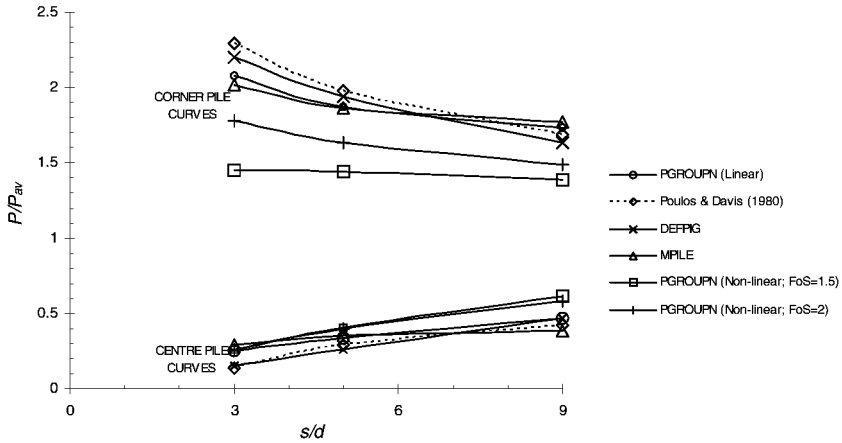


Figure 10.6 Comparison of axial load distribution to individual piles in 5x5 pile group.

Table 10.4 Parameters for the linear analyses reported in Figures 10.6–10.7

Parameter	Value
Pile length L (m)	25
Pile diameter, d (m)	1
Pile Young's modulus, E_p (GPa)	25
Soil Young's modulus, E_s (MPa)	25
Soil Poisson's ratio, ν_e	0.5

Lateral load distribution

As a pile group is subjected to a lateral load, this will result in a lateral deformation as well as a rotation of the group and hence the piles at the edge will be loaded axially in tension and compression. Thus, only if rotation of the cap is prevented, do the piles deflect purely horizontally and hence the lateral load deformation characteristics of the group can be analysed separately from the axial ones. For such fixed-head pile groups, the lateral load distribution to the individual piles predicted by selected numerical codes is examined by applying a lateral load of 15 MN to the same group of piles analysed in the previous section, and under the same soil conditions (refer to Tables 10.4 and 10.5). Similarly, Figure 10.7 shows the lateral load distribution (where H is the load acting on the individual pile head and H_{av} is the average load acting on each pile head) as a function of the normalised pile spacing (s/d).

In the linear range, the PGROUPN solutions compare favourably with DEFIG, while significant discrepancies with the MPILE analysis are observed in the corner load prediction. These differences may partially be explained with the approximations involved in the interaction factor approach which ignores the stiffening effects of piles within the soil mass, thereby leading to an overestimation of group interaction, as discussed in Section 3. Consideration of

Table 10.5 Additional parameters for the non-linear analyses reported in Figures 10.6–10.7

Parameter	Value
Initial soil Young's modulus, E_s (MPa)	75
Undrained shear strength, C_u (kPa)	50
Adhesion factor, α	0.5
Hyperbolic curve fitting constant R_f (shaft)	0.5
Hyperbolic curve fitting constant R_f (base)	0.99
Hyperbolic curve fitting constant R_f (lateral)	0.9

soil non-linearity results in a reduction of the load concentration at the corner pile and hence a more uniform load distribution. The amount of this reduction will depend on the load level. Finally, it should be emphasised that the numerical simulations presented herein take no account of possible failure by yielding of the pile section, i.e. the pile is assumed to remain elastic.

Pile group under general loading conditions

The deformations and load distribution in a 3-pile group under a combination of axial load, lateral load and moment are examined in the linear range (refer to Figure 10.8). Results from selected numerical analyses are compared in Table 10.6 in which w_3 , u and θ are the vertical head displacement of pile no. 3, the horizontal cap displacement and the rotation of the cap, respectively. There is a good agreement between the solutions which consider pile-soil-pile interaction (even if with different degrees of rigour), whereas the equivalent-bent analysis (reported in Poulos and Davis, 1980) gives quite different results, thereby showing the pitfall of attempting to model a complex pile-soil system by means of a simple structural frame.

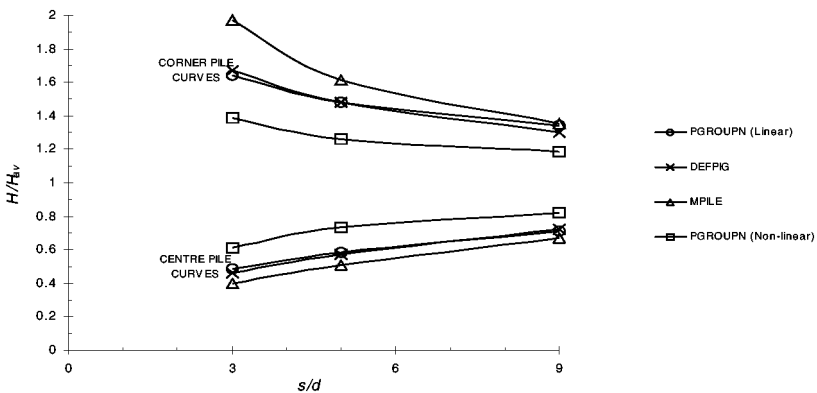


Figure 10.7 Comparison of lateral load distribution to individual piles in 5x5 pile group.

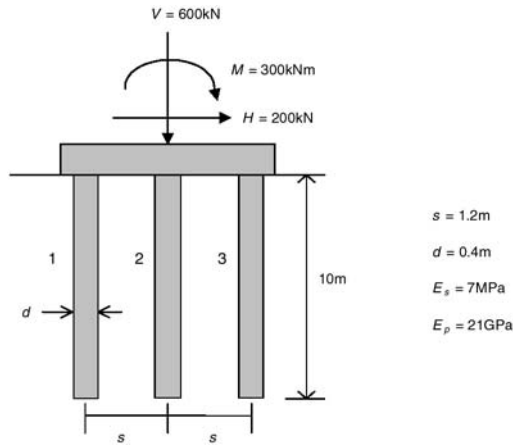


Figure 10.8 Group of 3 piles considered in comparison of methods.

Selection of soil parameters

In predicting the behaviour of pile foundations, the designer is faced with a number of decisions, including the selection of the method of analysis and the soil parameters to be adopted. It is crucial to recognise that the latter aspect is generally of greater importance than the method of analysis, provided that a soundly based method is employed.

Attention will be focused here on the estimation of the soil Young's modulus (E_s), which is the key geotechnical parameter for pile deformation predictions. The most reliable means of determining E_s is by backfiguring from the results of full-scale pile load tests, using the same theory that will be used for the actual deformation prediction. However, this is not always possible, at least in the preliminary stages of design, and hence resort is made to the results of laboratory or *in situ* soil tests.

The PGROUPN analysis is based on a non-linear hyperbolic interface model. For this kind of analysis, previous experience has shown that the initial ("low strain") value of E_s may be successfully employed in the prediction of the initial stiffness of the load-settlement curve of pile foundations (Poulos, 1989; Randolph, 1994; Mandolini and Viggiani, 1997). The use of an initial tangent soil modulus represents an advantage over a purely linear analysis which requires a secant value of soil modulus, relevant for the applied load level. Indeed, selection of an appropriate secant modulus is by no means straightforward, whereas the initial modulus is a more reproducible quantity. Some indication of the typical ratio of secant modulus to initial modulus as a function of the applied load level has been presented by Poulos *et al.* (2001).

It is important to recognise that the value of E_s for the soil in the vicinity of the pile shaft will be influenced by both the loading of the pile and the installation

Table 10.6 Comparison of different analyses for 3-pile group under general loading conditions

Quantity	Equivalent-bent analysis	DEFPiG	PIGLET	GEPAN	PGROUPN
V_1 (kN)	67.2	55.8	55.7	54.0	49.6
V_2 (kN)	200.0	155.1	155.0	156.0	153.0
V_3 (kN)	332.8	389.1	389.3	390.0	397.0
H_1 (kN)	66.8	72.0	80.4	73.7	68.9
H_2 (kN)	66.7	56.0	39.3	50.9	53.5
H_3 (kN)	66.6	72.0	80.4	75.4	77.6
M_1 (kNm)	-6.2	-35.8	-42.0	-38.5	-41.5
M_2 (kNm)	-6.2	-28.5	-16.3	-26.1	-31.8
M_3 (kNm)	-6.2	-35.8	-42.0	-38.6	-44.0
w_3 (mm)	17.5	13.4	9.9	10.8	14.1
u (mm)	8.9	11.6	11.4	10.5	11.5
θ (rad)	0.00581	0.00242	0.00242	0.00241	0.00263

process, and would be expected to be different for bored piles and for driven piles. As discussed by Randolph (1994), for driven piles, the soil modulus may be expected to be higher in the zone immediately around the pile, while for bored piles the soil modulus will be reduced. The near-pile E_s will tend to influence strongly the deformation of the single pile, whereas initial values of E_s will affect interaction effects between piles. Typical values for the near-pile soil modulus for bored and driven piles have been reported by Poulos (1993) and Poulos (1994), respectively. The discussion below will give some indication on the assessment of the initial soil modulus.

It is now well understood that the values of E_s determined from conventional triaxial tests with external measurement of axial strain of the soil sample (which is highly inaccurate at strains less than about 0.1%) are usually much smaller (typically one-fourth to one-tenth) than the initial modulus (Jardine *et al.*, 1984). The most reliable means of obtaining the low strain shear modulus (G_o), which is connected with E_s by the formula $E_s=2G_o(1+\nu_s)$, is to carry out *in situ* shear wave velocity measurements. Mandolini and Viggiani (1997) showed that there is a substantial agreement between low strain shear moduli derived from cross-hole data and those backfigured from pile loading tests, with a trend of the latter to fit the lower limit of the geophysical measurements. If *in situ* shear wave velocity measurements are not available, G_o may be determined in the laboratory using bender elements (Viggiani and Atkinson, 1995).

However, all of these means of measuring shear moduli are expensive and time-consuming, and are rarely available in the early stages of design. Thus, a preliminary assessment of initial soil modulus may be obtained from empirical correlations with the results of conventional *in situ* and laboratory tests.

For clays, a correlation between initial E_s and SPT N -value (blows/300 mm, corrected to a rod energy of 60%) has been proposed by Poulos (1993), based on the work by Wroth *et al.* (1979):

$$E_s = 25N^{0.77} \quad [\text{MPa}] \quad (10.11)$$

For convenience, a linear correlation may also be adopted, as suggested by Hirayama (1991, 1994) and Poulos (1993, 1994):

$$E_s = 14N \quad [\text{MPa}] \quad (10.12)$$

However, it is probably more reliable to correlate the initial soil modulus with the undrained shear strength (C_u), and the following correlation is suggested by Hirayama (1991, 1994) and Poulos (1993, 1994):

$$E_s = 1500C_u \quad (10.13)$$

Several other correlations have been proposed, i.e. $E_s=1500-3000C_u$ (Jardine *et al.*, 1986), $E_s=1200-2700C_u$ (Kuwabara, 1991), $E_s=1900C_u$ (Kagawa, 1992). Thus, Equation (10.13) may give average values which are expected to be on the safe side.

For silica sands, the following correlation between initial E_s and SPT N -value may be used (Ohsaki and Iwasaki, 1973; Poulos, 1994):

$$E_s = 16.9N^{0.9} \quad [\text{MPa}] \quad (10.14)$$

Alternatively, the initial soil modulus may be correlated with the Cone Penetration Test (CPT) results, as proposed by Imai and Tonouchi (1982) and Poulos (1989, 1994):

$$E_s = 53q_c^{0.61} \quad [\text{MPa}] \quad (10.15)$$

where q_c is the cone resistance (in MPa).

It must be stated that the empirical correlations presented above (Equations (10.11)–(10.15)) can only be expected to provide an approximate estimate of initial soil modulus and may be rather inaccurate if applied to cases outside the scope of previous experience. Thus, as discussed by Gazetas (1991), their use may only be recommended in practice in some cases as follows: (a) in feasibility studies and preliminary design calculations; (b) for final design calculations in big projects as supplementary data or in small projects as main data; (c) for initial data in back analyses; (d) to provide an order-of-magnitude check against the experimentally determined values.

It should be emphasised that such correlations refer to the axial response of pile foundations. For piles under lateral loading, the effects of pile installation

and pile-soil separation on the upper soil layer can have a significant influence on the values of soil stiffness, and hence the values of E_s adopted for the axial response may be reduced up to 50% or more.

As regards the soil Poisson's ratio, its effect is quite minor when the analysis is based on the use of Young's modulus rather than shear modulus. For saturated clays under undrained conditions, a value of 0.5 is relevant while, for most clays and sands, the drained value is usually in the range 0.3–0.4 (Poulos, 1994). Values of Poisson's ratio may also be approximated using the empirical formula (Duncan and Mokwa, 2001):

$$v_s = \frac{1 - \sin \phi}{2 - \sin \phi} \quad (10.16)$$

where the value of ϕ (friction angle) should be the total stress shear strength parameter ϕ_u for short-term undrained conditions and the effective stress shear strength parameter ϕ' for long-term drained conditions.

For a non-linear analysis, it is also necessary to assess the axial and lateral pile shaft resistance, and the end-bearing resistance, as discussed in the earlier section on limiting pile-soil stresses. Further information on this subject is provided in the work by Poulos (1989), Fleming *et al.* (1992) and Tomlinson (1994).

Applications and design analysis

Attention is turned to the application of available numerical analyses to practical problems involving real soils. Three published case histories are considered, involving single piles and pile groups subjected to either axial or lateral loading. In each case, the rationale for the selection of the soil parameters is described briefly, and then the predictions from selected methods of analysis are compared with the field measurements.

North London railway viaduct

Before proceeding to the analysis of the case histories, it is found instructive to discuss the results obtained from different numerical codes in the analysis of a 3×3 pile group subjected to a combination of vertical loads, horizontal loads and moments and embedded in London Clay. This project was part of the foundation design of a high-speed railway viaduct in North London. The bored cast-in-situ reinforced concrete piles are 17 m long, 0.9 m in diameter, with a centre-to-centre spacing of three pile diameters, and with the underside of the pile cap assumed at the top of the London Clay. The assumed Young's modulus for the piles is 25 GPa. A profile of undrained shear strength (C_u) of $50+9.4z$ kPa has been adopted, where z is the depth in m below the top of the London Clay. An adhesion factor of 0.6 is employed, while the hyperbolic curve fitting constants

have been taken as 0.0 and 0.99 for the axial response of the shaft and the base, respectively, and 0.9 for the lateral response.

For the axial response, the profile of soil modulus has been derived from the correlation $E_s=400C_u$ for the linear analyses and from $E_s=1500C_u$ for the nonlinear analysis. For the lateral response, the profile of soil modulus has been assumed to increase linearly with depth from a value of zero at the top of the London Clay (conservatively) at a rate of 4.14 MPa/m for the linear analyses and 6.15 MPa/m for the non-linear analysis. The soil Poisson's ratio has been taken as 0.5.

The applied vertical loads (V) result from the combined effect of live and dead loads, whereas the horizontal loads (H) and moments (M) are generated by the high-speed trains braking and accelerating. For the load case presented herein, the loads acting on the cap have been estimated as $V=14,200$ kN, $H=470$ kN and $M=3200$ kNm.

This problem has been analysed using the computer programs MPILE, DEFPIG and PGROUPN (both the linear and non-linear versions). Table 10.7 summarises the main results obtained from the analyses. In the linear range, there is a reasonably good agreement between the group deformations and axial load distribution predicted by the different codes. However, it is important to note the significant differences between the predictions of the pile head lateral loads and bending moments. As discussed previously, due to the interaction between the axial and lateral responses of the piles, higher loads are expected to occur for the piles in the leading row than for the piles in the trailing row of the group. While this load-deformation coupling effect is modelled by the PGROUPN analysis, MPILE and DEFPIG disregard the interaction between the axial and lateral responses and therefore predict the same lateral loads and bending moments for both the leading and trailing rows of the group. This results in a significant underestimate of the maximum values of lateral load and bending moment and hence may lead to an unsafe design of the piles.

If the effects of soil non-linearity are accounted for by means of the PGROUPN analysis, two main features of behaviour are observed:

- 1 A prediction of lower (and more realistic) group deformations.
- 2 A decrease of predicted loads on the most heavily loaded row of piles (i.e. the leading row) and hence a more uniform load distribution between the piles.

It should be emphasised that in this case, due to the low load level, the differences between the linear and non-linear PGROUPN results are mainly a consequence of the higher value of soil modulus adopted in the non-linear analysis (i.e. an initial value), rather than the effect of soil non-linearity.

This observation confirms the view already expressed by other authors (Randolph, 1994; Mandolini and Viggiani, 1997): at low load levels (and hence

Table 10.7 Comparison of alternative numerical analyses for a railway viaduct in North London

	MPILE	DEFFIG	PGROUPN (Linear)	PGROUPN (Non-linear)
Group centre settlement (mm)	9.0	11.3	11.6	4.0
Group deflection (mm)	3.2	4.3	3.9	2.7
Axial load at corner piles of leading row (kN)	2220	2210	2230	2100
Axial load at corner piles of trailing row (kN)	1700	1670	1640	1520
Lateral load at corner piles of leading row (kN)	66	62	94	76
Lateral load at corner piles of trailing row (kN)	66	62	23	35
Bending moment at corner piles of leading row (kNm)	120	177	225	179
Bending moment at corner piles of trailing row (kNm)	120	177	87	124

for a high safety factor), soil non-linearity has a relatively small effect on pile group response, provided that the group response is calculated using the initial value of soil modulus. However, when the factor of safety is low, consideration of soil non-linearity becomes essential. It is hoped that the above philosophy will find a wider application in design practice.

Comparison with field test data by O'Neill et al. (1982)

O'Neill *et al.* (1982) reported the results of axial loading tests on single piles and pile groups driven into a stiff overconsolidated clay at a site located in Houston. The piles were closed end tubular steel pipes with Young's modulus of 210 GPa, external diameter 274 mm, wall thickness 9.3 mm and a penetration depth of 13.1 m. The group piles were connected by a rigid cap with a clearance of 0.9 m from the groundline and were arranged in a 3×3 configuration with centre-to-centre spacing of three pile diameters. The soil parameters adopted for the PGROUPN non-linear analysis are based on the data summarised by Poulos (1989) in his Rankine Lecture, i.e. a profile of the initial soil modulus of 100 MPa at ground level, increasing linearly to 400 MPa at the pile base level (as deduced from seismic cross-hole data), and a profile of undrained shear strength of 40 kPa at the surface, increasing linearly to 175 kPa at the level of the pile base (as deduced from laboratory triaxial tests). The soil Poisson's ratio and the adhesion factor have been taken as 0.5, while the hyperbolic curve fitting constants have been assumed to be 0.0 for the shaft and 0.99 for the base.

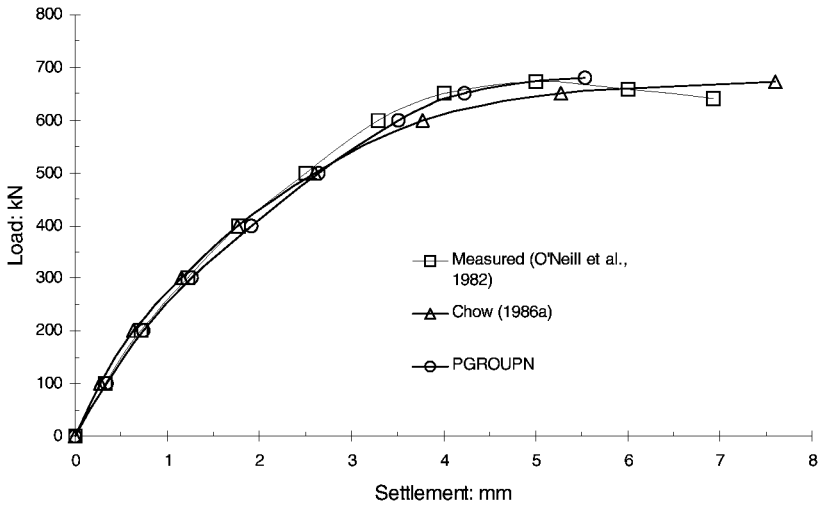


Figure 10.9 Comparison of load-settlement response for single pile.

Figures 10.9 and 10.10 show a favourable agreement between the computed and measured load-settlement behaviour of the single pile and the 9-pile group. The results show that the initial tangent soil modulus, as derived from seismic cross-hole data, may be successfully used in the prediction of the pile settlement, thereby confirming the findings of Mandolini and Viggiani (1997). It is worth noting that the adopted cross-hole profile of initial soil modulus corresponds to that which would have been derived from a correlation $E_s=2500C_u$.

Figures 10.9 and 10.10 also show the load-settlement curves obtained by the hybrid method by Chow (1986a) in which the individual pile response is modelled using the load-transfer method and the interaction between piles is effected using a BEM approach based on Mindlin's solution. It is important to note that the results obtained by Chow for the pile group have been based on parameters derived from back-analysis of single-pile test data, whereas the PGROUPN results have been obtained using soil parameters directly derived from the site investigation data. This confirms the usefulness of the PGROUPN approach for practical problems, particularly when no pile test results are still available.

Figures 10.11 and 10.12 report the computed and measured axial load distribution with depth among the piles in the 9-pile group at a working load of 2.58 MN and at a load nearing failure of 5.66 MN, respectively. In addition, Table 10.8 shows the computed and measured axial loads taken by the individual pile heads under the group loads mentioned above. The results also include the predictions obtained from MPILE and the linear version of PGROUPN using a secant value of the soil modulus based on the correlation $E_s=500C_u$.

It is worth noting that, even at a working load level, the linear solutions overestimate the load taken by the corner pile. Closer to the failure load of the

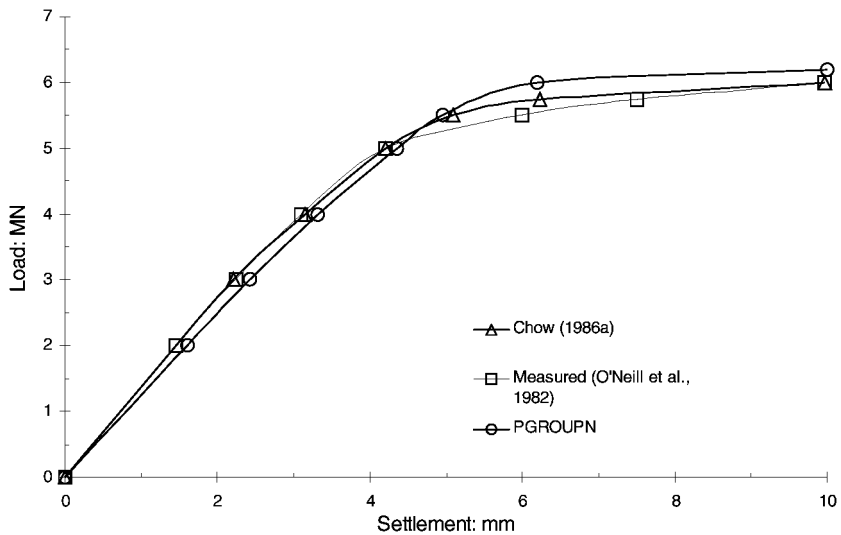


Figure 10.10 Comparison of load-settlement response for 9-pile group.

group, the effect of non-linearity is to cause a redistribution of the loads in the individual piles (i.e. the share of load carried by the corner piles progressively decreases and that of the central pile increases), leading to a more uniform distribution. It is clear that, at this load level, the degree of accuracy of the analysis would to a large extent depend on the agreement between the assumed ultimate pile capacities and the actual values in the field. For instance, O'Neill and colleagues report that the centre pile carried the highest load at failure, as contrasted to the lowest at working load, due to a slightly higher end-bearing load that may have resulted from higher effective confining stresses in the soil in the interior of the group. It should be emphasised that, at this load level, the linear analyses are not strictly applicable, but the actual trend is well reflected in the non-linear solutions.

Comparison with field test data by Briaud et al. (1989)

Briaud *et al.* (1989) described the results of axial loading tests on a single pile and a 5-pile group which were driven to failure in a medium dense sand at a site located in San Francisco. The piles were tubular steel pipes with Young's modulus of 160 GPa, external diameter 273 mm, wall thickness 9.3 mm, driven to a depth of 9.15 m through a 300 mm diameter hole predrilled to a depth of 1.4 m. The single pile was loaded at 1.5 m above the groundline. The group piles were arranged in the configuration shown in the inset to Figure 10.14, and connected by a rigid cap with a clearance of 0.6 m from the groundline. The soil profile consists of a hydraulic fill made of clean sand, about 11 m thick, overlain by 1.4 m of sandy gravel and underlain by sand interbedded with layers of stiff

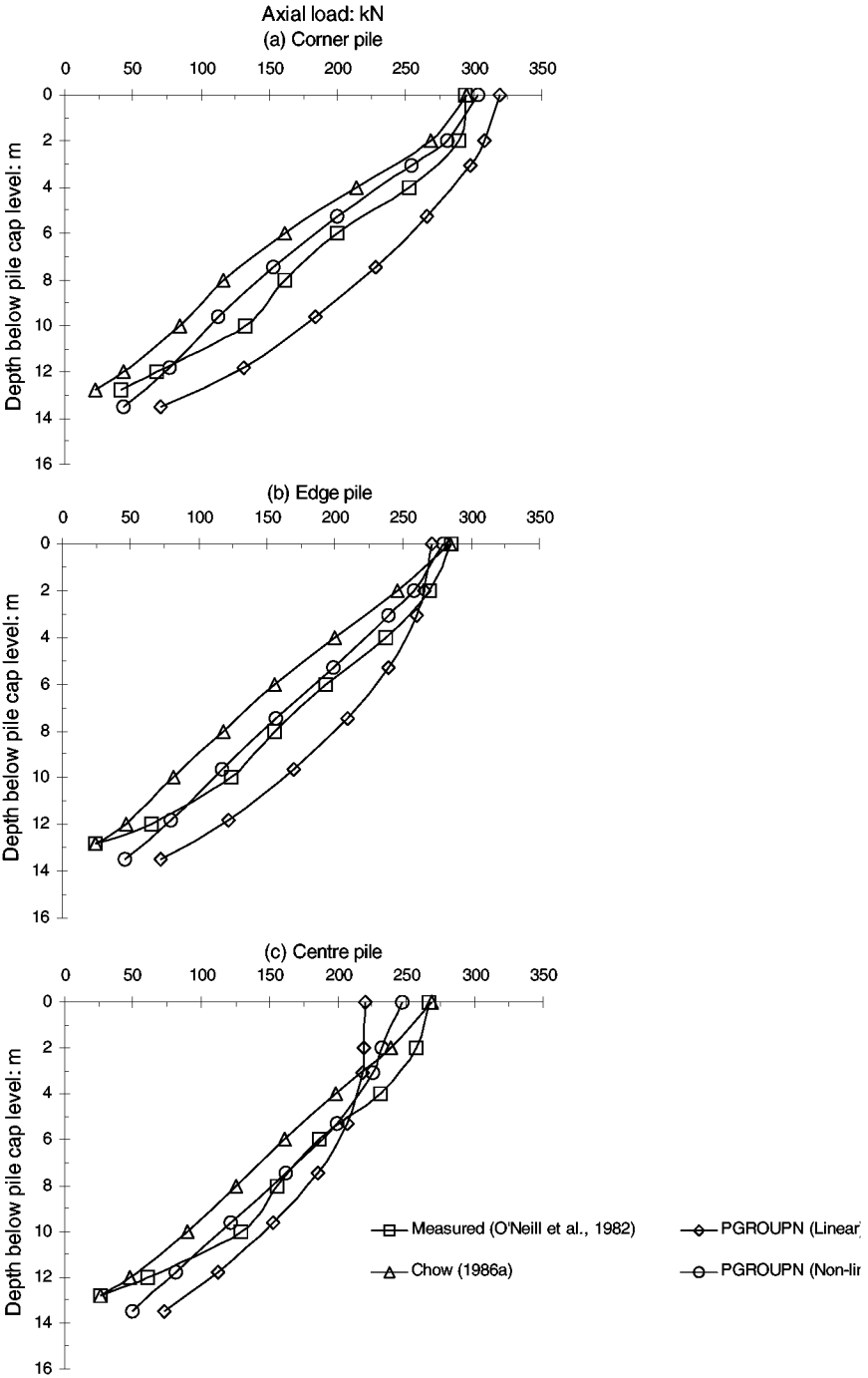


Figure 10.11 Comparison of axial load distribution in 9-pile group at a working group load of 2.58 MN (Note: curves by Chow (1986a) were reported in Chow (1986b)).

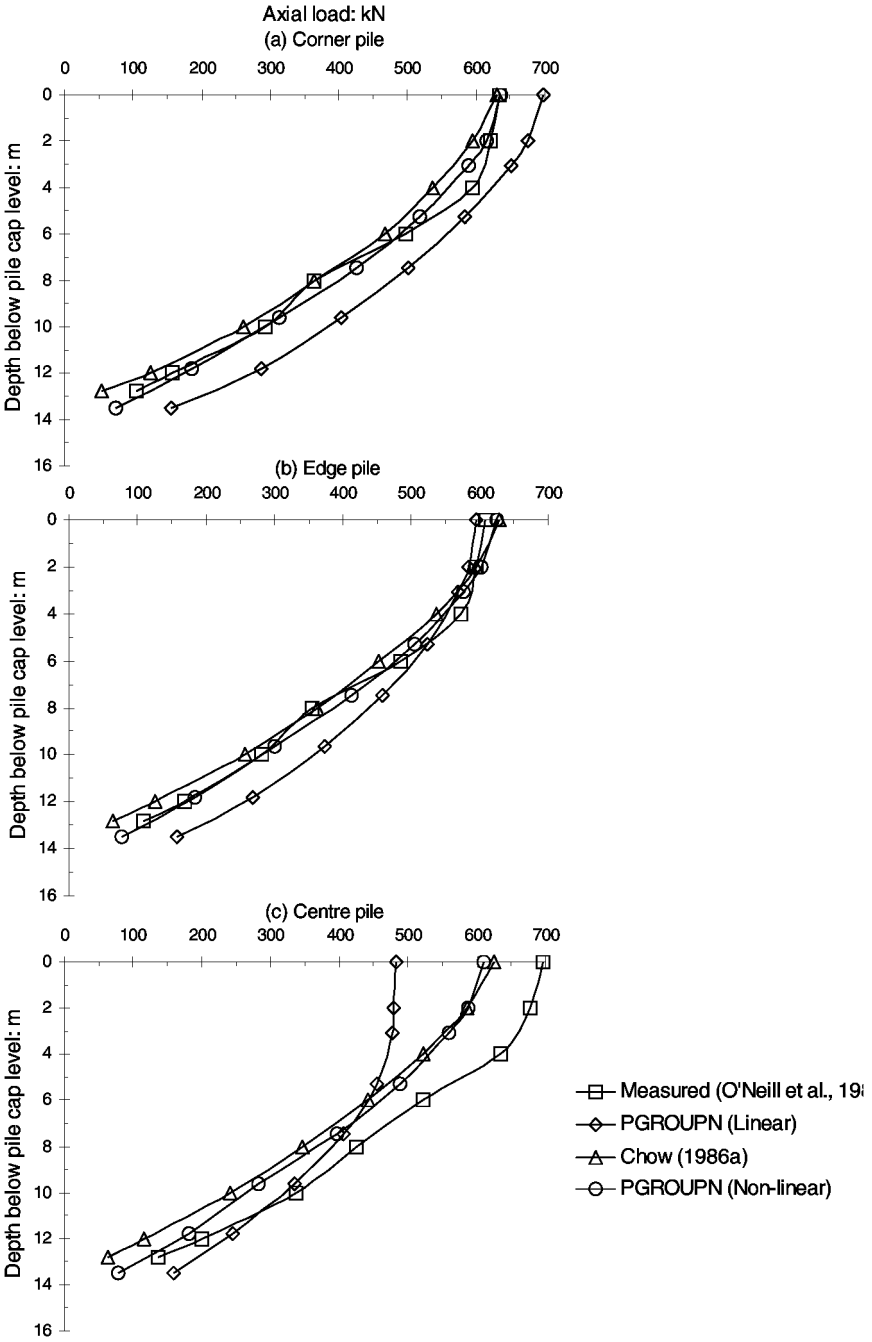


Figure 10.12 Comparison of axial load distribution in 9-pile group at a group load nearing failure of 5.66 MN (Note: Curves by Chow (1986a) were reported in Chow (1986b)).

Table 10.8 Comparison of axial load distribution to individual pile heads in 9-pile group

Method	Average pile loads (kN)					
	Total load = 2.58 MN			Total load = 5.66 MN		
	Corner	Edge	Centre	Corner	Edge	Centre
Measured (O'Neill <i>et al.</i> , 1982)	294	285	267	635	608	696
PGROUPN (Non-linear)	303	280	247	637	625	610
Chow (1986a)	295	284	269	631	629	626
PGROUPN (Linear)	319	271	220	699	595	482
MPILE	315	273	226	692	599	496

silty clay down to the bedrock found at a depth of 14.3 m below ground level. The water table is 2.4 m deep.

The soil parameters adopted for the PGROUPN analysis are based on a subsoil idealisation with two layers resting on a rigid base: for the lower soil layer (2.4–14.3 m), a profile of the initial tangent soil modulus of 138 MPa at a depth of 2.4 m, increasing linearly at the rate of 4.6 MPa/m (as deduced from the CPT profile using Equation (10.15)), a Poisson's ratio of 0.3 (from Equation (10.16)), a buoyant unit weight of 10.1 kN/m³ and a friction angle of 35.4° (from the soil investigation). The pile-soil interface angle may be taken as 5 degrees less than the friction angle, and the coefficient of horizontal soil stress (K_s) equal to 1.2 (Fleming *et al.*, 1992). For the upper soil layer (0–2.4 m), a constant value of soil modulus equal to 138 MPa has been adopted (it should be noted that the predrilled hole disconnects the piles from the top 1.4 m of gravelly soil). The remaining parameters are the same as those for the underlying layer, with the exception of the soil unit weight which is equal to the dry value, 15.7 kN/m³. The bearing capacity factor N_q may be taken as 51, following Tomlinson (1995). The hyperbolic curve fitting constants for the analysis have been assumed to be 0.5 for the shaft and 0.99 for the base.

Figures 10.13 and 10.14 show a favourable agreement between the computed and measured load-settlement behaviour of the single pile and the 5-pile group. It is worth noting that the measured ultimate capacity for the single pile was 505 kN while that for the pile group was 2499 kN, thereby giving a group efficiency of 0.99. Thus, in this case, no increase in pile shaft capacity due to the effects of driving neighbouring piles has taken place.

Comparison with field test data by Huang et al. (2001)

As part of the design of the high-speed rail system in Taiwan, Huang *et al.* (2001) reported the results of lateral load tests on single piles and pile groups installed at a site located in Taipao Township. The bored cast-in-situ reinforced concrete piles were 34.9 m long, 1.5 m in diameter, with a Young's modulus of 27.6 GPa.

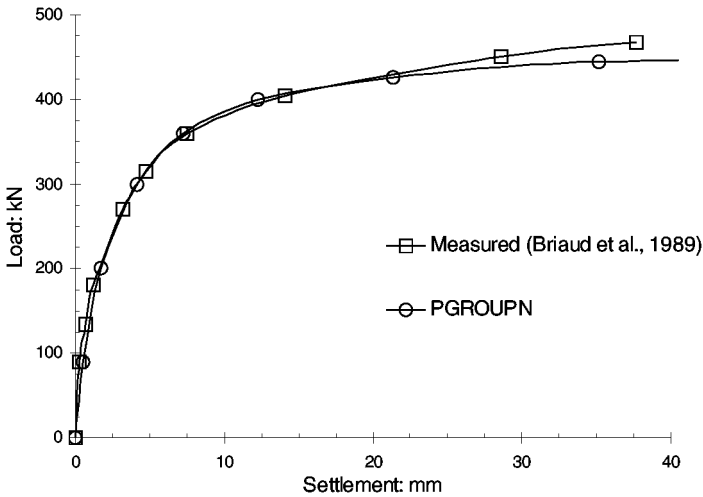


Figure 10.13 Comparison of load-settlement response for single pile.

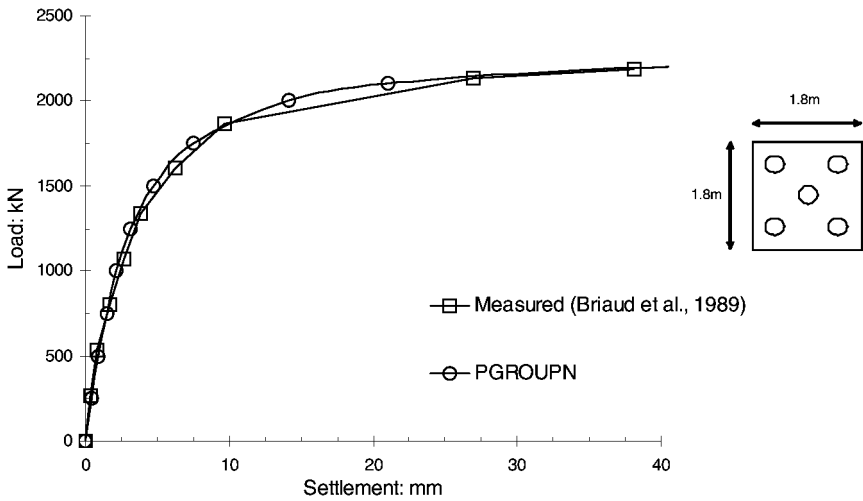


Figure 10.14 Comparison of load-settlement response for 5-pile group.

The group piles were connected by a massive reinforced concrete cap and arranged in a 2×3 configuration with centre-to-centre spacing of three pile diameters, as shown in the inset to Figure 10.16. The lateral load was applied at the level of the ground surface for both the single pile and the pile group. The soil was generally classified as silty sand or silt with occasional layers of silty clay. The water table is at approximately 1 m below the ground surface.

The soil parameters adopted for the PGROUPN analysis include a profile of the initial soil modulus of 77 MPa at a depth of 1 m (where the bottom of the pile

cap was located), increasing linearly at the rate of 9.5 MPa/m, as deduced from the seismic cone penetration test (SCPT) shear wave velocity measurements using a Poisson's ratio of 0.35 (from Equation (10.16)). Based on the soil stratification derived from CPT, and for the purpose of evaluating the response to lateral loading (for which the soil properties in the top eight pile diameters are most relevant), it is reasonable to idealise the soil profile as a single cohesionless layer with a friction angle of 30° . This has been derived from the widely adopted correlation with standard penetration test (SPT) data reported in Tomlinson (1995), using an N value of 10 for the soil in the top eight diameters. Other input parameters for the PGROUPN analysis include a pile-soil interface angle of 25° (i.e. 5 degrees less than the friction angle), a buoyant unit weight of 10 kN/m^3 (assumed), and a coefficient of horizontal soil stress (K_s) of 0.7 (Fleming *et al.*, 1992). The hyperbolic curve fitting constants have been taken as 0.5 and 0.99 for the axial response of the shaft and the base, respectively, and 0.9 for the lateral response (it should be noted that the value of the hyperbolic constants for the axial response has in effect no influence on the lateral response of the group).

Figures 10.15 and 10.16 report the computed and measured pile head load-deflection response of the single pile and the 6-pile group, respectively. The agreement for the single pile results is favourable, whereas, for the 6-pile group, the deflections computed by PGROUPN are slightly overestimated. These differences may partially be explained with the disregard of any shear resistance that might have developed along the base of the massive cap. In addition, other factors such as the cracking of the pile section and the rigidity of the connection of pile to pile cap can influence the lateral group response, particularly under large loads. These factors are not readily modelled in the PGROUPN analysis.

Figures 10.15 and 10.16 also report the results obtained by Huang and colleagues using the computer program GROUP, based on the use of p - y curves. They found that none of the p - y curves derived from the soil tests dilatometer test (DMT) yielded reasonable predictions of pile deflection profiles of the single pile and the pile group. The p - y curves were then adjusted until a good match between the measured and computed load-deflection profiles was achieved.

A comparison between the bending moment profiles predicted by PGROUPN and GROUP for the single pile and the 6-pile group is presented in Figures 10.17 and 10.18, respectively, showing a reasonable agreement between the analyses.

Overall, it may be concluded that the PGROUPN results are of comparable accuracy to those obtained from GROUP. However, it should be emphasised that the PGROUPN analysis is based on the assessment of intrinsic soil properties determined from the soil investigation, whereas the GROUP analysis made use of backfigured data from loading tests on the single pile and the pile group.

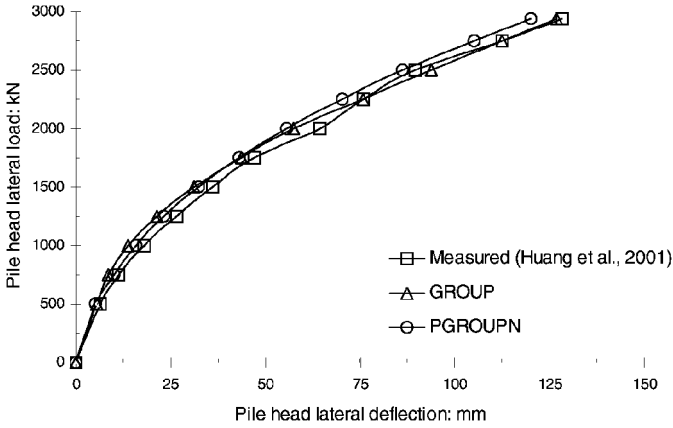


Figure 10.15 Comparison of load-deflection response for single pile.

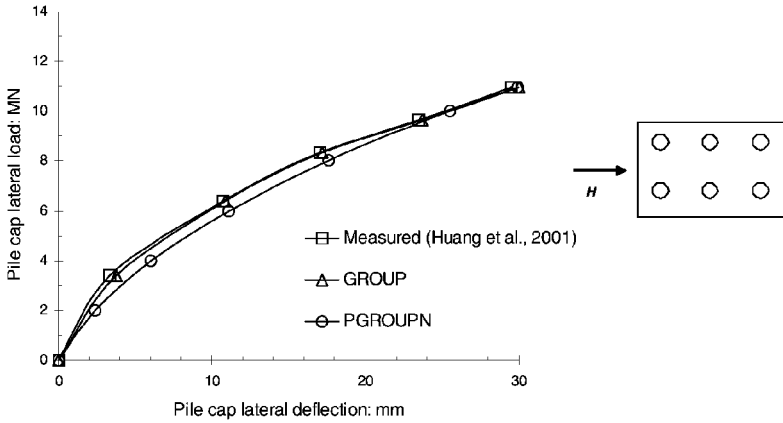


Figure 10.16 Comparison of load-deflection response for 6-pile group.

Final remarks

As early as 1977, Burland, Broms and de Mello pointed out that the primary reason for inclusion of piles as part of a foundation system is to satisfy a serviceability limit on deformations; nevertheless, traditionally pile designers have asked themselves how many piles are needed to carry the weight of the

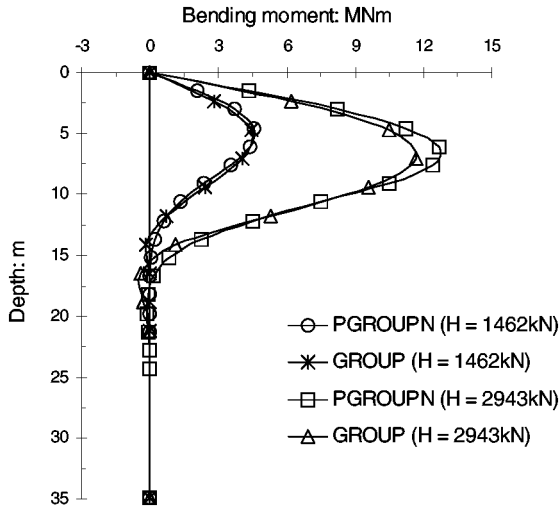


Figure 10.17 Comparison of moment profiles of single pile.

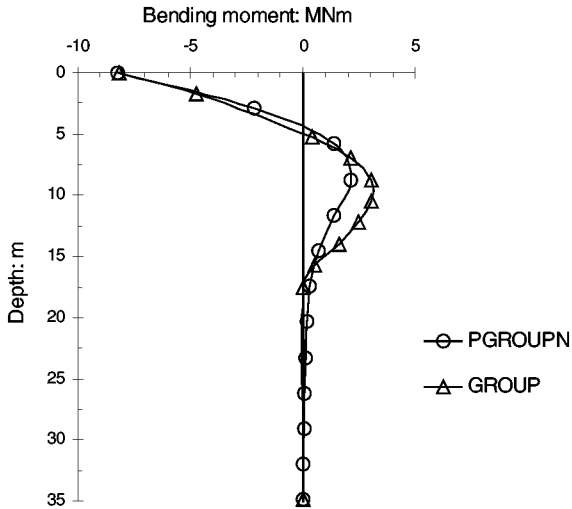


Figure 10.18 Comparison of moment profiles of leading row of piles in 6-pile group under the maximum applied lateral load $H=10,948$ kN.

building rather than asking themselves the question of how many piles are needed to reduce settlements to an acceptable level.

In spite of this primary purpose of piles, twenty-five years later, common practice in pile group design still concentrates on providing suitable capacity from the piles to carry the structural load, and estimation of the settlement is generally treated as a secondary issue. The dominance of capacity-based design,

which is evident in current revisions of national and regional design codes, may partially be attributed to the common belief that predicting deformations is more difficult and less reliable than predicting capacity. In reality, however, the reverse is often true for pile foundations (Randolph, 1994; Mandolini and Viggiani, 1997).

Thus, provided there is a minimum factor of safety, which may be as low as 1.5, pile group design should be approached in terms of satisfying the settlement criterion, rather than being based on a notional factoring of the ultimate state of each pile (Fleming *et al.*, 1992). If this design philosophy is adopted, and hence low safety factors are employed, consideration of non-linear soil behaviour becomes essential. This would result in an improved understanding of pile group behaviour and hence in more effective design techniques.

In this chapter, the effects of soil non-linearity on pile group response, as measured experimentally and as predicted by current numerical analyses, have been discussed. A computer program, called PGROUPN, for pile group analysis and design has been presented. It has been shown that the proposed method, by taking into account the continuous nature of pile-soil interaction, removes the uncertainty of empirical t - z and p - y approaches and provides a simple design tool based on conventional soil parameters.

Use of the program may lead to a number of significant advantages in practice. For example, even for a purely linear analysis, the PGROUPN solution is capable of modelling important features of group behaviour which are normally disregarded by the other numerical codes. Consideration of such features is essential in order to obtain a more realistic prediction of the load distribution between the individual piles of the group.

Another significant aspect of group behaviour which is not treated adequately by the other numerical procedures is the effect of soil non-linearity. The main advantage of a non-linear group analysis system over a linear one is that it has the desirable effect of demonstrating a relative reduction of the corner loads in large groups in both the horizontal and vertical senses. It has been shown that, even at typical working load levels, this reduction is significant. These observations are of basic importance in practice and may lead to tangible improvements in design procedures and worthwhile savings in construction costs.

Acknowledgements

The author is grateful to Dr Ken Fleming, Cementation Foundations Skanska, and Dr Nick Hurt, Halcrow Group, for reading the manuscript and providing valuable comments.

References

- Atkinson, J.H. (2000). Non-linear soil stiffness in routine design. *Geotechnique* **50**, No. 5, 487–508.
- Banerjee, P.K. and Driscoll, R.M. (1976). Three-dimensional analysis of raked pile groups. *Proc. Instn Civ. Engrs*, Part 2, Vol. 61, Dec., 653–671.
- Basile, F. (1999). Non-linear analysis of pile groups. *Proc. Instn. Civ. Engng, Geotech. Engng* **137**, No. 2, April, 105–115.
- Berezantzev, V.G., Khristoforov, V. and Golubkov, V. (1961). Load bearing capacity and deformation of piled foundations. *Proc. 5th Int. Conf. Soil Mech. Fdn Engng*, Paris **2**, 11–15.
- Briaud, J.L., Tucker, L.M. and Ng, E. (1989). Axially loaded 5 pile group and single pile in sand. *Proc. 12th Int. Conf. Soil Mech. Fdn Engng*, Rio de Janeiro **2**, 1121–1124.
- Broms, B.B. (1964). Lateral resistance of piles in cohesive soils. *J. Soil Mechs Fdn Division, Am. Soc. Civ. Engrs* **90**, No. SM2, 27–63.
- Brown, D.A. and Shie, C.F. (1990). Numerical experiments into group effects on the response of piles to lateral loading. *Computers and Geotechnics* **10**, No. 4, 211–230.
- Burghignoli, A. and Desideri, A. (1995). Analisi di un gruppo di pali sollecitati da forze orizzontali. *Riv. Ital. Geotecnica*, No. 3, 163–178.
- Burland, J.B., Broms, B.B. and de Mello, V.F.B. (1977). Behaviour of foundations and structures. *Proc. 9th Int. Conf. Soil Mech. Fdn Engng*, Tokyo **2**, 495–546.
- Butterfield, R. and Banerjee, P.K. (1971). The elastic analysis of compressible piles and pile groups. *Geotechnique* **21**, No. 1, 43–60.
- Chow, Y.K. (1986a). Analysis of vertically loaded pile groups. *Int. J. Numer. Anal. Meth. Geomechs* **10**, No. 1, 59–72.
- Chow, Y.K. (1986b). Discrete element analysis of settlement of pile groups. *Computers & Structures* **24**, 1, 157–166.
- Chow, Y.K. (1987). Three-dimensional analysis of pile groups. *J. Geotech. Engng, Am. Soc. Civ. Engrs* **113**, No. 6, 637–651.
- Cox, W.R., Dixon, D.A. and Murphy, B.S. (1984). Lateral load tests on 25.4-mm (1-in.) diameter piles in very soft clay in side-by-side and in-line groups. *Laterally loaded deep foundations: analysis and performance*, ASTM STP 835, J.A.Langer, E.T. Mosley, and C.D.Thompson (eds), American Society for Testing and Materials, 122–139.
- Duncan, J.M. and Chang, C.Y. (1970). Non-linear analysis of stress and strain in soils, *J. Soil Mechs Fdn Division, Am. Soc. Civ. Engrs* **96**, No. SM5, 1629–1681.
- Duncan, J.M. and Mokwa, R.L. (2001). Passive earth pressures: theories and tests. *J. Geotech. and Geoenv. Engng, Am. Soc. Civ. Engrs* **127**, No. 3, 248–257.
- Fleming, W.G.K., Weltman, A.J., Randolph, M.F. and Elson, W.K. (1992). *Piling Engineering* (2nd edn). Blackie Academic & Professional, Glasgow.
- Fraser, R.A. and Wardle, L.J. (1976). Numerical analysis of rectangular rafts on layered foundations. *Geotechnique* **26**, No. 4, 613–630.
- Gazetas, G. (1991). Foundation vibrations. In H.-Y.Fang (ed.), *Foundation Engineering Handbook*, Van Nostrand Reinhold, New York, 553–593.
- Geocentrix (2002) *Repute 1.0*, Pile Group Design software; www.geocentrix.co.uk

- Hirayama, H. (1991). Pile-group settlement interaction considering soil non-linearity. *Computer methods and advances in geomechanics* (eds Beer, Booker and Carter), Balkema, 139–144.
- Hirayama, H. (1994). Secant Young's modulus from N -value or C_u considering strain levels. *Proc. 1st Int. Conf. on Pre-failure Deformation of Geomaterials*, Sapporo 1, 247–252.
- Hoit, M.I., McVay, M., Hays, C. and Andrade, P.W. (1996). Non-linear pile foundation analysis using Florida-Pier. *J. Bridge Engng, Am. Soc. Civ. Engrs* 1, No. 4, 135–142.
- Huang, A.B., Hsueh, C.K., O'Neill, M.W., Chern, S. and Chen, C. (2001). Effects of construction on laterally loaded pile groups. *J. Geotech. and Geoenv. Engng, Am. Soc. Civ. Engrs* 127, No. 5, 385–397.
- Imai, T. and Tonouchi, K. (1982). Correlation of N value with S -wave velocity. *Proc. 2nd Eur. Symp. on Penetration Testing, Amsterdam*, 67–72.
- Jardine, R.J., Symes, M.J. and Burland, J.B. (1984). The measurements of soil stiffness in the triaxial apparatus. *Géotechnique* 34, No. 3, 323–340.
- Jardine, R.J., Potts, D.M., Fourie, A.B. and Burland, J.B. (1986). Studies of the influence of non-linear stress-strain characteristics in soil-structure interaction. *Géotechnique*, 36, No. 3, 377–396.
- Kagawa, T. (1992). Moduli and damping factors of soft marine clays. *J. Geotech. Engng, Am. Soc. Civ. Engrs* 118, No. 9, 1360–1375.
- Kimura, M. and Adachi, T. (1996). Analyses on laterally loaded cast-in-place concrete piles. *Proc. 6th Int. Conf. Piling and Deep Foundations, Deep Foundation Institute, Bombay*, 3.9.1–3.9.6.
- Kuwabara, F. (1991). Settlement behaviour of non-linear soil around single piles subjected to vertical loads. *Soils and Fdns* 31, No. 1, 39–46.
- Mandolini, A. and Viggiani, C. (1997). Settlement of piled foundations. *Géotechnique* 47, No. 4, 791–816.
- Mindlin, R.D. (1936). Force at a point in the interior of a semi-infinite solid. *Physics* 7, 195–202.
- Murchison, J.M. and O'Neill, M.W. (1984). Evaluation of p - y relationships in cohesionless soils. In J.Mayer (ed.), *Analysis and design of pile foundations*, EASCE, New York, 174–191.
- Ng, C.W.W., Zhang, L. and Nip, D.C.N. (2001). Response of laterally loaded large-diameter bored pile groups. *J. Geotech. and Geoenv. Engng, Am. Soc. Civ. Engrs* 127, No. 8, 658–669.
- Ohsaki, Y. and Iwasaki, R. (1973). On dynamic shear moduli and Poisson's ratios of soil deposits. *Soils and Fdns* 13, No. 4, 61–73.
- O'Neill, M.W., Ghazzaly, O.I. and Ha, H.B. (1977). Analysis of three-dimensional pile groups with non-linear soil response and pile-soil-pile interaction. *Proc. 9th Annual Offshore Technology Conf.*, Houston, Paper 2838, 245–256.
- O'Neill, M.W., Hawkins, R.A. and Mahar, L.J. (1982). Load transfer mechanism in piles and pile groups. *J. Geotech. Engng, Am. Soc. Civ. Engrs*, 108, No. GT12, 1605–1623.
- Ottaviani, M. (1975). Three-dimensional finite element analysis of vertically loaded pile groups. *Géotechnique* 25, No. 2, 159–174.
- Poulos, H.G. (1979). Settlement of single piles in nonhomogeneous soil. *J. Geotech. Engng, Am. Soc. Civ. Engrs* 105, No. GT5, 627–641.

- Poulos, H.G. (1989). Pile behaviour—theory and application. *29th Rankine Lecture, Géotechnique* **39**, No. 3, 365–15.
- Poulos, H.G. (1990). *User's guide to program DEFPIG—Deformation Analysis of Pile Groups, Revision 6*. School of Civil Engineering, University of Sidney.
- Poulos, H.G. (1993). Settlement prediction for bored pile groups. *Proc. 2nd Int. Geot. Sem. on Deep Foundations on Bored and Auger Piles, BAP II*, Ghent, 103–117.
- Poulos, H.G. (1994). Settlement prediction for driven piles and pile groups. *Proc. Conf. on vertical and horizontal deformations of foundations and embankments*, College Station, Texas, Geotechnical Special Publication, Vol. 2, No. 40, 1629–1649.
- Poulos, H.G. and Davis, E.H. (1980). *Pile foundation analysis and design*. Wiley, New York.
- Poulos, H.G. and Hewitt, C.M. (1986). Axial interaction between dissimilar piles in a group. *Proc. 3rd Int. Conf Num. Methods in Offshore Piling*, Nantes, 253–270.
- Poulos, H.G., Carter, J.P. and Small, J.C. (2001). Foundations and retaining structures—research and practice. *Proc. 15th Int. Conf. Soil Mech. Fdn Engng*, Istanbul, second plenary session, 2527–2606.
- Randolph, M.F. (1980). PIGLET: *A computer program for the analysis and design of pile groups under general loading conditions*. Cambridge University Engineering Department Research Report, Soils TR91.
- Randolph, M.F. (1994). Design methods for pile groups and piled rafts. *Proc. 13th Int. Conf. Soil Mech. Fdn Engng*, New Delhi 5, 61–82.
- Randolph, M.F. and Wroth, C.P. (1979). An analysis of the vertical deformation of pile groups. *Géotechnique* **29**, No. 4, 423–439.
- Reese, L.C. and Van Impe, W.F. (2001). *Single piles and pile groups under lateral loading*. Balkema, Rotterdam, 463 pp.
- Reese, L.C., Cox, W.R. and Koop, F.D. (1975). Field testing and analysis of laterally loaded piles in stiff clay. *Proc. 7th Annual Offshore Technology Conf.*, Houston, 671–690.
- Reese, L.C., Wang, S.T., Arrellaga, J.A. and Hendrix, J. (2000). *Computer program GROUP for Windows user's manual, version 5.0*. Ensoft, Austin, Texas.
- Rollins, K.M., Peterson, K.T. and Weaver, T.J. (1998). Lateral load behaviour of full-scale pile group in clay. *J. Geotech. and Geoenv. Engng, Am. Soc. Civ. Engrs* **124**, No. 6, 468–478.
- Rollins, K.M., Sparks, A.E. and Peterson, K.T. (2000). Lateral load capacity and passive resistance of full-scale pile group and cap. *Transportation Research Record 1736, Paper No. 00-1411*, Transportation Research Board, 24–32.
- Steinbrenner, W. (1934). Tafeln zur Setzungberechnung. *Strasse* **1**, 221.
- Tomlinson, S.J. (1994). *Pile design and construction practice* (4th edn). E & FN Spon, London.
- Tomlinson, S.J. (1995). *Foundation design and construction* (6th edn). Longman, Singapore.
- Viggiani, G. and Atkinson, J.H. (1995). Interpretation of bender element tests. *Géotechnique* **45**, No. 1, 149–154.
- Wroth, W.P., Randolph, M.F., Houlsby, G.T. and Fahey, M. (1979). A review of the engineering properties of soils, with particular reference to the shear modulus. *Cambridge University Research Report*, CUED/D-Soils TR75.
- Xu, K.J. and Poulos, H.G. (2000). General elastic analysis of pile groups. *Int. J. Numer. Anal. Meth. Geomechs* **24**, 1109–1138.

Chapter 11

Reservoir compaction, subsidence and well damage

L.Brun Hilbert, Jr.

Introduction

This chapter is concerned with the numerical simulation of compaction of hydrocarbon-bearing rocks, more commonly referred to as *reservoir rock*. With respect to operations in the petroleum industry, rock compaction may be defined as the reduction in overall volume of a subsurface stratum of rock as a result of production of fluids (oil, water and gas) stored within the pore space of the reservoir rocks. During production, both the volume of fluid and the fluid pressure decrease. The weight of the Earth's crust above the reservoir provides a near-constant state of vertical compressive stress on the reservoir, which results in vertical compressive strain within the reservoir rock as pore pressure is reduced during production. While rock compaction can be an important factor to be considered in reservoir engineering and analysis in gravity drained reservoirs, large amounts of compaction can lead to significant subsidence at the surface above the reservoir and can lead to damage and failure of wells in and around the reservoir. Reservoir compaction in the petroleum industry has been responsible for large financial losses to the operators of oil or gas fields due to well repairs and failures, and even costly damage to offshore platforms. Therefore, the numerical simulation of compaction has played an important role in the development of many fields and in the continued development of fields with compaction-sensitive rocks.

First, a brief synopsis of the nomenclature associated with compaction is presented. The most common mechanisms for casing damage due to compaction are discussed, with the focus placed on damage due to localized shear deformation as a result of shearing of thin weak clay layers, faults or fractures. Then historical compaction problems in the petroleum industry are reviewed, with a focus on efforts to analyze compaction, subsidence and casing damage. The theory of deformation of fluid-filled porous media is presented. The finite element approximation of the governing equations of such media is presented incorporating both coupled and uncoupled forms. Finally, the results of a finite element analysis of the compaction and casing damage which occurred at the South Belridge field near Bakersfield, California, USA are presented. The South

Belridge field analysis was performed in an effort to reduce or to mitigate the high rate of well failures associated with the severe compaction problem.

Petroleum industry compaction and subsidence problems

Reservoir compaction and surface subsidence

Compaction is generally taken to mean the increase in density of soil or rock due to a reduction in porosity. With reference to geological processes, compaction is a result of the increase in overburden above a layer of sediment due to deposition on a geological time scale (i.e., lithification); in civil engineering compaction is usually the result of the application of a mechanical force at the surface (densification through vibratory compactors, rollers, or an additional layer of soil); and in petroleum engineering compaction is usually associated with the decrease in pore pressure and pore volume during production. *Consolidation* is more strictly related to the transient expulsion of fluid (usually water) from the pores of a soil. With restriction to reservoir rock behavior, pore compaction, or simply compaction, is defined in this chapter to mean the change in volume of a sample of rock due to a change in pore volume. Since the focus of the work covered in this chapter is on compaction of a hydrocarbon reservoir, compaction means the reduction in the volume of reservoir rock due to a decrease in reservoir pressure as a result of production.

Some nomenclature associated with oil and gas reservoir compaction and surface subsidence is reviewed in this section. [Figure 11.1](#) is a cross section of a reservoir. The depicted cross section is the east to west cross section of the South Belridge field, an analysis of which is presented later in this chapter. In this case, the reservoir is comprised of layers of diatomite rock, which is at a depth of from 500 to 1000 feet (152 to 305 metres) below the surface. The dome-shaped diatomite reservoir is about 1000 feet (305 metres) at its thickest and about 5000 feet (1524 metres) wide. The rock above the reservoir is referred to as the *overburden*. The volume and weight of the overburden rock remains constant during field development. It may be noted that in the specific case of the South Belridge field, oil and gas has also been produced from the Tulare sands within the overburden, but the effect of this production has been neglected in the analysis of the Belridge diatomite reservoir compaction. The weight of the overburden constitutes the vertical load applied to the top of the reservoir, which is in part responsible for driving the compaction of the reservoir rock. As fluid is withdrawn from the reservoir and pore pressure decreases, the portion of the overburden stress supported by the pore fluid is transferred to the rock surrounding the pores, a notion that is captured within the concept of *effective stress*, to be addressed in a later section. The rock directly underneath the reservoir is referred to as the *underburden*. In the case of soft-rock, compactive reservoirs, the underburden rock is usually stiffer and stronger than the reservoir

rock. Therefore, the underburden is usually assumed to provide a non-deformable boundary at the bottom of the reservoir. The rock boundaries at the sides of the reservoir are called *flanks*.

Ubiquitous to any large, subsurface rock unit, and as indicated in [Figure 11.1](#), are faults, fractures and interfaces between rocks of differing mechanical properties, and geologic unconformities. Generally, these various geologic features are referred to as *discontinuities*.^{1,2} Thin layers of weak, plastic shale or clay, often present as a natural consequence of depositional processes, are classified herein as discontinuities. Geological unconformities may be the locations of significant changes in mechanical stiffness, which can be responsible for focusing shear deformation, and these are also classified as discontinuities for the purposes of this chapter. Additionally, changes in pore pressure can initiate slip on faults and fractures.³ Discontinuities have low shear strength or resistance to shear displacement, so they may be the location of large shear deformations. Water or oil wells that penetrate actively shearing discontinuities may be deformed to the extent that they may be considered damaged, which is the focus of the discussion on well damage and failures in this chapter.

As a prelude to later discussions, consider a petroleum reservoir that has undergone significant reservoir compaction as a result of eighteen years of field operation. Depicted in [Figure 11.2](#) is a cross section from a finite element analysis of the South Belridge field reservoir compaction and subsidence process, which is presented later in this chapter. The displacements calculated in the analysis have been exaggerated by ten times to illustrate the effects of reservoir compaction. The cross section shown has superimposed on it a color contour plot of reservoir pore pressures at the end of a simulation of eighteen years of field operation. The color contours in the center of the cross section represent the total pressure reduction due to production from wells. As fluids (oil, gas and water) are produced from the reservoir through wells, pore pressure and pore volume decrease. As a result, compressive effective stress and compressive vertical strain both increase, along with a reduction of the thickness of the reservoir. The vertical compressive strains in the reservoir result in “sagging” of the overburden layers, resulting in downward displacements at the surface. The decrease in elevation of the surface is termed *surface subsidence*. Water may be pumped into the reservoir for pressure maintenance to sustain productivity, or sometimes above the reservoir in an attempt to “pump up” the reservoir to counteract compaction and subsidence. The dark contours in [Figure 11.2](#) are contours of pressure increase due to water injection. One important feature that can be seen in [Figure 11.2](#) is that the rock units on the flanks of the reservoir are “dragged” toward the center of the field, which are the result of the horizontal components of strain. This effect may exacerbate well damage near the flanks.

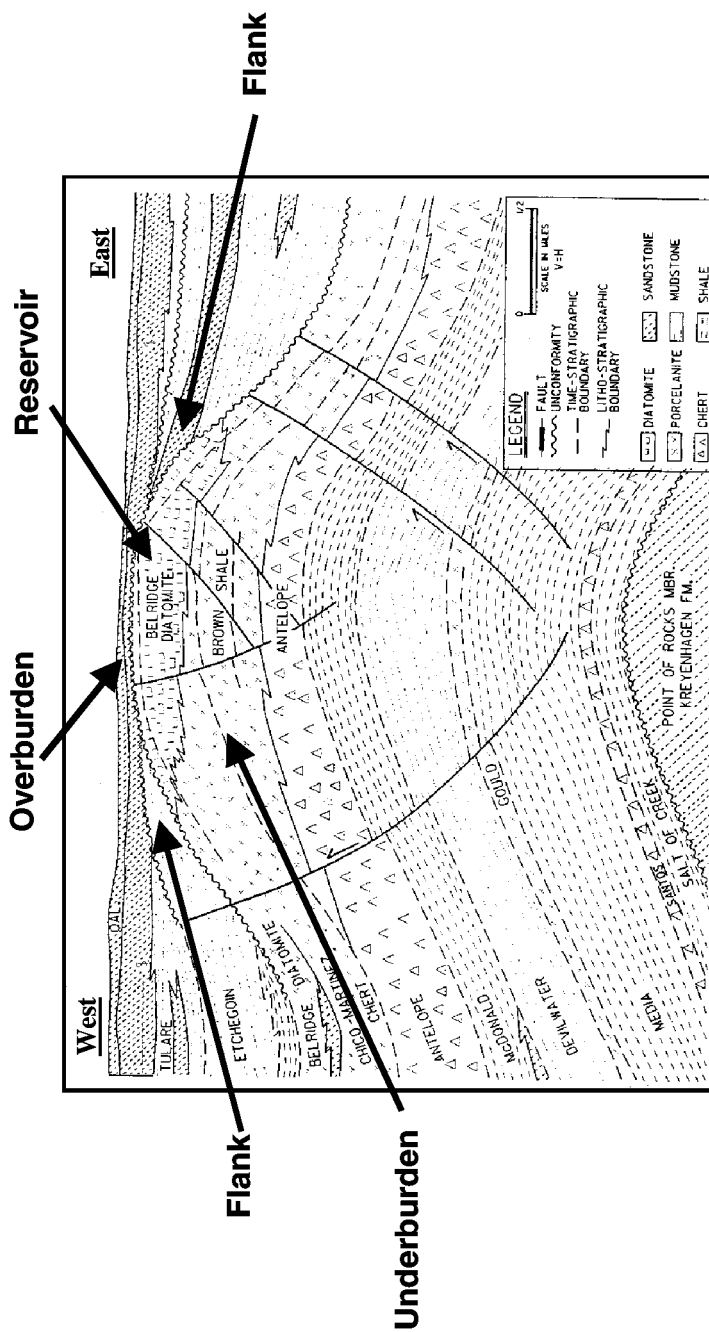


Figure 11.1 East to west cross section of the South Belridge field.

Historical perspectives on compaction and subsidence

Subsidence is an age-old problem and its effects on man and man-made structures, which range from a nuisance to catastrophic, have been well documented.^{4,5} Subsidence may be caused by the recovery of hydrocarbon reserves,^{6,7} pumping water from aquifers,⁸ geothermal fluid withdrawal,⁹ mining^{10,11} and tunneling.¹² Compaction of oil and gas reservoir rock is the source mechanism for costly problems in petroleum fields all over the world. Major problems have been documented in Norway, Russia, Italy, Venezuela, Japan, and in the United States in California, Texas, and the Gulf of Mexico.⁷ For example, reservoir compaction in the Ekofisk field in the North Sea has reportedly caused subsidence greater than 16 ft, resulting in costs of \$400 million to jack up offshore platforms and repair related damage.¹³⁻²¹ Reservoir compaction and casing damage associated with it has also been a continuing problem in other North Sea fields.^{22,23}

Extensive and costly problems associated with subsidence and reservoir compaction in the United States have occurred in the San Joaquin Valley near the cities of Los Angeles and Bakersfield in Southern California. Reservoir compaction in the Wilmington field near Long Beach, California, caused earthquakes, resulted in surface subsidence of as much as 33 feet, and hundreds of well failures and damage to surface facilities and structures.²⁴ By 1962, the problems in the Wilmington field and surrounding areas required expenditures exceeding \$100 million for repairs and damage mitigation. As a result, effort has been expended towards developing mathematical models of the Wilmington field.²⁵⁻²⁸

The Belridge field in the San Joaquin Valley near Bakersfield, California also has a long history of subsidence and compaction problems.²⁹⁻³² It has been producing since 1911 and is now recognized as one of the largest oil-producing reservoirs in the United States.³³ It has well-documented problems associated with reservoir rock compaction, which are discussed later in this chapter. The Lost Hills field, also in the San Joaquin Valley in the same geographic location as the Belridge field, has a history of compaction and well damage problems almost identical to the Belridge field.^{34,35}

A problem of scale

Reservoir compaction is often viewed as a *large-scale* problem. The areal extent of measurable surface subsidence may be of the order of square miles and the lateral extent of the reservoir of the same order. Hydrocarbon reservoirs that have significant compaction and surface subsidence have been thick, of the order of hundreds to thousands of feet. However, actual compaction-induced surface subsidence may be of the order of only several inches to a few feet, which may be sufficient to cause distress to buildings and other surface structures.³⁶ Moreover, compaction causes significant operational problems for hydrocarbon

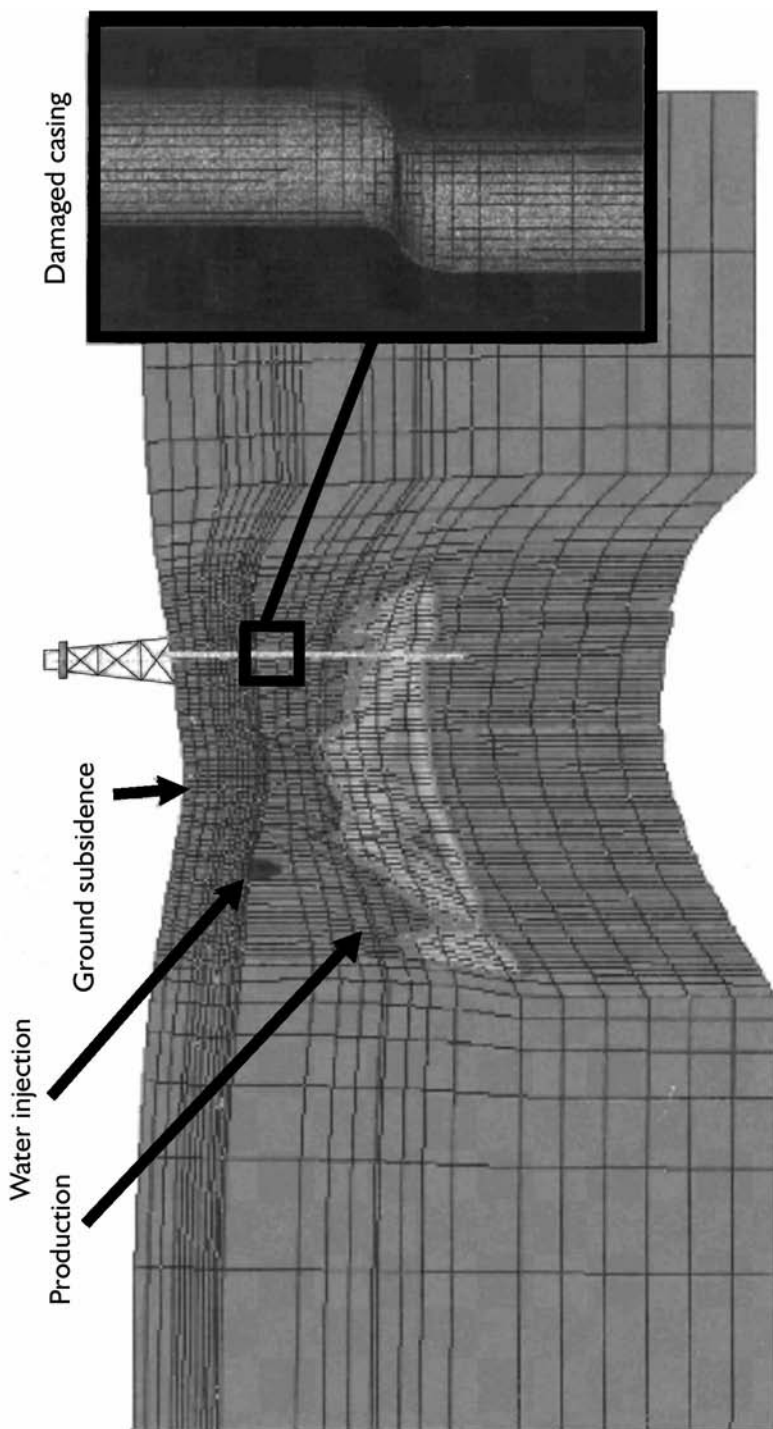


Figure 11.2 Cross section of a reservoir that has undergone significant reservoir compaction (discrepancies exaggerated by 10 times).

reservoirs and water aquifers, the dimensions of which are on an even smaller or local scale, that of the *wellbore*. In particular, compaction-induced shearing causes severe localized deformation of a casing over small lengths, often less than 10 feet (3 metres). The interaction of soft rock with the casing, and moreover the stiffness and strength of the rock, governs the geometry of the damaged, deformed casing. If effective and lasting damage mitigation and failure prevention measures are to be designed and implemented, then an understanding of the mechanisms of shear-induced casing damage is required.

Compaction induces bending and shearing deformations around the edges of the area of surface subsidence, or the “subsidence bowl”. Under such shearing, thin weak-rock layers and geologic unconformities fail or undergo significant shear deformations. Shear-induced, relative motions between layers, called “slip”, cause localized shear deformation. Such shearing can cause deformation and failure of wells penetrating the layers. It is not feasible to include the details of a wellbore in field-scale models in order to determine a relation between compaction and wellbore deformation. Instead, it is necessary to develop a correlation between shear-induced slip computed from large-scale models to either observations of casing shear damage or the results of wellbore-scale modeling. This procedure was followed in the study of the South Belridge field discussed later in this chapter.³⁷

Casing damage

Casing *damage* is herein defined as a change in the dimension of the casing which may affect the usability or serviceability of the casing, but for which the casing may be repaired to render it useable once again. Casing *failure* is defined as a change in casing dimension, which renders the casing irreparable or unusable, or separates the casing into one or more pieces, which is referred to as a *catastrophic failure*. Damage and failure of the casing due to shear deformation is focused upon in this chapter. Damage to the casing due to reservoir compaction has been the focus of several investigators. Casing deformation in the Ekofisk field and other fields of the North Sea has resulted in considerable operational difficulty.^{18–23} Similarly, reservoir compaction has caused significant difficulty and expense in the oilfields of southern California, most prominently in the Wilmington field,^{24, 28,40} the Belridge field,^{28,32,37–42} and in the Lost Hills field.^{34,35} Rock-casing interactions leading to damage and failure have also occurred in Montana and North Dakota⁴³ and in the Gulf of Mexico.^{43,44} Deforming salt has been studied as a mechanism for casing collapsed and failure.⁴⁵ In addition, salt and permafrost, a mixture of ice and rock, will thaw due to heating of the wellbore during production, which can result in high compressive strain and casing deformation.^{46,47} Perforation holes in the casing can also lead to casing deformation due to compaction or flow of weak, plastically deforming rock.^{48,49} Finally, numerous general studies of casing damage due to casing-

structure interactions for a variety of rock types, rock deformation mechanisms, and casing configurations (i.e., casing inclination) have been conducted.^{50–54}

With respect to compaction-induced shearing damage to casing, which is the mechanism for casing damage focused upon in this chapter, such damage can result from shearing of a thin, weak shale layer as depicted in the insert of Figure 11.2. Such shearing of thin, weak shale layers occurs in the overburden due to the bending (or sagging) of the overburden as a result of reservoir compaction. While the overall displacements in the overburden strata appear to be large in the figure, larger shear displacements are “focused” on the weak shale layer. That is, the weak layers “absorb” most of the shear deformation. As a result, the shear deformation of the casing is termed *localized*. Shearing reaches maximum magnitudes nearest the flanks of the reservoir. Faults and fractures can similarly affect casing damage. In fact, earthquakes have been induced by increases in shear stress in and around compacting reservoirs, resulting in a completely severed casing.²⁴

In addition to localized shearing, several other modes of casing damage due to reservoir compaction are possible, which have been discussed in some detail by Cernocky and Scholibo.⁴⁵ and Dusseault *et al.*⁵³ Casing damage caused by vertical compressive strains includes axial column-type or Euler buckling, if the well is vertical or nearly vertical. Crushing or collapse of the casing cross section may occur when the well is inclined (i.e., deviated), the worst case occurring when the casing is horizontal. Depending on the stiffness of the surrounding rock and the ratio of the casing outside diameter to its wall thickness, the pipe may experience cross-sectional, “can-type” buckling near the threaded connections. This type of compressive failure mode has been documented for compression caused by the thawing of permafrost.⁴⁷ In some cases, under sufficiently high compressive strains, threads in threaded connections may shear off, resulting in a “telescoped” connection. Tensile failure modes are also associated with compaction, but occur most often within the overburden strata. Large tensile strains may occur in the overburden due to vertical straining as the overburden rock layers sag downward, much as the roof of an unsupported tunnel. Such tensile strains can result in the “pull-out” failure of threaded connections. Such a failure mode may also occur if a connection is placed in a zone of localized shearing.

Mechanics of porous media

The mechanics of geologic materials has come to be referred to as *geomechanics*. Both experimental and computational geomechanics have subtleties unique from the study of solid, non-porous continua. The materials of interest are typically rocks or soils, with air and liquids residing in the pores. The cornerstones of the theory of the mechanics of porous media are a stress decomposition principle, the balance laws of linear momentum and mass, the balance of energy, and an appropriate constitutive model. Beginning with the

fundamental assumptions being stated, the governing equations for deformation fluid-filled porous media are derived, with the unknown variables being displacements and pore pressure. In the following section a mathematical formulation for deformation of fluid-filled, porous media is presented. The presentation follows that of Hibbitt, Karlsson and Sorensen⁵⁵ and Borja and Alarcón.⁵⁶ A finite element approximation to these governing equations is presented as implemented in the ABAQUS general-purpose, nonlinear finite element software, which was used for simulations of the reservoir compaction and casing damage discussed later in this chapter. The important effects of *coupling* between overall stress on the solid-fluid volume and pore pressure are discussed, as well as the effects of simplification by uncoupling the equations. Linear and nonlinear constitutive models are presented; including a constitutive model for fluid-filled porous media which incorporates a *Drucker-Prager* shear failure surface and an elliptical *Cap* yield surface to capture the effects of permanent deformation under volumetric strains.

Linear momentum balance

The material under consideration is assumed to be composed of a mixture of solid and fluid. Grains, or particles, of soil or rock constitute the solid portion. The particles may be cemented or bonded at contact points, or may slide, translate and rotate relative to one another. The framework of solid material is often referred to as the *matrix*. The interstitial space, or pore space, amongst the particles is assumed in the following developments to be completely filled with a single-phase fluid. That is, it is assumed that the media is *saturated*. It may be noted that the assumption that the media is saturated is not completely necessary, as only very general developments have been laid out for partially saturated media and multiphase flows of pore fluid.⁵⁵⁻⁵⁷ The processes that take place during compaction are assumed to be *quasi-static*, inertia forces and contributions to momentum from chemical reactions are assumed negligible.

Now consider a fluid-saturated body denoted by $B \subset R^n$ and let U be any open subset of B with piecewise C^1 boundary. Let $\phi_t: B \rightarrow R^n$ be the motion, or set of configurations of the body B . Let the motion of the fluid be denoted \cdot . Denote the volume of the subset U in an assumed reference or *undeformed* configuration by dV and the volume in the *deformed* configuration, after the motion $\phi_t(U)$, by dv . The position of a material point in the body will be denoted by the X in the reference configuration and by $x = \phi_t(X)$ in the deformed configuration. Let the volume of solid matrix in the deformed configuration be denoted by dv_g . Then the porosity may be defined as:

$$\phi := \frac{dv_p}{dv} = 1 - \frac{dv_g}{dv} = 1 - \frac{dv_g}{dV_g} \frac{dV}{dv} \frac{dV_g}{dV} = 1 - J_g J^{-1} (1 - \phi^0) \quad (11.1)$$

where

The linear momentum of a saturated body can be derived by considering it as a mixture of solid and fluid phases. In this context, define the Cauchy partial stress tensors on the solid and fluid arising from inter-particle and fluid stresses as σ^g and σ^f , respectively.^{56,58,59} Also, denote by \mathbf{n} the unit normal vector to the surface (U) of the deformed body. Then, the linear momentum balance of the solid phase in the current (deformed) configuration is:

$$\int_a \sigma^g \cdot \mathbf{n} da + \int_v \mathbf{h}^g dv + \int_v \rho_g (1 - \phi) \mathbf{g} dv = \mathbf{0} \quad (11.2)$$

The momentum balance for the fluid phase is:

$$\int_a \sigma^f \cdot \mathbf{n} da + \int_v \mathbf{h}^f dv + \int_v \rho_f \phi \mathbf{g} dv = \mathbf{0} \quad (11.3)$$

In the above momentum balance equations, \mathbf{g} is the gravitational acceleration vector, ρ_g and ρ_f are the solid and fluid mass densities, \mathbf{h}^g is a vector of force per unit volume arriving from the frictional force of the flowing pore fluid on the solid, and \mathbf{h}^f is the reaction on the fluid arising from \mathbf{h}^g . Since \mathbf{h}^g and \mathbf{h}^f are internal forces, their sum is zero. Summing Equations (11.1) and (11.2) gives the linear momentum balance for the solid and fluid mixture, as follows:

$$\int_a \sigma \cdot \mathbf{n} da + \int_v \rho \mathbf{g} dv = \mathbf{0} \quad (11.4)$$

where the Cauchy total stress tensor has been defined as

$$\sigma := \sigma^g + \sigma^f \quad (11.5)$$

and the mass density of the mixture, referred to as the saturated mass density, is

$$\rho := \rho_g (1 - \phi) + \rho_f \phi \quad (11.6)$$

The concept of effective stress

Terzaghi⁶⁰ is generally credited with first recognizing that the deformation of fluid-filled, porous media is governed by an *effective stress*. The effective stress has been used as an alternative to the total stress decomposition of Equation (11.5) based on the physical intuition of Terzaghi, experimental validation by many investigators in soil and rock mechanics, and more recently has been shown to have a rational interpretation in solid mechanics. The fundamental concept is that given an idealized volume of water-saturated soil, on the boundary of which is imposed a state of stress, given by the Cauchy total stress tensor, σ , that stress is shared by the soil and water in the following way:

$$\boldsymbol{\sigma}' = \boldsymbol{\sigma} - \alpha p \mathbf{I} \quad (11.7)$$

where $\boldsymbol{\sigma}'$ is the effective stress tensor, α is a material parameter referred to as the effective stress coefficient, p is the fluid pressure in the pores, and \mathbf{I} is the second order identity tensor.

In considering finite, elastoplastic deformations and using the Kirchhoff total stress tensor, defined by in the balance of mechanical energy of a mixture of incompressible solids and fluids, Borja and Alarcón⁵⁶ showed that the effective stress, is defined as

$$\boldsymbol{\tau}' = \boldsymbol{\tau} - p \mathbf{I} \quad (11.8)$$

where $\boldsymbol{\tau}' = p \mathbf{I}$ is a rational concept for effective stress. They showed that, since the fluid is assumed to be incompressible and has no shear strength, the component of stress in the fluid phase, does not perform mechanical work on the system, which is a clear distinction from the partial stress $\boldsymbol{\tau}^f$. Thus, the effective stress is intuitive and provides a rational and convenient framework for describing the stress within a saturated solid. Since the Kirchhoff stress will be used below, note that it is defined with reference to the undeformed configuration, while the Cauchy stress is defined with respect to the deformed configuration.

Nur and Byerlee⁶¹ showed that for linear, isotropic theory of the mechanics of porous media, the effective stress can be defined and written exactly as:

$$\boldsymbol{\sigma}' := \boldsymbol{\sigma} + \left(1 - \frac{C_r}{C_{bc}}\right) p \mathbf{I} \quad (11.9)$$

where the term in parentheses is identified by the effective stress coefficient α of Equation (11.7). The form of Equation (11.9) adopts the notation proposed by Zimmerman, *et al.*,⁶² in which C_r is the compressibility of the rock matrix and C_{bc} is the compressibility of the bulk rock under the action of the confining stress in a drained test. In an analysis of the linearized theory of Biot^{63–67} and the development of solutions to problems using that theory, Rice and Cleary⁶⁸ showed that while the effective stress law of Equation (11.9) occurs naturally in the equations of equilibrium, it arrives from the constitutive assumption, not from considering the pore pressure p in an analysis of equilibrium.

In the development that follows for finite deformation, elastoplastic finite element analysis, the effective stress law is taken to be:

$$\boldsymbol{\sigma}' = \boldsymbol{\sigma} + \chi p \mathbf{I} \quad (11.10)$$

where χ is an effective stress coefficient dependent upon saturation and surface tension between the pore fluid and solid. The coefficient χ is assumed to be 1.0 for a fully saturated medium. It may be noted that the effective stress coefficient

in Equation (11.10) becomes 1.0 when the rock material is assumed to be incompressible, or when C_r is zero.

Mass balance

Considering the total mass of pore fluid within a control volume in the current, or deformed, configuration, the mass continuity equation is:

$$\int_v \left\{ \frac{\partial(\rho_f \phi)}{\partial t} + \text{div}(\rho_f \phi \mathbf{v}_f) \right\} dv = 0 \tag{11.11}$$

where \mathbf{v}_f is the average fluid velocity of the pore fluid.

Variational forms of governing equations

Let the space of configurations be $C_\phi = \{ \phi: B \rightarrow R^n \mid \phi_i \in H^1, \phi = \phi_d \text{ on } \partial B \}$ and let the space of variations of the spatial variables be $V_\phi = \{ \eta: B \rightarrow R^n \mid \eta_i \in H^1, \eta = 0 \text{ on } \partial B \}$, where H^1 is the space of Sobolev functions of degree one. Now define the space of pore fluid pressures as $C_\psi = \{ \Pi: \phi_t(B) \rightarrow R^n \mid \Pi \in H^1, \Pi = \Pi_d \text{ on } \partial \phi_t \}$ and the space of variations of $V_\psi = \{ \psi: \phi_t(B) \rightarrow R^n \mid \psi \in H^1, \psi = 0 \text{ on } \partial \phi_t \}$. The fluid potential Π is defined by:

$$\text{grad } \Pi = \frac{1}{g \rho_w} \left(\frac{1}{\rho_w} \text{grad } p - \mathbf{g} \right) \tag{11.12}$$

where $\mathbf{g} := -g \partial z / \partial \mathbf{x}$ is the gravitational acceleration and $\text{grad} := \partial / \partial \mathbf{x}$ is the gradient with respect to the current configuration. The space of configurations may be identified with the deformation vector \mathbf{u} and the variations of the deformation field with $\eta = \delta \mathbf{u}$.

A variational form, or weak form, of the linear momentum balance, written with respect to the undeformed configuration, is:

$$G(\mathbf{u}, p, \delta \mathbf{u}) = \int_V (\boldsymbol{\tau} : \delta \boldsymbol{\varepsilon} - p \text{div } \delta \mathbf{u} - \rho_o \delta \mathbf{u} \cdot \mathbf{G}) dV - \int_A \delta \mathbf{u} \cdot \mathbf{t} dA \tag{11.13}$$

where the identity $\delta \boldsymbol{\varepsilon} := \text{grad } \delta \mathbf{u} = \text{sym}(\text{grad } \delta \boldsymbol{\varepsilon})$ has been used, and \mathbf{t} are the surface tractions per unit area. The first term within the volume integral is the internal virtual work, the second term exhibits the coupling between the deformation and the pore pressure, and the third term accounts for the weight of the fluid.

The variational form for the mass balance of fluid, Equation (11.12), is:

$$H(\mathbf{u}, \Pi, \delta \Pi) = \int_V (\delta \Pi \dot{J} - \text{grad } \delta \Pi \cdot \mathcal{F} \nabla) dV - \int_A \delta \Pi Q dA \tag{11.14}$$

where is the prescribed volumetric flow rate of fluid per unit undeformed area across the boundary.

The constitutive model for pore fluid flow is assumed to be Darcy's law:

$$\phi \mathbf{v}_f = \mathbf{k} \frac{1}{g \rho_f} (\text{grad } p - \rho_f \mathbf{g}) \quad (11.15)$$

where \mathbf{k} is the permeability tensor of the fully saturated medium, and \mathbf{g} is the vector of gravitational acceleration. Substituting Equation (11.15) into Equation (11.14) and using the divergence theorem, results in the variational form for the mass balance as follows:

$$H(\mathbf{u}, p, \delta p) = \int_V \left(\delta p \dot{J} + \frac{1}{\rho_w g} \text{grad } \delta p \cdot \mathbf{k} \cdot (\text{grad } p + J \mathbf{G}) \right) dV - \int_A \delta p Q dA \quad (11.16)$$

It can be seen that this equation is coupled due to the products of the pore pressure and its variation and the Jacobian J .

The weak form of the boundary value problem for flow in a saturated porous medium composed of an incompressible solid matrix is to find ϕ , C_ϕ and p , C_p such that

$$G(\mathbf{u}, p, \delta \mathbf{u}) = H(\mathbf{u}, p, \delta p) = 0 \quad (11.17)$$

This weak form of the problem forms the basis for the finite element approximation used in this chapter.

Finite element discretization

The finite element approximation of the Equation (11.13) and Equation (11.16) is developed for this problem by using the following discretizations of the virtual velocity and the virtual rate of deformation:

$$\delta \mathbf{u} = \mathbf{N}^N \delta \mathbf{u}^N \quad (11.18)$$

and

$$\delta \boldsymbol{\varepsilon} = \boldsymbol{\beta}^N \delta \mathbf{u}^N \quad (11.19)$$

where \mathbf{N}^N (S_i) are the nodal interpolation functions with respect to the material coordinates S_i . Usually, the interpolation function is defined as:

$$\boldsymbol{\beta}^N = \text{sym} \left(\text{grad } \delta \mathbf{N}^N \right) \quad (11.20)$$

though more general forms can be developed (e.g., for element formulations involving incompatible modes).

The pore pressure field is discretized such that a single scalar pore pressure is computed at a defined node.

Linearization of variational forms

Linearization provides a means for properly and easily developing a linear theory from the more general nonlinear equations. Linearization is also used to develop exact expressions for the variations of the weak forms of the momentum and mass conservation equations, $G(\mathbf{u}, p, \delta\mathbf{u})$ and $H(\mathbf{u}, p, \delta p)$, for use in a Newton-type iterative solution of the governing equations. Newton procedures for the solution of nonlinear, multivariate equations are described by Oden.⁶⁹ Briefly, given a system of nonlinear equations, for example, $\mathbf{F}(\mathbf{x})=\mathbf{0}$, where \mathbf{F} may be scalar, vector, or tensor valued, the function is expanded as a Taylor series about some suitably selected point:

$$\mathbf{F}(\mathbf{x}) = \mathbf{F}(\mathbf{x}_i + \mathbf{c}_{i+1}) = \mathbf{F}(\mathbf{x}_i) + \mathbf{DF}(\mathbf{x}_i) \cdot \mathbf{c}_{i+1} + \mathbf{D}_2\mathbf{F}(\mathbf{x}_i) \cdot \mathbf{c}_{i+1} + \dots = \mathbf{0} \quad (11.21)$$

where the point x_i is a close approximation to the actual solution, \mathbf{x} , after the i -th iteration, and \mathbf{c}_{i+1} is the difference between the actual solution and its estimation, which should be small. The second term on the right-hand side, \mathbf{DF} , is the derivative of \mathbf{F} at the point \mathbf{x}_i . Neglecting higher-order terms provides an approximate solution of \mathbf{F} after the i -th iteration using the iterate, \mathbf{c}_{i+1} , to the solution:

$$\mathbf{c}_{i+1} = -[\mathbf{DF}] \cdot \mathbf{F}(\mathbf{x}_i) \quad (11.22)$$

The matrix \mathbf{DF} is referred to as the “stiffness matrix,” and is equivalent in this case to the first variation of the function \mathbf{F} . To solve the governing equations for flow in a deforming porous medium requires the determination of the first variations of the functions $G(\mathbf{u}, p, \delta\mathbf{u})$ and $H(\mathbf{u}, p, \delta p)$. As indicated by Equation (11.21), these first variations can be obtained by linearizing the functions G and H .

Following the procedures in Marsden and Hughes⁷⁰ and Borja and Alarcón,⁵⁶ the first variation is obtained by the linearization of $G(\mathbf{u}, p, \delta\mathbf{u})$:

$$\begin{aligned} \mathbf{L}[G(\mathbf{u}, p, \delta\mathbf{u})] &= G^0 + \int_V \text{grad } \delta\mathbf{u} : (\mathbf{d}^0 + \boldsymbol{\tau}^0 \oplus \mathbf{1}) : \text{grad } \delta\mathbf{w} dV \\ &\quad - \int_V (\delta p \text{ div } \delta\mathbf{u} - p^0 \text{ grad}^T \delta\mathbf{u} : \text{grad } \delta\mathbf{w}) dV \\ &\quad - \int_V \rho_w J^0 (\text{div } \delta\mathbf{u}) \delta\mathbf{w} \cdot \mathbf{g} dV - \int_A \delta\mathbf{u} \cdot \delta\mathbf{r} dV \end{aligned} \quad (11.23)$$

The first variation of the weak form of the mass conservation equations is complication by the occurrence of time derivatives.

$$\begin{aligned}
 \mathbf{L}[H_{\Delta t}(\mathbf{u}, p, \delta \mathbf{u})] &= H_{\Delta t}^0 + \int_V \delta p (\mathbf{1} : d\boldsymbol{\varepsilon}) dV \\
 &+ \int_V \Delta t \left[\text{grad } \delta p \cdot \frac{\mathbf{k}}{\rho_w g} \cdot (\text{grad } p - \rho_w \mathbf{g}) \mathbf{1} \right] : d\boldsymbol{\varepsilon} dV \\
 &+ \int_V \Delta t \left[\text{grad } \delta p \cdot \frac{\mathbf{k}}{\rho_w g} \cdot \text{grad } dp \right] dV \\
 &- \int_V \Delta t \left[\text{grad } \delta p \cdot \text{grad } \delta w \cdot \frac{\mathbf{k}}{\rho_w g} \cdot (\text{grad } p - \rho_w \mathbf{g}) \right] dV \\
 &- \int_V \Delta t \left[\text{grad } \delta p \cdot \frac{\mathbf{k}}{\rho_w g} \cdot \text{grad } p \cdot \text{grad } \delta w \right] dV
 \end{aligned} \tag{11.24}$$

Upon discretization and using a Newton iteration scheme, the above system can be written as spatially discretized governing equations at a node as:

$$\begin{bmatrix} \mathbf{K}_s(\boldsymbol{\sigma}', \mathbf{d}) + \mathbf{L}(\mathbf{d}, u) + \mathbf{K}_{gd}(\mathbf{d}) & B(\mathbf{d}) \\ \mathbf{B}^T(\mathbf{d}) + \Delta t \mathbf{L}_c(\mathbf{d}, e) & \Delta t k(\mathbf{d}, e) \end{bmatrix} \begin{bmatrix} \mathbf{d}_c \\ u_c \end{bmatrix} = \begin{bmatrix} \mathbf{F}_r \\ \Delta V_r \end{bmatrix} \tag{11.25}$$

The components of the nodal stiffness matrix derive from the following: \mathbf{K}_s is a stiffness matrix associated with nonlinear material properties and nonlinear deformation geometry, \mathbf{L} is due pore pressure coupling, \mathbf{K}_{gd} is a load stiffness due to gravity loading, B is due to pore volumetric strain, \mathbf{B} is due to bulk volumetric strain, \mathbf{L}_c is related to permeability terms, and k is due to permeability changes during deformation. The corrections to the nodal displacement vector and the nodal pore pressure are represented by pore \mathbf{d}_c and u_c , respectively, while \mathbf{F}_r and V_r are the force and pore volume change residuals, respectively. The terms with the parentheses indicate the dependence of various stiffness factors on the displacement, \mathbf{d} , effective stress, $\boldsymbol{\sigma}'$, pore pressure, u , and the void ratio, e .

The above-stated system of equations is coupled, highly nonlinear and nonsymmetric. The system of equations has been written at one instant in time and includes only a semi-discretization in the time, indicated by t in the permeability terms. For transient problems in which fluid inertia must be considered, complete temporal discretization is not a trivial matter and should be approached with care. In this chapter, we are concerned with steady state solutions and as such the system is simplified, but remains nonlinear, nonsymmetric, and coupled. However, under steady state conditions, the coupling is not as complex. Moreover, the dependence between pore pressure and effective stress can be completely uncoupled as a further simplification.

Constitutive theories for fluid-filled rock

Linear and nonlinear models for the constitutive behavior of fluid-filled rocks are reviewed in this section. An elastoplastic, *Drucker-Prager* model modified to incorporate a Cap surface is applied in later sections in a computational application.

Linear constitutive theory

It is useful to review the general theory of poroelasticity, or Biot theory, which is a formulation of a theory of the stress and strain relations for geomaterials. Biot⁶³ presented a constitutive equation for fluid filled, porous material (e.g., rock or soil) assumed to behave linearly and isotropically under isothermal conditions. It is assumed that the pores are filled completely, or saturated, with a fluid under a pressure p , and that the volume of the pores is characterized by the specific volume $v = V_f/V_b$ where V_f is the volume of the pore fluid and V_b is the volume of the bulk sample of porous, saturated solid. If the rock is saturated with pore fluid and the fluid is incompressible, the specific volume may be recognized as the porosity, ϕ . Biot's linear constitutive equations may be written in the following form:

$$E\varepsilon_{ij} = (1 + \nu)\sigma_{ij} - \nu\sigma_{kk}\delta_{ij} + \frac{E}{3H}p\delta_{ij} \quad (11.26)$$

and

$$v - v_o = \frac{\sigma_{kk}}{3H} + \frac{p}{R} \quad (11.27)$$

where ε_{ij} and σ_{ij} are the components of the infinitesimal strain and stress tensors, respectively, and E and ν are the Young's modulus and Poisson's ratio determined from a "drained" laboratory test of a sample of rock. It may be recalled that the shear and bulk moduli can be computed from Young's modulus and Poisson's ratio by $G = E/2(1 + \nu)$ and $K = 2G(1 + \nu)/3(1 - \nu)$, respectively. The drained test provides the moduli of the porous solid. The two material properties H and R are known as Biot's constants. H and R are often referred to as *coupling* constants, since they relate the deformation of the porous solid to changes in the pore pressure or pore volume changes. It can be shown that:^{71,72}

$$\frac{1}{H} = C_{bc} - C_r \quad (11.28)$$

$$\frac{1}{R} = \phi(C_{pp} + C_f) \quad (11.29)$$

and

$$\frac{1}{R} - \frac{1}{H} = \phi(C_f - C_r) \quad (11.30)$$

where, using the notation of Zimmerman,⁶² C_{bc} is the compressibility of the bulk solid measured from a drained test, C_r is the compressibility of the rock or soil grains (sometimes referred to as the matrix material), C_f is the compressibility of the pore fluid, and C_{pp} is the compressibility of the pores (i.e., the change in volume of the pores due to a change in pore pressure).

Equations (11.26) and (11.27) make clear the *coupling* between pore pressure and deformation of a porous, fluid-filled medium. The first two terms on the right-hand side of Equation (11.26) are easily recognized as deriving from Hooke's law for a linear, elastic solid, while the third term arises from the effect of the fluid pressure within the pores. When such a material is deformed, the pore pressure will change according to the moduli E and H , and the stress will change as well. Equation (11.27) expresses the effect of changes in mean stress, $\sigma_{kk}/3$, and pore pressure upon the change in pore fluid volume in the sample.

For hydrocarbon reservoir compaction, the condition far from a well is that of an undrained rock. A material parameter known as Skempton's coefficient,⁷³ B , which characterizes the dependence between changes in pore pressure and mean stress, may be recovered from the mass balance of the pore fluid:

$$\Delta p = B \frac{\Delta \sigma_{kk}}{3} \quad (11.31)$$

where

$$B = \frac{C_{pp} + C_r}{C_{pp} + C_f} \quad (11.32)$$

It can be seen that for saturated soils and rocks, in which the pore fluid and rock matrix are incompressible, $B=1$, but ranges between about 0.5 and 0.99 for actual rocks.⁷¹

A simple expression for the change of thickness of a reservoir due to compaction resulting from a pore pressure reduction, or drawdown, p , can be derived from Equation (11.27) by:

- (1) assuming a reservoir of large lateral extent compared with its thickness,

- (2) assuming that the vertical stress due to the weight of the overburden does not change and
 (3) assuming that the horizontal stresses at the boundaries do not change.

These assumptions are those for the condition of plane strain and lead to the following expression for the compaction (i.e., the change in thickness), Δh , of the reservoir with initial thickness h or a rock sample of height h :

$$\Delta h = C_m h \Delta p \quad (11.33)$$

where C_m is referred to as the *one-dimensional compressibility* or *uniaxial compaction coefficient*:

$$C_m = \frac{1}{3} \left(\frac{1+\nu}{1-\nu} \right) (C_{bc} - C_r) \quad (11.34)$$

Typical deep-water Gulf of Mexico (GOM) reservoirs have been reported to be composed of unconsolidated to slightly consolidated Miocene, Pliocene and Pleistocene age turbidite sands.⁷⁴ These sands are prone to compaction, since they are young and under-consolidated.⁶² Martin and Serdengecti⁷⁵ presented data on the bulk compressibility of unconsolidated sandstones ranging from about 0.7 to 7.0 μ sips, they also reported that C_m ranges from $0.45C_{bc}$ to C_{bc} . As a further approximation, if C_r is assumed to be much less than C_{bc} , then C_m has an effect on C_{bc} that is a function only of Poisson's ratio. If Poisson's ratio ranges from 0.2 to 0.45 for consolidated to unconsolidated rock, then C_m ranges from $0.5C_{bc}$ to $0.88C_{bc}$.

Nonlinear, elastic-plastic constitutive model

Failure of rocks and soils under shear stress is well known and understood.^{1,76,77} For reservoir rocks, depletion of pore pressure results in increased stress carried by the rock matrix, reduction of pore volume, and possibly pore collapse. High porosity, weakly cement rocks are most susceptible to pore collapse.^{74,78-80} On the micro-scale, pore collapse is the result of the failure of bonds between particles and the subsequent rearrangement of the particles. Under sufficiently high stress and associated high volumetric strain, rock grains can fracture or become fragmented, a situation not often encountered in soils due to the relatively lower overburden stress near to the Earth's surface. For clastic rocks with weak grain bonds, shear stress can enhance compaction by the rearrangement of intact or fragmented particles. Pore collapse results in unrecoverable deformation and thus plasticity theories are amenable to developing a constitutive model. One such model, which has been used widely and successfully for both soils and rocks, is the generalized cap model of

DiMaggio and Sandier.⁸¹ This is a multi-surface plasticity model, which includes a non-associative shear failure surface and an associative cap plasticity surface.

The ABAQUS program, used for the computations presented later in this chapter, includes a linear *Drucker-Prager* shear failure surface, combined with a Cap plasticity surface.⁵⁵ This constitutive model is not identical to that implemented by DiMaggio and Sandler, but is based on the same phenomenological framework and is similar in many respects. A sketch of the yield envelope is shown in Figure 11.3. The *Drucker-Prager* linear failure surface is given by:

$$S_f = t - p(\tan\beta) - d \quad (11.35)$$

where t is a deviatoric stress measure, p is the mean stress, β is the internal friction angle, and d is the cohesion. The deviatoric stress measure in Equation (11.35), which is the ordinate in Figure 11.3, is defined as:

$$t = \frac{1}{2}q \left[1 + \frac{1}{K} - \left(1 - \frac{1}{K} \right) \left(\frac{r}{q} \right)^3 \right] \quad (11.36)$$

where

$$p = -\frac{1}{3} \text{trace}(\boldsymbol{\sigma}) \text{ is the equivalent pressure stress,}$$

$$q = \sqrt{\frac{2}{3}} \mathbf{S} : \mathbf{S} \text{ is the Von Mises equivalent stress,}$$

$$r^3 = \frac{9}{2} \mathbf{S} : \mathbf{S} \cdot \mathbf{S} \text{ is the third stress invariant,}$$

$$\mathbf{S} = \boldsymbol{\sigma} + p\mathbf{I} \text{ is the deviatoric stress tensor.}$$

The parameter K in Equation (11.36) is a material parameter that controls the dependence of the yield surface on the value of the intermediate principal stress. In this model, the surface is constructed so that K is the ratio of the yield stress in triaxial tension to the yield stress in triaxial compression, so $K=1$ gives a von Mises (circular) yield surface plotted in the 0 plane. Convexity of the yield surface is assured if $K > 0.778$.

The Cap yield surface is given by:

$$S_c = \sqrt{(p - p_a)^2 + \left[\frac{R\tau}{1 + \alpha - \alpha / \cos\beta} \right]^2} - R(d + p_a \tan\beta) \quad (11.37)$$

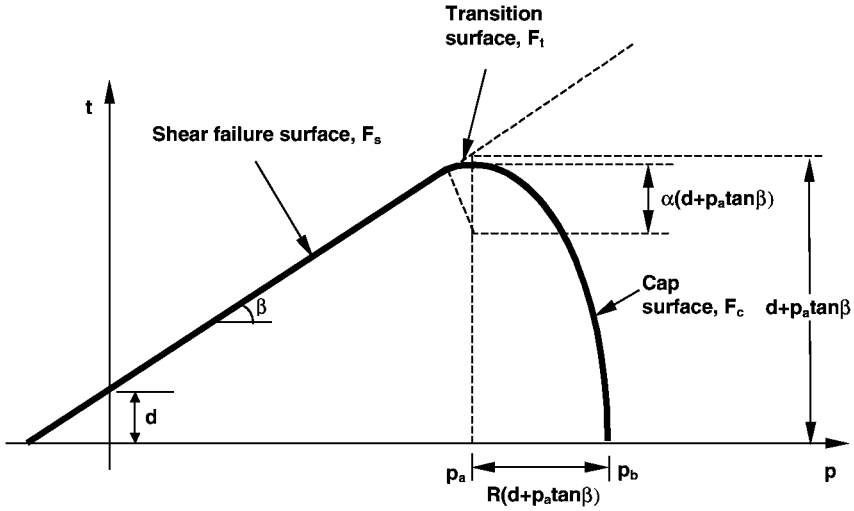


Figure 11.3 The yield envelope used in the ABAQUS program.

where R is a material parameter that controls the shape of the elliptical cap surface, p_a is an evolution parameter for volumetric plastic, strain-driven hardening and softening of the cap, and α is numerical parameter used to construct a smooth transition surface between the shear failure and the cap plasticity surfaces.

Hardening and softening of the cap surface is governed by the piecewise linear, functional dependence of the hydrostatic compression yield stress, p_b , on the volumetric plastic strain, :

$$p_b = f\left(\varepsilon_{\text{vol}}^{\text{pl}} \Big|_0 + \varepsilon_{\text{vol}}^{\text{pl}}\right) \quad (11.38)$$

where describes the initial state of the material when the analysis is beginning. Figure 11.4 is an example of a typical relationship between p_b and, which indicates that the plastic volumetric strain increases in compression with increasing hydrostatic pressure (i.e., the pore volume shrinks). The evolution of the cap surface is captured by the parameter, p_a , in Equation (11.37) as:

$$p_a = \frac{p_b - Rd}{1 + R \tan \beta} \quad (11.39)$$

To ensure a smooth, continuous transition from the shear failure surface to the cap surface, a circular arc transition surface is used, defined by:

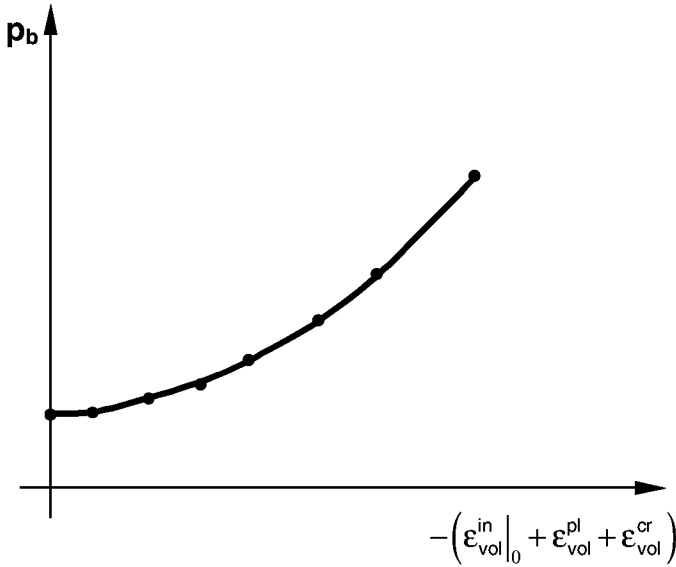


Figure 11.4 A typical relationship between p_b and .

$$S_t = \sqrt{(p - p_a)^2 + \left[t - \left(1 - \frac{\alpha}{\cos \beta} \right) (d + \tan \beta) \right]^2} - \alpha (d + p_a \tan \beta) \quad (11.40)$$

where α is a small number, typically chosen as between 0.01 to 0.05 to control the shape of the transition surface. The transition from the cap to the shear failure surfaces is not a trivial issue in computational geomechanics, since the normal to the surfaces at the transition may not be well defined.⁸²

The flow potential surface, shown in Figure 11.5, is a smooth, continuous surface in the meridional plane consisting of two elliptical surfaces. Plastic flow driven primarily by shear is governed by a non-associated flow rule:

$$G_s = \sqrt{[(p - p_a) \tan \beta]^2 + \left[\frac{t}{1 + \alpha - \alpha / \cos \beta} \right]^2} \quad (11.41)$$

Plastic flow driven by volumetric compaction is governed by an associated flow rule:

$$G_c = \sqrt{[(p - p_a)]^2 + \left[\frac{Rt}{1 + \alpha - \alpha / \cos \beta} \right]^2} \quad (11.42)$$

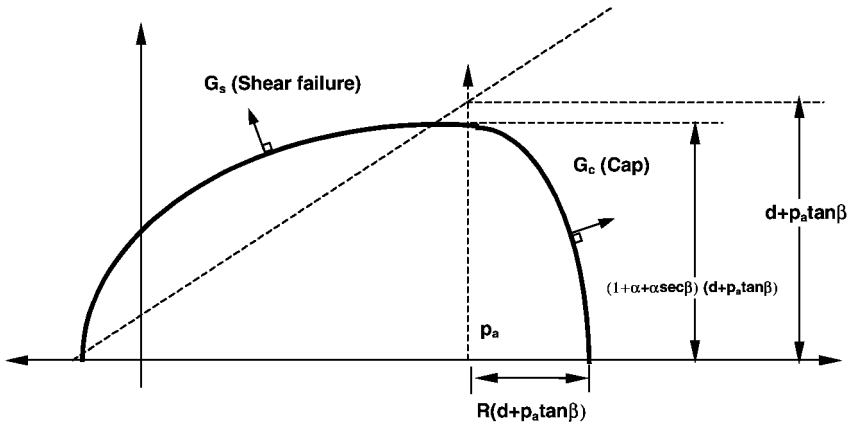


Figure 11.5 The flow potential surface.

Constitutive model input data requirements

As indicated above, a large number of material parameters can be required to specify the complete behavior of a geomaterial, which requires numerous complicated and often expensive laboratory tests. A listing of the material parameters required for a coupled geomechanical analysis of reservoir compaction using the ABAQUS program modified *Drucker-Prager/Cap* model is shown in Table 11.1.⁸³ Weakly cemented and unconsolidated elastic rocks and soils exhibit significant elastic nonlinearity at low stress, due to the nonlinear grain-to-grain contact deformation or closing and sliding of micro-cracks. A nonlinear, logarithmic bulk modulus, K , may be used to simulate this behavior. In most cases, this level of detail is not necessary, and a linear elastic modulus would provide acceptable accuracy. In some cases, particularly for highly unconsolidated rocks and sandy soils in the vadoze zone, the pore fluid may be compressible and the grains may be considered compressible. In the development of the finite element equations given in the previous section, the assumption was made that the grains were incompressible and the pores were fully saturated. Most commonly, for reservoir scale compaction simulations, the elastic behavior is modeled by providing the Young's modulus and the Poisson's ratio as determined from uniaxial or triaxial compressive stress tests. For unconsolidated materials, uniaxial compressive tests may be difficult, if not impossible.

The post-yield or post-failure behavior of rock is difficult to determine easily and inexpensively. The shear failure surface may in fact be nonlinear. Typically, at least three triaxial compression tests are required to establish the *Drucker-Prager* shear failure surface and its hardening behavior. A single hydrostatic compression test involving loading and unloading multiple times could be conducted to determine the compaction evolution curve for the Cap surface and

Table 11.1 Material parameters required for a coupled geomechanical surface

Elastic properties	
C_r	Compressibility of grain
C_f	Compressibility of permeating fluid
κ	Logarithmic bulk modulus
G	Shear modulus
P_i^{el}	Elastic tensile limit
ν	Poisson's ratio
Cap surface	
d	Cohesion
β	Intact rock friction angle
R	Cap eccentricity parameter
$\epsilon_{vol}^{pl} _0$	Initial cap yield surface position
α	Transition surface radius parameter
K	Ratio of flow stress in triaxial tension to flow stress in triaxial compression
$p_c^y, \epsilon_{vol}^{pl}$	Table of hydrostatic pressure yield stress and volumetric inelastic strain
Flow Properties	
k_y	Components of permeability tensor
$k(s), s$	Table to define saturation dependent permeability, s = wetting fluid saturation
β'	Velocity dependent coefficient
e	Void ratio

its hardening behavior. These tests are often difficult to perform, especially for very soft, highly compactive sands. Moreover, once the general shear failure parameters, d and β , and compactive yield data, and , have been generated from tests, the constitutive model parameters, such as R and α must be determined by fitting data. For very unconsolidated sands with high porosity, such as are found in the Gulf of Mexico off the southern coast of the United States, Cernocky *et al.*⁸⁵ have developed a procedure for using uniaxial strain, compaction tests (referred to by civil and geotechnical engineers as oedometer tests) to develop the constitutive parameters for the *Drucker-Prager/Cap* model in the ABAQUS program. The uniaxial strain tests are used in lieu of the hydrostatic compression test, since such tests are generally easier to perform.

Coupling between pore pressure and rock deformation

It is clear from Biot's linear elastic constitutive theory that deformation of a fluid filled rock depends on both the pore pressure in the rock and the total stress on the rock. That is, the deformation depends on a *coupling* between stress and pore pressure. Given a volume of fluid-filled rock and subjecting it to an increase in confining compressive stress, the pore pressure will increase if the pore fluid is

prevented from flowing (i.e., if the stress state is undrained). Alternatively, if the pore pressure is increased or decreased, then the effective stress on the volume of rock will change depending on the boundary conditions applied to the rock.

For large deformation, elastoplastic analysis of compaction, the complete set of governing equations defines a transient nonlinear system, which must be integrated numerically in the time domain. The system of equations is difficult to solve even for small problems, but especially difficult for large problems, such as a large-scale reservoir compaction simulation. The theory and numerical solution of the nonlinear, completely coupled system by finite element methods has been presented by a number of authors for applications in geotechnical engineering (i.e., consolidation and liquefaction) and petroleum engineering (i.e., compaction).^{55–57,86–88}

Though the fully coupled problem is highly nonlinear, some general observations regarding the effects of coupling can be stated. The state of stress in the reservoir rock under compacting conditions is compression. The weight of the overburden is the mechanism responsible for the compression, and hence drives the compaction. Compaction, which is in part the reduction in pore volume, drives fluid from the pores, or causes an increase of the pore fluid pressure, if the fluid is prevented from flowing. By the same token, the stress is affected by the pore pressure change, which affects the overall stress state in and around the reservoir, and hence affects the amount of compaction. Both of these effects are the salient effects of the coupling between rock deformations and pore fluid pressure. Historically, it has been the case that most reservoir flow simulators have no geomechanical capability, and therefore do not include coupling. That is, the rock matrix is incompressible, though the fluid may be compressible and multiphase. In such simulators, measured volumes of oil, water and gas, produced or injected, are “history matched” to the wells and reservoir pressure behavior computed with the simulator. The resulting pressure fields are used for predicting field life and operating conditions. Yale *et al.*⁸⁹ implemented an improvement to their reservoir simulator by incorporating a variable rock compressibility into a reservoir simulator, but that modification was not an implementation of full coupling.

In some recent case studies, the solution of the governing equations has been simplified by assuming a steady-state solution for the pore pressure. The steady state solution is still coupled, but the coupling is milder, without transient effects. Computing pore pressures with a standard uncoupled reservoir simulator been used as a further simplification. The computed pore pressures are prescribed as pore pressure boundary conditions at discrete intervals of time (e.g., yearly) in a nonlinear geomechanical finite element model and deformations are computed based on the effective stress.^{37–40} In this approach, a sophisticated reservoir simulator was used to compute reservoir pressure based on the production and the injection of literally hundreds of wells, thus a highly heterogeneous pore pressure field was used in the finite element model to compute compaction and its effects. However, this approach results in coupling

in only “one direction,” since pore pressures change the state of stress, but the pressures are not affected by the change in stress. This approach also reduces significantly the number of material model input data required for the geomechanical modeling, and a full transient analysis is not required. The computations using this decoupled approach were shown to agree well with subsidence measurements, as will be shown later in this chapter. Yale *et al.*⁸⁶ compared this technique of decoupled geomechanical analysis, using independently computed pore pressure, with full coupling in the simulation of production from a single well in a compacting reservoir to determine the magnitude of approximation from decoupling. The magnitude of the differences in the pore pressures and the overall stress state is dependent on many factors, including reservoir dimensions, fluid and rock compressibilities, and overburden rock mechanical properties.

Modeling rock discontinuities

Geologic discontinuities such as faults, fractures and weak rock layers have a finite, measurable thickness which can lead to casing damage up to tens of feet. However, on the scale of the thickness of most highly compactive hydrocarbon reservoirs, which is on the order of hundreds to thousands of feet, the discontinuities can be reasonably approximated as zero-thickness, frictional sliding, surfaces. Shear deformations of discontinuities can be modeled generally as frictional slip or sliding between the surfaces. The slip can be episodic (i.e., stick-slip) or continuous sliding, depending on the constitutive behavior of the frictional surface. A simple model for such frictional sliding is Coulomb’s law, typically written as:

$$\tau_f = \mu\gamma \quad (11.43)$$

where τ_f is the shear stress acting on the layer or surfaces, γ is the relative shear displacement or slip across the surfaces, and μ is a friction factor. Thin layers of weak rock and gauge-filled faults actually have constitutive behavior,^{2,90} which governs the amount of shear deformation. Most frequently, however, such constitutive behavior is modeled by the friction factor. Thus, the magnitude of the friction factor should be correlated from measurements of slip obtained during actual field operations. As will be shown later, the magnitude of the friction factor has been found to range from 0.2 to 0.6.

Initial geostatic field

The geologic process of lithification results in a tectonic stresses below the surface. This state of stress changes with depth, the vertical component being, of course, zero at the surface. Geologic processes determine the other stress tensor components. One of the most important and principal complications of

geomechanical analysis is that the initial geostatic stress must be included in the model. Rock behavior depends on the confining stress and at any depth in the subsurface the geostatic stress state acts as the confining stress. Changes in the effective stress, due to the pore pressure changes, result in local changes in the stress field from the initial geostatic stress.

The stress state at any depth is generally characterized by the principal stresses: one vertical and two principal stresses oriented horizontal to the surface (i.e., in the plane perpendicular to the vertical). The vertical stress at any depth is taken to be the pressure due to the weight of the material above that point. The horizontal principal stress components may not be equal and their magnitude depends upon the geologic processes, are difficult to determine with even reasonable accuracy, but can be estimated from hydraulic fracturing tests or borehole ellipticity measurements.^{91,92} Horizontal principal stresses are usually expressed as fractions of the vertical component, so that if the vertical component is σ_v , then:

$$\sigma_H = K_{oh}\sigma_v \text{ and } \sigma_h = K_{oh}\sigma_v \quad (11.44)$$

where usually $\sigma_v > \sigma_H > \sigma_h$. The factors, K_{oH} and K_{oh} are referred to as horizontal stress factors.

Modeling casing damage and failure under shearing

The mechanisms of compaction-induced casing damage may be categorized into two general forms: *localized shear damage* and *gross casing deformation*. Localized shear damage occurs due to displacements, frequently called *slip*, along rock discontinuities (i.e., faults and fractures), or due to plastic deformation of weak layers of soft rock as a result of yielding. Gross deformations of the casing are due generally to large, compaction-induced vertical strains. Modeling these modes of casing damage is discussed below.

Localized shear damage of the casing occurs due to the relative displacement, or slip, at discontinuities. Typically, casing shear damage is manifested as the relative offset of the casing centerline, thus producing a “kink” in the casing string. The length over which the offset, or kink, can occur varies, depending on the width of the discontinuity and the strength and stiffness of the rock layers on either side of the discontinuity, but this length has been observed to be between six inches to a few feet (0.152 to 3 metres). If the offset is sufficiently large, well maintenance can be made difficult due to the inability to pass tools through the kinked section of the casing. In the most dramatic cases involving large slip displacements on faults, which produce detectable micro-quakes and even large earthquakes, complete and catastrophic failure of the casing (i.e., separation of the casing into two pieces) can occur.

If compaction-induced deformation of the rock is sufficient, shear failure of the rock mass may occur, thus generating new faults or fractures. The generation of such failure surfaces, or the displacements on such new surfaces, are often known as “localization” or “shear bands”. Although computational models exist for the generation of shear bands, faults and fractures in rock, such simulations are not yet sufficiently efficient for simulations involving a full scale hydrocarbon reservoir. Therefore, inclusion of such geological features is based on field evidence of their existence, or they are assumed to exist at specific locations based on the field data, and the discontinuities explicitly included as part of the model.

If compaction deformations are sufficiently large, layers of weak rock, such as soft shale, can yield and undergo significant plastic flow, leading to relative motion between harder, stiffer rock layers on either side of the weak rock layer. Again, deformation is manifested as an offset in the centerline of the casing, producing an observable “kink” in the casing string. The amount of offset in the casing is dependent upon the properties of the surrounding rock and the thickness of the weak rock zone, but has been observed typically to occur over the order of several to tens of feet.

A model of the shear deformation of casing has been developed from analysis of compactive hydrocarbon reservoirs.³⁷ The model was constructed from finite elements available in the ABAQUS program for problems in which the initial geometry is axisymmetric, but for which the deformations produce a non-axisymmetric geometry.⁵⁵ The deformed geometry of the model must have a plane of symmetry. The geometry of the shear-damaged casing satisfies the requirements for the application of this element. In this case, the nodal displacements can be expressed with a general interpolation function including a Fourier expansion in the circumferential, or θ , direction as:

$$u_n = \sum_{m=1}^M H^m(g, h) \left(u_n^{m0} + \sum_{q=1}^Q \left(\cos q\theta u_{nc}^{mq} + \sin q\theta u_{ns}^{mq} \right) \right) \quad (11.45)$$

In the implementation of the ABAQUS program, the Fourier expansion terms correspond to discrete locations around the circumference of an axisymmetric solid, such as a pipe. Nodal displacements are calculated on these planes, rather than on only one plane, as is usual for axisymmetric finite elements. As with general Fourier approximations, increasing the number of terms included in the expansion increases the accuracy of the approximation. Increasing the summation index, Q , increases the number of terms of the expansion. In terms of angular position around the model, $Q=1$ means that displacements are calculated at $\theta=0^\circ$ and 180° . $Q=2$ corresponds to planes at $\theta=0^\circ$, 90° and 180° . It should be noted, however, that while increasing the number of terms in the Fourier series results in increased accuracy, there is a point of diminishing returns for the large

model and a fully three-dimensional model may, in fact, be more economical and efficient.

Example computation: the South Belridge field

The Belridge field is located about 45 miles west of Bakersfield, California, as shown in [Figure 11.6](#).

Reservoir geology

Detailed descriptions of the geology of the Belridge field have been published by Bowersox,⁹³ and a brief synopsis of the facts relevant to the compaction problem is included here. A geologic cross section of Section 33 of the field is shown in [Figure 11.1](#). The South Belridge field is a northwestward trending anticline. The Belridge diatomite is a massive reservoir, in some locations, more than 1000 feet (305 metres) thick. The porosity of the diatomite is high, varying from 45% to 75%, but the matrix permeability is low, 0.1 mDa or less. However, this feature of the Belridge diatomite also makes it highly susceptible to compaction as the reservoir is depleted. Overlying the Belridge diatomite are the Tulare sands, which are produced simultaneously with, but independently of, the diatomite. In fact, to date about 75% of the production in the Belridge field has been from Tulare sands. Thin layers of laterally continuous shales (i.e., mudstones), 10 to 50 feet thick (3.0515 to 15.24 metres), have been identified throughout the Tulare, separating major sand intervals, and at the unconformity between the lower Tulare sand and Belridge diatomite. Unsaturated alluvium, near the surface, along with the Tulare sands, comprises the *overburden* above the Belridge diatomite.

Historical well failures

Aggressive production in the early 1970s was spurred by improvements in techniques to hydraulically fracture diatomite reservoirs.⁹⁴ However, with the increased production came reservoir compaction, surface subsidence and well damage and failures.³¹ Measurements taken from 1987 to 1995 show that surface subsidence reached 12.5 feet (3.8 metres) in Section 12,³¹ greater than 9 feet (2.74 metres) in Section 19,⁴⁰ more than 10 feet (3.05 metres) in Section 33,³² and nearly 20 feet in other areas of the field. Surface subsidence in Section 12 was so severe that surface fissures formed at the edges of the subsidence bowl.³¹

Problems servicing wells and casing failures followed the trend of increasing subsidence. In some areas of the field 20% of the wells were damaged or failed. In Section 33, the well failure rate averaged about 4% per year between 1985 and 1996, reaching a peak of almost 8% in mid-1988. To stem the rate of subsidence and mitigate the apparently related trend in well failure rates, water injection programs were initiated in many areas of the field in the early 1980s.



Figure 11.6 Showing that the South Belridge field is a north westward trending anticline.

However, while subsidence decreased, and in some cases surface elevation was recovered,^{32, 38} the annual well failure rate remained constant at about 2% to 5%. Although low, failure rates of the magnitude had a sufficiently adverse impact on field economics to warrant implementation of additional well failure mitigation measures.

Throughout the South Belridge field up to 90% of the failures occur in the overburden.³⁹ In Section 33, most casing damage and failures occur at three discrete depths: at the Tulare-diatomite unconformity from about 500 to 700 feet (152 to 213 metres), and at locations of about 300 feet and 350 feet (91 to 107 metres) above the unconformity. The most frequent failure locations in the overburden of the diatomite have been identified with thin shale or mudstone layers, referred to here as the A1 shale and the D1 shale, with the D1 shale being the deeper of the two strata. In Section 33 the shale layers are fairly continuous across the section, though in other sections the shales are not continuous. A study of well workover records for Section 33 showed that the casing damage and

failures at these depths involved mainly the shearing mode, although other modes of failure in tension and compression have also occurred.

Field-scale model

The objective of the field-scale modeling was to develop relationships between field operations and the global mechanisms that cause casing damage. The results of the field-scale modeling are presented in this section.

Field-scale, two-dimensional, plane-strain finite element models developed for this work were constructed from slices of a field-scale, three-dimensional, finite element model developed during a simultaneous independent study of the South Belridge field.^{39,40} The three-dimensional finite element model was developed from the grid system of a three-dimensional, finite-difference reservoir flow model of Section 33. Two-dimensional slices of this finite difference grid were oriented in roughly North-South and East-West directions. The North-South oriented models capture the cross section of the field as shown in [Figure 11.7](#), while the East-West oriented models were aligned with the longitudinal axis of the field. Only the North-South oriented model results are discussed in this chapter.

The mesh for the model is shown in [Figure 11.7](#). The model represented a slice that is over 2 miles (3.2 km) wide and almost 1 mile (1.6 km) deep. The mesh consisted of 2720 eight-node, porous continuum elements, resulting in 9675 nodes. There were 27 layers of elements comprised of 13 distinct lithologies. Of these 13 lithologies, the lighter shaded layers in the upper third of [Figure 11.7](#) represent the diatomite reservoir rock. The depositional features of the diatomite have resulted in distinct lithological cycles, each with different material behavior. The diatomites were further broken down into 7 different cycles defined here as the G through to M cycles as shown in [Figure 11.8](#). The diatomite materials follow the *Drucker-Prager*/Cap plasticity constitutive model, while all other rock types in the material model follow a linear *Drucker-Prager* plasticity model. The constitutive parameters for the models are summarized in [Tables 11.2](#) and [11.3](#).

As discussed earlier, field observations and well logs showed that the shear-damaged casing is confined to only a very short length of the casing, as short as 7 to 10 feet (2.1 to 3 metres). These deformations occurred at the depths of weak shale layers or at the Tulare—diatomite unconformity, which has also been shown to include a thin shale layer. This and other evidence suggested that the shear deformations were also due to rock failure under shear. Shear failure of rock resulted in relative slip between the failure surfaces. Rather than attempt to model the rock failure mechanism (i.e., shear banding and localization), it was decided to capture the kinematics of the localized shearing deformation using frictional contact elements. Contact elements were defined by two curves in the two-dimensional model and two surfaces in the three-dimensional model. Although the weak rock layers do have a finite thickness, the shearing deformations were

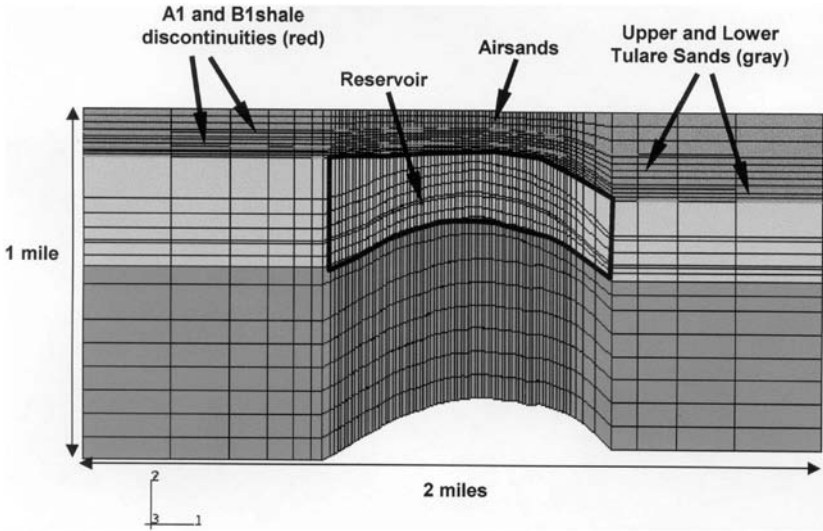


Figure 11.7 The finite element mesh for the model presented in this chapter.

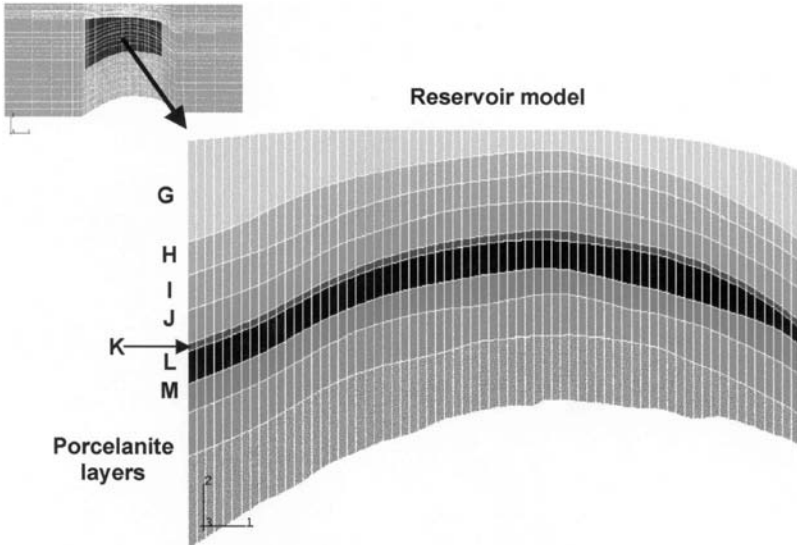


Figure 11.8 Detail of the diatomite reservoir rock.

modeled using zero-thickness contact elements. A linear Coulomb friction law relating the shear slip with the shear stress on the contact surface governed the surface interactions. In this work, frictional contact elements were placed at the depths of the A1 and D1 shales, and at the Tulare-diatomite unconformity. The friction factor was varied as a study parameter, with values of 0, 0.2, and 0.6 being used. These friction factors were consistent with previous studies of

Table 11.2 Density and elastic moduli for lithologies used in model

Lithology	Drucker–Prager			Drucker–Prager/Cap					
	β [deg]	K	ψ [deg]	d [psi]	β [deg]	R	ϵ_{vol}^{pl} [in/in]	α	K
Airsands	42.0	1.0	0.0						
Upper Tulare	36.0	1.0	0.0						
Lower Tulare	36.0	1.0	0.0						
Diatomite cycles:									
G				200	36.9	0.33	0.0	0.01	1.0
H				200	39.4	0.33	0.0	0.01	1.0
I				200	42.0	0.34	0.0	0.01	1.0
J				174	40.1	0.30	0.0	0.01	1.0
K				200	40.4	0.30	0.0	0.01	1.0
L				247	50.2	0.23	0.0	0.01	1.0
M				247	58.5	0.23	0.0	0.01	1.0
Upper porcelanite	38.0	1.0	0.0						
Lower porcelanite	38.0	1.0	0.0						

Table 11.3 Elasto-plastic constitutive parameters for rock units in model

Lithology	ρ [lb _f /in ³]	E [10 ³ psi]	ν
Airsands	0.06864	18	0.30
Upper Tulare	0.03826	300	0.25
Lower Tulare	0.03826	300	0.25
AI and DI shales	0.03500	235	0.25
Diatomite cycles:			
G	0.01951	477	0.17
H	0.01951	630	0.17
I	0.01951	792	0.19
J	0.01951	600	0.20
K	0.01951	716	0.17
L	0.01951	1124	0.17
M	0.01951	1626	0.17
Upper porcelanite	0.02854	680	0.22
Lower porcelanite	0.03396	3600	0.29

localized shear deformations and they bracket the behavior expected of sliding rock surfaces.^{28,37,38}

Simulated field operational history

An 18-year history of Section 33 field operation, from 1978 to 1995, was simulated with the three-dimensional, finite difference flow model, including oil,

water, and gas production, and water injection. Some details of the reservoir flow modeling were presented by Fredrich *et al.*⁴⁰ Hydraulic fracturing introduces considerable heterogeneity and anisotropy to the reservoir pore pressure field. The flow model was history-matched to volumetric data from production and injection wells. For the two-dimensional models to capture the spatial effects of the pore pressure field (e.g., the effects of the hydraulic fracturing), pore pressures from the three-dimensional model were averaged over 12 grid blocks perpendicular to the plane of the model and projected onto the nodal coordinates. Pore pressures were prescribed only on elements corresponding to the delineated reservoir, which is confined in Figure 11.7 to the center of the model in the lightly shaded elements which represents the diatomite and upper porcelanite layers.

The two-dimensional, field-scale finite element modeling was performed as a quasi-static analysis. Reservoir pore-pressure fields computed in the flow model were prescribed as boundary conditions on the nodes of the finite element model. Displacement boundary conditions on lateral edges and the bottom of the model were also prescribed.

The 18-year field history was simulated in nineteen steps. The first step developed the geostatic, or tectonic, *in situ* stress field. In this first step, pore pressures were prescribed to be 0 psi. The vertical stress at any depth was computed from the unit weight of the rock. The horizontal stress factors in Equation (11.44) were taken to be $K_{oh}=0.80$ and $K_{oH}=1.20$. These factors were determined from studies of regional tectonic stresses in the Belridge field.^{32,95} Since the materials are elastoplastic and the geologic layering is not purely horizontal, the computation of initial stresses was not straightforward. A trial-and-error procedure was developed to compute the *in situ* stress field. After the geostatic stress step was completed, pore pressures were changed incrementally for each year of the 18-year simulated field history.

As noted, pore pressures were prescribed as boundary conditions, hence the change in the state of effective stress was not the result of deformation of pores or changes in permeability of the rock. In this sense, this geomechanical analysis was not fully coupled. The elastoplastic deformation of the rock was in response to the change of effective stress. A fully coupled analysis would include the coupling between transient flow of pore fluids and pore deformations.

Computational results

As discussed earlier, modeling was performed on two scales, that of the reservoir and that of an individual well, with two separate computational models. Computations from these models and comparisons to historic field measurements and data are described in this section.

Field-scale model

Contours of the pore pressure field for four of the eighteen years of the simulation, 1978, 1980, 1989, and 1995, are superposed on the deformed mesh in [Figure 11.9a](#) to d. For clarity, the deformations were exaggerated by a factor of 75. The contours in the center of the reservoir were due to decreases in pore pressures from production. The pore pressure field varied considerably in the horizontal direction due to the detailed representation of individual wells and hydraulic fractures, as well as vertically due to the gravitational effect. Two darker areas above and to the left and right of the reservoir were due to water injection. Vertical shortening of elements within the reservoir illustrates reservoir compaction, which produces ground subsidence. Moreover, rock has been dragged towards the center of the reservoir, which illustrates the mechanism of shearing of rock. Local well deformations can also be observed. Elements laterally shorten around production wells due to the local reduction in pore pressure, while elements laterally expand around water injection wells. These deformations can cause shearing of wells within their area of influence, an effect referred to as “well-to-well interactions.”³⁸

A field program to monitor surface subsidence using surface monuments has been in place for several years in the Belridge field. Computed surface subsidence is compared with data collected from a surface monument array for 1991 and 1995 in [Figure 11.10](#). In 1995, the subsidence reached a maximum of approximately 10 feet (3 metres) in this area of the field. The agreement between computed and measured subsidence as a function of time verifies the accuracy of the magnitude of the pore pressures, as well as the transient nature of simulated field operations. However, subsidence is a large-scale effect produced by deformations on the reservoir scale. Local effects, such as deformations around individual wells, are more difficult to capture accurately on such a scale with the resolution of a field-scale model. Changing the friction factor for the contact surfaces did not affect the magnitude of the subsidence substantially. Also, there is considerable spatial variation in subsidence within Section 33, as production and injection programs vary over the field.^{39,40}

Relative slip between the A1 and D1 shale horizons and between the Tulare-diatomite unconformity is shown in [Figure 11.11](#) for the 1995 simulation. For the shown curves the sliding friction factor was assumed to be 0.2. Relative slip is observed to be highly heterogeneous along each interface, due to local variations in the pore pressure field. In addition, relative slip is observed to increase as the depth to the interface increases, which is due to the increase in shearing deformations with depth. Relative slip is observed to reach a maximum of about 11 inches in 1995.

The transient nature of the relative slip is illustrated by comparing plots of slip on the Tulare-diatomite unconformity computed in the 1987 and 1995 simulations, as plotted in [Figure 11.12](#). Both the magnitude and the character of the slip change with time.

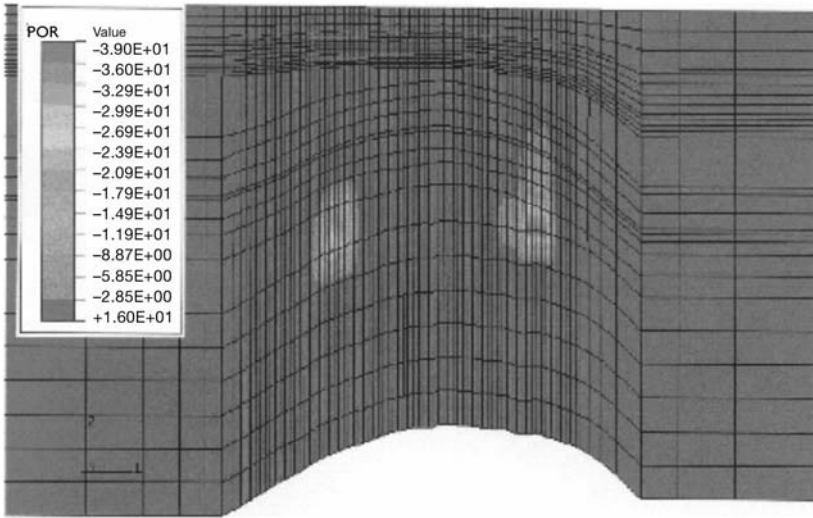


Figure 11.9a Pore pressure field contours for 1978.

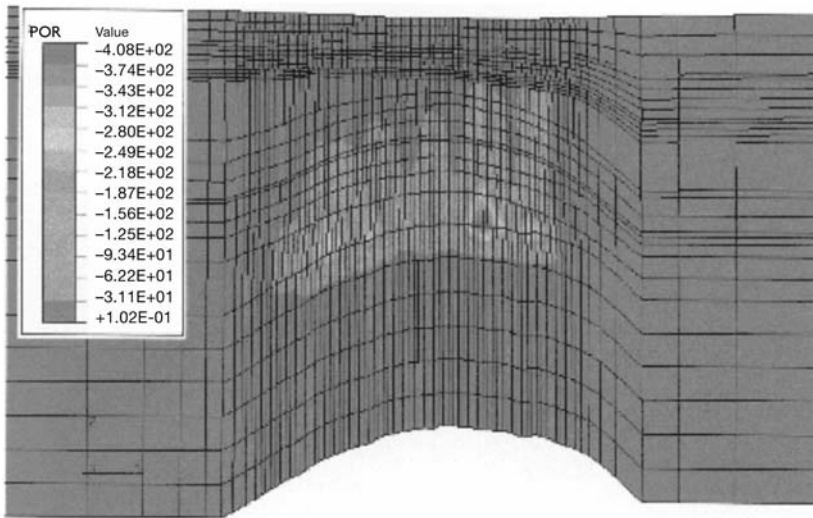


Figure 11.9b Pore pressure field contours for 1960.

Wellbore scale results

The compaction-induced deformations that drive subsidence and shearing on the field-scale were used as a basis for displacements applied to the wellbore scale model. At the beginning of the field-scale simulation, all nodes were vertically aligned, as shown in [Figure 11.7](#). Vertical lines of nodes were identified with wells, where a given well location was determined from its field coordinates and

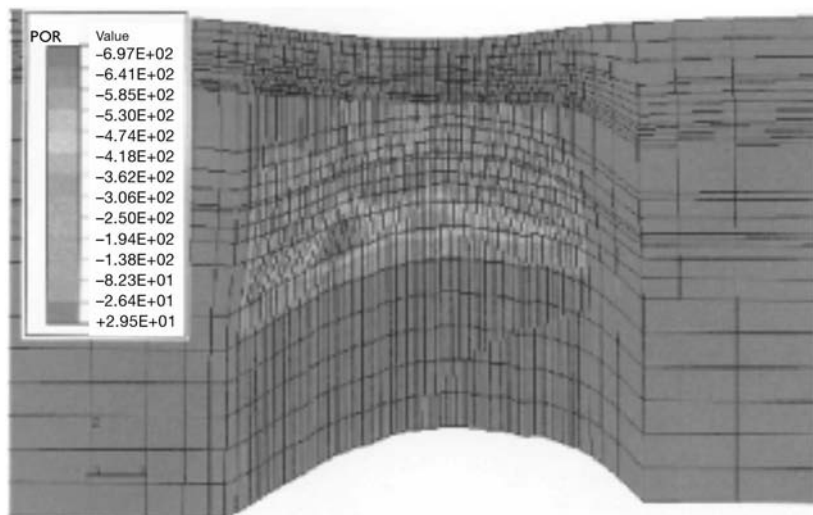


Figure 11.9c Pore pressure field contours for 1989.

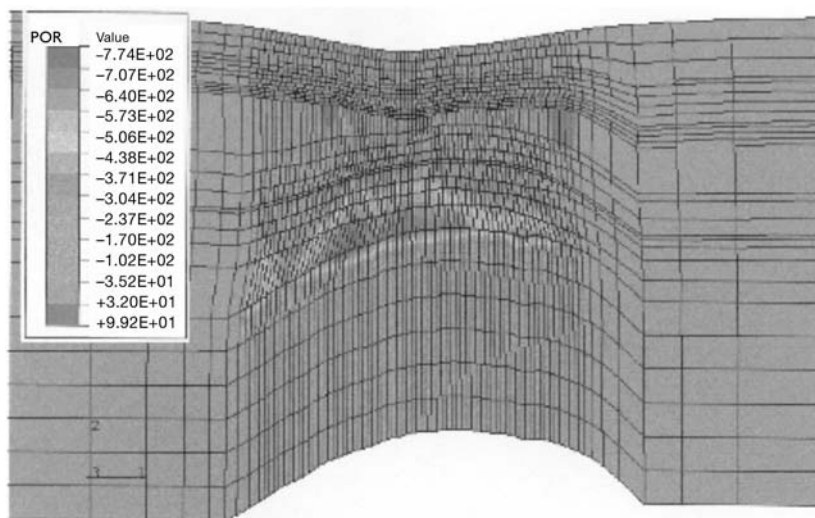


Figure 11.9d Pore pressure field contours for 1995.

then correlated with a “surface” node in the model. The horizontal displacements of the line of vertical nodes were assumed to represent the deformations of a well. As an example, well deformations for the nodes corresponding to the location of well 551G in Section 33 are shown in [Figure 11.13](#). This well was located near the northern edge of the Section 33 cross-sectional model, in an area where shear deformations were significant. The plotted deformations show that the well was dragged laterally toward the center of the subsidence bowl about 40

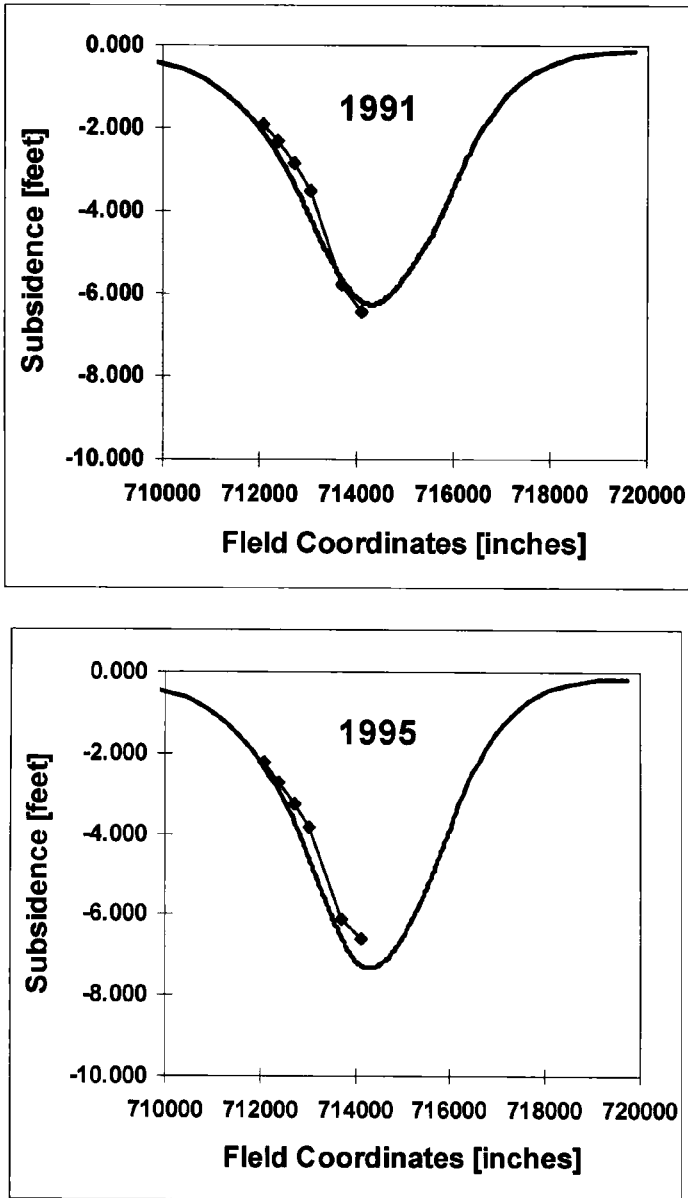


Figure 11.10 Computed and actual surface subsidence from 1991 to 1995.

inches (1 metre) since the beginning of the simulation. The sharp discontinuities in the curves of the well displacements from about 300 to 800 feet (91 to 244 metres) are the locations of the frictional slip surfaces.

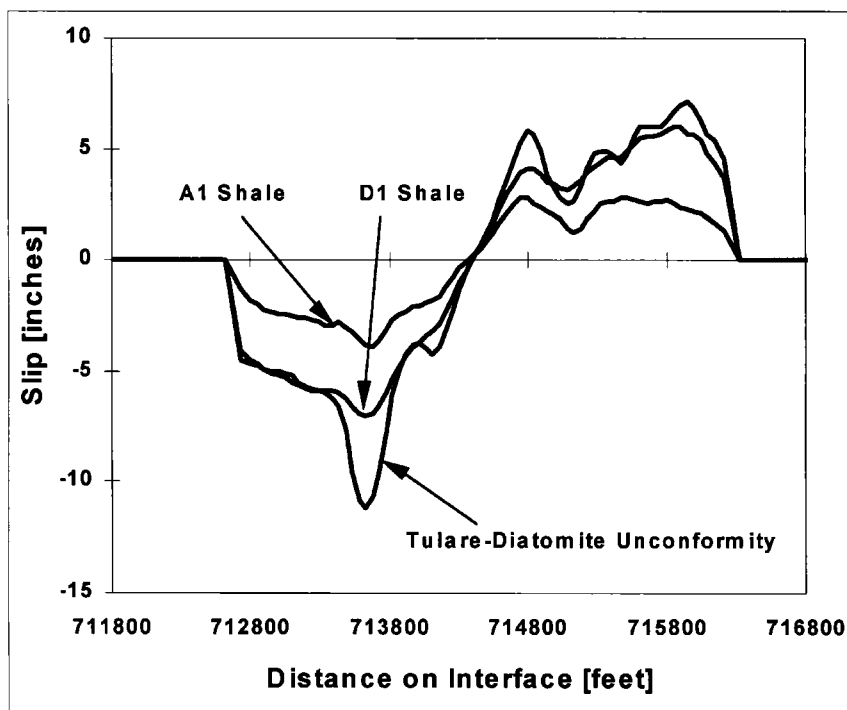


Figure 11.11 Relative slip between the A1 shale, D1 shale and the Tulare-diatomite unconformity as of 1995 in the simulation.

A three-dimensional model of a single wellbore was constructed to determine more accurately casing damage mechanisms and to assist in developing damage mitigation measures. The three-dimensional wellbore model is shown in Figure 11.14. The model included 7 inch (0.178 metres) OD, 26 lb/ft (37.8 kg/m), K-55 casing and an 8.75-inch (0.222 metres) OD cement-filled annulus. Outside of the cement were layers of Tulare sand and G-cycle diatomite rock, separated by a frictional sliding surface. The model was 100 feet (30.5 metres) long and 20 feet (6.1 metres) in diameter. The wellbore model used elements with $Q=2$ (see Equation (11.45)). The model shown in Figure 11.14 included 318 quadratic finite elements resulting in 2226 nodes.

A simulation of shearing included a sequence of two steps. The first step was to generate compressive stress equivalent to that of the *in situ* vertical stress at a depth of 600 feet (183 metres), the approximate location to the Tulare-diatomite unconformity. The second step was to prescribe lateral displacements at the outside diameter of the model to simulate shearing, prescribed in opposite directions on the upper and lower halves of the model.

The deformed casing from a shearing simulation is shown in Figure 11.15 (for clarity the rock and cement are not plotted). Even though the lateral

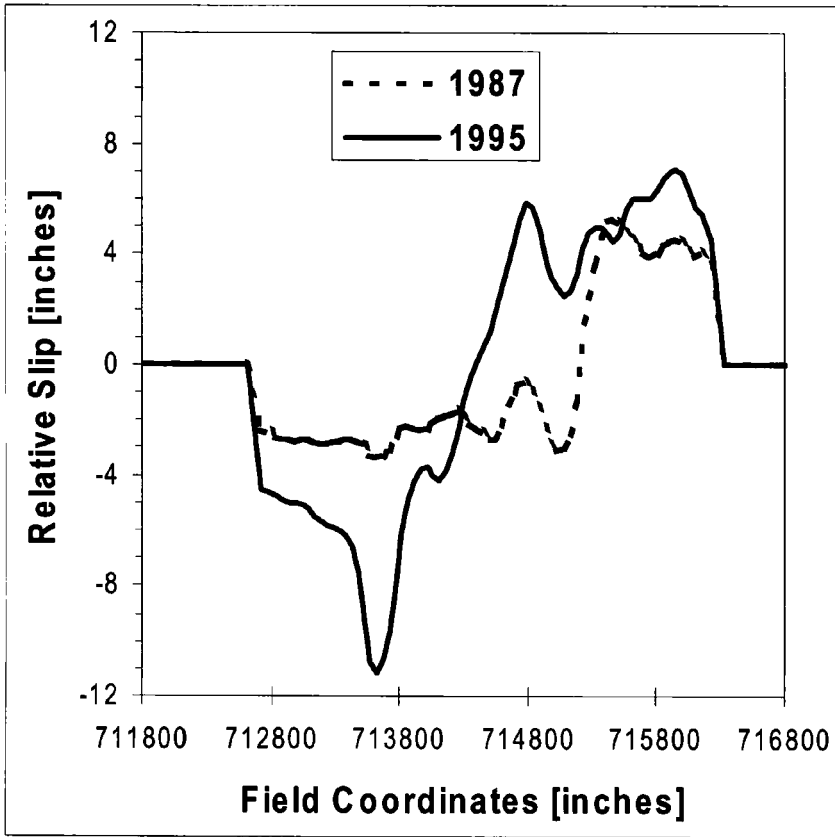


Figure 11.12 Slip on the Tulare-diatomite unconformity computed in 1987 and the 1995 simulations.

displacement far from the casing is localized on a plane, shear deformations are distributed over a finite length of casing in the detailed wellbore-scale model.

Logging tools have been developed or modified to measure the geometry of shear-deformed casing. Such tools are capable of measuring the inclination of the casing in the shear-damaged interval; this inclination has been referred to as the “kink angle.”⁴² The lateral offset of the casing from above to below the shear interval can also be measured, and the geometry of the deformed casing can be resolved. The computed deformed casing geometry is compared with measurements from a casing log in Figure 11.16 (the nodes on the inner surface of the casing are plotted). Shearing is distributed over about 7 feet of the casing in both the model and the field measurements.

Shearing deformations are distributed over a finite length as a result of the mechanical interaction between the stiff, strong casing and the soft, weak rock. The rock fails or “flows” as it deforms around the casing, thus the casing

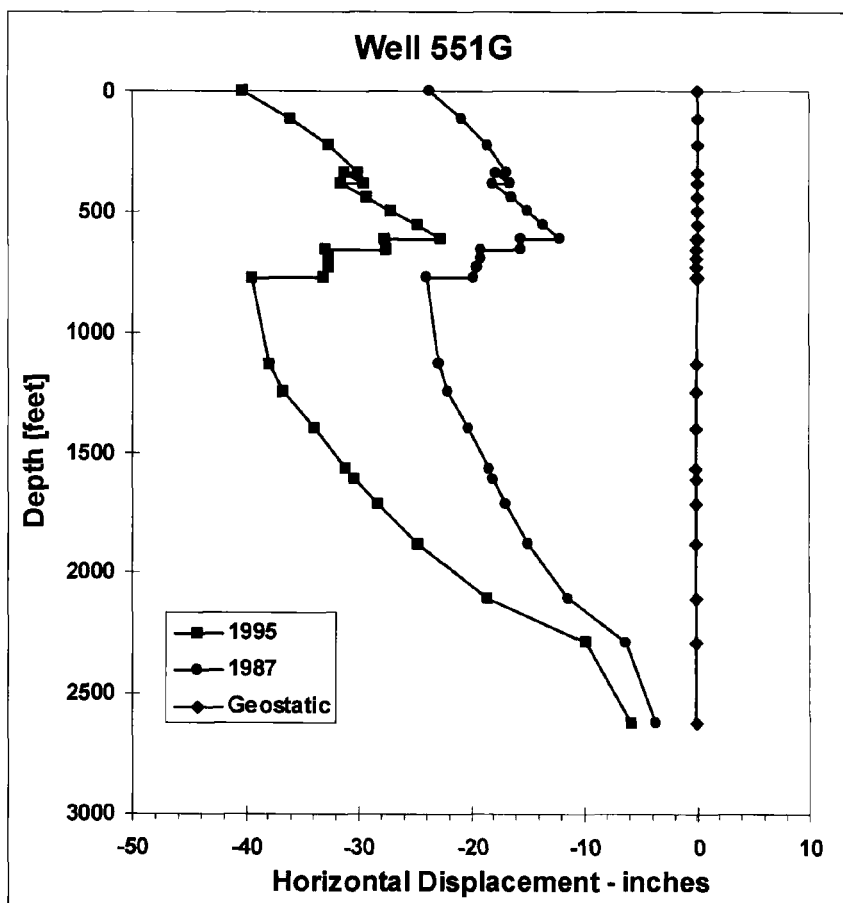


Figure 11.13 Well deformations corresponding to Well 551G.

deforms less than the rock. This is illustrated in Figure 11.17, in which the lateral offset of the casing is plotted against the lateral shearing displacement prescribed at the outside surface of the model. The slope of the plotted curve is less than 1.0, showing that the casing displaced less than the prescribed shear. Figure 11.17 is the link between the wellbore scale and the field scale. The plot shows that the slip computed from a field-scale model is likely to be overly conservative, that is, field-scale models over-predict the true lateral offset of the casing. The results of wellbore scale modeling shows that field-scale models, which do not include the detail to account for the casing-rock interaction, cannot be used alone to correlate casing damage with weak-layer slip or to subsidence.

The calculations of the field-scale model were compared with historical field data. An extensive inspection of well workover records was conducted from the files in the Section 33 operations. For the model discussed in this chapter, only

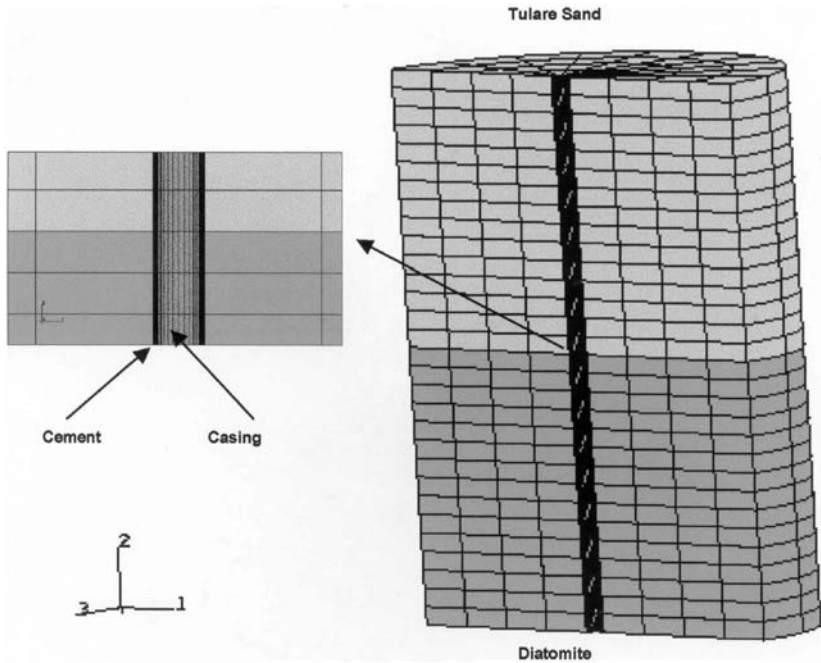


Figure 11.14 Three-dimensional wellbore model.

wells in the immediate vicinity of the two-dimensional, field-scale model were checked against model calculations. The data set of wells for this model included 23 failed wells, with various failure modes, not just in shear. Wells without apparent damage or failure were also included in the database. The first occurrence of well damage was defined as the inability to run or pull tools, such as packers, scrapers, or plugs, into or out of a well. The real elapsed time in the life of the well at which this occurred was compared with the simulated time in the field-scale model calculation. Often, field personnel noted the size of the tool on the workover ticket, which could be checked against the wellbore model. Permanently bent tubing pulled during a workover also indicated sheared casing, and this was checked.

The relative slip on the AI and DI shale layers and the Tulare-diatomite unconformity for simulated wells was tracked and plotted. Workover records for these wells were checked to determine if problems occurred. If problems did occur, the depth at which problems were encountered in the well was noted. This field data was compared with the relative slip in the simulated well. For the example shown in [Figure 11.18](#), well 551G did incur damage in about 1987 and a survey tool would not pass at the depth of the Tulare-diatomite unconformity in 1995.

The capability of the two-dimensional, field-scale model to predict the onset of well damage was fairly reliable. In areas of Section 33 where casing damage

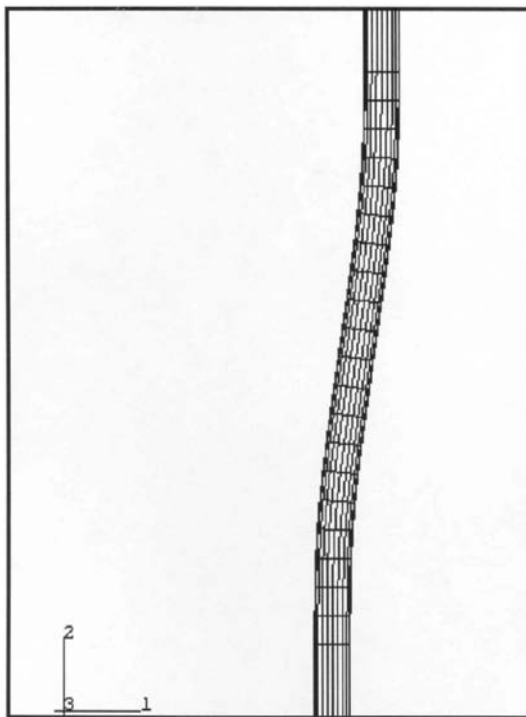


Figure 11.15 Deformed casing from a shearing simulation.

and failures were pervasive, the model was successful. However, in areas where damage or failure was sparse, the model was not as successful. These comparisons showed that the two-dimensional model may have lacked the detail to capture variations in field operation, that the pore pressure field may not be accurate in some areas of the flow model, or that important three-dimensional effects on field-scale deformations occur that the two-dimensional model could not capture. A similar history comparison for a three-dimensional model of Section 33 is discussed in Refs. 39 and 40.

Tool length

Wireline tools are instruments or equipment lowered into the wellbore from a steel wire for investigatory or maintenance purposes. If the casing is sufficiently deformed, then such tools may not be able to pass through the deformed section of casing, or worse yet, the tool may become stuck in the casing, thus requiring further efforts to recover them. In the operation of the Belridge field, if tools could not pass through the casing, then the well was noted as damaged on a workover ticket. However, there were several instances when one tool could not pass through the casing, but a second attempt with a smaller OD tool was

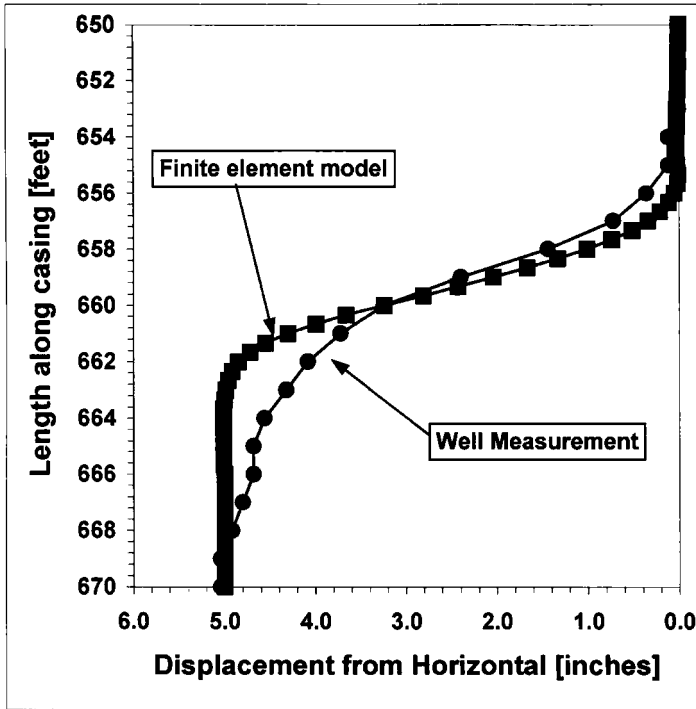


Figure 11.16 Comparison of computed and measured casing deformation.

successful. An apparent correlation exists between the tool dimensions, length and diameter, passable through the casing. The computed casing deformations of the wellbore model were used to develop a simplified geometric model of sheared casing, from which a formula was derived relating tool length and diameter to the deformed casing geometry:

$$l_t^2 = d_{ot}^2 - d_{ic}^2 \cos^2 \phi - d_{ic} \sin \phi \sqrt{l_t^2 + d_{ot}^2 - d_{ic}^2 \sin^2 \phi} + \left(\sqrt{l_t^2 + d_{ot}^2 - d_{ic}^2} \right) \times \left(d_{ic} - \sqrt{l_t^2 + d_{ot}^2 - d_{ic}^2 \cos^2 \phi} \right) \cos \phi \tag{11.46}$$

The terms in Equation (11.46) are defined in Figure 11.19, which is a schematic of the deformed casing geometry with a tool lodged in the sheared segment. Since Equation (11.46) is nonlinear, it is solved by trial-and-error. For a tool of given diameter, the equation provides the maximum tool length which can fit in the shown configuration. Plots of passable tool lengths as a function of casing lateral displacement, or slip, for two realistic example tool dimensions are shown in Figure 11.20. Workover tickets and well logs revealed that the Equation (11.46) provided results that were consistent with damaged wells. Therefore, if tools

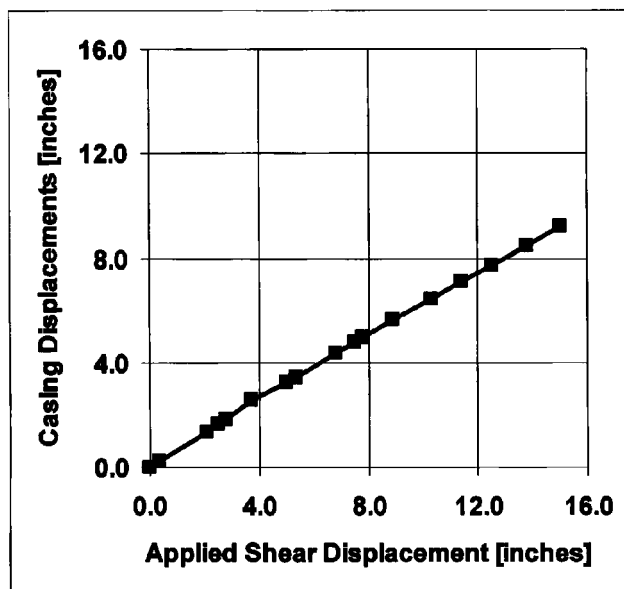


Figure 11.17 Casing displacement plotted against shear displacement.

of known length or diameter cannot pass through a damaged section, then the extent of damage could be determined. On the other hand, if the extent of damage was known, then the size of the tool to service the well could be determined prior to a workover.

Permanently bent tubing

Pulling bent tubing from a well during a workover has not been uncommon in fields undergoing severe shearing deformations, such as in the Belridge field. Using simple formulas from beam theory,⁹⁶ the shear slip to cause permanent bending of the tubing can be calculated. Plots of the bending stress required to result in permanent bending of inch (60 mm) OD and inch (73 mm) OD, J-55 tubing are shown in Figure 11.21. This analysis showed that inch (73 mm) OD tubing would become permanently bent when the slip reached about 5 inches (127 mm), and about 6 inches (152 mm) of slip was required to permanently bend inch (60 mm) OD tubing. Greater radial clearance for inch (60 mm) OD tubing results in its greater tolerance for slip than for inch (73 mm) OD tubing. A review of workover tickets and discussions with workover personnel indicated that these calculations were consistent with field observations.

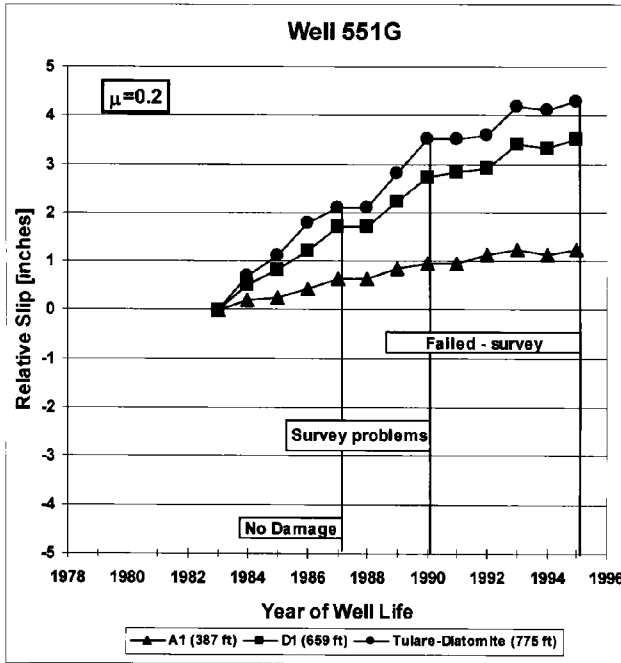


Figure 11.18 Relative slip plotted against the year of well life.

Mitigation of well damage

Several casing damage mitigation procedures have been investigated during the course of this work. A method of damage repair proposed by Dale *et al.*⁴² involved reaming the damaged section of casing to reduce the curvature of the sheared casing, thus enabling the passage of through-casing tools after the repair. Under-reaming the hole during drilling has been proposed as a means of allowing large displacement of a fault before rock can contact the casing and transmit shear.²⁴ The under-reamed section of the hole was referred to as a “bell hole.” The utility of this design was investigated in this work by modifying the three-dimensional wellbore model. Elements were removed from the model just outside of the casing and above and below the slip surface. The deformed shape of the casing for a standard well design is compared with that for the bell hole design simulation in Figure 11.22. The effect of the bell hole is to distribute the shear deformation over a greater length, thereby reducing the curvature of the casing in the sheared section. The curvature is what causes workover tools to get stuck and tubing to become permanently bent. The plots show that increasing the length of the under-reamed section significantly reduces the casing curvature. The primary requirement for a bell hole design is an annulus fluid that transmits little or no shear load to the casing.

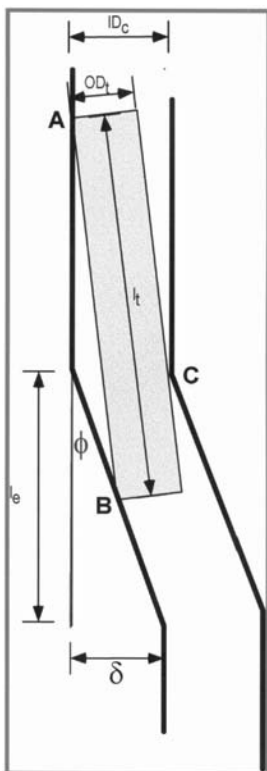


Figure 11.19 Tool passing through a sheared casing.

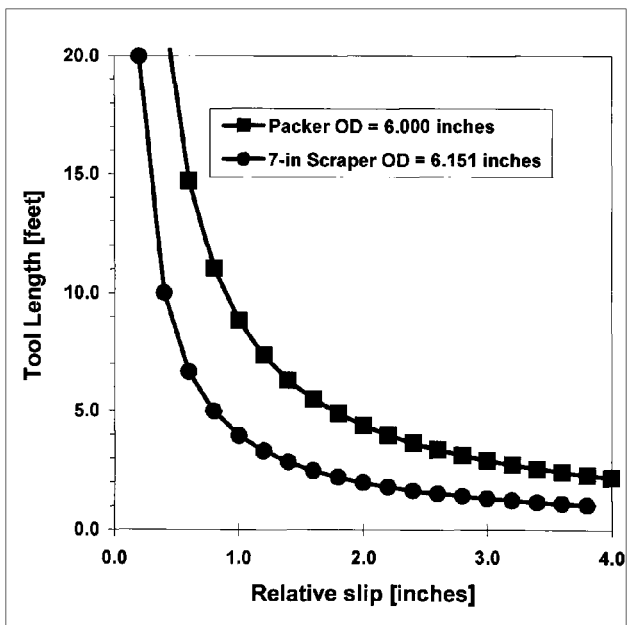


Figure 11.20 Passable tool length as a function of casing lateral damage.

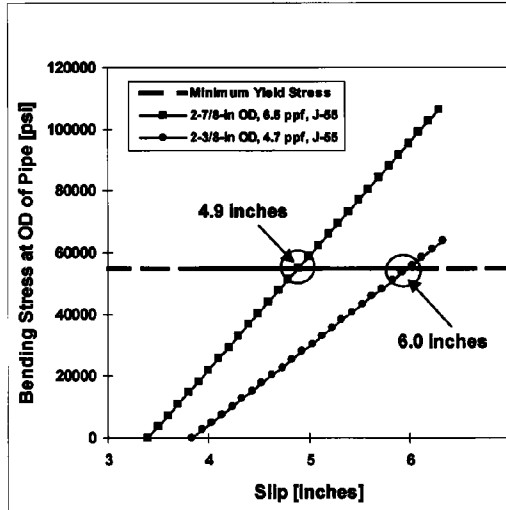


Figure 11.21 Bending stress that produces permanent bending in two sizes of tubing.

Acknowledgements

This chapter is based on the article “Field scale and wellbore modeling of compaction-induced casing failures,” which appeared in the June 1999 edition of the journal *SPE Drilling and Completion*. The author acknowledges the contributions of the co-authors of the original publication, Robert L.Gwinn and Tom A.Moroney of Aera Energy, LLC, and Greg L.Deitrick of Shell International Exploration & Production, Inc. The author also wishes to thank the management of Exponent Failure Analysis Associates, Inc., Aera Energy, LLC, and Shell E&P Technology Company for their permission to publish these results.

References

- 1 Jaeger, J.C. and Cook, N.G.W., *Fundamentals of Rock Mechanics*, 3rd Edition, Chapman and Hall, New York, 1979.
- 2 Cook, N.G.W., The Jaeger Memorial Lecture: Natural Joints in Rock, *Int. J. Rock Mech. Sci. & Geomech. Abstr.*, **29**, 198–223, 1992.
- 3 Rudnicki, J.W., “Effect of pore fluid diffusion on deformation and failure of rock,” *Mechanics of Geomaterials*, Bazant, Z. (ed.), John Wiley, 1985.

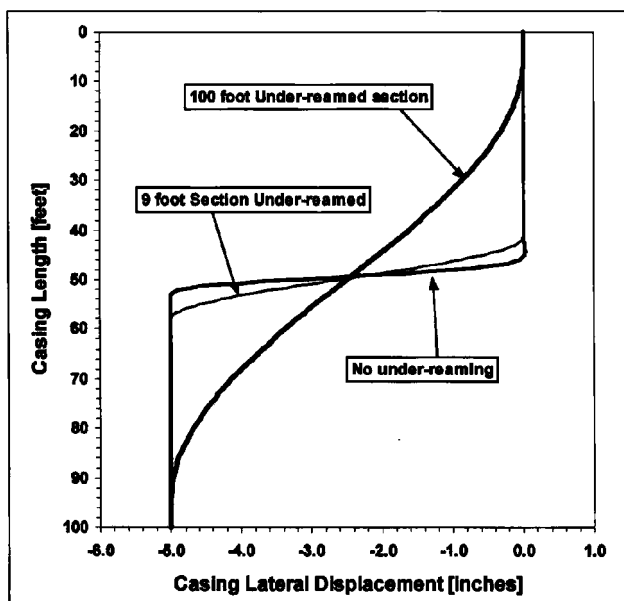


Figure 11.22 Casing length plotted against lateral displacement.

- 4 Geological Society of America (GSA), *Man-Induced Land Subsidence*, Holzer, T.L. (ed.), Inc., Boulder, CO, 1984.
- 5 Association of Engineering Geologists (AEG), *Land Subsidence Case Studies and Current Research: Proceedings of the Dr. Joseph F. Poland Symposium on Land Subsidence*, Special Publication No. 8, Borchers, J.W. (ed.), Star Publishing, Belmont, CA, 1998.
- 6 Geertsma, J., "Land subsidence above compacting oil and gas reservoirs," *Journal of Petroleum Technology*, June, 1973.
- 7 Martin, J.C. and Serdengecti, S., "Subsidence over oil and gas fields," *Man-Induced Land Subsidence*, Holzer, T.L. (ed.), Geological Society of America, Boulder, CO, 1984.
- 8 Holzer, T.L., "Ground failure induced by ground-water withdrawal from unconsolidated sediments," in *Man-Induced Land Subsidence*, Holzer, T.L. (ed.), Geological Society of America, Boulder, CO, 1984.
- 9 Narasimhan, T.N. and Goyal, K.P., "Subsidence due to geothermal fluid withdrawal," *Man-Induced Land Subsidence*, Holzer, T.L. (ed.), Geological Society of America, Boulder, CO, 1984.
- 10 Association of Engineering Geologists (AEG), *Proceedings: Mine Subsidence and Control*, Star Publishing, Belmont, CA, 1990.
- 11 American Society of Civil Engineers (ASCE), "Mine induced subsidence: Effects on engineered structures," *Geotechnical Special Publication No. 19*, Siriwardane, H.J. (ed.), American Society of Civil Engineers, New York, 1988.
- 12 Rodriguez, L.B. and Ruelas, S.A., "Ground settlements from the excavation of tunnels in soft clay," *Soft-Ground Tunneling: Failures and Displacements*,

- Reséndiz, D. and Romo, M.P. (eds), A.A. Balkema, Rotterdam, Netherlands, pp. 57–64, 1981.
- 13 Snyder, R.E. and McCabe, C.R., “Ekofisk jack-up: the story behind the story,” *Ocean Ind.*, **23**, 1, 1988.
- 14 Johnson, J.P., Rhett, D.W., and Siemers, W.T., “Rock mechanics of the Ekofisk reservoir in the evaluation of subsidence,” *Journal of Petroleum Technology*, **41**, pp. 717–722, 1989.
- 15 Rhett, D.W., “Ekofisk revisited: A new model of Ekofisk reservoir geomechanical behavior,” SPE/ISRM Paper No. 47273, *Proceedings of the SPE/ISRM Rock Mechanics in Petroleum Engineering*, Trondheim, Norway, pp. 367–376, July 8–10, 1998.
- 16 Teufel, L.W., Rhett, D.W., and Farrell, H.E., “Effect of reservoir depletion and pore pressure drawdown on in situ stress and deformation in the Ekofisk field, North Sea,” *Proceedings of the 32nd U.S. Symposium on Rock Mechanics*, Roegiers, J.C. (ed.), A.A.Balkema, Rotterdam, July 10–12, 1991.
- 17 Boade, R.R., Chin, L.Y., and Siemers, W.T., “Forecasting of Ekofisk reservoir compaction and subsidence by numerical simulation,” OTC Paper No. 5622, *Proceedings of the 20th Annual OTC*, Houston, TX, pp. 51–62, May 2–5, 1988.
- 18 Schwall, G.H., Slack, M.W., and Kaiser, T.M.V., “Reservoir compaction well design for the Ekofisk field,” SPE Paper No. 36621, *Proceedings of the 1996 SPE Annual Conference and Exhibition*, Denver, CO, October 6–9, 1996.
- 19 Bickley, M.C., and Curry, W.E., “Designing wells for subsidence in the greater Ekofisk area,” SPE 24966, *Proceedings of the 1992 SPE European Petroleum Conference*, Cannes, France, 1992.
- 20 Yudkovich, A., Chin, L.Y., and Morgan, D.R., “Casing deformation at Ekofisk,” *Journal of Petroleum Technology*, **41**, 7, pp. 729–734, 1989.
- 21 De Silva, F.V., Debande, G.F., Pereira, C.A., and Plischka, B., “Casing collapse analysis associated with reservoir compaction and overburden subsidence,” SPE Paper No. 20953, *Proceedings of Europec 90*, The Hague, Netherlands, pp. 127–133, October 23–24, 1990.
- 22 Kenter, C.J., Blanton, T.L., Schreppers, G.M.A., Baaijens, M.N., and Ramos, G.G., “Compaction study for the Shearwater Field,” SPE/ISRM Paper No. 47280, *Proceedings of the SPE/ISRM Rock Mechanics in Petroleum Engineering*, Trondheim, Norway, pp. 63–68, July 8–10, 1998.
- 23 Patillo, P.D., Kristiansen, Sund, G.V., and Kjelstadli, R.M., “Reservoir compaction and seafloor subsidence at Valhall,” SPE/ISRM Paper No. 47274, *Proceedings of the SPE/ISRM Rock Mechanics in Petroleum Engineering*, Trondheim, Norway, pp. 377–386, July 8–10, 1998.
- 24 Frame, R.G., “Earthquake damage, its cause and prevention in the Wilmington oil field,” *Annual Report, California Dept. Natural Resources, Div. Oil & Gas*, San Francisco, CA, **38**, No. 1, 1952, p. 5.
- 25 Mayuga, M.N. and Alien, D.R., “Subsidence in the Wilmington oil field, Long Beach, California, U.S.A.,” *Proceedings of the Tokyo Symposium: International Association of Scientific Hydrology*, IASH-Unesco-WMO, Pub. No. 88, Vol. 1, 1969, pp. 66–79.
- 26 Kosloff, D., Scott, R.F., and Scranton, J., “Finite element simulation of Wilmington oil field subsidence: I. Linear modelling,” *Tectonophysics*, **65**, 1980, pp. 339–368.

- 27 Kosloff, D., Scott, R.F., and Scranton, J., "Finite element simulation of Wilmington oil field subsidence: II. Nonlinear modelling," *Tectonophysics*, **70**, 1980, pp. 159–183.
- 28 Hamilton, J.M., Maller, A.V., and Prins, M.D., "Subsidence-induced shear failures above oil and gas reservoirs," *Proc. 33rd U.S. Symposium on Rock Mechanics*, Tillerson and Wawersik (eds), Santa Fe, NM, 1992, pp. 273–282.
- 29 Strickland, F.G., "Reasons for production decline in the diatomite, Belridge oil field: a rock mechanics review," *Journal of Petroleum Technology*, **37**, 1985, pp. 521–526.
- 30 Chase, C.A., Jr., and Dietrich, J.K., "Compaction within the South Belridge diatomite," *SPE Reservoir Engineering*, 1989, pp. 422–428
- 31 Bowersox, J.R. and Shore, R.A., "Reservoir compaction of the Belridge diatomite and surface subsidence, South Belridge field, Kern County, California," *Structure, Stratigraphy and Hydrocarbon Occurrences of the San Joaquin Basin, California*, Kuespert and Reid (eds), Pacific Sections of SEPM and AAPG, 1990, p. 225.
- 32 de Rouffignac, E.P., Bonder, P.L., Karanikas, J.M., and Kara, S.K., "Subsidence and well failure in the South Belridge diatomite field," SPE No. 29626, *Proceedings 1995 SPE Western Regional Meeting*, Bakersfield, CA, 1995.
- 33 *Oil and Gas Journal*, "South Belridge 15th billion barrel oil field in U.S.," Oct. 1995, p. 119.
- 34 Bruno, M.S. and Bovberg, C.A., "Reservoir compaction and surface subsidence above the Lost Hills field, California," *Proc. 33rd U.S. Symposium on Rock Mechanics*, Tillerson and Wawersik (eds), Santa Fe, NM, 1992, pp. 263–272.
- 35 Bruno, M.S., "Subsidence-induced well failure," *SPE Drilling and Completion (SPEDE)*, 1992, pp. 148.
- 36 The Institution of Structural Engineers, *Subsidence of low rise buildings*, SETO, London, England, 1994.
- 37 Hilbert, L.B., Gwinn, R.L., Moroney, T.A., and Detrick, G.L., "Field-scale and wellbore modeling of compaction-induced casing failures", *SPE Drilling and Completion*, **14**, 1999.
- 38 Hilbert, L.B., Jr., Fredrich, J.T., Bruno, M.S., Detrick, G.L., and de Rouffignac, E.P., "Two-dimensional nonlinear finite element analysis of well damage due to reservoir compaction, well-to-well interactions, and localization on weak layers," *Proc. 2nd North American Rock Mechanics Symposium*, Montreal, PQ, Canada, 1996.
- 39 Fredrich, J.T., Detrick, G.L., Argüello, J.G. and de Rouffignac, "Reservoir compaction, surface subsidence, and casing damage: A geomechanics approach to mitigation and reservoir management," SPE 47284, *Proceedings of the SPE/ISRM Rock Mechanics in Petroleum Engineering Conference*, Trondheim, Norway, July 8–10, 1998.
- 40 Fredrich, J.T., Argüello, J.G., Thorne, B.J., Wawersik, W.R., Detrick, G.L., de Rouffignac, Myer, L.R., and Bruno, M.S., "Three-dimensional geomechanical simulation of reservoir compaction and implications for well failures in the Belridge diatomite," SPE 36698, *Proceedings of the 1996 SPE Annual Technical Conference and Exhibition*, Denver, CO, Oct. 6–9, 1996.
- 41 Roberts, D.L., "Shear prevention in the Wilmington field," *Drilling and Production Practices*, API, 1953, pp. 146–155.

- 42 Dale, B.A., Narahera, G.M., and Stevens, R.M., "A case history of reservoir subsidence and wellbore damage management in the South Belridge field," SPE 36658, *Proceedings of the 1996 Western Regional Meeting*, Anchorage, AK, May 22–24, 1996.
- 43 Clegg, J.D., "Casing failure study—Cedar Creek anticline," *Journal of Petroleum Technology*, 1971, pp. 676–684.
- 44 McCauley, T.V., "Planning workovers in wells with fault-damaged casing—South Pass Block 27 Field," *Journal of Petroleum Technology*, 1974, pp. 739–745.
- 45 Cernocky, E.P. and Scholibo, F.C., "Approach to casing design for servicing compacting reservoirs," *Proc SPE Ann Technical Conference and Exhibition*, 1995, p. 731.
- 46 Cheatham, J.B. and McEver, J.W., "Behavior of casing subjected to salt loading," *Journal of Petroleum Technology*, 1964, pp. 1069–1075.
- 47 Hirshberg, A.J., Moyer, M.C., and Rickenbach, R.M., "Surface casing strain capacity for north slope operations," *SPE Drilling Engineering*, 1988.
- 48 Smith, M.B. and Patillo, P.D., "A finite element analysis of collapse of perforated casing," *Transactions of the ASME*, **105**, 1983, pp. 234–240.
- 49 Patillo, P.D. and Smith, M.B., "The effect of formation flow on the integrity of perforated casing," *Society Of Petroleum Engineers Journal*, 1985, pp. 637–646.
- 50 Bradley, D.A. and Chia, Y.-P., "Evaluation of reservoir compaction and its effects on casing behavior," SPE 14985, *Proceedings of the Deep Drilling and Production Symposium*, 1986, pp. 113–123.
- 51 Chia, Y.-P. and Bradley, D.A., "Effects of nonlinear reservoir compaction on casing behavior," SPE 15469, *Proceedings 61st SPE Annual Conference and Exhibition*, 1986, pp. 1–8.
- 52 Wooley, G.R. and Prachner, W., "Reservoir compaction loads on casing and liners," *SPE Production Engineering*, 1988, pp. 96–102.
- 53 Dusseault, M.B., Bruno, M.S., and Barrera, J., "Casing shear: causes, cases, cures," *SPE Drilling & Completion*, 2001, pp. 98–107.
- 54 Morita, N. and McLeod, H.O., "Oriented perforations to prevent casing collapse for highly inclined wells," SPE 28556, *Proceedings 69th SPE Annual Conference and Exhibition*, 1994, pp. 427–437.
- 55 Hibbitt, Karlsson and Sorensen, Inc., *ABAQUS Theory Manual*, version 5.8, Pawtucket, RI, 1998.
- 56 Borja, R.I. and Alarcón, E., "A mathematical formulation for finite strain elastoplastic consolidation. Part I: Balance laws, variational formulation, and linearization", *Comput. Methods Appl. Mech. Engrg.*, **20**, 1995, pp. 145.
- 57 Lewis, R.W. and Schrefler, B.A., *The Finite Element Method in the Deformation of Porous Media*, John Wiley, Chichester, UK, 1987.
- 58 Truesdell, C. and Toupin, R., "The classical field theories", *Handbuch der Physik III(1)*, S.Flügge (ed.), Springer Verlag, Berlin, 1960.
- 59 Truesdell, C. and Noll, W., "The nonlinear field theories of mechanics", *Handbuch der Physik III(3)*, S.Flügge (ed.), Springer Verlag, Berlin, 1965.
- 60 Terzaghi, K., Die Berechnung der Durchlässigkeitsziffer des Tonen aus dem Verlauf der hydrodynamischen Spannungserrechnungen. Akademie der Wissenschaften in Wien, Sitzungsberichte, Mathematisch-naturwissenschaftliche Klasse, Part IIA, **132**, 1923, p. 124.

- 61 Nur, A. and Byerlee, J.D., "An exact effective stress law for elastic deformation of rock with fluids," *J. Geophys. Res.*, **76**, 1971, p. 6414.
- 62 Zimmerman, R.W., Somerton, W.H., and King, M.S., "Compressibility of porous rocks," *J. Geophys. Res.*, **91**, 1986, p. 12, 765.
- 63 Biot, M.A., "General theory of three-dimensional consolidation," *J. Appl. Phys.*, **12**, 1941, p. 155.
- 64 Biot, M.A., "Theory of elasticity and consolidation of a porous anisotropic solid," *J. Appl. Phys.*, **26**, 1955, p. 182.
- 65 Biot, M.A., "General solutions of the equations of elasticity and consolidation for a porous material," *J. Appl. Mech.*, **78**, 1956, p. 91.
- 66 Niot, M.A., "Theory of deformation of porous viscoelastic anisotropic solid," *J. Appl. Phys.*, No. 5, 27, 1956, pp. 459–467.
- 67 Biot, M.A. and Willis, D.G., "The elastic coefficients of the theory of consolidation," *J. Appl. Mech.*, **24**, 1957, p. 594.
- 68 Rice, J.R. and Cleary, M.P., "Some basic stress diffusion solutions for fluid-saturated elastic porous media with compressible constituents," *Rev. Geophys. Space Phys.*, 14, p. 227.
- 69 Oden, J.T.R., *Finite Elements of Nonlinear Continua*, McGraw-Hill, New York, 1972.
- 70 Marsden, I.E. and Hughes, T.J.R., *Mathematical Foundations of Elasticity*, Dover Publications, Mineola, NY, 1983.
- 71 Green, D.H. and Wang, H.F., "Fluid pressure response to undrained compression in saturated sedimentary rock," *Geophyscis*, **51**, 4, 1986, pp. 948–956.
- 72 Geertsma, J., "The effect of fluid pressure decline on volumetric changes in porous rocks," *Petroleum Transactions of the AIME*, **210**, 1957, pp. 331–340.
- 73 Skempton, A.W., "The pore pressure coefficients A and B," *Geotechnique*, **4**, 1954, pp. 143–147.
- 74 Ostermeier, R.M., "Compaction effects on porosity and permeability: Deepwater Gulf of Mexico turbidites," *Journal of Petroleum Technology*, 2001, pp. 68–74.
- 75 Martin, J.C. and Serdengecti, S., "Subsidence over oil and gas fields", in *Reviews in Engineering Geology, Volume VI, Man-Induced Land Subsidence*, T.L.Holzer (ed.), Geological Society of America, Boulder, CO, 1984, pp. 23–34.
- 76 Atkinson, B.K. (ed.), *Fracture Mechanics of Rock*, Academic Press, San Diego, CA, 1987.
- 77 Terzaghi, K., Peck, R.B., and Mesri, G., *Soil Mechanics in Engineering Practice*, John Wiley, New York, 1996.
- 78 Wong, T.F., Szeto, H., and Zhang, J. (1992), "Effect of loading path and porosity on the failure mode of porous rocks," *Applied Mechanics Reviews*, **45**, 8, pp. 281–293.
- 79 Jones, M.E. and Leddra, M.J., "Compaction and flow of porous rocks at great depth," *Rock at Great Depth*, Maury and Fourmaintraux (eds), Balkema, Rotterdam, 1989, p. 891.
- 80 Yale, D.P. and Crawford, B., "Plasticity and Permeability in carbonate: dependence on stress path and porosity," *SPE/ISRM 47852, Proceedings SPE/ISRM Eurock '98*, 1998, p. 485.
- 81 DiMaggio, F.L. and Sandler, I., "Material model for granular soils," *Journal of the Engineering Mechanics Division*, ASCE, **97**, EMS, 1971, pp. 935–950.

- 82 Simo, J.C., Ju, J.W., Pister, K.S., and Taylor, R.L., "An assessment of the cap model: Consistent return algorithms and rate-dependent extension," Report No. UCB/SESM-85-05, Department of Civil Engineering, University of California at Berkeley, May 1985.
- 83 Hibbit, Karlsson and Sorensen, Inc., *ABAQUS/Standard User's Manual*, Pawtucket, RI, 2001.
- 85 Cernocky, E.P., Paslay, P.R., and Scholibo, F.C., "Approach to fitting the stress-strain behavior of highly stressed unconsolidated sands with the modified *Drucker-Prager* cap model," *Proceedings of the 7th ABAQUS User's Conference*, Hibbit, Karlsson and Sorensen, Pawtucket, RI, 1994, pp. 155-165.
- 86 Yale, D.P., Lyons, L.L., and Qin, G. "Coupled geomechanics-fluid flow modeling in petroleum reservoirs: coupled versus uncoupled response," *Proceedings of the 4th North American Rock Mechanics Symposium*, Balkema, Rotterdam, 2000, pp. 137-146.
- 87 Gutierrez, M. and Hansteen, H., "Fully-coupled analysis of reservoir compaction and subsidence," SPE 28900, *Proceedings EUROPEC '94*, 1994, pp. 339-347.
- 88 Koutsabeloulis, N.C. and Hope, S.A., "Coupled stress/fluid/thermal multi-phase reservoir simulation studies incorporating rock mechanics," SPE/ISRM 47393, *Proceedings Eurock '98*, Trondheim, Norway, 1998, pp. 449-545.
- 89 Yale, D.P., Nabor, G.W., Russell, J.A., Pham, H.D., and Yousef, M., "Application of variable formation compressibility for improved reservoir analysis," SPE 26647, *Proceedings of the 68th Annual SPE Technical Conference and Exhibition*, Houston, TX, 1993, pp. 435-450.
- 90 Scholz, C.H., *The Mechanics of Earthquake Faults and Fractures*, Cambridge University Press, New York, 1990.
- 91 Hubbert, M.K. and Willis, D.G., "Mechanics of hydraulic fracturing," *Transactions of the AIME*, **210**, 1957, pp. 153-166.
- 92 Zoback, M.D., Moos, D., and Mastin, L., "Wellbore breakouts and in situ stress," *Journal of Geophysical Research*, **90**, 1985, pp. 5523-5530.
- 93 Bowersox, J.R., "Geology of the Belridge diatomite, northern South Belridge field, Kern County, California," *Structure, Stratigraphy and Hydrocarbon Occurrences of the San Joaquin Basin, California*, Kuespert and Reid (eds), Pacific Sections of SEPM and AAPG, 1990, p. 215.
- 94 Strubhar, M.K., Medlin, L.W., Nabi, S.M., and Andreani, F.S., "Fracturing results in the diatomaceous earth formations, South Belridge field, California," *Journal of Petroleum Technology*, 1984, pp. 495-502.
- 95 Hansen, H.K., Prats, M., and Chan, C.K., "Finite-element modeling of depletion-induced reservoir compaction and surface subsidence in the South Belridge oil field, California," SPE 26074, paper presented at the 1993 Western Regional Meeting, Anchorage, AK, May 26-28.
- 96 *Steel Construction Manual of Allowable Stress Design*, 9th Edition, American Institute of Steel Construction, Chicago, IL.

Index

- abstract 1, 101, 165, 197, 254
- accelerograms 225
- acknowledgements 57, 98, 162, 195, 274, 313, 361
- activity rates 225
- air flow 26, 31, 44
- air loss prediction 31
- air losses 26, 36
- air pressure 47
- analysis 240, 300
- analysis methods 227
- anisotropic soil behaviour 86
- apparatus 46
- application(s) 64, 66, 84, 237, 244, 300
- area selection 238
- attenuation relationships 225
- axial load distribution 293

- back analysis 165, 166, 169, 174, 177, 185, 202
- background 198
- basic soil characteristics 88
- Bayesian method 197, 198, 199
- Bedfordshire 149
- bent tubing 358
- BESOIL program 232
- boundary conditions 33
- boundary value problem 60
- brickwork wall 157
- buildings 133
- buried gas main 158

- caisson 94
- caisson geometry 94
- caisson interaction 83

- calibration 145, 151
- camouflet, depths of zones 13
- camouflet deflection model 8
- camouflet determination 11
- camouflet finite element program 10
- camouflet material requirements 6
- camouflet numerical model 8
- camouflet numerical results 15
- camouflet size 6
- camouflet void 13
- case histories 263
- case study 39, 210
- casing damage 322, 340
- casing failure 340
- Catania 263
- Cesi village 244
- characteristics 237
- Chebyshev spectral element method 254
- cohesionless soil 288
- cohesive soil 287
- Colfiorito village 245
- compaction 317, 319
- comparison with field test data 302, 304, 308
- compressed air 28
- compressed air tunnelling 25
- computational modelling 129
- computational procedure 150
- computational results 347
- concluding remarks 218
- conclusion 21, 56, 94, 161, 194, 273
- constitutive model 332
- constitutive model input data 335
- constitutive theories 330
- contours 84
- coupling 337

- cover layer 75
- cross anisotropic soil behaviour 86
- current study 134

- data 240
- data preparation 206
- deficiencies in compressed air tunnelling 28
- deflection model 8
- design analysis 300
- designing for compressed air 28
- direct solution technique 167
- discretisation 257, 258
- discussion 15, 52
- displacements 204
- driving model 145

- earthquake catalogue 223
- effective stress 325
- elastic back analysis 166, 177
- elastic-plastic constitutive model 332
- elasto-plastic calculations 180
- element verification 136
- equations 33
- equations of motion 255
- evaluation 193, 206
- example computation 341
- experimental study 25
- extended Bayesian method 197, 199

- feedback system 202
- field operational history 346
- field test data 302, 304, 308
- field-scale model 343, 347
- final remarks 312
- finite element discretization 328
- finite element model 59, 63, 135
- finite element program 10
- finite soil layer 286
- Flintwick 149, 152
- fluid-filled rock 330
- formulation 199
- framework 202
- free surface ground motion 270

- gas main 158
- general loading conditions 296

- genetic algorithm 38
- geologic data 240
- geologic overview 238
- geometry 71
- geomorphologic overview 238
- geostatic field 339
- geotechnic data 240
- geotechnical problems 165
- GFEM-WSSI 63, 66, 84
- governing equations 33, 326
- granular deposit 174
- ground 26
- ground condition 211
- ground motion modelling 254
- ground shaking 263
- ground to air permeability 27
- ground wave applications 155
- ground wave modelling 155
- ground waves 129
- group shadowing effect 288

- hammers 132, 133
- hazard analysis 221
- historical perspectives 319
- historical well failures 342
- humans 133

- identification 225
- impact driving 145, 149
- impact driving model 145
- impact hammers 129, 141
- implementation 260
- increasing air pressure 47
- increasing suction 50
- infinite element models 135
- infinite elements 137
- initial geostatic field 339
- input data requirements 335
- introduction 1, 25, 102, 129, 165, 197, 220, 254, 278, 316
- inverse method 166
- issues 260
- Italy 263

- laboratory tests 45
- lateral load distribution 295
- limiting pile-soil stresses 287

- linear constitutive theory 330
- linear momentum balance 324
- linearization of variational forms 328
- load distribution 284, 293, 295
- loading conditions 296

- M66 145
- mass balance 326
- massive structure 270
- material requirements 6
- mathematical formulation 255
- measured displacements 204
- measurement 212
- mechanics of porous media 323
- method demonstration 263
- mitigation of well damage 359
- model identification 198, 214
- model parameters 214
- model parameters 201, 202
- modelling 26, 129, 254
- modelling casing damage 340
- modelling failure 340
- modelling rock discontinuities 339
- models 228, 232
- momentum balance 324
- multi-layer soil profiles 286

- non-linear constitutive model 332
- non-linear soil behaviour 289
- North London railway viaduct 300
- numerical analysis 42
- numerical comparison 42
- numerical method 202, 278
- numerical model 31, 32
- numerical modelling 26, 220
- numerical procedure 64
- numerical results 15, 290
- numerical solution 34
- numerical study 25

- objectives 134
- one-dimensional model 228

- parameter estimation 197, 208, 216
- parameter identification 36
- perimeter walls 36
- permanently bent tubing 358

- permeability 27
- petroleum industry 317
- PGROUPN 285
- PGROUPN method of analysis 285
- physical domain 257
- pile domain 287
- pile driving 129
- pile group analysis 278
- pile group settlement 293
- pile group(s) 278, 284, 296
- pile-soil stresses 287
- pipe geometry 71
- pipe interaction 65
- plane brickwork wall 157
- pore pressure 337
- pore pressure distribution 84
- pore-air pressure control 47
- pore-water pressure control 46
- porous media 323
- portal frame 155
- practical application 248
- pressure control 46, 47
- probabilistic back analysis 169
- problem formulation 38
- proposed scheme 206

- QUAD4M program 235

- railway viaduct 300
- recent developments 262
- rectangular steel portal frame 155
- references 22, 57, 98, 162, 195, 218, 251, 275, 313, 361
- reservoir compaction 316, 317
- reservoir geology 341
- reservoir subsidence 316, 317
- response parameters 242
- response spectra 225
- results 52
- rock deformation 337
- rock discontinuities 339
- rock mass 185
- rubble mound 94

- saturated soil 50
- scale 321
- seabed interaction 59, 63, 65, 83

Second Severn crossing 152
 seismic input 221
 seismic microzoning 220
 seismic sequence 237
 seismic sources 222
 selection of model parameters 202, 214
 sensitivity 133
 sensitivity analysis 206
 settlement 293
 shadowing effect 288
 shear strength 26, 44,
 shear strength parameters 190
 shearing 340
 Sicily 263
 simulated field operational history 346
 single pile response 290
 soil 44, 50
 soil behaviour 86, 289
 soil characteristics 68, 88
 soil domain 286
 soil layer 286
 soil parameters 297
 soil profiles 286
 solution technique 167
 South Belridge field 341
 special hammers 133
 SPEM 255
 stage 141, 142, 144
 steel portal frame 155
 structure interaction 59, 63
 subsidence 317, 319
 suction 50
 surface ground motion 270
 surface subsidence 317
 system solution 287

 test series 47, 50
 testing procedure 47
 testing programme 46
 theoretical formulations 60
 theory 44
 tool length 357
 treatment of measured displacements 204
 tunnel 174, 185
 tunnel characteristics 174, 185
 tunnel face 31
 tunnel model 186

tunnel perimeter walls 36
 tunnelling 25, 197
 two-dimensional model 232, 254

Umbria-Marche earthquake 237
 uncertainty evaluation 201, 218
 unsaturated soils 44

variational forms 326, 328
 viaduct 300
 vibratory hammers 132
 vibrodriver model 151
 vibrodrivers 149
 vibrodriving 152
 viscosity coefficient 193
 viscous rock mass 185
 void 13

wall 36, 157
 wave equation 258
 wave interaction 59, 63, 65, 83
 waves 129
 well damage 316, 359
 well failures 342
 wellbore scale results 351

zone 13
 zone depths 13